



The 27th Conference of the Israel Nuclear Societies

February, 11-13, 2014, Daniel Dead Sea Hotel, Israel

Program

Oral Presentations Papers

Poster Presentations List and Papers

Organized by:





הכנס ה-27 של האגודות הגרעיניות בישראל 11-13 בפברואר 2014, מלון דניאל, ים המלח

The 27th Conference of the Israel Nuclear Societies
February, 11-13, 2014, Daniel Dead Sea Hotel, Israel

PROGRAM

TUESDAY, FEBRUARY 11, 2014

10:30-12:00 Arrival and Registration

12:00-13:00 Lunch

13:00-15:15 Plenary Session I

Halls BC

Chair: Uzi German

13:00

Opening Remarks

Yigal Ronen, *President, Israel Nuclear Societies and Conference Chair*
Gustavo Haquin, *President, Israel Society for Radiation Protection*

13:15

Health & Safety of the IAEC Employees

Shaul Chorev,
Head, Israel Atomic Energy Commission

13:45

Flexblue®: A Subsea SMR for Enhanced Safety and Competitivity

Geoffrey Haratyk (invited)
DCNS Group, France

14:15

The Impact of the Fukushima Accident on LWR Safety and the Nuclear Power Risks

Bal Raj Sehgal (invited)
Nuclear Power Safety, KTH, Royal Institute of Technology, Sweden

14:45

An Approach to Compensation for Radiation-linked Diseases - an Example from the Nuclear Industry in the UK

Richard Wakeford (invited)
Institute of Population Health, University of Manchester, UK

15:15-15:45 Coffee Break

15:45-17:30 Plenary Session II

Halls BC

Chair: Ilan Yaar

15:45

Latest development on the SA Strategy In-Vessel Retention (for Existing NPPs)

Jiri Zdarek (invited)
Chairman, Consortium JHR, Czech Republic

16:15

The European COST Network

Wouter Schroeyers,
Chair, COST Action NORM4BUILDING TU1301, Belgium

16:25

Panel: A Nuclear Power Plant in Israel: Challenges & Prospects

Eugene Shwageraus, Shlomo Wald, Yishai Levanon

17:30-21:00 Dinner (for hotel guests)

08:30-10:30, Arrival, Registration and Exhibition Visit

08:30-10:15 Plenary Session III

Halls BC

Chair: Gustavo Haquin

08:30

Current Challenges in Medical Radiation Protection

Madan Rehani (invited)
European Society of Radiology, Austria

09:00

Attribution and Nuclear Forensics: Science in Support of Law Enforcement & National Security

Michael Kristo (invited)
Lawrence Livermore National Lab, USA

09:30

Remedy for Radiation Fear — Discard the Politicized Science

Jerry Cuttler (invited)
Cuttler & Associates Inc, Mississauga, Ontario, Canada

10:00

A National Survey of Exposure to Power Frequency Magnetic Fields ("ORCHID")

Ronen Hareuveny¹, I. Eliyahu¹, Y. Yaffe¹, I. Ben David¹, M. Riven², S. Kandel², L. Kheifets³
¹*Soreq Nuclear Research Center, Yavne, Israel*
²*Independent Consultant, Israel*
³*UCLA, Los Angeles, California, USA*

10:15-11:30 Coffee Break and Poster Session I

11:30-13:00 Reactor Physics and Technology I

Hall B

Chair: Guy Makov

11:30

Theoretical Simulations of Materials for Nuclear Energy Applications

Igor A. Abrikosov^{1,2} (invited), Alena V. Ponomareva², Anton Yu. Nikonov³, Svetlana A. Barannikova^{3,4},
Andrey I. Dmitriev^{3,4}
¹*Linköping University, Sweden*
²*National University of Science and Technology MISIS, Russia*
³*Institute of Strength Physics and Materials Science, Siberian Branch of Russian Academy of Science, Russia*
⁴*Tomsk State University, Russia*

12:00

One-Group Cross Sections Generation for Monte Carlo Burnup Codes

Dan Kotlyar¹, Eugene Shwageraus², Emil Fridman³
¹*Nuclear Engineering, Ben Gurion University, Israel*
²*Department of Engineering, University of Cambridge, UK*
³*Helmholtz-Zentrum Dresden-Rossendorf, Germany*

12:15

Improving Conversion Ratio of PWR with Th-U233 Fuel Using Boiling Channels

Marat Margulis¹, Eugene Shwageraus²
¹*Energy Engineering, Ben Gurion University, Israel*
²*Nuclear Engineering, Ben Gurion University, Israel*

12:30

A Multi Region, Multi Energy Formalism for the Feynman-Alpha Formulas

Tal Malinovitch, Chen Dubi
Physics, Nuclear Research Center of the Negev, Israel

12:45

Fuel Management Optimization of Pebble-Bed Reactors Using Particle Swarm Algorithm

Barak Tavron¹, Eugene Shwageraus²
¹*Israel Electric Corporation, Haifa, Israel*
²*Nuclear Engineering, Ben-Gurion University, Israel*

Chair: Yair Shamai

11:30

Age Dating of Nuclear and Radiological Materials and its Role in Nuclear Forensics

Michael Kristo (invited)

N Program, Lawrence Livermore National Laboratory, USA

11:45

Experimental Dating of ^{252}Cf Sources

Michal Brandis, Ofer Aviv, Zohar Yungrais, David Hershkovich, Gustavo Haquin

Radiation Safety Division, Soreq NRC, Israel

12:00

Nuclear Analytical Methods and Nonproliferation Studies at the University of Texas at Austin

Steven Biegalski, Sheldon Landsberger, Erich Schneider, Kendra Foltz-Biegalski

Nuclear Engineering Teaching Lab, University of Texas, USA

12:15

A Liquid Xe Detector for Contraband Detection

Itamar Israelashvili^{1,4}, Marco Cortesi², David Vartsky¹, Doron Bar³, Amos Breskin¹

¹*The Weizmann Institute of Science, Israel*

²*Paul Scherrer Institut (PSI), Switzerland*

³*Soreq Nuclear Research Center (SOREQ NRC), Israel*

⁴*Nuclear Research Center of Negev (NRCN), Israel*

12:30

Ground Deposition Pattern of an Explosive Radiological Dispersal Device (RDD)

Avi Sharon, Itzhak Halevy, Daniel Sattinger, Zvi Berenstein, Rony Neuman, Moriel Pinhas, Pini Banaim, Ilan Yaar

NRCN, Israel

12:45

Atmospheric Transport Modeling of Radio-Xenon Detections Possibly Related to the Announced Nuclear Test in North Korea on February 12, 2013

Kobi Kutsher¹, Menachem Stern²

¹*Radiation Safety Division, Soreq-NRC, Israel*

²*Physics and Nuclear Engineering Division, Soreq-NRC, Israel*

Chair: Jean Koch

11:30

Fukushima Update and Current Status

Suzuki Toshikazu

Department of Nuclear Safety and Security, International Atomic Energy Agency, Austria

11:45

Production of DNA Double Strand Breaks in Human Cells due to Acute Exposure to Tritiated Water (HTO)

Raphael Gonen¹, Uzi German¹, Zeev Alfassi², Ester Priel²

¹*Radiotoxicology, Nuclear Research Center, Negev, Israel*

²*Immunology and Nuclear Engineering, Ben Gurion University, Israel*

12:00

The Treatment of Uncertainty in Compensation Schemes for Cancer Based on the Probability of Causation Methodology

Jean Koch

Radiation Safety Division, Soreq Nuclear Research Center, Israel

12:15

Development of a Method to Assess the Radiation Dose due to Internal Exposure to Short-lived Radioactive Materials

David Benmaman¹, Jean Koch¹, Joseph Ribak²

¹*Radiation Safety Division, Soreq Nuclear Research, Israel*

²*School of Public Health, Tel-Aviv University, Israel*

12:30

A Combined Shielding Design for a Neutron Generator and a Linear Accelerator at Soreq NRC

Lior Epstein

Soreq Nuclear Research Center, Israel

12:45

Shielding Calculations for Industrial 5/7.5MeV Electron Accelerators Using the MCNP Monte Carlo Code

13:00-14:00 Lunch

14:00-15:30 Reactor Physics and Technology II (In memory of Dr. Uri Mintzer)

Hall B

Chair: Eugene Shwageraus

14:00

Nuclear Licensing and Safety Office (NLSO) regulatory practices of IAEC Research Reactors

Yacov Barnea¹, Uri Mintzer (Deceased)¹, Hanoch Hirshfeld¹, Meir Markovits²

¹*RRS/NLSO, IAEC, Israel*

²*NLSO, IAEC, Israel*

14:30

Zirconium Ignition in an Exposed Fuel Channel

Yuri Nekhamkin, Dov Hasan, Ezra Elias

Mechanical Engineering, Technion, Israel

14:45

Extending Two-Phase Capabilities of Thermal-Hydraulic Module in BGCORE

Marat Margulis¹, Eugene Shwageraus²

¹*Ben Gurion's Center for Global Engineering, Israel*

²*Nuclear Engineering, Ben Gurion University, Israel*

15:00

An In-Pile Kinetic Method for Determining the Delayed Neutron Fraction β_{eff}

Erez Gilad¹, Oleg Rivin¹, Hanania Ettetdgui¹, Ilan Yaar¹, Benoit Geslot², Alessandro Pepino², Jacques Di-Salvo², Adrien Gruel², Patrick Blaise²

¹*Nuclear Research Center NEGEV (NRCN), Israel*

²*DEN/CAD/DER/SPEX/LPE, CEA, France*

15:15

Protective Alternatives of SMR against Extreme Threat Scenario – A Preliminary Risk Analysis

Igal M. Shohet¹, David Ornai^{1,2}, Erez Gal¹, Yigal Ronen³, Mijal Vidra¹

¹*Department of Structural Engineering, Faculty of Engineering Sciences, Ben-Gurion University of the Negev, Israel*

²*Protective Technologies Research & Development Center, Ben-Gurion University of the Negev, Israel*

³*Department of Nuclear Engineering, Faculty of Engineering Sciences, Ben-Gurion University, Israel*

14:00-15:30 Radiological Risk Assessment

Hall C

Chair: Ilan Yaar

14:00

Legal and Political Obstacles and Opportunities for Successful Nuclear Projects

Moshe Yanovskiy

Institutional Development, Gaidar Institute for Economic Policy, Russia

14:15

Inclusion of Premeditated Threats in the Safety Methodology for NPPs

Ishay Levanon

Ishay Levanon Consulting Ltd., Israel

14:30

Protecting National Critical Infrastructure against Radiological Threat

Ilan Yaar¹, Itzhak Halevy², Zvi Berenstein², Avi Sharon²

¹*Chief Scientist Office, Ministry of National Infrastructures, Energy and Water Resources, Israel*

²*Nuclear Research Center Negev (NRCN), Israel*

14:45

Development of a Risk-Based Decision-Support-Model for Protecting an Urban Medical Center from a Nuclear Explosion

Gabi Ben-Dor^{2,3}, Igal M Shohet¹, David Ornai^{1,3}, Benny Brosh¹

¹*Structural Engineering, Ben-Gurion University of the Negev, Israel*

²*Mechanical Engineering, Ben-Gurion University of the Negev, Israel*

³*Protective Technologies Research & Development Center, Ben-Gurion University of the Negev, Israel*

15:00

Time Dependent Radio-toxicology of Fission Products

Menachem Stern, Asher Baram, Shlomo Pistinner

Nuclear Physics & Engineering, Soreq NRC, Israel

15:15

Fast Multispectral Fireball Analyses and the Relation to Particles' Aerosolization

Avi Sharon, Itzhak Halevy, Daniel Sattinger, Zvi Berenstein, Rony Neuman, Moriel Pinhas, Pini Banaim, Ilan Yaar
NRCN, Israel

15:30-16:30 Coffee Break and Posters Session II

16:30-18:00 Dosimetry

Hall B

Chair: Uzi German

16:30

Automation at NRCN Dosimetry Laboratory

Adi Abraham¹, Israel Arad², Menachem Mesing¹, Shmuel Levinson¹, Marcelo Weinstein¹, Omer Pelled¹, Amir Broida¹, Uzi German¹

¹*Nuclear Research Centre Negev, Israel*

²*Rotem Israel Arad Ltd, Israel*

16:45

About Background Correction for LiF:Mg,Ti Readout

Tova Yifrah^{1,2}, Adi Abraham¹, Marcelo Weinstein¹, Omer Pelled¹, Uzi German¹, Moshe Mintz^{1,2}

¹*Nuclear Research Centre Negev, Israel*

²*Ben-Gurion University of the Negev, Israel*

17:00

The Enigma of Linear/Supralinear Thermoluminescence Dose Response Mixed Localized/Delocalized Recombination describes a solution

Ilan Eliyahu^{1,2}, Yigal Horowitz¹, Leonid Oster³, Israel Mardor²

¹*Ben Gurion University of the Negev, Israel*

²*Soreq Nuclear Research Center, Israel*

³*Sami Shamoon College of Engineering, Israel*

17:15

Characterization of Soreq Whole Body Counter

Ofer Aviv, Erez Daniely, Sharon Moskovici, Zohar Yungrais, Hanan Datz, Yair Shamai, Gustavo Haquin
Soreq NRC, Israel

17:30

Comparison Study of the Response of Several Passive PDA Based Personal Dosimeters to Gamma and X-Ray Radiation

Shai Cohen¹, Adi Abraham¹, Omer Pelled¹, Yair Tubul¹, Esti Kresner², Asaf Ashkenazi³, Ilan Yaar¹

¹*Nuclear Research Center-Negev, Israel*

²*Chief Scientist for CBRN Defense, Ministry of Defense, Israel*

³*Asaf Ashkenazi Ltd, Israel*

17:45

Suitability of Israeli Household Salt for Retrospective Dosimetry

Hanan Datz¹, Sofia Druzhyzna², Leonid Oster³, Itzhak Orion², Itzhack Darras², David Hershkovich¹, Yigal Horowitz⁴

¹*Radiation Safety Division, Soreq Nuclear Research Center, Israel*

²*Department of Nuclear Engineering, Ben-Gurion University of the Negev, Israel*

³*Physics Unit, Sami Shamoon College of Engineering, Israel*

⁴*Physics Department, Ben Gurion University of the Negev, Israel*

16:30-18:30 NORM & Environmental Radioactivity

Hall C

Chair: Konstantin Kovler

16:30

A New European COST Network 'NORM4Building' (TU1301) for the Reuse of NORM Containing Residues in Building Materials

Wouter Schroeyers, Sonja Schreurs

UHasselt, Diepenbeek, Limburg, Belgium

16:45

Usability of Clay Mixed Red Mud as Building Material in Transdanubian (Hungary) Region

Zoltan Sas, Janos Somlai, Jacint Jonas, Gabor Szeiler, Tibor Kovacs

Institute of Radiochemistry and Radioecology, University of Pannonia, Hungary

17:00

Air Change Rates and Radon Concentrations in Residential Protected Rooms

Rachel Becker¹, Konstantin Kovler¹, Gustavo Haquin²

¹Faculty of Civil & Environmental Engineering, National Building Research Institute, Technion, Israel

²Radiation Safety Division, Soreq Nuclear Research Center, Israel

17:15

Radiation Exposure to Concrete in Israel

Gustavo Haquin¹, Konstantin Kovler², Govert de With³, Zohar Yungrais¹, Nathan Lavi⁴

¹Radiation Safety Division, Soreq Nuclear Research Center, Yavne, Israel

²National Building Research Institute, Technion - Israel Institute of Technology, Israel

³Radiation & Environment Division, NRG, ES Arnhem, the Netherlands

⁴Department of Nuclear Engineering, Ben-Gurion University, Israel

17:30

Scintillation vs. Semiconductor Spectrometers for Determination of NORM in Building Materials

Konstantin Kovler¹, Shmuel Levinson², Nathan Lavi³, Uzi Gherman², Boris Dashevsky¹, Hisham Nassar⁴,

Sergey Antropov⁵

¹National Building Research Institute, Technion - Israel Institute of Technology, Israel

²Nuclear Research Center Negev, Israel

³Department of Nuclear Engineering, Ben-Gurion University, Israel

⁴Ministry of Environmental Protection, Israel

⁵"Amplituda" Research Center, Russia

17:45

Radioactive Waste in Oil Exploration

Sheldon Landsberger¹, Shauna Landsberger², Graham George²

¹Nuclear and Radiation Engineering, University of Texas, USA

²Enviroklean Product Development Inc., USA

18:00

A Detailed Gamma-ray Survey for Estimating the Radiogenic Power of Sardinian Variscan Crust

Merita Xhixha^{1,5}, Marica Baldoncini^{2,5}, GiamPietro Bezzon³, GiamPaolo Buso³, Luigi Carmignani⁴, Leonardo

Casini¹, Ivan Callegari⁴, Tommaso Colonna⁴, Stefano Cuccuru¹, Enrico Guastaldi⁴, Giovanni Fiorentini^{2,3,5},

Fabio Mantovani^{2,5}, Giovanni Massa⁴, Liliana Mou³, Giacomo Oggiano¹, Antonio Puccini¹, Carlos Rossi

Alvarez³, Virginia Strati^{2,5}, Gerti Xhixha^{2,3}, Alessandro Zanon³

¹Department of Natural and Land Sciences, University of Sassari, Italy

²Department of Physics and Earth Sciences, University of Ferrara, Italy

³Legnaro National Laboratory, Istituto Nazionale di Fisica Nucleare (INFN), Italy

⁴Center for GeoTechnologies (CGT), University of Siena, Italy

⁵Ferrara Section, Istituto Nazionale di Fisica Nucleare (INFN), Italy

18:15

Measurement of Tritium Activity in Plants by Ice Extraction Method

Omer Pelled, Shimon Ovad, Yair Tobol, Shimon Tsroya, Rafi Gonen, Adi Abraham, Marcelo Weinstein,

Uzi German

NRCN, Israel

17:30-21:00 Dinner (for hotel guests)

21:00-23:00 Happy Hour – Scottish Pub, Daniel hotel

THURSDAY, FEBRUARY 13, 2014

08:30-10:30 Arrival, Registration and Exhibition Visit

09:00-10:30 Reactor Physics and Technology III

Hall B

Chair: Erez Gilad

09:00

Damage Curves of a Nuclear Reactor Structure Exposed to Air Blast Loading

Irada Brandys^{1,2}, David Ornai^{2,3}, Yigal Ronen²

¹Nuclear Research Center Negev, Israel

²Faculty of Engineering Sciences, Ben-Gurion University of the Negev, Israel

³Protective Technologies Research & Development Center, Ben-Gurion University of the Negev, Israel

09:15

Numerical Simulation of a Single-Phase Closed-Loop Thermo-Syphon in LORELEI Test Device

Dima Gitelman¹, H. Shenha¹, Ch. Gonnier³, D. Tarabelli³, A. Sasson¹, Y. Weiss¹, M. Katz²

¹Mechanical Engineering, ROTEM Industries, Israel

²NRCN, P.O.Box 9001 Beer Sheva, 84190, Israel

09:30

Thermal Design of the LORELEI Test Device Using a COMSOL Inverse Solver

Hadas Shenha⁽¹⁾, D. Gitelman⁽¹⁾, I. Preker⁽¹⁾, M. Arbel-Haddad⁽²⁾, L. Ferry⁽³⁾, A. Sasson⁽¹⁾, Y. Weiss⁽¹⁾, M. Katz⁽²⁾

¹Mechanical Engineering, ROTEM Industries, Israel

²NRCN, P.O.Box 9001 Beer Sheva, 84190, Israel

³French Atomic Energy Commission (CEA) – Cadarache Centre, France

09:45

Concept of the LORELEI test device for LOCA experiment in the JHR reactor

Moti Santo¹, N. Moran¹, L. Ferry², A. Azulay¹, O. Mileguir¹, Y. Weiss¹

¹Mechanical Engineering, ROTEM Industries, Israel

²French Atomic Energy Commission (CEA) – Cadarache Centre, France

10:00

Numerical ballooning and burst prediction of fuel cladding during LOCA transients in LWR

Eran Landau¹, Y. Weiss², M. Szanto²

¹Ben Gurion University, P.O.B. 653 Beer-Sheva 8410501 Israel

² Mechanical Engineering, Ben-Gurion University, Israel

10:15

Preliminary I&C Design for LORELEI

Sami Korotkin¹, Yacov Kaufman¹, Erez Grosman¹, Betty Guttmann¹, Shahar Levy¹, David Amidan¹, Erez Beer¹, Benny Gdalyho¹, Tzahi Cahana¹, Amir Ellenbogen¹, Meir Arad¹, Yishay Weiss², Avner Sasson², Lionel Ferry³, Francois Bourrelly³, Yosef Cohen¹

¹NRCN POB 9001, Israel

²Rotem Industries Ltd, Israel

³CEA, Cadarache, DER/SRJH, France

09:00-10:30 Medical and Applied Physics

Hall C

Chair: Raquel Bar-Deroma

09:00

Biodistribution of 212Pb Conjugated Trastuzumab in Mice

Nate Schneider¹, Megan Lobaugh¹, Peter Sandwall¹, Samuel Glover¹, Maisha Murry¹, Zhongyun Dong², Henry Spitz¹

¹Nuclear & Radiological Engineering, University of Cincinnati, USA

²Division of Hematology-Oncology, University of Cincinnati Cancer Institute, USA

09:15

A Novel Drug Delivery System for Preventing the Extension of the Telomeric Ends of DNA and Preventing the Unlimited Proliferation of Cancer Cells

Brenda Laster¹, Carol Isaacson¹, Maha Msamra¹, Ekterina Perez², Joseph Kost²

¹Nuclear Engineering, Ben Gurion University, Israel

²Chemical Engineering, Ben Gurion University, Israel

09:30

DNA Topoisomerase 1: A Novel Radiation Exposure Biomarker

Raphael Gonen¹, Uzi German¹, Zeev Alfassi², Ester Priel²

¹Radiotoxicology Dpt., Nuclear Research Center, Israel

²Immunology and Nuclear Engineering, Ben Gurion University, Israel

09:45

A New Concept in Radiation Damage Studies: Model System for Self-Induced Radiation Damage Experiments in Thin Films

Michael Shandalov¹, Tzvi Tempelman², Rafael Hevroni³, Itzhak Kelson³, Eyal Yahel¹, Yuval Golan²

¹NRCN, Israel

²Ben-Gurion University, Israel

³Tel Aviv University, Israel

10:00

Numerical Analysis of the Microwave Auditory Effect

Nir Mordechay Yitzhak, Raphael Ruppin, Ronen Hareuveny

Radiation Safety Division, Soreq NRC, Israel

10:15

Archaeological Ceramics: Provenience Based on Neutron Activation Analysis

Joseph Yellin

Hebrew University of Jerusalem, Israel

10:30-11:00 Coffee Break

11:00-11:30 Young Scientists Awards Ceremony

11:30-13:30 Accelerators / SARAF

Hall B

Chair: Asher Shor

11:30

The SARAF Accelerator in 2012-2013

Leo Weissman, A. Kreisel, D. Berkovits, A. Arenshtam, Y. Ben-Aliz, Y. Buzaglo, O. Dudovitch, I. Eliahu, Y. Eisen, D. Har-Even, Y.F. Haruvy, S. Halfon, T. Hirsh, D. Hirshmann, Z. Horivitz, I. Gertz, A. Grin, G. Feinberg, I. Fishman, B. Keizer, D. Kijel, G. Lempert, Y. Luner, E. Reinfeld, J. Rodnizki, G. Shimel, A. Shor, I. Silverman, E. Zemach

SARAF, Soreq NRC, Israel

11:45

Superconducting Accelerating Cavity Pressure Sensitivity Analysis

Jacob Rodnizki, Zvi Horvits, Leo Weissman, Yakir Ben Aliz, Asher Grin

SARAF, Soreq NRC, Israel

12:00

Redesign of SARAF RFQ Modulation for CW Deuteron Acceleration

Jacob Rodnizki, Asher Shor

Nuclear Physics and Engineering, Soreq NRC, Israel

12:15

Fast Beam Chopper at SARAF accelerator via RF deflector before RFQ

Boaz Kaizer, Asher Shor, Leonid Weissman

Nuclear Physics and Engineering, Soreq NRC, Israel

12:30

First Demonstration of High-Power Proton Irradiation and Neutron Production with a Liquid-Lithium Target

Shlomi Halfon^{1,2}, Alexander Arenshtam¹, Danny Kijel¹, Michael Paul², Leonid Weissman¹, Dan Berkovits¹, Yosef Eisen¹, Ilan Eliyahu¹, Gitai Feinberg^{1,2}, Arik Kreisel¹, Israel Mardor¹, Guy Shimel¹, Asher Shor¹, Ido Silverman¹, Moshe Tessler²

¹*Soreq NRC, Israel*

²*Racah Institute of Physics, The Hebrew University of Jerusalem, Israel*

12:45

Nuclear Astrophysics at SARAF with LiLiT

Gitai Feinberg^{1,2}, Michael Paul¹, Alex Arenshtam², Ofer Aviv², Dan Berkovits², Dan Cohen¹, Ofer Dudovitch², Yossi Eisen², Ilan Eliyahu², Moshe Friedman¹, Yehoshua Ganon¹, Shlomi Halfon^{1,2}, Dany Kijel², Arik Kreisel², Guy Shimel², Asher Shor², Ido Silverman², Moshe Tessler¹, Leo Weissman², Zohar Yungrais²

¹*The Hebrew University of Jerusalem, Israel*

²*Soreq NRC, Israel*

13:00

Status of Cross Section Measurement for the Deuteron Induced Reaction $^{23}\text{Na}(d,p)^{24}\text{Na}$ in the Energy Range 1-20 MeV at NPI Rez and SARAF

Arik Kreisel¹, T.Y. Hirsh¹, Y. Eisen¹, J. Mrazek², E.Simeckova², M. Stefanik²

¹*SARAF, Soreq NRC, Israel*

²*NPI Rez, Rez, Czech Rep*

13:15

Proton Irradiation of LiF:Mg;Ti at SARAF: Optical Absorption Relative Efficiency Calculations using Track Structure Theory

Ilan Eliyahu^{1,2}, Yigal Horowitz², Leonid Oster³, Leo Weissman¹, Arik Kreisel¹, Sofia Druzhyna², Israel Mardor¹

¹*Soreq Nuclear Research Center, Israel*

²*Ben Gurion University of the Negev,, Israel*

³*Sami Shamoon College of Engineering,, Israel*

Chair: Yagil Kadmon

11:30**The SVM Method for Fissile Mass Estimation through Passive Neutron Interrogation: Advances and Developments**

Chen Dubi, Itamar Israelshvili

Physics, Nuclear Research Center of the Negev (NRCN), Israel

11:45**Alpha Beta Monitoring System Based on a Pair of Simultaneous Multi Wire Proportional Counters**

David Amidan^{1,2}, Udi Wengrowicz², I. Orion¹, Y. Yehuda-Zada², Y. Levin², T. Mazor², Y. Kadmon², Y. Cohen²

¹*Nuclear Engineering, Ben-Gurion University of the Negev, Beer Sheva, Israel*

²*Electronics, Nuclear Research Center-Negev, Beer Sheva, , Israel*

12:00**Aerial Measuring System (AMS) / Israel Atomic Energy Commission (IAEC) Joint Comparison Study**

Itzhak Halevy¹, Peter Wasiolek²

¹*Physics, NRCN, Israel*

²*U.S. Department of Energy, Remote Sensing Laboratory, USA*

12:15**Design of Stack Monitoring System for PET Medical Cyclotron Facilities with Isotope Identification and Released Activity Concentration Measurement**

Alon Osovizky¹, Dmitry Ginzburg¹, Vitaly Pushkarsky¹, Dima Shmidov¹, Eran Vax², Yakir Knafo¹, Natan Semyonov¹, Laurence Kaplan¹, Yagil Kadmon², Yosef Cohen², Tzachi Mazor²

¹*Radiation Detection Department, Rotem Industries Ltd, Israel*

²*Electronics & Control Laboratories, Nuclear Research Center Negev, Israel*

12:30**Radon Daughters Background Reduction in Alpha Particles Counting System**

Shay Shalom Dadon¹, Omer Pelled¹, Itzhak Orion²

¹*NRCN, Israel*

²*Nuclear Engineering, Ben-Gurion University of the Negev, Israel*

12:45**Monte Carlo Simulation for Optimizing 6LiF:ZnS(Ag) based Neutron Detector Configuration**

Yaacov Yehuda-Zada^{1,4}, Itzhak Orion¹, Lee Dongwon², Or Hen⁵, Arie Beck⁴, Yagil Kadmon⁴, Yossi Cohen⁴, Jeffrey Zigler², Nicholas Maliszewskyj², Alon Osovizky^{2,3}

¹*Nuclear Engineering, Ben Gurion University of the Negev, Israel*

²*NIST Center for Neutron Research, USA*

³*Rotem Industries Ltd, Israel*

⁴*Nuclear Research Center Negev, Israel*

⁵*Tel Aviv University, Israel*

13:00-14:00 Lunch**END OF CONFERENCE**

ORAL PRESENTATIONS PAPERS

49

Plenary Session I (Tuesday, February 11, 2014 13:00)

The Impact of Fukushima Accidents on LWR Safety and the Nuclear Power Risks

B. R. Sehgal

Nuclear Power Safety, KTH (Royal Institute of Technology), Stockholm, Sweden, 10691

INTRODUCTION

The history of the consideration of severe accidents (SA) safety begins really with WASH-1400 [1] initiated by USNRC in early 1970's. The WASH-1400 considered accidents of decreasing probability and increasing consequence (see **Tables I** extracted from WASH-1400).

The accidents considered, occurred due to successive faults which lead to at least the melting of the core and a possible radioactivity release to the environment. The increasing consequence accidents would entail additional failures e.g., vessel failure, late containment failure, containment bypass, early containment failure etc. These additional failures would lead to larger releases of radioactivity and thus larger consequences for the public in the vicinity of the plant.

Chance per Reactor-Year	Early Fatalities	Early illnesses	Total Property Damage \$10 ⁹	Decontamination Area ~Square Miles	Relocation Area Square Miles
One in 20,000 ^(a)	<1.0	<1.0	<0.1	<0.1	<0.1
One in 1,000,000	<1.0	300	0.9	2000	130
One in 10,000,000	110	3000	3	3200	250
One in 100,000,000	900	14	8	-	290
One in 1,000,000,000	3300	45	14	-	-

^(a) This is the predicted chance- of core melt per reactor year

Table 1 - Early consequences of Reactor accidents for various probabilities for one Reactor.

WASH -1400 did not provide estimates of the costs for cleanup of the contaminated land area. Also there were no estimates of the economic costs involved in removal of the molten fuel and the decommissioning of the stricken plant. The emphasis in WASH-1400 was primarily with physical damage to the population in the vicinity of the plant and peripherally with the societal, social and economic costs of a severe accident in a large LWR plant.

CONSEQUENCES OF ACTUAL SEVERE ACCIDENTS

The TMI-2 accident (1979)

This was the first severe accident in an operating commercial nuclear power reactor plant. The TMI-2 accident was quite benign in terms of public consequences. There were only negligible releases of the dangerous fission products: I, Cs, Sr etc. Nobody suffered any serious exposure to radioactivity and there was no land contamination.

The Chernobyl accident (1986)

This accident occurred in the reactor no.4 of the 4 RBMK reactors located in a complex called the Chernobyl nuclear power plant (NPP). The RBMKs in 1986 had large positive void coefficients and rather unstable behavior at power levels below 30% nominal.

The Chernobyl accident consequences were not confined to the vicinity of the plant. The tremendous energy generated in the explosion time-scale resulted in a plume reaching very high in the atmosphere and radioactivity travelling long distances.

The immediate effect of the Chernobyl severe accident was on the plant workers who performed some heroic deeds to limit the consequences of the accident. It was determined that there were 31 early fatalities and considerable number of illnesses. The costs of cleanup in the evacuation area around the Chernobyl plant were estimated to be 7 billion rubles.

The Fukushima accidents (2011)

The Fukushima accidents occurred on March 11, 2011 when a giant tsunami wave (14 meters high) climbed over the 10 meters high embankment provided for the Fukushima reactors 1 to 4. The tsunami wave flooded the emergency diesel generators (EDGs) for the 4 reactors making them inoperable. The tsunami also inundated the D.C. batteries, making the D.C. electricity unavailable. These four reactors suffered total black out of long term duration

Much has been written about the accident scenarios in the unit 1-3 of Fukushima station [2, 3, 4, 5, and 6]. Suffice it to say that the 3 plants suffered core melt down and vessel failures. Substantial fractions of the core melt of the 3 reactors are out of the respective vessels. In addition, the hydrogen produced during the core heat-up in unit-1 and unit-3 leaked into the respective reactor buildings. It underwent combustion and blew out the roofs of the buildings leading to direct containment by-pass for these 2 units. Some of the hydrogen from unit 3 went to the reactor building of unit 4 and on combustion there extensively damaged that building.

The core melt accident in each of the 3 reactors, unit 1-3 resulted from the loss of water in the core and the loss of heat sink. The outcome was that cores of each of these 3 reactors were without water supply for 6-8 hours each, which resulted in core melt downs and subsequent vessel failures.

The Japanese government stated that the fission product releases from Fukushima 1-3 were in the range of 5-10% of the Chernobyl releases. This may sound, somewhat, comforting but it should be realized that the Chernobyl releases were dispersed over an enormously larger area than the dispersal land area for the Fukushima releases. A fortunate occurrence was that much of the time the winds were blowing toward the ocean and land contamination was much smaller than it could have been.

One must be grateful to the Japanese government for evacuating the population in the affected areas in due time, thereby no member of the public died or was injured due to radiation exposure. It is estimated that approximately 114,000 persons were evacuated and most of them cannot go back to their homes. In this context, there will be controversy as to the extent of clean up i.e., the radioactivity level of the cleaned land, houses, vegetation before the population will accept the "move back".

The economic consequences of the Fukushima accidents are beyond belief. The TEPCO, an enormously rich and valuable electric utility company is going bankrupt and may be nationalized. The costs of the Japanese Government's forty year plan for remediation of the Fukushima accidents have been estimated but are indeterminate. Currently, there are many other costs to the Japanese nation since all the reactors, except two are shutdown. The costs incurred by the Japan government (Japanese people) for the import of oil, natural gas and coal to replace nuclear electricity are of the order of a few billion USD per month. The overall costs of the Fukushima accidents have been estimated to be 500 billion USD.

LESSONS LEARNED FROM THE ACCIDENTS

We study the safety of nuclear power intensively only after a severe accident (SA) occurs and the public is affected or aroused. The "wake-up" call from TMI-2 was that in spite of the many years of earnest efforts to prevent a core melt accident, such an accident can occur. The other lesson learned from the TMI-2 accident was that the non-technical aspects, e.g., operator training, emergency procedures, organization and management were of equal importance to the technical aspects.

The "wake-up" call from Chernobyl accident was that large-scale environmental damage and the enormous costs of radioactivity clean-up could be incurred if the containment is absent or fails early during the accident. The impact of Chernobyl accident on the SA safety concerns in USA and the large nuclear countries in the West and the Asia was, however, quite small, since the argument was made that; (1) RBMK reactors are different from western LWRs, (2) there were serious design flaws, e.g., positive void coefficient, common-mode failure of all core-outlet pipes and (3) there were serious and successive operator errors

The Fukushima accidents generated much response from the agencies and societies concerned with nuclear energy all over the world. The American Nuclear Society (ANS) published their report in March 2012. The American Society of Mechanical Engineers (ASME) report published in June 2012 urges the forging of a new nuclear safety "construct".

We believe that the above cited reports and papers have not addressed some lessons with respect to the attitudes of the public to nuclear emergencies. We believe that the first and the most-important lesson that should be learned is that radioactivity is a "fear complex" in the minds of most populations. In particular, mothers have to be convinced that very small doses of radiation, for even long durations, will not be a health hazard for their young children.

The second lesson with respect to the public attitude to nuclear emergencies derived from the Fukushima accidents is that the public is most upset when they have to leave their homes and possessions and they cannot return readily back to their homes.

The third lesson; also evident, is that operator performance (errors, omissions, initiatives, skills) all matter for the public consequence as a SA progresses. Operator actions can turn-off a budding SA or make its consequences worse. Thus operator skills are important and perhaps skill-based response to nuclear emergencies should be encouraged.

The fourth lesson is about the lack of instrumentation to track the progression of the severe accident for the operator. Thermocouples installed on the vessel wall from outside could have identified the melt and vessel behavior during the time the vessels were almost fully devoid of water.

SOME SHORTCOMINGS OF THE CURRENT SAFETY PRACTICE

a. Societal and economic consequences

The concern in the accident consequences has been with fatalities, injuries and latent cancers, i.e.; the individual health effects. Estimates were provided of the contamination of the land and property damage. However, in WASH-1400, there was no mention or discussion of the social upheaval caused by the spread of radioactivity deposited by a large release from a severe accident, necessitating the relocation of a significantly large population. The social upheaval and anxiety is also magnified by the unknown duration of the loss of habitat, employment and other daily amenities. Clean-up of ground contamination is a long arduous process, requiring large teams and it can take months. There will be controversy on the re-entry conditions. All of these cause anxiety and fear in the population.

The economic costs of Chernobyl and Fukushima have been mentioned earlier in this manuscript. A large release causes huge costs for remediation and clean-up. The insurance by an individual utility company cannot cover the costs incurred, or to be incurred. The costs beyond the insurance are primarily borne by the nation.

b. Acceptance of residual risk

The concept of residual risk has been invoked when an event in the SA scenario is considered to be highly improbable ('rare') coupled with the inability to estimate the consequences of such an event. The consequences of such events are not assessed. Their risks are accepted, even if they could have very large consequences. But the consequences of the very low probability Fukushima accidents are too large. They cannot be accepted.

c. Cost-benefit and back fit rules

The cost-benefit rule may be invoked in USA when expensive back-fits or major improvements may be proposed for Gen-II or Gen-III plants. It is not the practice in Europe however, costs are always a factor for a public utility company. The cost-benefit rule may become a large issue if the lessons learned from the Fukushima accidents point to some expensive back fits in the currently installed plants.

d Safety design basis

Severe accidents were not prescribed as safety design basis for GEN II plants and not even for GEN III+ plants in USA and other countries. The design basis for U.S. LWRs is still the same that was prescribed more than 35 years ago.

d. Diagnostic instrumentation for severe accidents

The current GEN II plants have not installed instrumentation which could help the operator to diagnose the progression of a SA and the status of the plant during the SA; e.g., hydrogen meters, thermocouples in the lower head, fission product detectors in the primary system and the containment etc. The operator is basically "flying-blind" during a SA and is unable to diagnose the plant status.

WHAT SHOULD BE THE PUBLIC SAFETY GOALS FOR NUCLEAR POWER PLANTS?

We believe that the Fukushima accidents have demonstrated that it will be beneficial (in terms of subsequent cost-avoidance) for nuclear power to adopt the safety goal of "no large release of radioactive fission products" from any accident in a nuclear power plant. The complementary goal of "no long-term evacuation" should also be adopted to safeguard against the societal upheaval caused by such forced mass movements and prolonged periods before return of evacuees back to their homes.

The normal leakage of $\leq 0.1\%$ per day from the containment could be acceptable as per the siting rules. "No large failure of containment" implies that the containment would have to be strong enough to survive intact the loads from possible hydrogen deflagrations and explosions and conservatively estimated steam explosions.

The 'no large release' goal should also include the "no base-mat melt-through" goal, since that event could threaten large scale land contamination and a danger of water table contamination.

Finally, the goal of "no land contamination beyond the exclusion area" of a plant suffering a SA should also be adopted.

The above goals are tough but they are necessary for good health of nuclear power.

CONCLUSIONS

The Fukushima accidents have created a crisis situation for the nuclear enterprise in the world. Already some rich European countries have resolved to forsake nuclear power as a long term resource-base for electricity generation. We have experienced more severe accidents than estimated from PRA studies. The nuclear power enterprise cannot function with the frequency of accidents that have occurred, in spite of the climate change fears.

Summarizing; a "safe" LWR nuclear power plant design should both prevent and mitigate SA caused by external and internal initiators. Stabilization and termination of the SA should be rapid so that any evacuation of the population in the vicinity is very brief. Containment cooling systems should be provided to reduce the containment pressure. A filtered vent system should be provided for possible early or late releases. Hydrogen control should be provided in all buildings. Qualified instrumentation should track a SA to provide accurate information to operator, the technical support team and the public. In this context, education of public to recognize the slow but long term hazards of fossil plants should be promoted, so that there is a realization that electricity is not risk-free. Similarly, education to provide realistic health hazards of very low level of radioactivity on populations should also be promoted.

REFERENCES

- [1]. **U.S. Nuclear Regulatory Commission**, Reactor Safety Study, "An Assessment of Accident Risks in the U.S. Commercial Nuclear Power Plants", USAEC report WASH -1400 (1975)
- [2]. **B.R. Sehgal**, editor "Nuclear Safety in Light Water Reactors, Severe Accident Phenomenology", Elsevier, Academic Press Publishers (2012)
- [3]. **American Nuclear Society (ANS)**, "Fukushima Daiichi: ANS committee report, published by ANS", (March 2012)
- [4]. **American Society of Mechanical Engineers (ASME)**, "Forging a New Nuclear Safety Construct", Published by ASME (June 2012).
- [5]. **Institute of Nuclear Power Operations**, "Special Report on Nuclear Accident at Fukushima Daiichi Nuclear Power Station", (November 2011)
- [6]. **Japanese Government**, "Interim Report of the Japanese Government Investigation Committee on the Accidents at Fukushima Nuclear Power Stations of Tokyo Electric Power Co. ", (December 26, 2011)

Panel (Tuesday, February 11, 2014 16:25)

The Need for Nuclear Power Stations in Israel

S. Wald and I. Yaar

Ministry of National Infrastructures, Energy and Water Resources

Corresponding author: Dr. Shlomo Wald; shlomow@energy.gov.il

One of the recommendations given in the master plan for energy economy in Israelⁱ is to consider construction of Nuclear Power Plants (NPP's) as a part of the electrical production system in Israel, starting from 2030. This recommendation is based on the considerations listed below,

- The maximum electrical power production from natural gas starting from 2030 should not exceed 50-60% of the total production.
- The electrical power production from renewable sources will be about 20% and 25% in 2030 and 2050, respectively.
- The electrical power production from coal will be about 10% and 5% in 2030 and 2050, respectively.

Based on these assumptions together with the predictions for the increase in the total consumption of electrical power in Israel, a need for a first NPP in Israel around 2030 is established, with a need for a steady increase in the number of operational NPP's towards 2050.

Based on this recommendation, a pre-feasibility study of an Israeli NPP was conducted by the Ministry of National Infrastructures, Energy and Water Resourcesⁱⁱ. This report has identified several possible obstacles in the way to the construction of a first NPP in Israel (the major obstacles that were identified during this study will be presented in a different presentation).

In this work, the need for NPP's in Israel and the motivation for starting the pre-feasibility study will be presented.

References:

ⁱⁱⁱ Master plan for the energy economy in Israel, TAHAL Group and the Ministry of Energy and water, report No. 147420-713-307 (Dec. 13) final draft, in Hebrew.

^{iv} Ministry of Energy and Water Resources, Pre-Feasibility Study for the Construction and operation of an NPP in Israel - Final Report, in Hebrew (2012).

Plenary Session III (Wednesday, February 12, 2014 08:30)

Remedy for Radiation Fear — Discard the Politicized Science

J. Cuttler

Cuttler & Associates Inc, Mississauga, Canada

ABSTRACT

While seeking a remedy for the crisis of radiation fear in Japan, the author reread a recent article on radiation hormesis. It describes the motivation for creating this fear and mentions the evidence, in the first UNSCEAR report, of a factor of 3 reduction in leukemia incidence of the Hiroshima atom-bomb survivors in the low dose zone. Drawing a graph of the data reveals a hormetic J-curve, not a straight line as reported. UNSCEAR data on the lifespan reduction of mice and Guinea pigs exposed continuously to radium gamma rays indicate a threshold at about 2 gray per year. This contradicts the conceptual basis for radiation protection and risk determination that was established in 1956-58. In this paper, beneficial effects and thresholds for harmful effects are discussed, and the biological mechanism is explained. The key point: the rate of spontaneous DNA damage (double-strand breaks) is more than 1000 times the rate caused by background radiation. It is the effect of radiation on an organism's very powerful adaptive protection systems that determines the dose-response characteristic. Low radiation up-regulates the adaptive protection systems, while high radiation impairs these systems. The remedy for radiation fear is to expose and discard the politicized science.

INTRODUCTION

Almost three years have passed since a major earthquake and devastating tsunami damaged the Fukushima-Daiichi nuclear power plant. An evacuation order forced 70,000 people to leave the area, while an additional 90,000 left voluntarily and subsequently returned. Many of those who left under the forced order have not gone back to their homes as removal of radioactivity continues. Approximately 1,600 people died, mainly due to psychological stress, in the evacuation process (Mainichi 2013)—about the same number of deaths in the Fukushima Prefecture from the earthquake and tsunami combined (Japan National Police Agency 2013). The precautions taken to avoid hypothetical health risks have proved to be more harmful than the asserted risks.

The tragedy is that the radiation dose-response characteristic for leukemia in humans had been determined in 1958, but it was disregarded because of the policy decision to adopt the linear no-threshold (LNT) dose-response model. The threshold model had been the "gold" standard for medicine and physiology since the 1930s; however, in 1956, the US National Academy of Sciences adopted the LNT model for evaluating genomic risks due to ionizing radiation. The Genetics Panel members believed there was no safe exposure for reproductive cells. They thought that the mutation risk increased with even a single ionization. In 1958, the National Committee for Radiation Protection and Measurement generalized the LNT concept to somatic cells and cancer risk assessment. Soon after, the other national and international organizations adopted this model for radiation-induced genetic and cancer risks (Calabrese 2013a, 2013b).

RADIATION HORMESIS - A REMEDY FOR FEAR

The enormous social fear and media frenzy surrounding the release of radioactivity from the damaged Fukushima NPP led the author to study again the facts in a remarkable paper by Jaworowski (2010) on radiation hormesis. He described the exaggerated fear of irradiating healthy tissues that arose during the Cold War period with its massive production and incessant testing of nuclear weapons. Radioactive materials from the atmospheric tests spread over the whole planet. People were quite rightly scared of the terrifying prospect of a global nuclear war and large doses of radiation from fallout. However, it was the

leading physicists responsible for inventing nuclear weapons who instilled a fear of small doses in the general population. In their highly ethical endeavour to stop preparations for atomic war, they were soon joined by many scientists from other fields. Eventually, this developed politically into opposition against atomic power stations and all things nuclear.

Although the arguments of physicists and their followers were false, they were effective; atmospheric tests were stopped in 1963. However, this was achieved at a price—a terrifying specter had emerged of small, near zero radiation doses endangering all future generations. This became a long-lived and worldwide societal affliction nourished by the LNT assumption, according to which any dose, even that close to zero, would contribute to the disastrous effect. Radiation hormesis (Luckey 1991) is an excellent remedy for this affliction, and it is perhaps for this reason that it has been ignored and discredited over the past half century. What happened more than 50 years ago still influences the current thinking of both the decision makers and those who elect them.

The linearity assumption was not confirmed by early or later epidemiological studies of Hiroshima and Nagasaki survivors. No hereditary disorders were found in the children of highly irradiated parents. The United Nations Committee on the Effects of Atomic Radiation (UNSCEAR) was concerned mainly with the effects of nuclear tests, fulfilling a political task to stop weapons testing. The committee had mixed opinions regarding the LNT model, and its first report, UNSCEAR 1958, contains conflicting statements. Jaworowski states: "hormesis is clearly evident . . . in a table showing leukemia incidence in the Hiroshima population, which was lower by 66.3% in survivors exposed to 20 mSv, compared to the unexposed group (p.165). This evidence of radiation hormesis was not commented upon. Since then, the standard policy line of UNSCEAR and of international and national regulatory bodies over many decades has been to ignore any evidence of radiation hormesis and to promote LNT philosophy."

The very important data in UNSCEAR 1958, Table VII were not presented in graphical form. Figure 1, given here, shows these data (96,000 survivors) together with the LNT model from 1300 to 0 rem. A line through 100 rem was added to take into account Footnote c, which states that the doses in Zone C "were greater than 50 rem."

These Hiroshima leukemia data strongly contradict the LNT model, which predicts an increased degree of risk as the radiation dose increases. The data clearly indicate a reduction in incidence, by a factor of 3, in the dose range from about 0.1 to 10 rem (1 to 100 mSv). The threshold for increased risk is about 50 rem (0.5 Sv). The leukemia data fit a hormetic J-curve; they do not fit a straight line.

UNSCEAR 1958, page 165 in paragraph 31, states: "In zones A (1300 rem), B (500 rem), and C (50 rem), the values of P_L were calculated¹ to be . . . This finding was taken to support the suggestion that the extra leukemia incidence is directly proportional to radiation dose, and conversely to argue against the existence of a threshold for leukemia induction."

The discussion in paragraph 33 states "that a threshold for leukemia induction might occur. In fact, according to table VII a dose of 2 rem is associated with a decreased leukemia rate." But this observation was rejected because "the estimates of dose ... are much too uncertain ..." UNSCEAR should not have marginalized, because of dose uncertainty, the observation of this strong reduction in leukemia incidence for the 32,692 survivors in Zone D, which was far below the leukemia incidence of the 32,963 survivors in Zone E (the controls). This data disproved the LNT dose-response model, and UNSCEAR should have rejected the LNT model in its report.

Flidner et al (2012) pointed out that bone marrow stem cells, which produce the blood cell components, are very sensitive to radiation, yet they are remarkably resistant to chronic low-dose exposure regarding

¹ P_L is the extra probability of leukemia occurring in an exposed person per rem and per year elapsed after exposure.

function and maintenance of blood supply. Moreover, no increased cancer deaths occurred at doses below 700 mGy per year despite the fact that the latency time for leukemia is much shorter than for other radiation-induced cancers. This clear evidence of radiation hormesis—an absence of cancer risk at low dose radiation—adds to many other data of this kind and should cause UNSCEAR, the NAS and all radiation protection organizations to revoke the generalized link they created in 1958 between low radiation and a risk of cancer; this link is the basis for the fear we see today.

Regarding the present concern about radiation-induced "health effects" on the residents around the Fukushima NPP, UNSCEAR states that that none were observed (UNSCEAR 2012, Chapter IIB, Section 9(a)) and discusses in Chapter III, Section 1 the difficulties in attributing health effects to radiation exposure and inferring risks. Section 2 points out that failure to properly address uncertainties can cause anxiety and undermine confidence among the public, decision-makers and professionals. If it wished, UNSCEAR could have attributed beneficial health effects to the low radiation, based on the extensive evidence in Annex B of its UNSCEAR 1994 report. This report contains summaries of 192 studies on *adaptive responses*. There have also been hundreds of additional scientific studies published during the subsequent 20 years. The World Health Organization's health risk assessment report (WHO 2013) contains estimates of lifetime risks of cancer; however, it uses the invalid LNT methodology.

BENEFICIAL EFFECTS

Positive health effects were identified by medical scientists and practitioners soon after x-rays and radioactivity were discovered in 1895-96. High, short-term exposures were harmful, but low acute doses or low dose-rate long-term exposures were beneficial. Often this was found inadvertently, while diagnosing bone fractures or other medical conditions. Recent review papers describe accepted medical applications, such as, accelerated healing of wounds and infections, cancer cures, and treatments of inflammations and arthritis that occurred before the introduction of the cancer scare in the late 1950s (Cuttler 2013). A new review discusses the historical use of low radiation to cure pneumonia (Calabrese 2013c), a very common occurrence in hospitals.

Beneficial effects have been known and studied for well over a century. The mechanism is explained in a medical textbook, in a chapter by Feinendegen et al. (2013). The key point is the discovery more than 25 years ago that spontaneous (endogenous) DNA damage, by the attack of reactive oxygen species (ROS), occurs at a relatively very high rate compared to the damage rate caused by natural background radiation. The natural rate of single-strand breaks from ROS attacks per average cell is many millions of times greater than the rate induced by ~ 1 mGy per year. Single-strand breaks are readily repaired, but double-strand breaks (DSBs) are relevant to induction of cancer and other genetic changes. Non-irradiated cells contain from about 0.1 to numerous DSBs at steady state. This agrees with the calculated probability of 0.1 for a DSB to occur per average cell in the human body per day from endogenous, mainly ROS sources (Polycove and Feinendegen 2003). The probability of a radiogenic DSB to occur per day in background radiation is on average only about 1 in 10,000 cells. So the ratio of spontaneous to radiogenetic DSBs produced per day is about 1,000; i.e., the natural damage rate is a thousand times greater than the damage rate due to background radiation.

The critical factor is the effect of radiation on an organism's very powerful biological defences, its protection systems, which involve the actions of more than 200 genes. They act on all the damage that is occurring (and its consequences) due to both internal causes and the effects of external agents. A low radiation dose or low level radiation causes cell damage, but it up-regulates adaptive protection systems in cells, tissues, animals and humans that produce beneficial effects far exceeding the harm caused by the radiation (Feinendegen et al. 2013). The net beneficial effects are very significant in restoring or improving health. The detailed behaviours of the defences are very complex, but the evidence is extremely clear. They range from prevention/cure of cancers to the very important medical applications of enhanced adaptive protections in the responses to stresses and enhanced healing of wounds, curing of infections, and reduction of inflammation, as mentioned earlier. In contrast, high level irradiation impairs these systems.

THRESHOLDS FOR HARMFUL EFFECTS

The evidence of net beneficial effects requires the determination of the threshold for harmful effects. This was known through more than thirty years of human experience when the first radiation protection *tolerance dose*, 0.2 roentgen per day or ~ 700 mGy per year, was established for radiologists in the early 1930s (Henriksen et al. 2013). Figure 2 is the result of a recent assessment of lifespan data for dogs exposed to cobalt-60 gamma radiation (Cuttler 2013). The threshold for net harm is also ~ 700 mGy per year. Similar data are found in UNSCEAR 1958, Annex G, page 162. The threshold for lifespan reduction of mice and Guinea pigs exposed to radium gamma rays is 4 roentgen per week or ~ 2000 mGy per year. Their mean survival time is 7% longer than the controls at a dose rate of 0.5 roentgen per week, which is about 240 mGy per year.

The accepted threshold for recognizing harmful late effects after a short-term exposure, according to a large set of experimental and epidemiological data, is an absorbed dose of about 100 mGy. However, the UNSCEAR data for leukemia incidence among 96,000 Hiroshima survivors, shown in Figure 1, suggests a threshold of about 500 mGy for leukemia.

INVALID BASIS FOR THE LNT MODEL

Calabrese reviewed the evolution of radiation protection from the tolerance dose (threshold) concept to the LNT concept. It began when early geneticists discovered that large numbers of mutations could be induced in germ cells of fruit flies by ionizing radiation. This would enable eugenicists to modify organisms for utilitarian purposes (Muller 1927). A high dose, at a high rate, produced a mutation rate that was 150 times greater than the spontaneous rate. This and other high-dose studies indicated that the mutation rate was proportional to the dose. A radiation target theory was developed by physicists to model the process of radiation-induced mutation, with mathematical calculations related to quantum mechanics (Calabrese 2013a). They established a conceptual framework for gene structure, target theory for the induction of mutations by ionizing radiation, the single-hit mechanism hypothesis to account for the shape of the LNT dose response and the application of this dose-response model for what was to become modern cancer risk assessment. However, bio-organisms do not behave according to this model. The Caspari and Stern (1948) study that irradiated 50,000 fruit flies to a dose of ~ 50 roentgen at a low rate, revealed a mutation rate that was the same as the 50,000 controls. This study was ignored. Recent studies on fruit flies at very low dose rate indicate a mutation frequency far below the spontaneous rate—genetic benefit instead of risk—below an absorbed dose of about 1 gray, see Figure 3 (Cuttler 2013). This evidence clearly falsifies the LNT model.

DISCUSSION

Many researchers use the LNT model to predict the lifetime risk of cancer from a small dose of radiation. They calculate the expected cancer incidence from a very low dose by connecting a straight line between the zero-dose, zero-incidence point and the high-dose cancer incidence data of the atom-bomb survivors. This procedure can only yield a risk of cancer. Most epidemiological studies are designed to measure radiation-induced cancer incidence, so they do not report any observations of beneficial effects. The data are fitted to the LNT model, presuming it is valid. Scott et al. (2008) list seven approaches that make it difficult to recognize bio-positive effects and thresholds, concluding that there is no credible evidence to support the contention that CT scans will cause future cancers. Scott (2008) points out three epidemiological "tricks" that are commonly employed to obtain a LNT curve. Relative risk and odds ratio values are often shown instead of cancer incidence data. In view of the extensive evidence of beneficial health effects and reduced health risks from low doses, misrepresentations of data and deceptions are needed to fit the LNT model.

CONCLUSIONS AND RECOMMENDATIONS

Social concerns about the safety of all nuclear technologies is caused by ideological linkage of any (human-made) radiation exposure to a risk of health effects, namely cancer and genetic harm, using the LNT model

to calculate health risks. This link, created in the 1950s to stop the development and production of nuclear weapons, is maintained in spite of the extensive biological evidence of beneficial effects from low dose or low dose rate exposures. Ignoring biological facts and refusing to revert to the threshold model concept for radiation protection has created an enormous barrier against social acceptance of nuclear energy and the use of radiation-based medical diagnostics. The remedy is to discard this politicized science.

This enormous radiation scare surrounding the Fukushima-Daiichi is a very serious crisis. It should be looked upon as an opportunity to make changes in attitudes and concepts that would not otherwise be possible.

The following three fundamental messages should be communicated to everyone in order to explain the real effect of radiation on health and to eliminate the irrational fear.

- 1 Spontaneous DNA damage, mainly from reactive oxygen species, occurs at very high rate; the rate of double strand breaks (DSBs) is more than 1000 times the rate of DSBs induced by a background radiation level of 1 mGy per year.
- 2 Biological organisms have very powerful adaptive protection systems against harm to their cells, tissues and the entire organism, regardless of whether the harm is caused by natural internal processes or by external agents.
- 3 Low radiation generally up-regulates adaptive protection systems resulting in a net health benefit to the organism in terms of response to stress. High radiation generally impairs protection systems and results in more net harm than benefit. The effect of radiation on the adaptive protection systems is what determines the health benefit or risk.

Other recommendations are:

- Scientific societies should organize meetings to discuss the health benefits and risks of radiation.
- Regulatory bodies and health organizations should examine the scientific evidence.
- Radiation protection regulations should be changed. They should be based on science instead of politicized science.
- The basis for radiation protection should be restored to the *tolerance dose* (threshold) concept, in light of more than a century of medical evidence.
- Calculation of cancer risk using unscientific concepts, such as the LNT model, should be stopped.
- Regulation of harmless radiation sources, such as radon in homes, should be stopped.
- Based on biological evidence, the threshold for evacuations from low dose rate radiation should be raised from 20 to no more than 700 mGy per year, i.e., from 2 to ≤ 70 rad per year.

REFERENCES

Calabrese EJ. 2013a. *Origin of the linear no threshold (LNT) dose-response concept*. Arch Toxicol DOI 10.1007/s00204-013-1104-7. Available at: <http://link.springer.com/article/10.1007%2Fs00204-013-1104-7>

Calabrese EJ. 2013b. *How the US National Academy of Sciences misled the world community on cancer risk assessment: new findings challenge historical foundations of the linear dose response*. Arch Toxicol DOI 10.1007/s00204-013-1105-6. Available at: <http://link.springer.com/article/10.1007/s00204-013-1105-6>

Calabrese EJ. 2013c. *How radiotherapy was historically used to treat pneumonia: Could it be useful today?* Yale Journal of Biology and Medicine 86: 555-570

- Caspari E and Stern C. 1948. *The influence of chronic irradiation with gamma rays at low doses on the mutation rate in Drosophila Melanogaster*. Genetics 33: 75-95. Available at: <http://www.genetics.org/content/33/1/75.full.pdf+html?sid=cb861a39-fb63-48c4-bcbe-2433bb5c8d6a>
- Cuttler JM. 2013. *Commentary on Fukushima and Beneficial Effects of Low Radiation*. Dose-Response 11: 432-443. Available at: <http://www.ncbi.nlm.nih.gov/pmc/articles/PMC3834738/>
- Feinendegen LE, Pollycove M and Neumann RD. 2012. *Hormesis by low dose radiation effects: low-dose cancer risk modeling must recognize up-regulation of protection*. In Baum RP (ed.). Therapeutic Nuclear Medicine. Springer. ISBN 973-3-540-36718-5. Available at: <http://db.tt/UyrhlBpW>
- Fliedner TM, Graessle DH, Meineke V and Feinendegen LE. 2012. *Hemopoietic response to low dose-rates of ionizing radiation shows stem cell tolerance and adaptation*. Dose-Response 10: 644-663. Available at: <http://www.ncbi.nlm.nih.gov/pmc/articles/PMC3526333/>
- Henriksen T and Biophysics and Medical Physics Group at UiO. 2013. Radiation and Health. Taylor & Francis. ISBN 0-415-27162-2 (2003 updated to 2013). University of Oslo. Available at: <http://www.mn.uio.no/fysikk/tjenester/kunnskap/straling/radiation-and-health-2013.pdf>
- Japan National Police Agency. 2013. *Damage situation and police countermeasures associated with 2011 Tohoku district - off the Pacific Ocean earthquake, November 8, 2013*. Available at: http://www.npa.go.jp/archive/keibi/biki/higaijokyo_e.pdf
- Jaworowski Z. 2010. *Radiation hormesis - A remedy for fear*. Human and Exper Toxicol 29(4) 263-270. Available at: <http://www.belleonline.com/newsletters/volume15/vol15-2.pdf>
- Luckey TD. 1991. Radiation Hormesis. CRC Press
- Mainichi. 2013. *Stress-induced deaths in Fukushima top those from 2011 natural disasters*. The Mainichi. September 9, 2013. Available at: http://worldnews.nbcnews.com/_news/2013/09/10/20420833-fukushima-evacuation-has-killed-more-than-earthquake-and-tsunami-survey-says?lite
- Muller HJ. 1927. *Artificial transmutation of the gene*. Science 66(1699): 84-87
- Pollycove M and Feinendegen LE. 2003. *Radiation-induced versus endogenous DNA damage: possible effect of inducible protective responses in mitigating endogenous damage*. Human and Exper Toxicol 22: 290-306. Available at: <http://www.belleonline.com/newsletters/volume11/vol11-2.pdf>
- Scott BR. 2008. *It's time for a new low-dose-radiation risk assessment paradigm—one that acknowledges hormesis*. Dose-Response 6: 333-351. Available at: <http://www.ncbi.nlm.nih.gov/pmc/articles/PMC2592992/>
- Scott BR, Sanders CL, Mitchel REJ and Boreham DR. 2008. *CT Scans May Reduce Rather than Increase the Risk of Cancer*. J Am Phys Surg 13(1): 8-11. Available at: <http://www.jpands.org/vol13no1/scott.pdf>
- UNSCEAR. 1958. *Report of the United Nations Scientific Committee on the Effects of Atomic Radiation*. United Nations. General Assembly. Official Records. Thirteenth Session. Supplement No. 17 (A/3838). New York. Available at: <http://www.unscear.org/unscear/en/publications/1958.html>
- UNSCEAR. 1994. *Adaptive Responses to Radiation in Cells and Organisms. Sources and Effects of Ionizing Radiation*. Report to the United Nations General Assembly, with Scientific Annexes. Annex B. Available at: <http://www.unscear.org/unscear/publications/1994.html>
- UNSCEAR. 2012. *Report of the United Nations Scientific Committee on the Effects of Atomic Radiation. Fifty-ninth session (21-25 May 2012)*. Available at: <http://www.unscear.org/>
- WHO. 2013. *Health risk assessment from the nuclear accident after the 2011 Great East Japan Earthquake and Tsunami, based on a preliminary dose estimation*. World Health Organization. Available at: http://apps.who.int/iris/bitstream/10665/78218/1/9789241505130_eng.pdf

UNSCEAR 1958. Table VII. Leukemia incidence for 1950–57 after exposure at Hiroshima^a

Zone	Distance from hypocentre (metres)	Dose (rem)	Persons exposed	L (Cases of leukemia)	\sqrt{L}	N ^b (total cases per 10 ⁶)
A	under 1,000	1,300	1,241	15	3.9	12,087 ± 3,143
B	1,000–1,499	500	8,810	33	5.7	3,746 ± 647
C	1,500–1,999	50 ^a	20,113	8	2.8	398 ± 139
D	2,000–2,999	2	32,692	3	1.7	92 ± 52
E	over 3,000	0	32,963	9	3.0	273 ± 91

^a Based on data in reference 13 (Wald N. Science 127:699-700. 1958). Prior to 1950 the number of cases may be understated rather seriously.

^b The standard error is taken as: N times (\sqrt{L}/L).

^c It has been noted (reference 15, 16) that almost all cases of leukemia in this zone occurred in patients who had severe radiation complaints, indicating that their doses were greater than 50 rem.

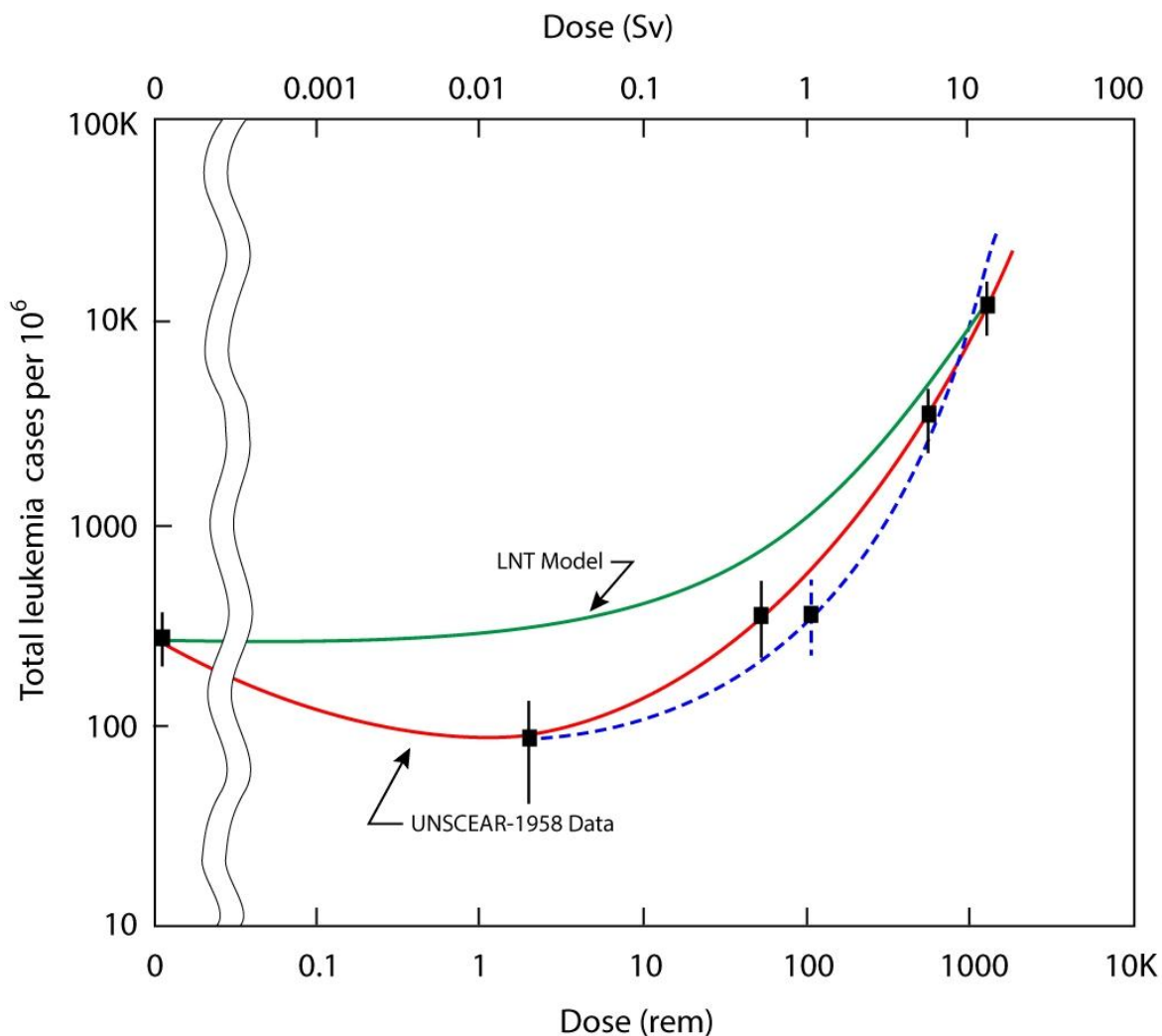


Figure 1. Leukemia incidence in the Hiroshima survivors for 1950-57

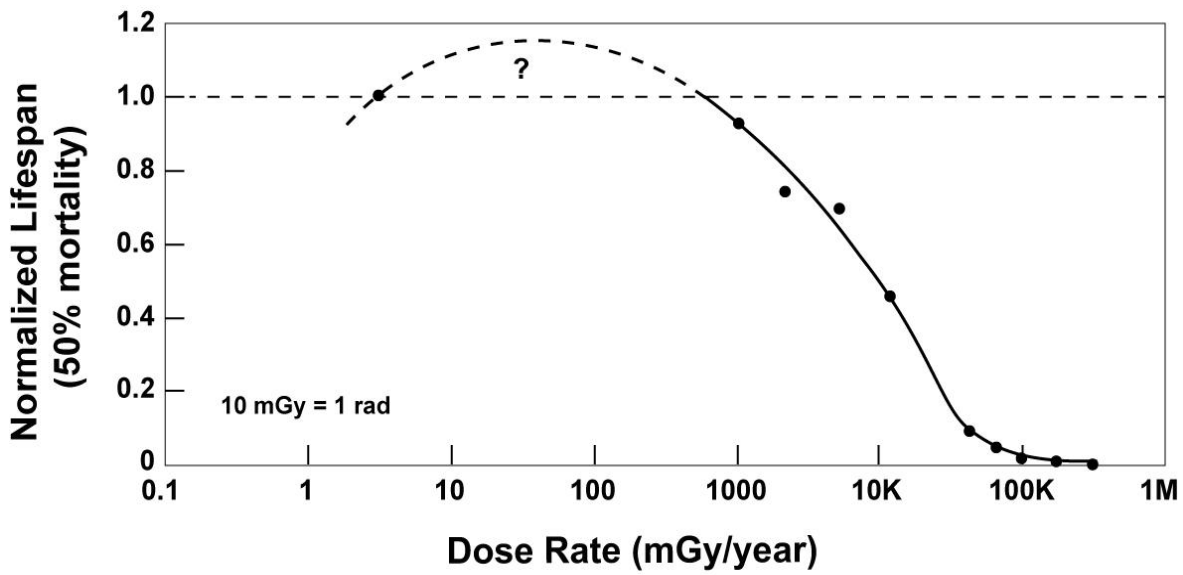


Figure 2. Lifespan versus radiation level (Cuttler 2013)

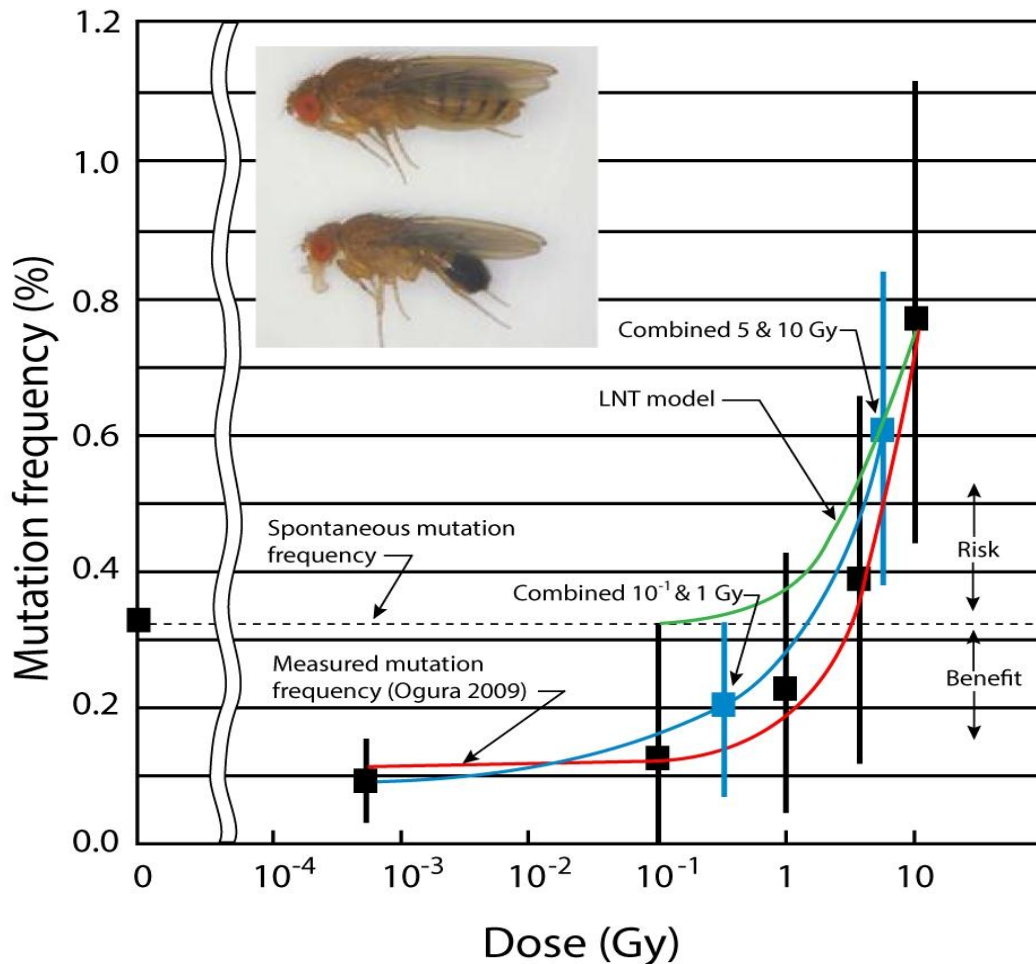


Figure 3. Fruit fly mutation frequency versus radiation dose (Cuttler 2013). A binomial distribution is assumed for the occurrence of the mutations. Each error bar is two standard deviations from the mean frequency. The data points at 0.3 Gy (0.19%) and at 7 Gy (0.61%) are obtained by "pooling" the Ogura et al (2009) data at 10⁻¹ and 1 Gy, and at 5 and 10 Gy, respectively. Note that the mean mutation frequency is below the spontaneous level (0.32%) when the dose is below 1 Gy.

Plenary Session III (Wednesday, February 12, 2014 08:30)

A National Survey of Exposure to Power Frequency Magnetic Fields ("*ORCHID*")

R. Hareuveny¹, I. Eliyahu¹, Y. Yaffe¹, I. Ben David¹, M. Riven², S. Kandel² and L. Kheifets³

¹ *Soreq NRC, Yavne, Israel*

² *Independent Consultant, Israel*

³ *UCLA, Los Angeles, California, USA*

INTRODUCTION

Since 1979⁽¹⁾, a lot of epidemiological research has been conducted examining the association between residential exposure to power frequency (50/60 Hz, Extremely Low Frequency - ELF) magnetic fields (MFs) and cancer in general, and childhood leukemia in particular. Two pooled analyses^(2,3) summarizing the results of important epidemiological research published up to 2000 pointed to a consistent increase in the risk of developing childhood leukemia in children exposed to residential MF levels above 0.3–0.4 μT (OR approximately 2). In 2002, the International Agency for Research on Cancer (IARC) categorized human exposure to ELF MFs as “possibly carcinogenic” (2B). The Scientific ambiguity and uncertainty about the nature of the observed association, implied in the IARC classification, has significant impact on worldwide national and local exposure policies, as well as public concerns. This situation is especially complicated in Israel, where MFs exposure limits to the general public are among the strictest in the world.

ORCHID project (Hebrew abbreviation of "*National Survey to MFs in Israel*") was initiated by SOREQ NRC and funded by the Ministry of National Infrastructures, Energy and Water Resources. The original aim of the project, the first of its kind in Israel, was to collect extensive and reliable information regarding the exposure of children to power frequency MFs. Beyond the scientific importance of this data, identification of major MFs sources might help to reduce general public exposure. Furthermore, *ORCHID* outcomes may be helpful for policy development.

The innovation of *ORCHID* is its educational aspect, namely the integration of gifted children as active scientific participants in the project. The goals of this aspect are to enable gifted children to gain experience in scientific research, and to directly learn from hands about ELF MFs. Furthermore, the involvement of the students in the research increases their willingness to participate in the survey (over 80% positive responses), and significantly improves the quality of the gathered information. The involvement of the children includes various activities such as full participation in the MFs exposure survey and data analysis, active learning, and personal research projects regarding different aspects of ELF MFs as described later.

This abstract briefly summarizes the major activities of the project up to the present time.

EXPOSURE SURVEY

Each child participates in two types of measurements - *Spot* measurements in his apartment, and *24 hours Personal Exposure Monitoring*. Measurements are performed using EMDEX II meters (Enertech Consultants, Campbell, CA, USA) operating in a broadband mode (40–800 Hz).

Spot measurements are performed during evening hours (typically 16:00–20:00, when children are more likely to be at home and electric consumption is expected to be at its peak) according to a predefined protocol, similar to one used in previous surveys⁽⁵⁾. Five points are measured in each room (except bathrooms, restrooms, storerooms, and balconies) at a height of 1 m – one at the center of the room and the other four at the midpoint of the diagonal pointing from the center to each of the room's four corners.

Additional spot measurements are performed at contact with the mattress of each bed in the apartment – one at its upper part and the other at its lower one. Appliances are left at the state they were found.

At the end of the spot measurement, an EMDEX II meter, continuously monitoring and recording the MFs each 1.5 s, is given to the participating child for 24 hours personal monitoring, together with written instructions. Generally speaking, the child is asked to continue his regular daily behavior with the meter attached to his body, and document his major activities. While sleeping, the meter is placed next to his bed. After some 24 hours the meter is picked up by our team, the data is downloaded to a PC, and sent back to the child for analysis. Survey results will be published in the future.

EDUCATIONAL ACTIVITIES

ORCHID project has been implemented at three centers for gifted and talented children. The pilot study took place at the *gifted children center* in the town *Rehovot*. 19 adolescent, mostly 9th grade students, went through a program of two hours weekly meetings. During the first semester they conducted different types of MFs measurements, analyzed the data themselves, and finally presented their results and conclusions, and discussed them with their classmates. Additionally, they assembled an electronic circuit as an introduction to the basic principles and limitations of commercial MF meters, and received frontal lectures about various related topics. In the second semester, the children were divided into seven working teams. Each team performed a *Personal Research Project*, as described briefly in the next paragraph. At the end of the year the projects were presented in posters and oral presentations in a conference organized for invited audience.

The second group that participated in the project was from the *gifted children center* at *Yavne*. 20 children, 6th grade pupils, went through the same process as those in the previously mentioned center at *Rehovot*. Following their own request, some of them perform personal research projects during their free time.

Currently, *ORCHID* project is ongoing at *Davidson-Institute-of-Science-Education* affiliated with the *Weizmann Institute of Science*. Nearly 100 adolescent, 10th grade students from all over Israel, participating in the "*Young Scientist*" program, are divided into two groups, each take part in three meetings during the year. These students are required to analyze their personal findings, insert them into a common data base on the web, and finally try to draw advanced conclusions based on this collective body of information.

PERSONAL RESEARCH PROJECTS

Currently, the most advanced personal research project, performed by two gifted children together with *ORCHID* team, is the characterization of the MFs inside vehicles. The MFs in the four seats of seven different car models, with either gasoline or diesel engines, were monitored either while the car was standing (60 seconds at 2500 or minimal RPM) or driven along nearly 1 km road at two distinct speeds (40 km/h and 80 km/h, two repetitions at each speed). Data is now analyzed and a manuscript with results will be developed.

Other personal research projects are already underway or are in preliminary stages. Four projects seek circumstances that might influence the results of both *Spot* measurements (The electric load in measurements of residential apartments and the protocol type for school surveys) and *Personal* monitoring (sampling rate and spatial meter movements). Other projects check the MFs in the vicinity of electric musical instruments (pianos and guitars) and amplifiers, and the shielding effectiveness of different construction materials. A project in preparation aims to study the biological effects of MFs on plants (*Arabidopsis* and *Nicotiana tabacum*).

SUMMARY

This abstract briefly presents *ORCHID* - a national survey of exposure to power frequency magnetic fields. While the initial focus of the project was the MFs survey, the extraordinary interest and skills of the gifted children and willingness to participate in the project, persuaded us to increase its educational component. Over 50 "double" measurements (*Spot* and *Personal*) out of 100 planned have been completed. 10-15

different educational centers in Israel already applied to join the project. Extension of this project into other countries is being considered.

REFERENCES

1. Wertheimer, N. and Leeper, E. *Electrical wiring configurations and childhood cancer*. Am. J. Epidemiol. **109**, 273-284 (1979).
2. Ahlbom, A., Day, N., Feychting, M., Roman, E., Skinner, J., Dockerty, J., Linet, M., McBride, M., Michaelis, J., Olsen, H. *et al. A pooled analysis of magnetic fields and childhood leukaemia*. Br. J. Cancer **83**, 692-698 (2000).
3. Greenland S., Sheppard A. R., Kaune W. T., Poole C. and Kelsh, M. A. *A pooled analysis of magnetic fields, wire codes, and childhood leukemia*. Childhood Leukemia-EMF Study Group. Epidemiology **11**, 624-634 (2000).
4. Mezei G. and Kheifets L. *Selection bias and its implications for case control studies: a case study of magnetic field exposure and childhood leukaemia*. Int. J. Epidemiol. **35**, 397-406 (2006).
5. Hareuveny R., Kandel S., Yitzhak N.M., Kheifets L. and Mezei G., *Exposure to 50 Hz Magnetic Fields in Apartment Buildings With Indoor Transformer Stations in Israel*, J. of Exposure Science and Environmental Epidemiology 21,365-371 (2011).

ACKNOWLEDGMENTS

The authors would like to thank Dr. R. Ruppin, N. Yitzhak, N. Refaeli and L. Stencel for their helpful assistance to the study. The project is funded by the Unit of Chief Scientist at the Israeli Ministry of National Infrastructures, Energy and Water Resources.

Theoretical Simulations of Materials for Nuclear Energy Applications

I. A. Abrikosov^{1,2}, A. V. Ponomareva², A. Y. Nikonov³, S. A. Barannikova^{3,4}, A. I. Dmitriev^{3,4}

¹*Linköping University, Linköping, Sweden*

²*National University of Science and Technology MISIS, Moscow, Russia*

³*Siberian Branch of Russian Academy of Science, Tomsk, Russia*

⁴*Tomsk State University, Tomsk, Russia*

INTRODUCTION

Ongoing development of next generation reactors strengthens demands on materials to be used in fission and future fusion reactors, which include good tensile and creep strength, as high as possible operational temperatures, a control over ductile to brittle transition temperature, resistance to irradiation, high thermal conductivity, low residual activation, compatibility with cooling media, and good weldability⁽¹⁾. A great challenge here is to identify potentially significant materials. New theoretical tools within the condensed matter physics allow one to capitalize on the power of modern computers, and greatly enhance a possibility for accelerated knowledge-based alloy design.

In this paper we discuss recent developments in the field of *ab initio* electronic structure theory and its use for studies of materials for nuclear energy applications. We review state-of-the-art simulation methods that allow for an efficient treatment of effects due to chemical and magnetic disorder, and illustrate their predictive power with examples of two materials systems, Fe-Cr-X alloys (X=Ni, Mn, Mo) and Zr-Nb alloys.

Ferritic body-centered cubic (bcc) Fe-Cr steels are used to manufacture reactor pressure vessels (RPV). Irradiation-induced accelerated ageing is considered to be a crucial issue that limits the lifetime of nuclear reactors. Fe-Cr steels with 7-18 at.% Cr are promising structural materials for fast neutron reactors due to their relatively low rate of swelling at elevated temperatures⁽¹⁾. Moreover, novel steels for RPV contain other elements, e.g. Ni, Mn, and Mo. Their effect on the stability of parent Fe-Cr alloy did not receive corresponding attention of the theory. We investigate the effect of multicomponent alloying on the mixing enthalpy of Fe-Cr alloys, and show that in the ferromagnetic state it reduces the alloy stability at low Cr concentrations.

Hexagonal closed packed (hcp) Zr-based alloys represent another material system widely used in nuclear energy applications, e.g. as fuel cladding materials. Alloying provides significant improvement of materials properties as compared to pure Zr. In particular, Zr-Nb alloys (with about 1 at.% Nb) show strengthening behavior due to polymorphous martensitic hcp \leftrightarrow bcc transition. However, an empirical approach is still taken for the selection of alloying additions [1], and improved understanding of Zr-based alloys is clearly required. Here we demonstrate how thermodynamic and elastic properties for these alloys can be systematically calculated from first-principles and argue that they can be used in higher-level simulations in the framework of the multiscale modeling.

THEORY

In this work we employ so-called *ab initio* or first-principles approach to simulate properties of alloy phases⁽²⁾. This means that we do not use any experimental or adjustable parameters in our simulations. Calculations are based on a solution to the quantum mechanical problem provided by the Density Functional Theory (DFT). However, in our case the application of the DFT formalism is highly non-trivial because substitutional solid solutions, considered in this work do not have any translational periodicity. The point is that in this case the group theory, which is the corner stone of the modern first-principles calculations, cannot be used directly. A detailed discussion of the problem can be found in Ref. ⁽²⁾.

In this work we employ the coherent potential approximation (CPA) for the description of chemical and magnetic disorder. Within CPA one reconstructs three-dimensional periodicity of the solid solution phase $A_{1-x}B_x$ by mapping it onto an ordered lattice of “effective” atoms, which describe the original system on the average. The effective atoms are placed at the sites of the original system. Their scattering properties have to be determined self-consistently from the condition that the scattering of electrons off the alloy components, embedded in the effective medium as impurities, vanishes on the average. The CPA is currently one of the most popular techniques to deal with substitutional disorder, and in this work we use it in the framework of the exact muffin-tin orbital (EMTO) theory as implemented in the EMTO-CPA software⁽³⁾. Details of the calculations for Fe-Cr alloys are the same as in Ref. ⁽⁴⁾, while for Zr-Nb alloys they are summarized in Ref. ⁽⁵⁾.

RESULTS

We start with the analysis of the mixing enthalpy ΔH^{mix} of Fe-Cr alloys. It often provides important insight into behavior of alloys upon ordering of phase separation. For a given system, an alloy or its pure components, the enthalpy $H = E + PV$ is calculated from their volumes V , CPA total energies E , and pressures P . For a binary system $A_{1-x}B_x$ one defines $\Delta H_{A_{1-x}B_x}^{mix} = H_{A_{1-x}B_x} - (1-x)H_A - xH_B$, where $H_{A(B)}$ represents the enthalpy of a standard state, taken in this work as enthalpies of pure alloy components. Positive values of ΔH^{mix} indicate a tendency towards phase separation of the solution phase, either into a mixture of pure elements or a mixture of ordered phases. However, the solution phases could be stabilized at high temperature, and remain metastable when the temperature is decreased. A condition for the spinodal decomposition of a binary alloy, which occurs in systems unstable to any concentration fluctuation, is given by inequality $d^2H/dx^2 < 0$. A generalization of this formalism for multicomponent systems is straightforward.

Calculated mixing enthalpy and its second derivative of ferromagnetic binary Fe-Cr alloys are shown in Fig. 1 with full orange lines. One sees that the alloy is stable at low Cr compositions, but has a tendency towards phase separation at higher concentrations. Experimentally it is known that though there is a miscibility gap for the alloy concentrations above 10 at. % Cr at room temperature, for lower concentrations of Cr the alloy is stable with respect to this decomposition. Therefore, our results are in excellent agreement with experiment. To investigate the effect of additional alloying elements on the stability of bcc Fe-Cr steels, we calculate the mixing enthalpies and their second derivatives for Fe-Cr-Ni and Fe-Cr-Ni-Mn-Mo systems. The results are shown in Fig. 1. One can see that these elements tend to destabilize solid solutions and enhance the tendency towards the spinodal decomposition. Indeed, ΔH is now positive for all Cr compositions, and d^2H/dc^2 changes sign at lower Cr concentrations.

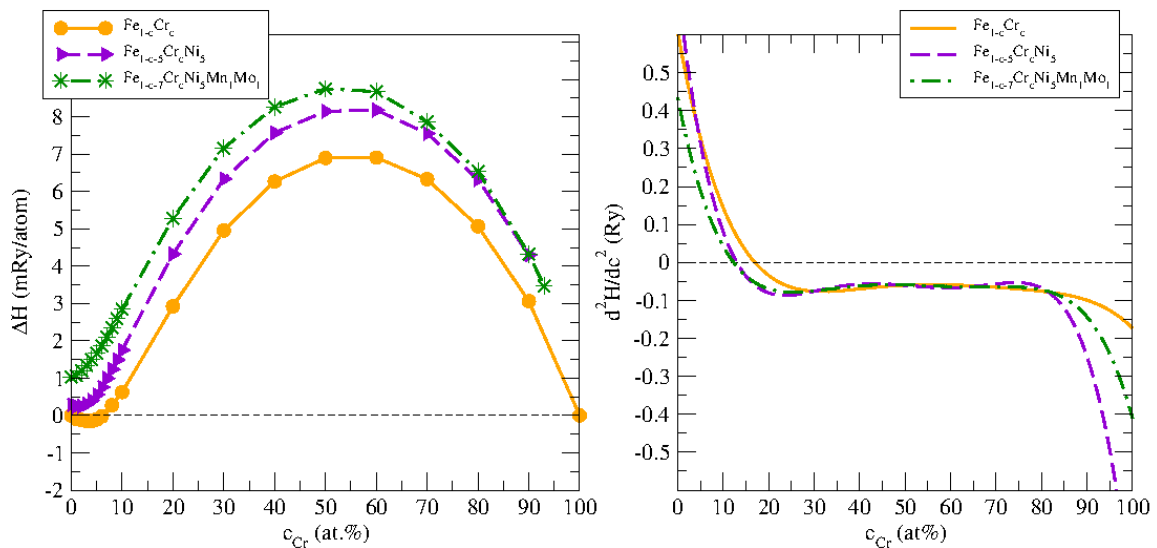


Figure 1. (left) Calculated mixing enthalpy and (right) its second derivative of ferromagnetic binary Fe-Cr alloys (full orange line, circles), as well as ternary alloys with 5 at. % Ni (dashed violet line, triangles), and

multicomponent alloys with 5 at. % Ni, 1 at. % Mn and 1 at.% Mo (dot-dashed green line, stars) as a function of Cr concentration

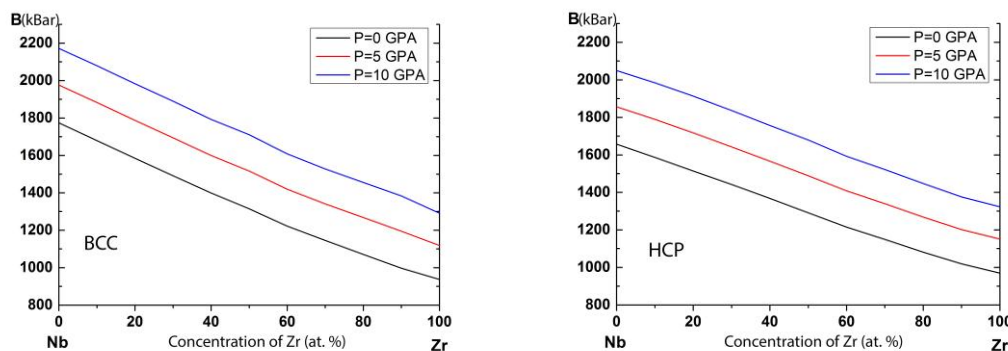


Figure 2. Calculated bulk moduli of Nb-Zr system as a function of Zr concentration in two crystal structures, bcc (left) and hcp (right), and at three values of external pressure, ambient pressure (black), 5 GPa (red) and 10 GPa (blue).

In order to illustrate capability of the theory to predict mechanical properties of alloys for nuclear energy applications, we show in Fig. 2 calculated bulk moduli of Nb-Zr system in the complete interval of concentrations and in two crystal structures, bcc and hcp. Here a comparison with experiment can be done for pure elements, and it is quite favorable. Indeed, for bcc Nb at ambient pressure and room temperature $B=1710$ kBar, while for hcp Zr it is 940 kBar, in good agreement with results, presented in Fig. 2. But theory can predict elastic properties even for systems which cannot be synthesized experimentally. This information is very useful, e.g. for higher level phenomenological models. For example, using this information it is possible to describe localized plastic flow auto-waves in deforming alloys⁽⁵⁾.

CONCLUSIONS

We have demonstrated that state-of-the art theoretical calculations have a capability to predict thermodynamic and mechanical properties of materials with very high accuracy, comparable to the experimental accuracy. Considering Fe-Cr alloys, we have investigated the effect of multicomponent alloying on their phase stability, and we have shown that alloying elements Ni, Mn, and Mo, present in RPV steels, reduce the stability of low-Cr steels against binodal, as well as spinodal decomposition. Considering Zr-Nb alloys, we have demonstrated a possibility of obtaining their elastic moduli from *ab initio* electronic structure calculations. We argue that theoretical simulations represent valuable tool for a design of new materials for nuclear energy applications.

ACKNOWLEDGMENTS

This study was supported in part by the Ministry of Education and Science of the Russian Federation within the framework of AMD3d project and Russian Foundation for Basic Researches (Grants No. 13-02-00606a, A.V.P. and No. 12-08-00960-a, I.A.D.)

REFERENCES

1. Marquis E. A. *et al.* *Nuclear reactor materials at the atomic scale*. *Materials Today* **12**, p.30-37, (2009).
2. Ruban A. V., Abrikosov I. A. *Configurational thermodynamics of alloys from first-principles: Effective cluster interactions*. *Rep. Prog. Phys.* **71**, p.046501-1 -30, (2008).
3. Vitos L., Abrikosov I. A., Johansson B. *Anisotropic lattice distortions in random alloys from first-principles theory*. *Phys. Rev. Lett.* **87**, p.156401-1-4 (2001)
4. Ponomareva A. V. *et al.* *Effect of pressure on phase stability of FeCr alloys*. *Phys. Rev. B* **84**, p.094422-6, (2011).
5. A. Barannikova, *et al.* *Significant correlation between macroscopic and microscopic parameters for the description of localized plastic flow auto-waves in deforming alloys*. *Solid State Commun.* **152**, p.784-787, (2012).

One-Group Cross Sections Generation for Monte Carlo Burnup Codes

D. Kotlyar¹, E. Shwageraus², E. Fridman³

¹*Ben Gurion University of the Negev, Be'er Sheva, Israel*

²*University of Cambridge, CB2 1PZ, Cambridge, United Kingdom*

³*Helmholtz-Zentrum Dresden-Rossendorf, Bautzner Landstraße 400, Dresden, Germany*

INTRODUCTION

Allowing Monte Carlo (MC) codes to perform fuel cycle calculations requires coupling to a point depletion solver. In order to perform depletion calculations, one-group (1-g) cross sections must be provided in advance. This paper focuses on generating accurate 1-g cross section values that are necessary for evaluation of nuclide densities as a function of burnup. The proposed method is an alternative to the conventional direct reaction rate tally approach, which is more computationally expensive. The method presented here is based on the multi-group (MG) approach⁽¹⁾, in which pre-generated MG sets are collapsed with MC calculated flux. In our previous studies⁽²⁾, we showed that generating accurate 1-g cross sections requires their tabulation against the background cross-section (σ_0) to account for the self-shielding effect. However, in previous studies, the model that was used to calculate σ_0 was simplified by fixing Bell and Dancoff factors. This work demonstrates that 1-g values calculated under the previous simplified model may not agree with the tallied values. Therefore, the original background cross section model was extended by implicitly accounting for the Dancoff and Bell factors. The method developed here reconstructs the correct value of σ_0 by utilizing statistical data generated within the MC transport calculation by default. The proposed method was implemented in BGCore code system. The 1-g cross section values generated by BGCore were compared with those tallied directly from the MCNP code. Very good agreement (<0.05%) in the 1-g cross values was observed. The method does not carry any additional computational burden and it is universally applicable to the analysis of thermal as well as fast reactor systems.

METHOD FOR 1-G CROSS SECTIONS GENERATION

BGCore is a system developed at Ben-Gurion University, in which MCNP4C⁽³⁾ is coupled with fuel depletion and decay module. BGCore utilizes MG methodology for calculation of 1-g transmutation cross-sections. In general, the 1-g cross section is an energy average, in which the reaction rate is conserved, and defined as:

$$\bar{\sigma} = \frac{\int \sigma(E)\phi(E)dE}{\int \phi(E)dE} \quad (1)$$

In the above formula, $\phi(E)$ is the energy dependent neutron flux (obtained from the neutron transport solution) and $\sigma(E)$ in the numerator is known (pre-generated) energy dependent microscopic cross section. In MG approach, Equation 1 is solved by transitioning from continuous to discrete representation of energy dependence (energy groups). In principle, increasing the number of energy groups, i.e. obtaining finer spectrum, is expected to improve the accuracy of the 1-g cross section value, at the limit approaching the continuous energy representation. However, MC codes cannot, in principle, recreate the fine group spectrum in unresolved resonances energy region because of probabilistic treatment of unresolved resonance parameters. This implies that averaging the cross section values over the unresolved resonances region may result in non-negligible error if Equation 1 is used directly.

In previous study⁽²⁾, the MG approach was extended by introducing the background cross sections (σ_0) tabulation into the calculation scheme. The background cross sections can take values between $0 < \sigma_0 < \infty$, since dilution is the concentration of the resonance absorber relative to concentration of all other nuclides. In order to calculate the background cross section, both energy and spatial contributions have to be accounted for. A typical approach for calculating background σ_0 used in many deterministic lattice codes⁽⁴⁾ is presented in Equation (2).

$$\sigma_{0,j} = \frac{\sum_{i=1}^M N_i \sigma_{p,i} + \frac{1/\bar{R}}{1/a + 1/\gamma - 1}}{N_j} = \frac{\sum_{i=1}^M N_i \sigma_{p,i} + 1/R^*}{N_j} \quad (2)$$

Where:

- i or j = isotope indexes number,
- M = total number of isotopes in the fuel,
- $\sigma_{0,j}$ = background cross-section of isotope j,
- N_j = atom density of isotope j,
- $N_i \sigma_{p,i}$ = potential macroscopic scattering cross-section of isotope i,
- a = Bell factor,
- γ = Dancoff factor,
- \bar{R} = mean chord length of a fuel element, which equals to $4V/A$, where V is the volume of the fuel region and A is the surface area.

In practice, a series of MG cross section sets is generated for selected isotopes with significant resonance cross-sections for several values of σ_0 .

However, this model was based on the assumption that the average chord length accounts for most of the spatial self-shielding effect, i.e. assumes $a = \gamma = 1$ (unless specified differently by the user). This assumption neglects the probability that a neutron born in a given fuel pin will experience next collision in another fuel pin (Dancoff factor) and also empirical correction to Wigner's rational approximation for the fuel pin escape probability (Bell factor). In order to execute BGCore, the user was required to provide the mean chord length as a part of the input to BGCore.

In some cases however, the assumption that $a = \gamma = 1$ is not universally applicable for calculating 1-g cross section. Here, we propose a modified approach for accounting for the spatial effects in the calculation of 1-g cross sections. The method relies on generated statistical data that allows calculating the term

$R^* = \frac{1/\bar{R}}{1/a + 1/\gamma - 1}$ in Equation 2 automatically without requiring any intervention or input from the user, and

consequently allows for more accurate prediction of the nuclide specific background σ_0 .

$R^* = R^*(\bar{R}, a, \gamma)$ is an "effective" mean chord length, which already includes all the spatial effects described by the Bell and Dancoff factors. The 1-g cross section calculation process based on the R^* evaluation can be broken down into following five stages:

1. Calculation of the 1-g absorption cross section $\bar{\sigma}_a^j$ for each nuclide j based on MCNP collision statistics (collected by default during neutron transport solution),
2. Reconstruction of R_j^* for each nuclide j based on linear interpolation of $\sigma_{0,j}$ vs. $\bar{\sigma}_a^j$,
3. Calculation of a single weighted average \bar{R}^* value to be used for calculation of self-shielding factors,
4. Calculation of $\sigma_{0,j}$ for each resonant nuclide j - the value is obtained by applying Equation 2
5. Linear interpolation to obtain self-shielded 1-g cross section value.

Detailed description of the implemented routine for estimation of R^* as used in BGCore is provided in Reference 5.

VERIFICATION OF THE PROPOSED METHODOLOGY

Verification of the proposed method was performed using the Sodium cooled Fast Reactor (SFR) assembly model developed in the framework of CP-ESFR project⁽⁶⁾. This case was chosen due to the high absorption rate (38.5% of the total absorption rate) in unresolved energy region, thus leading to substantial importance of the self-shielding effects in this region.

The examination of the \overline{R}^* (as defined in Equation 2) calculation procedure was performed with the cross section data evaluated at 300K because of the stronger self-shielding effect at low temperatures.

In order to demonstrate the effect of the cross section correction on the accuracy of the results, the depletion of the fuel assembly was performed twice: 1) using infinitely diluted cross sections, and 2) using cross sections that are reconstructed accordingly to the presented method (designated as corrected (a, γ)). The MG data set in this case was generated in 50,000 energy groups as proposed by Fridman et al.⁽²⁾. The depletion results are presented in Figures 1 through 2. The figures show k-inf as a function of burnup (Figure 1) and the burnup of Pu239 (Figure 2).

Clearly, the scheme of generating 1-g cross-sections based on universal set of infinitely diluted cross sections results in a systematic inaccuracy. For example, the difference in 1-g values between the infinitely diluted cross sections and the reference solution (direct tally) is 1.6% at zero burnup. This, in turn, leads to inaccuracies in the specific isotopes concentrations, such as Pu239 (Figure 2), resulting from the depletion calculations, and therefore limit the quality of the overall depletion results.

The proposed σ_0 tabulation model (with inherently correct a and γ values) improves the accuracy of the 1-g cross-sections. Omitting this correction results in a large deviation that affects the overall depletion results, as demonstrated in the burnup of Pu239 (Figure 2). Although, implementation of the simplified σ_0 model ($a=\gamma=1$) can reduce the deviations by a factor of 2 to 5, the assumption of $a=\gamma=1$ is not universally applicable. In the examined case, the deviation from the reference value in predicting the 1-g cross section for U238 by using the simplified model (i.e. $a=\gamma=1$) was 0.65%. The proposed method that accounts the Dancoff and Bell corrections demonstrated significant improvements in generating 1-g cross section for various nuclides.

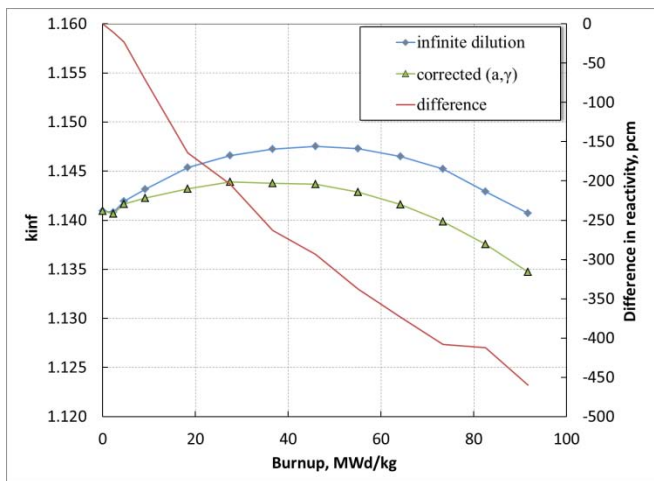


Figure 1. Comparison of k-inf, infinite dilution vs. corrected (a, γ) cross sections

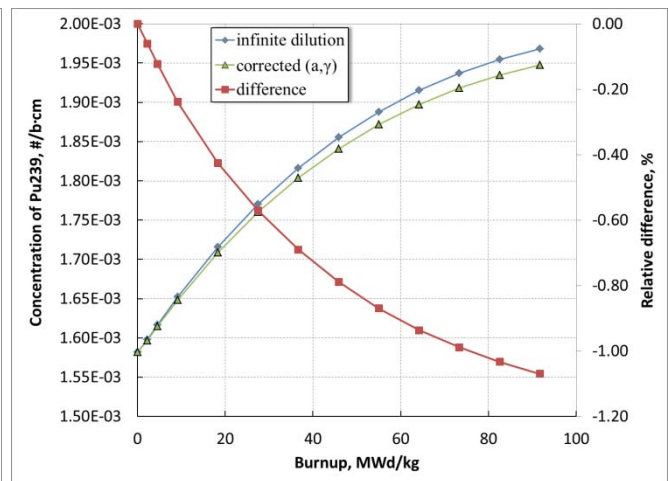


Figure 2. Comparison of Pu239 concentration, infinite dilution vs. corrected (a, γ) cross sections

SUMMARY AND CONCLUSIONS

Performing depletion calculations in coupled MC codes requires the knowledge of 1-g cross section for all relevant isotopes. The new subroutine implemented in BGCORE code for taking into account the spatial shielding effects typically represented by the Bell and Dancoff factors produces high accuracy results without requiring any additional calculation time. The modified MG method relies on automatically generated MCNP statistical data that allows reconstruction of the Bell and Dancoff factors. The method was tested on a typical Sodium cooled fast reactor assembly design. The results show that using the original MG approach⁽⁷⁾, e.g. in ALEPH code, leads to prohibitively large systematic errors. The main conclusion of this

work is that the correction for calculating the effective chord length introduced into BGCORE is essential in order for the code to be universally applicable to the analysis of a wide range of reactor systems. The presented method takes into account the fuel lattice geometry effects commonly described by the Bell and Dancoff factors and yields correct values of the 1-group cross sections for fast as well as thermal spectrum systems.

REFERENCES

1. Fridman E., Shwageraus E., Galperin A., *Implementation of multi-group cross-section methodology in BGCORE MC-depletion code*, In: Proceedings of PHYSOR 2008, Interlaken, Switzerland (2008).
2. Fridman E., Shwageraus E., Galperin A., *Efficient generation of one-group cross sections for coupled Monte Carlo depletion calculations*, Nuclear Science and Engineering, 159, 37-47 (2008).
3. Briesmeister J. F. Ed., *MCNP - A General Monte Carlo N-Particle Code, Version 4C*, Los Alamos National Laboratory, LA-13709-M (2000).
4. Segev M., *Applied Resonance Equivalence*, Nuclear Science and Engineering, 111,271 (1992).
5. Kotlyar D., *Development of new computational capabilities in BGCORE system*, M.Sc thesis, Ben Gurion University of the Negev, Be'er Sheva, Israel (2010).
6. Fiorini G.L., Vasile A., *European Commission – 7th Framework Programme: The Collaborative Project on European Sodium Fast Reactor (CP ESFR)*, Nuclear Engineering and Design, A., 3461 (2011).
7. Haack W., Verboomen B., Abderrahim H.A., *ALEPH-An Efficient Approach to Monte-Carlo Burn Up*, Proc. The Monte-Carlo Method Versatility Unbounded in a Dynamic Computing World, Chattanooga, Tennessee (2005).

Improving Conversion Ratio of PWR with Th-U²³³ Fuel Using Boiling Channels

M. Margulis, E. Shwageraus

Ben-Gurion University of the Negev, P.O.B. 653 Beer-Sheva 84105, Israel

INTRODUCTION

The goal of this study is to develop a Pressurized Water Reactor with improved fuel utilization. This can be achieved through the use of Th-U²³³ fuel cycle. In recent studies, a number of options for employing Th-U²³³ fuel cycle in a typical PWR core were investigated (Kotlyar and Shwageraus⁽¹⁾, Volaski et. al.⁽²⁾ and Boldova and Fridman⁽³⁾). These studies focused on achieving breeding through optimization of fuel geometry, pins arrangement within the assembly and fuel composition. The results indicated that creating a self-sustainable Th-U²³³ PWR fuel cycle requires transition from homogeneous to heterogeneous configuration, a fissile rich (seed) zone and the fertile (blanket) zone to improve the neutron absorption by Th²³². However, unavoidable consequence of this heterogeneous arrangement would be much higher than typical power peaking, leading to higher fuel temperature and heat fluxes in the high power locations. As a result, the safety constraints will inevitably limit the achievable core power density. Although the mentioned studies (1, 2, 3) presented designs that potentially could achieve conversion ratio advantage of the concept. This study presents the first attempt to optimize a high conversion ratio PWR without reducing the core power density below nominal 104 W/cc. The main idea is to create an intermediate spectrum by allowing partial two phase flow regime inside the seed zones. This in turn reduces moderation and improves the breeding performance. In addition, large latent heat of coolant phase transition allows removing much higher power from the same volume. Boiling heat transfer is also more efficient as long as bubbly flow regime is maintained. Although, in conventional PWRs, limited sub-cooled boiling is allowed, it is an undesired phenomenon because it leads to preferential deposition of crud, precipitation of soluble boron and resulting axial power shape distortion. In high conversion PWRs (1, 2, 3) however, the excess core reactivity is very small and may allow operation entirely without soluble boron using only mechanical (control rods) shim. In such case, boiling may no longer be an issue as long as the operating and safety envelope of the core is preserved. Some thermal hydraulic design issues however may still need to be addressed requiring further studies. The fuel center line temperature (T_{CL}) could remain above the limiting value of no melt incipient under anticipated transient conditions. A possible solution to reduce T_{CL} , is to increase the number of seed fuel pins by reducing their lattice pitch without changing the original seed region volume fraction. Larger number of seed pins would reduce the linear heat generation rate and the heat flux. This modification however, implies that seed and blanket pin lattices would no longer have the same pitch.

The high conversion partially boiling PWR core design would have to meet the following design objectives and constraints. The core design should have conversion ratio greater than unity to assure sustainable fuel cycle. Reasonably long fuel cycle length of at least one year of continuous operation should be maintained. Core safety margin at steady state should not be compromised and maintained similar to the conventional LWR designs. In addition, despite the boiling in the seed channels, the outlet core average coolant enthalpy should be the same as in a typical PWR. In other words, the coolant must still be sub-cooled at the core outlet after two-phase flow from the high power seed channels is mixed with a single phase coolant from the lower power blanket channels. Finally, the coolant flow pressure losses should not require replacement of the existing main recirculation pumps. The 2D analysis performed here, confirms that such PWR (with boiling channels) design is feasible in principle.

HIGH-CONVERSION Th-U233 FUEL ASSEMBLY OPTIMIZATION

A number of modifications were made to the original reference design (2) to allow boiling regime in the seed region, while keeping fissile inventory ratio (FIR) above unity:

1. Blanket size optimization (section 1).
2. FIR as a function of seed size (section 2).
3. Blanket fuel material - ThO₂ vs. ThH₂ (section 3).

The end of life (EOL) was chosen to be 900 days and requires adjustment of the initial fuel assembly enrichment. For each studied case, we examined the reactivity as a function of time behavior in order to determine the discharge burnup.

This study relied on two computational tools in order to perform the optimization. The first is BOXER code, which is a part of the ELCOS package for steady state simulation of light water reactor cores, Paratte et al.⁽⁴⁾. The second is SERPENT, which is a continuous energy Monte Carlo (MC) neutron transport code with burnup (BU) capabilities, Leppänen⁽⁵⁾.

1. Blanket size optimization

The effect of reduced moderation on breeding performance in PWRs was studied in detail by Utoinen et al.⁽⁶⁾. In their study, reduced moderation resulted in better breeding performance, which was also observed here. Introducing boiling in the seed region improves the breeding performance (i.e. higher FIR at EOL) compared to zero void value. This is because higher void fraction increases the leakage rate into the blanket and somewhat hardens the spectrum also increasing the resonance absorption in Thorium.

The blanket region size in the reference model (2) was selected to maximize the capture of neutrons leaking from the seed region. Due to the fact that the operating conditions in the seed region were changed, the blanket region had to undergo a modification in order to improve neutron captures. Moreover, we investigate the use of two possible fuel forms for the blanket region - ThH₂ and ThO₂. Each fuel form presents potential advantages. On one hand, admixing moderator material to the fuel in the ThH₂ case also improves the resonance captures in Th because of the lower self-shielding, ultimately resulting in better breeding performance. In addition, thermal conductivity of hydrides is much higher than in the oxide fuel. On the other hand, ThO₂ has a much higher melting point and its performance as a nuclear fuel is much better understood.

A model of seed assembly surrounded by a large blanket zone was created in SERPENT. We then examined the cumulative neutron captures in the blanket as a function of distance from the seed, while changing the seed coolant void fraction. The blanket region size was selected at the point where the cumulative captures reached 95% of total, as shown in Figure 1 for ThO₂ and ThH₂ blanket materials with the latter being much smaller. The results in Figure 1 are not surprising due to the less efficient neutron moderation in ThO₂ in comparison to ThH₂. The less expected result is that the void fraction in the seed has remarkably small effect of the capture rate distribution in the blanket.

2. FIR vs. seed assembly size and pin dimensions

In the next step, different seed assembly arrays of $N \times N$ pins were examined. The seed pins were placed in the assembly center and surrounded by the blanket with dimensions determined in the previous section. The core power density was assumed to be fixed at 104 W/cc and have different void fractions in the seed, varied from 10% to 30%. The fissile material content was adjusted to achieve the same cycle length of 300 days (or 900 days total in core residence time).

Furthermore, the effect of the seed pin geometry modifications on FIR was also examined. The reference seed pin radius selected to be that of a typical PWR, 0.4095 cm. Then, the pin radius was increased by 10% and 20%, while the cell pitch remained fixed at 1.26 [cm] (although it may need to be reduced to reduce the linear heat generation rate as discussed earlier). A setup example is shown in Figure 2. The results for the 2D simulations obtained from BOXER are shown in Figures 3 and 4.

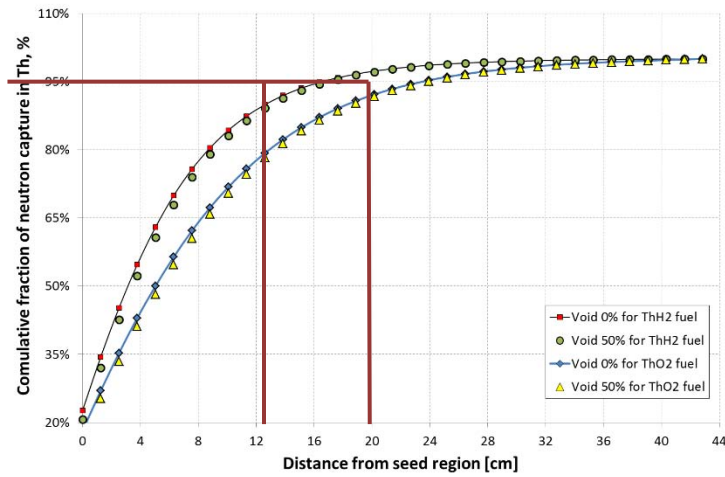


Figure 1. Cumulative fraction of neutron capture in Th for ThH₂ and ThO₂

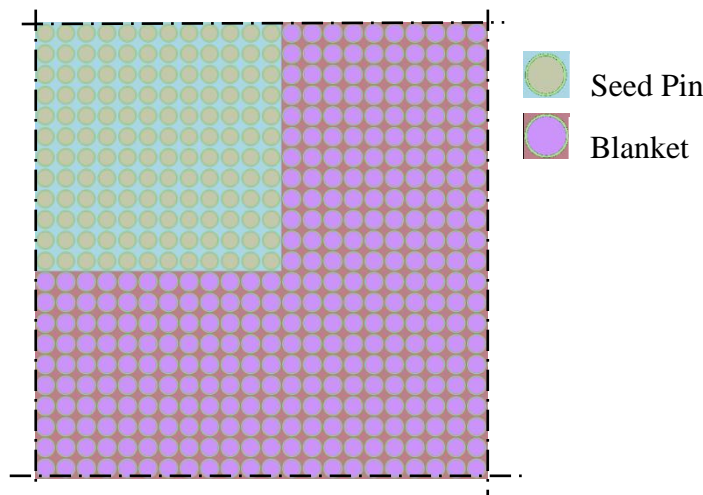


Figure 2. Quarter of a high-conversion Th-U233 fuel assembly

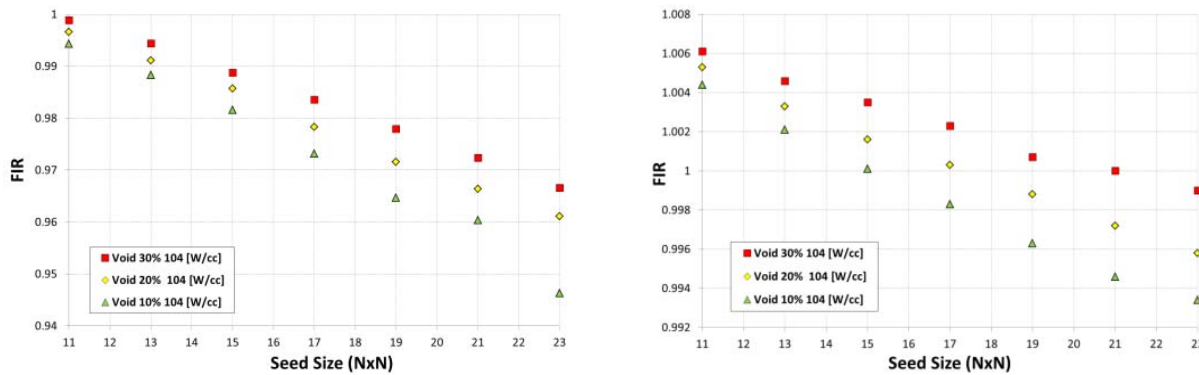


Figure 3. FIR at EOL as a function of seed size, ThO₂ fuel, $R_s=0.4095, 0.4914$ [cm]

The results presented in Figure 3 suggest high sensitivity of FIR to the seed pin dimensions and coolant void fraction. Reduced moderation (higher void fraction and larger pin diameter) improves the breeding significantly. The seed region size (total number of seed pins) also has significant effect on the breeding. Reducing the seed region size improves FIR but it also requires higher initial fissile content, as can be seen in Figure 4 for the void fraction of 20% and different fuel types. Smaller seed region also implies smaller relative volume fraction of the seed (Figure 5) and thus higher power peaking, which will most definitely challenge the core thermal design. Seed fuel pin radius of 0.4914, average void fraction of about 20% and

15x15 to 17x17 seed array size seem to provide reasonable combination of parameters to achieve FIR~1 at the reference core power density.

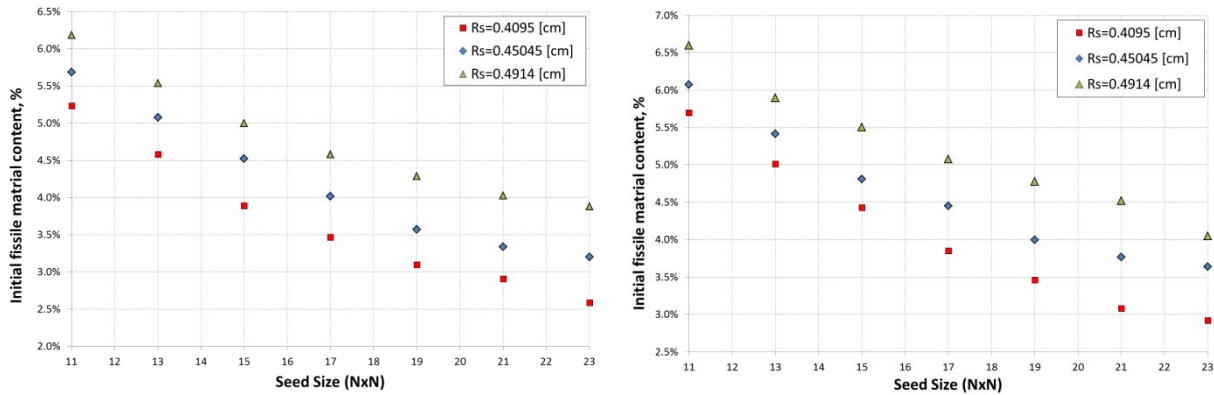


Figure 4. Initial fissile material content as a function of seed size with void fraction of 20% (Left – ThH₂, Right – ThO₂)

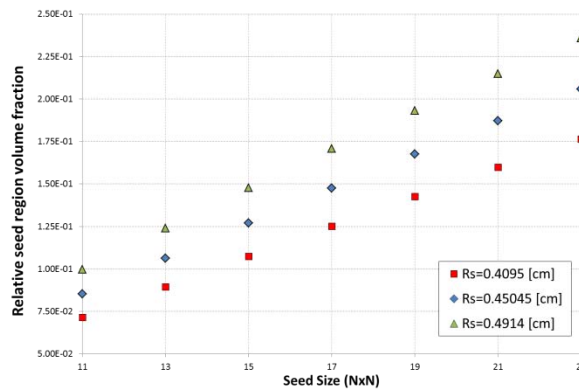


Figure 5. Relative seed region volume fraction vs. seed size

3. Blanket fuel material - ThO₂ vs. ThH₂

The calculation in the previous section suggested that ThO₂ fuel in the blanket would be preferred over ThH₂ fuel in order to achieve FIR above unity at EOL. However, the use of hydride fuel form improves the moderation and creates a much more thermalized neutron spectrum in the blanket region. This, in turn, should increase the neutron absorption in thorium and reduce the relative blanket volume fraction, consequently allowing tolerating higher seed region power density. Figure 1 clearly demonstrates that the blanket thickness should be only 17.64 cm as opposed to 25.2 cm in ThH₂ and ThO₂ cases respectively. Although, high thermal flux increases the probability of neutron capture in the thorium, it also increases the burnup rate of U²³³ once it is accumulated in substantial quantities resulting in less efficient breeding performance on the overall balance. Furthermore, absorption in hydrogen contained in the fuel is also non-negligible which also negatively affects breeding.

Therefore, it can be concluded that ThO₂ is a preferable choice of blanket fuel form from the breeding performance point of view. This assertion however will have to be confirmed by thermal hydraulic analysis in which power density distribution considerations may prove otherwise.

CONCLUSIONS

This work explored the basic neutronic design considerations of a PWR seed-blanket fuel assembly with boiling channels in order to achieve FIR above unity at EOL. More precisely, the effect of various parameters, such as – void fraction in the seed region, seed size (number of seed pins) and seed pin diameter, on breeding was investigated. The optimization process also included selection of the blanket size

and selection of the blanket fuel material. The results of the optimization suggest that certain combination of studied design parameters (void fraction, seed region size and pin radius) would indeed result in net breeding. It was found that, in general, reduced moderation improves the breeding performance. Such reduced moderation can be achieved through combination of void fraction on the order of 20% and larger than standard pin diameter.

The calculations performed in this work were based on the assumption of a uniform axial void distribution, which would clearly not be the case. Therefore, 3D fuel assembly analysis coupled with thermal hydraulic feedback would be required to confirm feasibility of this design concept.

AKNOWLEDGMENTS

This work was sponsored by research grant from the US-Israel Binational Science Foundation Grant #2009560.

REFERENCES

1. D. Kotlyar, E. Shwageraus, *Neutronic Optimization in High Conversion Th-233U Fuel Assembly With Simulated Annealing*, PHYSOR, Knoxville, TN USA (2012)
2. D. Volaski, E. Fridman, E. Shwageraus, *Thermal Design Feasibility of Th-233U PWR Breeder*, Proc. Global, Parish, France, p. 9248 (2009)
3. D. Boldova, E. Fridman, *High Conversion Th-U233 Fuel Assembly for Current Generation of PWRs*, **Before submission**
4. J. Parette, K. Foskolos, P. Grimm, C. Maeder, *Das PSI Codesystem ELCOS zur Stationären Berechnung von Leichtwasserraktoren*, Proc. Jahrestagung Kerntechnik, Travemünde, Germany p. 59, (1998)
5. J. Leppänen, *Development of a New Monte Carlo Reactor Physics Code*, D.Sc. Thesis, Helsinki University of Technology, VTT Publications 640 (2007)
6. V.O. Uotinen et al, *Technical Feasibility of Pressurized Water Reactor Design With a Low Water Volume Fraction Lattice*, EPRI NP-1833 Final Report (1981)

A Multi Region, Multi Energy Formalism for the Feynman-Alpha Formulas

T. Malinovitch¹, C. Dubi¹

¹ Nuclear Research Center of the Negev, Israel

INTRODUCTION

The stochastic transport equation, which describes the dynamics in time of neutron population in a nuclear system, is used to gain expressions for higher moments of the neutron population. Unlike the Boltzman equation, where the conservation laws are given in terms of the average neutron population in a given region and energy, the stochastic transport equation describes the conservation laws in the system in terms of the complete probability theorem, and thus enabling us to describe the distribution in its entirety rather than just the average number of neutrons in the system.

This type of analysis is especially important in "Noise experiments", originating from Feynman's seminal work⁽¹⁾, where the variance to mean ratio (or the Feynman-Y function) is used to determine the multiplication factor of a sub-critical system near criticality in the presence of a Poissonic source.

A second application for the stochastic transport equation is in the so-called Neutron Multiplicity Counting (NMC) methods. In NMC the first three moments of the detected neutrons are used to separate between neutrons originating from spontaneous fission and neutrons originating from induced fissions and alpha-neutron reactions, in order to estimate the mass of fissile material in a sample. It is important to note that in order to apply the results to NMC calculations, there is a need to derive the third moment of the number of detections, and not only the first two, as needed for the Noise experiments.

Feynman's original work (as well as all present NMC models) is done under the assumption of a single spatial region and a single energy group, taking into account only the prompt neutrons. Or, equivalently, we consider a single homogenized cross sections set and a single detection efficiency. Lately, there is an academic interest in expanding this theory into more complex settings. In particular, a two regions (single energy group) model has been introduced⁽²⁾, an expansion to two energy groups⁽³⁾ (and one region), and the effect of a time varying source⁽⁴⁾.

In the present study, we generalize the results introduced^(2,3) into the most general setting of N regions and M energy groups combined. In addition, the paper also deals with a general multiplicity of both the source and the fissions.

The basic idea which allows simplifying the formulas is the simple observation that from a mathematical point of view, there is almost no difference between spatial and energetic distribution. Or, in other words, we could treat the system, at least from a formal point of view, as a single vector of "space-energy" cells, distinguished only by their cross sections. Thus, fairly simple matrix expressions may be derived for the average and centralized variance matrix (in order to maintain applicability for NMC and Noise experiments, the first three moments of the number of detection is derived).

In the simple case of a finite detection window, opening long after the system reached equilibrium, a closed analytic formula may be derived for the N regions and M energy group the Feynman-Y function. The resulting expression for the Feynman-Y function is quite complicated, and in the general form contains an integral over a complicated matrix expressions, though it clearly contains the same time dependence as the classic one-region one energy group expression.

An interesting conclusion from the expression derived, is generalization to the well-known (and significant) fact that the single energy point-wise Feynman-Y function does not depend on the source strength. We show that the multi-region, multi-energy Feynman-Y function depends only on the relative strength of the source in the different energy-region cells. As a result, the Feynman-Y function does not depend on the source only if the source is either contained in one energy-region cell, or distributed homogeneously throughout the system.

REFERENCES

1. R.P. Feynman, F.de Ho_mann, R. Serber. *Dispersion of the neutron emission in U-235 fission*, Journal of Nuclear Energy, vol.3 (1956) 64.
2. J. Anderson, D. Chernikova, I. Pazsit, L.Pal and S. A. Pozzi. *Two-point Theory for the differential self-interrogation Feynman-alpha method*, Eur. Phys. J. Plus 127: 90 (2012).
3. L.Pal and I. Pazsit. *Two-Group Theory of the Feynman-Alpha Method for Reactivity Measurement in ADS*, Hindawi Publishing Corporation, Science and Technology of Nuclear Installations, Volume 2012 Article ID 620808 (2012).
4. M. Ceder, I. Pzsit. *Analytical solution for the Feynman-alpha formula for ADS with pulsed neutron sources*. Prog. nucl. Energy 43, 429 - 436 (2003)

Fuel Management Optimization of Pebble-Bed Reactors Using Particle Swarm Algorithm

B. Tavron¹, E. Shwageraus²

¹Israel Electric Corporation, Haifa, Israel

²Ben-Gurion University, Beer-Sheva, Israel

INTRODUCTION

The on-line fueling and thermo-mechanically stable fuel of the Pebble-Bed Reactors (PBR) allow flexible fuel management operation. PBR fuel pebble contains robust TRISO fuel particles which demonstrated safe operation at very high burnup of up to 140000 MWD/THM in test reactors and up to 7000000 MWD/THM in some experiments ⁽¹⁾. TRISO particles have been recently confirmed to retain fission products at temperature of 1800 C ⁽²⁾. Fissile and/or fertile fuel materials may be loaded into fuel pebbles. PBR fuel management deals with decisions on re-circulation of the different fuel pebbles through the core and optionally their radial loading location. Fuel pebbles may be re-circulated through the core several times (4-6) until reaching their target burnup, or they can reach their target burnup in single pass through the core (OTTO- Once-Through-Then-Out fueling Scheme). Pebble-bed reactors also feature efficient neutron economy since they operate with low excess reactivity which minimizes the use of neutron poisons and control rods. These features enable very flexible fuel management. Thus, meta-heuristic optimization technics for improving PBR performance with respect to fuel utilization can be applied. Traditionally, fuel cycle design decisions were made using expert decisions and parametric studies ⁽³⁾. In this work, we have used the Particle Swarm Optimization (PSO) meta-heuristic algorithm to optimize PBR fuel utilization.

Natural uranium utilization optimization was carried out for a large core design ⁽³⁾ running OTTO fuel management and for a modular core design (PBMR400 ⁽⁴⁾) with recirculating fuel management (also referred to as MEDUL for Mehffachdurchlauf, which is "multi-pass" in German). Optimization parameters include fuel enrichment, heavy metal loading at two radial fuel loading zones.

DEFINITION OF THE OPTIMIZATION PROBLEM

The optimization objective is to maximize natural uranium utilization, by searching for the most efficient fuel management operation under reactor operational constrains. The natural uranium fuel utilization is calculated by:

$$NUU = \frac{Q}{\sum_i m_{U,i} LR_i FF_i} ; FF_i = \frac{F}{P} = \frac{X_{p,i} - X_w}{X_f - X_w}$$

Where:

$m_{U,i}$ - Mass of uranium per pebble in zone i , kg,

LR_i - Pebbles feed rate in zone i , #/day,

FF_i - Natural Uranium enrichment feed factor for fuel pebbles in zone i ,

F - Mass of natural uranium (feed material), kg,

P - Mass of enriched uranium (product material), kg,

Q - Reactor power, MW,

For the material stream of enrichment process:

$X_{p,i}$ - Weight fraction of U235 in the product

X_f - Weight fraction of U235 in the feed (natural U - 0.7%)

X_w - Weight fraction of U235 in the waste (tails, we use 0.2%)

The natural uranium utilization (NUU) units are MWDth/kgNU. The NUU is calculated for the equilibrium core, in which the feed fuel enrichment is constant over time. Equilibrium cycle calculations were performed under common PBR operational constraints of maximum pebble power of 4.5 kW and maximum fuel temperature of 1150 C. These constraints are set to ensure that fuel temperature would not exceed the safety limit of 1600 C under worst accident (DLFOC - Depressurized Loss of Forced Cooling)

The VSOP code system is used to simulate the fuel cycle of the reactor ⁽⁵⁾. The VSOP is a system of codes for the simulation of pebble-bed reactors with treatment of its special features, such as "double heterogeneity" and on-line continuous fuel loading. Unit-cell spectrum calculations in VSOP are performed by the THERMOS, ZUT and GAM codes for the thermal, the resonance and the epi-thermal energy spectrum regions, respectively. These codes apply various approximations to the transport equation to accommodate special features of pebble-type fuel with coated fuel kernels. Power and neutron flux distributions are then calculated by the 2D diffusion program CITATION. Burnup calculations and fuel shuffling operations are performed by the FEVER code. Thermo-hydraulic and fuel cycle cost calculation are performed by THERMIX and KPD codes.

The fuel cycle optimization parameters are HM loading and fissile enrichment per pebble, for each fuel loading zone. The pebble feed rate which is calculated using dedicated MATLAB script for maintaining the equilibrium cycle, is dependent on these optimization parameters. In the equilibrium core, the neutron flux, power and material composition do not change considerably over time. The algorithm used in MATLAB script is described below:

Step 1: Initial core loaded with fresh fuel, operates until reaching criticality. Perform the fresh core burnup calculation until criticality is reached.

Step 2: Perform fuel management operations (core refueling with small batch fuel loading increments) and continue the core burnup simulating reactor life:

- Continuously load and discharge fuel pebbles from the core in small batches (in OTTO fuel management scheme load only fresh fuel). Iterate on feed rate to achieve critical core.
- Repeat core burnup cycles until equilibrium condition is reached (no change in fuel feed rate to maintain criticality).

Step 3: Check constraints compliance; Obtain fuel pebbles feed rate LR_i from equilibrium core and calculate Natural U utilization.

PARTICLE SWARM OPTIMIZATION

PSO is an evolutionary optimization algorithm that is inspired by the social behavior swarms like a flock of migrating birds trying to reach an unknown destination (or food)⁽⁶⁾. PSO has been found to have superior performance in several benchmarks [4]. This stochastic algorithm mimics the behavior of the birds in the flock, which communicate with one another as they fly. In PSO, each solution is a "bird" in the flock and is referred to as "particle". Each bird in the flock looks in a specific direction and also identifies the bird with the best location in the flock. The bird is then speeds to a new location depending on own search (own experience) and a global search (flock experience). The process repeats until it reaches desired destination (convergence).

The process is initialized with generating a swarm of N random particles (solutions), which, in our case, we generated using the Latin Hypercube⁽⁷⁾ sampling technic to ensure an even sampling from the search space. Each particle i is characterized by a location vector x_i and a speed vector v_i . The location quality of each particle p_i , is calculated by the objective function, i.e. the natural uranium utilization - NUU. G represents the global best location of the swarm up to the current time step. Advancing from time step k to $k+1$, each particle updates its location $x_i(k+1)$ by the speed vector $v_i(k+1)$. The updated speed vector depends on previous speed, previous best location and global best location weighted by the algorithm parameters w , c_1 , c_2 and with additional random weighting γ_1 and γ_2 . Hence the algorithm formulas are:

$$v_i(k+1) = wv_i(k) + c_1\gamma_1(p_i - x_i(k)) + c_2\gamma_2(G - x_i(k))$$

$$x_i(k+1) = x_i(k) + v_i(k+1)$$

Some PSO algorithm extensions found to improve its performance have been implemented: "Maximum velocity", "Queen Particle", "Constriction coefficient" and "Acceleration factor". These extensions are described in ref⁽⁸⁾. Based upon tuning experiments for a simplified PBR optimization case, population size of 15 and the learning factors of $c_1=1$ and $c_2=3$ have been selected.

RESULTS

OTTO fuel cycle optimization calculations were performed for a large two zone core of 3000MW thermal power and core dimensions of 5.89m radius and 5.5m height. Standard 6 cm fuel pebbles with TRISO type coated particles were used. Detailed core and fuel design parameters were adopted from reference 1. Optimization was carried out for all uranium fuel - LEU case (UO₂), for mixed oxide Thorium-Uranium fuel - Th-MOX case (Th-U)O₂ fuel and for separate seed (UO₂) and breed (ThO₂) pebbles – SEP case. Heavy metal loading ranged between 3 to 25 g per pebble and U enrichment ranged from natural enrichment (0.7%) up to 20% which is IAEA statutory proliferation limit. For the mixed oxide fuel, additional hypothetical case has been calculated allowing enrichment up to 90%. For the calculations of fuel cost, prices were obtained from the WISE internet site⁽⁹⁾ (accessed on 01/09/2013): Uranium ore purchase 32.15 \$/lb U₃O₈; Conversion: 9 \$/kg U; Enrichment: 105 \$/kg SWU, fabrication costs - 4100 \$/kg U (from Eskom estimations). Th costs are assumed to be low and hence neglected, Th pebble fabrication costs are assumed to be the same as for the uranium pebbles. OTTO fuel cycle optimization results of a two-zone core are presented in Table 1.

Table 1. OTTO fuel cycle Optimization Results.

		Optimization Results 2-loading zones core								
Case		LEU		Th-MOX U enrichment constrained to 20%		Th-MOX Unconstrained		SEP U enrichment constrained to 20%		
zones		1	2	1	2	1	2	1	2	
Input	Loading Fraction	0.735	0.265	0.735	0.265	0.735	0.265	0.735	0.265	
	HM Loading (g/pebble)	6.82	6.95	7.43	7.52	12.1	17.0	Seed: 7.08; Breed: 20.8; Graphite:0		
	Pebble Fraction (%)	-	-	-	-	-	-	S	B	G
								57	32	11
								64	26	10
	HM Enrichment	0.084	0.086	0.10	0.11	0.08	0.08	0.2		
	U Enrichment	0.084	0.086	0.2	0.2	0.734	0.775	0.2		
	Ave. Th fraction	-		54%		90%		60%		
Moderation Ratio	551	541	500	493	303	212	455	476		
Ave Moderation Ratio	548.73		497.8		278.7		461.2			
Output	Fuel residence time (days)	706.4		917		1250		987.2		
	Load rate (Pebble/day)	8608		6633		4863		6160		
	Power Peak Max/Ave	3.56		3.36		3.34		4.55		
	Max. Power (KW/ pebble)	3.28		3.1		3.08		4.2		
	Max. Fuel Temperature C	1062.5		1041.3		1185.2		1038.3		
	Discharge Burnup (MWD/kg)	105212		127394		94728		97822		
	Fuel Utilization (MWD_{th}/kg NU)	5.779		5.737		5.935		5.753		
	SWU Utilization (MWD _{th} /kg-SWU)	5.442		4.855		4.637		4.877		
	Plutonium production rate, (kg/GWe-Y)	24.942		12.836		1.764		11.315		
	Fuel Cycle Cost (mills/kWhe)	5.601		4.681		5.342		4.614		

MEDUL fuel cycle optimization calculations were performed for the South-African modular core design - the PBMR400⁽⁴⁾. PBMR400 has an annular core with fixed central reflector of 1 m radius, radial thickness of 85 cm and height of 11 m. Detailed core description is taken from ref 2. The number of fuel recirculation passes through the core significantly affects the axial core power distribution, as shown on fig.1 below. When the fuel pebble passes only once through the core (OTTO fuel cycle), power density distribution peaks significantly towards the top of the core. This high power means also high fuel temperature which limits OTTO fuel cycle cores overall power rating. In the cases where fuel pebbles recirculate more than once through the core, the axial power peak is reduced by as much as a factor of two. In the MEDUL fuel cycle, a mixture of fresh fuel with partly burned fuel is loaded to the core, lowering power density at the upper core area. Circulating the fuel pebbles more than 6 times through the core has no longer appreciable effect on the axial power shape. Therefore, in PBMR400 model, we adopted 6-passes MEDUL fuel cycle for the optimization study. Initial results indicate that MEDUL case allows achieving somewhat higher fuel utilization than OTTO cycle. Although this part of the analysis is still ongoing.

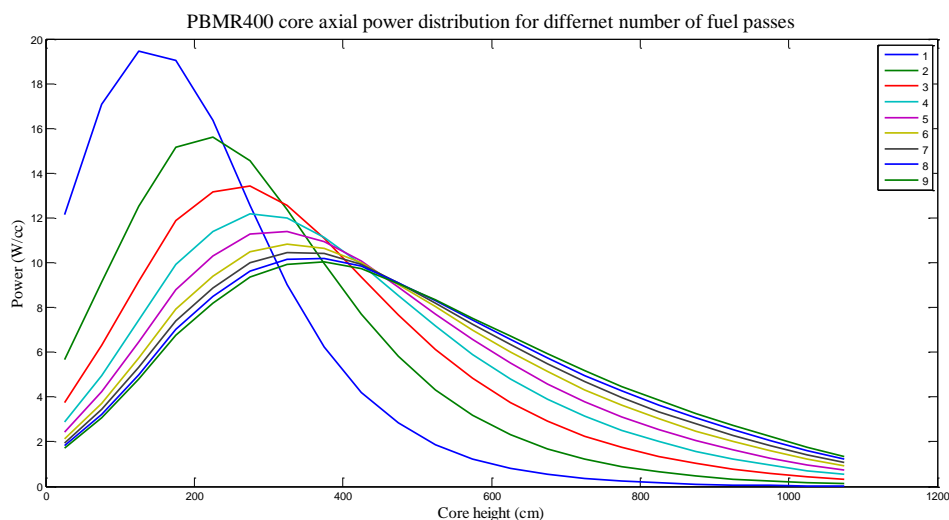


Figure 1: PBMR400 core axial power distribution for different number of fuel passes

SUMMARY AND CONCLUSIONS

A procedure for the optimization of pebble bed reactors fuel management, utilizing PSO algorithm has been developed. This procedure has been used for optimizing the natural uranium utilization of a large 3000MWth core, operating with an OTTO fuel management scheme. Low enriched uranium and thorium fuel cycles have been investigated. Thorium was assumed to be loaded in the form of mixed Th-U oxide fuel and also in separate Th pebbles. The optimization results indicate that thorium introduction does not improve natural uranium utilization when constraining uranium enrichment to non-proliferation level of 20%, however it does decrease Pu production by 50% compared to the low enriched uranium cycle. Only 3% improvement in natural uranium utilization is gained with mixed oxide of highly enriched uranium and thorium fuel. In this case, Pu production is reduced by 95%. When introducing Th to the fuel, higher uranium enrichments are required, up to the 20% when constrained by the proliferation limit or more than 70% when unconstrained. This enriched uranium demand increases natural uranium requirements for the enrichment process, which is compensated by reduced overall core uranium loading. Optimized Th introduction also results in longer fuel residence time at to core, for the efficient buildup of U233. Th introduction also effects moderation ratio, from high value of 550 for LEU case, it reduces down to 497 and 461 for the proliferation constrained Th-MOX and SEP cases and down to 297 for the unconstrained Th-MOX case respectively. Th-MOX and SEP cases may have lower fuel costs by up to 17%. Fuel management with fuel loading in two zones has only slightly improved performance since in this large core, the radial flux distribution is already relatively uniform. MEDUL fuel cycle axial distribution resembles the cosine shape with reduced power density and hence maximum fuel temperatures.

REFERENCES

1. D. Petti, J. Maki, *"The Challenges Associated with High Burnup and High Temperature for UO₂ TRISO Coated Particle Fuel"*, MIT NGNP Symposium, INL/CON-05-00038, 2005
2. WNN internet site, *"Triso fuel triumphs at extreme temperatures"*, http://www.world-nuclear-news.org/ENF-Triso_fuel_triumphs_at_extreme_temperatures-2609137.html, 26 September 2013.
3. E. Teuchert, *"Once Through" Cycles in Pebble-Bed HTR*, KFA, Jul-1470, 1977.
4. NEA publication, "PBMR COUPLED NEUTRONICS/THERMAL-HYDRAULICS TRANSIENT BENCHMARK THE PBMR-400 CORE DESIGN", NEA/NSC/DOC (2013).
5. E. Teuchert, et al., "VSOP ('94) – Computer Code System for Reactor Physics and Fuel Cycle Simulation – Input Manual and Comments",
6. E. Elbeltagi, T. Hegazy, A. Colorni, *"Comparison among five evolutionary optimization algorithms"*, *Advanced Engineering Informatics*, 19, 43-53, 2005.
7. MCKAY, M. D., BECKMAN, R. J. and CONOVER, W. J., "A comparison of three methods for selecting values of output variables in the analysis of output from a computer code". *Technometrics* **21** 239-245 1979.
8. E. K. Burke, G. Kendall. *Search Methodologies*. s.l. : Springer, 2005. ISBN-10:0-387-23460-8.
9. "WISE Uranium Project ", <http://www.wise-uranium.org/index.html>.

Nuclear Forensics and Security (Wednesday, February 12, 2014 11:30)

Experimental Dating of ^{252}Cf Sources

M. Brandis¹, O. Aviv¹, Z. Yungrais¹, D. Hershkovich¹, G. Haquin¹

¹Radiation safety Division, Soreq NRC, Yavne 81800, Israel

INTRODUCTION

One of the primary objectives of the Nuclear Forensic Laboratory (NFL) at Soreq Nuclear Research Centre (SNRC) is the attribution of radioactive evidences taken from a scene (either pre or post dispersion) to an individual or entity involved in illegal or terrorist activities. The attribution has several aspects: the radioactive material production site, the route of the material from its production site to the scene and the intended use of the material.

A material of interest due to its wide spread and potential risk is ^{252}Cf ($T_{1/2}=2.65$ years), which undergoes radioactive alpha decay to ^{248}Cm as well as spontaneous fission (SF). Each fission event gives off multiple neutrons with a broad spectrum of energies. The fission rate is 6.2×10^5 SF/s/ μg and the average number of neutrons per fission is 3.7 (the probability of spontaneous fission is 3.1%) [1]. Therefore, the neutron emission rate is 2.3×10^6 neutrons/s/ μg with a specific activity of 20 MBq/ μg . The variations in fission fragment sizes and number of neutrons emitted per fission provide variable neutron energies over the range of 0-5.5 MeV (with few neutrons going up to 10 MeV [2]), with average neutron energy of approximately 2.3 MeV.

Sources of ^{252}Cf are commercially available for a range of applications such as prompt-gamma neutron activation analysis of coal and cement, petroleum contamination analysis in soil, detection of explosives and landmines, calibration of neutron monitors, neutron radiography and cancer therapy.

Most of the contributions to the gamma spectrum are from Fission Products (FP), most of which have short half-lives, activation products from the shielding and casing materials, and impurities in the source. The activity of long lived (compared to that of ^{252}Cf) FP such as ^{137}Cs ($T_{1/2}=30.02$ years) continue to grow with time, while the activity of short lived FP such as ^{132}I ($T_{1/2}=2.3$ h) remains constant. Those FP emit gamma-rays at 662 and 667 keV respectively [3]. Other nuclei that are present in commercially available ^{252}Cf sources are ^{249}Cf ($T_{1/2}=351$ years), ^{250}Cf ($T_{1/2}=13.08$ years) and ^{251}Cf ($T_{1/2}=898$ years) isotopes which are created during the production of the source via irradiation of ^{250}Cf in high flux reactors [4]. Even though the source is chemically purified at the end of the production process these isotopes remain present.

Only two sites in the world produce ^{252}Cf : the Oak Ridge National Laboratory in the United States and the Research Institute of Atomic Reactors in Dimitrovgrad, Russia. As of 2003, both sites produce 0.25 grams and 0.025 grams of ^{252}Cf per year, respectively [5].

Gehrke et al. [3] studied the gamma spectrum of a new and an aged ^{252}Cf sources and observed several major differences:

- The 388 keV line from ^{249}Cf (351 years) is stronger at the aged source.
- The 661 keV line from ^{137}Cs (30 years) is stronger at the aged source.
- The 177 keV line from ^{251}Cf (898 years) is stronger at the aged source.

The presence of ^{249}Cf and ^{251}Cf is the results of trace elements introduced during the source production process, whereas ^{137}Cs is a FP of ^{252}Cf .

The age of a ^{252}Cf source (the time from its chemical purification) is determined by the ratio of two FP, ^{137}Cs and ^{132}I . Having that ^{132}I has a short half-life compared to ^{252}Cf , its activity represent the current ^{252}Cf activity, which is not the case for ^{137}Cs with its long half-life relative to ^{252}Cf .

The gamma emission rate ratio:

$$R = I_{\gamma}(^{137}\text{Cs}) / I_{\gamma}(^{132}\text{I})$$

is calculated using the growth and decay equations, assuming that the ancestor FP of ^{137}Cs have short half-lives:

$$I_{\gamma}(x) = \frac{\lambda_2}{\lambda_2 - \lambda_1} \cdot P_{\gamma}(x) \cdot S \cdot Y_{cx} \cdot A(^{252}\text{Cf})^0 \cdot (e^{\lambda_1 \cdot 1^t} - e^{\lambda_1 \cdot x^t})$$

Where $I_{\gamma}(x)$ is the emission rate of x (x is 662 or 667 keV) at time t , $P_{\gamma}(x)$ is the gamma-ray emission probability, λ is the decay constant and S is the number of SF per decay and Y_{cx} is the cumulative yield of each FP.

The ratio R can be written and then solved graphically or numerically. In our dating method we used the graphic solution appearing in [3].

RESULTS

Two old ^{252}Cf sources were found in a storeroom in Soreq NRC. They were found inside explosive detectors delivered by the U.S. army at an unknown date. The source assigned “source A” (seen in Figure 1a) was separated from its detector, mounted inside a stainless steel casing, about 5 mm in diameter, and the source assigned “source B” was still incased in the original detector (seen in Figure 1b). The effective dose from both sources was measured using a BF3 proportional counter the results are presented in Table 1.



(a) Source A, separated from the detector.

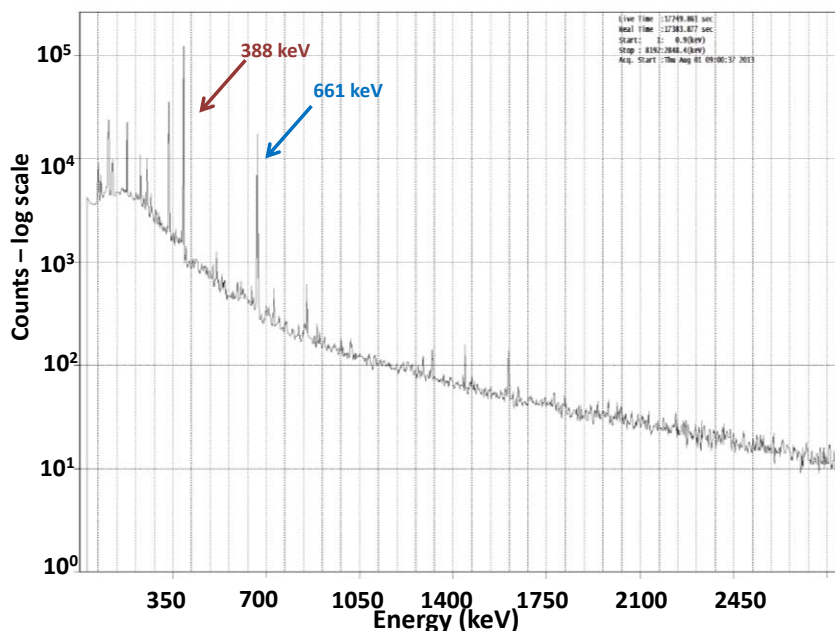


(b) The detector casing, Source B is encased in the detector.

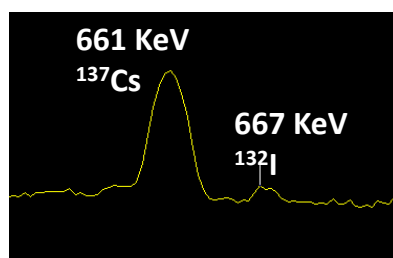
Figure 1. The two ^{252}Cf sources, separated and inside the original casing.

Table 1. Measured effective dose of ^{252}Cf sources

	Neutrons (mRem/h)	Gamma-rays (mRem/h)
Source A	0.05±0.01	2.7±0.2
Source B	0.15±0.03	5.5±0.3
Background	0.004±0.002	-



2(a) The gamma spectrum of source A as measured with an HPGe detector. The blue arrow marks the 661 keV line from ^{137}Cs and the red line marks the 388 keV from ^{249}Cf .



2(b) The 661 and 667 keV peaks used for dating, zoomed.

Figure 2. Measured gamma spectra of the ^{252}Cf source A.

The gamma spectrum of both sources was measured with an HPGe detector, at a 10 cm distance between the source and the detector which enables approximate point-source geometry, with a 10% accuracy. The gamma spectrum of source A is presented in Figure 1, along with a zoomed image of the 661/667 keV peak area. The other most prominent peak in the spectrum is 388 keV from ^{249}Cf . Other peaks that are seen in the spectrum are from other FP such as 331 keV from $^{130}\text{Sb} + ^{144}\text{Cs}$ and 255 keV from ^{142}Ba . The analysis of the entire gamma spectrum is challenging due to the large number of FP.

The peak ratio of ^{137}Cs and ^{132}I was estimated to be 124 for source A, which correspond to 28 ± 5 years, according to the graphic solution to the FP ratio equation found in [3]. The determined age of the source is in agreement with its estimated arrival time at Soreq. The presence of ^{250}Cf in the source influences the SF rate as a function of time. Further analysis of this influence is being conducted.

The age of source B was not determined yet due to uncertainty in the location of the radioactive source inside its detector casing. To overcome this limitation X-ray radiography of the detector casing is under implementation.

CONCLUSIONS

The gamma spectrum of a ^{252}Cf neutron source holds a large number of peaks from the FP, their products and other Cf isotopes present in the spectrum. The differences between a new and an old ^{252}Cf neutron source gamma spectrum are mainly in the size of 661, 388 and 177 keV peaks from ^{137}Cs , ^{249}Cf and ^{251}Cf , respectively.

A technique to identify the traces of ^{252}Cf sources and to determine their age was developed based on previous work [3], using ^{252}Cf sources found at Soreq NRC. In the future, measurement of more, well known sources will be conducted to quantify the accuracy of this dating method.

REFERENCES

1. M. L'Annunziata, *Handbook of Radioactivity Analysis*, 3rd Edition, Academic Press, 2012.
2. J. W. Meadows, ^{252}Cf Fission Neutron Spectrum from 0.003 to 15.0 MeV, *Phys. Rev.*, **157(4)**, p. 1076-1082, (1967).
3. R.J. Gehrke, R. Aryaeinejad, J.K. Hartwell, W.Y. Yoon, E. Reber, J.R. Davidson, *The γ -ray spectrum of ^{252}Cf and the information contained within it*, *Nucl. Instr. and Meth. B*, **213**, p.10-21, (2004).
4. N. J. Roberts and L. N. Jones, *The Content of ^{250}Cf and ^{248}Cm in ^{252}Cf Neutron Sources and the Effect on the Neutron Emission Rate*, *Radiat. Protection Dosimetry*, **126 (1-4)**, p. 83-88 (2007).
5. National Research Council, *Radiation Source Use and Replacement: Abbreviated Version*, National Academies Press, Washington D.C. 2008

Nuclear Forensics and Security (Wednesday, February 12, 2014 11:30)

Nuclear Analytical Techniques and Nonproliferation Studies at the University of Texas at Austin

S. Landsberger, S. Biegalski, E. Schneider, and K. Foltz-Biegalski
Nuclear Engineering Teaching Laboratory, University of Texas at Austin, Texas, USA

INTRODUCTION

Since the terrorist attack on September 11, 2001, and even going back before the 1991 collapse of the former Soviet Union, there has been a national security focus on nuclear terrorism and the production, acquisition, theft, and use of nuclear materials, including special nuclear materials. Out of this concern has come an evolving field of study, nuclear analytical techniques in nonproliferation and Homeland Security which incorporates the analysis of nuclear materials recovered from either the capture of unused materials or from the radioactive debris following a nuclear explosion for the purpose to contribute significantly to the identification of the sources of the materials and the industrial processes used to obtain them. In a 2008 at an American Nuclear Society presentation¹, Dr. Heino Nitsche from Lawrence Berkeley National Laboratory (LBNL) noted that there is a continuing need for nuclear and radiochemists in a wide range of nuclear areas, including nuclear power and new fuel cycle/reprocessing developments, Homeland Security and anti-terrorism challenges, nuclear stockpile stewardship, and in maintaining programs to ensure adequate education in nuclear and radiochemistry. Nitsche also noted that in nuclear and radiochemistry over the past several decades there were shrinking numbers of research and teaching faculty, departments, offered college courses, and awarded PhD degrees. Efforts to counter these downward trends have been limited but they include summer schools sessions for creating undergraduate interest. Finally, Nitsche noted the solution would require a commitment to improve nuclear and radiochemistry science and education across the board. The US Government of Accountability Office GAO² had issued to various government agencies a report outlining how U.S. efforts are hampered by equipment, infrastructure, personnel issues, and a lack of baseline program requirements. The GAO restated such concerns about the limited pool of experts and the education/training of future radiochemists and other nuclear scientists. In 2010 National Academy of Science also pointed out succinctly out the similar concerns³. In 2008 the Joint Working Group of the American Physical Society and the American Association for the Advancement of Science published a report on the role, state of the art, and program needs of nuclear analytical techniques in nonproliferation⁴.

Beginning with two successive three-year educational grants in radiochemistry (2002-2005 and 2005-2008) and then another two successive three grants in nuclear analytical techniques in nonproliferation (2009-2012, 2012-2105) the faculty of the Nuclear and Radiation Engineering Program at the University of Texas has been intricately involved in developing courses in support of these areas, conducting research, and placing students in the national laboratories and the US government. The research has involved a wide area of pre and post detonation scenarios, non-proliferation and nuclear fuel cycle. We have established very close collaborations with many national laboratories and have received funding from the Department of Homeland Security (DHS), Defense Threat Reduction Agency (DTRA), Department of Defense (DOD), National Nuclear Security Administration (NNSA), Department of Energy (DOE) as well as various Department of Energy's national laboratories. The areas that have been covered include low-level fission product identification using Compton suppression and gamma-gamma coincidence methods, radioxenon signatures, argon and radioxenon subsurface transport, β - γ coincidence data, design of an aerosol sampler for nuclear explosion monitoring, software for predicting germanium detector absolute full-energy peak efficiencies, development of logic for nonproliferation assessment tool software package, assessment of non-traditional isotopic ratios by mass spectrometry for analysis of nuclear activities and ¹³⁷Cs in soil. Some current and recent work the faculty have been involved with include development of the multi-isotope

process for spent fuel, advancement of delayed neutron counting for uranium and plutonium identification at the high flux isotope reactor (HIFR) reactor and fast neutron imaging both at Oak Ridge National Laboratory, development of the clover gamma ray system for characterization of ultra-low level fission product identification at Los Alamos National Laboratory, investigation of nuclear fuel cycles for nonproliferation, active interrogation systems for detection of special nuclear material, and a generalized physics-based model for reactor and fuel cycle system simulation. A comprehensive overview of the interaction with national laboratories is shown in Figure 1.

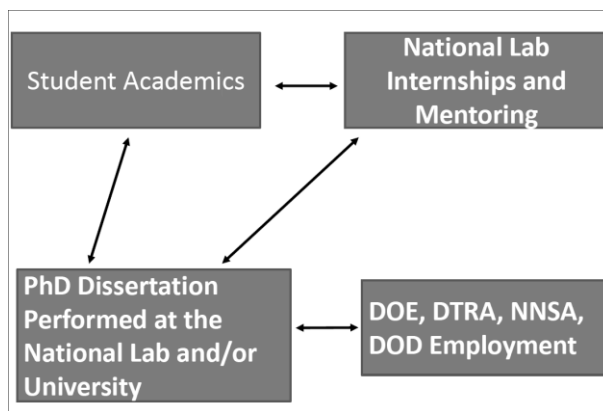


Figure 1. An Overview of the Educational Collaboration with the National Laboratories

RESULTS

Educational awards won by the Nuclear and Radiation Engineering program have also been judiciously used to fund to seed projects in conjunction with national laboratories to support travel to set up collaborations, to attend conferences for the students and to buy small amounts of supplies and pay for equipment usage. This approach has allowed many of our PhD students to work with staff members at national laboratories for their dissertation research which among other benefits, fostered a relationship that has led to increased collaboration and improved student placement within the Department of Energy and other government agencies during their graduation education and full time positions after graduation. This relationship has also allowed the majority of our graduate students to receive multiple internship opportunities at national labs. As well a high fraction of our students, many of whom are also supported on various prestigious fellowships, have participated in summer-internship programs at Lawrence Livermore National Laboratory (LLNL), Sandia National Laboratory (SNL), Oak Ridge National Laboratory (ORNL), Los Alamos National Laboratory (LANL), and Pacific Northwest National Laboratory (PNNL).

CONCLUSIONS

The faculty members in the Nuclear and Radiation Engineering Program have made significant contributions to the placing of PhD and MS students in various programs at the national laboratories and US government. The success and foundation of the program is based on a strong collaboration with staff members at these various laboratories, peer-reviewed publications, and continued financial support.

REFERENCES

1. May, M., Abedin-Zadeh, R., Barr, D. A., Carnesale, A., Coyle, P. E., Davis, J., Dorland, B., Dunlop, B., Fetter, S., Glaser, A., Hutcheon, I. D., Slakey, F., Tannenbaum, Reza Abedin-Zadeh, Joint Working Group of the American Physical Society and the American Association for the Advancement of Science, February 20, 2008.
2. US GAO, GAO-09-527R, April 30, 2009.
3. National Academy of Sciences <http://www.nationalacademies.org/morenews/20100729.html> (2010).
4. American Physical Society <http://cstsp.aaas.org/files/Complete.pdf> (2008)

ACKNOWLEDGEMENTS

This material is based upon work supported by the U.S. Department of Homeland Security under Grant Award Number, 2012-DN-130-NF0001-02. The views and conclusions contained in this document are those of the authors and should not be interpreted as necessarily representing the official policies, either expressed or implied, of the U.S. Department of Homeland Security.

A Liquid Xe Detector for Contraband Detection

I. Israelashvili^{1,4}, M. Cortesi², D. Vartsky¹, D. Bar³ and A. Breskin¹

¹The Weizmann Institute of Science, Rehovot 76100, Israel

²Paul Scherrer Institut (PSI), Villigen PSI 5232, Switzerland

³Soreq Nuclear Research Center (SOREQ NRC), Yavne 81800, Israel

⁴Nuclear Research Center of Negev (NRCN), Beer-Sheva 9001, Israel

INTRODUCTION

Recently, a new detector concept, for combined imaging and spectroscopy of fast-neutrons and gamma rays, was presented ⁽¹⁾. It encompasses a fast liquid-xenon (LXe) converter-scintillator coupled to a UV-sensitive gaseous imaging photomultiplier (GPM) (see figure 1).

Our research was concentrated on validating this new idea on efficient neutron/gamma screening techniques for simultaneous detection of hidden explosives (low-Z, with fast neutrons) and fissile materials (high-Z, with gammas). The range of both probes is 1-20 MeV, obtained with pulsed mixed neutron/gamma radiation beams; neutron spectroscopy relies on Time-of-Flight; gamma energy - on measuring the deposited energy of absorbed or scattered gammas. Imaging of both is relying on scintillation-light localization from dedicated liquid-xenon converters, with a UV-sensitive Gas Photomultiplier (GPM) - a novel Thick-Gas Electron Multiplier, THGEM ^(2, 3, 4), coated with a CsI photocathode, developed at our research group.

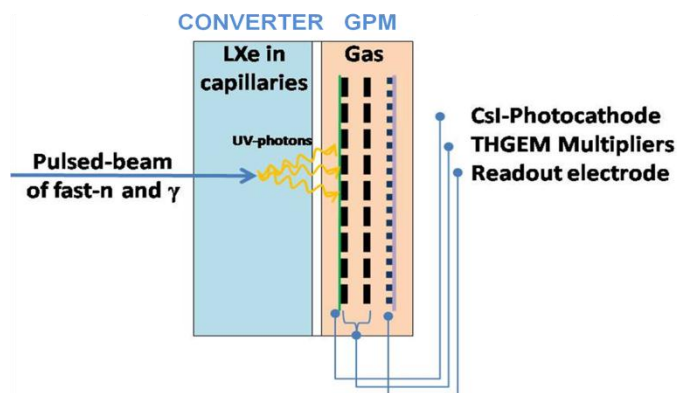


Figure 1. Schematic view of the combined gamma & fast-neutron imaging detector. Radiation interacts with liquid-xenon, e.g. contained in small capillaries; the resulting UV photons are guided through the capillaries and are detected, after traversing a UV-window, with a CsI-coated gas avalanche electron multiplier- here a double-THGEM followed by a segmented readout anode.

Within this project we have carried out comprehensive computer simulations, using GEANT4 toolkit (version 9.3.2) ⁽⁵⁾, to evaluate the expected performances of four suggested radiation-converter concepts incorporating a plain LXe volume and LXe-filled capillaries (made of Teflon, Polyethylene or hydrogen containing Teflon-Tefzel), with fast neutrons and gammas in the relevant energy range of 2 to 14 MeV. The simulations encompassed: the physics processes of radiation conversion and light production (photon yields) & propagation in different converter geometries; detection processes, e.g. photoemission into gas, electron collection, multiplication etc; and detector performance assessment in different configurations.

In this work we will present the expected performances (detection efficiency and spatial resolution) of the four possible radiation-converter variants, and will show some preliminary results of gamma and neutron radiography and material reconstruction.

RESULTS

Detection efficiency and spatial resolution

The detection efficiency and spatial resolution for the suggested radiation-converter variants, are shown in figure 2. The detection efficiency is defined as the number of particles (neutron/gamma) interacting in the LXe sensitive volume resulting in at least one photoelectron, detected by the GPM, normalized to the total number of particles impinging on the detector. The spatial resolution was obtained by computing event-by-event, the centers-of-gravity (CG) of the detected photoelectron-cloud distributions on the GPM's photocathode surface (Fig. 1).

For *fast-neutrons*, detection efficiency values of ~20% were calculated over the whole 2-14 MeV range, for a 50mm long LXe converter. LXe-filled Polyethylene or Tefzel capillaries yielded the best spatial resolutions (~2.5mm FWHM), due to moderation of the scattered neutrons - preventing them from reaching distant capillaries. For *gammas*, all converter configurations yielded similar spatial resolutions (~3 mm FWHM); the plain-LXe converter provided the highest detection efficiency, e.g. of ~45% for 2-14MeV.

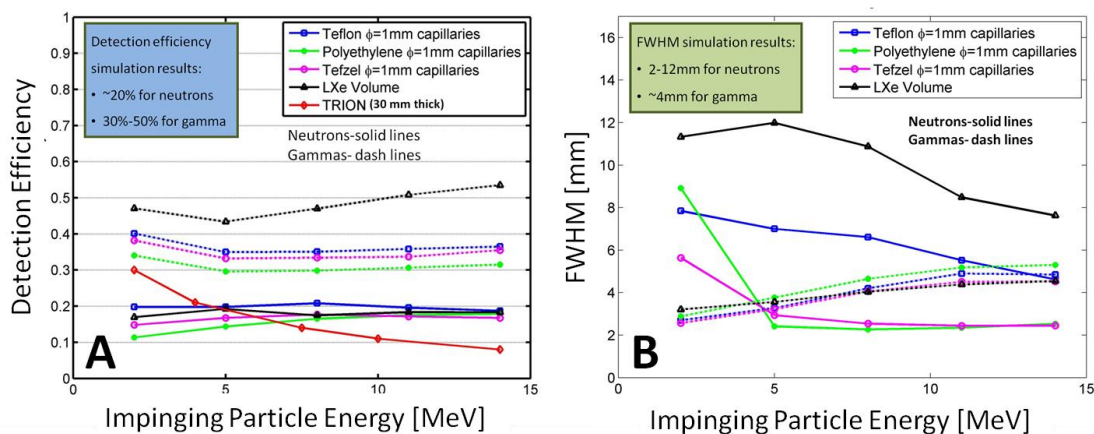


Figure 2: Calculated detection efficiency (fig A) and spatial resolution (fig B) as a function of the impinging neutrons' energy (solid lines) and gammas' energy (dash lines) for radiation converters of Teflon capillaries (squares), Polyethylene capillaries (diamonds) and LXe plain volume (triangles). For comparison, the neutron detection efficiencies for TRION [6] detector, are shown (red diamonds). The average spatial resolution of TRION for neutrons is ~0.7mm.

The calculated detection efficiency of the proposed detector is larger by factor of ~2 than that of the TRION detector ⁽⁶⁾ (30mm thick scintillation screen/intensified CCD), for neutron energies above 8MeV. The calculated neutron spatial resolution of the detector with Tefzel capillaries is about 4-5 times worse compared to that of the TRION sub-mm resolution; however it should be sufficient for the planned application. The calculated gamma detection efficiency of our detector is expected to be better than that of TRION due to the high Z and high density of LXe.

Gamma and neutron radiography and material reconstruction

GEANT4 simulations were carried out in order to evaluate the expected performance, of the plain LXe volume radiation-converter for gamma and neutron radiography and in material separation. Nine objects (20x20x20mm³ for gammas and thicker ones, 20x20x60mm³ for neutrons) of various materials (Lead, Tungsten, Uranium, Polyethylene, Graphite, Aluminium, PETN (=explosive), Iron and silicon) were "irradiated" by uniform beams of gammas (4.4 MeV and 15.1 MeV) and neutrons (**continuous** spectrum 2-10MeV). The transmitted radiation was "measured" by the GPM detector. Typical simulated radiography results are shown in figure 3. The images were enhanced using Lucy-Richardson deconvolution method.

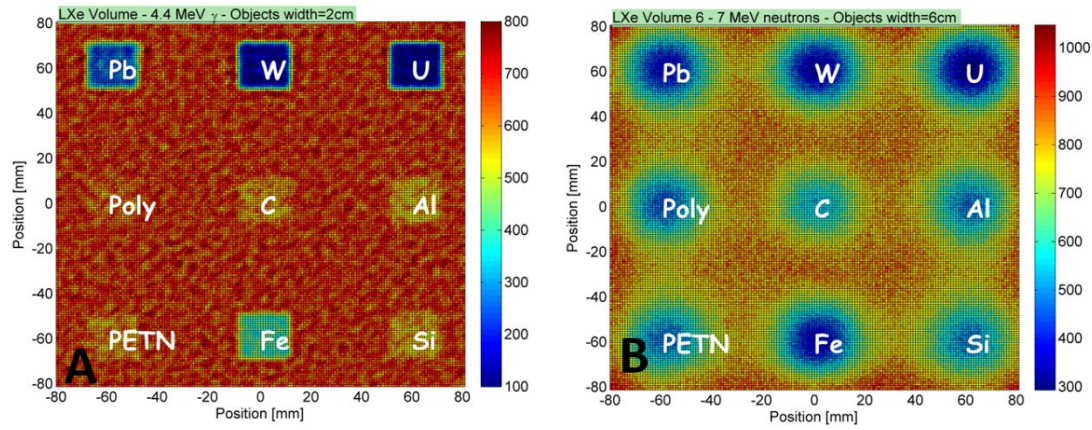


Figure 3: Typical simulated radiography results for objects of various materials, with 4.4MeV gammas (fig A) and 6-7MeV neutrons (fig B).

Materials reconstruction using dual-energy **gamma** radiography (DEGR) was done using the R-value defined, for each element, as the ratio between mass attenuation coefficients of gammas in two energies. Materials with low, medium or high Z would result in R-values of different number regions, independently of the object density or thickness, and hence would enable materials reconstruction. The equation for R-value is:

$$R_{Value}(E_1, E_2) = \frac{\ln(I_\gamma(E_1)/I_\gamma^0(E_1))}{\ln(I_\gamma(E_2)/I_\gamma^0(E_2))} = \frac{\mu_\gamma(E_1)}{\mu_\gamma(E_2)}$$

Where E_1 is 15.1MeV, E_2 is 4.4MeV, I_γ^0 is the impinging flux, I_γ is the transmitted flux and μ is the mass attenuation coefficient. Table 1 shows the R-values calculated from the simulation, and the theoretical ones, obtained from tabulated values ⁽⁷⁾.

Fast-neutron resonance radiography (FNRR) exploits cross-section fluctuations to detect specific elements within inspected items. For example, the Carbon neutron cross-section has resonance in energies of 7.7-8.83MeV and dips in energies of 6.85-7.2MeV. Dividing the image received with neutrons of 6.85-7.2MeV by the image received with neutrons of 7.7-8.83MeV would emphasize materials containing high carbon concentration, e.g. graphite (see figure 4A). Similarly, the ¹⁶O neutron cross-section has resonance in energies of 3.26-3.79MeV and dip in energies of 2.31-2.37MeV. Dividing the image received with neutrons of 2.31-2.37MeV by the image received with neutrons of 3.26-3.79MeV would emphasize materials containing high oxygen concentration, e.g. an explosive in our case(see figure 4B).

Table 1: Theoretical and calculated R-values.

	R value		
	Theory	Simulation	Bias
Pb	1.34	1.38	-3.0%
W	1.33	1.35	-1.2%
U	1.35	1.35	-0.3%
Polyethylene	0.56	0.64	-15.2%
Graphite	0.59	0.54	8.2%
Al	0.73	0.65	11.8%
PETN	0.61	0.71	-15.6%
Fe	0.96	1.04	-8.9%
Si	0.75	0.78	-3.3%

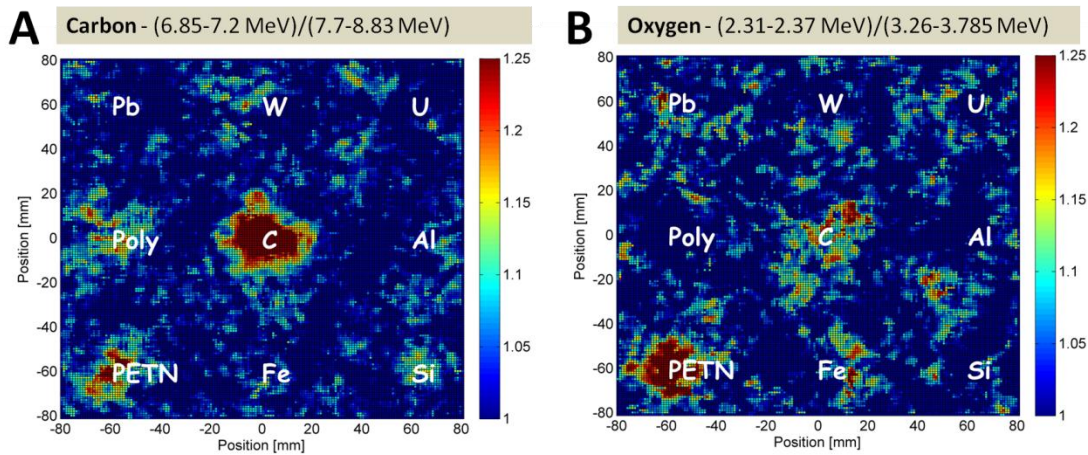


Figure 4: Simulation results. Materials reconstruction using fast-neutron resonance radiography. Figure A- ratio between the image received with neutrons of 6.85-7.2MeV and the image received with neutrons of 7.7-8.83MeV emphasizes the graphite object. Figure B- ratio between the image received with neutrons of 2.31-2.37MeV and the image received with neutrons of 3.26-3.79MeV emphasizes the oxygen-rich (explosive) object.

CONCLUSIONS

A new cost-effective, large-area and robust detector concept, for simultaneously detection of hidden explosives (low-Z, with fast neutrons) and fissile materials (high-Z, with gammas) is proposed, using pulsed mixed neutron/gamma radiation beams.

GEANT4 simulations were carried out to evaluate the expected performances of four suggested radiation-converter concepts incorporating LXe-filled capillaries or a plain volume.

The simulation results indicate that the proposed detector fulfills the efficiency and resolution requirements of screening systems (e.g. high detection efficiency (>10%) for both, fast-neutrons and gamma and spatial resolution better than 5-10 mm).

Preliminary qualitative results with fast neutrons and gamma radiography and elemental separation were presented. They will be followed by more detailed ones, to assess the potential quantitative resolution of specific materials.

ACKNOWLEDGMENTS

This work was partly supported by the Israel Science Foundation grant 477/10, Minerva Foundation with funding from the German Ministry for Education and Research, and from the Benozio Foundation. A. Breskin is the W.P. Reuther Professor of Research in The Peaceful Use of Atomic Energy.

REFERENCES

- [1] A. Breskin, I. Israelashvili, M. Cortesi, L. Arazi, S. Shchemelinin, R. Chechik, V. Dangendorf, B. Bromberger and D. Vartsky. 2012 JINST 7 C06008. <http://dx.doi.org/10.1088/1748-0221/7/06/C06008>
- [2] C. Shalem, R. Chechik, A. Breskin, and K. Michaeli, Nucl.Instr.Meth.A 558, 475 (2006).
- [3] M. Cortesi, R. Alon, R. Chechik, A. Breskin, D. Vartsky, and V. Dangendorf, Journal of Instrumentation 2, P09002-P09002 (2007).
- [4] A. Breskin, R. Alon, M. Cortesi, R. Chechik, J. Miyamoto, V. Dangendorf, J. Maia, and J. M. F. dos Santos, Nucl.Instr.Meth.A 598, 107 (2009).
- [5] S. Agostinelli, et. Al., NIM A 506 (2003), 250-303.
- [6] I. Mor et al, 2009 JINST 4 P05016
- [7] <http://physics.nist.gov/PhysRefData/Xcom/html/xcom1.html>

Ground deposition pattern of an explosive radiological dispersal device (RDD)

A. Sharon^{1*}, I. Halevy¹, D. Sattinger¹, Z. Berenstein¹, R. Neuman¹, P. Banaim¹, M. Pinhas², and I. Yaar¹

¹Nuclear Research Center Negev (NRCN), P.O.Box 9001, Beer-Sheva, Israel

²Israel Atomic Energy Commission (IAEC), POB 7061, Tel Aviv, Israel 61070

*Corresponding author: Avi Sharon, asharon68@gmail.com, avish@nrcn.org.il

ABSTRACT

"Green Field" (GF) project conducting in Israel, between the years 2010-14, aimed at increasing the preparedness for possible terrorism events, where a radioactive (RA) material disperse via an explosive charge. About 20 atmospheric dispersion tests were conducted using 6-8 Ci of ^{99m}Tc which were coupled to TNT charges within the range of 0.25-25 kg. Different typical urban ground surfaces were used below the charges, in order to study its effect on the activity ground deposition pattern. We have used efficient aerosolizing devices, means that most of the RA particles were initially in the size of fine aerosols. Ground activity measurements were performed both around the dispersion point and up to few hundred meters down wind. Micrometeorology parameters (wind intensity and direction, potential temperature, relative humidity, solar radiation and atmospheric stability) were measured allowing comparisons to atmospheric dispersion models' predictions¹. Based on the experimental results, new model parameterizations were calculated. Improvements in the models' predictions were achieved and a set of thumb rules for first responders was formulated. This paper describes the project objectives, some of the experimental setups and results obtained.

INTRODUCTION

Health and environmental consequences of an explosive RDD event depend on many parameters. Among them: type and amount of high explosive (HE), type of RA material, device geometry, surface type below the detonation and local meteorology conditions. A given set of these parameters will define the severity of the event by means of the total dose levels that people might be exposed to (both externally and internally) and the level (and size) of the contaminated area. The dispersion of fine respirable size (<10 micron) is mainly a risk via inhalation while the dispersion of large size particles and aerosols is a hazardous via external exposure. The final RA particle size distribution following such an event is the key question for a reliable risk assessment calculations and preparedness for explosive RDD events.

GF project includes three phases (I, II and III) with different aims for each one. GFI included a wide set of detonation tests where simulant material were dispersed and the explosion cloud were detected up to the effective height, before its downwind motion. One of the important achievements of this phase is the formulation of a model² for the elevation of the explosion cloud up to the effective height as a function of: time elapsed, horizontal wind speed, atmospheric stability class and HE amount up to 100 kg (equivalent to TNT).

The latter two phases included atmospheric dispersion of an explosive RDD devices using a short live RA material (^{99m}Tc with T_{1/2}=6.02 hr. and gamma photon on 141 keV). The device used was such that, initially, most of the RA particles created were within the length scale of fine aerosols. The HE amount used was up to 25 kg of TNT.

The main GF II, III objectives were:

- Measuring the surface activity concentrations around ground zero (GZ), where meteorology is not yet influence, and up to a few hundred meters downwind. Existing models are weak in very near area predictions.

- Study the fireball–ground interaction by means of the amount of activity deposited on the ground in the close vicinity where the fireball “kisses” the ground.
- Measuring the aerial distribution of the activity around the detonation point.
- Measuring the effect of different HE amounts and different surfaces on the ground activity deposition pattern.
- Comparison between predictions of atmospheric and health physics dispersion codes (Hotspot, ERAD, LODI, RODOS, ARGOS) and field results.
- New models’ parameterizations based on the experimental results and comprehensive calculations.

1. Experimental setup

Phases II and III of the project included 20 tests where 6-8 Ci of ^{99m}Tc dispersed by 0.25-20 kg of TNT charges. Shots were done above clean or dirt surfaces in order to study the effect of the different amount of dirt entrained into the fireball. While clean (steel) surface do not involve much of dirt entrainment into the fireball, dirtier surfaces (packed sand soil, grass, concrete, asphalt) involve dirt in the fireball and hence reduce the amount of fine RA particles, due to agglomeration-condensation processes.

We study the effect of different heights of detonation above ground level and compare it to ground detonation.

High resolution radiation detection (about 40 points collected) was done in order to get an accurate 2D radiation fields. Special attention was given to few meters circle around the detonation point, called "Ground Zero" (GZ).

RA concentrations in the air were measured by high volume air samplers around the detonation point.

Particles were collected by stubs from the GZ area and were analyzed by SEM and EDS for the sake of size distribution, morphology and chemical composition. Agglomerates of dirt and RA material were detected.

All tests were documented and recorded by three video cameras, high speed camera, thermal camera (part of the shots), fast multispectral radiometer (part of the shots) and stills camera.

Radiation detection was done by LnBr_3 , personal detection system PDS (CsI crystal), HPGE, NaI (different volumes) and beta surface detectors. Each point were measured shielded (by Lead plates) and unshielded for local and integrated (including the GZ “hot zone”) radiation levels, respectively. The test field area (GZ and far distance) and some of detecting devices can be seen in figures 1 and 2 respectively.



Figure 1: The GZ area (on concrete surface - right) and far field look (left) of the test site. Height reference balloon and a video camera are on the left.



Figure 2: Portable LnBr_3 detector with a lead shield plate and a PDS (right) and 25 kg of TNT cloud 4 s following the detonation (left).

RESULTS AND DISCUSSIONS

A comparison between raw data (gross counts per second) and analyzed data (surface activity) for 0.25 kg of TNT shot is shown in figure 3.

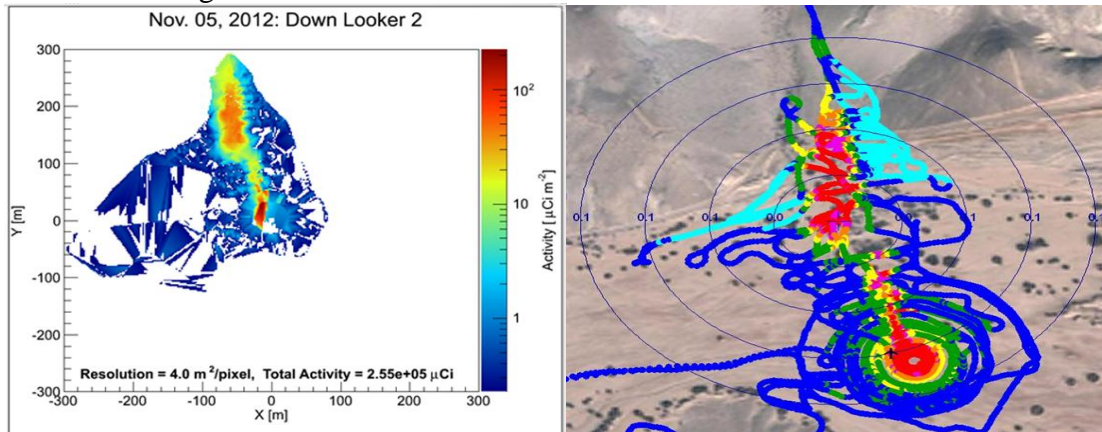


Figure 3: Raw (right) vs. analyzed (left) data of activity ground deposition following detonation of 0.25 kg of TNT combined to RA source of 6.6 Ci of $^{99\text{m}}\text{Tc}$.

Note that the 2D maps in figure 3 do not include the activity in the GZ “hot” area where most of it was deposited. Based on the analyses of GF experiments, it was found out that 3-25% of the total activity was deposited on the GZ area inside a circle of 3-4 fireball radii. Since most of the RA particles dispersed as fine, respirable, aerosols another 2% of the total activity was found on the ground up to 300 m downwind. This means that most of the activity, initially dispersed, was not recover. The GZ activity of the same test is shown in figure 4.

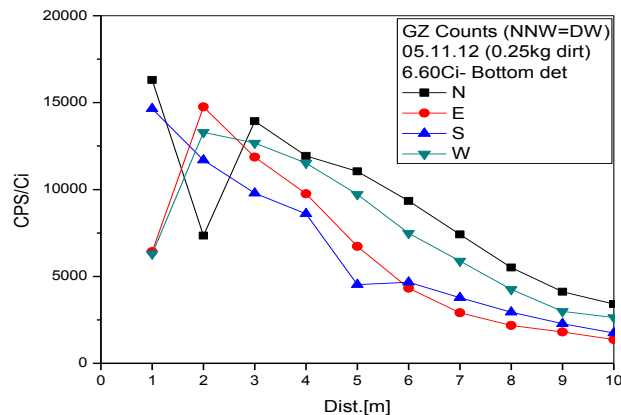


Fig. 4: GZ activity [cps/Ci] distribution along four directions from the detonation point (North, South, East and West). This area contains up to 25% of the total activity and its influence can be up to few hundreds of meters.

SUMMARY

Activity deposition pattern of outdoor explosive RDD experiments were discussed and analyzed. In cases of fine, respirable size, aerosols dispersion, most of the activity deposited inside a circle of up to 4 fireball radii around the detonation point. About an order of magnitude less was deposited in the rest of the wide open area, in the downwind direction. The effects of different RA particles size distribution on the ground deposition pattern is still being studying under the framework of GF project.

REFERENCES

1. Hotspot 2.07.2, Health physics and atmospheric dispersion code, LLNL-USA, Sep. 2011. See also in Hot Spot user guide Sharon et al.
2. A. Sharon, I. Halevy, D. Sattinger, I. *Yaar*, Cloud rise model for RDD events, Atmospheric Environment 54 (2012) 603-610.

Nuclear Forensics and Security (Wednesday, February 12, 2014 11:30)

Atmospheric Transport Modeling of Radio-Xenon Detections Possibly Related to the Announced Nuclear Test in North Korea on February 12, 2013

K. Kutsher¹, M. Stern²

¹*Radiation Safety Division, Soreq-NRC, Israel*

²*Physics and Nuclear Engineering Division, Soreq-NRC, Israel*

INTRODUCTION

On February 12th 2013, monitoring stations of the Preparatory Commission of the Comprehensive Nuclear-Test-Ban Treaty Organization (CTBTO) detected a seismic event with explosion-like underground characteristics in the Democratic People's Republic of Korea (DPRK) ⁽¹⁾. The location was found to be in the vicinity of the two previous announced nuclear tests in 2006 and 2009 (Lat.: 41.313 degrees north; long.: 129.101 degrees east) and the signal had the characteristics of a shallow event ⁽¹⁾. The nuclear test was also announced by the government of the DPRK.

After an underground nuclear explosion (UNE), radioactive fission products (mostly noble gases) can seep through layers of rock and sediment until they escape into the atmosphere. The fission products are dispersed in the atmosphere and may be detected thousands of kilometers downwind from the test site.

Indeed, more than 7 weeks after the explosion, unusual detections of noble gases was reported at the [radionuclide station in Takasaki, Japan \(JPX38\)](#). The radionuclide station is a part of the International Monitoring System (IMS), operated to verify the CTBT.

The purpose of this study is to provide an estimation of the possible source region and the total radioactivity of the release using Atmospheric Transport Modeling (ATM).

METHODS

During the period of 8-9 April 2013, unusual concentration of ^{131m}Xe and ¹³³Xe (half-lives of 11.8 and 5.2 days, respectively) were measured at the radionuclide station in Takasaki, Japan, shown in Table 1*.

Table 1. Measured concentrations of ^{131m}Xe and ¹³³Xe at the radionuclide station at Takasaki, Japan in the period of 8-9 April 2013

Collection time	^{131m} Xe [mBq/m ³]	¹³³ Xe [mBq/m ³]	Ratio ^{131m} Xe / ¹³³ Xe
08-APR-2013 06:54	0.27	2.08	0.13
08-APR-2013 18:54	0.73	3.05	0.24
09-APR-2013 06:54	0.35	1.87	0.19
09-APR-2013 18:54	0	0.72	0

Assuming that the detections were the result of fission, the isotopic ratio indicates that the fission occurred approximately 52 days before the detections (+/- 4 days). Therefore, it is possible that the unusual radio-xenon detections at Takasaki are related to the DPRK nuclear test on February 12th 2013.

Based on the radio-xenon concentration, ATM was performed using the Lagrangian particle dispersion model FLEXPART version 6.2 ⁽²⁾. The model was assimilated by meteorological grid every 3 hours for the entire simulation period.

* The data was received by the Israeli NDC from the International Data Center (IDC), which is part of the CTBTO.

RESULTS

The simulation was performed in two modes:

1. Backward ATM, which identifies the area from which radionuclides may have been released, calculated backward in time from Takasaki. This mode provided an estimate of the dilution factor (the ratio between the detected concentration and the released concentration) and can indicate possible source regions as a function of time. A map of dilution factor contours on 7 April 2013 (24 hours before the first detection) is shown in Figure 1.

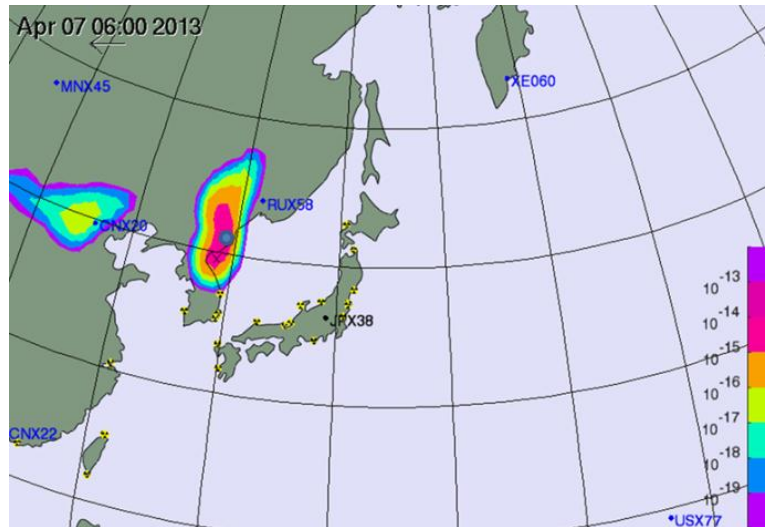


Figure 2. Backward ATM - dilution factor contours of radio-xenon on 7 April 2013 calculated from Takasaki, Japan (indicated in the map as JPX38) to the DPRK test site (indicated by blue circles); blue dots indicate nearby international radionuclide stations, radioactivity symbol indicates nuclear power plants.

The results in Figure 1 correspond to a possible source in the region of the DPRK test site, 24 hours before the first detection at Takasaki. Assuming that the possible source caused the detection at Takasaki, the released activity was found to be 15 orders of magnitude higher than the concentrations at Takasaki. Hence, the total released activity is estimated to be of the order of 10^{12} Bq.

2. Forward ATM, which predicts where radionuclides may travel from their known point of release. Based on the backward ATM, we define a release of 10^{12} Bq of radio-xenon isotopes at the DRPK test site on April 7, 2013. The isotopes are transported by the atmospheric flow as a function of time. Each time-step the model calculates the concentration at each grid point. A map of predicted concentrations on 06:00 UTC April 8, 2013 is shown in Figure 2.

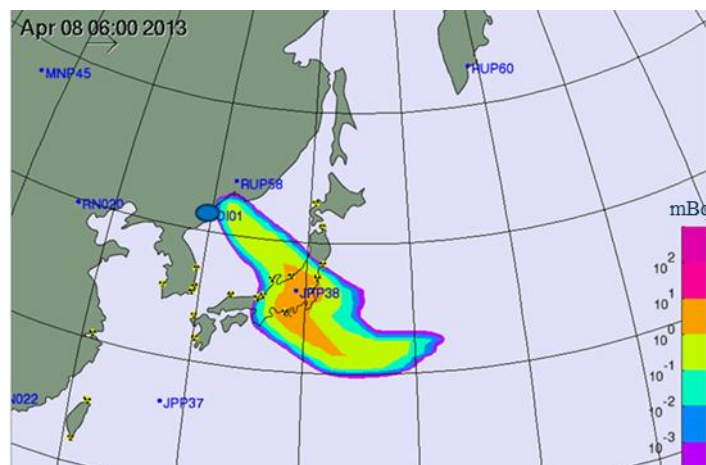


Figure 3. Forward ATM - predicted concentrations of radio-xenon on 06:00 UTC April 8, 2013, assuming a release of 10^{12} Bq from the DPRK test site on April 7, 2013 (indicated by blue circles); Blue dots indicate nearby international radionuclide stations.

The results in Figure 2 show that the winds transported the emitted radionuclides to the east, from the site over the Sea of Japan. The predicted concentrations at Takasaki station are in agreement with the actual measured values. For a release occurred on April 7th, the forward ATM suggests that no other international station would be significantly affected.

CONCLUSIONS

The fact that two radioactive isotopes of the noble gas xenon, ^{131m}Xe and ^{133}Xe , were identified provided reliable information on the nuclear fission nature of the source.

A release from the DPRK test site was found to be consistent with the possible source region results from the ATM. The ATM also showed that the detections in Takasaki are consistent with a release activity of 10^{12} Bq, early in the morning of 7 April 2013, i.e. 54 days after the explosion.

Any actions possibly performed at the DPRK test site (and their timing) are unknown. However, according to American estimations, based on UNE at the Nevada Test Site (NTS), 1-10 % of the noble gases total activity could be released to the atmosphere ⁽³⁾.

Based on the above, the nuclear yield of the explosion is in the range of 1-10 kilotons TNT equivalent. This estimation is in agreement with the estimated yield in another study based on the CTBT international monitoring system ⁽⁴⁾.

REFERENCES

1. CTBTO press release. *On the CTBTO's detection in North Korea*. <http://www.ctbto.org/press-centre/press-release/2013/on-the-ctbtos-detection-in-north-korea/> (2013).
2. Stohl, A., Forster, C., Frank, A., Seibert, P., Wotawa, G. *Technical note: the Lagrangian particle dispersion model FLEXPART version 6.2*. Atmos. Chem. Phys. **5**, 2461-2474 (2005).
3. J.J. Zucca et al. *Signatures of Testing: On-Site Inspection Technologies*, in Monitoring a CTBT, ed. E.S. Husebye and A.M. Dainty. Kluwer Academic (1996).
4. A. Ringbom et al. *Radi xenon detections in the CTBT international monitoring system likely related to the announced nuclear test in North Korea on February 12, 2013*. J. Environ. Radio. **128**, 47-63 (2013).

Radiation Protection (Wednesday, February 12, 2014 11:30)

Fukushima Update and Current Status

T. Suzuki

International Atomic Energy Agency, Vienna, Austria

On 2nd Apr. 2011, highly contaminated water which flowed into the cable trench of unit 2 brought ambient dose rate up to 1,000mSv/h at the cable pit near the sea water intake of the unit. This was the first sign of the leakage of contaminated water.

As for the alternative water injection by fire engines to the reactor pressure vessel (RPV), the majority of injection volume streamed into the steam condenser as a bypass flow through the water seal of the low-pressure condensation pump. Nevertheless, a large quantity of seawater was injected into RPV, which flowed into the basement of the turbine building (T/B) via gaps or cable penetrations. For example in unit 3, this highly contaminated water did not exist until 23rd Mar.2011, and “lukewarm water” which three workers felt around their ankle on the next day during their cable repair work in the basement floor was the very thing. From a measurement right after that, the surface dose rate of the water was found to be approximately 400mSv/h in unit 3 and above 1000mSv/h in unit 2.

The gross volume of the highly contaminated water stagnating in the basement of R/B, T/B, C/B, Rw/B of unit 1 to 4 by 29th Oct.2013 is 80,900 tons and 19,120 tons in process main building and high temperature incinerator building of centralized radioactive waste treatment facility.

Furthermore, stagnating water of the same concentration exists in the cable trench of unit 2.

On the other hand, the cooling of fuel debris is continuing by two water injection systems, core spray (CS) system and feed water (FDW) system, in RPV. The water which contributed to the cooling falls to primary containment vessel (PCV) through the damaged RPV bottom and cools the fuel debris which dropped into PCV. It makes the temperature keep less than 30°C-40°C at the RPV bottom and 35°C-45°C in the PCV. A circulation cooling system in which Cesium is adsorbed after oil separation process and Strontium is eliminated by reverse osmosis membrane and the distillation process is used for this injection.

As 1,000 tons of groundwater flows per day through the permeable layer from the mountain side to the sea side, 850 tons of water was drawn a day from sub-drain in order to control the groundwater level to keep lower than the foundation of buildings in Fukushima Daiichi Nuclear Power Station before the accident. However, with the loss of the sub-drain function, the groundwater level rose, and approximately 400 tons per day flows into the basement of buildings after the accident. Therefore, in a day, 770 tons in conjunction with 370 tons of fresh water to use for RPV cooling became targeted for the treatment of circulation cooling system. As a result, concentrated contaminated water (mainly Sr-Y) is produced 400 tons every day from the desalination process.

This groundwater inflow will be settled if the level is lowered by pumping-up but the present condition also prevents contaminated water stagnating inside the basement from draining into the groundwater.

Accordingly, a production of two storage tanks (1,000 tons ea.) per day in average may be indispensable for the time being. Leaks of Strontium contaminated water, the concentration of which was 20kBq/cm³ occurred from a flange type tank which was made in earlier period for this purpose.

The final solution for this is supposed to be full operation of sub-drain with complete repair of the PCV boundary. So various kinds of measures are in progressing towards the destination.

Radiation Protection (Wednesday, February 12, 2014 11:30)

Production of DNA Double Strand Breaks in Human Cells due to Acute Exposure to Tritiated Water (HTO)

R. Gonen¹, U. German¹, Z. B. Alfassi², E. Priel²

¹ Nuclear Research Center, Negev, P.O.B 9001 Beer Sheva, 84190, Israel

² Ben Gurion University of the Negev, Beer Sheva, 84105, Israel

INTRODUCTION

The average and maximum energies of the beta emission from ³H are 5.69 keV and 18.6 keV respectively. The average range in water (or soft tissues), around 0.5 μm (500 nm), is considerably less than the typical diameter of a cell (10-30 μm), and even of a cell nucleus (5-10 μm), thus the micro-location of the tritium atom may well be crucial in determining its biochemical consequences. Due to the high ionization density of the beta particles emitted by tritium (about 400 ion pairs/μm) possible interaction of tritium beta radiation with DNA may play a significant role.

Tritiated water (HTO) is the main chemical form in which tritium is found in the environment. In the body it may be retained as organically bound tritium (OBT), binding to biological molecules or remaining as OBT with various degrees of solubility. OBT can be retained in the human body much longer than HTO and therefore the dose arising from OBT can reach 50% of the total tritium dose ⁽¹⁾.

Histones are major protein components of chromatin. They function as spools around which DNA winds and play an important role in the regulation of gene expression. In the absence of histones, the DNA in chromosomes would be unmanageably long, as human cells each have about 1.8 m of DNA. During mitosis, DNA is duplicated and condensed, resulting in about 120 μm of chromosomes ⁽²⁾. It was recently reported that the phosphorylation of histone H2AX on serine residue 139 (γ-H2AX) is associated with Double Strand Breaks (DSB) sites in DNA ⁽³⁾, which indicates the possibility of research based on the detection of DSBs in DNA. The phosphorylated megabase chromatin domain surrounding the DSB can be immunostained and visualized as discrete foci by fluorescence microscopy ⁽⁴⁾, as each DNA DSB formed produces a visible γ-H2AX focus ⁽⁵⁾. Since 1 Gy of radiation produces approximately 60 DSBs/cell, doses of a few mGy should be distinguishable from the background, and it was recently shown that the exposure to 1 mGy of X-rays induces a significant increase in H2AX phosphorylation in primary human fibroblasts ⁽⁶⁾. Thus, immunostaining of γ-H2AX may represent a sensitive biomarker of exposure ⁽⁷⁾.

The scientific literature contains practically no information about the effect of acute exposure from HTO on the integrity of the DNA, and the present work presents some preliminary results on this subject. The investigation on the formation of the Double Strand Breaks was done by the detection of the phosphorylated histone, γH2AX. For this research we used Human malignant osteoblast MG-63 cells, and normal peripheral blood lymphocytes.

EVALUATION OF THE EXPOSURE DOSES IN HTO MEDIA

For investigation of the DSBs effects in DNA, cells were exposed to various activities in tritium liquid solutions. A tritium concentration of 13,220 Bq/ml in solution was defined as 1 Ac. The exposure effect was tested using solutions from 0.5 Ac to 16 Ac. Evaluation of the tritium dose in the HTO medium was done based on the basic definition of energy absorbed per mass unit (Grey units).

The average energy of a beta particle emitted from tritium is 5.7 keV. Assuming that all beta particles are absorbed in the aqueous volume (due to their short range), the energy absorbed in 1 kg of a 16 Ac solution is:

$$2.115 \cdot 10^5 [\text{Bq/ml}] \cdot 5.7 [\text{keV}] \cdot 1.6 \cdot 10^{-16} [\text{joule/keV}] \cdot 10^3 [\text{ml/kg}] = 1.93 \cdot 10^{-7} [\text{joule/kg/sec}]$$

1 Gy is defined as 1 [joule/kg]; therefore, the dose rate corresponding to a tritium activity of 16 Ac is $1.93 \cdot 10^{-7}$ [Gy/sec]. For an incubation time of 3 h, the total dose will be:

$$1.93 \cdot 10^{-7} [\text{Gy/sec}] \cdot 1.08 \cdot 10^4 [\text{sec}] \cdot 10^3 [\text{mGy/Gy}] = 2.09 [\text{mGy}]$$

Scarpa et al. ⁽⁸⁾ also evaluated the absorbed dose for a β -emitting isotope uniformly distributed in a homogeneous medium. Applying the Equation used by Scarpa to the tritium solution described above gives a dose value of 1.51 mGy, which is close to that evaluated above, based on the most basic definitions.

The exposure of 2.09 mGy corresponds to a solution containing a tritium activity of 16 Ac (211,533 Bq/ml) and an exposure time of 3 hours. Thus the basic exposure factor is $0.0435 \text{ Bq} \cdot \text{Ac}^{-1} \cdot \text{hr}^{-1}$. Based on this factor, the exposure for each tritium concentration and exposure time can be calculated. The doses used in this study ranged from 0.065 mGy to 16.72 mGy, which were obtained with HTO activities in the range $6.61 \cdot 10^3$ Bq/ml to $2.11 \cdot 10^5$ Bq/ml (0.5 - 16 Ac). These doses are classified in the literature as low doses ^(9, 10, 11).

RESULTS

Detection by Immunofluorescence

One group of cells was incubated for 3 h and for 24 h in media containing different HTO concentrations. The second group was exposed for the same total incubation time to 1 μM etoposide (known to cause DSBs). At the end of incubation, the cells were detached from the plastic flasks by trypsinization, rinsed twice with large volumes of PBS, diluted to the desired concentration, and dispersed onto glass slides. After performing a micro assay using an incubation step of monoclonal antibody against γH2AX (Biolegend™, cat#: 613402), they were diluted 1:100 and an additional incubation step with DAPI (a minor groove dye of DNA that is used for staining nuclei) was performed. The cells were then analyzed by fluorescence microscopy for cy-3 and DAPI emissions.

The immunofluorescence results (Figures 1-4) for different tritium exposures show that DSBs occurred in DNA only after the exposure of the cells to 1 μM etoposide for 24 h and after to 16 Ac HTO for 24 h (Figures 2 and 3). Typical fluorescent foci were only observed after exposure to 16 Ac activity in the DAPI nuclear staining area (~10% of total cells exhibited fluorescent foci).



Figure 4: 16 Ac HTO exposure for 3 h (2.09 mGy).

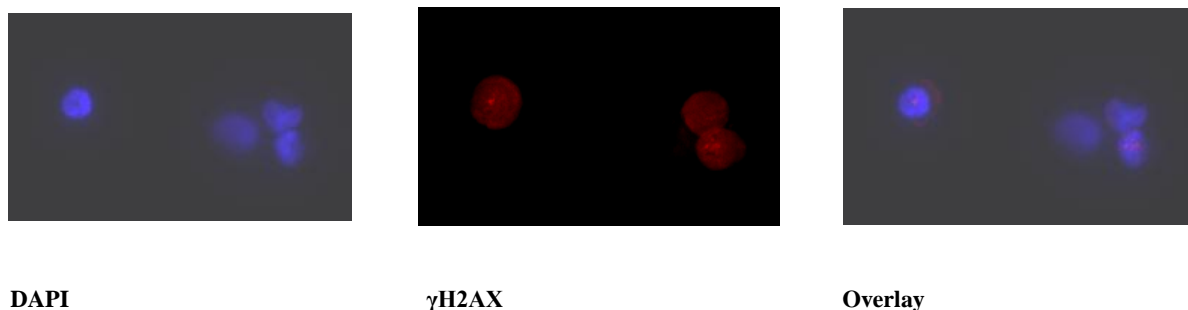


Figure 5: Exposure to 1 μ M etoposide for 24 h

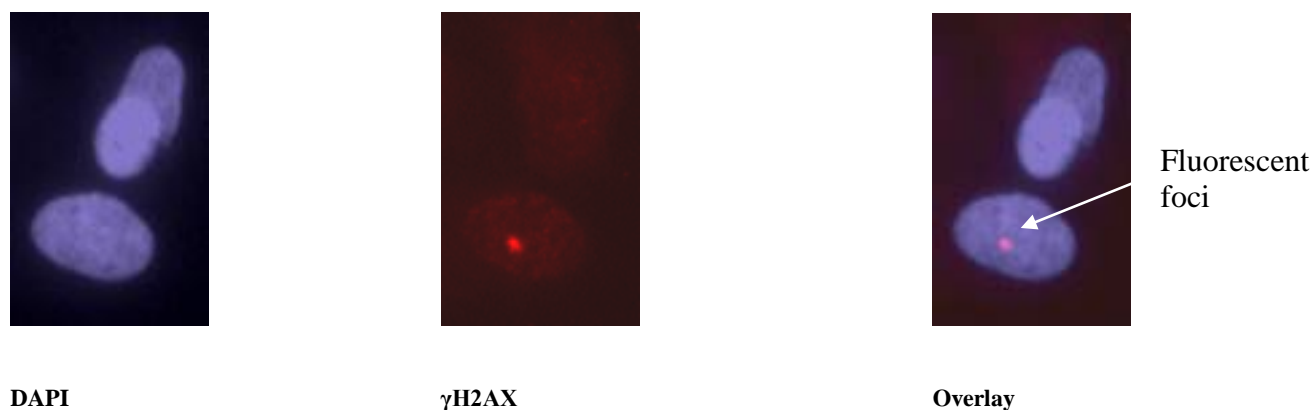


Figure 6: 16 Ac HTO exposure for 24 hours (16.72 mGy).



Figure 7: 16 Ac HTO exposure for 3 hours (2.09 mGy).

Detection by Western Blot

The western blot analytical technique was used to detect the formation of the phosphorylated protein (serine-139), γ - γ H2AX. To lyse the cells, the different cellular mixtures (of cells exposed to HTO for 3 h) were treated with RIPA buffer. The membranes and the DNA fraction were separated from the cellular extracts, and the DNA fraction was treated once more with RIPA buffer supplemented with SDS to achieve a final concentration of 0.1% (or according to Abcam's procedure). Equivalent amounts of 25 μ g (except 12 μ g for the Etoposide) of the membranes and DNA fraction from the various treatments were used for in the western blot analysis. The proteins that were transferred from the 15% acrylamide gel to the nitrocellulose membrane were reacted overnight with a 5 μ g monoclonal anti- γ H2AX antibody (BioLegend™, cat#:613402) diluted in 5 ml PBS containing 5% BSA (fraction 5, Sigma) and 0.05% Tween-20. The

nitrocellulose membrane was rinsed three times, 10 min each time, in PBS containing 0.05% Tween-20 and then reacted for 1 h with a secondary antibody, goat anti-mouse #HRP conjugated (Santa CruzTM), diluted 1:10,000 (in the same buffer), after which it was rinsed again in PBS containing 0.05% Tween-20. The immune complexes were detected by an ECL system followed by autoradiographs. Band intensities were quantified by densitometric scans using EZQuant-Gel image processing and analysis software (Rehovot, Israel).

The nitrocellulose membrane was also allowed to react with an anti H3 histone antibody (Abcam#Ab1791) to enable a quality control test of the protein quantities used (Figures 5 and 6).

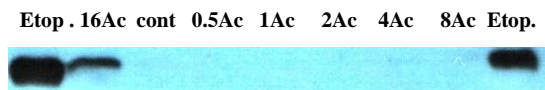


Figure 8: γ H2AX detection in control cells and in cells exposed to either 120 μ M etoposide or HTO for 24 h.

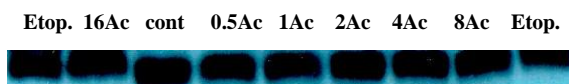


Figure 9: H3 histone detection in control cells and in cells exposed to either 120 μ M etoposide or HTO for 24 h.

The similar band areas exhibited by the different treatments indicate that the same quantities of fraction extracts were used (Figure 6). The densitometric analysis of the different samples also indicated that equal amounts of proteins were loaded on the gels. The variability among the samples was in the range of 6%. As the etoposide treatment was an important positive control for H2AX phosphorylation, two protein concentrations were used 25 μ g and 12 μ g.

As seen from the results presented in Figure 5, only the 24-h exposures to 16 Ac tritium and to 120 μ M of etoposide caused DSBs to form in DNA (Figure 5).

CONCLUSIONS

It was found that low HTO dose exposure of 16.72 mGy can cause DSBs after exposing MG-63 cells for 24 h. This dose did not cause any DSBs in normal stimulated peripheral blood lymphocytes (data are not shown), probably due to the inherent metabolism and replication differences between the two cell types.

The capability of tritium (as HTO) to cause DSBs, proves that this radionuclide has a potential to cause DNA damage.

REFERENCES

1. Kotzer, T., Trivedi, A., Waito, G., Workman, W. (1998). Ultra low-level of organically- bound tritium in bioassay samples. AECL-11956, COG-98-131-I.
2. Redon C, Pilch D, Rogakou E, Sedelnikova O, Newrock K, Bonner W (2002). Histone H2A variants H2AX and H2AZ. *Current Opinion in Genetics & Development*: 12;162-169.
3. Rogakou EP, Pilch DR, Orr AH, Ivanova VS, Bonner WM. (1998). DNA double- stranded breaks induce histone H2AX phosphorylation on serine 139. *J Biol Chem*: 273; 5858-5868.
4. Rogakou EP, Boon C, Redon C, Bonner WM (1999). Megabase chromatin domains involved in DNA double-strand breaks *in vivo*. *J Cell Biol*: 146; 905-916.
5. Sedelnikova OA, Rogakou EP, Panyutin IG, Bonner WM (2002). Quantitative detection of (125)IdU-induced DNA double-strand breaks with γ -H2AX antibody. *Radiat Res*: 158; 486-492.

6. Rothkamm K, Löbrich M. (2003). Evidence for a lack of DNA double-strand break repair in human cells exposed to very low X-ray doses. *Proc Natl Acad Sci USA* 2003: 100.
7. Bonner WM. (2003). Low-dose radiation: thresholds, bystander effects, and adaptive responses. *Proc Natl Acad Sci USA*. 100(9): 4973-4975.
8. Scarpa G, Vulpis N, De Santis ME, Vulpis G. (1981). The dose absorbed by lymphocytes irradiated in vitro with tritiated water. *Phys. Med. Biol.*, Vol. 26 No. 6, 1137-1144.
9. Gridley DS, Williams JR, Slater JM. (2005). Low-dose/low dose rate radiation: a feasible strategy to improve cancer radiotherapy? *Cancer Therapy* vol.3, 105-130.
10. Jha AN, Dogra Y, Turner A, Millward GE (2006). Are low doses of tritium genotoxic to *Mytilus edulis*? *Marine Environmental Research* 62: S297-S300.
11. Hagger JA, Atienzar FA, Jha AN (2005). Genotoxic, cytotoxic, developmental and survival effects of tritiated water in early life stages of marine mollusk, *Mytilus edulis*. *Aquatic Toxicology* vol. 74: 205-217.

Radiation Protection (Wednesday, February 12, 2014 11:30)

The Treatment of Uncertainty in Compensation Schemes for Cancer Based on the Probability of Causation Methodology

J. Koch

Soreq Nuclear Research Center, Yavne, Israel

INTRODUCTION

Since it is commonly accepted that exposure to ionizing radiation, even at the low levels encountered in the workplace, can cause malignant diseases^(1,2), radiation workers are at some risk, although much is done to optimize radiation protection and reduce occupational exposure to levels "as low as reasonably achievable". However, the causal relationship between exposure to radiation and malignant diseases is difficult to establish, since cancer is such a frequent disease and many other factors may contribute to its development. Ideally, those workers who developed cancer as a result of occupational exposure to radiation should be compensated. Guidance on procedures and methodology to assess attributability of cancer to occupational exposure to radiation and to assist decision-making in compensating workers is provided in a recent joint IAEA/ILO/WHO publication⁽³⁾. This guide also reviews compensation schemes in place in several countries, with an emphasis on those based on the probability of causation (POC), also known as assigned share (AS) methodology. The POC method provides a scientifically based framework to assess cancer attributability to occupational exposure and was extensively reviewed by Wakeford et al⁽⁴⁾. This paper presents a comparison of two well-known compensation schemes based on the POC approach with regard to their treatment of uncertainty.

UNCERTAINTY IN POC ESTIMATION

The sources of uncertainty are uncertainty inherent in the dosimetry data and uncertainty in the risk models. Uncertainty in the dose estimates are due to the degree of accuracy in the dosimetry records, to the fact that a whole-body dose is often used instead of the relevant organ dose which has not been monitored, to the fact that organ doses due to internal exposure are estimated from bioassay measurements. If dosimetry records are not available, a large degree of uncertainty is introduced by the process of dose reconstruction. The cancer risk models were mostly derived from the epidemiological studies conducted on the survivors of the atomic bombings of Japan. Uncertainty in the risk models is due to uncertainty in the dose estimates of the survivors and to various other factors, such as the method for transferring risk from the Japanese population to another population and the inclusion of a dose and dose rate effectiveness factor (DDREF).

TREATMENT OF UNCERTAINTY IN THE UK COMPENSATION SCHEME

The Compensation Scheme for Radiation Linked Diseases (CSRLD) is in place in the UK since 1981, as an agreement between employers in the nuclear industry and trade unions⁽⁴⁾. Its estimation of POC is based on the risk models presented in BEIR VII, which are mostly derived from the latest analysis of the epidemiological data collected from the Japanese survivors.

Uncertainty in the dosimetry data is dealt with by constructing dose histories by retrospectively applying current assessment standards to historical dose records⁽³⁾. Uncertainty in the calculation is not formally taken into account through a quantitative uncertainty analysis, but it is believed that this uncertainty is overcome by adopting a proportional recovery compensation system. Under this system claimants with POC values of 50% or above are fully compensated, but claimants with POC values below 50% are also partially compensated according to the following sliding scale: ¼ of full compensation for POC values between 20-

29.9%, $\frac{1}{2}$ for values between 30-39.9% and $\frac{3}{4}$ for values between 40-49.9%⁽⁴⁾. It is believed that this system ensures that no deserving claimant is denied compensation.

TREATMENT OF UNCERTAINTY IN THE USDOE COMPENSATION PROGRAM

The program was enacted in the US under the Energy Employees Occupational Illness Compensation Program Act (EEOICPA) of 2000. It is designed to provide compensation to the nuclear weapons production workers employed by the USDOE and its contractors, who developed cancer as a result of their occupational exposure.

Use is made of the radioepidemiological tables developed by the US National Institutes of Health (NIH), as periodically updated and implemented in the Interactive RadioEpidemiological Program (IREP) computer software. These tables are also based on epidemiological data derived from the Japanese atomic bombs survivors.

The method incorporates formal uncertainty analysis by describing the uncertainty in each of the parameters mentioned above by a subjective probability distribution and propagating these uncertainties through a Monte Carlo type calculation to obtain the full probability distribution of the POC (instead of its central estimate in the UK scheme).

Compensation is awarded if the POC value is 50% or above, but instead of using the central estimate of the POC, the EEOICPA mandates the use of the upper 99% confidence limit of its distribution.

CONCLUSIONS

Although the treatment of uncertainties in the USDOE Compensation Program is more formal and scientifically based than in the UK Compensation Scheme, the political decision to mandate by law the use of the upper 99% confidence limit of the POC distribution introduces some partiality: on one hand it ensures that no deserving claim would be denied, but on the other hand it may allow many non-deserving claims to be successful. The treatment of uncertainties in the UK Compensation Scheme, through the introduction of proportional recovery at POC values lower than 50%, seems therefore more balanced.

REFERENCES

1. NRC. *Health risks from exposure to low levels of ionizing radiation*. BEIR VII Phase 2. National Research Council of the National Academies. The National Academies Press, Washington, D.C. (2006).
2. ICRP. The 2007 recommendations of the International Commission on Radiological Protection. ICRP Publication 103. *Annals of the ICRP* 37(2-4) (2007).
3. IAEA/ILO/WHO. *Approaches to attribution of detrimental health effects to occupational ionizing radiation exposure and their application in compensation programmes for cancer*. Occupational Safety and Health Series No. 73. ILO, Geneva (2010).
4. Wakeford R., Antell B.A. and Leigh W.J. A review of probability of causation and its use in a compensation scheme for nuclear industry workers in the United Kingdom. *Health Physics* 74, 1-9 (1998).

Radiation Protection (Wednesday, February 12, 2014 11:30)

Development of a Method to Assess the Radiation Dose due to Internal Exposure to Short-lived Radioactive Materials

D. Benmaman¹, J. Koch¹, J. Ribak²

¹ *Soreq Nuclear Research Center, Yavne, Israel*

² *Tel-Aviv University, Tel-Aviv, Israel*

INTRODUCTION

Work with radioactive materials requires monitoring of the employees' exposure to ionizing radiation. Employees may be exposed to radiation from internal and/or external exposure. Control of external exposure is mostly conducted through personal radiation dosimeters provided to employees. Control of internal exposure can be performed by measuring the concentration of radioactive substances excreted in urine or through whole-body counting in which the entire body or target organs are scanned with a sensitive detector system ⁽¹⁾. According to the regulations in Israel an employee that may be internally exposed must undergo an exposure control at least once every three months. The idea lying behind the control of internal exposure by urine testing is that if radioactive material has penetrated into the employee body, it can be detected even if the test is performed once every three months. A model was fitted for each element describing its dispersion in the body and its excretion therefrom ⁽²⁾. By means of this model, one can estimate the activity that entered the body and calculate the resulting radiation dose to which the worker was exposed. There is a problem to implement this method when it comes to short-lived radioactive materials, for which it is very likely that the material that penetrated into the body has decayed and cannot be detected by testing once every three months. As a result, workers with short-lived radioactive materials are presently not monitored for internal exposure, in contradiction to the requirements of the Safety at Work Regulations. The purpose of the study is to develop an alternative method to assess the amount of radioactive material absorbed in the body and the resulting radiation dose due to internal exposure of workers to short-lived radioactive materials.

METHODS

Two methods for monitoring two radionuclides that enter the body were investigated in the study.

^{99m}Tc

The method is based on introducing a known activity of ^{99m}Tc in various organs inside a phantom (liver, stomach and other organs in the abdomen), and measuring the dose rate in front of the stomach area.

The bio-kinetic model of ^{99m}Tc determines its distribution among the different body organs.

The first step is to determine the activity that if introduced daily into the body will cause a dose of 1 mSv per year (the dose limit to members of the public), taking into account the physical and biological decay ("activity threshold").

The second step is to measure the dose rate corresponding to the activity threshold in front of the stomach of the phantom. This dose rate is used as a decision value above which employees are sent to a urine test or a whole-body counter test. In addition, the behavior of the dose rate as a function of the activity was examined, in order to ensure that this behavior is linear.

¹³¹I

The method is based on measuring the count rate produced by a known activity of ¹³¹I inside a capsule by means of an uptake counting instrument.

The same two-step procedure as for ^{99m}Tc is used for ^{131}I with two differences: the measurement is carried out in front of the thyroid and a count rate is measured in cpm (counts per minute).

RESULTS

^{99m}Tc

To determine the threshold value above which the employee should be sent to a urine test, a few radiation detectors were tested, functioning according to different principles (Geiger-Mueller (GM) counter, proportional counter and plastic scintillator). Measurement results were obtained in units of cps (GM counter and proportional counter) or $\mu\text{Sv/h}$ (plastic scintillator).

- a. The results obtained with the radiation detectors 1 and 2 (a GM counter and a proportional counter, respectively) show that the coefficients of variation for these radiation monitors are quite low (0.22 and 0.13, respectively) and the results are therefore highly reliable. In addition, there is a very good correlation between the activity introduced in the phantom and the count rate ($R^2 = 0.9856$ and $R^2 = 0.9615$, respectively). However, for radiation detectors that measure the count rate (cps), the size of the detector and its principle of operation have a strong influence on the results. Therefore, since it cannot be guaranteed that all employers possess a specific radiation detector, an instrument that measures the count rate is not suitable as a screening tool for radiotoxicology monitoring.
- b. The results obtained with the radiation detectors 3 and 4 (plastic scintillators) show that the coefficients of variation for these instruments are low (0 and 0.43, respectively). In addition, there is a very good correlation between the activity introduced into the phantom and the radiation dose rate ($\mu\text{Sv/h}$) ($R^2 = 0.972$ and $R^2 = 0.9298$, respectively). Therefore, both monitors are suitable as screening tools for radiotoxicology monitoring.

The radiation dose rate that was defined as the threshold value above which a urine test should be conducted is $0.1 \mu\text{Sv/h}$ above the background level.

- c. In spite of the recommendations in paragraphs (a) and (b) above, since the RAM GENE 1 GM device (Rotem Ltd.) is a relatively cheap instrument, workplaces involved in working with ^{99m}Tc that do not possess a plastic scintillator could use a RAM GENE 1 detector. The threshold value above which a urine test should be conducted is in this case 2 cps above the background radiation level.

^{131}I

The results of the experiments conducted show that the coefficient of variation is very low (0.15). In addition, a very good correlation exists between the activity of ^{131}I in the thyroid and the count rate (cpm) ($R^2 = 0.9987$). Therefore, a Model CAPTUS 2000 (Capintec Inc.) can be used as a screening tool for radiotoxicology monitoring. It was found that the measurement period should last at least two minutes.

The threshold value above which a urine test should be performed is 20 cpm.

CONCLUSIONS AND RECOMMENDATIONS

The following conclusions and recommendations can be drawn from the present study:

1. Workers with ^{99m}Tc should be checked at the end of each working day with a radiation detector of the plastic scintillator type positioned in front of the stomach. If the reading is higher than $0.1 \mu\text{Sv/h}$, a urine sample should be immediately sent to a radiotoxicology laboratory. Every reading lower than this value should be considered as negligible. A GM detector can also be used for this purpose, but because of the strong influence of the detector size, the use of a uniform device should be recommended. Economic considerations being taken into account, the most suitable device is the RAM GENE 1. The threshold value is in this case 2 cps above the background level.
2. Workers with ^{131}I should be checked at the end of each working week with an uptake device. The threshold value above which a urine sample should be sent to a radiotoxicology laboratory is 20 cpm (above the background level).

REFERENCES

1. ICRP. *Dose Coefficients for Intakes of Radionuclides by Workers*. Publication No. 68. Annals of the ICRP 24(4)(1994).
2. ICRP. *Individual Monitoring for Internal Exposure of Workers*. Publication No. 78. Annals of the ICRP 27(3/4)(1997).

Radiation Protection (Wednesday, February 12, 2014 11:30)

A Combined Shielding Design for a Neutron Generator and a Linear Accelerator at Soreq NRC

L.Epstein

Soreq Nuclear Research Center, Yavne, Israel

INTRODUCTION

A new radiography facility is designed at Soreq NRC. The facility will hold a neutron generator that produces $1.73 \cdot 10^9$ n/s with an energy of 14 MeV and a linear accelerator that accelerates electrons to an energy of 9 MeV. The two radiation sources will be installed in 2 separate laboratories that will be built in an existing building. Each laboratory will have its own machine and control room. The dose rates around the sources were calculated using the FLUKA Monte Carlo code^(1,2). The annual doses were calculated in several regions around the generator and the accelerator laboratories in accordance with the occupancy in each area. The calculated annual doses were compared with the dose limits specified in the Safety at Work Regulations⁽³⁾ and the IAEA Standard for Protection against Ionizing Radiation⁽⁴⁾. The shielding was designed to comply with the following dose constraints: 0.3 mSv/y for members of the public and 2 mSv/y for radiation workers.

Each radiation source is planned to produce radiation for a maximum of 500 hours per year. The dose rate in the direct beam of the accelerator is 30 Gy/min at 1 m from the source and it will be surrounded by a collimator with an opening of 30° horizontally and 2 mm vertically, 3 m from the radiation source. The leakage radiation dose will not be greater than 1.5 mGy/min (0.005% of the direct beam, according to the manufacturer). The leakage radiation will be produced isotropically.

The neutron generator will be surrounded by a shielding made of a 10 cm iron cylinder (density 7.87 g/cm³), surrounded by 50 cm of borated polyethylene (atomic percent: H (13.8%), C (82.2%), B (4%), density: 0.92 g/cm³) and 5 cm of lead (density 11.35 g/cm³). The neutron generator shielding was not designed or required in the present shielding design but was considered in the shielding calculations.

RESULTS

The FLUKA Monte Carlo code calculates the fluence rate in every unit of volume surrounding the radiation source according to the geometry of the building and converts it to annual dose using the conversion factors specified in Publication 74 of the ICRP⁽⁵⁾. The annual dose was calculated inside and outside the building and for various shielding options. The selected shielding design is the minimal shielding that complies with the dose constraints specified above and the requirements of the future user of the facility.

The annual doses take into account the occupancy factor in each surrounding area: full occupancy in the control room (500 hours annually), 1/25 occupancy in the machine room, 1/5 occupancy in the building corridors and 1/40 occupancy in the areas surrounding the building. The occupancy factors were selected according to data provided by the future user of the facility and the recommendations in Report 151 of the NCRP⁽⁶⁾.

Dose Rates due to Operation of the Accelerator

The future user of the facility required that shielding should not be installed around the accelerator, as opposed to the neutron generator. Table 1 presents the annual doses in the areas surrounding the accelerator laboratory (500 hours of operation).

Table 1. Annual doses around the accelerator laboratory.

	Occupancy factor	Occupants	Annual dose (mSv/y)
Control room	1	Rad. workers	2
Machine room	1/25	Rad. workers	2
Maze entrance	1/5	Members of the public	0.2
Parking lot	1/40	Members of the public	0.4*
Generator lab.	1	Rad. workers	16
South of building	1/40	Members of the public	0.3
Roof	-	-	2,200

* The annual dose 1 m from the northern wall is lower than the dose constraint for members of the public (0.3 mSv/y)

The highest annual dose in the control room and the machine room are equal to the dose constraint for radiation workers (2 mSv/y). The highest dose rate in the machine room exists in the south-east corner and is 0.1 mSv/h, while the dose rate in the other parts of the room is lower than 20 μ Sv/h. If workers are planned to stay in the machine room for long periods of time (higher occupancy factor than 1/25) during the accelerator operation one of the following should be done:

1. Restrict access to the south-east corner of the room.
2. Add shielding on the wall facing the accelerator laboratory (thickness of the shielding will be calculated according to the updated occupancy factor in the room).

The annual dose in the generator laboratory is higher than the dose constraint and equals 16 mSv/y (max. dose rate: 30 μ Sv/h). Presence of workers in the generator laboratory during the accelerator operation should be restricted to 60 hours annually or shielding should be added on the wall between the two laboratories. The high annual dose on the roof of the building requires restricting entrance to the roof during the accelerator operation.

A fence should be built that will not allow people to come closer than 1 m from the northern wall of the building.

Dose Rates due to Operation of the Neutron Generator

Table 2 presents the maximum annual doses in surrounding areas of the neutron generator laboratory (500 hours of operation).

Table 2. Annual doses around the neutron generator laboratory.

	Occupancy factor	Occupants	Annual dose (mSv/y)
Control room	1	Rad. workers	1.1
Machine room	1/25	Rad. workers	0.2
Maze entrance	1/5	Members of the public	0.2
Parking lot	1/40	Members of the public	0.4*
Accelerator lab.	1	Rad. workers	0.1
South of building	1/40	Members of the public	0.2
Roof	-	-	70

* The annual dose 1 m from the northern wall is lower than the dose constraint for members of the public (0.3 mSv/y)

The annual doses in the control room, the machine room and the accelerator laboratory are lower than the dose constraint for radiation worker (2 mSv/y). The annual doses to members of the public in the maze entrance, the parking lot and south of the building are lower than the appropriate dose constraint. Due to the high annual dose on the roof of the building (assuming full occupancy), this area should be restricted and entrance should not be permitted during operation.

Activation Calculations

FLUKA was also used to evaluate neutron activation of materials in the generator laboratory. The dose rates from the activated materials were calculated depending on the irradiation time and the cooling time after operation. The maximum irradiation time (48 h) and two cooling times (1 min and 10 min) were considered in the calculations. Several large metal objects made of iron, aluminum and lead surround the generator and their mass and distance from the generator were considered. The most common produced radionuclides are ^{56}Mn , ^{28}Al and ^{24}Na . It was found that after 48 hours of irradiation the highest dose rate in the room is 30 $\mu\text{Sv/h}$ in contact with to the shielding of the generator.

CONCLUSIONS

The shielding of the two laboratories that are planned to be built at Soreq NRC was designed to comply with dose constraints that were set based on the Safety at Work Regulations and the IAEC Standard. Few surrounding rooms (the control room and the machine room) were defined as controlled areas to which only radiation workers can access and the roof of the building was defined as an area to which access is denied during operation of the generator or the accelerator as a result of high radiation doses.

Prolonged operation of the neutron generator (longer than 48 hours) may cause considerable activation of the metals in the neutron generator laboratory that will require long cooling times. Entrance to the neutron generator laboratory after operation will only be permitted when the dose rate inside the room will be lower than 1 $\mu\text{Sv/h}$.

If occupancy in the machine room of the accelerator laboratory or the neutron generator laboratory is required during operation of the accelerator, shielding should be added on the wall facing the accelerator.

REFERENCES

1. Battistoni G., Muraro S., Sala P.R., Cerutti F., Ferrari A., Roesler S., Fasso` A. and Ranft J., *The FLUKA code: Description and benchmarking*. Proceedings of the Hadronic Shower Simulation Workshop 2006, Fermilab, 6-8 September 2006, M. Albrow, R. Raja eds., AIP Conference Proceedings 896, 31-49 (2007).
2. Fasso` A., Ferrari A., Ranft J. and Sala P.R., *FLUKA: a multi-particle transport code*. CERN-2005-10, INFN/TC_05/11, SLAC-R-773 (2005).
3. Ministry of Economy, *Safety at Work Regulation (Environmental and Biological Monitoring of Workers with Harmful Agents) - 2011*.
4. Israel Atomic Energy Commission, *The IAEC Standard for Protection against Ionizing Radiation - 2011*.
5. International Commission on Radiological Protection, *Conversion Coefficients for Use in Radiological Protection against External Radiation*. ICRP Publication 74 (1996).
6. National Council on Radiation Protection and Measurements, *Structural Shielding Design and Evaluation for Megavoltage X- and Gamma-ray Radiotherapy Facilities*. NCRP Report No. 151 (2005).

Radiation Protection (Wednesday, February 12, 2014 11:30)

Shielding Calculations for Industrial 5/7.5MeV Electron Accelerators Using the MCNP Monte Carlo Code

E. Peri, I. Orion

Ben-Gurion University of the Negev, Beer Sheva, Israel

INTRODUCTION

High energy X-rays from accelerators are used to irradiate food ingredients to prevent growth and development of unwanted biological organisms in food, in order to extend the shelf life of products. High energy photons can cause food activation due to (γ,n) reactions. Until 2004, to eliminate the possibility of food activation, the electron energy was limited to 5 MeV X-rays for food irradiation. In 2004, the FDA approved the usage of up to 7.5 MeV, but only with tantalum and gold targets ⁽¹⁾. Higher X-ray energy results an increased flux of X-rays in the forward direction, increased penetration, and higher photon dose rate due to better electron-to-photon conversion. These improvements could decrease the irradiation time and allow irradiation of larger packages, thereby providing higher production rates with lower treatment cost.

Medical accelerators usually work with 6-18 MV electron energy with tungsten target to convert the electron beam to X-rays. In order to protect the patients, the accelerator head is protected with a heavy lead shielding; therefore, the bremsstrahlung is emitted only in the forward direction. There are many publications and standards that guide how to design optimal shielding for medical accelerator rooms ^(2,3,4). The shielding data for medical accelerators is not applicable for industrial accelerators, since the data is for different conversion targets, different X-Ray energies, and only for the forward direction.

Collimators are not always in use in industrial accelerators, and therefore bremsstrahlung photons can be emitted in all directions. The bremsstrahlung spectrum and dose rate change as a function of the emission angle. The dose rate decreases from maximum in the forward direction (0°) to minimum at 180° by 1-2 orders of magnitude. In order to design and calculate optimal shielding for food accelerator rooms, there is a need to have the bremsstrahlung spectrum data, dose rates and concrete attenuation data in all emission directions, which are different for each conversion target and energy (5 MeV or 7.5 MeV). There are publications and standards available such as: NCRP 144 ⁽⁵⁾, IAEA Report 188 ⁽⁶⁾, ANSI N43.3 ⁽⁷⁾, to guide how to design shielding for industrial accelerator rooms. The shielding data in these guides is suitable for most industrial accelerators that have collimators, but does not contain angular dependence shielding data for 5 MeV and 7.5 MeV X-rays, such as used in food irradiation facilities.

OBJECTIVE

In this study we calculated essential data needed for a typical straightforward concrete shielding designs food accelerator rooms. These are the MCNP Monte Carlo code system evaluations made for this study: (1) Photon dose rate angular dependence ($0-180^\circ$) of 5 MeV and 7.5 MeV electron beams, on iron, aluminum, gold, tantalum, and tungsten targets. (2) Bremsstrahlung angular dependence energy distribution ($0-180^\circ$) simulations using 5 MeV and 7.5 MeV electron beams on gold, tantalum, and tungsten. (3) Photon attenuation calculations in concrete for several photon emission angles of 5 MeV and 7.5 MeV electron beams on a tantalum target. Based on the simulation, we calculated the expected increase in dose rate for facilities intending to increase the energy from 5 MeV to 7.5 MeV, and the concrete width needed to be added in order to keep the existing dose rate unchanged.

The data given in this paper is partial; the complete explanations and the full results can be found in the thesis submitted for M.sc degree by Eyal Peri and supervised by Itzhak Orion ^(Error! Reference source not found.).

MATERIAL AND METHODS

The simulations were carried out using the MCNP version 4C2 code package. The simulations were done by irradiating gold, tantalum, and tungsten targets with a narrow 5/7.5 MeV electron beam. The targets depth and radial dimensions were chosen to be slightly more than the electron maximum range. Target thickness of Ta, W and Au were 1.5, 1.3 and 1.3 mm for 5 MeV electrons, and target thickness of Ta and Au were 2.3 and 2.0 mm for 7.5 MeV electrons.

The material compositions and densities were defined by the compendium of material composition data for radiation transport modeling⁽⁸⁾, the shielding material was defined as an ordinary concrete.

The tally F6 in a cell volume was used for absorbed dose calculations. Tally F4 of photon fluence was used for the photon spectra graphs.

In order to validate the results, prior to the calculations, simulations were done with targets or energies which is available in the literature, all the results showed a good agreement. Usually 10^6 - 10^8 histories were used to obtain relative error less than 5%.

RESULTS

Figure 10 presents the angular dependence (0-180°) of photon dose rate (Gy h^{-1}) at 1 m from gold, tantalum, and tungsten targets as a function of beam current (mA) for 5 MeV and 7.5 MeV electron beams. Due to the larger atomic number of gold its dose rate is slightly higher, but only for the backward angles ($>90^\circ$). This is one of the reasons why a gold target is not cost effective. The 7.5 MeV dose rates are almost parallel to those of 5 MeV and higher by a factor of 1.5 to 2.6.

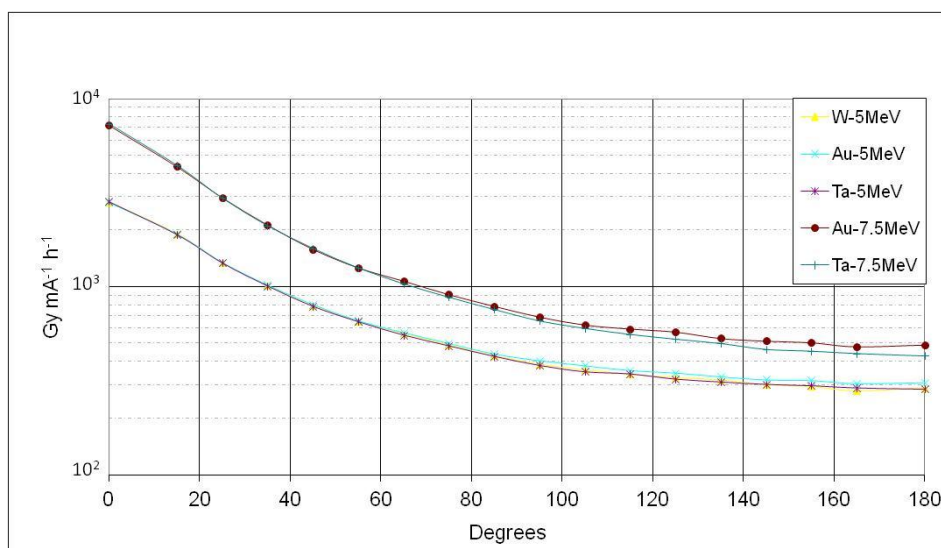


Figure 10: Angular dependence of photon dose rate (Gy h^{-1}) at one meter from Au, Ta, W targets as a function of beam current (mA) for 5/7.5MeV electron beam.

Figure 2 presents the energy distribution of bremsstrahlung emission for tantalum target by 5 MeV and 7.5 MeV electron beams. The spectrum of the forward direction photons is higher and "harder" than the spectrum in the backward emission. In the lower energy bins, the fluence in the forward directions is higher by an order of magnitude than the backward emission. As the energy bins increased, the gap increases up to three orders of magnitudes in the higher energy bins, from that we can understand why the dose rate is decreasing as the photon emission angle increases. The fact the spectrum of the backward direction is softer explains why the concrete shielding is more effective to attenuate backward photon emission.

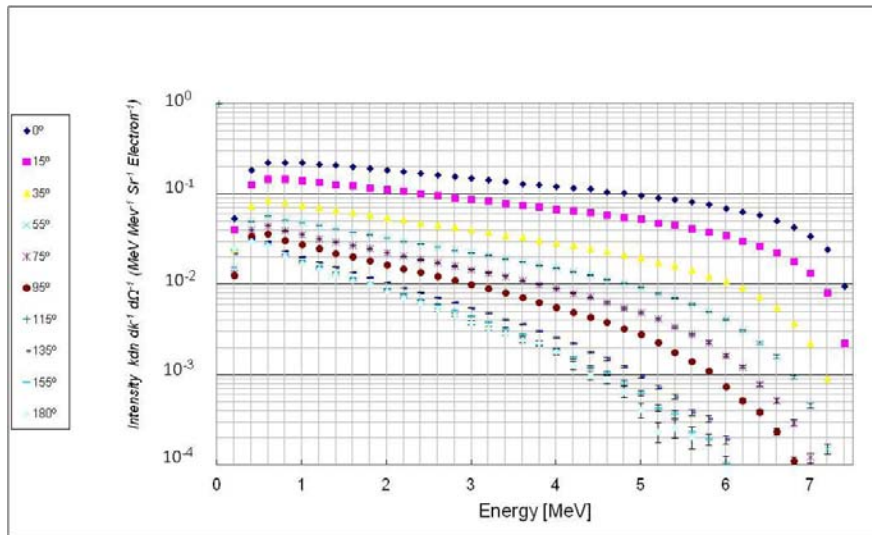


Figure 11: Energy distribution of 7.5 MeV bremsstrahlung in Ta Target.

Figure 12 presents the photon attenuation ratio in concrete (0-180 cm) of a tantalum target in selected photon emission angles (0° , 90° , 135° , 180°) for 5 MeV and 7.5 MeV electron beams. The attenuation ratio was obtained as the ratio between the dose without shielding, to the dose behind the concrete shielding. The photon attenuation in concrete for 5 MeV is higher than for 7.5 MeV by up to an order of magnitude. The attenuation is larger for the backward emitted photons compared to the forward ones by up to an order of magnitude.

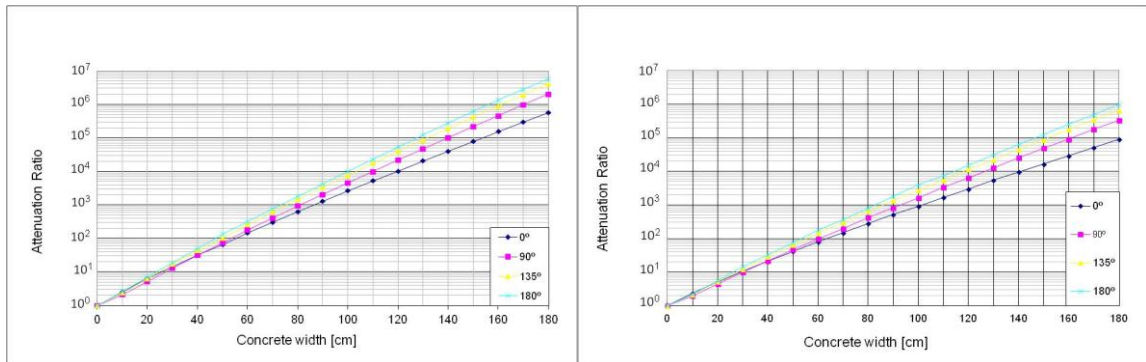


Figure 12: Dose attenuation in concrete of the bremsstrahlung emission from Ta target for electron beam energy of 5 MeV (left) and 7.5 MeV (right).

By using Table 2, facilities that plan upgrading their accelerator to 7.5 MeV can easily estimate the expected increase in dose rate around the shielded facility. It can also easily evaluate the quantity of concrete to be added in order to keep the existing dose rate around the facility, and by that to maintain the same safety status. The data are presented for three emission angles (0° , 90° , 180°) as a function of the existing concrete thickness in the facility.

Table 2: Dose rate ratios of bremsstrahlung emission between 5 MeV and 7.5 MeV beams Ta target as a function of existing concrete for a given angle (left), and the quantity of required concrete to be added for 7.5 MeV facility in order to keep the 5 MeV dose rate (right).

Existed Concrete (cm)	5 MeV and 7.5 MeV Dose Rate Ratio			Required Concrete addition (cm)		
	0°	90°	180°	0°	90°	180°
0	2.6	1.7	1.5	8	5	0.5
20	3.3	2.0	1.7	12	7	2
60	4.8	3.3	2.2	18	14	5
100	7.6	4.9	2.9	25	20	9
120	9.0	6.0	3.8	28	22	13
140	11.1	6.9	4.4	31	24	15
160	13.7	8.6	5.2	35	28	17
180	16.5	10.5	6.1	38	31	19

CONCLUSION

Angular dependence MCNP simulations of dose rate, bremsstrahlung, and concrete attenuation ratio were carried out for 5 MeV and 7.5 MeV accelerators for gold, tantalum, and tungsten targets. Since the targets' atomic numbers are similar, there was only a slight difference in dose rates and bremsstrahlung spectra of the targets. The dose rate of 7.5 MeV accelerators is higher than the 5 MeV dose rate by factor of about 2.6 in the forward direction, and a factor of 1.5 in the backward direction. The difference in dose rates from the forward to backward directions is almost two orders of magnitude. Photon attenuation ratios in concrete of 7.5 MeV beam is lower than that of 5 MeV beam by almost an order of magnitude for thick shielding for all emission angles. There is a significant difference in the bremsstrahlung spectrum between the forward emission angles to the backward angles. Since the bremsstrahlung spectrum of the backward angles is softer than in the forward direction, the concrete shielding is more effective in attenuating the backward direction. This difference is small for thin shielding, but for thick shielding of more than 150 cm, the attenuation of the backward emissions is larger than for forward direction by an order of magnitude, for the same concrete thickness.

REFERENCES

1. Federal Register, Vol. 69 No.246, December 2004, P. 76844.
2. NCRP Report No.49, Structural Shielding Design and Evaluation for Medical Use of X-Rays and Gamma-Rays up to 10 MeV, 1976.
3. NCRP Report No.151, Structural Shielding Design and Evaluation for Megavoltage X and Gamma Ray Radiotherapy Facilities, 2005.
4. IAEA, Safety Report Series No.47, Radiation Protection in the design of Radiotherapy Facilities, 2006.
5. NCRP Report No.144. Radiation Protection for Particle Accelerator Facilities; 2005.
6. IAEA, Technical Reports Series No.188, Radiological Safety Aspects of the Operation of Electron Linear Accelerators 1979.
7. ANSI/HPS N43.3-2008, For General Radiation Safety – Installation Using Non-Medical X-ray and Sealed Gamma-Ray Sources, Energy Up to 10 MeV, 2008.
8. E. Peri, Shielding calculations for industrial 5/7.5MeV electron accelerators using the MCNP Monte Carlo Code, Thesis submitted in partial fulfillment of the requirements for the M.Sc degree, November 2013.
9. Williams R.G., Compendium of Material Composition Data for Radiation Transport Modeling, DOE, April 2006.

Nuclear Licensing and Safety Office (NLSO) regulatory practices of IAEC Research Reactors²

Y. Barnea¹, U. Mintzer (Deceased)¹, H. Hirschfeld¹, M. Markovits²

¹*RRS/NLSO/IAEC, P.O.Box 7061, Tel-Aviv 61070*

²*NLSO/IAEC, P.O.Box 7061, Tel-Aviv 61070*

ABSTRACT

The achievement and maintenance of a high level of safety in the siting, design, construction, commissioning, operation and decommissioning of nuclear facilities, and in the closure of waste disposal facilities, requires a sound legal and governmental infrastructure, including a regulatory body with well-defined responsibilities and functions. The ISRAEL Atomic Energy Commission (IAEC) is committed to safe operation of its two nuclear Research Reactors (RRs) by implementing comprehensive safety practices such as the International Atomic Energy Agency (IAEA) Safety Standards and Technical Guides. These standards are studied, validated and adopted by the Nuclear Licensing and Safety Office (NLSO), the professional Regulatory Authority of the IAEC nuclear facilities. Following practices of regulatory bodies worldwide, the Research Reactor Section (RRS) of the NLSO has three basic functions: a) to develop and enact appropriate and clear safety requirements; b) to review, assess and verify compliance with these requirements; and c) in the event of departure from the license conditions, malpractice or wrongdoing by the operating organization (OO) under oversight, to revoke the operating license. The presentation refers to the principles of maintaining independent regulatory decision along with an overview of various regulatory activities of RRS/NLSO. These activities include the performance of the review and assessment (R&A) processes, such as: 1) the bases for process; 2) the verification of the safety analysis; 3) the regulatory inspection; 4) the records and documentation etc... Most of these practices were recently presented and evaluated by an IAEA Integrated Nuclear Safety Assessment of Research Reactors (INSARR) mission held in Israel from 7 to 11 July 2013. The purpose of the audit was to conduct a peer-review of the safety of the IRR-1 Pool type Research Reactor, located in the Soreq Nuclear Research Center (SNRC). Regardless the acknowledged successful review process, it is a permanent commitment of the NLSO to maintain and continuously improve nuclear facilities safety, and to assure public credibility.

INTRODUCTION

The ISRAEL Atomic Energy Commission (IAEC) is committed to safe operation of its two nuclear Research Reactors (RRs) by implementing comprehensive safety practices such as IAEA Safety Standards and Technical Guides [1]. These standards are studied, validated and adopted by the NLSO, the professional Regulatory Authority of the IAEC nuclear facilities. The Research Reactor section (RRS) of the NLSO has three basic regulatory functions: a) to develop and enact appropriate and clear safety requirements; b) to review, assess and verify compliance with these requirements; and c) in the event of departure from the license conditions or wrongdoing by the operating organization (OO) under oversight, to revoke the operating license. The present paper includes five chapters, where the first chapter includes the introduction, Chapter 2 construes the principles of maintaining independent regulatory decisions by following the IAEA guidance [2] and Chapter 3 explains the Review and Assessment (R&A) process, as the most important practice by the RRS/NLSO. Chapter 4 is addressing a recent external monitoring process of the RRS/NLSO activities, evaluated by an IAEA multinational expert mission review team (INSARR) carried out in the

² *In memoria* of Dr. Uri Mintzer (1967-2013)

IRR-1 Soreq-Nuclear Research Center (SNRC) Pool type reactor, and Chapter 5 includes the summary and some conclusions.

Regulatory Decision Making

In order to ensure independence in exercising the basic regulatory functions, there must be an effective separation between the regulatory body and the promoters of utilization and operation of the Research Reactors [2]. Nevertheless, at the same time, the NLSO must function within the national system of laws and under budget constraints. Key features of independence in regulatory decision making include: a) existence of appropriate mechanisms for external professional dialogue and consultations with the licensees; b) decisions taken on the basis of science and proven technology and relevant experience, accompanied by clear explanations of the reasoning underpinning the decisions; c) consistency and predictability, in relation to clear safety objectives and related technical criteria; d) transparency and traceability; and e) sufficient competence to ensure that decisions are firmly based on science and proven technology and relevant experience.

Review and Assessment Process

The R&A process is a critical appraisal, of information submitted by the operator to demonstrate the safety of the facility, undertaken by the RRS/NLSO, in order to enable the regulatory body to make a decision or series of decisions on the acceptability of the facility in terms of safety. The process consists of examining the operator's documents submissions on all aspects relating to the safety of the facility. It includes consideration of both normal operation and failures, and events, including human errors, which have the potential for causing the exposure of workers or the public or radiological hazards to the environment. Considering the bases for R&A, at all stages of the authorization process, the RRS/NLSO must have a clear understanding of the safety requirements that are used in the R&A. These requirements, communicated to the operator for guidance in preparing its documentation, must specify safety goals for levels of performance in the protection to be achieved. The RRS/NLSO may develop the safety requirements itself or it may adopt requirements that have been developed and issued by regulatory bodies in other States. The safety requirements must cover, among other things: a) prevention of faults rather than mitigation of their consequences; b) application of the principle of defense in depth; c) meeting the single failure criterion as well as redundancy, diversity and separation for safety related systems; d) preference for a "fail safe" passive system over an active or operator based system, for prevention and protection; e) criteria relating human-machine interface; f) dose limits and dose constraints (both occupational and public), amount of discharges to the environment and ALARA considerations; g) criteria for assessing radiological risks to workers and the public; i) minimization and management of waste generated and j) emergency preparedness. In formulating the content and structure of the requirements to be used in its review and assessment process, the RRS/NLSO considers a broad range of sources, including: (a) national laws and regulations; (b) advice obtained from consultants; (c) standards and guidance on nuclear physics and engineering, radiation, transport and radioactive waste safety as well as information issued by national and international organizations; (d) requirements and experience in other relevant industries; (e) technical results and experience from research and development. As so, the safety analysis must be as complete as possible, and one of the main tasks of the R&A is to confirm its completeness. Moreover, a basic objective of R&A is to determine whether the operator's submissions demonstrate that the facility complies throughout its lifetime with the safety objectives stipulated or approved by the regulatory body. Furthermore, the management of the R&A process is an important part of the process. The management of R&A has to include responsibility for: a) planning and directing the R&A process; (b) preparing the procedures to be followed in accordance with the overall quality management program; (c) coordinating all information exchange between the regulatory body and the operator; (d) keeping logs and records for all documents sent or received; (e) monitoring the progress of documents submitted by the operator and the progress of the R&A process against the tentative program agreed by the operator and the RRS/NLSO; (f) making the necessary arrangements whenever different disciplines of the regulatory body need to combine their expertise to make a decision in a timely manner; (g) making arrangements for co-ordination between

R&A activities and inspection activities, as appropriate; (h) making arrangements for liaison with consultants and dedicated public advisory committees as appropriate; (i) collating and disseminating the overall findings of the regulatory body following the completion of the R&A process; (k) planning for public committee consultation during the review process, as appropriate; Through the R&A, the regulatory body employs a plan to provide assurance that all topics significant to safety will be covered. This plan includes a series of steps that the RRS/NLSO will follow for all aspects and topics covered by the submission in order to identify those items for which applicable safety objectives and requirements have been met and those for which they have not. In practice, the scope and depth of the R&A will depend on several factors such as novelty, complexity, previous history, the experience of the operator and the associated risk. For regulatory efficiency, the findings of the preliminary review are prioritized on the basis of their potential implication for the overall safety assessment of the facility and associated hold points in the authorization process. For regulatory effectiveness, the R&A efforts are usually focused more on those aspects design or operation which involve untested (innovative) features. For the most important submissions by the operator (such as the safety analysis report) the RRS/NLSO is performing an acceptance review of the documentation. As a result of this review, an application or submission that is deficient in certain areas may be returned to the operator for correction and resubmittal. A major feature of the operator's submission will be its analysis of normal and fault conditions. It is imperative that the safety of a facility is based on sound engineering and good management, and safety analysis is a confirmation of the adequacy of these and not a substitute for them. As so, the value of safety analysis is in extending knowledge and understanding of the facility and process and in identifying shortcomings in areas in which safety can be improved. In the case that the RRS/NLSO may find that there are aspects of regulated facilities which are insufficiently understood. This may apply to existing or to future facilities. These aspects may involve, among other things, modelling techniques and processes or fault progression. Therefore, the RRS/NLSO may encourage the operator to carry out the necessary research and development work to extend understanding of safety related issues. Rarely, the regulatory body may decide to initiate research and development work where it considers that there is a need for additional studies beyond those undertaken by the operator. There may also be situations in which the regulatory body requires independent research and development work so that it can apply suitable critical considerations in its review and assessment. In all cases, scheduling of submission is considered necessary for the R&A process so as to facilitate the process and to minimize delays in the granting of any necessary authorizations. In scheduling the R&A program, the RRS/NLSO considers the fact that the information initially submitted by the operator may be incomplete. In such cases, it will take time to obtain adequate information so that R&A in full can be initiated. Considering the organization and technical resources for R&A, the number of consultants used by the section and the interaction with the dedicated public advisory committees, has to reflect the number and the size, the nature and type of its activity. In this regards, the RRS/NLSO is in a temporary shortage of manpower that will be addressed soon. Finally, the RRS/NLSO and the operator established formal relations based on independence and mutual respect, through proper channels of communication, and the operator, with its responsibility for the safety of the facility, is the only organization among those involved in the manufacture, construction, installation, operation and safety analysis of the facility with direct relations with the RRS/NLSO. In all the stages of the authorization process, the operator and the RRS/NLSO continue to hold meetings and discuss topics such as the bases for proposed changes to discuss matters under consideration. Written records are kept of such meetings, and of any decisions or agreements reached.

Monitoring Processes

The regulatory body has to ensure that the findings and decisions of the review and assessment process are subjected to a suitable process of peer review conforming to the national practices of the State and the overall quality assurance system of the regulatory body. Recently, the activity of the RRS/NLSO was audited through an International Atomic Energy Agency (IAEA) Integrated Nuclear Safety Assessment of Research Reactors (INSARR), held in Israel from 7 to 11 July 2013. The purpose of the mission was to conduct a peer-review of the safety of the IRR-1 Reactor, located in SNRC. The mission included IAEA safety experts as well as international experts in the field of nuclear safety from five countries, and covers all safety areas of research reactors. Key review areas include design, safety analysis, operational limits and

conditions, *Regulatory Supervision and Licensing Process*, reactor operation and maintenance, ageing management, radiation protection and waste management, and experiments and modifications. The team noted the strengthening of the national regulatory system to enhance independence and the efforts of the operator to enhance reactor safety, and recommended that the RRS/NLSO "should establish a human resource plan to maintain its technical expertise."

SUMMARY AND CONCLUSIONS

The paper contains an overview of the regulatory activities of the Research Reactors section of the NLSO, with special emphasize on the Review and Assessment process of the operator's submissions. These practices were structured during the last decade, and were proved to be efficient. Nevertheless, it is a commitment of the NLSO to maintain and continuously improve nuclear facilities safety, in order to assure public credibility.

REFERENCES

- [1] Review and Assessment of Nuclear Facilities by Regulatory Body, Safety Standards Series No. GS-G-1.2, IAEA, 2002.
- [2] Independence in regulatory decision making, INSAG-17, IAEA, December 2003.

Zirconium Ignition in an Exposed Fuel Channel

Y. Nekhamkin, D. Hasan and E. Elias

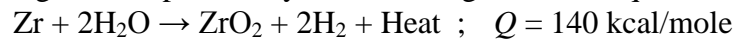
Technion – Israel Institute of Technology, 32000 Haifa, Israel

INTRODUCTION

The recent events at the Fukushima plants have underscored the importance of secondary heat generation sources, such as thermo-chemical reactions, to the overall safety of the reactor. The theory of metal oxidation and combustion has been extensively developed in the last century as part of the technological effort to develop efficient rocket propellants and later in conjunction with nuclear reactor safety. Extensive review of the basic theoretical and engineering literature is given in [1, 2]. This paper aims at surveying some of the classical models available for predicting the threshold ignition temperature related to Zr oxidation and outlines the possibilities for integrating chemical oxidation models in a full scale fuel channel transient analysis.

IGNITION OF METAL PARTICLES

Thermo-chemical reaction between steam and zirconium in the fuel cladding could become an important heat source under accident conditions. During normal operation of power reactors, the cladding temperature is about ten degrees higher than that of the coolant, i.e. about 330-350 °C. The oxidation rate at that temperature is generally low with minimal heat release. However, if the cooling deteriorates and the critical heat flux is exceeded in the core, the clad temperature could increase by several hundred degrees. At temperatures above about 900 °C, clad oxidation rate begins to significantly increase, leading to release of heat and formation of hydrogen, as expressed by the following chemical equation [4, 5]:



The heat of reaction, Q , is 6500 kJ/kg of Zr reacted (1540 kcal/kg) and the stoichiometric volume of hydrogen generated is 0.5 m³. Generally, the reaction rate depends strongly on the metal temperature, T , and on the rate of oxygen diffusion through the oxidized layer, of thickness, δ , which is formed on the outer surface of the metal. Thus, predicting the necessary conditions for ignition calls for simultaneous solution of heat and mass transfer equations. This conjugate problem was effectively approached by Khaikin et al. [3] as an extension of the classical theory of thermal explosion of a small metal sphere. Their model is slightly modified here to describe the ignition of a thin metal slab simulating the fuel cladding. A lumped parameter heat balance over a slab introduced instantaneously into a gaseous oxidizer yields,

$$mc_p \frac{dT}{dt} = \rho QS \frac{d\delta}{dt} - hS(T - T_0) \quad (1)$$

Where m and S are the mass and surface area of the metal; ρ and c_p are its density and specific heat, h the heat transfer coefficient, δ is the thickness of the oxide film at the surface, Q is the heat release per gram oxide multiplied by the oxide/metal density ratio, and T_0 is the ambient gas temperature. Equation (1) can be further manipulated by expressing the particle volume and surface area in terms of its initial thickness, a_0 , and by defining the heat transfer coefficient in terms of the Nusselt number and the metal conductivity, λ , ($h = Nu\lambda / a_0$), resulting in,

$$\rho c_p a_0 \frac{dT}{dt} = \rho Q \frac{d\delta}{dt} - \frac{\lambda}{a_0} Nu (T - T_0) \quad (2)$$

Various oxidation laws for $\delta(\tau)$ have been theoretically investigated by Khaikin et al. [3], the simplest takes the form,

$$\frac{d\delta}{dt} = \frac{A_\delta}{\delta^n} \exp\left(-\frac{E}{RT}\right) \quad (3)$$

where E is the activation energy, R the universal ideal gas constant and A_δ is a pre-exponent coefficient, which accounts for the oxidizer concentration at the surface. The parabolic law ($n=1$) will be used here as it coincides with the Baker-Just [4] model, which is broadly used in estimating Zr oxidation rate in nuclear reactors. We further adopt the following dimensionless variables,

$$\begin{aligned} \eta &= \frac{\delta - \delta_i}{\delta_i}; \quad \tau = t \frac{Q}{c_p} \frac{E}{RT_0^2} \frac{A_\delta}{a_0 \delta_i} \exp\left(-\frac{E}{RT_0}\right); \quad \chi = \frac{Q\rho}{\delta_i} \frac{E}{RT_0^2} \frac{a_0}{Nu\lambda} A_\delta \exp\left(-\frac{E}{RT_0}\right); \\ \beta &= \frac{RT_0}{E}; \quad \Theta = \frac{E}{RT_0^2} (T - T_0); \quad \Theta_i = \frac{E}{RT_0^2} (T_i - T_0); \quad \gamma = \frac{a_0 c_p RT_0^2}{\delta_i EQ} \end{aligned} \quad (4)$$

where c_p is the Zr specific heat and the index i refers to initial conditions. Equations (2) and (3) are then reduced to

$$\begin{aligned} \frac{d\Theta}{d\tau} &= (\eta + 1)^{-1} \exp\left(\frac{\Theta}{1 + \beta\Theta}\right) - \frac{\Theta}{\chi} \\ \frac{d\eta}{d\tau} &= \gamma (\eta + 1)^{-1} \exp\left(\frac{\Theta}{1 + \beta\Theta}\right) \\ I.C. : \quad &\tau = 0, \quad \eta = 0, \quad \Theta = \Theta_i \end{aligned} \quad (5)$$

The solution of (5) is determined to a considerable extent by the parameter γ in the second equation. In most cases relevant to cladding oxidation $\gamma \gg 1$ is a realistic condition. In fact, Khaikin et al. [3] have estimated the value of γ to be in the range of 10^2 to 10^5 . At values $\gamma \gg 1$ the system behavior depends on the exponent term in (5). To define the ignition conditions for $\gamma \gg 1$, Khaikin et al. [3] used the following change of variables in (5)

$$\begin{aligned} \frac{d\Theta}{d\tau'} &= \frac{1}{z} \exp\left(\frac{\Theta}{1 + \beta\Theta}\right) - \frac{\Theta}{\Omega} \\ \frac{dz}{d\tau'} &= \frac{1}{z} \exp\left(\frac{\Theta}{1 + \beta\Theta}\right) \\ z &= \frac{\delta}{a_0} \frac{QE}{c_p RT_0^2}; \quad \tau' = \frac{\tau}{\gamma}; \quad \Omega = \frac{\chi}{\gamma} \\ I.C. : \quad &\tau' = 0, \quad z = \frac{1}{\gamma}, \quad \Theta = \Theta_i \end{aligned} \quad (6)$$

The set of equations (6) was numerically solved for $\beta=0.0873$ and initial Zr thickness of $a_0=0.57$ mm, which corresponds to a PWR fuel cladding. The initial oxide thickness was 10 nm, resulting in $\gamma=430$. Figure 1 shows the Zr dimensionless temperature vs. time for two values of the parameter Ω . It is seen that, in the studied range, a small variation of Ω dramatically changes the temperature profile. The value of Ω corresponding to the abrupt temperature change is termed 'critical'. At $\Omega = \Omega_{cr}$ the oxidation heat generation exceeds the rate of convection cooling leading to rapid metal temperature escalation. The thickness of the oxide layer change significantly during the heating process, as shown in Fig. 2.

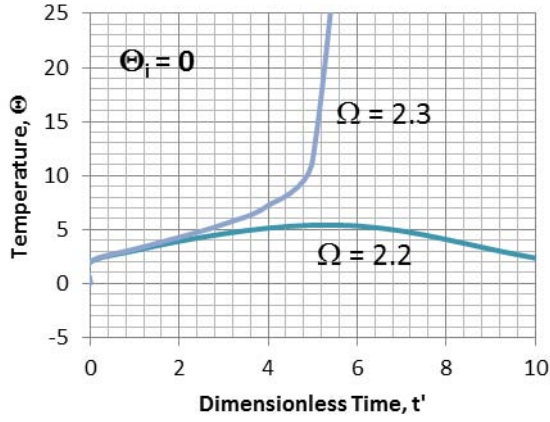


Fig. 1 Dimensionless temperature vs. dimensionless time for two values of Ω

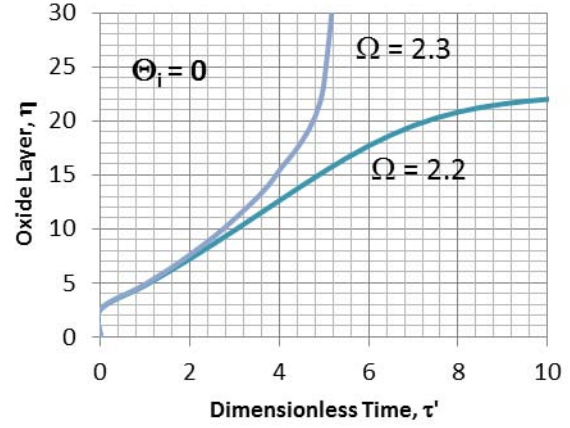


Fig. 2 Dimensionless oxide thickness vs. dimensionless time for two values of Ω

The critical condition in a slab, could be expressed as a function of ambient temperature as,

$$\Omega_{cr} = A_{\delta} \left(\frac{QE}{RT_{0,cr}} \right)^2 \frac{\rho}{Nu \lambda c_p k} \exp\left(-\frac{E}{RT_{0,cr}} \right) \quad (7)$$

where $T_{0,cr}$ is the ignition temperature, i.e., the oxidizing gas temperature corresponding to metal ignition. Figure 3 shows Ω_{cr} vs. $T_{0,cr}$ using $Nu=2$ according to [3]. The exact value of Nu must be determined according to accident conditions.

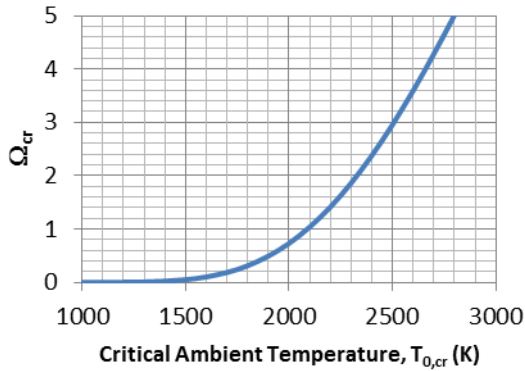


Fig. 3 Critical ignition parameter, Ω_{cr} , vs. temperature for Zr oxidation

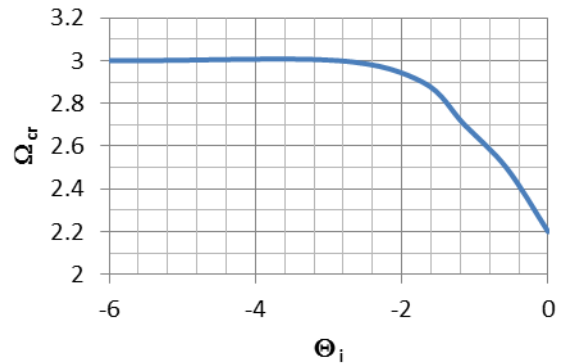


Fig. 4 Critical ignition parameter, Ω_{cr} , vs. initial Zr temperature

Using the data of Fig. 1, the value of Ω_{cr} is 2.3 for $\Theta_i=0$. Therefore, from Fig. 3, the ignition temperature is estimated as 2400 K. It is noted that the exact value of Ω_{cr} depends on the initial condition as shown in Fig 4.

CONCLUSIONS

A theoretical model based on simultaneous solution of the heat and mass transfer equations is developed for estimating the ignition temperature of Zr cladding subject to heating and oxidation in hot steam environment. The present solution will be integrated as part of a channel code for predicting the anticipating possible outcomes of different accident mitigation procedures in light water nuclear reactors under LOCA conditions.

ACKNOWLEDGEMENT: This work is supported by the Israel Atomic Energy Commission (IAEC) and the Ministry of Energy and Water Resources under Technion contract 2017804

REFERENCES

- [1].L. P. Yarin and G. Hetsroni, "Combustion of Two-Phase Reactive media", Springer-Verlag Berlin, 2004.
- [2]. Y. Nekhamkin, V. Rosenband, D Hasan, E. Elias, E. Wacholder and A. Gany, *Oxidation and Heat Transfer Considerations in Degraded Core Accident*, TOPSAFE98, Valencia, April 1998.
- [3].B. I. Khaikin, V. N. Bloshenko and A. G. Merzhanov, "On the Ignition of Metal Particles", UDC 536.46-662.215.1, Translated from *Fizika Goreniya i Vzryva*, No. 4, pp. 474-488, October-December, 1970, also in *Combustion, Explosion, and Shock Waves*, Vol. 6, No. 4 (1970).
- [4].Louis Baker, Jr. and Louis C. Just, "Studies of Metal-Water Reactions at High Temperatures", Argonne National Lab. ANL 6548, May 1962.
- [5].C. L. Whitmarsh, "Review of Zircaloy-2 and Zircaloy-4 Properties Relevant to N.S. SAVANNAH Reactor Design", ORNL-3281, 1982.

Extending Two-Phase Capabilities of Thermal-Hydraulic Module in BGCore

M. Margulis¹, E. Shwageraus²

¹Ben Gurion's Center for Global Engineering, P.O.B. 653 Beer-Sheva 84105, Israel

²Ben-Gurion University of the Negev, P.O.B. 653 Beer-Sheva 84105, Israel

INTRODUCTION

In recent studies we presented a system of codes, BGCore⁽¹⁾, which couples Monte Carlo (MC) with point depletion and TH solvers. The thermal hydraulic module, THERMO⁽²⁾, is responsible for the prediction of temperature and coolant density distributions. This paper describes the deficiencies of the previous models used in the TH module and presents the modifications that were implemented to improve the accuracy of the TH solver.

The main challenge of the TH solver is to predict correctly the development of the boiling regime in a heated channel. The previously implemented model in THERMO used a vapor quality correlation suggested by Ahmad⁽³⁾. This model neglects the vapor generation between the onset of nucleate boiling (ONB) and the onset of significant void (OSV), thus over estimates the coolant density in the region. This in turn may influence the neutronic parameters. In order to ensure accurate prediction of the vapor generation in the channel, we suggest to use an alternative correlation developed by Delhay⁽⁴⁾. The use of this correlation enables prediction of vapor generation between the ONB and the OSV.

Modified THERMO module was tested on a typical 7x7 BWR assembly and the results were compared against those of DYN3D⁽⁵⁾. Preliminary results showed a large deviation from the results obtained from DYN3D. Therefore, in order to reduce the discrepancy between the two codes, we adopted the void fraction and pressure drop correlation similar to DYN3D. The modified THERMO version showed good agreement with DYN3D and can be used as TH solver in coupled MC codes.

METHODOLOGY

This section presents the new models adopted in THERMO. First modification accounts for the two-phase regime between the ONB and OSV points and relies on the Delhay⁽³⁾ correlation which is presented in Eq. (1). The correction is based on a hyperbolic tangent function, which has zero derivative at the ONB point.

$$(1) \quad x' = 0.01\xi \left\{ x_{eq} - x_{ONB} \left[\tanh \left(\frac{x_{eq}}{x_{ONB}} - 1 \right) + 1 \right] \right\}$$

Where x_{ONB} is the quality at the onset of nucleate boiling and calculated according to Eq. 2 with ΔT_d calculated according to Eq. 3, which was suggested by Frost and Dzakowic⁽⁶⁾.

$$(2) \quad x_{ONB} = - \frac{C_{pl} \Delta T_{ONB-d}}{h_{lg}}$$

$$(3) \quad \Delta T_{ONB-d} = (\Delta T_{sat})_{ONB} = \left(\frac{8\sigma\Phi T_{sat}}{k_l h_{lg} \rho_g} \right)^{0.5} Pr_l$$

The constant ξ , in Eq.1, is adjusted to allow continuity of the quality between the sub-cooled boiling region and the Fully Developed Boiling (FDB). The constant ξ is calculated so that Eq. 1 and 4 give the same value of x' where their derivatives are equal.

$$(4) \quad x' = x_{eq} + [x_{OSV} - x_d] \exp\left(\frac{x_{eq}}{x_d} - 1\right)$$

Where x_{OSV} is the quality at the OSV point calculated according to Manon⁽⁷⁾ model and x_d is the equilibrium quality at the point of bubble detachment, given by Eq. 2 with ΔT_{ONB-d} replaced by Eq. 5.

$$(5.1) \quad \Delta T_d = 0.0022 \left(\frac{\phi D}{k_l} \right) \quad \text{for } Pe < 70000$$

$$(5.2) \quad \Delta T_d = 153.8 \left(\frac{\phi}{GC_{pl}} \right) \quad \text{for } Pe > 70000$$

In addition to vapor quality model, additional modifications were made in THERMO module.

In order to reduce the difference between THERMO and DYN3D, it was decided to switch from the drift flux model for void calculation to the Molochnicov⁽⁸⁾ correlation, which is used by DYN3D and shown in Eq. 6.

$$(6) \quad \alpha = 1 + \frac{0.6 + 1.5\beta^2}{\sqrt[4]{Fr}} \left(1 - \frac{P}{P_{cr}} \right) [1 - \exp(-20\beta)]^{3/2}$$

Where $Fr = \omega_0^2 / gd_H$ is the Froude number; $\omega_0 = G / \rho_l S$ is the circulation velocity; P is the system pressure and $P_{cr} = 22.56$ [MPa] is the critical pressure for water. β is calculated according to Eq. 7.

$$(7) \quad \beta = \left[1 + \frac{\rho_g}{\rho_l} \frac{1 - x'}{x'} \right]^{-1}$$

Furthermore, it was also found that the total pressure drop, Eq. 8, is strongly affected by distribution of the void fraction. Therefore, we replaced the previously used homogeneous model (HEM) for pressure drop calculation by the separate flow model (SFM). The SFM eliminates the basic assumption of HEM, that the liquid-gas phases are moving at the same velocity, thus allowing a more realistic calculation of the pressure drop in the core.

$$(8) \quad \left(\frac{dP}{dz} \right)_{tot-TP} = \left(\frac{dP}{dz} \right)_{fric-TP} + \left(\frac{dP}{dz} \right)_{g-TP} + \left(\frac{dP}{dz} \right)_{a-TP}$$

Both models evaluate gravity losses according to Eq. 9. Where ρ_m is the two-phase mixture density.

$$(9) \quad \Delta P_{g-TP} = \rho_m g L \sin \theta$$

The calculation of the acceleration pressure drop however must account for the different velocity of the two phases in the channel, as can be seen in Eq. 10.

$$(10) \quad \Delta P_{a-TP} = G_{tot}^2 \left[\left(\frac{(1-x)^2}{\rho_l(1-\alpha)} + \frac{x^2}{\rho_g \alpha} \right)_{out} - \left(\frac{(1-x)^2}{\rho_l(1-\alpha)} + \frac{x^2}{\rho_g \alpha} \right)_{in} \right]$$

Calculation of the friction losses term (Eq. 8) is made according to the correlation suggested by Osmachkin⁽⁹⁾, Eq. 11.

$$(11) \quad \Delta P_{fric-TP} = f_{TP} \frac{L}{d_H} \frac{G^2}{2\rho_l} \left[1 + x \left(\frac{\rho_l}{\rho_g} - 1 \right) \psi \right]$$

Where f_{TP} is the two phase friction factor; ψ is the correction coefficient calculated according to Eq. 12.

$$(12) \quad \psi = \left[1 + x \left(\frac{\mu_l}{\mu_g} - 1 \right) \right]^{-0.2x} \left\{ 1 + 0.57x^{0.125} (1-x)^2 \left[\left(0.2 + \frac{\rho_g}{\rho_l} \sqrt{Fr} \right)^{-1} - 5.2x^2 \right] \right\}$$

MODEL VERIFICATION

In order to verify the implementation of the modified THERMO module, a code to code comparison was performed. DYN3D code was used as a reference code to simulate a typical BWR 7×7 pins assembly lattice with 36 axial nodes each of 10.16 cm height.

DYN3D is based on four balance equations for mixture mass, momentum and energy as well as vapor mass balance. The two-phase flow model, in DYN3D, uses the following assumptions:

- One of the phases (vapor or liquid) is in saturation conditions.
- The relation between phase velocities is described by a quasi-stationary phase slip model, which means, an algebraic equation for the phase slip ratio is applied.

Table 1 summarizes the main parameters of the lattice configuration.

Table 1. BWR 7×7 lattice data

Parameter	Value	Units	Parameter	Dimension [cm]
Mass flow rate	29.4	[kg/sec]	Fuel Diameter	1.43002
Inlet pressure	7.13	[MPa]	Gap Diameter	0.01524
Inlet temperature	278.80	[°C]	Clad Diameter	0.9398
Flow area	93.247	[cm ²]	Assembly pitch	8.82
Heated diameter	220.13	[cm]	Unit cell Pitch	1.2600
Wetted diameter	220.13	[cm]		

In order to verify the correctness of the new modifications in THERMO, we investigated the effect of different power distribution shapes on TH properties and compared with the results obtained from DYN3D. More precisely, different void correlations were examined at two burnup points: beginning of life (BOL) and end of life (EOL), for which, power distributions were obtained directly from DYN3D calculations, as presented in Fig. 1.

These power distributions were then used by THERMO to perform stand-alone thermal hydraulic calculations. Two main parameters of interest have been compared: vapor quality and void fraction along the axial direction. Fig. 2 and 3 show the predictions by THERMO for three types of void correlations:

1. Ahmad quality calculation with Drift flux model, designated as *THERMO-2.0 Drift*
2. Delhay model with Molochnikov void correlation, designated as *THERMO-2.04 ONB*
3. Molochnikov correlation which is also used in *DYN3D*

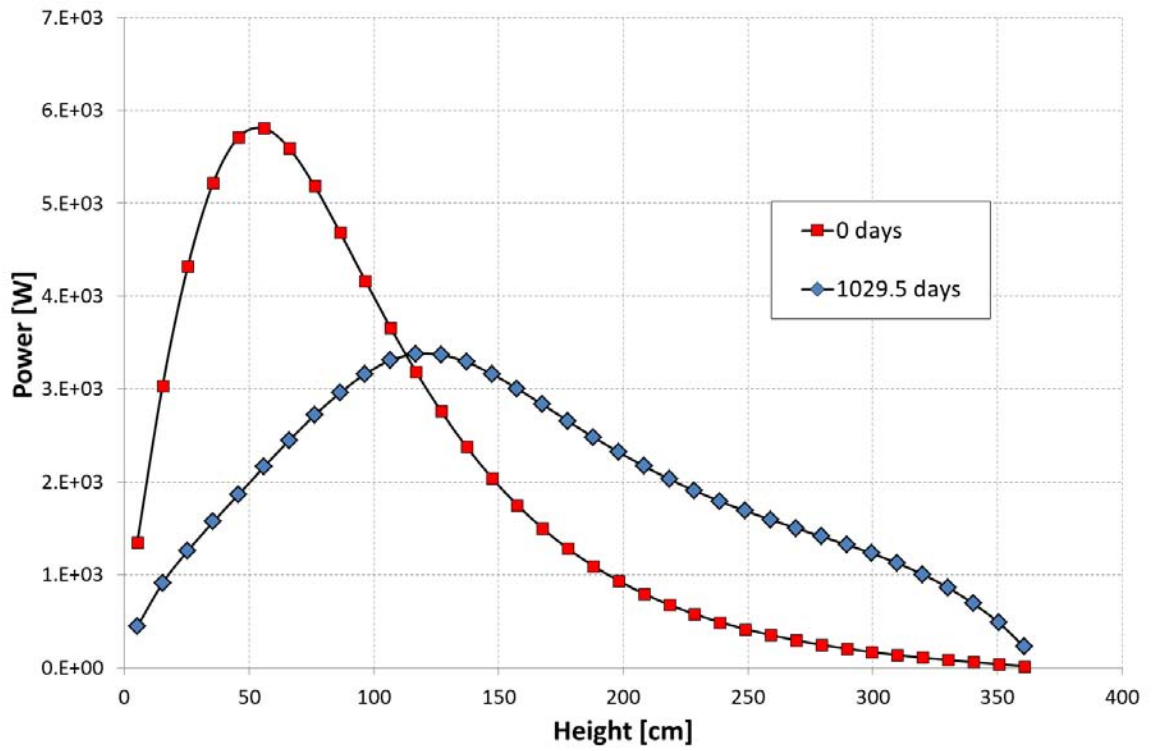


Figure 1. Power distribution for BOL & EOL

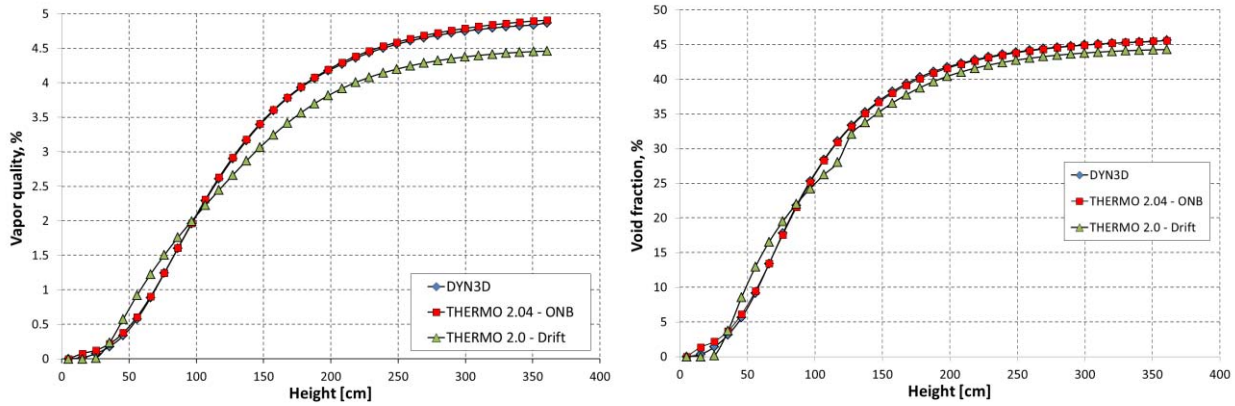


Figure 2. Void (left) and vapor quality (right) at BOL

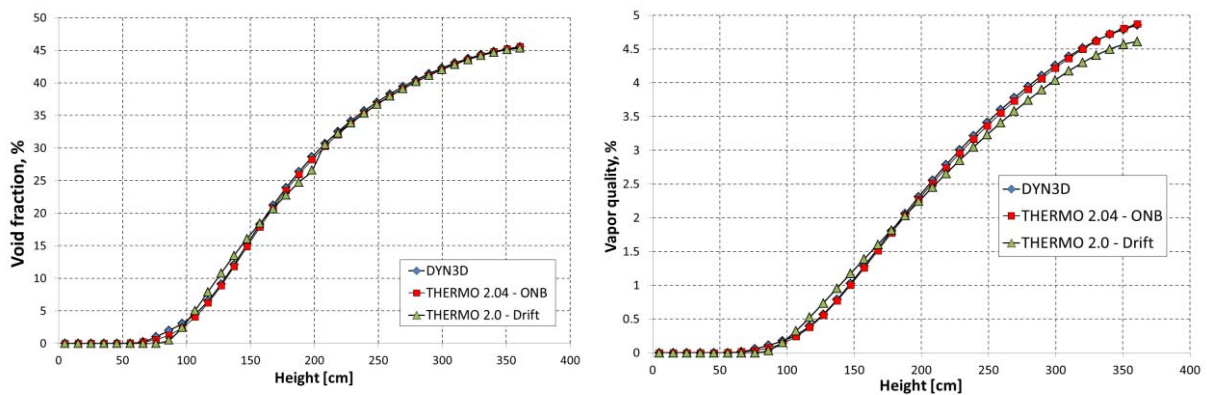


Figure 3. Void (left) and vapor quality (right) at EOL

The results presented in Fig. 2 and 3 clearly indicate that THERMO with previous implementation of vapor quality correlation does not agree with the results obtained from DYN3D. Two main differences can be seen from Fig. 2 and 3. The first is the formation of vapor quality in the channel, which is due to the use of Ahmad correlation that does not take into account the region between ONB and OSV. As a result, the first appearance of void (in drift flux model) always occurs at higher elevations in the channel (on the order of few centimeters). The second point is the different outlet vapor quality. This difference is a result of different models for pressure drop in the core. The mentioned above differences can affect significantly the neutronic parameters. As can be learned from Fig.2 and 3, these large differences disappear when the modified version of THERMO is used due to implementation of Delhay vapor quality model with Molochnikov's void fraction correlation and SFM model for pressure drop calculation.

CONCLUSIONS

The current work focused on developing reliable TH module for coupled MC codes. More precisely, different void models for two-phase flow regime were investigated. Different void models were implemented into THERMO, which is part of the BGCore reactor system of codes. The previous implementation vapor quality prediction model in THERMO was based on Ahmed correlation. The eigenvalue transport solution is obtained iteratively by including the TH feedback into the calculation scheme. Utilizing different correlation to predict void distribution will result in different coolant density profile. A typical BWR assembly test case confirms that there is a significant deviation of THERMO results obtained with previously used Ahmed model from the reference solution obtained with DYN3D. Therefore, two major modifications were applied to THERMO in order to account for the effects that were not taken into consideration by the previous drift flux model implementation. The first is more accurate prediction of ONB point which was resolved by the use of Delhay model. The second is the Osmachkin correction that allows more accurate prediction of the pressure drop. The modified THERMO results were compared against the state of the art DYN3D code certified for licensing applications in Germany. Very good agreement in all TH parameters (e.g. void and quality distribution) indicates that the current THERMO version can produce reliable results for cases with two-phase flow regime.

REFERENCES

1. D. Kotlyar, Y. Shaposhnik, E. Fridman and E. Shwageraus, *Coupled neutronic thermo-hydraulic analysis of full PWR core with Monte-Carlo based BGCore system* Nuclear Engineering and Design, **241**, p.3777-3786 (2011).
2. Y. Shaposhnik, E. Shwageraus, "Thermal-Hydraulic Feedback Module for BGCore System", Dep. Nuclear Engineering, Ben Gurion University, Israel (November 2008).
3. S. Y. Ahmad, *Axial distribution of bulk temperature and void fraction in a heated channel with inlet subcooling*, J. Heat Transfer **92** p.595-609 (1970).
4. J.M. Delhaye, F. Maugin, J.M. Ochterbeck, "Void fraction prediction in forced convective sub-cooled boiling of water between 10 and 18 MPa", Dep. Mechanical Engineering, Clemson University, Clemson, USA (2003).
5. U. Grundmann, U. Rohde, S. Mittag, *DYN3D – three dimensional core model for steady-state and transient analysis of thermal reactors* Proc. PHYSOR 2000, Pittsburgh, PA, USA (2000).
6. W. Frost, G.S. Dzakowic, "An extension of the method of predictive incipient boiling on commercially finished surfaces", ASME-AIChE Heat transfer Conference, Seattle (1967).
7. E. Manon, J.M. Delhaye, "Contribution to the analysis and the local modeling of convective sub-cooled boiling under pressurized water reactor conditions", Ecole centrale des arts et manufactures, Chatenay-Malabry, FRANCE (2000).
8. Yu. S. Molochnicov, N. G. Banashova, "Steam void fraction with tube subcooled water boiling", Achievements in heat transfer and hydraulics of two phase flow in power equipment components, Nauka, pp. 79-96, Leningrad (1973).
9. L.N. Polyanin, M. H. Ibragimov, G. I. Sabelev, "Heat transfer in nuclear reactors (Теплообмен в ядерных реакторах)", Nuclear engineering library, 5th edition, Moscow (1982).

An In-Pile Kinetic Method for Determining the Delayed Neutron Fraction β_{eff}

E. Gilad¹, O. Rivin¹, H. Ettetdgui¹, I. Yaar¹, B. Geslot², A. Pepino², J. Di Salvo²,
A. Gruel² and P. Blaise²

¹Nuclear Research Center NEGEV (NRCN), P.O. Box 9001, Beer-Sheva, 84190, Israel

²CEA/DEN/CAD/DER/SPEX/LPE, 13108 Saint Paul-les-Durance, France

INTRODUCTION

Delayed neutrons are of fundamental importance in the field of nuclear reactor dynamics and control. Although only a small fraction of the neutrons emitted by fission are not prompt, the knowledge of the delayed neutrons parameters is essential for transient analysis, such as startup or shutdown of the reactor, as well as for accidents analysis and control system design [1]. One of the main delayed neutron parameters used in the point reactor model equations is the effective delayed neutron fraction β_{eff} , which incorporates both delayed neutron spectral properties and core geometrical configuration [1,2]. Additional delayed neutron parameters include the fraction of fission neutrons emitted in each delayed group β_j , and the delayed neutron precursors decay constants λ_j .

Experimental efforts aimed at determining the value of β_{eff} , which provide experimental support for the evaluation of delayed neutron parameters, are extremely valuable. This is due to the fact that unlike other fields in reactor physics, e.g. criticality safety or shielding, the availability of experimental data and benchmark problems for validating delayed neutron parameters and its implementation in different models is highly limited [3,4]. Furthermore, the existing experimental data exhibit significant discrepancies between the different sets of parameter, which lead to substantial disparity in the analysis of kinetic experiments and reactor dynamic behavior [5].

In this work, a method for determining the effective delayed neutron fraction β_{eff} using in-pile reactivity oscillation and Fourier analysis is presented. The method is based on measurements of the reactor's power response to small periodic in-pile reactivity perturbations and utilizes Fourier analysis for reconstruction of the reactor zero power transfer function. Knowledge of the reactor transfer function enables the estimation of the β_{eff} value using multi-parameter nonlinear fit. The method accounts for higher harmonics, which are excited by the trapezoidal reactivity signal, thus showing that it is possible to reconstruct the reactor transfer function over a wide range of frequencies using only a single oscillation at a low frequency.

THEORETICAL BACKGROUND

Study of the reactor power level response to small reactivity perturbations is of great importance regarding the stability and control of the reactor. The reactor power level response is described by a transfer function, which summarizes the main physical parameters controlling the reactor's dynamics. For a critical reactor operating at low power (such that the reactivity is not affected by the reactor's power level), the transfer function is given by [1,2,6]

$$R(s) = \frac{1}{P_0} \frac{\delta P(s)}{\delta \rho(s)} = \left[s\Lambda + \sum_j \frac{s\beta_j}{s + \lambda_j} \right]^{-1} \xrightarrow{s \sim \lambda_j} \left[\sum_j \frac{s\beta_j}{s + \lambda_j} \right]^{-1}, \quad (1)$$

where $\delta \rho(s)$ is the Laplace transform of small reactivity perturbation $\delta \rho(t)$, $\delta P(s)$ is the Laplace transform of the consequent small power response $\delta P(t)$, P_0 stands for the mean power, s is a complex variable, and

$R(s)$ is the zero power transfer function. Note that the transfer function $R(s)$ is complex and its explicit representation in the frequency domain $R(i\omega)$ is obtained by substituting $i\omega$ for s [6].

EXPERIMENTAL SETUP

The oscillation experiments were performed at the MINERVE Zero Power Reactor located at CEA Cadarache Research Centre. MINERVE is a pool-type ($\sim 120 \text{ m}^3$) reactor operating at a maximum power of 100W with a corresponding thermal flux of $10^9 \text{ n cm}^{-2} \text{ s}^{-1}$. The core is submerged under 3 meters of water and is cooled through natural convection. The core is composed of a driver zone, which includes 40 standard highly enriched MTR type metallic uranium alloy plate assemblies surrounded by a graphite reflector. An experimental cavity (70x70 cm), in which various UO_2 or MOX clad fuel pins can be loaded in different lattices, reproducing various neutron spectra, is located in the center of the driver zone [7].

Our measurements at the MINERVE lasted 6 days using the MAESTRO core configuration. The experiment was performed using 16 different oscillation frequencies in the range of 5×10^{-3} to 0.25 Hz, with 100 full period cycles obtained for most frequency. The average power level during our measurements was approximately 10W, with maximal power oscillation of $\pm 2\%$ and an average power level drift of less than 1% per minute. The reactivity oscillations were introduced into the reactor using a dedicated mechanical piston, mounted with a light water sample. The water sample acted as an additional moderator, which introduced an additional reactivity of $3.79 \pm 0.02 \text{ pcm}$ into the core [8]. The neutron count rate was measured using a ^{10}B based Ionization Chamber (IC) and a high sensitivity Fission Chamber (FC).

RESULTS AND DATA ANALYSIS

An example of the reactivity perturbation worth and the corresponding IC and the FC acquired signals (total neutron count) for a 60s oscillation period is shown in Fig. 1. The prompt response of the neutron flux to the piston movement, as well as the delayed neutron dynamics, can be clearly observed. The sharp trapezoidal (nearly square) waveform of the reactivity perturbation is also evident (Fig. 1a). The statistical precision of the IC is significantly higher than that of the FC (Fig. 1b and 1c).

There are three main independent contributions for the experimental error associated with the transfer function measurements. The first contribution is due to the drift in the reactor power level during the oscillations with an average value of 2% (1σ). The second one is due to statistical fluctuations characterizing the neutron flux, the detectors response, and the electronic acquisition system, with an average value of 1% (1σ). The last one stems from the uncertainty in the reactivity worth of the induced perturbation with an average value of 1.5% (1σ). These errors are estimated for each value of the transfer function, i.e. for each harmonic value for each oscillation period.

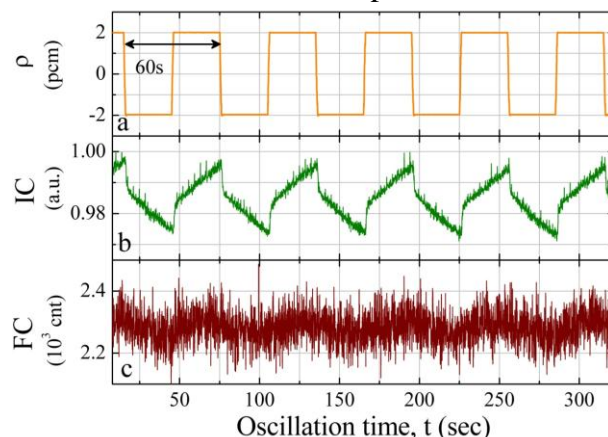


Figure 1. Example of the reactivity perturbation (a) and the corresponding IC and FC counts (b and c, respectively) obtained for a 60s oscillation period.

In order to determine the transfer function amplitude we apply Fourier transform to both the reactivity perturbation and the power response signals. An example of the 60s oscillation period analysis is shown in

Fig. 2 (left), where the power spectrum of the reactivity perturbation (Fig. 2a), and of the IC and FC detectors (Fig. 2b and 2c) are plotted. The fundamental mode and the higher harmonics are obtained at $\omega_n = 2\pi n/60$ rad/s for odd n . The transfer function amplitude values, corresponding to the first 17 harmonics of the 60s period measurement, are shown in Fig. 2d, along with the calculated theoretical curves plotted using ENDF/B-VII.1 JEFF-3.1.2 neutron data libraries. In all measurements, the number of harmonics obtained from the FC count is significantly smaller than that obtained using IC count, due to the large statistical uncertainty in the former. The obtained values of $|R(i\omega)|$ using all oscillation periods with their respective harmonics are presented in Fig. 2e (right). Also presented are calculated curves using available neutron data library. In addition, the calculated curve based on the neutron data derived in the present work is plotted. This curve exhibits good agreement with those of the literature.

The data points of the transfer function amplitude were used to fit curves of the theoretical form described in Eq. 1. The fitting procedure was applied using multi-parameter nonlinear weighted least-squares fit, where for each library, the delayed neutron precursors decay constants λ_j were fixed and the inverse of the errors were used as weights. The effective delayed neutron fraction is calculated according to $\beta_{\text{eff}} = \sum_j \beta_j$ for each library. The uncertainty in β_{eff} results from the propagation of the statistical errors, the uncertainty in the induced reactivity perturbation, and the uncertainty in the λ_j sets taken from different libraries. Assuming that these uncertainties are uncorrelated, the total uncertainty in the derived value of β_{eff} is ~ 17 pcm. The obtained value of β_{eff} is 711 ± 17 pcm (1σ), in agreement with the calculated value of 716 pcm [9].

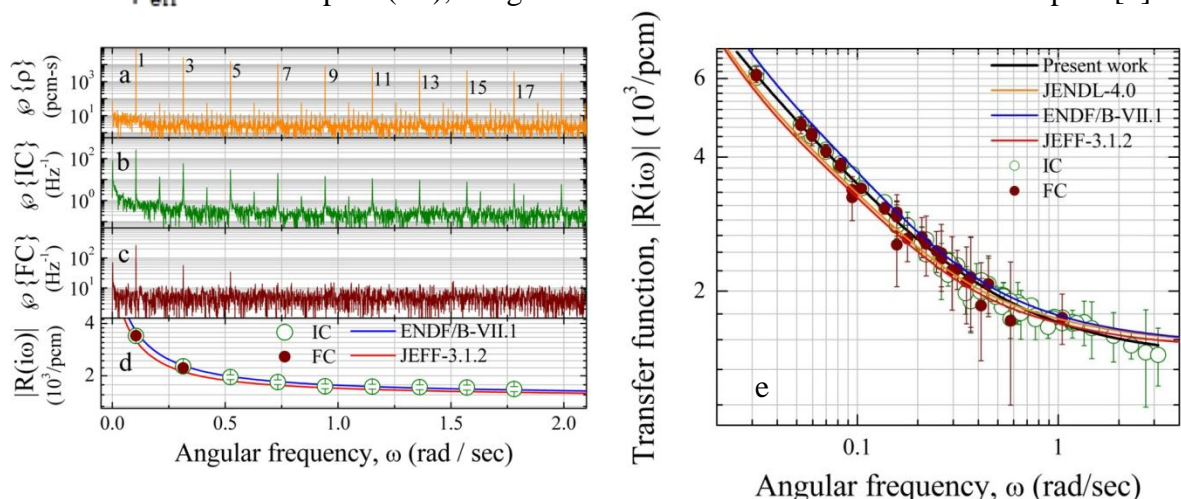


Figure. 2. Left: Power spectrum of the reactivity perturbation (a), the corresponding detectors signals (b,c), and the resulting transfer function amplitude compared to theoretical curves(d). Right: The obtained values of $|R(i\omega)|$ using the IC (open) and the FC (closed), including all oscillation periods and their higher harmonics (e).

CONCLUSIONS

A method for determining the effective delayed neutron fraction β_{eff} using in-pile oscillations and Fourier analysis is presented. The method developed in this work extends a previous work [4] by accounting for the higher harmonics excitation by the non-sinusoidal reactivity perturbation waveform. This work demonstrates that although previously overlooked [1,4], these higher harmonics store valuable information regarding the reactor transfer function. Furthermore, it is shown that the transfer function can be reconstructed with satisfactory precision over a wide range of frequencies using non-sinusoidal perturbation and a single oscillation frequency. The method is applied to a set of in-pile measurement performed at the MINERVE ZPR in order to determine the value of β_{eff} for the MAESTRO core configuration [7,9]. The obtained value of β_{eff} is 711 ± 17 pcm (1σ) which agrees with the calculated value of 716 [9]. The uncertainties associated with this result are small enough so that the method presented in this work can be regarded as qualified technique for this kind of measurements [3].

REFERENCES

1. G.I. Bell and S. Glasstone, *Nuclear Reactor Theory*, Wiley (Van Nostrand Reinhold), USA, (1970).
2. G.R. Keepin, *Physics of Nuclear Kinetics*, Addison-Wesley, USA, (1965).
3. A. Dos Santos et al., "A proposal of a benchmark for β_{eff} , $\beta_{\text{eff}}/\Lambda$, and Λ of thermal reactors fueled with slightly enriched uranium", *Ann. Nucl. Energy* **33**, pp. 848-855, (2006).
4. Y. Yedvab et al., "Determination of delayed neutrons source by in-pile oscillation measurements", Proc. Int. Conf. *PHYSOR 2006*, Canadian Nuclear Society, Vancouver, Canada, September 10-14, (2006).
5. G.D. Spriggs and J.M. Campbell, "A summary of measured delayed neutron group parameters", *Prog. Nucl. Energy* **41**, pp. 145-201, (2002).
6. D.L. Hetrick, *Dynamics of nuclear reactors*, University of Chicago Press, Chicago, USA, (1971).
7. J.P. Hudelot et al, "OSMOSE: An Experimental Program for the Qualification of Integral Cross Sections of Actinides", Proc. Int. Conf. *PHYSOR 2004*, American Nuclear Society, Chicago, Illinois, USA, April 25-29, (2004).
8. CEA, private communication.
9. G. Perret et al., "Modeling report of the CEA Cadarache MINERVE reactor for the OSMOSE project", ANL-04/18, (2004).

Protective Alternatives of SMR against Extreme Threat Scenario – A Preliminary Risk Analysis

*I. M. Shohet, D. Ornai, E. Gal, Y. Ronen, M. Vidra
Ben-Gurion University of the Negev, Beer Sheva 84105, Israel*

INTRODUCTION

The article presents a preliminary risk analysis of the main features in NPP (Nuclear Power Plant) that includes SMR - Small and Modular Reactors, given an extreme threat scenario. A review of the structure and systems of the SMR is followed by systematic definitions and analysis of the threat scenario to which a preliminary risk analysis was carried out. The article [outlines](#) the basic events caused by the referred threat scenario, which had led to (1) possible failure mechanisms according to FTA (Fault-Tree-Analysis), (2) critical protective circuits, and to (3) detecting critical topics for the protection and safety of the reactor.

RESULTS

The Threat Scenario

SMR may face many hazards which can potentially lead to failure in the reactor core. The main hazards are aircraft crash, missile hit, and car bomb explosion. One of this research main objectives is to examine the survivability (resilience) of the SMR to the effects of explosion, shock and ground movements that may lead to LOCA (Loss of Coolant Accident) resulting in a core melting. These scenarios have direct consequences on the destruction of the structure and the systems of the SMR, as well as indirect consequences, which could be caused as a result of indirect damage to vital cooling systems of the reactor, due to fractures and cracks in sensitive systems such as critical pipelines connecting coolant resources to the RV (Reactor Vessel). It is assumed that due to the RV remarkable toughness (geometry, thickness, and structure) it will remain intact under the extreme event hazards. It is also assumed that due to the spatial locations of the various protection systems, and their autonomous operation, not all of them will be hit due to single hit.

Definition of Basic Events and Consequences

Given the referred threat scenario, two "state of nature" were defined:

A. Warning systems did not identify the extreme event, and/or automatic shutdown systems did not shut down the reactor core successfully.

B. According to Smith and wright⁽³⁾ and Bajcs et al.⁽¹⁾, once the reactor protection system detects extreme event, it will perform automatic shutdown. Core shutdown will be accomplished thanks to gravity by the falling of the CRDM (Control Rod Drive Mechanism) into the reactor core. Alternatively, core shutdown may be accomplished by the injection of borated water into the RV. Following shutdown, the reactor's thermal power decreases quickly and drastically. According to El-Wakil⁽²⁾, the reactor's capacity declines to between 7% and 0.1% of the thermal output before shutdown, and later decreases to even lower values within a duration of an hour to several days, depending on the operation of the reactor before the break. In fact, within a few hours, the reactor's thermal power drops below 1% from its original capacity. Consequently, only one proper cooling system, with ongoing external power supply, is required to prevent core melting caused by LOCA. SMR has only five passive safety systems:

1. Emergency Heat Removal System (EHRS): is designed to transfer heat from the coolant to the environment during an accident.

2. Emergency Boration Tanks (EBT): two systems, providing way of alternative reactor shutdown by supplying borated water through the DVI (Direct Vessel Injection) lines into the RV. In addition, these containers provide a water source to the primary system during an emergency.

3. Pressure Suppression System (PSS): consists of six water tanks and a mutual gas storage tank. This system controls the CV pressure below 1.0 MPa.

4. Automatic Depressurization System (ADS): its role is ensuring equal pressure between the CV and RV. It consists of two 4-inch parallel pipes, each with two closed valves. The single line discharges into the Pressure Suppression System water tank through a sparger.

5. Long-Term Cooling System (LTCS): Implemented by a cavity at the bottom of the RV. This cavity accumulates the coolant and condensed liquid as well. In case of LOCA, it fills up above the level of the core allowing the core to be saturated in water.

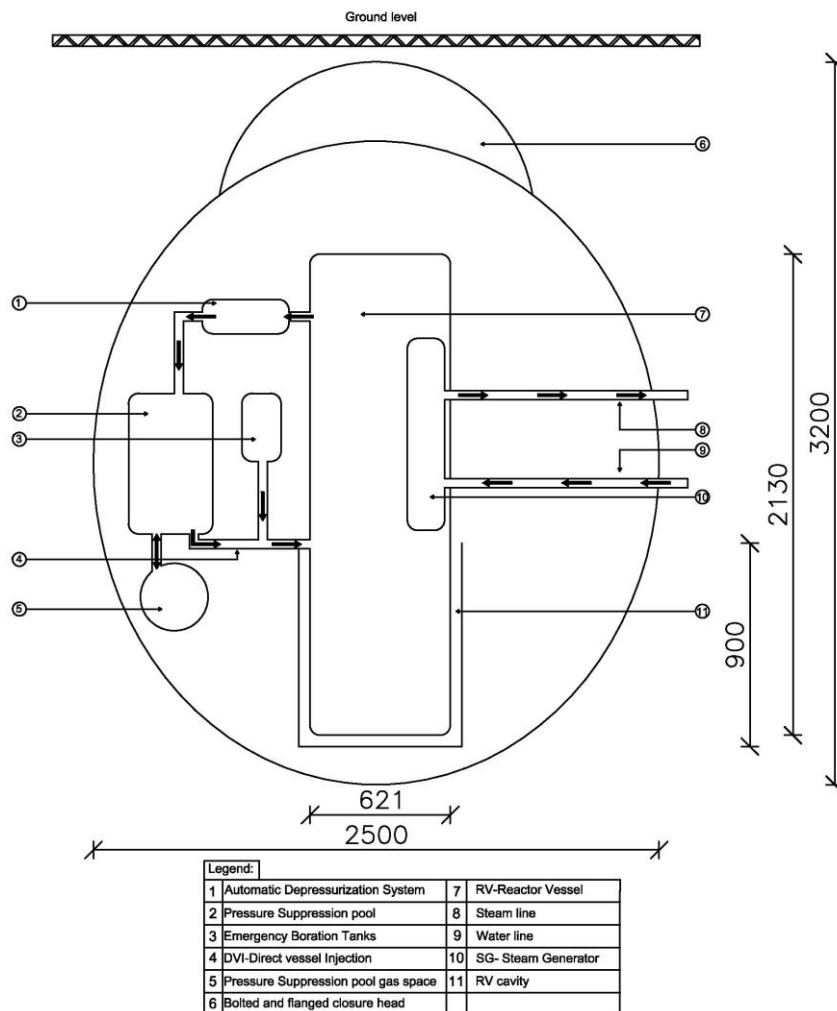


Figure 1. Scheme of SMR Containment Vessel

Qualitative FTA

Failure mechanisms in the SMR for the given threat scenario are modeled using a qualitative FTA, indicating the critical components in the failure mechanism. The primary failure event (Top Event) is Loss Of Coolant Accident (LOCA) event, which can lead to core melting. SMR has three protective circuits:

1. RV cooling.
2. Containment Vessel cooling.
3. External mechanisms of emergency cooling.

Assuming successful shutdown, the three protective circuits mentioned above are linked with an "OR" gate to the LOCA top event. Each of them has its own fault tree according to its own failure mechanisms:

CV loss of coolant failure occurs if one of the two following systems fails (Figure 2):

A. *DVI lines*: pipes failure due to a direct or indirect hit (shock or thrust).

B. *Simultaneous failure of the two safety systems located within the CV*:

1. *Pressure Suppression System (PSS)*: fails only if all the six pools fails simultaneously.

2. *Automatic Depressurization System (ADS)*: fails only if the two water lines fail simultaneously.

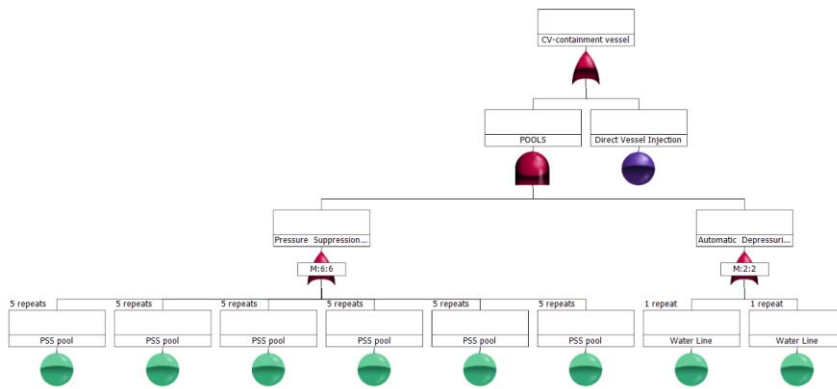


Figure 2. CV loss of coolant failure fault tree diagram.

Similarly, RV loss of coolant failure occurs if one of the main cooling systems, which are integrated in the RV, fails:

- A. *RCP-Reactor Coolant Pumps*: failure occurs when all eight pumps fail simultaneously.
- B. *SG-Steam Generators*: failure occurs when all eight SGs fail simultaneously.
- C. *Pressurizer*: fails due to a direct or indirect hit at the pressurizer containment.

External above-grade systems failure will occur only if the two following systems fail:

- A. *Emergency Heat Removal System (EHR)*: consists of Refueling Water Storage Tank (RWST) and four heat exchangers connected to four SGs. This system fails when failure occurs in the RWST or in the four heat exchangers simultaneously. The successful operation of these components is depended on the reliable operation of the exterior pipeline systems.
- B. *Makeup Tanks*: consists of eight SG makeup water tanks connected to all of SGs. Each container is connected to the steam and water lines of its SG. This system fails if failure occurs in the containers or in the steam and water lines respectively.

As mentioned above, these analyses are based on the hypothesis that the reactor shutdown performed successfully. Nevertheless, it is important to interpret the reactor shutdown failure:

A reactor shutdown failure will occur if the following systems fail simultaneously:

- A. *CRDM*: failure occurs if the rods do not fall into the reactor, and/or they do fall but do not perform shutdown.
- B. *EBT- Emergency Boration Tanks*: failure occurs when the two tanks fail simultaneously.

SUMMARY AND CONCLUSION

A preliminary risk analysis was carried out to explore the risks associated with operating an SMR given an extreme threat scenario that is a single extreme event that may cause failure of some protective systems. The risk analysis refers to the following "State of nature" situations:

1. Automatic shutdown systems did not identify the extreme event, and / or did not have time to perform shutdown as required.
2. Automatic shutdown systems identified the extreme event, and were able to perform shutdown of the reactor core successfully.

Initial qualitative analysis depicts that the safety systems of the SMR are of high reliability since they are based on three circuits, two of which are essentially passive (RV and CV)

The analysis, referred to the successful shutdown of the reactor, shows that the internal safety circuits have a high degree of redundancy. Both the interior cooling systems of the RV and CV are characterized by a high degree of redundancy. Consequently, focus on protecting the RV or CV, which according to the hypothesis

of this study will be underground, could ensure a safe shutdown of the reactor given a reference extreme event and assuming the shutdown of the reactor was reached.

REFERENCES

1. Bajs, T., Grgic, D., and Cavlina. N. "*LOCA Analysis of the IRIS Reactor*". International Conference: Nuclear Energy for New Europe Portorož, Slovenia, Sept. 8-11, 2003, **304**, p.1-8, (2003).
2. El-Wakil, M.M. "*Nuclear Heat Transport*", International Textbook Company, ISBN 978-0894480140. (1981).
3. Smith M.C and Wright R.F. "*Westinghouse Small Modular Reactor: Passive Safety System Response to Postulated Events*". International Congress on Advances in Nuclear Power Plants 2012, ICAPP 2012 2, Chicago, IL; United States; 24 June 2012 through 28 June 2012 **Paper 12517**, p.1001-1006, (2012).

Radiological Risk Assessment (Wednesday, February 12, 2014 14:00)

Legal and Political Obstacles and Opportunities for Successful Nuclear Projects

M. Yanovskiy

Gaidar Institute for Economic Policy, Moscow, Russia

INTRODUCTION

Every business suffers from excessive regulations, unpredictable changes in legislation, various kinds of the political rent, extorting practices like "big business social responsibility" and more. The industries with long-term return-of-investment (ROI) are most vulnerable to political and legal risks. For the nuclear industry, long-lasting public perception of radiation as an imminent threat caused the present over-regulation look natural. Therefore ROI is above two decades, essentially precluding private entrepreneurship activity. While durable solution includes changing public perception and updating regulation, both are "facts on the ground" and "habits are hard to break."

Political alliances, appeal to public opinion and lobbying are legitimate methods for promoting industry's interests in a democratic state. However in case of the nuclear industry, bureaucratic and political interests seem too strong to be overpowered by regular lobbying activities.

Durable solutions we are searching for should not only eliminate the present legal and political obstacles, but also prevent them in near- to middle-term future. Such solutions would mitigate risks and remove barriers in number of industries, including nuclear industry as well. Particularly, "not in my backyard" (NIMBY) attitude to nuclear installations is often viewed as a formidable problem. However, this problem has pretty old and reliable solution via compensation for real estate devaluation, if such takes place.⁽¹⁾ Such solution may preclude some projects, but makes others predictable and reliable (e.g. in sparsely populated or relatively poor areas).

RESULTS

In Israel, historical dynamics of the indices of Economic Freedom in the World (Fig. 1, top) and of Regulation (Fig. 1, bottom) do not provide evidence for a clear trend during the last decade. So in the sense of de-regulation, the difference between the two mainstream political forces (left-center and right-center) is not clearly pronounced (for additional statistical evidences see the paper of Yanovskiy et al.⁽²⁾). In search of potential future supporters of the nuclear energy agenda, it is informative to review the international experience.

Eastern and Central European countries' transition to democracy and market economy yielded a number remarkable cases in support of Sharansky theory of identity.⁽³⁾ Namely, these cases (Estonia, Slovenia, Poland etc) prove that appealing to national agenda is capable to promote and defend de-regulating pro-market economic reforms.

There are two main types of reasoning for pro-market choice of conservative hardliners. The first one was targeted by e.g. Ayn Rand⁽⁴⁾: it is conservatives' "religious" belief in the legitimacy of private property and business success. The second type of reasoning, developed by Zeev Jabotinsky, is purely pragmatic⁽⁵⁾. Namely, as economic success of private entrepreneurship proved to be solution for national problems (like absorption of Jews in the Land of Israel), business success should be welcomed.

Most parties in the post-socialist space, aiming at empowering their national states, turned to be strongly pro-market.⁽⁶⁾⁽⁷⁾ There are also opposite cases (easily detectable in ex-imperial nations like Russia or Serbia) when relatively small anti-market nationalist groups are successful. Anti-market nationalists are usually very concerned about weakening "bad" nations, instead of empowering their own.

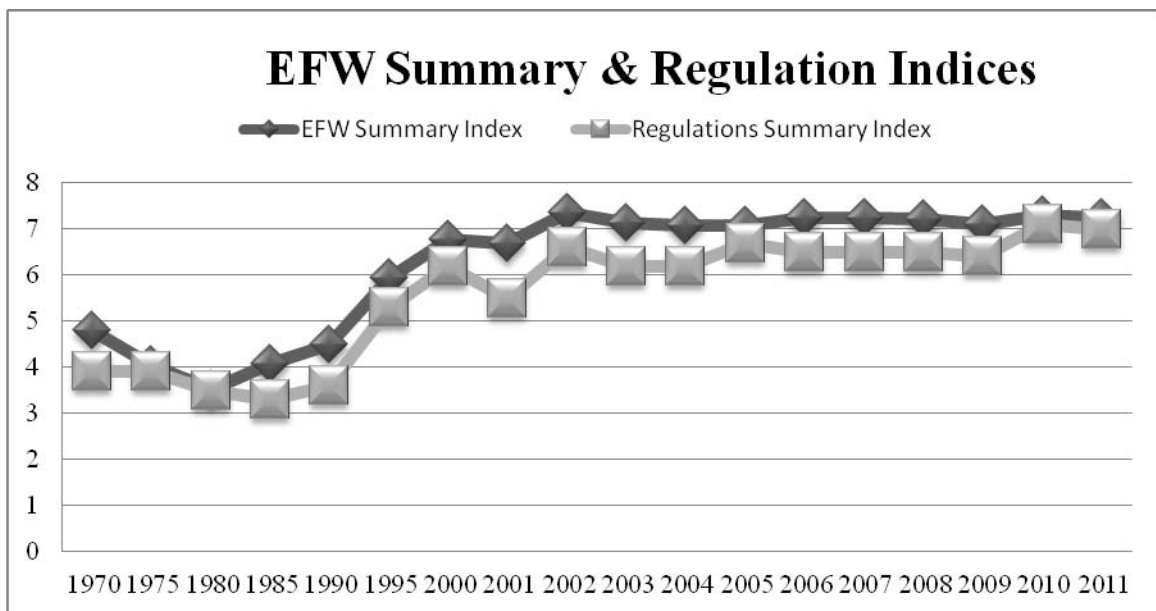


Figure 1. Economic Freedom in the World indices for Israel; Source: <http://www.freetheworld.com/reports.html>

In addition to the mentioned above positive examples of de-regulating in post-socialist states, one can use the examples of economic de-regulation in the USA and UK initiated and performed by R. Reagan and M. Thatcher, correspondingly. Both leaders should be definitely classified as hard-line right-wingers rather than mainstream conservatives. Both relied heavily on religious argumentation in their policy – stressing that the divine will comprises the moral grounds for de-regulated market economy (and just as a consequence of this will, the common sense supports the same values being just a projection of the divine will on human thought). De-regulation is exactly what the nuclear industry needs so urgently, so national and religious parties and groups are potentially the most reliable allies.

CONCLUSIONS

National and religious parties and groups, interested in national agenda promotion through economic success, are potentially the most reliable allies of nuclear and other national infrastructure industries. Therefore, the most prospective public-relations policy is to stress the immediate nation's interests. Respectable experts' direct appeal to the public with the message of Israel's energy independence – and its importance for defense and security, strong economy and independent policy – could turn to be fruitful to open the window of opportunities.

REFERENCES

1. Coase R., *The Firm, the Market, and the Law*, Univ. of Chicago Press, 1990
2. Yanovskiy K.M., Shestakov D., Zhavoronkov S., "Risks, Responsibility and Public Respect: Cases of Entrepreneurs Elected in the USA and Russia" (2013 wp1) // <http://ssrn.com/abstract=2267164>
3. Sharansky N., "Defending Identity: Its Indispensable Role in Protecting Democracy" *PublicAffairs*, 2008
4. Rand A., "Requiem for Man", in: "Capitalism: The Unknown Ideal", Signet; (Signet 1st Printing, 1967) edition (1986)
5. Jabotinsky "Zion and Communism" *Hadar*, NY, 1-3, February 1941
6. Mau V., S. Zhavoronkov, A. Shadrin, K. Yanovsky et. al. (2003), *Importirovannyye instituty v stranah s perehodnoi ekonomikoi: effektivnost' i izderzhki* (Imported Institutions in Transition Countries: Efficiency and Costs), IET, Moscow.(relevant fragment presented in Dabrowski, Mau, Yanovskiy, 2004 pp. 34-35)
7. Dabrowski, ed., et al "Russia: Political and Institutional Determinants of Economic Reforms" CASE wp # 56/2004, 2004 <http://ssrn.com/abstract=1431892>

Radiological Risk Assessment (Wednesday, February 12, 2014 14:00)

Inclusion of Premeditated Threats in the Safety Methodology for NPPs³

I. Levanon

Ishay Levanon Consulting Ltd., Tel Aviv, Israel

During the last decade the global effort to prevent terrorism or to mitigate its harm, if prevention fails, has increased. The nuclear power community was involved in this effort trying to prevent terrorist attacks on NPPs (Nuclear Power Plants). A natural extension of terror restraining is the prevention of any premeditated damage to the plant, including acts of state. The pre-feasibility study of an Israeli NPP, conducted by the Ministry of National Infrastructures, has identified the risk of hostile damage to the NPP as a major obstacle to the establishment of nuclear power in Israel, second only to the refusal of nuclear exporting nations to sell an NPP to Israel^v. The General Director of the Ministry and the Head of the IAEC (Israeli Atomic Energy Commission) have approved continuation of the pre-feasibility study.

This synopsis presents a study, regarding premeditated threats to NPPs, commissioned by the Ministry of National Infrastructures as part of the continuation. It focuses on the **safety** aspect of **premeditated** threats originating **outside** the plant, although a significant part of the analysis can be extended to other subjects such as theft or diversion of strategic materials. The study deals only with methodology and does not encompass specific threats or protection measures. Conclusions and recommendations are marked by **bold italics Arial font**.

The theory of nuclear safety regarding non-premeditated safety events (equipment failures, human errors, natural events, etc.) is well developed. The study refers to these events and the theory attached to them as "classical", distinguishing them from premeditated events.

The study defines two postulates, related to premeditated threats:

Correspondence – We should adopt the classical methodology whenever possible.

Regulation – The safety of an NPP from premeditated threats requires examination, approval and inspection by a regulator.

Key issues of the methodology with substantial differences from the classical one are:

- Rate of change of the threat;
- Design Basis Threat (DBT) and beyond it, including Defense in Depth (DID);
- State and licensee responsibility;
- Probabilistic Safety Assessment.

These key issues are discussed below in light of the above two postulates and related publications, mainly of the US NRC (Nuclear Regulatory Commission). Problems are detailed and partial solutions are suggested.

Rate of Change

A premeditated threat may change significantly during a period of several years as a result of technological changes, international-relations changes or a combination of both. We do not expect such rapid change of the classical risk for an NPP, although our knowledge about such risks may change rapidly. An example of a knowledge change is the discovery of a design error in the shutdown mechanism of RBMK NPP (1983)^{vi}.

Examination of the knowledge changes shows that a part of the necessary safety improvements was carried out only after an incident or an accident occurred, even when the operating organization had information regarding a design fault beforehand. A similar picture emerges regarding terror threats; strengthening the security against the threats was often made only after terrorist attacks on (non-nuclear) facilities were carried out.

³Work Commissioned by the Israeli Ministry of National Infrastructures, Energy and Water Resources, Office of Chief Scientist.

Partial solutions to the problem of rapid change of the threat are:

- a) Reliance on the plant's safety margin, i.e. reducing it^{vii};
- b) Prior analysis beyond the DBT^{vii};
- c) Response by the state. For example, screening of aircraft passengers or the development of defensive weapons^{viii,ix};
- d) Sharing intelligence regarding present threats and probable future ones with the nuclear community^{viii};
- e) Readiness for change, including the **extreme option of shutting down the plant.**

The partiality of the solutions requires a critical combination of them while maintaining an independent and determined regulator who is able to enforce them.

DBT and Beyond

New NPPs (Gen. 3/ 3+) are safer than older ones. The improved safety was achieved by redundant safety systems, some of them passive. Concurrently, the requirements for safety became more demanding. Safety goals turned out to be more ambitious and new terms were introduced to reflect the safety change. Loose reference to BDBA (Beyond Design Basis Accidents) was gradually replaced with formal requirements relating to "*design extension conditions*". IAEA safety standards^x state that these conditions, including core melt, will require "*only protection measures that are of limited scope in terms of area and time*" and that "*conditions that could lead to significant radioactive releases are practically eliminated*".

This requirement is achieved not by inherent safety, namely physical negation of states that cause "*large and early releases*", but by safety measures that mitigate incidents. It is not clear a priori that the safety measures will be adequate to endure energetic premeditated events that cause common mode failures. Therefore, parallel to the reinforcement of the classical safety, an enhancement of safety against premeditated threats is required and performed. A DBT (Design Basis Threat) is defined parallel to DBA. ***DBT is not the most serious possible threat ("safe is not the equivalent of risk-free"^{xi}), but rather a credible serious threat defined by a regulator. A formal requirement for partial defense against BDBT is also included^{xii}.***

DID model encompasses five independent defense layers for an NPP. However, it acknowledges that extreme (classical) energetic events may overcome more than a single layer simultaneously^{xiii}. An airplane colliding with an NPP, for example, may breach the first four layers – from obstructing the normal operation up to a containment breach. A recommended solution is the inclusion of several physically independent sub-layers in one logical layer, mainly in the first one. For a colliding airplane the sub-layers may be: passengers' screening, air defense and containment hardening.

State Responsibility and Operator Responsibility

Air defense was mentioned as one of the safety measures against the intention to crash an airplane on an NPP. This defense is the responsibility of the State, not the licensee. This is one of the cases in which the defense against premeditated threats lies with the State. Sharing responsibilities for safety between the State and the operating organization (operator) is unique to premeditated threats. As early as 1967, at the dawn of the nuclear power era, the US AEC (Atomic Energy Commission) regulated that operators of an NPP are not required to supply protection against an attack by an "enemy of the United States"^{xiv}. A similar principle, that a defense against premeditated threats lies partly with the State, was adopted by the IAEA and probably by all ~30 countries that operate NPPs. The division of the primary responsibility between the state and the operator raises two questions: *what is the boundary between State responsibility and operator's responsibility and who determines it?*

A broad interpretation of the "Enemy of the State" regulation could have been that the State and not the operator is responsible for protection against any deliberate action performed by a person or an organization hostile to the USA. However, the US NRC, which replaced the AEC as the nuclear regulator, has adopted a narrower interpretation: the duty to protect is imposed on the operator in any case where a private vendor can be "*reasonably expected to defend*"^{xv}. The operator's duty includes a security force defending against a well-trained and dedicated attackers ("*willing to kill and be killed*"^{xvi}) as well as the capability to fight fires

induced by a colliding airplane. On the other hand, the NRC has set limits to the operator's duty and has not required additional shielding structure for existing NPPs. ***The regulator determines the scope of the requirements of the operator and thus determines the boundary between the State and the operator. A similar policy, consistent with the correspondence and the regulation postulates is proposed for Israel.***

Security Regulator

The need for a regulator responsible to ensure safety against premeditated threats appears in the second postulate. Assigning responsibility (at least partially) to the operator to implement the required safety reinforces the need for a **security regulator**, a government agency that examines and determines that adequate safety is provided. The role of security regulator can be imposed on the classical safety regulator or on another agency. The US, from the beginning of civil nuclear power, and the UK, since 2007^{xvii}, have both adopted the first alternative. Similarly ***a single nuclear regulator for all safety issues is proposed for Israel.***

Relations with Other Agencies

The security/safety regulator supervises the safety achieved by the operator. It does not supervise the necessary protection supplied by the State. How does it determine that adequate safety is provided by the combined operations of State and operator? A **partial** solution is: ***The safety regulator is fully informed by other government agencies, it takes some part in their discussions and deliberations, but it does not regulate them. This issue needs further development by the regulator[s].***^{viii, ix}

Cost

Protection against hostile attacks carried out by the State or by the operator, will invoke an additional cost. The cost may be imposed either on the State (i.e. levied on the taxpayers), achieving socioeconomic or environmental policy goals, or it may be imposed on the utility (i.e. the consumers), achieving economic efficiency.

Secrecy and Transparency

It is necessary to bridge, as far as practicable, the gap between safety culture and security culture.

Safety Goals

The nuclear community has well-established goals for nuclear safety, e.g., requirement that LERF (Large and Early Release Frequency) is less than one per million reactor-years^{xviii}. The goals are stricter by an order of magnitude than previous generation ones. Vendors' assessments, endorsed by regulators, show that actual safety achieved, excluding external events, is superior to the goals by approximately an order of magnitude.

Proposal: ***adopt these goals for the total safety including premeditated events (consistent with the correspondence postulate).***

Opposing approaches (not adopted by the study) are:

1. Classical goals:

- a. Safety requirements for NPPs are unnecessarily more demanding than the requirements for other (non-nuclear) industries and go above and beyond "adequate safety". Therefore, we may use more relaxed goals. **Rejected:** not adopted in any country.
- b. Society cannot cope with catastrophic accidents like the ones in Fukushima or Chernobyl. Safety requirements should be more demanding. **Rejected:** this practically means a gradual elimination of current NPPs. Employed in Germany and Italy.

2. Goals for premeditated Threats:

People in Israel live with a larger (security) risk than in other countries:

- a. Using safety goals from "calmer" countries will impose a heavy burden on industry and society. **Rejected:** a large and early release is a catastrophic event. Like other countries we cannot allow it to happen.

- b. We should reduce the additional safety risk arising from hostile attacks on NPPs, by employing stricter goals than other countries. **Rejected:** the probability of the classical goals is small enough.

The Issue of safety goals should be further elaborated with the participation of the nuclear regulator, preferably with its leadership.

Safety Assessment

Including premeditated threats in a deterministic safety assessment is in principle straightforward. One should define the DBT and derive scenarios that require protection of the operator. BDBT should be included, analyzed and protection measures ought to be defined for some of the scenarios.

We encounter a different situation for PSA (Probabilistic Safety Assessment). The assessment starts with an estimation of the frequency of initiating events. For premeditated events the initiating event is the adversary's decisions bringing about an attack on the NPP. How should we estimate the frequency for this action?

F , the frequency of damage, e.g., LERF, can be written as $F=f \cdot P$, where f is the frequency of initiating an attack and P is the conditional probability that the attack will cause the damage (large and early release).

I suggest directing the question regarding the magnitude of f to the decision maker, and to phrase a simpler question than "*what is the value of f ?*" A safety goal for F , F_{goal} , should be defined, P should be ("objectively") estimated and thus a safety limit for $f_1 = F_{\text{goal}}/P$ can be derived. The question addressed to the decision maker will be "Do you estimate that f is smaller or larger than f_1 ?" To further facilitate the dialogue, the question should be formulated not in abstract terms of frequency, but rather in more common terms of the probability of occurrence (incidence) during a period similar to the lifespan of the plant (~50 years), i.e. "***Is the probability for attack in the next 50 years larger or smaller than 1%?*** (arbitrary values)". Another simplification could be achieved if it were possible to reduce the adversary's decision to attack to sub-events. I have not found a suitable way for this reduction and the issue remains for further examination.

A different and extreme approach is to assume that an assault during the lifetime of the reactor is certain. This approach is too severe and too crude. It does not take into account differences in motivation of different adversaries with diverse capabilities. It also ignores the possibility of successful deterrence and reduction in the willingness to attack (~ f) if the chances to succeed (P) are small.

Other topics requiring treatment for PSA of premeditated events are:

The chances of success of the attack, P , are determined by a bilateral struggle between aggressor and defender and add a degree of difficulty and complexity to the issue of reliability of human actions in extreme situations.

The source term resulting from an enemy attack can be larger and earlier than the classical one. This is not a fundamental difference, but it may necessitate a unique calculation by the vendor of the reactor. If the calculation shows that the release of radioactivity from an enemy attack is indeed earlier than that of classical accidents, then the effectiveness of intervention measures may be reduced.

Israel

Demographic criteria (1990) for an Israeli NPP are stricter than in other countries. They may compensate for a larger security threat and the possibility of an early release of radioactivity^{xix}.

CONCLUSIONS

Problems and solutions in the inclusion of premeditated threats in the Safety Methodology for NPPs were detailed. Further work in the subject should be carried out in collaboration with the NPP regulator.

REFERENCES (all internet sites were retrieved on 2013-12-29)

1. Ministry of Energy and Water Resources, Pre-Feasibility Study for the Construction and operation of an NPP in Israel - Final Report, Hebrew (2012).
2. IAEA, The Chernobyl Accident, INSAG-7 (Updating of INSAG-1), p. 13, 15 (1992).
3. USNRC, Feasibility Study for a Risk-Informed and Performance-Based Regulatory Structure for Future Plant Licensing, NUREG 1860, Vol. 2, App G. Table G-1, Page G-5 (2007).
4. USNRC, Protecting Our Nation, NUREG/BR-0314, Rev. 3, pp 10-11, (2013).
5. USNRC, Safety and Security Improvements at Nuclear Plants – Fact Sheet (2005).
6. IAEA, Safety of Nuclear Power Plants: Design, Specific Safety Requirements, No. SSR -2/1, Requirement 20 (2012).
7. United States Court of Appeals, Ninth Circuit, Public Citizen v. Nuclear Regulatory Commission... Nos. 07-71868, 07-72555 (2009).
8. USNRC, 10 CFR § 50.150, Aircraft Impact Assessment. (2009)
9. IAEA, Defence in Depth in Nuclear Safety, INSAG 10 (1996).
10. USNRC, 10 CFR, § 50.13 Attacks and destructive acts by enemies of the United States; and defense activities (1967),
11. US Federal Register, NRC, Design Basis Threat, Vol. 72, No. 52, March 19 2007, p. 12708, 12710, 12713.
12. USNRC, 10 CFR, Part 73, Physical Protection of Plants and Materials, § 73.1 (1), (2007).
13. a) UKHSE, about us>timeline>2000, HSE takes on responsibility for the security activities of the Office for Nuclear Security (OCNS) and UK Safeguards Office (UKSO);
b) UKHSE, HSE>ONR>Nuclear Security, Civil Nuclear Security.
14. a) USNRC, Safety Goals for the Operations of Nuclear Power Plants; Policy Statement, Federal Register 51 28044 ; 51 30028, (1986).
b) OECD/NEA, Probabilistic Risk Criteria and Safety Goals, NEA/CSNI/R(2009)16 (2009).
c) EUR, European Utility Requirements for LWR NPPs, Vol. 1, Ch. 1.3, Sec 4.1, Change C-04 (2001).
15. Pre-Feasibility Study, Ch. 11.

Radiological Risk Assessment (Wednesday, February 12, 2014 14:00)

Protecting National Critical Infrastructure against Radiological Threat

I. Yaar^{1,2}, I. Halevy², Z. Berenstein² and A. Sharon²

- 1) *Ministry of National Infrastructures, Energy and Water Resources, Chief Scientist Office, 14, Hartum St. POB 36148, Jerusalem 9136002, Israel*
- 2) *Nuclear Research Center Negev (NRCN), P.O. Box 9001, Beer-Sheva 84190, Israel*

INTRODUCTION

National Critical Infrastructure (NCI) such as transportation, water, energy etc., are essential elements in a developed country's economy. As learned after the 9/11 attack^{xx}, a terror attack on these complex system may cause thousands of casualties and significant economic damage. The attack can be a conventional one; like the train bombing in Spain^{xxi} or the bus bombing in London^{xxii}, or a non-conventional one; like the Sarin attack on the underground train in Tokyo, Japan^{xxiii}. A radiological attack on a NCI is also feasible^{xxiv}. This type of attack must be taken into consideration due to the vulnerability of an infrastructure to such an attack, and the severe economic outcome of it^{xxv}. The radioactive materials that might be used by terrorists were recently identified and categorized in one of the IAEA Nuclear Security Series publication^{xxvi,xxvii}. The most common and therefore reachable radio nuclides are the gamma emitters ⁶⁰Co, ¹³⁷Cs and ¹⁹²Ir, the beta emitter ⁹⁰Sr and the alpha emitters ²⁴¹Pu, ²³⁸Pu and ²⁴¹Am.

A radiological event can be any of two principle scenarios. In the first scenario, a radiological dispersion device (RDD) or "dirty" bomb is used. This device consists of a radiation source which is detonated using conventional or improvised explosives^{xxviii}. Most of the casualties in this event will be from the explosion blast wave. However, some people might become contaminated with different levels of radiation^{xxix}, some might need to go through some type of medical screening process and the costs of the total actions might be significant^{xxx}.

The second scenario involves a silent dispersion of radioactive material in a public site. In this event, there are no immediate known casualties, and the fact that people were exposed to radioactive material will be discovered only in the uncommon event when symptoms of radiation sickness will be identified due to exposure to high radiation dose^{xxxi}, or if the radioactive material is discovered by a first responder equipped with a radiation detector or a dosimeter. The main impact of such a radiological attack is the contamination of a large area^{xxxii}. The size of the contaminated area depends on the type and activity of the radioactive material, on the type and geometry of the dispersion device, on the micro-meteorology conditions and on the cross contamination caused by the movement of people inside the contaminated area^{xxxiii}.

Two experimental programs, "Green Field"^{xxxiv} (GF) and "Red House"^{xxxv} (RH) were recently conducted in Israel in order to increase the preparedness for a RDD event. The GF program aimed at evaluating the consequences of an outdoor and an indoor explosion of an RDD device; while the RH program aimed at evaluating the outcome of a silent dispersion of a radioactive material inside a building. Based on the results of these two experimental programs, the consequences of a possible RDD attack or a silent indoor dispersion of a radioactive material will be given and the necessary preventative steps that can be taken in order to secure NCI's against these threats will be specified.

EXPERIMENTAL SETUP AND RESULTS

2.1 Simulation of an outdoor RDD attack

An outdoor explosion of a RDD can be used by terrorists in the attempt to contaminate NCI's such as harbors docks, train stations, bus stations airports, water sources, power stations, etc., with radioactive

materials. In the last part of the GF program, a set of experiments using the short lived radioisotope ^{99m}Tc were conducted in order to study the consequences of such an event^{xxxvi}. Overall, fourteen tests were conducted using 5-7 Curies of ^{99m}Tc bottled in a 30 cc saline water and coupled to 0.25-2.5 kg of TNT, in each test. All of the experiments' results were recorded by three video cameras (taken from three different angles), by a high speed camera and some of them were also recorded by a thermal Infra-Red (IR) camera.

On site Gamma measurements were taken by several gamma detectors. A small personal detecting system based on a 1" by 1" cesium-iodide (CsI) crystal, a laboratory medium resolution detector based on a 1.5" by 1.5" lanthanum-bromide (LaBr₃) crystal and a spectral advanced radiological monitoring system (SPARCS) based on several sodium-iodide crystals. A high gamma resolution pure germanium (HPGe) detector was also used at the laboratory in order to count the radioactivity collected by the Petri dishes that were placed around the detonation point. The activity that was measured on the ground following one of the 2.5 kg tests, measured with the SPARCS system, is depicted in Figure 1 in units of $\mu\text{Ci}/\text{m}^2$.

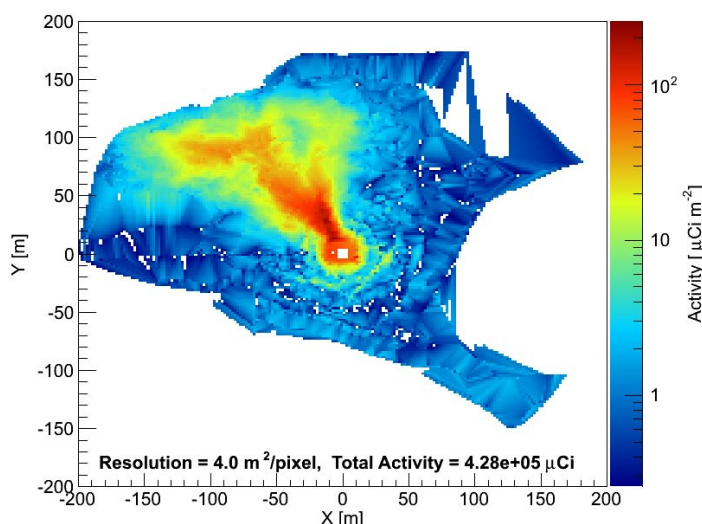


Figure 1. The activity on the ground after a 2.5 kg test, measured with the SPARKS system. The results are given in units of $\mu\text{Ci}/\text{m}^2$

The main findings concluded from these experiments, which can be relevant to a real RDD event inside a critical transportation system are that about 20 % of the total activity is found on the ground close to the detonation point and less than 1 % of the original activity is observed outside of this area. It should be mentioned, that this is true only for the cases where most of the particles created were fine aerosols due to the charge geometry and radioactive material type that enhanced the creation of such particles. In cases where most of the particles will be in the ballistic size range (>100 microns aerodynamic diameter), a reasonable assumption in the case of a RDD made of a metallic ^{60}Co or ^{192}Ir source, it is reasonable to assume that most of the particles will settle on the ground within the range of few hundred meters around the point of release.

2.2. Simulation of an indoor RDD attack

In this section, the results of a set of tests that were conducted in order to measure the consequences of an indoor RDD event are given^{xxxv}. This scenario is relevant to a terrorist attempt to contaminate NCI's installed inside buildings, such as power stations, water pumping station, train stations or airport terminals, with a radioactive material. When an RDD is detonated inside a building with openings part of the radioactive material will contaminate the building and the rest will be emitted out from doors and windows. In all of the experiments conducted in this part of the program, two identical charges were simultaneously detonated. One charge was placed outdoor and the second one was hanged at the center of a small steel chamber, 3 by 3 by 2 m³, with two 1 by 1 m² openings in the center of adjacent walls. Tests results were recorded by three video cameras, by a high speed camera and some of them were also recorded by a thermal IR camera. In addition to comparing between the heights of the clouds created inside and outside of the steel chamber, the amount and the size of the particles that were emitted from the openings after the blast and the

distribution of the material inside the chamber were also measured.

In six of the indoor shots non-radioactive CsCl and SrTiO₃ powders, simulating radioactive sources, were used. After each of these shots, samples were taken from the walls, the ceiling and the floor, and from samplers that were hanged outside of each window. These samples were analyzed using an Inductively Coupled Plasma Mass Spectrometry (ICP-MS) laser ablation technique, and the average material (CsCl or SrTiO₃) concentration on these areas was calculated. The results show that within this amount of explosive and chamber size, the material was dispersed homogenously over the walls and windows area. Therefore, the ratio between the fraction of radioactive material that will be dispersed outside and inside the building in an indoor RDD event, will be proportional to the ratio between the total openings' area (doors, windows etc.) and the total area of the building (including walls, floor and ceiling).

2.3 Simulation of a silent indoor dispersion of radioactive material

A set of experiments, which included silent dispersion of liquid ^{99m}Tc, were conducted as a part of the "Red-House" (RH) experimental program^{xxxv}. This part of the program was conducted in order to improve the preparedness and response to terrorism scenarios such as silence dispersion of radioactive material inside NCI's installed inside buildings. The tests were conducted (on July 2010) in the assigned Chemical, Biological, Radiological and Nuclear (CBRN) Israel Defense Force (IDF) home front command facility.

The CBRN training building is designed as a small size two-floor shopping mall. The main floor (ground floor) is about 24 by 24 m² size and includes an empty central part (18 by 18 m²) surrounded by shops and offices. The radioactive concentration in the air inside the building was measured by ten low volume (2 liters per minute) air samplers and five high volume air samplers (20 m³/10min). PDS and LnBr detectors were used for mapping the contamination level, both on the first and on the second floor. The dispersion was performed by an electric sprayer which can produce fine particles in an order of several microns. Each dispersion included 50 mCi of ^{99m}Tc mixed with 3.5 liters of water. The liquid drops size distribution was Gaussian-shaped with a mean value of 30 micron and a standard deviation of 10 microns. The time period for each release was 10 min. Upon spraying, the aerosol was dispersed by the building ventilation system. The aerosol was anticipated to dry in a short time period leaving a small micrometer size salt particle containing ^{99m}Tc. A typical spatial distributions of the floor surface deposition, depicted in µrem per hour (µrem/h), as measured in one of the tests is presented in Figure 2.

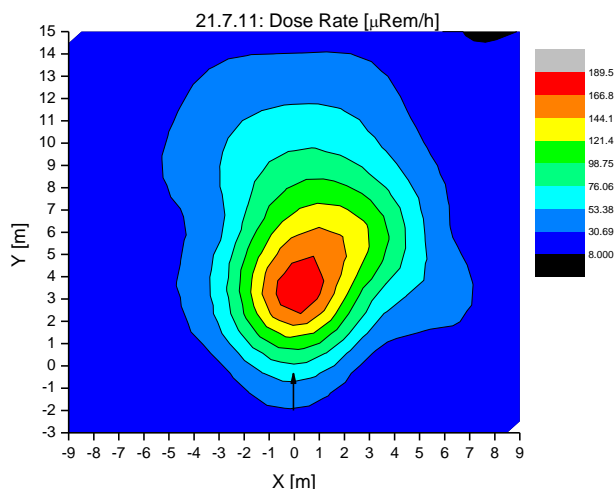


Figure 2. Spatial distribution of the floor surface deposition in µrem/h

DISCUSSION AND CONCLUSIONS

Based on the experimental results presented in this work and on other theoretical^{xxix,xxxvii,xxxviii} and experimental^{xxviii,xxx,xxxii,xxxiii,xxxix,xl,xli} work conducted in the past, some new insights regarding the security of NCI's can be obtained. As demonstrated in the Goiania accident^{xlii}, a detonation of an RDD or a silent

dispersion of radioactive material inside an airport terminal, train station, bus central station, subway system or harbor^{xliii}, even when a category 1 radiation source is used^{Error! Bookmark not defined.}, will only cause minor injuries and few casualties from high radiation doses. On the other hand, this event will probably have a huge economic impact on the country involved^{xliv}, and therefore cannot be ignored.

A coordinated radiological terror attack on international airports, main harbors or power stations, will probably close these facilities for periods of months or more, resulting in a big economic and physiologic effect^{xlv}. This long time period is needed for cleaning of the radioactive contamination to a point where these systems can be reopened according to IAEA guidelines for contaminated areas^{xlvi}. Additional general conclusions about the physical outcome of such events can be drawn from the experimental work presented here. First, it is clear that in a silent radiological event or in an RDD event where only a small quantity of explosives is involved, most of the radioactive material will be found in a close vicinity to the point of detonation or dispersion, resulting with high levels of contamination. The rest of the material will be found inside the ventilation system, especially on the surface of the filters, and will be carried by people to other parts of the infrastructure involved, or outside. In an RDD event that involves a large quantity of explosives, the damaged and contaminated central area will be larger, the radioactive material concentration inside the affected area will be lower and the area that will be contaminated will be much larger and mostly downwind from the detonation point.

The big question that has yet to be answered is: **what has to be done in order to minimize the chances for such an event to occur in one of the NCI's around the world?**

The most promising answer to this question is based on the multilayer security system approach^{xlvii,xlviii}. The first security layer is a personal screening process of people at the entrance to the main infrastructure transportation facility. This process is not simple to perform, in order to achieve a 100% screening coverage, all entrances must be secured by trained security teams having monitoring capabilities, which will allow them to hold everyone who enter the facility for a short screening procedure, after which the person is either allowed to enter into the facility or he has to go through a more comprehensive screening process. If an international airport will be taken as an example, all private vehicles entering the airport from any point of entry and all of the people coming via public transportation system (buses, trains, subway) have to be stopped for a short questioning process before they are allowed to enter into the main airport area.

The second security layer, which has to be integrated into the security system, is an explosive detection system^{xlix}. These systems are usually based on well-known techniques and they can prevent conventional as well as RDD terror attacks, or at least stop them at the entrance to the secured area.

The third security layer is one that can cope directly with any radiological terror threat¹. The most challenging ones are the alpha^{li} and beta^{lii} emitters. A detection system that will identify these radioisotopes will easily detect gamma emitters like ⁶⁰Co, ¹³⁷Cs and ¹⁹²Ir. The detection system can be a simple hand held radiation detector, operated by the security personnel posted at the first or second security layer; or a more complicated radiation detection portal suitable for the detection (and in some types identification) of radioactive material^{liii}. The screening of public, vehicles and cargo for radioactive material will result in some level of false alarm rate coming from the presence of Naturally Occurring Radioactive Material (NORM) and from people that had been treated or examined with radioisotopes several days before they went through the radiation detection portal^{liv}.

These security systems are aimed at prevention from a terrorist to enter into any NCI carrying a radioactive material. If this system fails to alert, a second line of radiation detectors, aimed at detecting and/or identification of radioactive material release, has to be installed inside the facility. According to the results obtained in the RH experimental program, the preferred place for the positioning of these detectors is inside the air-conditioning ducts, as close as possible to the filters of the air that is being sucked from the building and some other detectors have to be positioned outside the building in order to detect a release of radioactive material outside. The main purpose of this second line of radiation detectors is to raise an alert as soon as possible on the presence of radioactive material, in order to minimize the exposure of people involved and to prevent farther transportation of the contamination to other parts of the NCI that was attacked.

REFERENCES

1. G. Makinen, The Economic Effects of 9/11: A Retrospective Assessment, Report for Congress, RL31617 (2002).
2. F. Reinares, The Madrid Bombing and Global Jihadism, *Survival: Global Politics and Strategy*, 52 (2010) 83.
3. P. Murphy, Intelligence and Security Committee Report into the London Terrorist Attacks on 7 July 2005, ISC 105/2006, May 2006.
4. Natural and Selected Synthetic Toxins, A.T. Tu and W. Gaffield editors, ACS Symposium series, Vol. 745, Chapter 20, Overview of Sarin Terrorist Attacks in Japan, *Natural and Selected Synthetic Toxins*, pp 304–317 (1999).
5. The Terrorist Threat to the U.S. Commercial Passenger and Freight Rail System, Office of Intelligence and Analysis / Directorate for Preparedness, Homeland Infrastructure Threat & Risk Analysis Center (2006).
6. J.M. Acton, M.B. Rogers and P.D. Zimmerman, Beyond the Dirty Bomb: Re-thinking Radiological Terror, *Survival: Global Politics and Strategy*, 49 (2007) 151.
7. Code of Conduct on the Safety and Security of Radioactive Sources, International Atomic Energy Agency, Vienna, 2004.
8. Categorization of Radioactive Sources, IAEA Safety Standards for protecting people and the environment, Safety Guide No. RS-G-1.9, International Atomic Energy Agency, Vienna, 2005.
9. A. Sohler and F. Hardeman, Radiological Dispersion Devices: are we prepared? *Journal of Environmental Radioactivity*, 85 (2006) 171.
10. C.O. Slater, J.C. Gehin and R.T. Santoro, A Study of the Effects of a Radiation Dispersal Device, Oak Ridge National Laboratory, Nuclear Science and Technology Division (94), ORNL/TM-2003/128 (5/2003).
11. S.V. Musolino and F.T. Harper, Emergency Response Guidance for the First 48 Hours after the Outdoor Detonation of an Explosive Radiological Dispersal Device, *Health Physics*, 90 (2006) 377.
12. J.M. Acton, M.B. Rogers and P.D. Zimmerman, Beyond the Dirty Bomb: Re-thinking Radiological Terror, *Survival: Global Politics and Strategy*, 49 (2007) 151.
13. V.P. Reshetin and J.L. Regens, Estimation of Radioactivity Levels Associated With a ⁹⁰Sr Dirty Bomb Event, *Atmospheric Environment*, 39 (2005) 4471.
14. F.T. Harper, S.V. Musolino and W.B. Wentz, Realistic Radiological Dispersal Device Hazard Boundaries and Ramifications for Early Consequence Management Decisions, *Health Physics*, 93 (2007) 1.
15. A. Sharon, I. Halevy, D. Sattinger and I. Yaar, Cloud rise model for radiological Dispersal device events, *Atmospheric Environment*, 54 (2012) 603.
16. Sharon, I. Halevy, Z. Bernstein, M. Levy, S. Tabibzadeh, A. Ashkenazi, I. Yaar, The "Red House" Project, An Experimental Study of Indoor Dispersion of Radioactive Material, NRCN private communication (11/2011).
17. A. Sharon, I. Halevy, Z. Berenstein, P. Banaim and I. Yaar, "Green Fields III" - November 2012 Campaign, preliminary summary, NRCN Report, N972/0113 (12/2012).
18. A. Elliott, Security of Radioactive Materials for Medical Use, S. Apikyan and D. Diamond (eds.), *Countering Nuclear and Radiological Terrorism*, Springer, 2006, 95.
19. M. Durante and L. Manti, Estimates of radiological risk from a terrorist attack using plutonium, *Radiation Environment Biophysics*, 41 (2002) 125.
20. Z. Prouza, V. Beckova, I. Cespirova, J. Helebrant, J. Hulka, P. Kuca, V. Michalek, P. Rulik, J. Skrkal and J. Hovorka, Field tests using radioactive matter, *Radiation Protection Dosimetry*, 139 (2010) 519.
21. Z. Prouza, J. Helebrant, V. Beckova, I. Cespirova, J. Hulka, P. Kuca, V. Michalek, P. Rulik and J. Skrkal, Explosion Tests Using Radioactive Substances, in *Proceedings of Third European IPRA Congress*, Helsinki, Finland, 14-16 June 2010.
22. X. Cao, G. Roy, P. Brousseau, L. Erhardt and W. Andrews, A Cloud Rise Model for Dust and Soot from High Explosive Detonations, *Propellants Explosives Pyrotechnics*, 35 (2010) 1.
23. The radiological accident in Goiania, IAEA, VIENNA, 1988, STI/PUB/815, ISBN-92-0-129088-8.

24. M.K. Zaidi, Risk Assessment in Detection and Prevention of Terrorist Attacks in Harbors and Costal Areas, in I. Linkov et al. (eds.), Environmental Security in Harbors and Costal Areas, Springer 2007, 309.
25. A.P. Schmid, High Consequence Radiological Terrorism Scenarios - U.N., in W.D. Wood and D.M. Robinson (eds.), International Approaches to Securing Radioactive Sources against Terrorism, Springer 2009, 79.
26. E. Eraker, Cleanup After a Radiological Attack, U.S. Prepares Guidance, The Nonproliferation Review (2004) 167.
27. INTERNATIONAL ATOMIC ENERGY AGENCY, Remediation of Sites with, Dispersed Radioactive Contamination, Technical Reports Series No. 424, IAEA, Vienna (2004).
28. Protecting the Nation's Seaports: Balancing Security and Cost, Jon D. Haveman and Howard J. Shatz editors, PPIC Pub., San Francisco, Ca (2006).
29. J. Becker and L. Smit, Transport security, Annex XVIII of ASSESS Final Report, DG TREN, European Commission (2005).
30. C. Bruschini, Commercial Systems for the Direct Detection of Explosive for Explosive Ordnance Disposal Tasks, Subsurface Sensing Technologies and applications, 2 (2001) 299.
31. R.T. Kouzes, Challenges for interdiction of nuclear threats at borders, First International Conference on Advancements in Nuclear Instrumentation Measurement Methods and their Applications (ANIMMA), Marseille (7-10 June 2009) 1.
32. I. Yaar, I. Peysakhov and E.M.A. Hussein, Passive detection and identification of a concealed ^{241}Am source in transport, Packaging, Transport, Storage and Security of Radioactive Material, 19 (2008) 189.
33. I. Yaar and Esam M.A. Hussein, Passive Detection of Concealed ^{90}Sr RTGs in Transport, Packaging, Transport, Storage and Security of Radioactive Material 15 (2004) 149.
34. I. Yaar and I. Peysakhov, A Multiple-Detector Radioactive Material Detection Spectroscopic (RMDS) Portal, Nuclear Instrumentation and Methods in Physics Research A, Vol. 712 (2013) 62.
35. R.T. Kouzes and E.R. Siciliano, "The response of radiation portal monitors to medical radio-nuclides at border crossings," Radiat. Meas., 41 (2006) 499.

Radiological Risk Assessment (Wednesday, February 12, 2014 14:00)

Development of a Risk-Based Decision-Support-Model for Protecting an Urban Medical Center from a Nuclear Explosion

G. Ben-Dor, I. M. Shohet, D. Ornai, B. Brosh
Ben-Gurion University of the Negev, Beer Sheva, Israel

INTRODUCTION

Nuclear explosion is the worst man-made physical threat on the human society. The nuclear explosion includes several consequences, some of them are immediate and others are long term. The major influences are: long duration blast, extreme thermal release, nuclear radiations, and electro-magnetic pulse (EMP). Their damage range is very wide. When nuclear explosion occurs above or in an urban area it is possible that one or more medical centers will be affected. Medical centers include several layers of structures defined by their resistance capacity to the nuclear explosion influences, beginning with the structure's frame and ending with different systems and with vulnerable medical critical infrastructures such as communications, medical gas supply, etc. A comprehensive literature survey revealed that in spite of the necessity and the importance of medical centers in the daily life and especially in emergency and post nuclear explosion, there is a lack of research on this topic.

The Nuclear Threat Scenario

Nuclear warheads are classified mainly by their equivalency to conventional TNT explosive charge, often called as nuclear weapon yield that ranges between kilotons (kT) to megatons (MT). The enormous bombs that were used in Hiroshima and Nagasaki were less or equal to 21kT. Current Ballistic Missiles have sub-warheads that sums together to the MT scale. The closest point on the ground surface to the above ground explosion is called ground zero (GZ). The burst altitude can vary between decades of kilometers above ground with almost just electromagnetic effect, hundreds of meters above ground for maximizing the blast and the prompt radiation effects, and above ground burst with lower blast effect but with additional radioactive fallout, which has long term hazardous effects. Medical centers will not be a target of nuclear weapon, but being in the centers of big and medium size cities would make them susceptible to late effects of the nuclear explosion. They could be located a few hundred meters (a scenario which is not cost effective to prepare for) to a few kilometers away from GZ, meaning that they are outside the burst main influence depending on the warhead yield. The model which will be presented can be applied to many threats. Nevertheless the scenarios that will be examined will match a blast of 30 kT located above ground ranges between hundreds of meters up to a few kilometers away from GZ.

Implications and consequences of the threat scenario in department of emergency care of the medical center.

There are several possible types of hazards to medical centers that depend on their location, their distance from the blast and their physical characteristics. These hazards can occur exclusively, simultaneously and at different levels at different sections in the facility as described subsequently:

- a) No structural or physical hazard but necessity to evacuate the facility because of radioactive fallout or fallout fear in its vicinity and lack of preparedness of sealing and long duration stay;
- b) No physical hazard but lack of full availability of the medical, nursing and administrative staff because of their or their relatives' injuries or evacuations;
- c) Electromagnetic effect that causes malfunctioning of electrical and electronic devices;
- d) Light hit in the exterior envelope such as windows etc.;
- e) Fire;
- f) Survivability of buildings but hazard to surrounding infrastructures;

- g) Survivability of the buildings' skeleton but hazard to brick walls, interior partitions, infrastructures and exterior envelope components.
- h) Comprehensive or partial collapse but survivability of shelters and protective spaces.
- i) Partial or complete structural collapse but survivability of the shelters and protected areas.
- j) Comprehensive collapse that includes protected areas.
- k) Injuries to the staff, patients and visitors directly from the blast (irradiation for example) in addition to different degrees of structural damage.
- l) Radioactive activation of structural elements.

The blast loading with its main parameters such as incident and reflective pressures and impulses (integration of pressure by time), and duration time can be calculated. A typical medical center department facility made of reinforced concrete, is relatively similar to 900 square meters above ground structure, including two stories described with its pressure-impulse (P-I) damage curves, ranges between no damage (0%) up to severe damage and collapse (100%) depicted by SAFER technical manuals (part of the U.S. Department of Defense manuals). In most cases the non-structural elements, such as masonry walls, will suffer at least one damage level above the structural elements. If the current structural resistance to the nuclear blast, is below the dynamic loading expressed by the calculated P-I, then it needs to be improved by various protective techniques such as strengthening the walls and ceilings, adding protective layers, etc.

Research objective

The research goal is to develop a decision-making model for optimal protection, and the means of its execution for a medical center, which has to continue performing in a nuclear attack event. The model is aimed at finding the optimal working point for investment in protection, based on getting the minimum point of the curve that includes cost scheme:

- a. The cost of investment in protective measures;
- b. Risk expectancy;

The Risk Management Model

The risk management model is composed of three main functions: (1) the risk function (R); (2) the Cost of Protective Effectiveness (CPE), (3) the Total Cost of Protective Effectiveness (TCPE). The following paragraphs delineate the rationale of the Risk function.

The consequence expectancy function expresses the consequence as follows:

$$C = f \{M, I, D, P_{(M,I,D)}\}$$

Where C, the consequences of the event expressed in units of cost, is a function of:

M – direct mortalities

I – direct injuries

D – cost of physical damage

$P_{(M,I,D)}$ – mortalities, injuries and physical damage caused by the medical center's malfunction (partial or complete)

The risk function is expressed as follows:

$$R = f \{P_a, 1-P_E, C\}$$

Where R, the risk attributed to the threat realization (in US\$), is a function of:

P_a - the probability of an attack

$1 - P_E$ - the lack of protective effectiveness (vulnerability) of the protection measures that were taken.

C- the general consequence of the attack.

In addition, the Cost of Protective Effectiveness (CPE) and the Total Cost of Protective Effectiveness (TCPE) functions will be developed.

Figure 1 delineates the typical linkages between the CPE and the R, given the threat scenario vs. P_E - The decision variable (independent variable).

The dashed line represents the Cost of Protective Effectiveness, CPE, related to the level of Protective Effectiveness [%], P_E . The dotted line represents the Risk Expectancy vs. the Protective Effectiveness [%], P_E . The solid line expresses the Total Cost of Protective Effectiveness: a superposition of the two above-mentioned functions, TCP, Total Cost of Protective Effectiveness, expresses actually the total cost of the CPE and the Risk Expectancy. The minimum of this curve is the optimal point of investment in protective policy.

The main research assumption is that the Risk curve, R, in the decision diagram is not linear in a nuclear scenario but climbs steeply against reduction in the level of the protective effectiveness level. This is because of the fact that the damage expectancy effects diverge beyond the physical damage and include also indirect mortality caused by loss of healthcare performance in addition to direct injuries and mortalities.

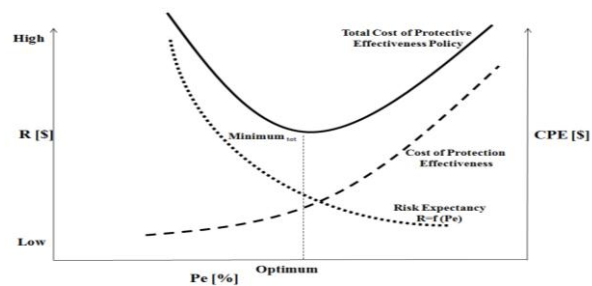


Figure 1: Decision diagram for the optimal investment point for nuclear explosion scenario

The statistical parameters in the proposed model are:

- The probability distribution of the distance between the blast and the medical center building. This depends on the distances to the city center, to strategic facilities, etc.
- The probability distribution of the building or its members failure, given specific dynamic loads profile, according to acceptable calculating tools and guidelines.
- The probability distribution of the number of people of the building, as a function of time, day, night, season, etc.
- The probability distribution of casualties' rate in the building caused by the direct effects of the explosion and by the building failure.
- The probability distribution of the number of people that will need medical treatment in the medical center in the area, due to the charge weight, population density, regional distribution of medical centers and the discussed medical center capacity.
- The probability distribution of mortality for several types of injuries with and without medical treatment.

SUMMARY AND INTERMEDIATE CONCLUSIONS

- Although the consequences of nuclear explosion are highly severe, they can be estimated and preparedness for the threat can be established to mitigate the consequences.
- The physical effects and hazards of the nuclear explosion at various locations are compared to the medical center current resistance. Additional protective means will be provided and evaluated if necessary.
- Although the probability of effective nuclear attack is considered to be low, the consequences and the derived risk expectancy are high and can be analyzed rationally from economic measures.
- Given a successful nuclear attack event, medical centers have an important role in mitigating disaster consequences.
- The relevant literature dealing with this issue does not relate to medical center preparedness, probably due to the assumption that medical centers will be beyond the effective range of the blast effect or too close to be considered.

Time Dependent Radio-toxicology of Fission Products

M. Stern , A. Baram , S. Pistinner

Soreq NRC, Yavne 81800, Israel

INTRODUCTION

Ionizing radiation, emitted by radiological materials, is known to cause damage to biological tissue. Prolonged exposure to radiation may cause a vast array of harmful medical effects, from enhancing future probability of cancer, up to Acute Radiation Syndrome resulting in multi-system failure.

In complex radiologic release events involving fission products (nuclear fallout, reactor failures), the products' physical decay chains dictate a time dependent product inventory. As the ratios between different products vary, so does the toxicology of the radioactive inventory as a whole. The temporally varying toxicological factors should be taken into account when producing radiological risk assessments for populations. In this paper we study the time varying toxicology of fission products, using a specialized model named Koala, developed in Soreq NRC.

A significant and monotonous rise in the aggregate toxicity of ingested fission products was noted. This result carries important implications for risk assessment, as it partially cancels out the fission product physical decay. A similar, albeit less pronounced rise was found for external exposure. Factoring activity and toxicity together allows computation of effective source terms for simple events involving fission products. We demonstrate one such source term, based on fallout from a nuclear explosion. This source term may be easily introduced into suitable atmospheric dispersion models.

THE RADIOACTIVE INVENTORY

Several important classes of radiological risk assessments involve fission products. These materials are product of nuclear reactions in fissile material (such as Uranium or Plutonium), used to release energy in nuclear reactors or weapons. The fission products are usually radioactive, and may pose a threat to the population. Characterization of the fission products is thus an important step in preparing radiological risk assessments for events like nuclear accidents or fallout.

The fission products are divided into decay chains, such that the quantity of a single isotope satisfies the equation

$$(1) \quad \frac{dN_i(t)}{dt} = -\lambda_i N_i(t) + \sum_j \lambda_j \alpha_{ji} N_j(t)$$

Where $N_i(t)$ is the quantity of the isotope, λ_i is its decay constant (reciprocal mean lifetime), and α_{ji} are the branching ratios of other isotopes into the considered isotope. This relation corresponds to a large number of connected first order differential equations, one for each isotope involved in the problem. To solve this set of equations, we have developed a model named Koala, which utilizes several independent techniques to obtain solutions of the time dependent inventory⁽¹⁾. The currently preferred method is based upon solving the eigenvalue problem of the decay matrix represented by

$$(2) \quad \mathbf{C}_{ij} \equiv \lambda_i (\alpha_{ij} - I)$$

Where I is the unity matrix.

Obtaining the time dependent solution of the fission products inventory allows the computation of a crucial function for risk assessment, the inventory activity

$$(3) \quad a_i(t) = \lambda_i N_i(t)$$

Koala's results were validated by comparing them to both analytical solutions of simple isotope systems, and experimental data. The following figures present comparison of Koala to experimental and numerical results for aggregate fission product inventories (for U^{235} and Pu^{239}). Millage⁽²⁾ considered numerically the decay of Pu^{239} using numerical programs, while Petrov et al.⁽³⁾ studied activity measurements the inventory of U^{235} . The results are normalized by the Way-Wigner approximation⁽⁴⁾ denoted by $a \sim t^{-1.2}$

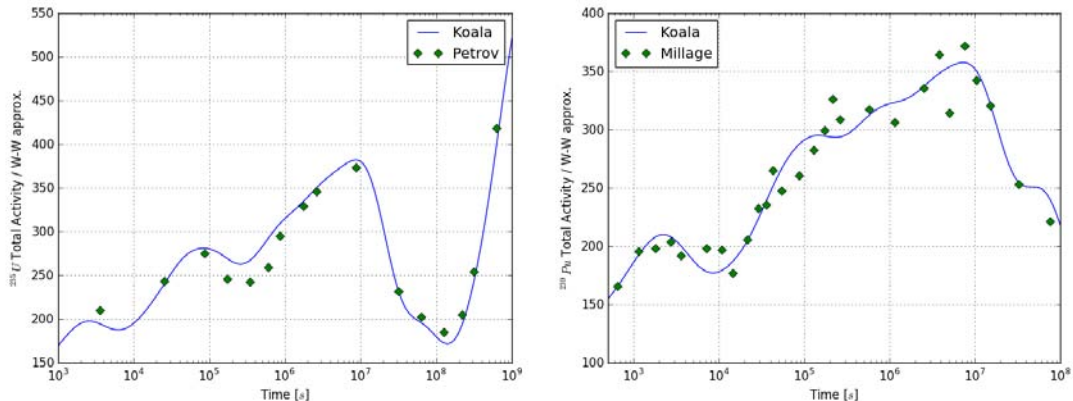


Figure 13. Comparison of Koala results to decay data. a) Millage's^[2] numerical data for decay of Pu^{239} (using DKPOWR and ORIGIN2), b) Petrov et al.^[3] experimental results for decay of U^{235} . Activities are divided by the Way-Wigner⁽⁴⁾ approximation $a \sim t^{-1.2}$. According to this approximation, the activity on these graphs should form a straight line. The deviation from the Way-Wigner Approximation is clearly demonstrated.

The nontrivial temporal behavior of the decay products is well reconstructed by the Koala model. This test and others show that the model is compatible for calculation of decay inventory for fission products in instantaneous events. A modification of the model allows computation of the time dependent decay inventory in the more complex settings of a reactor core.

RADIO-TOXICITY OF FISSION PRODUCTS

Performing risk assessments for events involving fission products require a further elaboration on the aforementioned computation. Each of the isotopes may be assigned numbers, relating its instantaneous activity to the biological damage it may cause. These factors depend on the pathway of exposure:

1. Inhalation⁽⁵⁾ – each inhaled Becquerel causes aggregate damage over decades. Toxicity for inhalation is assigned the units of Sv/Bq .
2. External exposure due to the radioactive cloud⁽⁶⁾ (Immersion) – proportional to the time integral of the airborne activity concentration ($Sv \cdot m^3/Bq \cdot s$).
3. External exposure due to ground shine^[6] – proportional to the ground activity concentration ($Sv \cdot m^2/Bq \cdot s$).

Computing the risk of each isotope at a certain time entails finding its activity, and multiplying it by the relevant toxicity factors. This process facilitates the construction of an effective source term, comprised of an "effective isotope", with activity equal to the total inventory activity, and a time dependent toxicity conversion factor. It is convenient to group the isotopes according to their reactivity: Ideal gasses are non-reactive and are not deposited on the surface. This property also dictates that their radio-toxicity due to inhalation is null. Therefore, we will consider two effective isotopes referred to as "Solids" and "Ideal Gasses". The following figures show the time dependence of the effective toxicity conversion factors for the two effective isotopes, due to an instantaneous fission of Pu^{239} by fast neutrons.

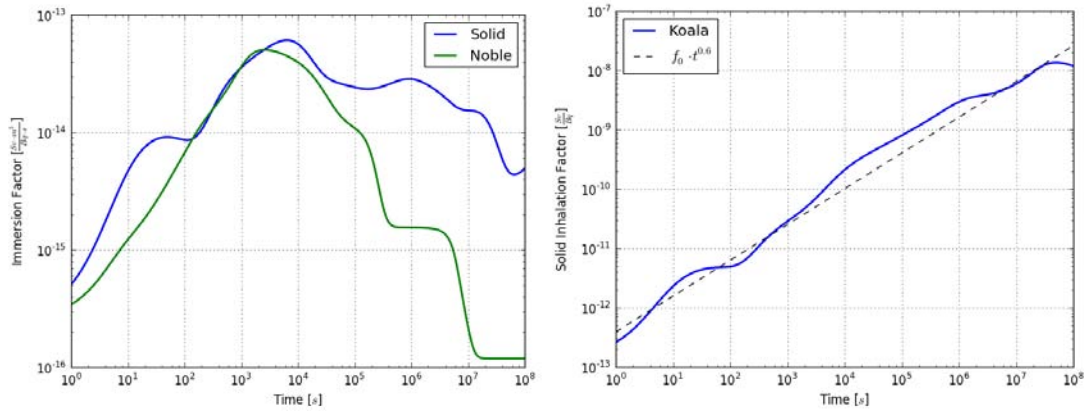


Figure 14. Time dependent radio-toxicity of the two effective isotopes ("Solids" and "Ideal Gasses"), due to a) inhalation of fine particles, b) immersion in the radioactive cloud.

In figure (2a) we find an unexpected phenomenon: The effective radio-toxicity due to inhalation significantly grows over time, as the inventory gradually accommodates more toxic isotopes. In the first two years following fission it may be approximated by a power law with exponent 0.6. This growth indicates that the inventory decay rate provides a poor estimate for the radiological risk to population. In fact, the inventory physical decay is partially offset by the sharp increase in radio-toxicity. The effective radio-toxicity due to external exposure (2b) does not show growth of such magnitude, but still displays a non-trivial temporal dependence. It is noteworthy that during the first few hours after the fission (the time window most relevant for risk assessment), one may still detect an effective radio-toxicity increase of nearly two orders of magnitude compared to the initial value.

Let us now discuss a simple source term, due to a nuclear explosion of 1kt, which will result in fission of $\sim 1.5 \cdot 10^{23}$ Pu²³⁹ nuclei. Koala allows calculating the activity of each radioisotope, and multiplying it by the relevant radio-toxicity factors. Factoring in a typical human respiration rate facilitates placing the radiological exposures due to inhalation and external radiation on the same footing. The following figure illustrates the "potential doses" due to the effective isotopes in each path of exposure. It is important to stress that the potential dose does not represent a real exposure a person may contact, but a measure of the source term, representing the hazardous materials in the atmosphere following the explosion. To obtain risk assessments for the exposures of the population, the source term is inserted into a suitable atmospheric dispersion model.

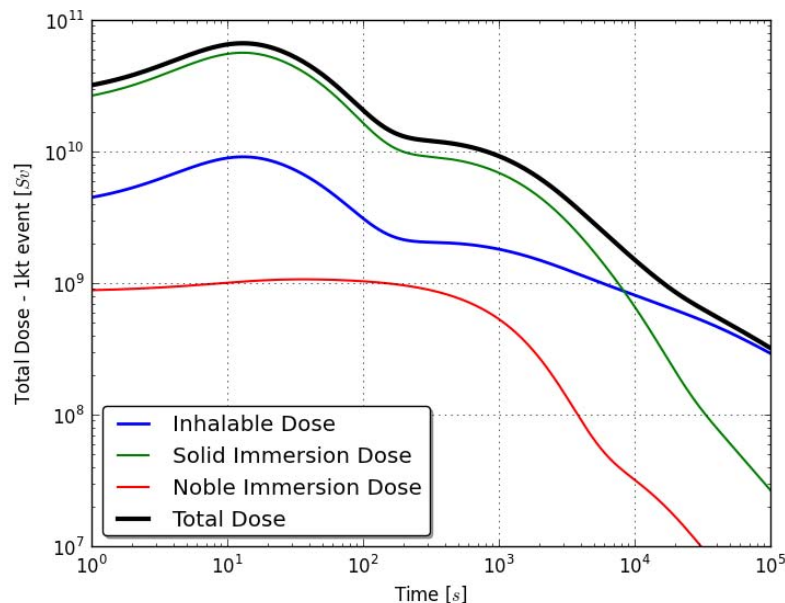


Figure 15. The potential dose due to a 1kt nuclear explosion.

In the first two hours, most of the radiological exposure is caused by external exposure to solids. In later times, the primary cause of radio-toxicity is inhalation of radioactive aerosols. The noble gasses seem to contribute very slightly to the source term at all times. Let us remark that the comparison between external and internal exposures has an important caveat. The external exposure is immediate, and the internal exposure will be accumulated over the following 50 years. It is thus recommended to initially treat the external exposure, which may cause more severe biological effects.

REFERENCES

1. J. Harr, Precise Calculation of Complex Radioactive Decay Chains, AFIT/GNE/ENP/07-03 (2007).
2. K. K. Millage, Fission Product Decay Characteristics, AFIT/GNE/ENP/86M-5 (1989).
3. R. V. Petrov et al, Radioactive Fallout, Appendix IV (1963).
4. K. Way, E. P. Wigner, The Rate of Decay of Fission Products, *Physical Review*, Vol 73, 11 (1948).
5. International Basic Safety Standards for Protection Against Ionizing Radiation and for the Safety of Radiation Sources, Safety Series No. 115, International Atomic Energy Agency, Vienna (1996).
6. K. F. Eckerman, J. C. Ryman, External Exposure to Radionuclides in Air, Water, and Soil, Federal Guidance Report No. 12, EPA-402-R-93-081 (1993).

Radiological Risk Assessment (Wednesday, February 12, 2014 14:00)

Fast Multispectral Fireball Analyses and the Relation to Particles' Aerosolization

A. Sharon^{1*}, I. Halevy¹, D. Sattinger¹, Z. Berenstein¹, R. Neuman¹, P. Banaim¹, M. Pinhas², and I. Yaar¹

¹*Nuclear Research Center Negev (NRCN), P.O.Box 9001, Beer-Sheva, Israel*

²*Israel Atomic Energy Commission (IAEC), POB 7061, Tel Aviv, Israel 61070*

* Corresponding author: Avi Sharon, asharon68@gmail.com, avish@nrcn.org.il

ABSTRACT

One of the key questions in analyzing the consequent risk following an explosion of radiological dispersal device (RDD) is the final radioactive particles' size distribution caused by the detonation. Fine, respirable, aerosols behave different when compare it to large, non respirable, aerosols or to inertial particles. While aerosols (both, respirable and non respirable) are trapped inside the detonation cloud moving downwind with the cloud, heavier, inertial particles escape the initial fireball and settled on the ground at a short distances due to hydrodynamic drag. Respirable aerosols are mostly risky when inhaled into the body (internal radiation) while non respirable are risky as an external exposure agents (both on the skin and from a distance). Knowing the size distribution of the radioactive particles will, thus, enable more realistic risk assessment predictions of such events.

Fast multispectral radiometry of detonation fireballs can be used as novel tool for the estimation of the RA material final size distribution.

INTRODUCTION

During Green Field1 experimental project, ColoRad C7, fast multispectral radiometer (FMR) of IARD-Israel2 was used. This unique tool was aimed to detect the fast temporal evolution of the fireball in time scales of micro seconds (sampling frequency of 250 kHz).

The fireball average radiant intensity was measured every four microseconds in four different spectral bands. The aim of using such an advance tool is to be able to quantify the contribution of the different particles and detonation products involved, to the total energy released following the explosion. The measurement of the radiant intensity of the aerosols and other particles involved (detonation products, soot, carbon monoxide, carbon dioxide and dirt entrained into the fireball) and a comparison between clean and dirt shots enable to study the effect of agglomeration processes occur in different fireballs. Analyses done on the radiant intensity data enable us to calculate the fireball temperature and its radiant area temporal variation. This can be done from the ratio between radiant intensities of different spectral bands.

Aerosolization of particles due to detonation shock wave depends on the fast and complicated evolution of and processes inside the fireball where the RA particles exist. The results will indicate the possible agglomeration processes of RA particles and dirt material entrained into the fireball.

The after burn stage which is typical to explosive types which are under balanced to oxygen (like TNT, for example, which is (-74%) under balanced, or C4 which is (-21%)) can be only exist if there is available ambient oxygen, material to be oxidized ("fuel") and high enough temperatures. During the after burn process, the C atoms of the explosive oxidize and become CO molecules and then CO₂ molecules if there is still available oxygen and high temperatures of more than 1750oK degrees. The interaction of the detonation products, soot and other hot aerosols with the RA particles and the dirt entrained into the fireball (from the ground or from the explosive case, for example) will dramatically influence the temporal temperature variation and thus the final particles' size distribution following the detonation. Hence, the radiological consequences will be affected as well.

Enhanced amount of dirt entrained into the fireball reduce its temperature and suppress the after burn process and thus, most of the energy involve in the detonation will come out of the early detonation stage

rather than from the after burn. TNT is an example of explosive which is very (by -74%) underbrace to oxygen. This means that in the case of clean detonation (with no dirt entrainment and a certain amount of free available oxygen) the first part of the process yields only one third of the total available (combustion) energy, called the detonation energy³ and the rest two third of the total energy appear in the after burn stage. Based on this phenomenology we have used the ColoRad C7 of IARD in different explosive atmospheric dispersion tests of RA material, during GF III project¹.

The spectral bands (all in the SWIR and MWIR range) were chosen in order to capture the molecular emission of the detonation products and the CO₂ as an after burn indicator.

Figure 1 shows the ColoRad C7 radiometer used during GFIII tests.



Figure 1: The IARD ColoRad C7 (right) and high speed fireball snapshot 10 ms following TNT detonation

2. Experimental results: radiant intensity and temperatures

A comparison between two shots of the same explosive charge (0.25 kg of TNT), one is hanging in the air above clean steel surface (on the left) and the other is on packed soil, dirt surface, (on the right) is presented on figure 2.

The fireball radiant intensity of each of the four spectral bands is presented for each of the two shots.

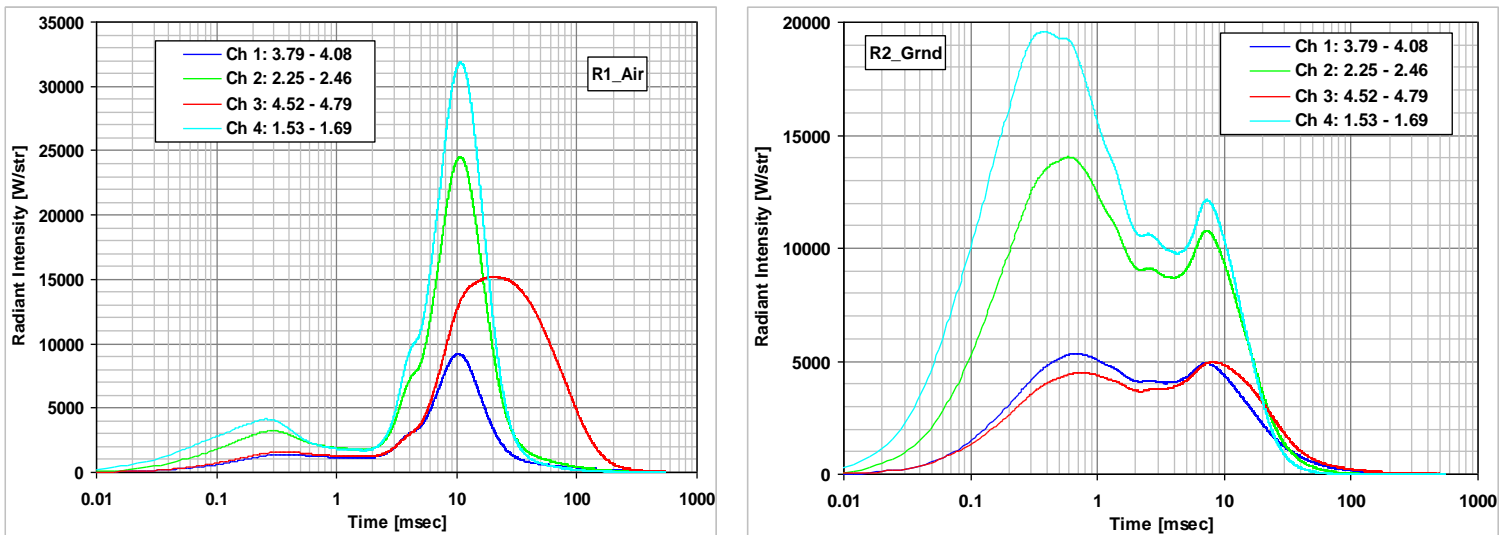


Figure 2: Fireball radiant intensity of clean (left) and dirt (right) 0.25 kg of TNT charges, as measured during GFIII experiment.

As described before, it is easy to recognize the two peaks of the energy emission: the first one (around 200-300 μs) is related to the detonation energy and the second (around 10 ms) is the after burn contribution of later oxidation, mainly due to the emission of the CO_2 . The total energy is the time integral of these curves. One can see that the two peaks ratio, of each fireball is completely different when comparing the clean and the dirt shots. In the case of the clean shot, no ambient dirt was entrained into the fireball and thus high temperatures were exist to support full after burn process. On the other hand, the dirt shot involves high amount of soil that entrained by the fire ball strong vortices, reduce the temperature and suppress the oxidation of the C atoms into CO_2 , thus resulting in a lower after burn peak.

RA particle size distribution will be different for the two shots, even though the charges were similar. Due to the fact that the radiant intensities that were measured in channels 1,2 and 4 are from the contribution of the aerosolos of the deronation products then it is possible to calculate (based on gray body radiation assumpton) from each two of the channels, the equivalent temperature and the effective fireball projected area. The results for two shots are presented in figure 3.

As can be seen from the two cases the temperatures after 40 microseconds are almost completely overlap for each two channels ratios (per each shot), which are in principle independent of each other. This means that the algorithm using for calculating the temperatures can yield the real value of the fireball average temperature. The CO_2 contribution to the total radiant intensity can be calculated as well, since channel no. 3 is reflecting the emission intensities of mainly the CO_2 and the detonation products aerosols.

Temperature diffences of a given fireball, at early times following detonation (10-30 μs) are possibly due to low signal to noise ratio and / or due to some diviation from the gray body radiation assumption, and it is under current study.

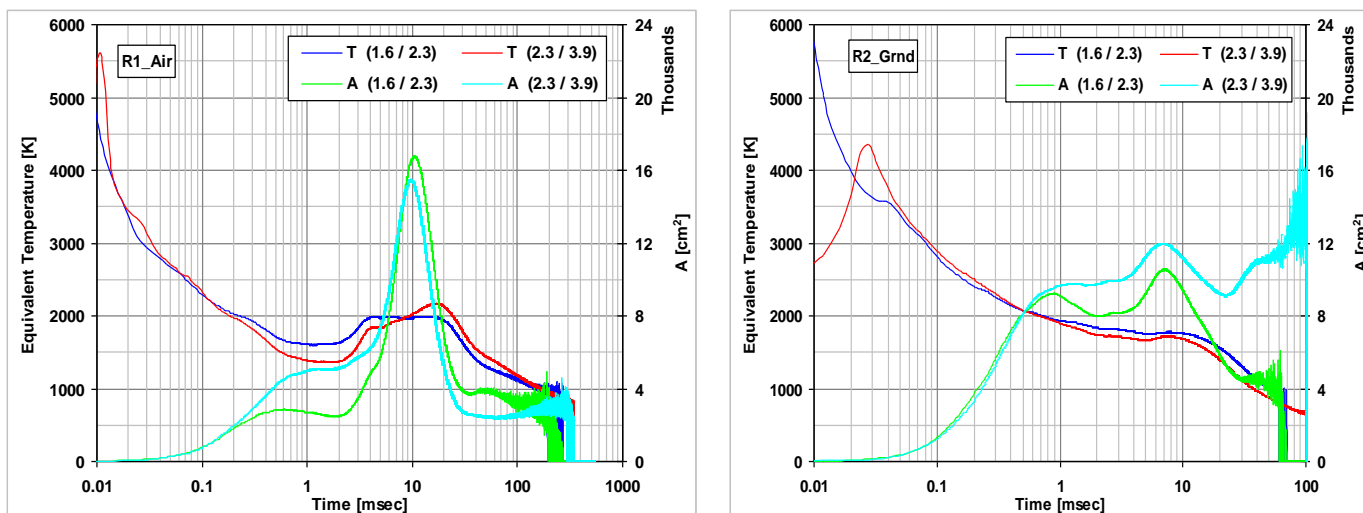


Figure 3: Equivalent (radiant) temperature and fireball effective area for the clean (left) and the dirt (right) shots.

SUMMARY

Fast multispectral radiometry of detonation fire balls is using for the study of the dynamic physical and chemical processes in the fireball. The after burn intensity, mainly due to CO_2 emission can used as an indicator for the fireball cleanness which affect the final size distribution of RA particles which dispersed by high explosive charges.

REFERENCES

1. A. Sharon et al. Ground deposition pattern of an explosive RDD, Israel Nuclear Society conference, February 2014, Dead sea, Israel.
2. IARD – Sensing solutions Ltd., Yagur, 30065, Israel.
3. P. A. Cooper, Explosive Engineering, WILEY-VCH, ISBN-0-471-18636-8 1996.

Dosimetry (Wednesday, February 12, 2014 16:30)

Automation at NRCN Dosimetry Laboratory

A. Abraham⁽¹⁾, I. Arad⁽²⁾, M. Mesing⁽¹⁾, S. Levinson⁽¹⁾, M. Weinstein⁽¹⁾,
O. Pelled⁽¹⁾, A. Broida⁽¹⁾, U. German⁽¹⁾

⁽¹⁾ *Nuclear Research Centre Negev, POB 9001, Beer-Sheva 84190, Israel*

⁽²⁾ *Rotem Israel Arad Ltd., POB 275, Kefar-Saba 44102, Israel*

INTRODUCTION

Running a dosimetric service based on TLD technology such as at the Nuclear Research Centre Negev (NRCN) requires a large group of workers to carry out simple mechanical actions such as opening and closing TLD badges, placing and removal of TLD cards from the badges and operating the TLD reader. These actions can be automated to free human resources for other assignments and to improve the quality assurance.

At NRCN a project was undertaken to design and build a robotic system based on a manipulator arm. The design was based on the experience achieved with an earlier prototype ^(1,2). The system stores the TLD badges in special designed boxes, which are transported and stored in computer defined bins. The robotic arm loads and unloads TLD cards to the badges, and loads/unloads the cards to a magazine for the TLD reader. At the Nuclear Research Center Negev (NRCN) each badge is assigned to a specific worker and bears a sticker containing the worker's personal details, also in a machine readable form (barcode). In order to establish a proper QA check, a barcode reader records the information on the badge and on the TLD card placed in this badge and checks their compatibility with the information contained in the main database. Besides the TLD cards loading/unloading station, there is a contamination check station, a cards cleaning station and a UV irradiation box used to reduce the history dependent residual dose.

The system was installed at the NRCN dosimetry laboratory. It was successfully tested for several hundreds of cycles and will become operational in the first quarter of 2014. As far as we know, there is no similar product available for automatic handling in a TLD laboratory. A general view of the whole system is seen in Fig. 1.

THE SYSTEM AND THE PROCESSES

The whole system is managed by an automatic controller that manages the movement of each component (TLD cards, badges and boxes) to and from specific locations defined by the required task and by the information from the various sensors. The central component of the system is a robotic arm with 6 degrees of freedom equipped with a gripper, which includes custom made fingers and a vacuum nose. The function of the fingers is to seize the badge and bring it to a certain location. The fingers are designed to apply a pre-designed pressure.

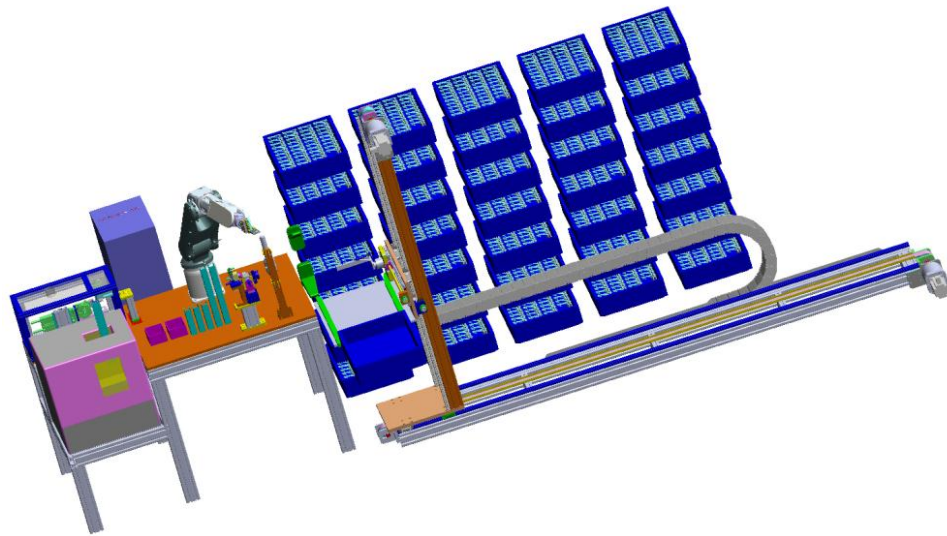


Fig. 1. A general view of the robotic system.

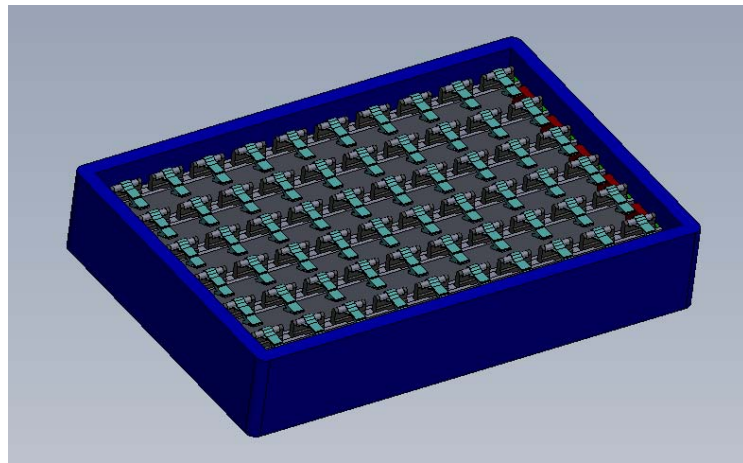


Fig. 2: The boxes containing the TLD badges

The Mechanized Storage System

The system is based on specially designed boxes that are used to store, handle and move the TLD badges. A box contains aluminum strips that hold the TLD badges in a fixed location (see fig. 2). Each box can hold 1-50 TLD badges. The storage of boxes is based on a XYZ system that can move the boxes to and from the shelves and to and from the working table. The storage system has a special "insert boxes shelf" which automatically registers the box and determines its location according to the momentary map of free shelves.

The Working Table

The working table includes the following stations:

- **External contamination check.** A radiation detector is mounted at this station and the badge is held in front of it for a pre-determined time to ensure that no contamination of the badge occurred during the field operation.
- **Barcode reading station.** It identifies the TLD card number and the information on the badge containing this card to check their match, as defined in the main database.
- **TLD badge opener.** It opens the TLD badges to allow the robotic arm to remove / return the TLD card to the badge.

- **TLD system cartridge.** It stores the TLD cards which were taken out of the badges and after being filled is transferred to the TLD reader.
- **Cleaning station.** It is operated to remove dust and dirt from the TLD cards by inserting them in an ultrasonic bath filled with alcohol and a drying the cards using a stream of nitrogen. The cleaning process is not part of the routine day to day work and can be run separately.
- **UV irradiation station.** It is operated to irradiate the TLD cards by a UV lamp at a pre-determined temperature to enhance background reduction..
- **TLD reader (optional).** The operation of the TLD reader can be made fully automatic. The robotic arm can take the TLD system cartridges into and out of the TLD reader and the controller can give read commands to the reader and get end signals from it.
- **CR39 station (optional).** Can be used to handle the registration and changing of the CR39 dosimeters from the TLD badges.

The system can perform a combination of different tasks. An example for such a task is shown in the flow chart in Fig. 3 for the unloading and read process.

The process of loading/unloading a full 50 TLD badge box including all QA checks takes about 25 minutes. Loading a box with cards that passed readout and unloading a new box can be undertaken while the TLD reader reads a cartridge of TLD cards (the readout rate is about 60 cards per hour), thus the operation time can be optimized by planning suitable parallel tasks.

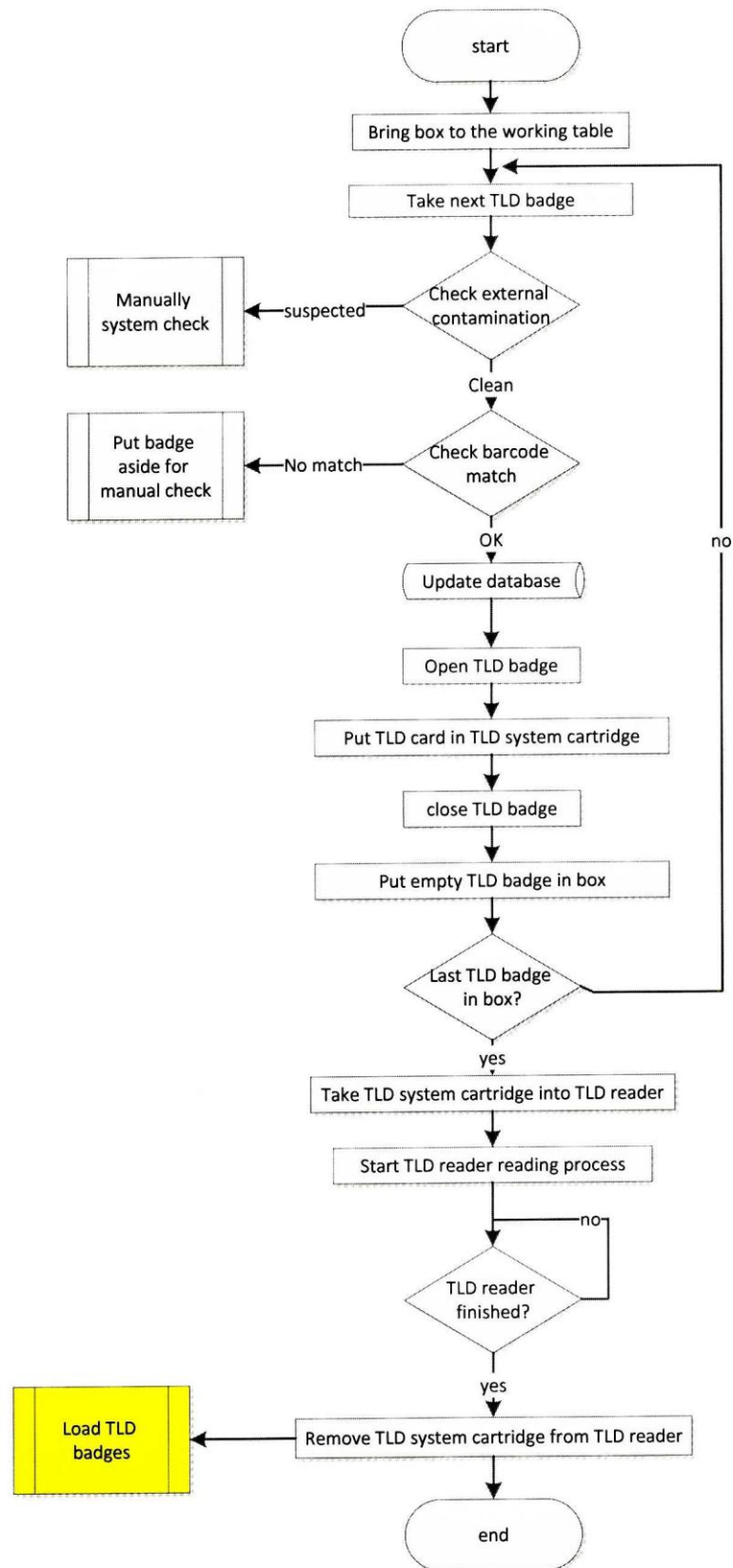


Fig. 4: Flow Chart - Unloading and Reading Process of a Single Box.

SUMMARY

An automatic robotic system based on a mechanized storage system combined with a robotic arm system for handling of TLD badges was designed, built and tested at the NRCN dosimetry laboratory. The system was designed to fit the NRCN dosimetry laboratory procedures and can handle any load of TLD badges, with the

only limitation of the size of the storage area. The system is in the stage of final checks and will be soon fully operational.

REFERENCES

1. Gorelik V., Rozenfeld R., Levinson S., German U., Weinstein M., Hillel S., Rodnay G., *Robotic Implementation in Handling of Harshaw/Bicron TLD Badges*, The 23th Conference of the Nuclear Societies in Israel, 15-16 Feb. 2006, pp. 137-139.
2. S. Levinson, M. Weinstein, A. Abraham, U. German, V. Gorelik, R. Rozenfeld, S. Hillel, G. Rodnay, "A Robotic Manipulator for Handling of TLD Badges ", The Radiation Safety Journal (Health Physics), p. S190-S193, Nov. 2008

Dosimetry (Wednesday, February 12, 2014 16:30)

About Background Correction for LiF:Mg,Ti readout

T. Yifrah^(1,2), A. Abraham⁽¹⁾, M. Weinstein⁽¹⁾, O. Pelled⁽¹⁾, U. German⁽¹⁾, M. Mintz^(1,2)

⁽¹⁾ Nuclear Research Center Negev, POB 9001, Beer-Sheva 84190, Israel

⁽²⁾ Ben-Gurion University of the Negev, Beer Sheva, Israel

INTRODUCTION

Nowadays, the regulations require an accurate and reliable measurement of exposures according to the principle of ALARA (As Low As Reasonably Achievable), which emphasizes the need to handle correctly the background issue. Background signals can be radiation and non-radiation related and are produced during the readout process in the TL reader systems. The source of the non-radiation related signals can be the reader itself or effects in the TL crystal due to heating. The main contributions from the reader are dark current and electronic spikes, which are monitored continuously during the readout of a batch of TLD cards. Their contribution is constant during normal operation and can be easily subtracted. Non-radiation related contributions from the TLD chips may be caused by dirt which may be present on the TLD cards or light emitted by the Teflon layer which covers the chips⁽¹⁾. These spurious signals can be detected by checking the shape of the glow curves.

However, there is also a radiation related contribution originated by the exposure history of the specific chips. A TLD card contains TLD chips (most commonly LiF:Mg,Ti) held between two layers of Teflon, which are read out in routine work by using high heating rates. A readout temperature limitation of 300°C is also set, as the Teflon may be damaged at higher temperatures. Besides, due to the high amount of cards used in a routine dosimetry laboratory, usually no annealing procedure is applied. As a result, the electronic traps of the TLD crystals are not completely emptied during routine readouts and previous exposures leave a residual record, which increases the background and makes it history dependent. This contribution is mostly unknown and cannot be predicted.

Different attitudes were published in the literature to handle the TLD background issue. Clark et al.⁽²⁾ tried to fit a Boltzmann function to describe the background signal under the glow peak. Delgado and Gomez Ros⁽³⁾ determined several regions in the glow peak distribution and used the experimental ratios of some regions to predict the background contribution. The same authors tried a similar solution to handle the background issue for GR-200 glow curves⁽⁴⁾. Horowitz and Moscovitch⁽⁵⁾ mention a "conventional manner" to evaluate the background via a second readout immediately following the first. This simple and direct method was applied also in other works^(6,7), but its accuracy is questionable, as the first residual readout contains also a part of the measured dose itself and in addition the unknown history residual. In view of the complexity of the background contribution, a possible solution is to override the issue. Stadtmann and Ashbacher⁽⁸⁾ used a statistical handling of the bulk of results at their institution to correct generally for background, while Weinstein et al.⁽⁹⁾ used on purpose low dose exposure and UV irradiation handling to make the background issue insignificant.

A first step to handle in more depth the residual dose background issue of LiF:Mg,Ti readout was presented earlier⁽¹⁰⁾. The present paper describes a continuation of the effort to determine more accurately the background contribution present in each TLD readout due to its irradiation history.

THE METHOD

Due to the incomplete emptying of the deep traps during routine readout, a residual dose is left in the TLD crystal. Each readout frees a part of the charges, and with each consecutive reading less residual dose

remains trapped. This process was described elsewhere ⁽¹⁰⁾ and it is the reason why for every readout, there is a background contribution dependent on the dose in the past exposure and the number of times the crystal was read since then. As in a routine dosimetry laboratory many readout cycles are performed after various exposures, the residual dose background will be a superposition of tails from historical exposures, determined by the dose received and the number of readouts after each occurrence.

Suppose a virgin TLD crystal with no exposure history exposed to a dose D. The first readout (dose readout) will give the dose D, with no residual contribution from the past. Consecutive readouts will give decreasing readings, according to the residual dose in the crystal after each readout. Let $f(d, n)$ represent the readout values as a function of the exposure (d) and the number of readings from the exposure (n). If I exposures will occur at different times, the total resulting residual dose for a specific readout (R_I) can be expressed mathematically by:

$$(1) \quad R_I = \sum_{i=1}^I R_i = \sum_{i=1}^I f(d_i, n_i)$$

Where i is a serial number of the total I past exposures.

If the crystal is exposed to a new (unknown) dose D and then read, the reading (V) will be the actual dose value superposed on the residual tail from previous readings:

$$(2) \quad V = D + R_{I+1}$$

If j successive readouts will be performed next, the residual dose will contain combined residual doses from history and from the last exposure, expressed by:

$$(3) \quad R'_j = R_{I+j+1} + f(D, j)$$

$f(d, n)$ is a function which can be found by optimal fit to the experimental values of successive readouts of an exposed virgin crystal. If R will be described by a parametric function, several successive readouts will provide a series of equations in the form of Eq. (3), which can be solved to calculate the unknown parameters, including the last exposure D, which is the unknown to be determined.

Materials and Experiments

TLD cards which were used in the past in the dosimetry laboratory at NRCN were repeatedly read until achieving a constant readout value, which can be considered the "Initial Zero Value", free of history contribution. Next they were exposed and read several times. By analyzing the sequential residual dose readouts, a "Residual Response" function $f(d, n)$ can in principle be determined.

The experiments were performed using LiF:Mg,Ti cards (Thermo Inc. USA), randomly chosen from the stock of the dosimetry laboratory at Nuclear Research Centre Negev. Two sets of TLD cards were used. One set contained three TLD-100 crystals and the second set contained two TLD-600 and two TLD-700 crystals. The only precondition for choosing the TLD cards was that the residual dose of all the un-irradiated chips should be less than 0.02 mSv. In order to obtain this low residual dose, the TLD cards were prepared by irradiating them with an UV lamp (15 W, 254 nm) which followed by a series of readouts, until the reading was less than 0.02 mSv. This initial readout was marked as readout number -1 and was regarded as the zero value. Cards containing chips that could not reach this low zero reading were discarded.

The cards from the different sets were separated into 5 groups. Each group was irradiated to a different dose in the range up to 500 mSv. The irradiated cards were read up to 11 consecutive readouts. The first readout after the irradiation (the dose readout) was marked as readout number 0 and the following residual readouts were marked as readouts 1 to 10. All readouts were performed by a standard TLD6600 reader (Thermo Inc.). The heating of the TLD crystals was done by a hot nitrogen gas jet controlled by a PC. The Time Temperature Profile (TTP) used consisted of a pre-heat to 50°C (0.5 s), after which a linear heating rate of 25°C/s was applied up to a maximum temperature of 300°C for a pre-determined total time of 30 s. After each reading, the crystals were immediately cooled to room temperature by the nitrogen stream. The results of the readout process were digitized by the readout system to a 200 channel glow curve.

The Residuals Function

Fig 1 shows the averages of the results obtained from the successive readouts of all TLD chips exposed to 500 mSv, normalized to the dose readout (readout #0). The residual readings are #1 to #10.

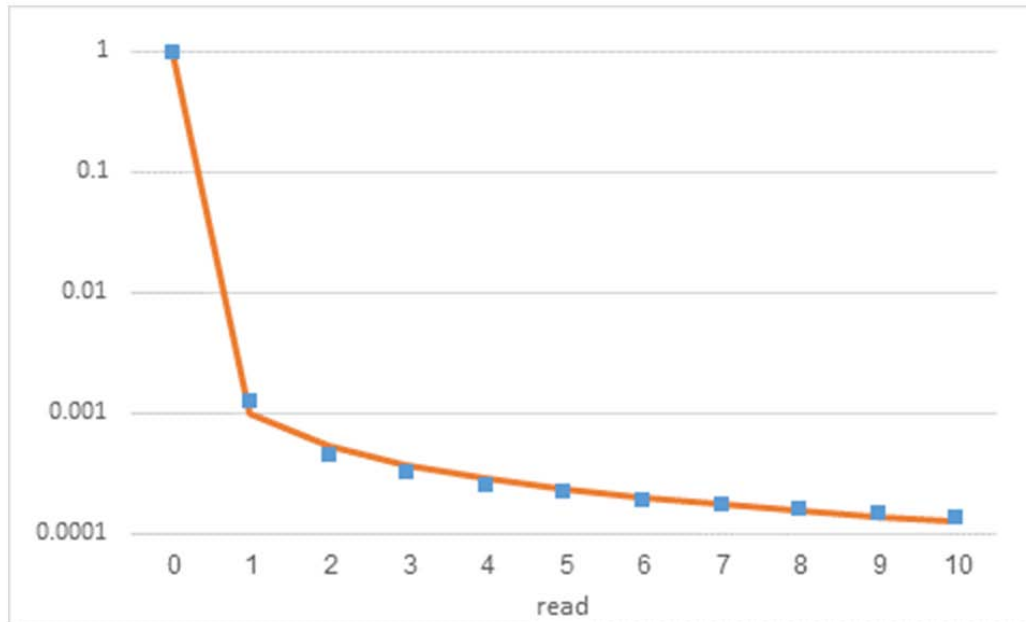


Figure 16 - The average successive readouts relative to dose readout of all 500 mSv irradiated TLD chips and the fitted function (Eq. 4).

A function, as given in Equation 4, was chosen which could describe as accurate as possible the steep descend from read #0 (dose readout) to read#1 (first residual readout) and a much more slower descend thereafter.

$$(4) \quad R(n) = \frac{1}{A + B \cdot n^C}$$

For $n=0$ (dose readout $=D$) Equation 4 becomes:

$$(5) \quad R(0) = D = \frac{1}{A}$$

Thus, from the case of a virgin crystal irradiated to a dose D the value of constant A is obtained: $A=1/D$. For the normalized readouts given in Fig. 1, $A=1$. The parameters B and C were determined by least squares fitting of function (4) to the experimental points in Fig. 1, which gave the values $B=988.9$ and $C=0.907$. The magnified region $n>0$ showing the experimental points and the fitted function for this region are shown in Fig. 2. The resulting final equation which describes all readouts (the dose readout and the residual readouts) is given in Equation (6).

$$(6) \quad R(D,n) = \frac{1}{1/D + 988.9 \cdot n^{0.907}}$$

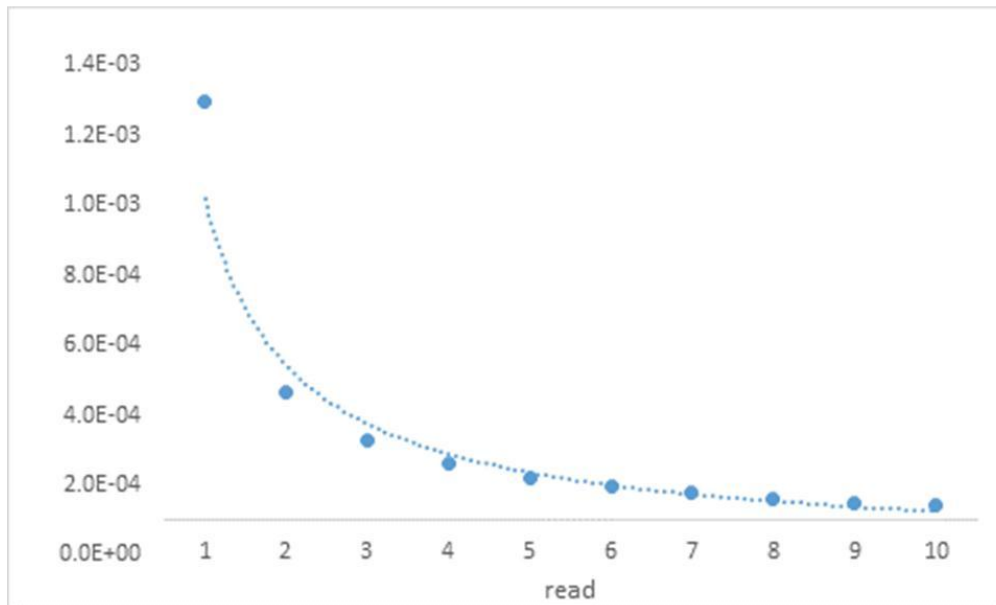


Figure 2 - The experimental successive readouts relative to dose readout and the fitted function (Eq. 4) for the residual dose range (detailed).

DISCUSSION AND CONCLUSIONS

A function could be found which accurately describes the total range of readouts, including the dose readout and the consecutive residual readouts. It represents the basic response of a virgin crystal irradiated to a certain dose and can serve as a basis of all other forthcoming considerations. The complete history of a TLD crystal is a superposition of these functions, each with its characteristic dose and read number.

An important feature is that the function described above is general, as the measured points used in the function fitting process are averages of all crystals used, of all types (TLD-100, TLD-600 and TLD-700). Thus, the function found is the basis for an universal handling of the background issue of LiF:Mg,Ti dosimeters.

The next step will be to find a parametric function which describes the superposition of any combination of the given basic function for different doses and read numbers, which will be the history component. Each new residual dose readout will contain the history component and the last exposure residual component (function 6). By performing several residual readouts, an extrapolation to readout #0 can be made, and the accurate total residual background can be subtracted to obtain the dose (see "The Method" section).

REFERENCES

1. U. German, M. Weinstein, "Non-Radiation Induced Signals in TLD dosimetry". Rad. Prot. Dosim. 101, (2002). 81-84.
2. W.J. Chase, M.D. Bezaire, F.P. Vanderzwet, C.E. Taylor, "A glow curve analyzer (GCA) for routine analysis of personnel thermoluminescent dosimeter results". Rad. Meas. 43 (2008), 621-625.
3. A. Delgado, J.M. Gomez Ros, "A simple method for glow curve analysis improving TLD-100 performance in the dose region below 100 μ Gy". Rad. Prot. Dosim. 34 (1990), 357-360.
4. A. Delgado, J.M. Gomez Ros, J.L. Muniz. "Computerized analysis of GR-200 TL signals: Application to dose measurements in the μ Gy range". Rad. Prot. Dosim. 60 (1995), 147-153.
5. Y.S. Horowitz, M. Moscovitch. "LiF-TLD in the microgrey dose range via computerized glow curve deconvolution and background smoothing", Rad. Prot. Dosim. 17 (1986), 337-342.
6. M. Osvay, S.Deme, "Comparative investigation of the LiF dosimeters using low and high LET radiation fields", Rad. Prot. Dosim. 85, (1999), 469-472.

7. S.Miljanic, M.Ranogajec-Komor, J.Blagus, D.Miljanic, M.Osvay, "TLD-700 for proton dosimetry in the presence of low-energy X-rays". Nucl. Instr. and Methods A, 519, (2004), 667-673.
8. H. Stadtmann, A. Ashbacher, "Background correction of personal dose distribution by a novel unfolding algorithm". Rad. Prot. Dosim. 125 (2007), 395-398.
9. M.Weinstein, U. German, A. Abraham, S. Dubinsky, Z.B. Alfassi, " On the linearity of the high temperature peaks of LiF:Mg,Ti". Rad. Meas. 39 (2005). 489-494.
10. A. Abraham, M. Weinstein, O. Pelled, U. German, Z.B. Alfassi, "Minimizing the residual signal of LiF:Mg,Ti readouts". The 26th Conference of the Nuclear Societies in Israel, 21-23 Feb. (2012), 357-360.

Dosimetry (Wednesday, February 12, 2014 16:30)

The Enigma of Linear/Supralinear Thermoluminescence Dose Response Mixed Localized/Delocalized Recombination describes a Solution

I. Eliyahu^{1,2}, Y.S. Horowitz¹, L. Oster³ and I. Mardor²

¹ *Ben Gurion University of the Negev, Beersheva, 84105, Israel*

² *Soreq Nuclear Research Center, Yavne, 81800, Israel*

³ *Sami Shamoon College of Engineering, Beersheva, 84100, Israel*

Kinetic models of thermoluminescence (TL) dose response have recently been proposed (1) which propose to solve the long-standing conundrum (2) concerning the dependence of the TL dose response on ionization density. Many TL materials exhibit an initially linear dose response over several decades of dose which then turns supralinear before entering into saturation. LiF:Mg,Ti is perhaps the most outstanding and widely studied example. The dose response of the major dosimetric glow peak (composite peak 5) is strictly linear from the lowest level of dose measurable of $\sim 10^{-4}$ Gy to ~ 1 Gy and then turns supralinear reaching maximum values of the normalized TL dose response $f(D)$ of 3-5 at levels of dose between 300 -500 Gy (3). This behaviour coupled with the dependence of the supralinearity on particle type and energy (i.e., on ionization density) has presented a formidable challenge to conventional kinetic theories of dose response. It has been gradually recognized over the past decade that this behaviour in LiF:Mg,Ti requires both nanodosimetric input coupled with a mixture of both localized and delocalized recombination mechanisms. This due to the complex nature of the trapping structure giving rise to the TL. Following irradiation the trapping center (TC)- luminescent center (LC) can be populated by a locally trapped electron-hole (e-h) or an electron (e) only. The former giving rise to geminate (localized) recombination the latter to mainly delocalized recombination via charge transfer migration in the conduction band. The relative concentrations of these configurations are dependent on ionization density (1). In this paper we present the latest developments in which we attempt to simulate (i) the linear/supralinear dose response, (ii) the dependence of the supralinearity on electron energy and (iii) the shape of composite glow peak 5 as a function of electron energy. In order to predict all three characteristics the simulations require the incorporation of band tail states (4) allowing semi-localized recombination from the e-only configuration.

The Kinetic Model

The conduction band/valence band model for the recombination stage is shown in Figure 1 and the differential equations describing the traffic of the charge carriers during heating are shown below. The total population of trapping centers, N_{TC2} , giving rise to peak 5, is composed of a certain fraction of trapping centers, N_{e-h} , which are spatially correlated/coupled to the luminescent centers, It is these trapping and luminescent centers, in close proximity to one another, which when populated by an e-h can give rise to geminate recombination. The remaining fraction of the TCs is denoted by N_e .

Following irradiation, the ratio, n_{e-h}/n_e , of the density of e-h to e-only populated TC/LC complexes is given by:

$$n_{e-h} / n_e = a \times (1 - e^{\beta_{e-h} \times D}) + b \quad (1)$$

The combined densities must, of course, yield the total density of occupied TCs as given

$$n_{e-h} + n_e = n_{tot} = N_{TC2} \times (1 - e^{\beta_{TC2} \times D}) \quad (2)$$

The parameters a, b and β_{e-h} are assumed to depend on photon/electron energy. Further information is given in ref 1 concerning the differential equations governing the transport of charge carriers in the irradiation

stage and the final values of the parameters. The dose filling constant, β_{TC2} , of the 4 eV OA band associated with glow peak5 has been measured experimentally. It is important to point out that the value of N_{e-h}/N_{TC2} chosen in the irradiation stage must be consistent with the calculated population densities, n_{e-h} and n_e at saturation (full population) as given by equation 3 below. It follows therefore, of course, that m_{e-h} is equal to n_{e-h} .

$$\frac{N_{e-h}}{N_{TC2}} \approx \frac{n_{e-h}}{n_e} \rightarrow D > 10^3 [\text{Gy}] \quad (3)$$

The irradiation stage parameters were constrained to yield the experimentally observed dose filling rates of the 4 eV optical absorption (OA) and 5.45 eV OA bands which are the major OA bands associated with the TL mechanism of composite peak 5.

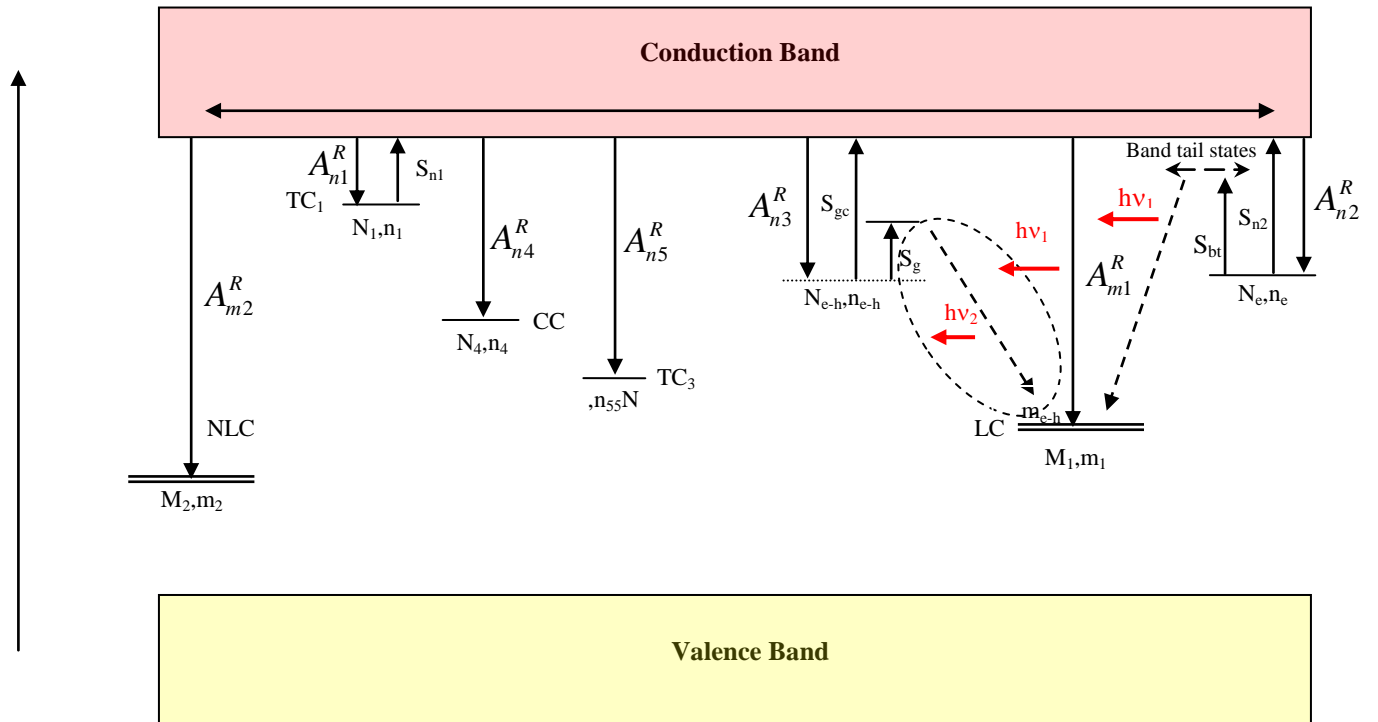


Figure 1. The conduction band/valence band kinetic model in the recombination stage.

The differential equations governing the traffic of charge carriers in the recombination stage are shown below.

$$\frac{dm_1}{dt} = -A_{m1}^R \cdot m_1 \cdot n_c - n_{e-h} \cdot S_g \cdot e^{-\frac{E_g}{kT}} - n_e \cdot S_{bt} \cdot e^{-\frac{E_{bt}}{kT}} \quad (4)$$

$$\frac{dm_2}{dt} = -A_{m2}^R \cdot m_2 \cdot n_c \quad (5)$$

$$\frac{dn_1}{dt} = -n_1 \cdot S_{n1} \cdot e^{-\frac{E_{LT}}{kT}} + A_{n1}^R \cdot (N_1 - n_1) \cdot n_c \quad (6)$$

$$\frac{dn_e}{dt} = -n_e \cdot S_{n2} \cdot e^{-\frac{E_{TC}}{kT}} - n_e \cdot S_{bt} \cdot e^{-\frac{E_{bt}}{kT}} + A_{n2}^R \cdot (N_e - n_e) \cdot n_c \quad (7)$$

$$\frac{dn_{e-h}}{dt} = -n_{e-h} \cdot S_g \cdot e^{-\frac{E_g}{kT}} - n_{e-h} \cdot S_{gc} \cdot e^{-\frac{E_{gc}}{kT}} + A_{n3}^R \cdot (N_{e-h} - n_{e-h}) \cdot n_c \quad (8)$$

$$\frac{dn_4}{dt} = A_{n4}^R \cdot (N_4 - n_4) \cdot n_c \quad (9)$$

$$\frac{dn_5}{dt} = A_{n5}^R \cdot (N_5 - n_5) \cdot n_c \quad (10)$$

$$\frac{dn_c}{dt} = n_1 \cdot S_{n1} \cdot e^{-\frac{E_{IT}}{kT}} + n_e \cdot S_{n2} \cdot e^{-\frac{E_{IC}}{kT}} + n_{e-h} \cdot S_{gc} \cdot e^{-\frac{E_{gc}}{kT}} - n_c \cdot [A_{m1}^R \cdot m_1 + A_{m2}^R \cdot m_2 + A_{n1}^R \cdot (N_1 - n_1) + (11) \\ + A_{n2}^R \cdot (N_e - n_e) + A_{n3}^R \cdot (N_{e-h} - n_{e-h}) + A_{n4}^R \cdot (N_4 - n_4) + A_{n5}^R \cdot (N_5 - n_5)]$$

RESULTS

The results of the simulations are shown in Figure 2 3 and 4. Figure 2 shows the theoretically simulated values of $f(D)$ for 8 keV and 500 keV electron energies respectively. Figure 3 shows the value of n_{e-h}/n_e as a function of dose chosen to yield normalized dose response with $f(D)_{\max} = 1.8$ and 3.3 corresponding to electron/gamma irradiation energies of 8 keV and greater than ~ 100 keV respectively. The low dose value of $n_{e-h}/n_e = 0.2$ for 8 keV photons compared to ~ 0.1 for the higher energy photons is consistent with increased ionization density with decreasing energy. The values of n_{e-h}/n_e begin to increase at a dose level of ~ 10 Gy corresponding to the onset of supralinearity in the dose response of peak 5 and reach saturation values of ~ 0.4 - 0.5 at dose levels in excess of 10^3 Gy. Figure 4 shows the theoretically simulated dose response of the ratio of peak 5a/5 measured following irradiation with $^{90}\text{Sr}/^{90}\text{Y}$ beta rays of ~ 500 keV average energy. The over-all agreement with the experimental data is good although the 5a/5 ratio is over-estimated at the highest levels of dose. The theoretically simulated 5a/5 ratio at 8 keV is $\sim 20\%$ greater than at 500 keV and this difference is maintained for the two electron energies until their values merge at high levels of dose (10^4 Gy). Confirmation of this behaviour requires dose response measurements at 8 keV which are being planned.

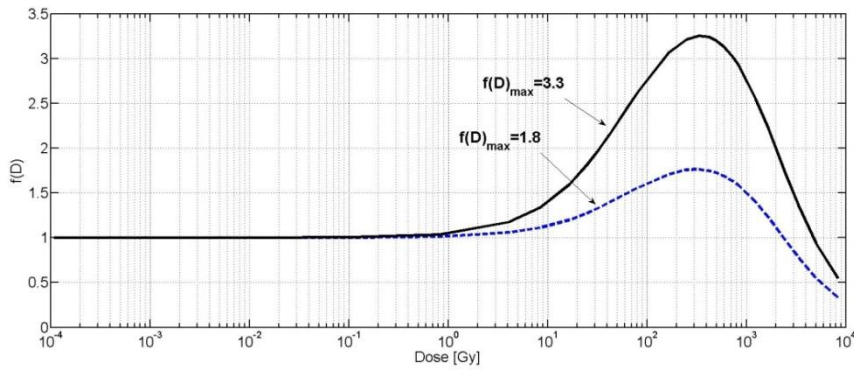


Figure 2. The theoretically simulated values of $f(D)$ for 8 keV and 500 keV electron energies respectively.

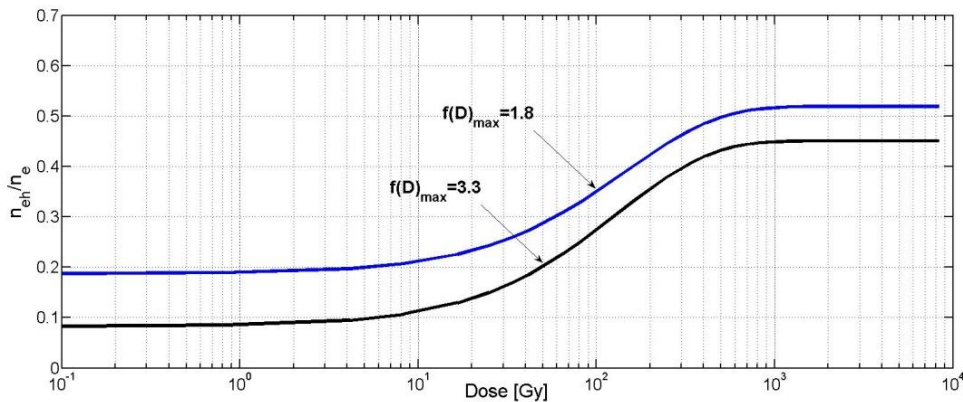


Figure 3. The values of n_{e-h}/n_e as a function of dose for two irradiation energies of 8 keV and 500 keV leading to maximum values of the supralinearity $f(D)_{\max}$ of 1.8 and 3.3 respectively.

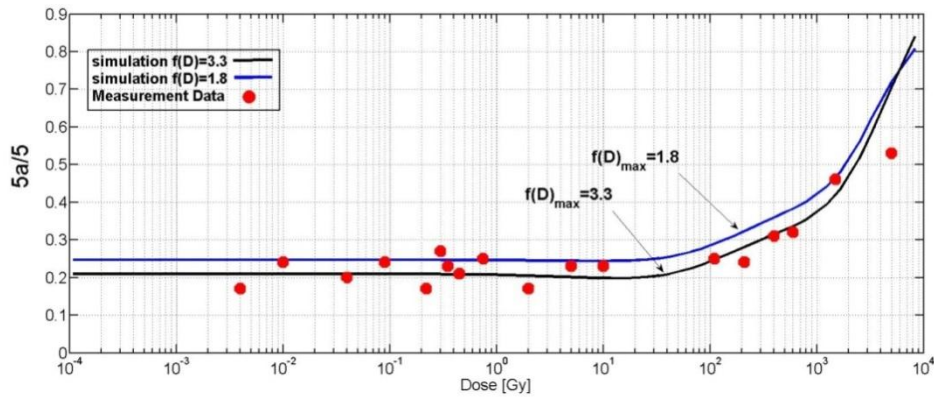


Figure 4. Comparison the the theoretically simulated values of $5a/5$ as a function of dose with the experimentally measured values.

CONCLUSIONS

A kinetic model including both localized and delocalized recombination has been developed which is capable of simulating the dependence of the ratio of the intensity of peak 5a to peak 5 as a function of dose as well as simulating the behaviour of the dose response supralinearity as a function of photon energy.

REFERENCES

1. Eliyahu, I., Horowitz, Y.S., Oster, L., and Mardor, I., A kinetic model incorporating both localized and delocalized recombination: Application to the dependence of the TL dose response on photon energy, *J. Lumin.*, 145 (2014) 600-607.
2. Chen, R and Pagonis, V., *Thermally and optically stimulated luminescence: A Simulation approach*, Wiley, 2011.
3. Horowitz, Y., Fuks, E., Datz, H., Oster, L., Livingstone, J. and Rosenfeld, A., Mysteries of LiF TLD response following high ionization density density irradiation: glow curve shapes, dose response, the unified interaction model and modified track structure theory, *Radiat. Meas.*, 46 (2011) 1342-1348.
4. Li Bo and Li S-H, The effect of band-tail states on the thermal stability of the infra-red stimulated luminescence from K-feldspar, *J. Lumin.*, 136 (2013) 5-10.

Dosimetry (Wednesday, February 12, 2014 16:30)

Characterization of Soreq Whole Body Counter

O. Aviv, E. Daniely, S. Moskovici, Z. Yungrais, H. Datz, Y. Shamai, G. Haquin

Soreq Nuclear Research Center, Yavne 81800, Israel

INTRODUCTION

The Whole Body Counting (WBC) technique is a widely used technique for the determination of the intake of radionuclides emitting X-rays or gamma-rays. Internal contamination might have been caused by inhalation, ingestion, injection, or insertion through wounds of radionuclides. Information about the intake, chemical composition and exposure pathway, serves as input for committed dose assessment. For the majority of radionuclides, WBC is complementary to other dosimetric methods such as the personal dosimeter and urine sample analysis. The major advantage of in-vivo measurement is the rapidity and direct assessment of the level of contamination in the body. Determination of the system counting efficiency is usually performed either by realistic ⁽¹⁾ or computerized (voxel) phantoms ⁽²⁾. Realistic phantoms can be comprised of calibrated amount of radionuclides embedded in surrogate organs having similar density and volume as organs in the human body. The minimal detectable activity per nuclide depends on the efficiency, background counts and measurement time.

In this paper we characterize the WBC system at the Soreq Nuclear Research Centre (SNRC) ⁽³⁾. A study was performed testing the response of the WBC to a Lawrence Livermore torso lung phantom. Minimum detection activities (MDA) of selected nuclides were calculated for several configurations of the system and are presented in this work.

MATERIALS AND METHODS

The system consists of four HPGe detectors (Model GEM-FX8530, ORTEC), each with relative efficiency of ~50% and resolution of up to ~1.9 keV for 1332.5 keV gamma energy of ⁶⁰Co. The experimental system is shown in Figure 1 with and without a torso phantom. Two detectors are located above and two detectors are located below a movable bed. The height of the top detectors can be modified by motorized movement, depending on the subject dimensions. The used energy range in whole body counting is 12-3000 keV, covering the low energy (X-rays) and up to high energy gamma rays. The signal from each detector is fed through a spectroscopy amplifier (Model 672, ORTEC) into a MCA (model ASPEC927, ORTEC) and then to PC via USB. Data acquisition and analysis as well as the bed positioning, are performed by the software Renaissance32 (both individually as well as grouped detectors). The software allows the summation of spectra and follow-up analysis in terms of peak identification, quantification of nuclide activity and MDA calculations. The total count rate is displayed continuously throughout the measurement which allows for rough indication of the contamination along the body. The software also offers data management capabilities such as subject database which includes personal data (ID, height, weight, etc.) linked to the acquired spectra. Records of routine quality control of the four detectors in terms of efficiency, resolution, energy calibration and background count rate are stored into files and can be displayed on demand. Each pair of detectors is surrounded by 8.5 cm of old lead (2.8 Bq/kg) in a ∞ like shaped and for the lower detectors cave, a lead lining (50 mm x 700 mm x 700 mm) was constructed. In addition, two lead walls (10 cm X 100 cm X 200 cm) are located in both sides of the bed. The bottom part of the bed is made from 5 mm of wood to support a 50mm mattress both with low attenuation material.

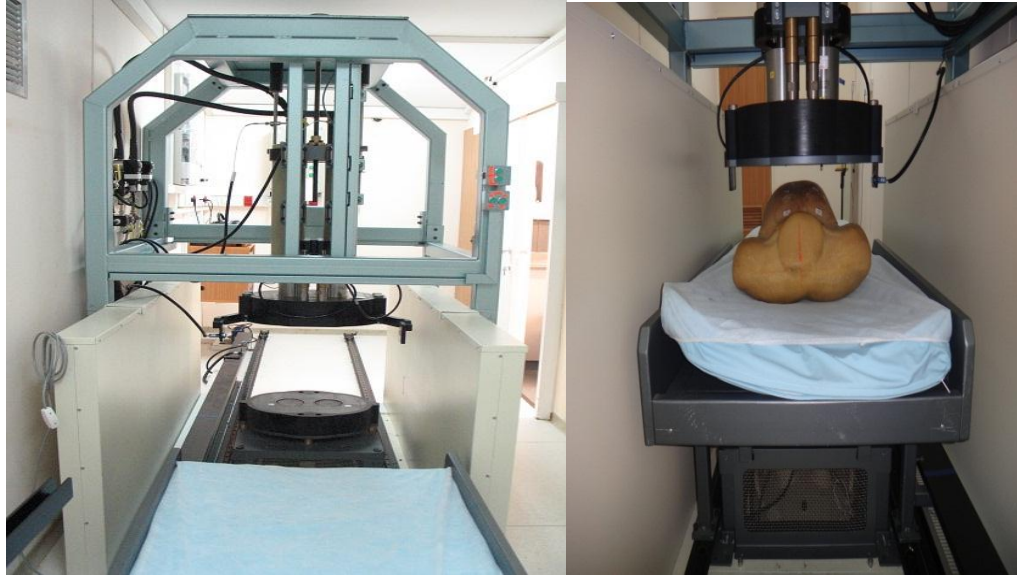


Figure 17: Whole Body Counter at Soreq NRC with (left) and without (right) torso phantom..

WBC SYSTEM CHARACTERIZATION

The WBC system exhibits an average count rate of 50 counts/sec for the sum of the four HPGe detectors in the energy range of 12-3000 keV. Table 1 summarizes the count rate in the region of interest for some of the dominant nuclides observed in the background spectrum. The MDA following Curie formulation ⁽³⁾ was determined from the contribution of background counts in the region-of-interest (which in turn depends on the detectors' resolution) as well as the efficiency measured by a realistic Lung phantom ⁽⁵⁾ embedded with ¹⁵²Eu having chest thickness of ~2 cm. MDA calculations were performed for several configurations with a moving bed (Figure 1) for a group of detectors. Figure 2 shows the full-width-half-maximum (FWHM) of the sum of the four detectors which was done with a set of reference sources. The efficiency curve for the sum of the four detectors is presented in Figure 2 together with a polynomial fit.

Table 3: Background total count rates in the region of interest (ROI) for selected nuclides for the grouped detectors in SNRC WBC system.

Nuclide	Energy [keV]	Count rate in ROI [counts/sec]
^{212/214} Pb	74.8	1.030
²²⁶ Ra	186.1	0.055
²¹⁴ Pb	351.9	0.246
²⁰⁸ Tl	583.2	0.689
²¹⁴ Bi	609.3	0.035
²¹⁴ Bi	1120.3	0.050
⁴⁰ K	1460.8	0.133
²⁰⁸ Tl	2614.5	0.045

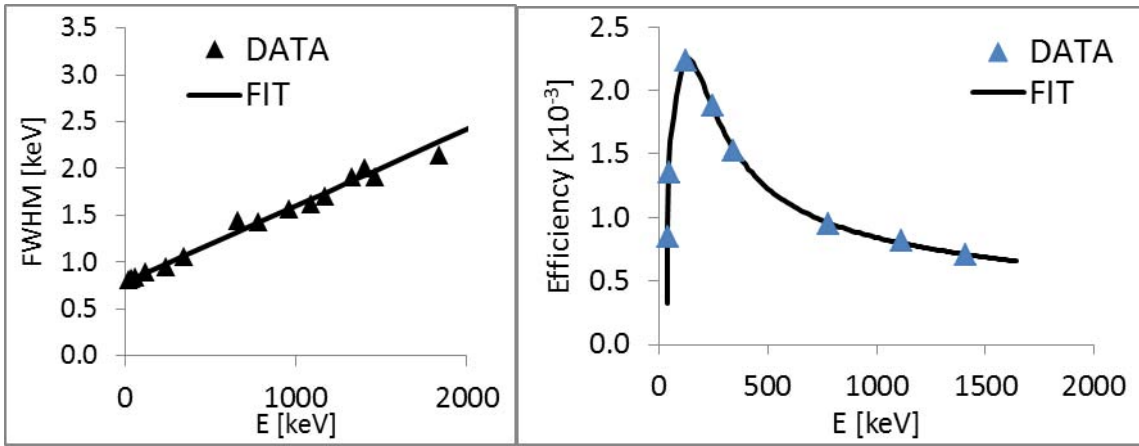


Figure 18: Peak FWHM of grouped spectra versus gamma energy (Left) and grouped detection efficiency from lung torso (Right).

The MDAs for ¹³⁷Cs and ²⁴¹Am for several configurations of grouped detectors (2 above and 2 below, 2 above 1 below and so on) is shown in Figure 3, assuming a common measurement live time of 1850 seconds. The lowest MDA was achieved for ¹³⁷Cs (29 Bq) with the four detectors and for ²⁴¹Am (71 Bq) with the two upper detectors. For ¹³⁷Cs the MDA improves with increasing number of detectors. The strong variations in the MDA for ²⁴¹Am for the different detector configurations is explained by the trade-off between the overall detection efficiency (source-detector distance and attenuation by the wooden bed) and the contributions of background counts among the different groups of detectors in the region of interest. Thus, it is recommended to operate the upper detectors only when performing whole body counting for ²⁴¹Am in the lungs.

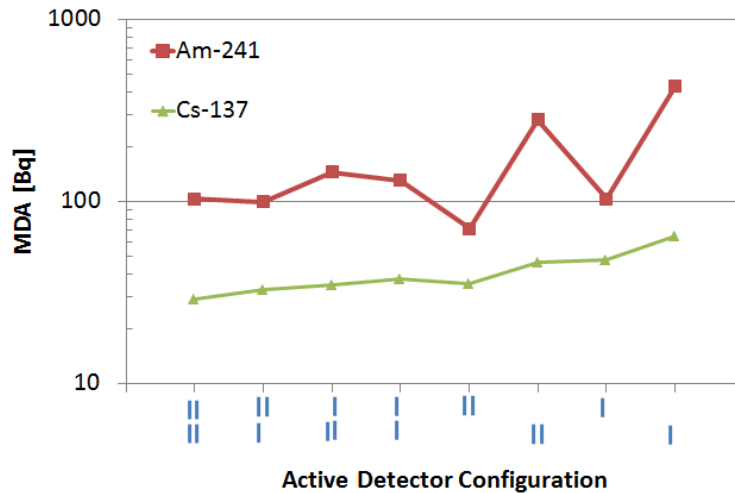


Figure 19: Calculated MDA for several nuclides in the Lungs for several detection configurations. Measurement duration was 1850 seconds for all configurations.

The measured values for the MDA are relatively similar in size compared to other similar systems ^(1, 6). An extensive study is underway with the aim of characterizing SNRC system efficiency to various voxel phantom geometries and sizes through Monte-Carlo simulations using GEANT4 and FLUKA.

ACKNOWLEDGMENTS

The authors thank Shimon Tsroya and Omer Pelled from NRCN for helpful discussions and advices.

REFERENCES

1. T. Ishikawa, "Performance of a whole-body counter with five high purity germanium detectors". Appl. Radiat. Isot. **64**, p. 386-389 (2006).

2. J. Atanackovic, G.H. Kramer, M. Hugue, "*Monte Carlo model of HPGe detectors used in routine lung counting*". Appl. Radiat. Isot. **79**, p. 94-102 (2013).
3. G. Haquin, H. Datz, T. Riemer, Z. Yungrais, Y. Ben-Hemo, D. Katz, E. Sayag and D. Rendlich. "*A New High-Purity Germanium based Whole Body Counter for Internal Dose Assessments at Soreq Nuclear Research Center*". 26th Conference of the Nuclear Societies in Israel (2012).
4. Currie, L.A. Limits for Qualitative Detection and Quantitative Determination. Anal. Chem. 40,586-593, 1968
5. O. Pelled, S. Tsroya, U. German, G. Haquin, Z.B. Alfassi, "Locating a hot spot in the lungs when using an array of four HPGe detectors". Appl. Radiat. Isot. 61, p. 107-111 (2004).
6. G.H. Kramer, R.M. Loesch and P.C. Olsen, "*The 1993 Intercomparison of the measurement of in-vivo radioactivity*". Radiat. Prot. Dosim. **86**, p. 197-205 (1999).

Dosimetry (Wednesday, February 12, 2014 16:30)

Comparison Study of the Response of Several Passive PDA Based Personal Dosimeter to Gamma and X-Ray Radiation

S. Cohen¹, A. Abraham¹, O. Pelled¹, Y. Tubul¹, E. Kresner², A. Ashkenazi³ and I. Yaar¹

¹*Nuclear Research Center-Negev, POB 9001, Beer-Sheva 84190, Israel*

²*Chief Scientist for CBRN defense, MOD, Tel Aviv, Israel*

³*Asaf Ashkenazi LTD, Tel Aviv, Israel*

INTRODUCTION

In the case of a radiological terror event or a nuclear accident, there is a need to perform a fast and reliable personal dosimetry measurements for first responders and other intervention forces. The dosimeters should be (i) simple, instant and cumulative readout (ii) small and lightweight (iii) energy independent (iv) wide dose range (v) withstand intense environments (vi) cheap, and disposable. In the last decade, two simple dosimeters were presented for radiological emergencies (i) self-indicating radiation alert dosimeters (SIRAD) and (ii) RADview by J.P Labs⁽¹⁾ and M/s RADeCO⁽²⁾, respectively. Both dosimeters contain radio-chromic films based on PDA (poly-di-acetylene) material that change the colors in their active window as a function of radiation dose⁽³⁾.

In the current study, the dose response of SIRAD and RADview personal dosimeters to ¹³⁷Cs and M150 X-Ray radiation at the range of 0.01-11 Sv is presented. In addition, the environmental, fading effects and usage effects on the response of these dosimeters is evaluated.

MATERIALS AND METHODS

Three types of dosimeters in two configurations (credit card\badge and stamp size) were irradiated by ¹³⁷Cs and M150 X-ray sources, according to category I (photons, accidents) of the ANSI/HPS N13.11-2009 standard⁽⁴⁾. All three types of dosimeters were mounted on a poly-methyl methacrylate (PMMA) phantom surface facing the central ray of the radiation sources at a distance of at least 1 m. Five dosimeters of each configuration type were exposed to gamma and X-Ray radiation doses in the range of 0.01-11 Sv. In addition, the angular response of each dosimeter to radiation was evaluated at 40°, 60° and 180° degrees for exposure of 1 Sv. At the end of each irradiation, both SIRAD and RADVview dosimeters were scanned by a CANON 5600F scanner and MP Navigator Ex software. The scanned images were evaluated by an image processing software in order to analyze the RGB color values of the active material as a function of radiation dose.

Visual Readout Test

A visual estimation of the readout of delivered dose to the radiochromic films was performed by 16 employees of NRCN working as first responders and radiation supervisors. The visual readout test used 36 dosimeters irradiated to doses ranging from 0 to 11 Sv. Each participant was given instruction to evaluate if the dosimeter has been exposed and to estimate the absorbed dose.

Fading Effect

Dosimeters were measured at different time intervals after irradiation to different doses (0.1, 0.5 and 1 Sv) in order to determine the fading (time dependence of the readout after exposure) effect on the RGB color (dose) readout. The dosimeters were evaluated each day for a period of one month. In addition, dosimeters reading were also taken at the end of each month for a period of one year.

Environmental and Usage

Environmental and usage condition were performed in order to verify the manufactures specifications

and test the dosimeters performance at extreme conditions. Three dosimeters of each type were exposed to temperatures ranging from 20 to 100 °C and relative humidity of 30%-90% at 40 °C for one hour. In addition, the color change of the dosimeters were evaluated after UV exposure (1-24h), laundry cycle and applied stress ranging from 1 to 4 Tons.

RESULTS AND DISCUSSION

The red and green color intensity for all three types of dosimeters after exposure to ^{137}Cs radiation source as a function of absorbed dose are presented in Fig 1 and Fig. 2. For all three types of dosimeters, the change of the blue color absolute intensity was small (compared to the red and green) and therefore found impractical for dose calculation (this result is not presented in the current work).

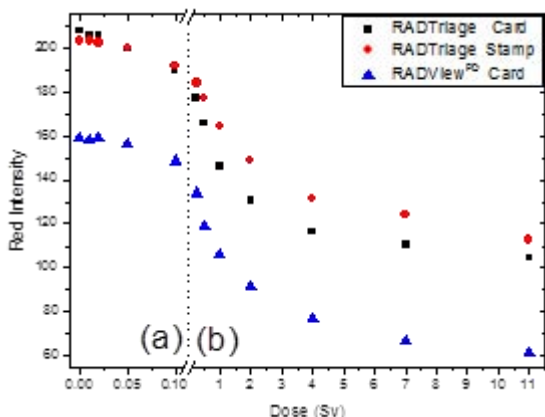


Figure 1. Red color Intensity vs. Absorbed Dose of RADTriage and RADview Dosimeters

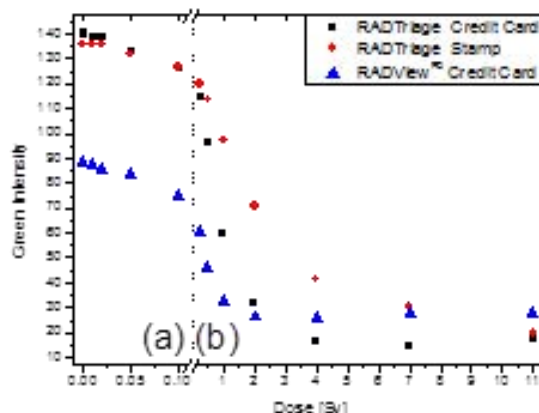


Figure 2. Green Color Intensity vs. Absorbed Dose of Radtriage and RADview Dosimeters

For low doses (up to 0.05 Sv) the change of the green and red color intensity (area (a) in Fig. 1 and 2) on all dosimeters is negligible. In addition, all the PDA materials have completely reacted at doses above 4 Sv (area (b) in Fig. 1 and 2). The red and green intensity decreases significantly above 0.1 Sv, with increasing dose (area (b) in Fig. 1 and 2) for all dosimeters. However, the absolute and the gradient of the color intensity measured in each dosimeter type is different.

The change in the red intensity of RT card is higher for the high dose range and therefore will be more appropriate for accurate dose estimation.

The relative standard deviations for green and red intensities were up to 10% and 40% for blue intensity. The corresponding X-Ray beam experiments (this result is not presented here) show similar curve behavior results for all colors and dosimeters. However, RV card and ST stamps green and red intensities were lower compared to results obtained after exposure to the ^{137}Cs source radiation. This is probably due to energy dependence of this two dosimeters. Yet, the RT card didn't reveal any energy dependence and X-ray RGB intensity results were with good agreement with the ^{137}Cs RGB results.

Angular dependence test didn't indicate on any change of the dose response for all three dosimeters types at 40° and 60° degrees. At 180° degree, after 1 Sv radiation exposure, the dose is attenuated by ~50% compared to 0° due to the radiation absorbance by the phantom. In conclusion, all three dosimeters were found to be appropriate for accurate dose estimation by image processing tools for doses in the range of 0.1-4 Sv according to the red and green intensities. The RV card was found more sensitive to dose change then the red intensity analysis while the RV and ST cards are more sensitive to change in the green intensity. The RT card has the most sensitive film to dose changes (for the green intensity) and has no energy dependence.

Visual Readout Test

Visual dose for RT and RV cards were performed by NRCN first responders and radiation supervisors as a function of delivered dose. The results showed large variation of the visual dose estimation compared to the 20% error declared by both manufactures; but this error decreases with increasing dose.

All of the subjects were able to identify exposure for doses above 0.1 Sv, similar to the RGB analysis results. ST stamps visual test results (not presented here) were similar to the RT and RV cards, but the first responders were able to identify only radiation exposure above 0.25 Sv.

Fading Effect

The relative change in the green and red intensity for all dosimeters after 0.5 Sv and 1 Sv exposure, as function of time are presented at Figs. 3 and 4, respectively.

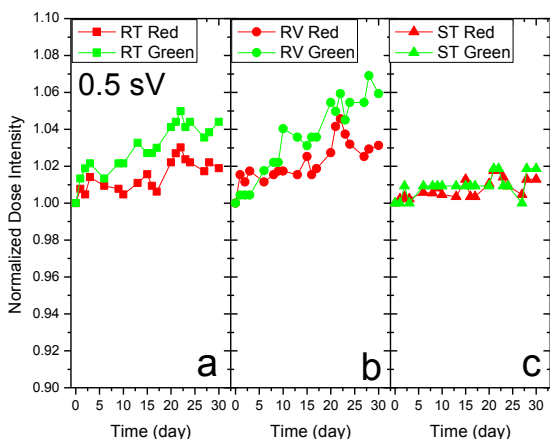


Figure 3. Daily Fading Effect of (a) RT card

(b) RV card (c) ST stamp

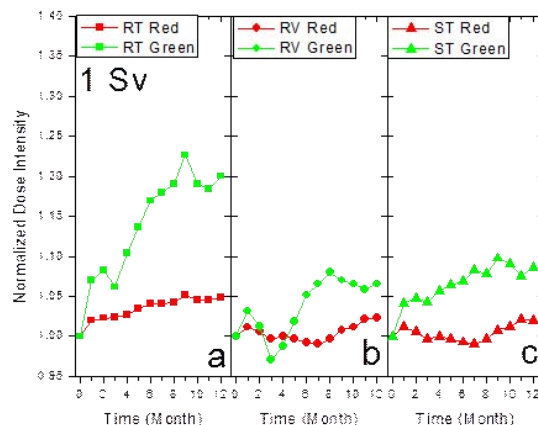


Figure 4. Monthly Fading Effect of (a) RT card

(b) RV card (c) ST stamp

For all three dosimeters types there is a fading effect (darkening) within a month from the radiation exposure (Fig 3) due to continuation of the polymerization reaction. It seems that the fading effect of the green color intensity is larger compared to the fading effect of the red intensity due to its higher sensitivity to radiation exposure. RT (Fig. 3a) and RV (Fig. 3b) radio-chromic films exhibited an average color increase of 3% after five days, while no significant color change was observed for the ST stamps (Fig. 3c) up to 20 days later. At the end of the first month, the RV cards had the highest darkening effect. However, for all dosimeters this post-irradiation colorations is less than 10% after 30 days and therefore does not alter significantly the accuracy of the dose readings.

The general trend of the green intensity fading effect continues for all PDA films up to one year post irradiation time (Fig. 4). Both RT and ST dosimeters (Figs. 4a and 4c) present a steady red color intensity (~5% darkening) but the green coloration increases up to 10% and 23% for the ST and the RT dosimeters, respectively. In contrast to the other two dosimeters, the RV card (Fig. 3b) show a somewhat different time dependent behavior with initially decrease in the color intensity (up to 6 month post irradiation) and later both RV colors intensities increase with time. It is therefore concluded that for all PDA's a fading effect dose correction after one month is needed in order to estimate accurate absorbed dose. The red color intensity is less sensitivities to fading effects and therefore is more adequate for accurate dose calculation after long time periods.

Environmental and Usage

The environmental tests aimed to assess the dosimeter performance under wide range of environmental conditions and extreme usage. Relative dose response of all three dosimeter types after 0.5 Sv exposure as a function of temperature and relative humidity at 40 °C is presented in Figures 5 and 6.

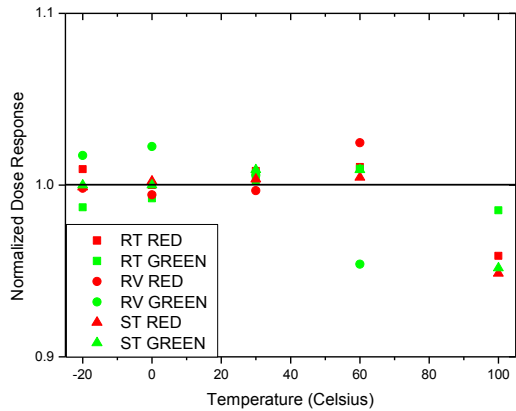


Figure 5. Relative Dose Response vs. Temperature for RT, RV and ST dosimeters

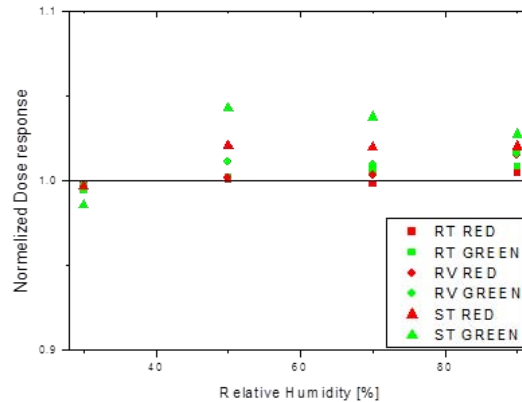


Figure 6. Relative Dose Response vs. Relative Humidity for RT, RV and ST dosimeters

Analysis of the normalized green and red intensity at the temperature range of 20-60 °C after 0.5 Sv exposure (Fig.5) do not show any change from the target value and it is within the statistical error (up to 4%). After exposure to 100 °C for 1 hour the efficiency decreases by more than 5% for all dosimeters types. Both manufactures stated that the dosimeters can withstand temperatures of up to 60 °C, and therefore all of these dosimeters are still compliant within their specification. Relative humidity tests after 0.5 Sv exposure (Fig. 6) didn't reveal any measurable change compared to the expected dose and therefore are with accordance within the manufactures specifications.

The influence of extreme usage that the first responders might encounter was estimated by exposing the dosimeters to UV light, applied mechanical pressure and laundry cycle. No coloration were identified after 24 H exposure to UV-C light. This result is due to a UV light protective filter that cover the dosimeter. However, it is important to note that both manufactures state that the dosimeters do react after long UV light exposure. Applying pressures of 1-4 tons for one min and then exposing the dosimeters to 0.5 Sv didn't exhibit any change in the dose response. This result is consistent with the manufactures statement that the dosimeters can withstand falling and heavy loads. However, after one laundry cycle in all three dosimeters water penetration into the active matrix was observed, causing the green and red color intensity to decrease by up to 10% even before exposure. After exposure to 0.5 Sv, dosimeters showed variations of 10-37% lower compared to the expected dose.

CONCLUSIONS

The physical response of RADview and SIRAD personal dosimeters to gamma and X-Ray radiation was measured according to the ANSI/HPS N13.11-2009 standard⁴. It has been found that all three dosimeters can determine accurate dose measurements in the 0.1-4 Sv dose range by image processing analysis of the red and green color intensity. Visual readout tests indicated that first responders can identify doses above 0.1 Sv. Fading experiments show a coloration increase of up to 20% but by the red color analysis, and an accurate dose estimation of 6% can be achieved. Environmental and usage tests indicate that the dosimeters performance is compliant with manufacturer specification (temperature, relative humidity, etc) except for the laundry cycle experiments.

REFERENCES

1. M/s J P Lab USA, Technical Specifications, <http://jplabs.com/> (Last accessed at 10/1/14).
2. RADeCo USA, Technical Specifications, http://www.radecohealth.com/index.php?option=com_content&view=article&id=8&Itemid=11 (Last accessed at 10/1/14).
3. S.G. Vajapurkar and A. Bera, Present status of radiochromic techniques for nuclear radiation measurements, Indian J. of Pure & Applied Physics, **48**, p.830-836, (2010).
4. American National Standards Institute, Personnel dosimetry performance – criteria for testing, ANSI/HPS N13.11-2009.

Posters (Thursday, February 13, 2014 14:00)

Suitability of Israeli Household Salt for Retrospective Dosimetry

H. Datz¹, S. Druzhyna², L. Oster³, I. Orion², I. Darras²,
D. Hershkovich¹ and Y. Horowitz²

¹ *Soreq Nuclear Research Center, Yavne, Israel*

² *Ben-Gurion University of the Negev, Beer-Sheva, Israel*

³ *Sami Shamoon College of Engineering, Beer-Sheva, Israel*

INTRODUCTION

Following a nuclear accident or a terror attack involving the dispersal of radioactive material, radiation dose assessment to first responders and the members of the public is essential. This information may be used by medical personnel to decide whether to refer the exposed individual for medical treatment or not. Few people, if any, will be wearing standard dosimeters at the exposure scene, so the need for a retrospective assessment of the radiation dose is an acute necessity.

Previously developed methods for retrospective dosimetry (RD) have suggested various types of materials such as tiles, bricks, CDs, electronic components, mobile phones, electron paramagnetic resonance of tooth enamel, hair, nails, biological dosimetry techniques etc^(1,2,3). These techniques involve significant disadvantages such as: (i) the long time required to prepare the samples for measurement (ii) the considerable expense of the measuring equipment, (iii) invasive procedure and others. The need for an RD technique which will be fast, inexpensive, reliable, non-invasive and, if possible, portable, remains an on-going challenge.

The ideal retrospective dosimeter must fulfill the following basic criteria:

- a) Availability in the contaminated area,
- b) Adequate dose measurement capability in the relevant range of dose levels,
- c) Negligible or known fading between exposure and measurement.

OBJECTIVES AND METHODOLOGY

The present study examines the potential use of Israeli household salt as a retrospective dosimeter. Salt is readily available and sensitive to ionizing radiation^(4,5,6) and inexpensive.

The experiments were carried out on Israeli salt samples following Nielsen market track survey based on scanning data representing the barcoded market, including organized and independent retail chains and a sample of private minimarkets and supermarkets. The data is representative of the entire Jewish population of Israel.

The dosimetric technique used was thermoluminescence (TL) dosimetry. TL is a well-known phenomenon in crystalline solids, in which the TL is the luminescence emitted from an irradiated sample during exposure to heat. The emitted TL signal is dependent on the dose absorbed by the sample following exposure. The TL measurements used a Thermo 3500 manual reader. Samples were read-out in a high purity N₂ atmosphere from 50°C to 350°C with a linear heating rate of 1°Cs⁻¹. Each salt sample was dispensed into a stainless steel cupel (~ 0.3 mm thick), weighed before measurement, and exposed to a dose levels from 1 mGy to 300 Gy at the Israeli Secondary Standard Dosimetry Laboratory of the Soreq Nuclear Research Center using a calibrated ¹³⁷Cs source.

RESULTS

Household salt market in Israel: In 2012, ~10,200 tons of household salts were sold in Israel. As listed in Table 1, the 4 and 10 bestselling salts constitute 76% and 92% of the total market respectively. This information is useful to assess the feasibility for RD, since it allows focusing the investigation on a limited range of types of common salt.

Table 1: Israeli Household salt market survey for 2012

Brand name	Lab name	Quantitative sold [ton]	Market share [%]
Salit - Finest table salt (1 kg pack)	A	3,512	34
Sugat - Fine table salt (1 kg pack)	B	2,128	21
Shufersal - Table salt (1 kg pack)	C	1,075	11
Salit - Table salt (1 kg pack)	D	1,025	10
Sugat - Crude table salt (1 kg pack)	E	534	5
Shufersal - Crude salt (1 kg pack)	F	395	4
Salt of The Earth - Red sea salt (500 gr shaker pack)	G	378	4
Salt of The Earth - Dry sea salt (1 kg pack)	H	303	3
Sugat - Iodine enriched sea salt (250 gr pack)	K	3.8	0.04
Remainders		840	8
Total		10,194	100

Sensitivity: The glow curves following irradiation and readout of the Israeli salt samples to a dose level of 0.3 Gy using a ^{137}Cs gamma ray source are shown in Fig. 1. The significant TL sensitivity demonstrates that dose measurement in all the brands of salts with 10% (1 SD) precision is possible in the relevant range of doses. The glow curve consists of 3 main glow peaks, with the dominant peak at $\sim 220^\circ\text{C}$.

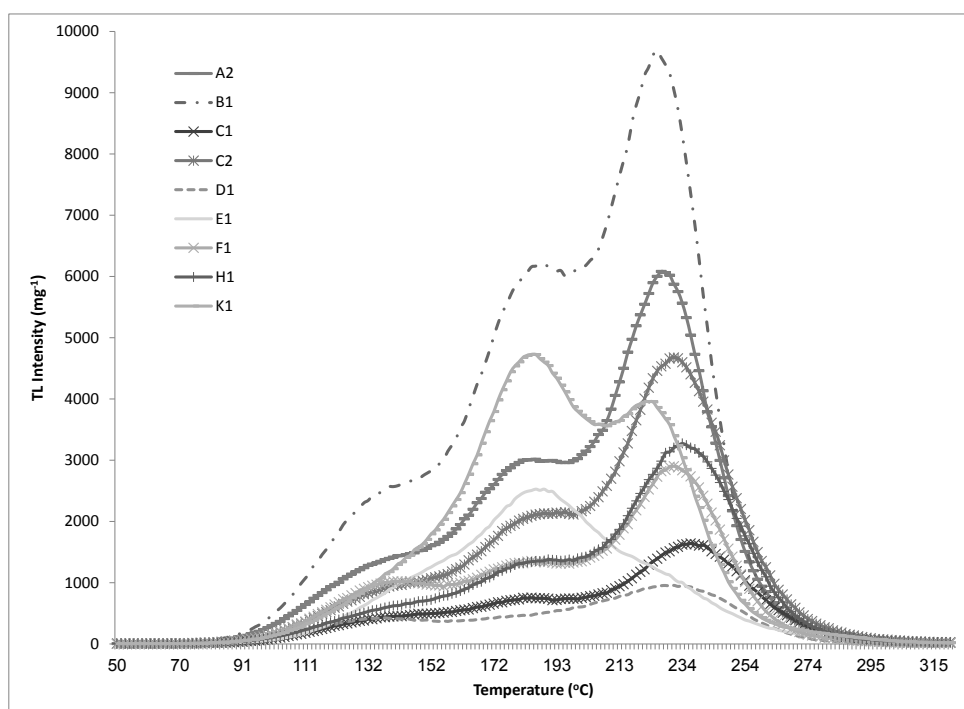


Figure 1 - TL glow curves of gamma irradiated brands of Israeli household salt. Dose: 0.3 Gy; heating rate: 1°C s^{-1}

Fading: Figure 2 demonstrates the glow curves of the Israeli best-selling household salt samples (Lab name A) versus storage time from exposure to measurement. In the interim between exposure and measurement, the samples were stored in the dark to eliminate exposure to light. The total TL intensity decreased by ~20% following readout 48 hours after exposure but remained constant thereafter up to 2 weeks following exposure.

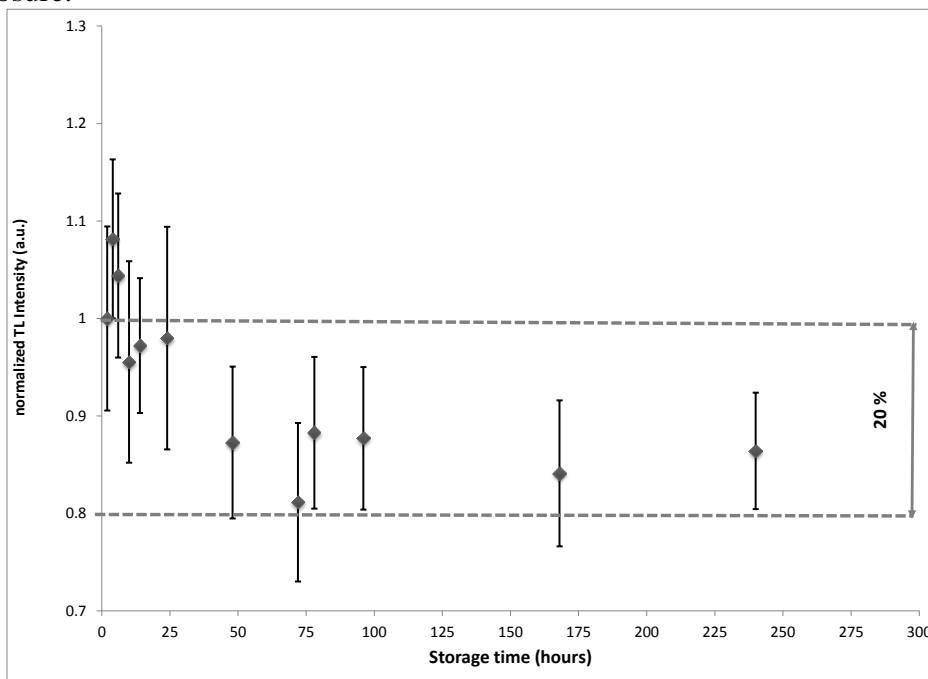


Figure 2: Fading of the TL signal normalized to initial intensity (measured 2 hours after irradiation) following storage in the dark for the best-selling Israeli household salt type A. Each point is the integral of the glow curve, averaged for 3 samples.

Figure 3 demonstrates the glow curves of sample A following storage in the dark and under normal fluorescent room lighting. During storage in the dark, readout 48 hours after exposure showed negligible fading but following 48 hours continuous exposure to room light a decrease of up to 60% of the total TL intensity was observed.

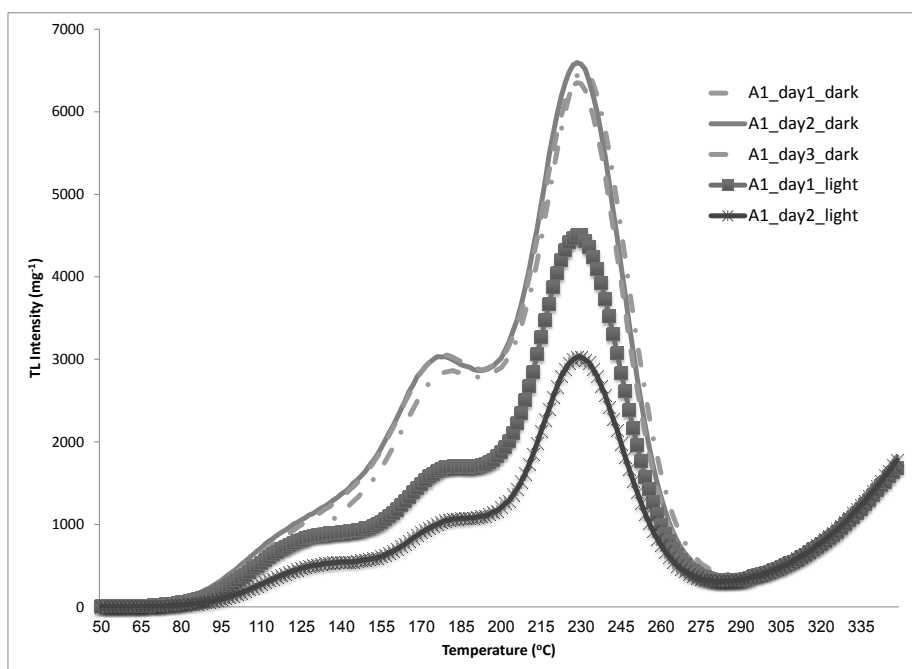


Figure 3: TL signal fading salt type A following storage in the dark and under room light.

CONCLUSIONS

The common Israeli household salts are a pragmatic potential candidate for RD. Light induced fading indicates that storage in the dark during (use of salt irradiated in packaged material) and following exposure is necessary to reduce uncertainties in the estimation of the delivered dose. Further studies are being carried out in order to evaluate the other relevant dosimetry characteristics of the salt.

ACKNOWLEDGEMENTS

This work was supported by the IAEC-UPBC Joint Research Foundation in memory of Prof. Amnon Pazi.

REFERENCES

1. Alexander, G.A., Swartz, H.M., Amundson, S.A., Blakely, W.F., Buddemeier, B., Gallez, B., Dainiak, N., Goans, R.E., Hayes, R.B., Jones, R.L., Lowry, P.C., Nosaka, M.A., Okunieff, P.G., Salner, A.L., Schauer, D., Trompier, F., Turteltaub, K.W., Voisin, P., Wiley, Jr, A.L., Wilkins, R., *BiodosEPR-2006 Meeting: Acute dosimetry consensus committee recommendations on biodosimetry applications in events involving uses of radiation by terrorists and radiation accidents*, Radiation Measurements, **42**, 972-996, (2007).
2. Haskell, E.H., *Retrospective Accident Dosimetry Using Environmental Materials*, Radiation Protection Dosimetry, **47**(1-4), 297-303, (1993).
3. Mesterházy, D., Osvay, M., Kovács, A., Kelemen, A., *Accidental and retrospective dosimetry using TL method*, Radiation Physics and Chemistry, **81** (9), 1525-1527, (2012).
4. Gartia, R.K., Arunkumar Sharma, B., Ranita, Usham, *Thermoluminescence response of some common brands of iodised salts*. Indian Journal of Engineering & Materials Sciences. **11**, 137-142 (2004).
5. Spooner, N.A., *Analysis of luminescence from common salt (NaCl) for application to retrospective dosimetry*, Radiation Measurements, **46**, 1856-1861 (2011).
6. Christiansson, M., Mattsson, S., Bernhardsson, C., Rääf, C.L., *Optimizing a Readout Protocol for Low Dose Retrospective OSL-Dosimetry Using Household Salt*, Health Physics, **102**(6), 631-636 (2012).

NORM & Environmental Radioactivity (Wednesday, February 12, 2014 16:30)

A New European COST Network 'NORM4Building' (TU1301) for the Reuse of NORM Containing Residues in Building Materials

W. Schroeyers , S. Schreurs,

University of Hasselt, Diepenbeek, Belgium

BACKGROUND

The depletion of energy resources and raw materials demands introduction of sustainability in construction sector and construction material production. In the development of new synthetic building materials the reuse of residue streams becomes a necessity.

A specific class of residues, for which building materials offer an interesting reuse option, originates from NORM (naturally occurring radioactive materials) processing industries. Existing NORM residues being studied for reuse in are among others: (i) coal fly-ash, slag and bottom ash from coal-fired power plants, (ii) phosphorous slag from thermal phosphorus production, (iii) phosphogypsum from phosphoric acid production, (iv) red-mud from alumina production, (v) unprocessed slag from primary iron production and steel or stainless steel, lead, copper and tin slags from primary and secondary production.

Current innovations in the building industry, such as the emerging field of Alkali-Activated Materials⁽¹⁻⁴⁾, can open up promising new reuse pathways for these NORM residues in building materials.

Using NORM residues in the production of new types of building materials raises concerns among authorities, public and scientists on the potential gamma exposure from building materials to occupants and on indoor air quality.

The draft of the new Euratom Basic Safety Standards directive (EU-BSS)⁽⁵⁾, expected in December 2013, specifically addresses the topic of NORM in building materials and sets the requirement of a radiological screening and further characterisation of building materials before they can be distributed on the market.

OBJECTIVES 'NORM4BUILDING' network:

The new EU sponsored COST action 'NORM4BUILDING' stimulates the collaboration of scientists, industries and regulators. The goal is to gather knowledge, experiences and technologies, to stimulate research on the reuse of residues containing enhanced concentrations of natural radionuclides, originating from NORM processing industries, in tailor-made building materials in the construction sector while considering the impact on both external gamma exposure of building occupants and indoor air quality.

By improving radiological impact assessment models⁽⁶⁾ for the reuse of NORM residues in building materials the COST Action aims to further stimulate justified uses of NORM residues in different types of newly developed building materials. Based on these models, the Action aims at investigating realistic legislative scenarios so that the authorities concerned can allow reuse pathways for NORM that can be accepted from a radioprotection and chemical point of view in concordance with the Lead Marked Initiative (LMI) and sustainable construction.

The focus of the NORM4BUILDING network is on NORM based building materials that are under research for the production of ceramics, cement, concrete, and in particular Alkali-Activated Materials.

PRACTICAL ASPECTS:

The new COST action was initiated on the 1st of January 2014 and runs for four years. COST is supported by the EU RTD Framework Program. In the presentation more information on how to participate in the network will be provided.

In the presentation the new approach and new initiatives of the NORM4BUILDING network, that has its first meeting here in the DEAD SEA Hotel on the 12-13/02/2014, will be introduced.

The NORM4Building materials network will be an open network of researchers. An Advisory Board consisting mainly from NORM processing and construction industries and relevant associations and regulators are invited to work in collaboration with the scientists that will populate the various working groups and the management committee of the new COST action.

REFERENCES

1. Bakharev, T., *Durability of geopolymer materials in sodium and magnesium sulfate solutions*, Cem. Concr. Res., 35 (6), p 1233-1246 (2005)
2. Davidovits, J., *Geopolymers - inorganic polymeric new materials*, J. Therm. Anal., 37 (8), 1633–1656 (1991)
3. Duxson, P., Provis, J.L., Lukey, G.C., van Deventer, J.S.J., *The role of inorganic polymer technology in the development of 'Green concrete'*, Cement and Concrete Research., 37 (12), 1590-1597 (2007)
4. Duxson, P., Fernández-Jiménez, A., Provis, J.L., Lukey, G.C., Palomo, A., van Deventer, J.S.J., *Geopolymer technology: The current state of the art*, J. Mater. Sci., 42 (9), 2917-2933 (2007)
5. EC (European Commission) is currently in the process of recasting five Council Directives: Basic Safety Standards Directive (96/29/Euratom); Medical Directive (97/43/Euratom); Directive on High Activity Sealed Sources (2003/122/Euratom); Directive on Outside Workers (90/641/Euratom); Directive on Public Information (89/618/Euratom) (2013)
6. Risica, S., Bolzan, C., Nuccetelli, C., *Radioactivity in building materials: room model analysis and experimental methods*, Sci. Tot. Environ., 272, 119-26 (2001)

NORM & Environmental Radioactivity (Wednesday, February 12, 2014 16:30)

Usability of Clay Mixed Red Mud as Building Material in Transdanubian (Hungary) Region

Z. Sas, J. Somlai, J. Jónás, G. Szeiler, T. Kovács

University of Pannonia, H-8200, Veszprem, Egyetem str. 10 Hungary

INTRODUCTION

The most commonly used building materials in Hungary and in numerous country of the world are the bricks, which made from clays. Due to the congenial internal structure properties of the clays these raw materials can be mixed with other materials, provides great possibility to reuse industrial by-products as additive material.

The production and inbuilt of new types of synthetic building materials based on NORM (naturally occurring radioactive materials) by-products is raising concerns among authorities, public and scientists. Several NORM residues produced in large quantity, such as: phosphogypsum (phosphate industry), red mud (aluminium processing industry), fly ash, coal slag (coal burning and steelworks) and so on are presently under investigation⁽¹⁻⁴⁾.

The aluminum manufacturing in Ajka (Hungary) started in 1943. As a result of the bauxite refining activities up to now approximately 30 Mt of red mud has been produced in Hungary, stored in reservoirs. The radionuclide content of the bauxite usually exceeds the world average in soils (WA), which entirely remains in the by-product during Bayer process. The exposure pathways in case of application of NORM residues have to be explored in order to reveal the potential risks of NORMs on residents. The gamma radiation originated from the primordial radionuclides (K-40; U-238; Th-232) and their daughter elements found in nature and in building materials as well increase the external dose of the human body. In the EU the Radiation Protection 112 (RP 112) guideline serves for classification of building material, wherein the gamma exposure is limited by I-index⁽⁵⁾.

MEASUREMENTS AND METHODS

SAMPLE COLLECTION

In this study 14 clay samples were taken, used in 9 Hungarian building material factories in Transdanubian region of the country. Furthermore five red mud samples were collected from 1-2 m depth of "IX" red mud reservoir and eighteen samples of "X" red mud reservoir of Ajka (Hungary). The location of the gathered samples are illustrated in Figure 1.

The dried and sieved samples were stored for 30 d in air-tight aluminum Marinelli beakers with volume of 600 cm³ to reach the secular equilibrium between the Ra-226 and the Rn-222. The determination of the Ra-226 activity concentration occurred via the radon progenies Pb-214 (295 keV) and Bi-214 (609 keV) by high resolution gamma ray spectrometry, using an ORTEC GMX40-76 HPGe detector with efficiency of 40 %, and an energy resolution of 1.95 keV at 1332.5 keV. The data and spectra recorded by a Tennelec PCA-MR 8196 MCA. The system was calibrated with clay reference material certified by Hungarian National Office of Measures. The sample measuring time was 80.000 s in every case.



Figure 1. Provenience of the clay samples.

RESULTS

The results of gamma-spectrometry measurements are shown in Table 1. and Table 2. In case of red mud samples the Ra-226 and Th-232 activity concentration were significantly higher than the world average (Ra-226 32 Bq/kg and Th-232 45 Bq/kg) and the K-40 contents were lower than the 420 Bq/kg world average according to UNSCEAR 2008.

The calculated I-indexes were approximately two times higher than the recommended 1.0 value.

Table 1. Ra-226, Th-232 and K-40 activity concentrations of red mud samples

Sample ID	Activity concentration [Bq/kg]						I-index
	Ra-226	±	Th-232	±	K-40	±	
Reservoir IX	348	27.8	261	31.3	55.2	50	2.48
Reservoir X	182	21.8	247	19.7	284	312	1.94

The average Ra-226 activity concentration of clay samples was 44.4 ± 7.6 Bq/kg (21.9 to 100.5 Bq/kg), the mean Th-232 40.9 ± 8.5 Bq/kg (31.8 to 48.6 Bq/kg) and the average of the K-40 content was 850 ± 98.0 Bq/kg (690 to 1127 Bq/kg). The obtained results exceed the average of the soils (UNSCEAR 2008) eleven times in case of the Ra-226 and three times in case of the Th-232, whilst the K-40 contents transcend the reference value in every samples. The obtained results are not unusual because the clay-based building materials have higher K-40 content than the world average of other soils or building materials (UNSCEAR 2008).

The I-indexes of the investigated clay samples were lower than the maximal 1.0 value in all cases. The average of them was 0.64. Due to that fact all of them can be used as building material in case of bulk amount inbuilt.

Table 2. Ra-226, Th-232 and K-40 activity concentrations of Transdanubian clay samples

Sample ID	Activity concentration [Bq/kg]						I-index
	Ra-226	±	Th-232	±	K-40	±	
BSZGY I	32.2	5.9	34.2	7.3	726	87.6	0.52
BSZGY II	54.6	8.7	47.6	9.7	1113	122	0.79
BSZGY III	37.2	7.2	31.8	7.4	689	91.0	0.51
BSZ I	105	17.4	41.9	8.7	743	86.1	0.81
BSZ II	21.9	4.2	35.5	7.5	753	87.4	0.50
SMR I	30.3	6.6	37.5	9.8	787	114.3	0.55
SMR II	29.9	5.4	38.2	8.3	852	101.1	0.57
KB	32.6	5.0	42.1	7.8	885	88.9	0.61
KSZ	37.1	6.7	48.6	10.7	731	89.5	0.61
SP	44.4	6.9	43.9	7.9	1127	118	0.74
SMB	85.4	14.8	39.4	8.6	832	101	0.76
DEVK	38.4	5.6	48.3	7.5	993	94.2	0.70
DEVS	32.4	4.9	43.1	6.8	755	72.5	0.58
TKV	40.0	7.7	40.4	10.8	907	118	0.64
Min	21.9	4.2	31.8	7.4	690	91.0	0.50
Max	105	17.4	48.6	10.7	1127	118	0.81
AVG	44.4	7.6	40.9	8.5	850	98.0	0.64

DETERMINATION OF RED MUD MIXING RATIO

In function of the radionuclide content the mixing proportion of red mud can be calculated according to I-index, recommended by RP 112 guideline. On the basis of the obtained results the maximum red mud mixing ratios were calculated (Table 3.) with all of the investigated Transdanubian clays used in building material factories.

The obtained mixing ratios allow on an average 19.5 % red mud content in the case of red mud samples originated from reservoir IX. The obtained minimum mixing proportion of red mud was 11.6 % in the case of sample “BSZ I” and the maximum was 25.2 % in the case of “BSZ II”. The average radionuclide content of the red mud sample originated from reservoir “X” allow on the average 27.6 % red mud content, which is 8 % higher than in case of reservoir “IX”. The minimal proportion was 17.1% and the maximal red mud content was 34.7 %.

Table 3. mixing ratios of red mud and Transdanubian clay samples

Clay ID	Mixing ratio [%]		Mixing ratio [%]	
	Clay	Red mud IX	Clay	Red mud X
BSZGY I	75.6	24.4	66.1	33.9
BSZGY II	87.7	12.3	81.8	18.2
BSZGY III	75.3	24.7	65.8	34.2
BSZ I	88.4	11.6	82.9	17.1
BSZ II	74.8	25.2	65.3	34.7
SMR I	76.8	23.2	67.6	32.4
SMR II	77.7	22.3	68.8	31.2
KB	79.4	20.6	70.8	29.2
KSZ	79.2	20.8	70.6	29.4
SP	85.2	14.8	78.5	21.5
SMB	86.0	14.0	79.5	20.5
DEVK	83.2	16.8	75.8	24.2
DEVS	77.7	22.3	68.8	31.2

TKV	80.4	19.6	72.1	27.9
Min	74.8	11.6	65.3	17.1
Max	88.4	25.2	82.9	34.7
AVG	80.5	19.5	72.4	27.6

CONCLUSIONS

Due to the obtained results it can be clearly stated that all of the investigated red mud samples have higher I-index than the recommended 1.0 value recommended by RP 112 guideline. The surveyed clay samples used in Transdanubian building material factories have lower I-index (on an average 0.64) than the 1.0 limit, which proves, all of them can be used as building material for bulk amount inbuilt. The maximum mixing ratios of the red mud samples and the investigated clay samples were calculated. The mixing proportions of the red mud varied between 11.6 to 34.7 %, which make the reuse of mud possible in significant amount.

ACKNOWLEDGEMENT

This work was supported by the Hungarian State and the European Union projects Grant No. TÁMOP-4.2.2.A-11/1/KONV-2012-0071 and the European Union and the State of Hungary, co-financed by the European Social Fund in the framework of TÁMOP 4.2.4. A/2-11-1-2012-0001 'National Excellence Program'

REFERENCES

1. Kovler K., Haquin G., Manasherov V., Ne'eman E., Lavi N., *Natural radionuclides in building materials available in Israel*. Build Environ, **37**, p. 531-537, (2002)
2. Nuccetelli C., *In situ gamma spectroscopy in environmental research and monitoring*. Appl Radiat Isot, **66**, p. 1615-1618, (2008)
3. Somlai J, Jobbágy V., Somlai K, Kovács J., Németh Cs., Kovács T., *Connection between radon emanation and some structural properties of coal-slag as building material*. Radiat Meas, **43**, p. 72-76, (2008)
4. Beretka J., Mathew P.J. *Natural radioactivity of Australian building materials, industrial wastes and by-products*. Health Phys, **48**, p. 87-95, (1985)
5. RP-112. *Radiological protection principles concerning the natural radioactivity of building materials*. Luxembourg, European Commission; (1999)

Air Change Rates and Radon Concentrations in Residential Protected Rooms

R. Becker¹, K.Kovler¹, G. Haquin²

¹ *Technion – Israel Institute of Technology, Haifa, 32000, Israel*

² *Soreq Nuclear Research Center, Yavne, 81800, Israel*

INTRODUCTION

According to national regulations, every Israeli dwelling must include a Residential Protected Room (RPR), which is intended for shelter against artillery threats and protection from chemical or biological gases. These rooms are multi-purpose, but must be equipped with only one window of limited size and one entrance door, both extremely airtight. The door is required to open out of the room. Another regular (inward opening and less tight) door may be added on the same frame and serve the everyday functions. The tight window cannot be replaced nor can a less tight window be added. The entire envelope (walls and slabs) of the RPR must be made of 20-25 cm thick reinforced concrete.

Due to economic and environmental reasons there is an increased tendency to use recycled industrial by-products containing Technologically Enhanced Natural Occurring Radioactive Materials (TENORM) in the building material industry. Fly ash (FA), produced as a by-product in the combustion of coal, is extensively used in Israel since the early 1990's in concrete and as an additive to cement.

The increase of ²²⁶Ra activity concentration, the mineralogical characteristics of the FA and of the concrete may affect the radon exhalation rate and consequently the radon exposure in RPRs. In addition, due to its special features, the RPR is expected to experience, under regular use conditions, a lower air change rate than any of the other rooms in the dwelling. Consequently, concern was raised with regard to long term radon exposure in RPRs.

The paper presents results derived in a research project that studied in-situ air change rates and radon concentration evolution under various ventilation scenarios in 6 RPRs in a high-rise building, and compared evaluated free radon exhalation rates from the walls with values derived from laboratory samples of the same concretes.

METHODOLOGY

The investigation was composed of an experimental phase of in-situ and laboratory measurements, and a modelling phase, which was based on basic mass transfer and conservation principles. This paper is devoted to the results of the experimental part only, with data analysis based on the methods and equations derived in the theoretical part^(1,2).

IN-SITU TESTS

Tests were performed in a western and eastern RPR on floors 12, 15, and 19 (F12, F15, F19, respectively) of a tall building. All RPRs were equipped with the especially airtight window and outward opening door. An additional inward opening regular wooden door was installed in the RPRs on F12. Concrete cast on F15 was a pure Portland cement concrete (without addition of fly ash or other pozzolanic additives), whereas on the other floors fly ash replaced part of the cement. Fly ash used in F12 concrete had relatively low radioactivity, and that in F19 concrete was richer in ²²⁶Ra. Radon concentration was measured continuously, at 1 hour intervals, in all RPRs. In the eastern RPRs a passive radon monitor (pulse height ionization chamber), Alphaguard PRO 2000 (AG), of Saphymo GmbH was used. In the western RPRs a semiconductor alpha detector, RTM 1688-2, of Sarad GmbH was used. Tests in the eastern RPR on F12 included also simultaneous monitoring with a second continuous radon monitor, RAD-7 (DurrIDGE Company Inc.). Tracer gas measurements with SF₆ were performed in the two RPRs on F12. A few tens of grams of gas were first released into the closed room and stirred with fans to ensure a homogenous well mixed spatial distribution.

The window and door were then maneuvered into the tested position. Continuous monitoring (at a 1-minute interval for the cases of the extremely airtight scenario, and 0.5-minute interval for all the other cases) was performed with an MIRAN infra-red analyzer calibrated to the range 1-1000 ppm. Figure 1 shows the experimental setup in the eastern RPR on F12.

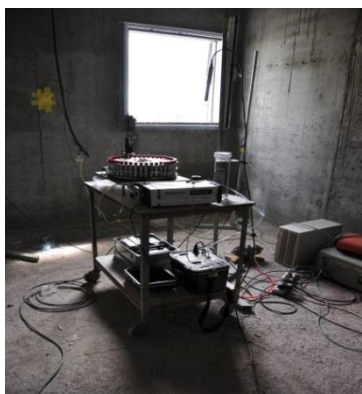


Figure 1. Representative experimental setup for in-situ tests (eastern RPR on F12).

LABORATORY TESTS

Concrete prisms (10 cm × 10 cm × 20 cm) were taken while casting the walls and floors of the tested RPRs. Radon exhalation rates from fully exposed concrete specimens were measured in the laboratory using the sealed chamber test method⁽³⁾. Figure 2 shows the test setup.



Figure 2. Setup for radon exhalation measurements using the sealed chamber method.

RESULTS

The estimated free radon exhalation rates based on the laboratory measurements of the concrete used in the test building are given in Table 1. E_0 is the average prism free exhalation rate, and $E_{0,sr}$ is the estimated RPR wall surface free exhalation rate.

Table 1. Measured prism free exhalation rates, E_0 , and estimated RPR wall surface free exhalation rates, $E_{0,sr}$, for the cast in situ concrete samples (Bq/m^2h).

Floor	Fly Ash (kg/m^3)	Testing Age (d)	E_0 (Bq/m^2h)	$E_{0,sr}$ (Bq/m^2h)
12	120	94	1.73±0.12	6.5±0.5
12	120	58	1.73±0.12	
12	120	83	1.73±0.12	
15	0	60	2.39±0.17	8.9±1.0
15	0	60	2.33±0.17	
15	0	55	2.35±0.17	
15	0	44	2.34±0.17	
15	0	44	2.46±0.17	
19	140	76	2.08±0.17	7.6±1.1

19	140	76	1.95±0.17	
----	-----	----	-----------	--

Apparently, the different concretes used on the various floors had somewhat different characteristic free exhalation rates, with the fly ash free concrete (used on F15) exhibiting the highest rate, and the one with the low radioactivity fly ash (F12) the lowest one. Significant differences were observed, however, only between the F12 and F15 concretes.

Table 2 presents the air change rates, N, measured using the tracer gas method. The SF₆ monitored data was analyzed using several methods, yielding different values of N for the same case. The average and ranges of these values are given, addressing also the uncertainties stemming from these different calculations. Despite the large spread of the results within each scenario, it was apparent that there is a significant difference between the airtightness levels for the various scenarios. With the especially airtight door, air change rates in RPRs were extremely small, including near zero levels. With a regular interior door they were much higher (>0.1 ACH), but stayed below 0.3 ACH, indicating the need for additional ventilation in order to ensure a generally proper indoor air quality (IAQ), which implies that occupants would refrain from staying long periods under these conditions in order to prevent stale air, moisture accumulation, etc. Tilting the window on its horizontal axis raised the air change rate to the range of >1 ACH, which is proper for IAQ, but excessive for proper energy performance, and for this reason would usually not be used when heating or cooling equipment is on. Based on these findings, it could be concluded that the air change rates during long occupancy periods of the RPR would not be kept lower than 0.1

Results obtained for E_{0,sr} and N from the continuous radon concentration measurements in the RPRs are given in Table 3.

The independent analyses performed by the two research groups for the same datasets yielded similar results for the apparent radon decay, λ_{eff}, and all the orders of magnitude of the obtained values of Δλ=λ_{eff} - λ_{Rn} compared well with those of the independently measured N. The differences between the values of Δλ and N were, however large and inconsistent, with an average difference of ±30.7% and extremes of 111.2% and -54.5%.

Table 2. Air change rates, N, measured using the tracer gas method (ACH).

Case	Window Position	Door Position	Calculate Average Air Change Rate, N (ACH)		Total Range for scenario* (ACH)
			Eastern RPR	Western RPR	
A1	Closed	Special Tight	11E-4	6.9E-3	9.6E-4 – 7.1E-3
B1	Closed	Regular Closed	0.13	0.26	0.13 – 0.26
B2	Closed	Regular Closed	0.14	0.26	
C1	Tilted	Regular Closed	1.23	2.70	0.9 – 3.1
C2	Tilted	Regular Closed	1.30	2.93	
D1	Closed	Open	15.1	13.4	9 – 21
D2	Closed	Open	11.5	14.8	
E1	Open	Regular Closed	4.48	6.13	3.2 – 14
E2	Open	Regular Closed	4.76	12.4	
F1	Tilted	Regular 1/3	-	31.2	11 – 51
F2	Tilted	Regular 1/3	15.2	28.4	
G1	Open	Regular 1/3	35.4	52.2	21 – 105
G2	Open	Regular 1/3	49.5	50.1	

*The total range includes the margins of the various uncertainty ranges.

Table 3. Δλ (h⁻¹), and RPR wall surface free radon exhalation rates, E_{0,sr} (Bq/m²h) obtained from radon monitoring.

Case	$\Delta\lambda$ (1/h)	$E_{0,sr}$ (Bq/m ² h)
A _{1,F12east}	48E-4	8.38
B _{1,F12east}	0.24	7.34
A _{1,F12west}	7.1E-3	7.05
B _{1,F12west}	0.19	7.44

The estimated values of $E_{0,sr}$ were within the range 4.9 – 8.7 Bq/m²h, with an average of 7.6±1.3 Bq/m²h, which compared quite well with the value 6.5±0.5 Bq/m²h obtained independently from the laboratory samples of the F12 cast concrete. For the other cases of scenario A on Floor 12 (which were not accompanied by tracer gas measuring of the air change rate) $\Delta\lambda$ was used instead of N in the calculation of $E_{0,sr}$. The range of the estimated values of $E_{0,sr}$ on floor 12 for these case was 7.7 – 10.3 Bq/m²h, with an average of 8.6±0.7 Bq/m²h. Similarly, for Floors 15 and 19 concretes the ranges of the estimated values of $E_{0,sr}$ were 7.8 – 9.4 Bq/m²h, and 4.9 – 9.7 Bq/m²h, respectively, with averages of 7.2±2.0 Bq/m²h and 7.2±1.5 Bq/m²h, respectively, comparing quite well with the laboratory measured values.

CONCLUSIONS

The orders of magnitude of the estimated air change rates using radon monitoring data were similar to the orders of magnitude of the directly measured values obtained by the tracer gas method, but differences between the values were large with no consistent tendency. Radon monitoring alone could not, thus, serve as a sole means for estimating the air change rate in rooms.

Room-surface free radon exhalation rates calculated from the radon monitoring data matched well the values obtained from the analysis of independently measured material samples, with relatively small differences.

Consequently, exposure risks in closed RPRs were performed using laboratory-based upper limits of free radon exhalation rates (e.g. 12 Bq/m²h) together with tracer gas-based lower limits of air change rates (e.g. 0.1 ACH). The estimated maximal exposure risk for a 10 hour period in a closed RPR under normal service conditions was 171 Bq/m³, and for a 5 hour period in a tightly sealed RPR under sheltered conditions 136 Bq/m³. The consequent annual average exposure risk was thus estimated to be well below the stipulated action level of 200 Bq/m³.

REFERENCES

1. Kovler, K., Becker, R., Haquin, G. *Radon exhalation from concrete containing coal fly ash*. Publication of the National Building Research Institute and the Soreq Nuclear Research Center, Israel, p.1-137, (2011).
2. Becker, R., Haquin, G., Kovler, K. *Air-change rates and radon accumulation in rooms with various levels of window and door closure*. In print, Journal of Building Physics. Published online before print, 1744259113506071 (2013).
3. SII, "SI 5098: Content of radioactive elements in building products". The Standards Institution of Israel, Tel-Aviv, Israel, (2009).

ACKNOWLEDGEMENTS

The Israeli Ministry of Construction and Housing and the National Coal Ash Board are acknowledged for supporting the entire set of experimental and theoretical research activities. In addition, the work of the assistant researchers, Zakhar Prilusky from Technion, and Lior Epstein and Zohar Yungreis from Soreq NRC is fully appreciated. The authors are also obliged to Ayala Ronen and the technical team of the Israel Institute for Biological Research who supplied the SF₆ instrumentation and participated in these tests.

Radiation Exposure to Concrete in Israel

G. Haquin¹, K. Kovler², G. de With³, Z. Yungrais¹ and N. Lavi⁴

¹*Soreq Nuclear Research Center, Yavne, 81800, Israel*

²*Technion - Israel Institute of Technology, Haifa 32000, Israel*

³*NRG, 6800 ES Arnhem, The Netherlands*

⁴*Ben Gurion University of the Negev, Beer Sheva, 84105, Israel*

INTRODUCTION

Most building materials of terrestrial origin contain small amounts of radionuclides of natural origin, mainly from the Uranium (^{238}U) and Thorium (^{232}Th) decay chains and the radioactive isotope of potassium, ^{40}K . The external radiation exposure is caused by gamma emitting radionuclides, which in the uranium series mainly belong to the decay chain segment starting with Radium (^{226}Ra). The internal (by inhalation) radiation exposure is due to Radon (^{222}Rn), and its short lived decay products, exhaled from building materials into the room air.

Due to economical and environmental reasons there is an increased tendency to use industrial by-products containing relatively high concentrations of radionuclides of natural origin in the building material industry. Fly ash (FA), produced as by-product in the combustion of coal, is extensively used in Israel since mid eighties of the last century in concrete and as an additive to cement ⁽¹⁾.

The increase of ^{226}Ra activity concentration, the mineralogical characteristics of the FA and of the concrete may influence on the radon exhalation rate and consequently on the radon exposure of the public.

The recently published Israeli Standard 5098 (IS 5098) "Content of natural radioactive elements in building products" ⁽²⁾ limits the content of natural radionuclides as well as the radon emanation from concrete.

This paper presents a compilation of three studies conducted at Soreq Nuclear Research Centre (SNRC), Technion, NRG and Environmental Lab BGU (ELBGU) to investigate and quantify the influence of FA addition in concrete.

MATERIALS AND METHODS

Seventy four batches (at least 3 concrete samples per batch) containing raw building materials from all over Israel having different concentrations of FA (0 to 150 kg/m³ of concrete) were prepared at the lab and at the concrete plant. Samples were cured according to the standard procedure (7 days).

The natural radionuclides content in the concrete was determined by gamma spectrometry method as indicated in the IS 5098 standard.

The free exhalation rate and the emanation coefficient were measured at the Israeli laboratories by the close chamber method according to IS 5098 standard procedure. Uncoated samples of dimensions 10 cm x 10 cm x 20 cm were placed in a close chamber and the radon concentration was monitored using a continuous radon monitor or activated charcoal canisters.

For comparison purposes twenty one concrete samples were also measured at NRG in The Netherlands. The natural radionuclides content was determined also by gamma spectrometry while the Rn exhalation rate was measured using the Dutch standard ⁽³⁾ based on a purge and trap method.

The radiation exposure in a full concrete room was evaluated by two means: according to IS 5098 and using a mathematical simulation method described by De Jong ^(4,5) and De With ⁽⁶⁾.

RESULTS

The addition of FA to concrete increases the activity concentration of ^{226}Ra and ^{232}Th proportionally to the amount of FA at an average rate of 0.67 and 0.54 Bq per 10 kg of FA respectively ($R=0.90$ and 0.997), while the influence on ^{40}K is not statistically significant as shown in Figure 1.

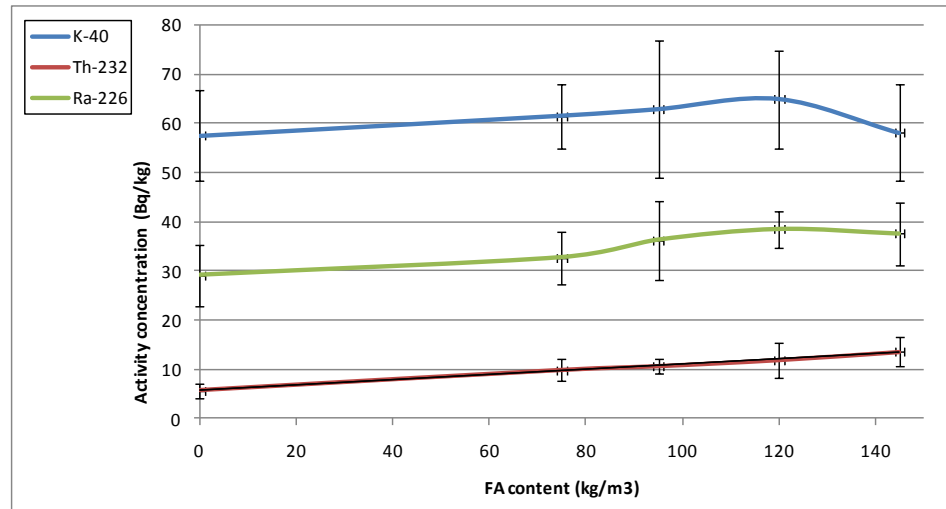


Figure 1: Average activity concentration in concrete with and without FA.

The influence of FA addition to ^{222}Rn emanation is ambiguous as it was shown by Becker et al. ⁽⁷⁾ with a slight trend to decrease at a rate of 0.1% per 10 kg of FA, as shown in Figure 2.

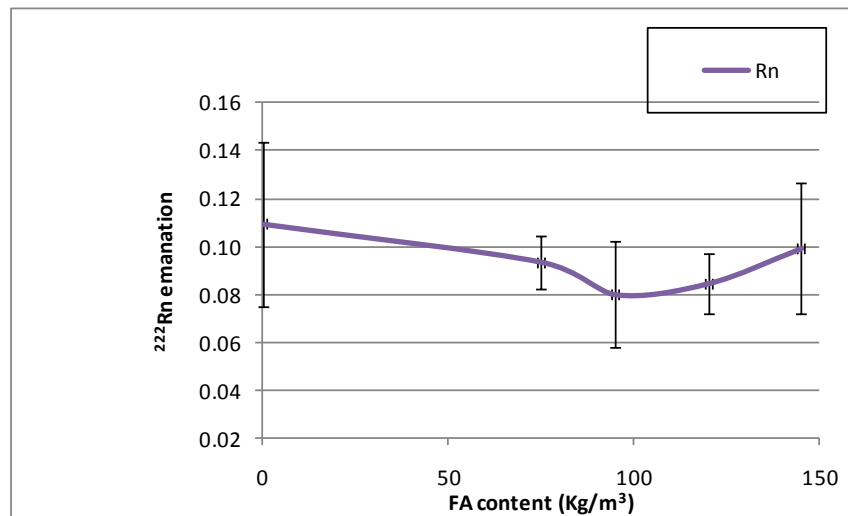


Figure 2: ^{222}Rn emanation from concrete with and without FA.

The radiation exposure was calculated according to IS 5098, by two means considering only the external exposure from gamma emitting radionuclides (^{226}Ra , ^{232}Th and ^{40}K , respectively), and taking into account the influence of the internal exposure due to ^{222}Rn and its decay products.

The annual average external exposure in the center of a 3 m x 3 m x 2.7 m room of 0.2 m concrete thickness was 0.19 mSv and the total exposure, including ^{222}Rn (equilibrium factor 0.4) under conservative living conditions (air exchange rate of 0.5 h^{-1}) was 0.61 mSv per year. Figure 3 shows almost normal distributions of the gamma and total exposure in concrete rooms.

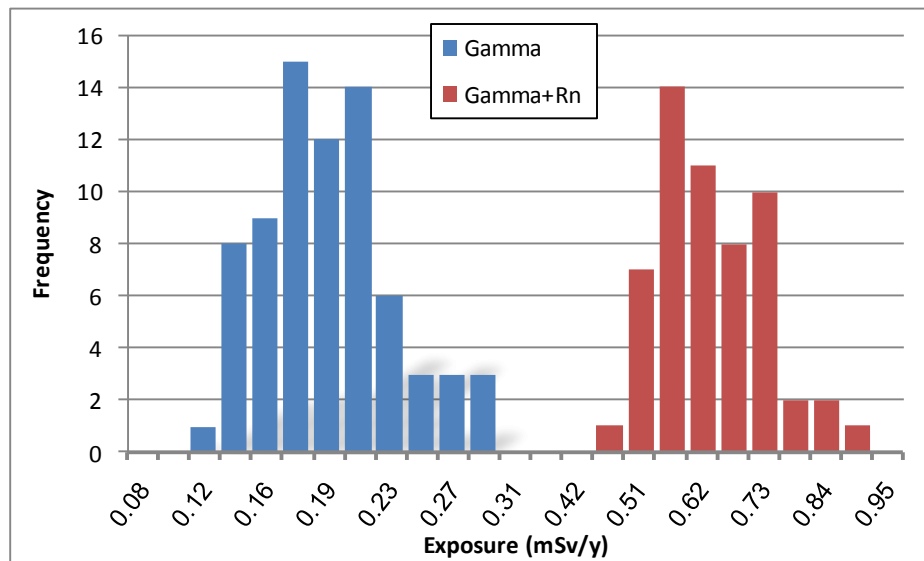


Figure 3: Radiation exposure to gamma and Rn from concrete in Israel.

COMPARISON TO THE DUTCH APPROACH

As a new standard the IS 5098 a benchmark against another parallel approach was performed. In The Netherlands the radioactivity from building materials is searched since several years and the Dutch authorities developed various standard methods for measuring the activity concentrations of gamma emitting radionuclides and the exhalation of radon from building materials. In addition a standard method is developed to assess the radiation exposure in dwellings from external radiation (from gamma emitting radionuclides) and internal radiation (^{222}Rn).

Figure 4 shows the good correlation between the SNRC and NRG activity concentration results. The comparison of the emanation coefficient calculated from the exhalation rate measurements performed at NRG and at SNRC is shown in Table 1.

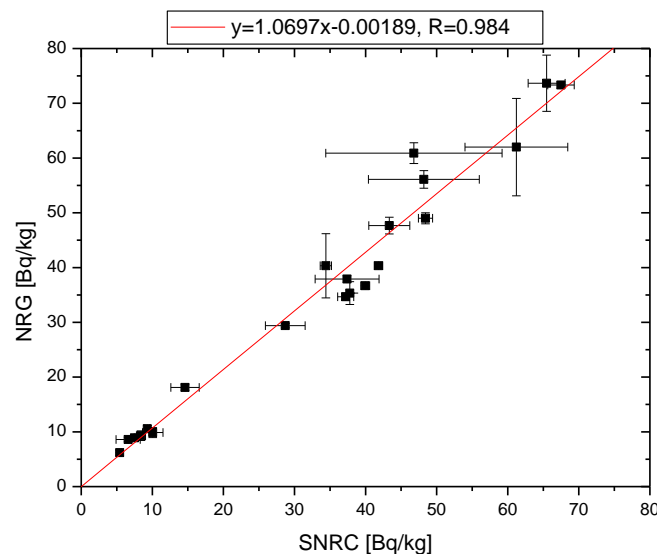


Figure 4: Correlation between SNRC and NRG activity concentration results.

Table 1: Emanation coefficient of concrete samples as measured at NRG and SNRC

FA content	SNRC ϵ (%)	NRG ϵ (%)	Deviation
0	7.8	8.6	10.8%
120	8.3	8.2	-0.9%
120	8.4	9.3	11.2%
120	7.0	7.0	-0.4%
120	6.6	6.9	3.8%

The external radiation exposure was found to vary for the different concrete mixtures 0.20-0.26 mSv/y. The internal exposure to ^{222}Rn was found to be 0.55-0.62 mSv/y, giving an overall total exposure of 0.78 – 0.86 mSv/y.

CONCLUSIONS

Concrete mixtures commonly used in Israel were measured for their natural radionuclide content and Rn emanation coefficient according to the standard procedure described at the National standard IS 5098.

The addition of up to 150 kg/m³ of FA to concrete increased the activity concentration of ^{226}Ra and ^{232}Th in the concrete while the ^{222}Rn emanation tended to decrease slightly.

Benchmarking of the IS 5098 methodology was performed using the Dutch approach. Few concrete samples were measured at SNRC, ELBGU and NRG giving similar activity concentration and Rn emanation results. The external exposure calculated at NRG was 20-40% higher due to different room characteristics and the influence of adjacent rooms. The total exposure calculated at NRG was 35-70% higher due to the different Rn concentration assessment in the room and its influence to the internal exposure.

The average annual external radiation exposure in Israel in the center of a standard room built with concrete is 0.19 mSv and the total exposure (external and internal) is 0.61 mSv/y.

ACKNOWLEDGMENT

The work was supported by the National Coal Ash Board and partially by the Ministry of Construction and Housing.

REFERENCES

1. Haquin, G. *Natural Radioactivity and Radon in Building Materials*. Proc. 12th IRPA congress, Buenos Aires (2008).
2. Israeli Standard IS 5098, *Content of natural radioactive elements in building products*, The Standards Institution of Israel (2009) (in Hebrew).
3. NEN (2001) Radioactivity measurements – Determination method of the rate of the radon exhalation of dense building materials. NEN 5699(en). Nederlands Normalisatie-instituut, Delft, The Netherlands.
4. De Jong, P. and Van Dijk, W. (2008), Modeling gamma radiation in dwellings due to building materials. *Health Phys.* 94: 33-42.
5. De Jong, P. and Van Dijk, J.W.E. (2008), Calculation of the indoor gamma dose rate distribution due to building materials in the Netherlands. *Radiat. Prot. Dosim.* 132:381-389.
6. De With G. and De Jong P. (2011) *CFD modelling of thoron and thoron progeny in the indoor environment*. *Rad. Prot. Dosim.*, 145 (2-3): 127-132.
7. Becker, R., Haquin, G., Kovler, K. *Air-change rates and radon accumulation in rooms with various levels of window and door closure*. *Journal of Building Physics*. Published online before print, 1744259113506071 (2013).

NORM & Environmental Radioactivity (Wednesday, February 12, 2014 16:30)

Scintillation vs. Semiconductor Spectrometers for Determination of NORM in Building Materials

K.Kovler¹, S.Levinson², N.Lavi³, U.Gherman², B.Dashevsky¹, H.Nassar⁴, S.Antropov⁵

¹ *Technion - Israel Institute of Technology, Haifa 32000, Israel*

² *Nuclear Research Center, Negev, POB 9001, Beer Sheva, 84190, Israel*

³ *Ben-Gurion University, Beer Sheva 84105, Israel*

⁴ *Ministry of Environmental Protection, POB 34033, Jerusalem 95464, Israel*

⁵ *"Amplituda" Research Center, POB 120, Moscow 124460, Russia*

INTRODUCTION

Most common gamma spectrometers include systems equipped with either scintillation or semiconductor detectors. The most popular scintillation detectors are based on sodium iodide crystals doped with thallium (NaI(Tl)), while semiconductor detectors are usually made of high-purity [germanium](#) (HPGe) crystals. NaI(Tl) detectors are simpler and cheaper, but have poor energy resolution. For this reason they are often considered as not suitable for identification of complicated mixtures of γ -ray-emitting materials and for quantitative determination of their radionuclide composition. The current paper continues the series of publications aimed to check whether the scintillation detectors, in spite of their poor energy resolution, can accurately determine the content of natural radionuclides in building materials with different radionuclide composition [1, 2].

HPGe detectors have better energy resolution than NaI(Tl) detectors and suit for the determination of the unknown radionuclide mix composition. However, the HPGe detector can only function if cooled to liquid-nitrogen temperatures, otherwise electrons are thermally excited into the conduction-band and generate a high level of noise. In addition, in order to provide a stopping power equivalent to a commonly available size of scintillation spectrometer, the germanium crystal becomes very expensive to fabricate. As a consequence, HPGe detectors are significantly more expensive than NaI(Tl) detectors [3].

NaI(Tl) detectors are commonly used for identification and measuring activities of low-level radioactive sources. The NaI(Tl) spectrometer produced by Amplituda (Russia), are equipped with a special software based on the matrix method of least squares, which provides an accurate quantitative analysis of the radionuclides mixtures of known composition. It was used in parallel with HPGe spectrometer for determination of the NORM (Naturally Occurring Radioactive Materials) in the previous series of tests [2]. The materials studied in this series included (a) synthetic compositions with activity concentrations varying in a wide range, from 1/5 to 5 times median activity concentrations of the natural radionuclides available in the earth crust, and (b) samples of popular building materials, such as concrete, pumice and gypsum, with the density of the tested samples varying in a wide range: from 860 up to 2,410 kg/m³. The main feature of the applied software is that the entire spectrum is represented as a sum of the functions of the response individual radio-nuclides, instead of the treatment of the peaks of the full energy absorption (photo-peaks).

RESULTS AND DISCUSSION

The present paper describes the results of the last series of the tests, which included masonry blocks made of lightweight concrete of three types - lightweight aggregate (pumice) concrete, no-fines concrete and aerated autoclaved concrete, Portland cement of types CEM I, CEM II A and CEM II B, coal bottom ash and sand. The background measurements were conducted during 50,000 sec. In total 66 specimens representing different materials were tested using both HPGe and NaI(Tl) spectrometers, while several specimens were measured twice and even more times (till 5); totally 79 measurements have been analyzed.

These results include some previous results, which were reported recently [2], and are presented in Figs. 1 - 4.

It can be seen that the results obtained by the scintillation spectrometer are very similar to those obtained with the HPGe spectrometer (the regression coefficients in Fig. 1 are close to 1 for all cases), mostly within the uncertainty range (see Figs 2 – 4). The results of the measurements by NaI(Tl) on the same specimen were well reproduced. The limits of detection in the measurement of the radioisotopes ^{226}Ra , ^{232}Th and ^{40}K , using NaI(Tl) spectrometer, did not exceed 2, 2 and 13 Bq/kg, respectively, being within the limits required by the Israeli Standard for measuring the radioactive content in building materials [4]. The limits of quantification in the measurement of these radionuclides did not exceed 4, 5 and 28 Bq/kg, respectively.

CONCLUSIONS

The better efficiency (for the same detector size), and the lower cost of the NaI(Tl) spectrometer can be traded-off against the better resolution of the HPGe spectrometer. The NaI(Tl) spectrometer equipped with the special software based on the matrix method of least squares provides an accurate quantitative analysis of the NORM in building materials and soils, and has the potential to be successfully used for the assessment of radio-nuclide content in mass construction products.

REFERENCES

1. Kovler K., Priluzky Z., Antropov S., Antropova N., Bozhko V., Alfassi Z., Lavi N., *Determination of Radionuclide Content of Building Materials by Means of Scintillation Spectrometry*, The 25th conference of the nuclear societies in Israel, 16-18 February 2010, Dead-Sea, Israel, pp. 284-289.
2. Kovler K., Prilutskiy Z., Antropov S., Antropova N., Bozhko V., Alfassi Z., Lavi N., *Can scintillation detectors with low spectral resolution accurately determine radionuclides content of building materials?* Applied Radiation and Isotopes 77 (2013) 76-83.
3. IAEA, *Safeguards Techniques and Equipment*. Vienna: IAEA, International Nuclear Verification Series (2011).
4. SI 5098. Content of radioactive elements in building products. The standards institution of Israel (2009).

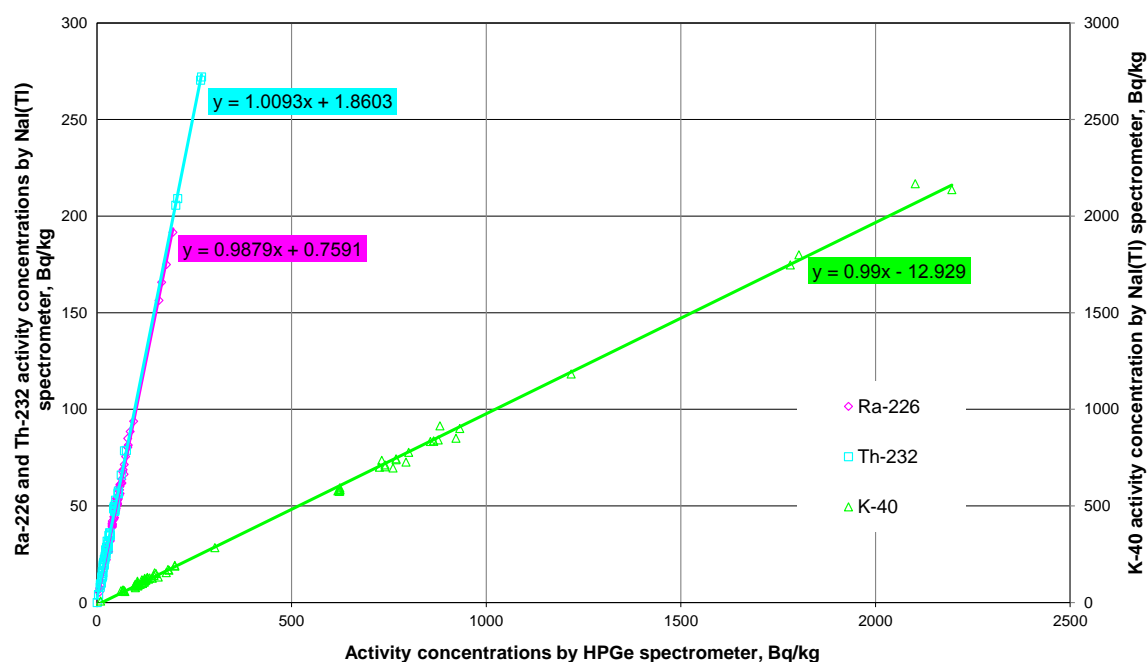


Figure 20. NORM activity concentrations measured by NaI(Tl) vs. HPGe spectrometers.

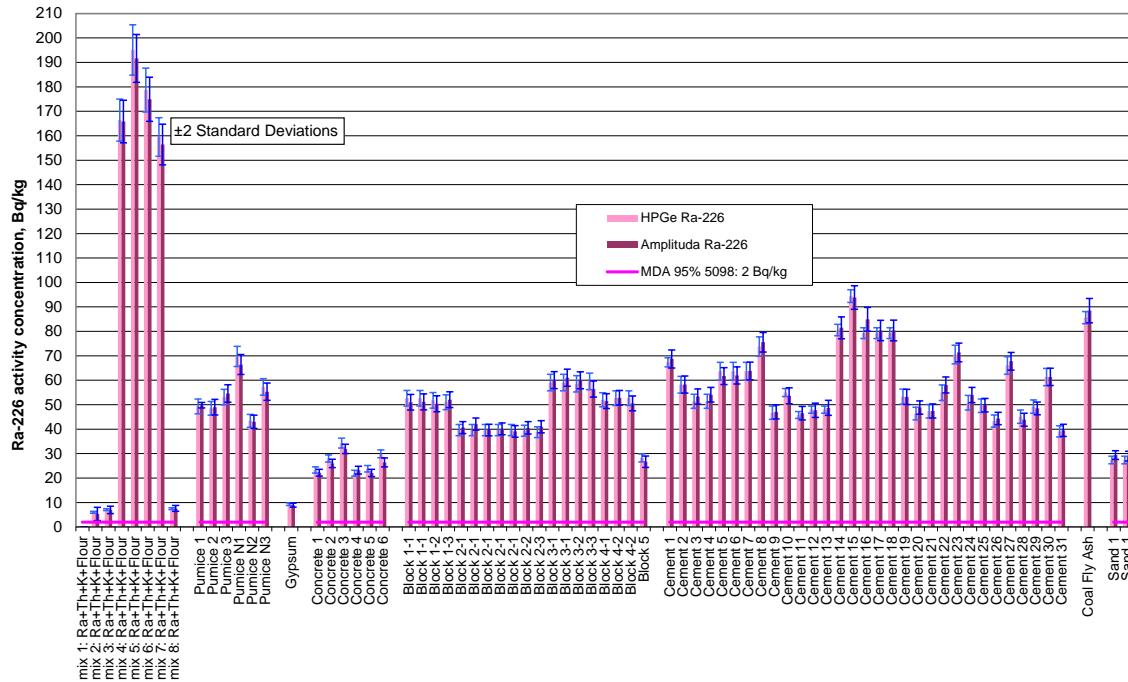


Figure 21. ^{226}Ra activity concentrations measured in different materials by two types of spectrometers, HPGe and NaI(Tl).

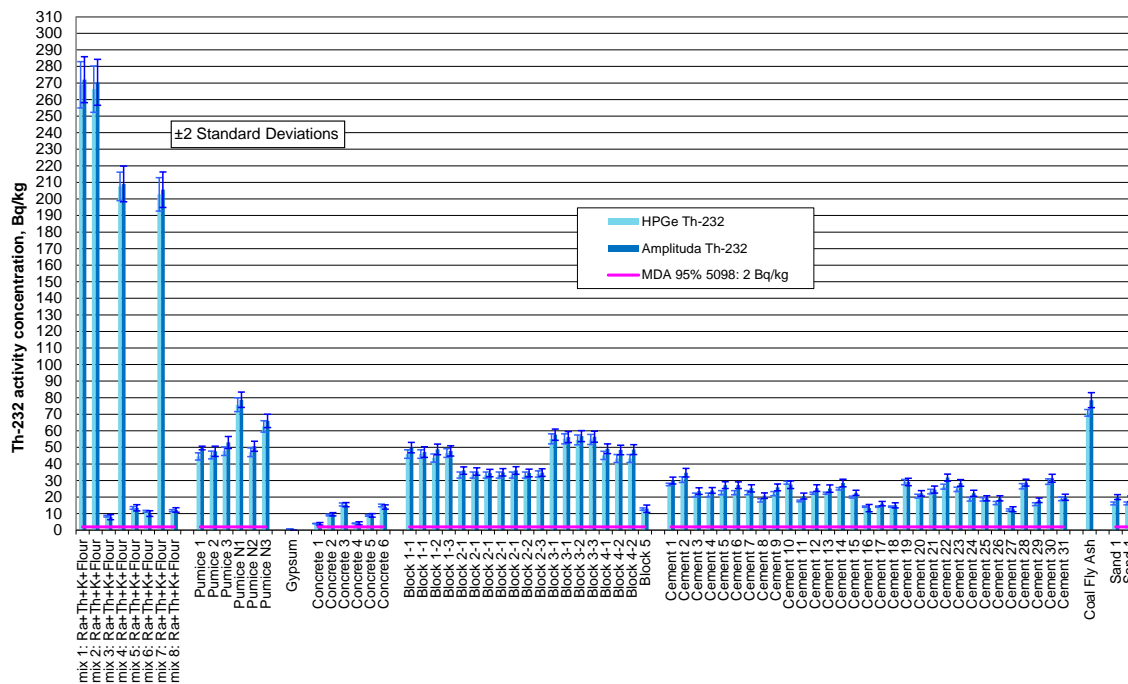


Figure 22. ^{232}Th activity concentrations measured in different materials by two types of spectrometers, HPGe and NaI(Tl).

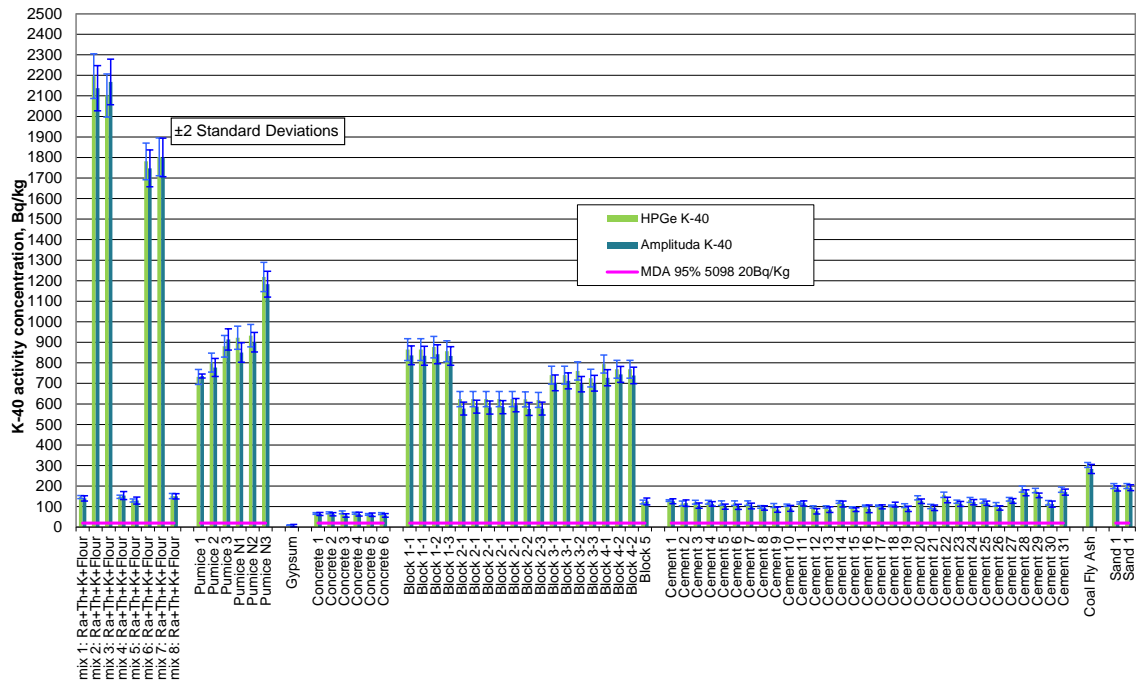


Figure 23. ⁴⁰K activity concentrations measured in different materials by two types of spectrometers, HPGe and NaI(Tl).

NORM & Environmental Radioactivity (Wednesday, February 12, 2014 16:30)

Radioactive Waste in Oil Exploration

S. Landsberger¹, S. G. Landsberger², G. Graham²

¹University of Texas at Austin, Texas, USA

²Enviroklean Product Development, Inc. (EPDI), Houston, Texas, USA

INTRODUCTION

Naturally occurring radioactive material commonly known as NORM composes the majority of the dose received by a person each year at approximately 80% of the total amount. However, there is a noticeably higher concentration of radioisotopes present in technologically enhanced NORM, often called TENORM, which results directly from human industrial activities. NORM is formed in the process of mineral mining including phosphate production, where the end goal is to concentrate high quantities of metals or elements (e.g. phosphorous). However, NORM has also become a widely recognized problem in the oil and gas industry. It is approximately one hundred and fifty years since oil was discovered in the continental United States and the mention of radioactivity in mineral oils and natural gases occurred in 1904, just eight years after the discovery of radioactivity by Henri Becquerel in 1896. In just over three decades the problems from naturally occurring radioactive material (NORM) wastes arising from the oil and gas industry have been much more scrutinized. In the 1980's ²²⁶Ra began to be noticed when scrap metal dealers would detect unacceptably high levels of radiation from oil-field piping¹. In 1991 Raloff² published an article on the *new hot wastes* in NORM and in 1992 Wilson *et. al*³ described the health physics aspects of radioactive petroleum piping scale. NORM will develop in high concentrations in by-product oil and gas waste streams⁴⁻⁷. The NORM will chemically separate from other piped material in the process of the extraction of oil, resulting in high concentrations of ²²⁶Ra, ²²⁸Ra and ²¹⁰Pb and other radioisotopes in a densely caked layer on the inner surfaces of the piping¹. The activity of the ²²⁶Ra from NORM ranges from 185 to several tens of thousands Bq/kg of sample. By comparison, the NORM concentrations of radium in rock and soil is, at a natural level, 18.5 - 185 Bq/kg¹. Disposal of NORM becomes more problematic as higher concentrations of radioactivity and demand even higher degrees of separation from the general populace. Very low levels of NORM can be dispersed along the surface, but higher concentrations require containment in abandoned wells or salt domes¹. ²²²Rn a product of the decay of ²²⁶Ra is also a major component of dose to oil and gas workers from NORM¹. Radon buildup is particularly hazardous in places where air ventilation is limited, such as underground mining operations. In the oil and gas industry, radon tends to preferentially follow gas lines, and thus is a major concern in the extraction of natural gas where concentrations of 5 - 200,000 Bq/m³ can be reached⁸. US EPA has also placed the set rules for contaminated soil to be at 1.11 Bq/g (30 pCi/g). The obvious concern is that any elevated concentrations in radionuclides in soil may eventually leach into the ground water. Enviroklean Product Development, Inc. (EPDI) and the Nuclear Engineering Teaching Lab have been involved in the cleanup and identification of NORM wastes in west Texas.

RESULTS

NORM samples from oil and gas exploration contain a complex matrix as a result of the precipitation of radium, barium, calcium and strontium sulphates. Barium, calcium and strontium are in group II of the periodic table thus they have very similar chemical characteristics. Thus the determination of low energy photons of ²²⁶Ra (186 keV) and ²¹⁰Pb (45.6 keV) may be severely compromised due to self-attenuation of the gamma-rays in the sample. This is especially true if the samples are gamma-ray counted in large volumes such as Marinelli® containers which may hold up to 250-500 grams of material. To overcome this problem we used Petrie® dishes containing 20 grams of material. In our experiments we used a 1 µCi

calibrated water based solution containing isotopes from 46 to 1836 keV to derive a standard efficiency curve. A program called SELFABS⁹ was used to estimate the attenuation in the water and soil. For soil the estimated concentrations of elements above 0.1% were based on universal published on crustal earth data¹⁰. The transmission factors were as follows: 45.2% for the 46.5 keV photon belonging to ²¹⁰Pb; 76.8% for the 186.2 keV photon belonging to ²²⁶Ra and 87.3% for the 911 keV photon of ²²⁸Ac, which is in secular equilibrium with ²²⁸Ra. All samples were heat sealed and let stand for one month to achieve secular equilibrium, were counted for 12 hours on a hyperpure germanium detector with an efficiency of 28% and a FWHM resolution of 2.0 keV for the 1332.4 keV photon belonging to ⁶⁰Co. The radioactivity results for soil, scale, sludge and processed water samples are shown in Table 1. A quality assurance on the efficiency curve was performed by analyzing the IAEA-375 radionuclides in soil¹¹. Our result of 5024 ± 163 Bq/kg for ¹³⁷Cs (with all uncertainties propagated) is in good agreement with the consensus value of 5280 ± 80 Bq/kg, which is ~5% higher. A simple sensitivity analysis revealed that the dominant factor for any variation in a result is the calculation of the calculated transmission factor (or self-absorption) of photons. The analytical uncertainties based on counting statistics for the ²¹⁰Pb, ²²⁶Ra and ²²⁸Ra for the sludge, soil and scale varied between 0.1 - 6%. Detection limits for ²¹⁰Pb, ²²⁶Ra and ²²⁸Ra varied depending on the type of matrix that was determined. However, in all four cases there were adequate statistics to achieve good precision. Two additional interferences were taken into consideration. One is the interference of the 185.2 keV gamma-ray of ²³⁵U on the 186.2 keV of ²²⁶Ra. This interference is well known and explained in detail by Gilmore¹². However, in these NORM samples the activity of ²³⁵U is from one to several orders of magnitude less than that of ²²⁶Ra, thus having a negligible interference effect. The second systematic problem is coincidence summing. Again, this is a well-known effect, and for naturally occurring radioactivity these corrections have been tabulated for Marinelli® and Petri® holders¹³. For ²¹⁰Pb and ²²⁶Ra the correction factors are negligible but for the 911 keV photon for ²²⁸Ac used to determine ²²⁸Ra there is a 9% effect. Figure 1 shows a typical spectrum of radioactive oil waste byproduct. The results in Table 1 reflect this correction factor.

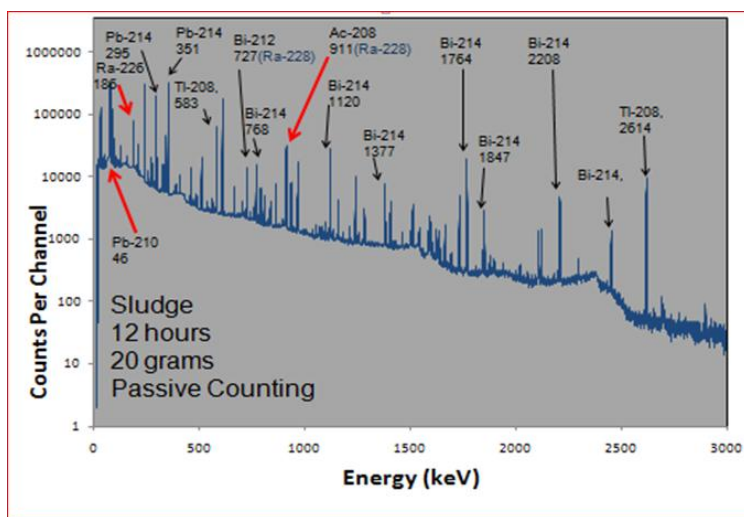


Figure 1. Typical spectrum showing the ²¹⁰Pb, ²²⁶Ra and ²²⁸Ra byproducts from oil exploration

More recently, we have used a more standard way of determining the self-attenuation by using a ¹⁵²Eu source and placing it on top of the Petrie® dish with and without the NORM sample. Once an attenuation curve is plotted self-absorption factors for photons for any sample less or more dense can be easily calculated by normalizing the original plot with just one photon. Results for ²¹⁰Pb, ²²⁶Ra and ²²⁸Ra are shown in Table 1.

Table 1. Radioactivity results for ^{210}Pb , ^{226}Ra and ^{228}Ra

Radionuclides	Sludge (Bq/kg)	Scale (Bq/kg)	Soil (Bq/kg)
^{210}Pb	5148 ± 222 (139 ± 6 pCi/g)	1370 ± 74 (37 ± 2 pCi/g)	$22,889 \pm 740$ 618 ± 20 pCi/g
^{226}Ra	$59,000 \pm 300$ (1593 ± 81 pCi/g)	2630 ± 148 (71 ± 4 pCi/g)	$65,296 \pm 3296$ (1763 ± 89 pCi/g)
^{228}Ac (^{228}Ra)	$28,501 \pm 1493$ (770 ± 340 pCi/g)	565 ± 40 (15 ± 1 pCi/g)	154 ± 12 (4.1 ± 0.3 pCi/g)

CONCLUSIONS

Our collaboration with EPDI industry in NORM in oil exploration has been very fruitful. We have implemented analytical protocols in determining radionuclides in the waste products and determining self-attenuation properties for samples that exhibit unusually high atomic number elements such as iron, barium and strontium.

REFERENCES

- Zielinski, R.A., Otton, J.K. *Naturally Occurring Radioactive Materials (NORM) in produced water and oil-field equipment – An issue for the energy industry*. U.S. Geological Survey. <http://pubs.usgs.gov/fs/fs-0142-99/fs-0142-99.pdf>. (1999).
- Raloff J. *NORM-The new hot wastes*. Science News **140**, p.264-267 (1991).
- Wilson A.J., Scott L.M. *Characterization of radioactive petroleum piping scale with an evaluation of subsequent land contamination*. Health Phys. **63**, p 681-685 (1992).
- Heaton, B., Lambley, J. *TENORM in the oil, gas and mineral industry*. Appl. Radiat. Isotopes, **46**, p.577-581 (1995).
- Al-Masri, M.S., Sunam, H. *NORM waste management in the oil and gas industry: The Syrian experience*. J. Radioanal. Nucl. Chem. **256**, p.159-162 (2003).
- Al-Saleh, F.S., Al-Harshan, G.A. *Measurements of radiation level in petroleum products and wastes in Riyadh City Refinery*. J. Environ. Radioact. **99**, p.1026-1031 (2008).
- Gazineu, M.H.P., Hazin, C.A. *Radium and potassium-40 in solid wastes from the oil industry*. Appl. Radiat. Isotop. **66**, p.90-94 (2008).
- World Nuclear Association. *Naturally Occurring Radioactive Materials (NORM)*. <http://www.world-nuclear.org/info/inf30.html>. (2011).
- Jaegers P., Landsberger S. *Selfabs: A PC computer code for the determination of the self-absorption fractions of gamma rays for neutron activation analysis*. Nucl. Instrum. Meth. Phys. Res. **B44**, p.479-483 (1990).
- Wedepohl K.H. *The composition of the continental crust*. Geochimica et Cosmochimica Acta. **59**, p.1217-1239 (1995).
- International Atomic Energy Agency “*IAEA-375 Radionuclides and Trace Elements in Soil*”, http://nucleus.iaea.org/rpst/Documents/rs_iaea-375.pdf (2000).
- Garcia-Talavera M., Laedermann J.P., Decombaz M., Daza M.J., Quintana B. *Coincidence summing corrections for the natural decay series in γ -ray spectrometry*. J. Appl. Radiat. Isotop. **54**, p.769-776 (2001).
- Gilmore, G. *Practical Gamma-Ray Spectrometry*, 2nd edition, John Wiley, eds. (2008).

A Detailed Gamma-ray Survey for Estimating the Radiogenic Power of Sardinian Variscan Crust

M. Xhixha^{1,5}, M. Baldoncini^{2,5}, G.P. Bezzon³, G.P. Buso³, L. Carmignani⁴,
L. Casini¹, I. Callegari⁴, T. Colonna⁴, S. Cuccuru¹, E. Guastaldi⁴, G.
Fiorentini^{2,3,5}, F. Mantovani^{2,5}, G. Massa⁴, L. Mou³, G. Oggiano¹, A.
Puccini¹, C. Rossi Alvarez³, V. Strati^{2,5}, G. Xhixha^{2,3}, A. Zanon³

¹*University of Sassari, Sassari, Italy*

²*University of Ferrara, Ferrara, Italy*

³*Istituto Nazionale di Fisica Nucleare (INFN), Legnaro, Italy*

⁴*University of Siena, San Giovanni Valdarno, Italy*

⁵*Istituto Nazionale di Fisica Nucleare (INFN), Ferrara, Italy*

INTRODUCTION

The N-E Sardinia batholith is part of the European Variscan belt which is generally considered an example for hot collisional orogens. After a period of crustal thickening characterized by lower gradients, during Late Carboniferous and Early Permian times, higher geothermal gradients were diffusively established. The sources which contributed to the thermal budget of late Variscan high-temperature events are still debated. One of the hypothesis⁽¹⁾ considers an extra contribution by radioactive heating of felsic crust tectonically emplaced at the bottom of a Palaeozoic orogenic root.

It is apparent that a detailed characterization of heat-producing elements (K, U and Th) of Sardinian Variscan crust are needed by the Earth Science community. This study focus on this goal reporting the results of an extensive survey on the base of gamma-ray measurements performed in the laboratory and in situ. The K, U and Th abundances obtained for the main lithotypes of Sardinia batholiths will be used as input for modeling the geodynamic and thermal evolution of the South Variscan Belt.

RESULTS

An area of about 4165 km² was investigated with 531 in-situ measurements and 167 laboratory measurements on rock samples (**Figure 1**). In-situ measurements were performed by placing on fresh rock outcrops a portable NaI(Tl) gamma-ray detector⁽²⁾. While, laboratory measurements on rock samples were performed using a HPGe gamma-ray spectrometer⁽³⁾. The frequency distribution functions of the abundances of K (%), U (µg/g) and Th (µg/g) obtained by both methods of investigation are found to be comparable within the standard uncertainty. Therefore, we consider a unique dataset of 698 records. The geological map in scale of 1:250.000 used for sampling is described in details in Carmignani et al. (2012)⁽⁴⁾: the most frequent lithotypes in the N-E Sardinia batholith are shown in **Figure 1**.

The first step of data analysis was to study the distribution of measured ⁴⁰K, ²³⁸U, ²³²Th abundances in 698 samples, in order to have a first insight into the data structure. Furthermore, we graphically determined either a distribution is normal or lognormal according to a univariate statistics based on percent-probability P-P plot. A more formal statistical test (Kolmogorov-Smirinoff test) is applied to all data: it provides a p-value (usually p < 0.05) that can be used to decide whether or not the null hypothesis can be rejected. We verify that the distributions of ⁴⁰K and ²³²Th are well approximated by normal distributions, while the distributions of ²³⁸U are well approximated by a lognormal distribution.

The abundances (±1σ standard deviation) of K (%), U (µg/g) and Th (µg/g) in different lithotypes are summarized in **Table 1**. The radioelement concentrations show a good agreement at 1σ level with the data reported in literature⁽⁵⁾. The K, U and Th abundances were used to calculate the radiogenic heat production

rates⁽⁶⁾ for different lithotypes (**Table 1**). The calculated Th/U ratio varies in the range 1.22-5.21, to compare with 3.9 reported in Rudnick and Gao (2003)⁽⁷⁾. The uncertainty propagation for isotopic ratios and radiogenic heat production rates was calculated by Monte-Carlo method. In **Figure 2, 3** and **4** are shown the radiometric maps obtained using Kriging interpolator.

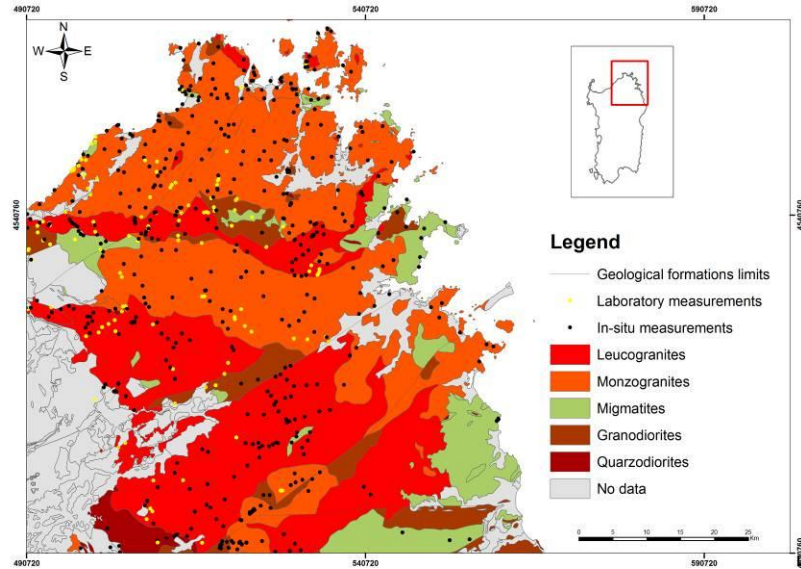


Figure 1. The distribution of the main lithotypes of N-E Sardinia batholith following Carmignani et al. (2012)⁽⁴⁾. Black and yellow circles show respectively the location of in-situ measurements and rock sample collected.

Table 1. The abundances of K (%), U ($\mu\text{g/g}$), Th ($\mu\text{g/g}$), the ratio of Th/U and the heat production rate A ($\mu\text{W/m}^3$) within 1σ standard deviation for the main lithotypes.

rock-type	No.	K (%)	U ($\mu\text{g/g}$)	Th ($\mu\text{g/g}$)	Th/U	A ($\mu\text{W/m}^3$) [*]
monzogranite	446	4.02 \pm 0.60	4.85 ^{+2.40} _{-1.62}	18.70 ^{+7.11} _{-5.17}	3.85 ^{+2.63} _{-1.56}	3.12 ^{+0.83} _{-0.63}
granodiorite	87	2.92 \pm 0.87	2.97 ^{+1.10} _{-0.81}	12.41 \pm 4.16	4.07 ^{+2.29} _{-1.63}	2.51 ^{+0.71} _{-0.55}
migmatite	25	3.42 \pm 0.60	4.55 ^{+1.40} _{-1.07}	13.10 \pm 4.76	2.81 ^{+1.48} _{-1.14}	2.52 ^{+0.51} _{-0.46}
granite	21	3.77 \pm 0.94	4.18 ^{+4.08} _{-2.07}	16.13 \pm 7.07	3.62 ^{+4.51} _{-2.16}	2.73 ^{+1.16} _{-0.81}
leucogranite	16	4.09 \pm 0.74	4.24 ^{+4.17} _{-2.11}	19.99 \pm 8.67	4.43 ^{+5.45} _{-2.63}	3.07 ^{+1.24} _{-0.91}
leuco-monzogranite	16	4.43 \pm 0.50	7.37 \pm 2.74	23.09 \pm 8.31	3.12 ^{+2.28} _{-1.31}	4.08 ^{+0.97} _{-0.95}
orthogneiss	13	3.31 ^{+0.93} _{-0.73}	4.40 ^{+2.42} _{-1.56}	12.78 ^{+5.96} _{-4.02}	2.91 ^{+2.26} _{-1.28}	2.51 ^{+0.77} _{-0.56}
amphibolite	12	1.56 \pm 0.70	2.11 \pm 0.71	8.01 ^{+2.90} _{-2.14}	3.89 ^{+2.57} _{-1.39}	1.57 ^{+0.34} _{-0.32}
eclogite	11	0.22 ^{+0.27} _{-0.12}	0.31 ^{+0.34} _{-0.16}	0.37 ^{+1.78} _{-0.31}	1.22 ^{+6.79} _{-1.04}	0.20 ^{+0.22} _{-0.09}
sienogranite	11	4.52 \pm 0.51	5.58 ^{+4.27} _{-2.40}	26.31 \pm 5.46	4.64 ^{+3.80} _{-2.14}	3.87 ^{+1.20} _{-0.78}
alkaline-granite	10	3.96 \pm 0.19	4.16 \pm 1.33	19.85 ^{+5.19} _{-4.16}	4.86 ^{+2.71} _{-1.52}	2.95 ^{+0.52} _{-0.48}
porphyry	7	4.45 \pm 0.46	4.92 \pm 1.84	18.88 \pm 6.08	3.82 ^{+2.71} _{-1.51}	3.11 \pm 0.67
monzo-granodiorite	6	3.54 \pm 0.67	4.65 \pm 1.76	14.03 \pm 1.96	3.01 ^{+1.89} _{-0.90}	2.60 \pm 0.50
quarzodiorite	6	1.14 \pm 0.35	1.28 \pm 0.81	3.93 \pm 1.92	2.73 ^{+3.81} _{-1.72}	0.73 \pm 0.26
tonalite	6	1.94 \pm 0.92	1.93 \pm 0.77	10.15 \pm 3.35	5.21 ^{+3.99} _{-2.13}	1.44 \pm 0.33
monzo-sienogranite	5	4.40 \pm 0.26	8.65 \pm 3.63	29.26 \pm 2.98	3.36 ^{+2.36} _{-1.04}	4.87 \pm 1.00

* The heat production rate was calculated taking a density of 3.30 g/cm^3 for amphibolites and eclogites, and 2.75 g/cm^3 for the other lithotypes.

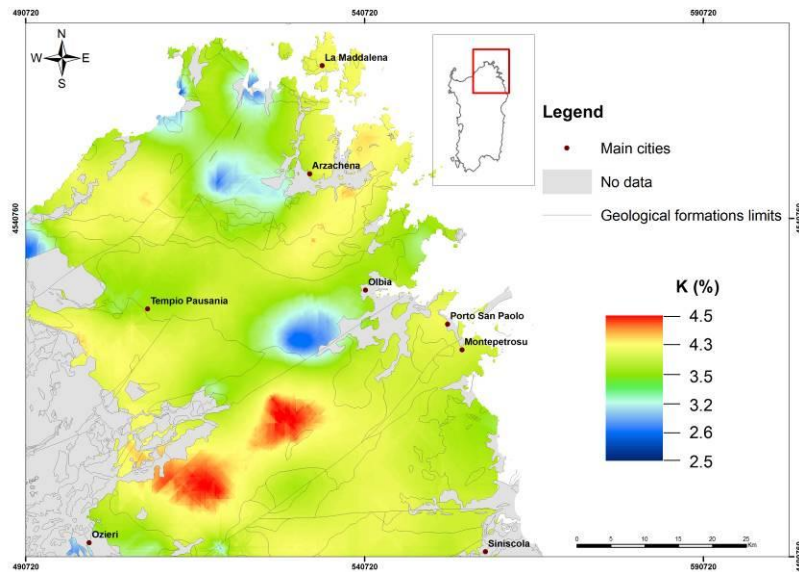


Figure 2. The distribution of K (%) in the N-E Sardinia batholith.

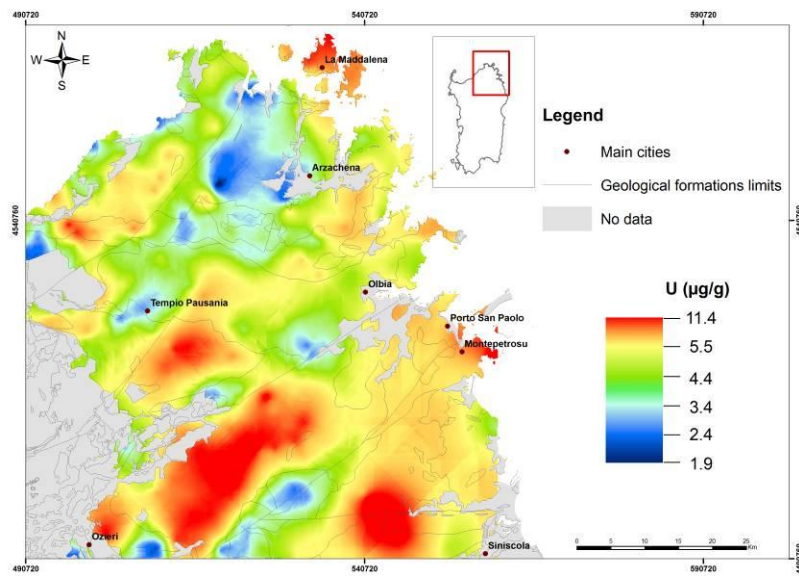


Figure 3. The distribution of U ($\mu\text{g/g}$) in the N-E Sardinia batholith.

CONCLUSIONS

The radioactivity content of Sardinia Hercynian basement (4165 km^2) was investigated on the base of 698 data, corresponding to an average of 1 sample per 6 km^2 . The statistical data analysis shows a Gaussian distribution for K and Th, and log-normal distribution for U abundances. The average K, U and Th abundances in the upper-crust rocks are higher than those typical reported in Rudnick and Gao (2003)⁽⁷⁾.

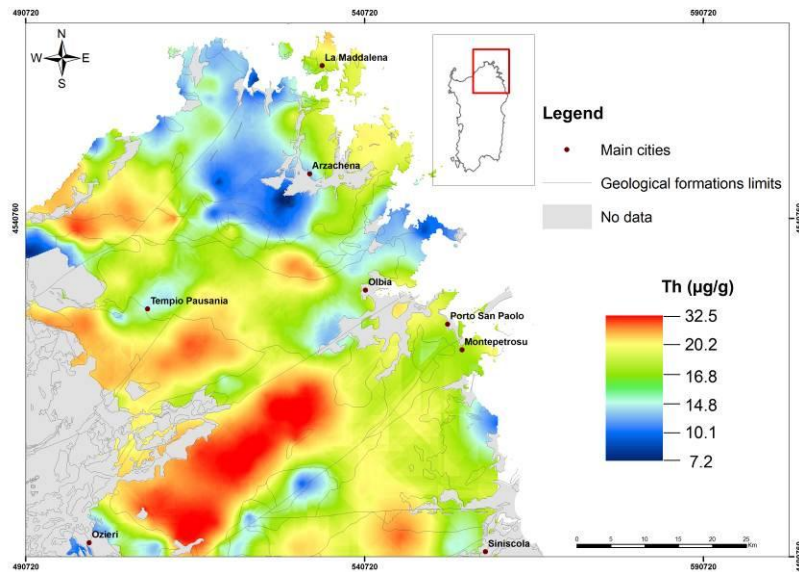


Figure 4. The distribution of Th ($\mu\text{g/g}$) in the N-E Sardinia batholith.

The spatialization of the heat-producing elements concentrations in the crustal rocks is obtained by ordinary Kriging interpolation. The maps of K, U and Th content not only show clearly the main geological and tectonic structures (i.e. the oceanic crust remnants in the northern part of the island and the Variscan and metamorphic complexes) but they permit to outline different metamorphic grade of the basement. The heat production rate calculated for the main lithotypes will be a benchmark for constraining the models which describe the early Permian high-temperature metamorphism of the Sardinia Variscan belt.

REFERENCES

1. Lexa O., et al. *Heat sources and trigger mechanisms of exhumation of HP granulites in Variscan orogenic root.* *J. Metamorph. Geol.* **29**, p.79-102, (2011).
2. Caciolli A., et al. *A new FSA approach for in situ gamma-ray spectroscopy.* *Sci. Tot. Environ.* **414**, p.639-645, (2012).
3. Xhixha G., et al. *The worldwide NORM production and a fully automated gamma-ray spectrometer for their characterization.* *J. Radioanal. Nucl. Chem.* **295**, p.445-457, (2013).
4. Carmignani, L., et al. *Carta Geologica della Sardegna. Scala 1:250.00.* (2012).
5. Merita K. Xh. *New gamma-ray spectrometry methods for estimating K, U, Th concentrations in rocks of the Sardinia Batholith.* PhD. Thesis in Natural Sciences, University of Sassari, p.204 (2013).
6. Fiorentini G., et al. *Geo-neutrinos and earth's interior.* *Phys. Rep.* **453(5-6)**, p.117-172, (2007).
7. Rudnick R. L., Gao S. *Composition of the Continental Crust.* In *Treatise on geochemistry.* Eds. H.D. Holland and K.K. Turekian. pp. 659. Elsevier, p.1-64, (2003).

Measurement of Tritium Activity in Plants by Ice Extraction Method

O.Pelled, S.Ovad, Y.Tubul, S.Tsroya, R.Gonen, A.Abraham, M.Weinstein, U.German

Nuclear Research Center, Negev, P.O.B 9001 Beer Sheva, 84190, Israel.

INTRODUCTION

Tritium is produced primarily by interactions of cosmic rays with the atmosphere. However, nuclear installations may add significantly tritium to the surroundings, increasing its concentration. The main sources of tritium released by man are linked to the nuclear power cycle: nuclear power stations, nuclear fuel reprocessing plants or tritium production plants⁽¹⁾. Tritium is found in the environment mainly as tritiated water, in gaseous or liquid form (HTO, T₂O), in the surrounding air and in soil. It accumulates in plants, which may use as a measure to the level of tritium concentration in the environment.

The most common routes of tritium uptake from the environment in plants are from atmospheric humidity and by precipitation water which entered the soil⁽²⁾. The fraction of tritium bound to the plant tissue is small compared to that present as tritiated water in the plant (from 0.06% to 0.3% for growing crops). The tritiated water uptake is through the roots, as tritiated water from the soil follows a pathway similar to that of ordinary water. As most tritium in plants consists of tritiated water, the measurements of only the tissue free water tritium concentration (as HTO or T₂O) gives an accurate estimate of the tritium content in the plant.

Analyzing free tritium in biological matrices usually requires using the freeze-drying method to extract the water from the sample, and then measure the water collected in a cold trap with a Liquid Scintillation Counter (LSC). The "freeze-drying" occurs because of the sublimation of the frozen water inside the plant, that takes place when the temperature is beneath the triple point and the vapour pressure is low. In the temperature range of -5° to -10° C the mechanism that plants use to avoid freezing is drawing of water from the [cell protoplasm](#) into the [intercellular](#) spaces^(3,4,5). Changes in [cell membrane permeability](#) allow water to leave the cell and enter the spaces between the cells where it freezes instead of freezing within the cell and causing its death. This process continues until the cells are almost totally dehydrated. In the temperature range of -20° to -60° C the intra-cellular water freeze forms "sharp" ice crystals that cause the [death](#) of the cells. Water (H₂O) and tritiated water (HTO) behave nearly identically in both liquid and vapour phases⁽⁵⁾.

The freeze-drying method, although relatively simple, requires the use of dedicated systems and is time consuming. When a plant is frozen in a closed bag, ice is accumulated on the exterior surface of the plant and in the plastic bag that contained the sample, producing a "self-freeze drying" effect. This ice may be directly used for tritium evaluation if the tritium measurement results are compatible with the generally accepted freeze-drying (lyophilization) method. The present work presents a comparison of this simple Ice Extraction Method (IEM) for tritiated water analysis with the standard lyophilization method.

MATERIALS AND METHODS

More than 100 desert plants samples containing stem and foliage were collected, put in a double plastic bags and were frozen to -20°C for more than 3 months, allowing formation of enough ice (to produce more than 15 cc of water).

The ice from each sample was collected, melted and filtrated through filter paper (Whatman No-41), to separate solids. In some cases, when the final water sample was turbid, a distillation process was employed. After collecting the ice from the bag, the remaining plant was lyophilized and a second sample was obtained. This was done by placing the plant in a glass container, which was part of a vacuum system intended to maintain the sublimation condition and a cold trap for the water vapour collection.

The two liquid samples obtained by both methods, were counted in a liquid scintillation (LSC) system for 20 minutes. Quenching correction was applied as usual in liquid scintillation counting.

RESULTS

The vegetation used for the investigation was random plants in the Negev area. From 100 samples, only 40 results were above the Minimal Detection Activity (MDA) of the LSC system and were suitable for comparison. Fig.1 shows the tritium activity ratio $A_{\text{IEM}}/A_{\text{lyophilization}}$ of the samples prepared by the two methods. The blue (triangle) marks indicate results with a large standard deviation ($>50\%$) caused by a very low tritium activity, near the MDA of the LSC system (0.01Bq/cc). The red (circle) marks are related to results with a standard deviation lower than 30% .

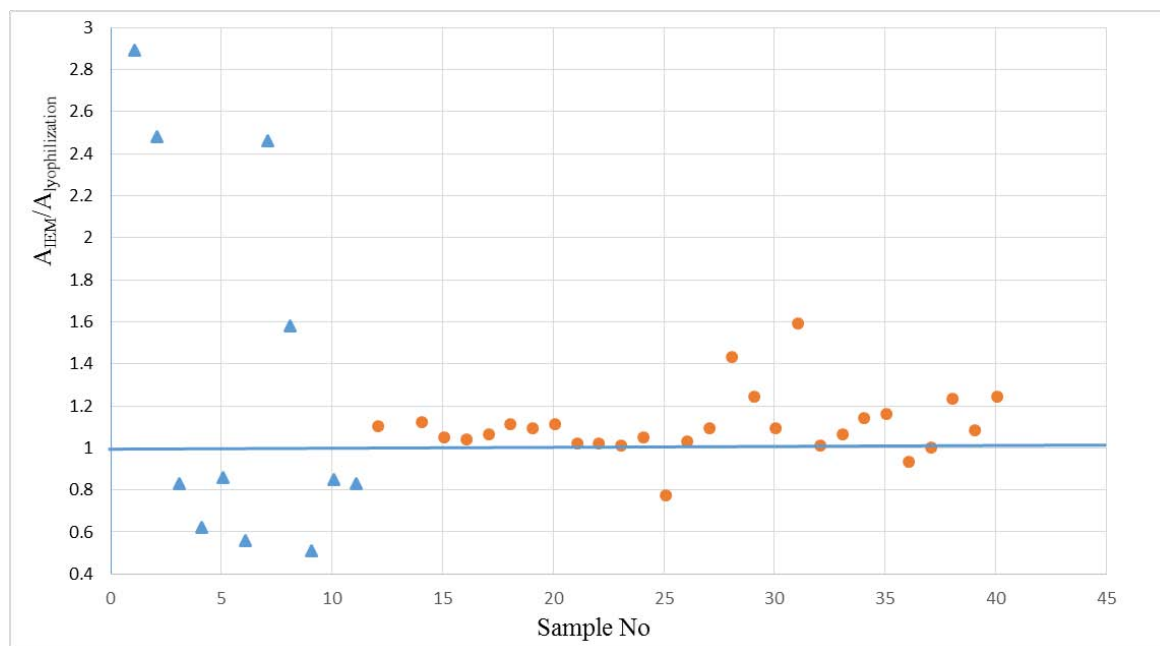


Fig.1: The tritium activity ratio $A_{\text{IEM}}/A_{\text{lyophilization}}$ for samples containing tritium activities higher than the MDA of the LSC system.

It can be seen that most results, except the values for very low activities with very high associated statistical uncertainties, show an agreement of up to about 20% between the IEM and the standard lyophilization methods. The average ratio is 1.14 ± 0.26 , which indicates a slightly bias of approximately 15% in favour of the IEM method. However, this bias is within the standard error of the average.

CONCLUSIONS

A very simple method named Ice Extraction Method (IEM) for tritiated water analysis in plants was checked in comparison to the standard lyophilization method. No preparation system is needed, as the ice which is formed in the bags containing the plants during their stay in the freezer is directly used. Plants from the natural environment in the Negev were used for this check, which contained very small tritium activities (mostly below MDA), therefore the statistical uncertainties are high. A comparison to the standard lyophilization method indicates a good agreement, within the statistical constraints. More in-depth investigation is needed to validate the method with plants containing higher tritium activities, as growing them in a controlled tritium environment.

REFERENCES

1. Okada, S., Momoshima, N., Overview of tritium: characteristics, sources and problems. *Health Phys.* 65, (1993) 595–608.
2. C. Boyer, L. Vichot, M. Fromm, Y. Losset, F. Tatin-Froux, P. Guetat, P.M. Badot. Tritium in plants: A review of current knowledge. *Environmental and Experimental Botany* 67, (2009) 34–51.
3. J. S. McKenzie, C. J. Weiser, E. J. Stadelmann, M. J. Burke. Water Permeability and Cold Hardiness of Cortex Cells in *Cornus stolonifera* Michx. *Plant Physiol.* 54, (1974) 173-176.
4. R. S. Pearce. Plant Freezing and Damage, *Annals of Botany* 87, (2001) 417-424.
5. B. J. Andraski, M. W. Sandstrom, R. L. Michel, J. C. Radyk, D. A. Stonestrom, M. J. Johnson, and C. J. Mayers. Simplified Method for Detecting Tritium Contamination in Plants and Soil. *J. Environ. Qual.* 32, (2003) 988–995.

Damage Curves of a Nuclear Reactor Structure exposed to Air Blast Loading

I. Brandys^{1,2}, D. Ornai², Y. Ronen²

¹*Nuclear Research Center Negev, P.O.Box 9001, Beer-Sheva, Israel*

²*Ben-Gurion University of the Negev*

INTRODUCTION

Nuclear Power Plant (NPP) radiological hazards due to accidental failure or deliberated attacks are of most concern due to their destructive and global consequences: large area contaminations, injuries, exposure to ionizing radiation (which can cause death or illness, depends on the levels of exposure), loss of lives of both humans and animals, and severe damage to the environment. Prevention of such consequences is of a global importance and it has led to the definition of safety & design guidelines, and regulations by various authorities such as IAEA, U.S. NRC, etc. The guidelines define general requirements for the integrity of a NPP's physical barriers (such as protective walls) when challenged by external events, for example human induced explosion⁽¹⁾. A more specific relation to the design of a NPP is that its structures and equipment (reactor building, fuel building, safeguards building, diesel-generator building, pumping station, nuclear auxiliaries building, and effluent treatment building) must function properly: shutdown the reactor, removal of decayed heat, storage of spent fuel, and treatment and containment of radioactive effluents) under external explosion. It requires that the NPP's structures and equipment resistance to external explosion should be analyzed and verified. The air blast loading created by external explosion, as well as its effects & consequences on different kinds of structures are described in the literature⁽²⁾. Structural elements response to the air blast can be analyzed in general by a Single Degree of Freedom (SDOF) system that converts a distributed mass, loads, and resistance to concentrated mass, force, and stiffness located at a representative point of the structure's element where the displacements are the highest one. Proper shielding should be designed if the explosion blast effects are greater than the resistance capacity⁽³⁾. External explosion effects should be considered within the Screening Distance Value (SDV) of the NPP since its critical systems must withstand the blast loading⁽³⁾. This research on the NPP blast damages due to an external blast loading enables better protectiveness and resilience of NPP that is exposed to blast.

AIR BLAST PHENOMENA

A shock wave (Fig. 1a) is a result of an explosion. In the free air the pressures rises immediately to a peak incident pressure, P_{so} , which decreases exponentially while crossing the ambient pressure after duration time, t_o , towards a suction phase that lasts t_o^- in which the pressure is lower than the ambient pressure. If the shock wave hits normally a structural element such as structure's wall, it reflects back and the peak reflected pressure, P_r , is at least two times greater than P_{so} . Fig. 1b displays a pressure-time history of above ground explosion. Based on experimental data⁽⁴⁾, due to 100 kgs of TNT hemispherical explosion 10m away a wall, the incident pressure is 239.2kPa and the reflected pressure is 842.3kPa with positive duration of 9.6 milliseconds.

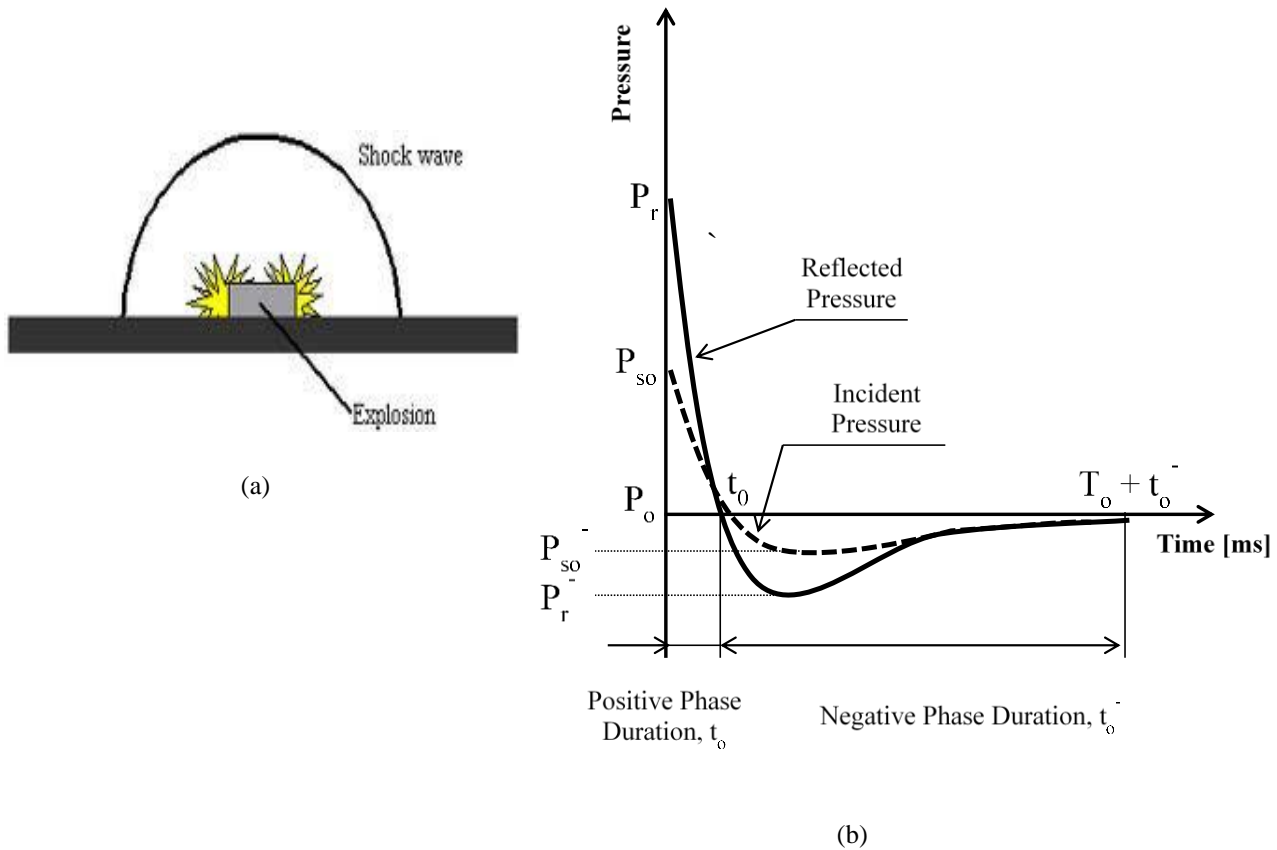


Fig. 1: (a) Shock wave caused by explosion, (b) Pressure-time variation of above ground explosion

RESEARCH METHOD

This work presents a structural dynamic analysis of a typical nuclear reactor reinforced concrete wall exposed to an external blast loading, as shown in Fig. 2. In this study there is a standoff between the explosion and the wall, as it may happen for most of the missile, air bomb, and artillery hits. The wall should not fail or harm its occupants, the internal equipment and systems since they are essential for the NPP safety⁽³⁾. The nuclear reactor containment structure may be even analyzed against a direct hit because of its importance. The analysis method is based on the following assumptions, definitions and approximations:

1. The dimensions of a representative vertical strip of the wall are 1x5x0.4 m (width x height x thickness). It includes $\phi 12@100/100$ mm reinforcement bars meshes at the front and at the back sides of the wall with concrete cover of 30 mm.
2. The concrete type is B-30 (compressive strength of 30 MPa) according to the Israeli standard.
3. The wall is fixed both to the floor at its bottom and to the roof at its top.
4. The suction phase is ignored⁽²⁾.

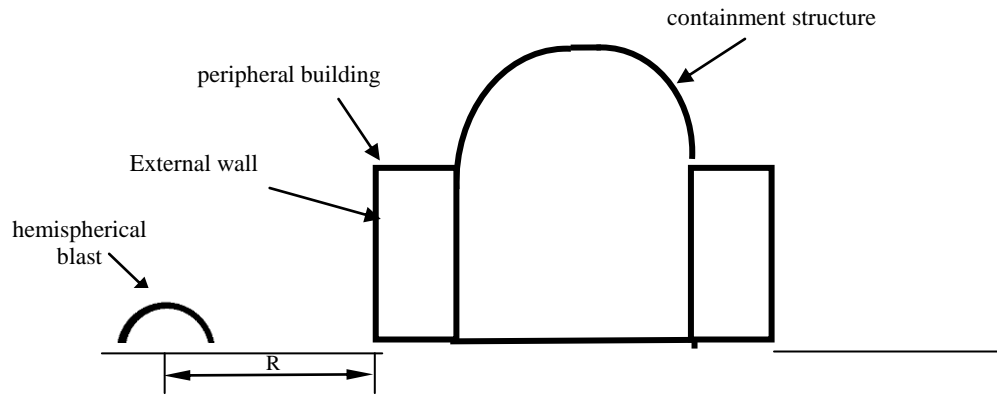


Fig. 2: Nuclear reactor structure elevation (for example: Pressurized Water Reactor)

The NPP's structural damages due to external blast loading will be described by using Pressure-Impulse (P-I) diagram, that is also called damage curves⁽²⁾ of the structural elements (columns, load bearing walls, beams, etc.), as shown in Fig. 3. The impulse is the integration of pressure by time. Each structural damage level between no damage (0%) to severe damage or destruction (100%) is based on the results of a structural dynamic analysis of many P-I pairs. Then they are compared to specific explosion scenario and by that the NPP's resistance and vulnerability is estimated.

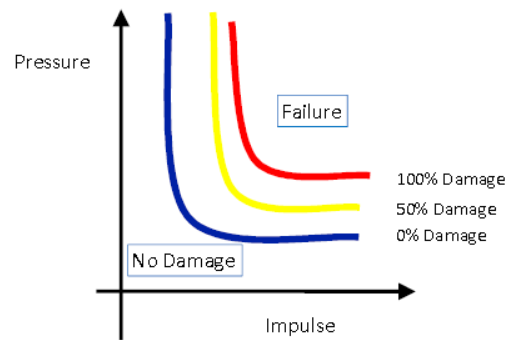


Fig. 3: Typical P-I diagram

FUNDAMENTAL RESULTS

The resistance curve of a reinforced concrete wall was calculated, considering the midpoint as the representative point where the concentrated mass, stiffness, and force is acting. A failure was defined when the angle at the supports reached 2° . Several hemispherical blast charges at different distances were defined, as shown in Table 1.

The calculations predict that the wall will be breached and fail while causing casualties and damages to the interior spaces under blast loading of 100kgs TNT (Trinitrotoluene) charge at a distance of 5m and 1000kg TNT charge at 5m and 10m. Spalling (the thrown concrete debris from the wall internal face) is supposed to occur due to 100 kgs TNT charges located at 10m and 5m from the wall and for 1000 kgs TNT at 20m, 10m, and 5m.

R [m]	5		10		20	
W [kgs TNT]	P_{so} [kPa]	I_s [kPa·ms]	P_{so} [kPa]	I_s [kPa·ms]	P_{so} [kPa]	I_s [kPa·ms]
10	202.1	252.6	49.3	136.7	16.5	71.8
100	1155.8	1064.1	239.2	583.1	56.5	314.6
1000	4848.5	1655.2	1308.2	2310.9	284.5	1336.6

Table 1 :Explosive charge weights, locations, and related pressures & impulses

SUMMARY

A typical nuclear reactor reinforced concrete wall resistance to blast loading was examined. Explosive charges at certain locations might cause casualties and damages to the interior parts of the NPP due to spalling, breaching or wall failure. The protectiveness and the resulted NPP's safety can be improved according to the requirements, based on advanced retrofit techniques.

REFERENCES

- *External Human Induced Events in Site Evaluation for Nuclear Power Plants*, IAEA Safety Standards Series, NS-G-3.1, (2002).
- Krauthammer T. *Modern protective structures*, Boca Raton, Florida, CRC Press, (2008).
- *External Events Excluding Earthquake in the Design of Nuclear Power Plants*, IAEA Safety Standards Series, NS-G-1.5, (2003).
- Kingery, C. N. and Bulmash, G., *Airblast Parameters From TNT Spherical Air Bursts and Hemispherical Surface Bursts*, ARBRL-TR-02555, (1984).

Numerical Simulation of a Single-Phase Closed-Loop Thermo-Siphon in LORELEI Test Device

D. Gitelman¹, H. Shenha¹, Ch. Gonnier³, D. Tarabelli³, A. Sasson¹, Y. Weiss¹, M. Katz²

¹*Rotem Ind, Mishor Yamin, D.N Arava, Israel*

²*NRCN, P.O.Box 9001 Beer Sheva, 84190, Israel*

³*French Atomic Energy Commission (CEA) – Cadarache Centre, France*

INTRODUCTION

The LORELEI experimental setup in the Jules Horowitz Reactor (JHR)⁽¹⁾ is dedicated for the study of fuel during a Loss of Coolant Accident (LOCA). The main objective of the LORELEI⁽²⁾ (Light-Water One-Rod Equipment for LOCA Experimental Investigation) is to study the thermal-mechanical behavior of fuel during such an accident and to produce a short half-life fission products source term. In order to study those phenomena, the fuel sample will experience a transient neutron flux field, which in turn will generate a Linear Heat Generation Rate (LHGR) and determine the temperature of the fuel and its cladding, simulating the behavior of the fuel and the cladding during a LOCA accident.

In order to reproduce a LOCA-type transient sequence, the experimental test device will be located on a displacement device. The displacement device moves the test device in the flux field in order to generate a representing LHGR in the fuel or temperature of its cladding.

The LOCA-type transient sequence has four major features:

- An adiabatic heating of the fuel up to the ballooning and burst occurrence.
- High temperature plateau which will promote clad oxidation.
- Passive precooling by thermal inertia.
- Water re-flooding and quenching.

The challenge in the thermo-hydraulic design of the LORELEI test section is in defining a one closed water capsule design that can operate as a thermo-siphon at re-irradiation phase and also can reproduce all LOCA-type transient sequence phases. This design should be validated and verified to fill all safety and regulation requirements.

This work aims to investigate fluid flow behavior of a single-phase thermo-siphon in the LORELEI test device, as part of the conceptual design and optimization study. The complexity of the flow field in the LORELEI test device, as a closed-loop thermo-siphon, is due to the opposing forces in the device - buoyancy forces and natural convection flow generated (mainly) by the fuel power in the hot channel, opposed by buoyancy forces generated by non-uniform gamma power generated in the device structure.

As a first stage, an average 2D axisymmetric model was studied and compared with a 1D CATHARE analysis. Modeling of a 3D power distribution in the system, generated by gamma heating, presents a very complex flow field due to the asymmetric opposed buoyancy forces.

NUMERICAL MODEL

The numerical calculations were performed by FLUENT, commercial CFD software. As a consequence of a non-uniform axial and azimuthal power distribution of heat sources shown in Figure 1 and in order to have complete view of the flow, 3D geometry was used.

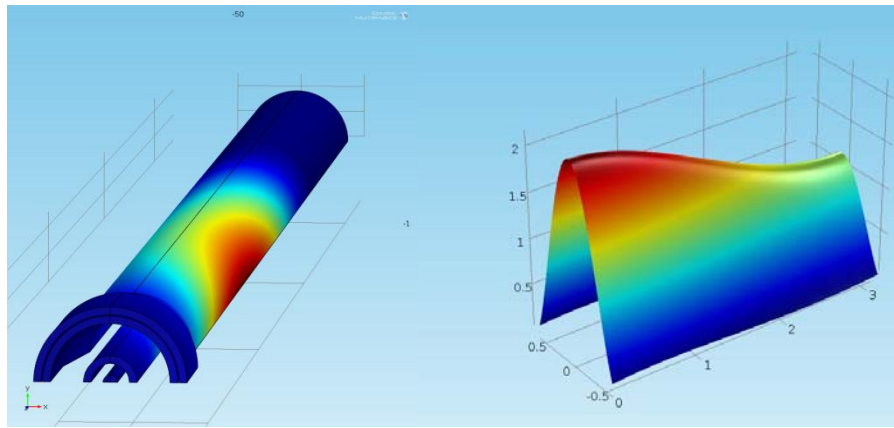


Figure 1. Non-uniform axial and azimuthal gamma heating distribution.

Assuming axial middle plane symmetry, only a half of the experimental capsule body was simulated. Mapped mesh method was chosen for the model for its best fit for the flow direction. Solutions from different mesh size models were compared in order to insure solution mesh independence. The final mesh shown in Figure 2 consists of about 1.5M elements.

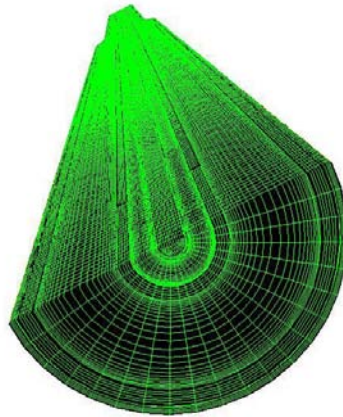
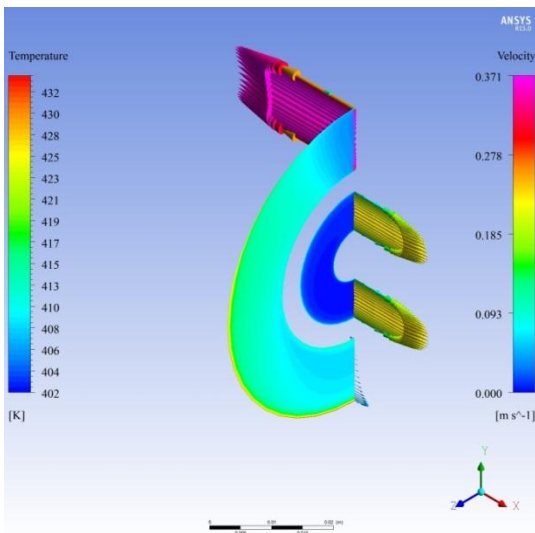


Figure 2: Numerical mesh in a 3D model. 1.5M elements.

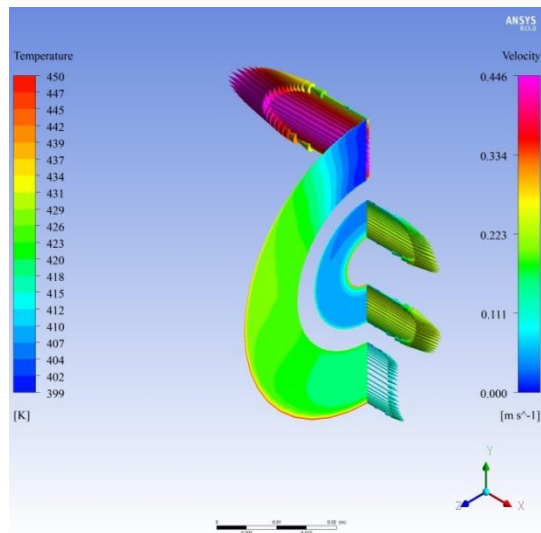
Conjugated turbulent natural convection with heat transfer model was solved. As a viscous model for the flow, a RNG $k-\epsilon$ turbulence model with enhanced wall treatment was chosen. The pressure of the system was set to 70 bars, which is the nominal pressure of the re-irradiation phase.

RESULTS

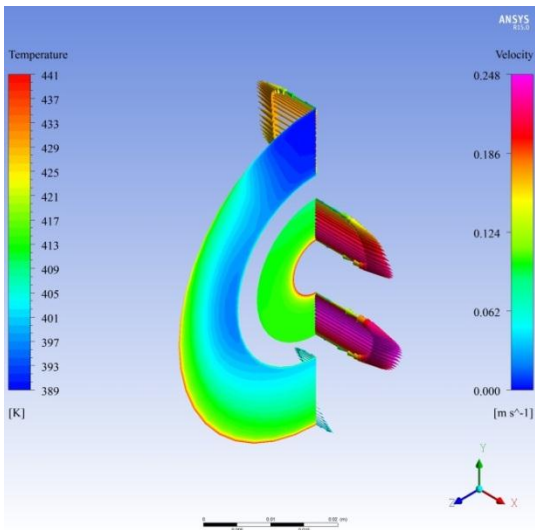
The simulation shows that at the influx part of inner flask there is an azimuthal temperature distribution as a result of the azimuthal gamma heating distribution. This thermal azimuthal distribution generates local circulations in flow field. Figure 3 presents temperature and velocity radial and azimuthal distribution for water channels at fuel rod inlet, center and outlet cross sections respectively.



a. Fuel bottom end cross section



b. Fuel middle cross section



c. Fuel top end cross section

Figure 3: Velocity vectors and temperature contours at different cross sections

CONCLUSIONS

In this study, the thermosyphon flow in the LORELEI test device during the re-irradiation phase was analyzed. The strong gamma radiation field surrounding the test section generates non-uniform gamma power in the structure. The consequent flow field is irregular where circulations occur in the cold channel due to strong buoyancy forces. In order to improve the flow field, the balance between buoyancy forces and friction losses should be changed.

REFERENCES

1. Estrade J. et al, *The Jules Horowitz Reactor: a new performance European MTR (Material Testing Reactor) with modern experimental capacities – Building an international user facility*. Research Reactor Fuel Management 2013. 21-25 April, St-Petersburg, Russia, (2013).
2. Gonnier C. et al, *Fuel and material irradiation hosting systems in the Jules Horowitz Reactor*. Joint IGORR 2013 & IAEA Technical Meeting, 13-18 October, DCC, Daejeon, Korea, (2013).

Thermal Design of the LORELEI Test Device Using a COMSOL Inverse Solver

H. Shenha⁽¹⁾, D. Gitelman⁽¹⁾, I. Preker⁽¹⁾, M. Arbel-Haddad⁽²⁾,
L. Ferry⁽³⁾, A. Sasson⁽¹⁾, Y. Weiss⁽¹⁾ and M. Katz⁽²⁾

(1)Rotem Ind., Mishor Yamin, D.N Arava 86800, Israel

(2)NRCN, P.O.Box 9001 Beer Sheva, 84190, Israel

(3)French Atomic Energy Commission (CEA) – Cadarache Centre, France

INTRODUCTION

The LORELEI (Light-Water One-Rod Equipment for LOCA Experimental Investigation) test device in the Jules Horowitz Reactor (JHR) is dedicated to study fuel thermo-mechanical behavior during Loss of Coolant Accident (LOCA) in power reactors. By using a displacement device, the fuel sample moves in the neutron flux field and generates heat according to its location. A typical fuel clad temperature variation has been defined which simulates some specific thermal conditions as in a real LOCA scenario. The design of the LORELEI test device should be able to produce this temperature variation profile by the movement of the experimental setup on the displacement device.

The goal of this study was to develop a numerical model that calculates, for a given geometry, the transient device position that will generate the desired clad temperature profile. The LOCA-type transient sequence has four major features:

- An adiabatic heating of the fuel up to the ballooning and burst occurrence.
- High temperature plateau which will promote clad oxidation.
- Passive precooling by thermal inertia.

This work will present the thermal analysis of the LORELEI test device, performed using the COMSOL model. The sensitivity of cladding temperature to various parameters such as cladding strain level, fuel porosity and oxidation reaction model was investigated. Figure 1 presents schematic representation of the cladding ballooning and strain level and experimental observation of cladding burst. Some results of the parametric study will be presented.

THE NUMERICAL MODEL

A 2D axisymmetric model was developed in COMSOL Multiphysics software. The power generated by the oxidation reaction of the Zirconium cladding, during the thermal sequence has been defined as a first order differential equation and was coupled to the temperature variation in the model. The system position was defined using a mathematical simulator (differential equation) of a PID controller that was respectively implemented in the same model. The PID controller calculates the position of the system and as an outcome the power that is generated in the fuel sample, for a required clad temperature profile. Another simulator of a PID controller was defined and implemented to meet the adiabatic conditions for the fuel sample, during the adiabatic heating phase.

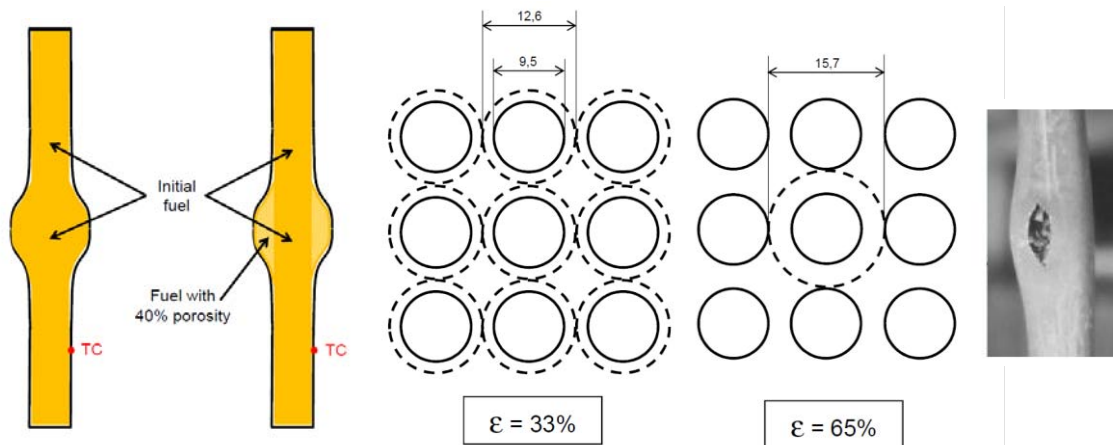


Figure 24: Thermo-mechanical behavior of the cladding during LOCA scenario (ballooning, different strain levels, and burst).

RESULTS

Figure 2 presents a typical result of the transient maximum cladding temperature profile (at the hot spot) and the corresponding position of the displacement device. The hot spot temperature variation in time is similar to the required profile according to the experimental objectives and the displacement device position (in red line) throughout the experimental phases is in its range of motion.

Measuring the hot spot temperature directly is not possible due to the possibility to interfere with the thermo-mechanical process (ballooning and burst). Measuring the hot spot temperature by a thermocouple located on the peripheral heating element was proposed. Figure 3 presents the fuel cladding temperature and the heater temperature. As one can see, the inner wall temperature of the heater is typically following the temperature profile of the fuel cladding and gives indications for the ballooning higher temperature. This result support the feasibility to predict the hot spot temperature on the clad by measuring temperature on the heater.

CONCLUSIONS

According to the study presented, the conceptual design of the LORELEI test device has the ability to generate the conditions needed for all experimental phases. The current design is sufficiently robust to ensure safety in critical abnormal scenarios.

The sensitivity of the device temperature to the occurrence of the ballooning was defined with the coupled COMSOL model and a method to control the experiment without direct measurement of the temperature on the clad, was suggested and verified.

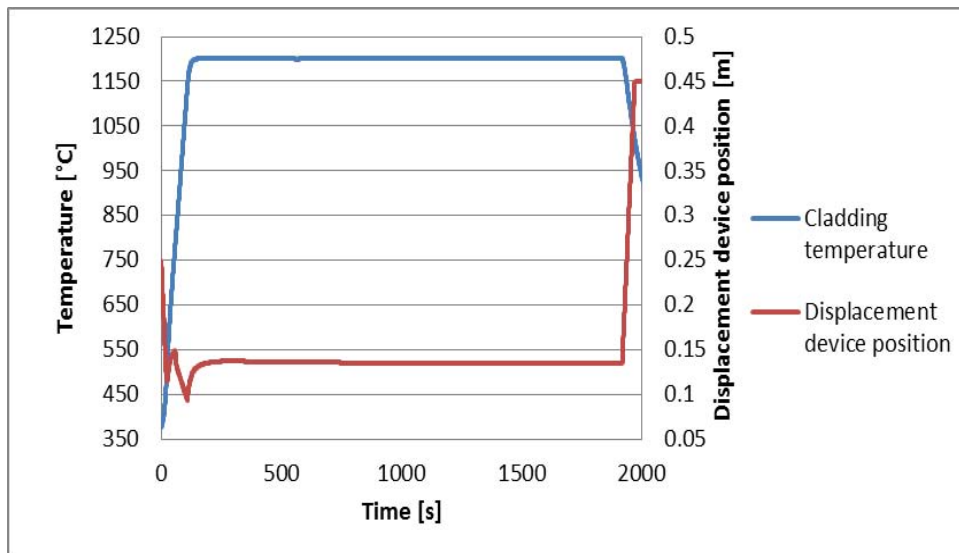


Figure 25. Displacement device position and cladding maximal temperature throughout the experimental sequence

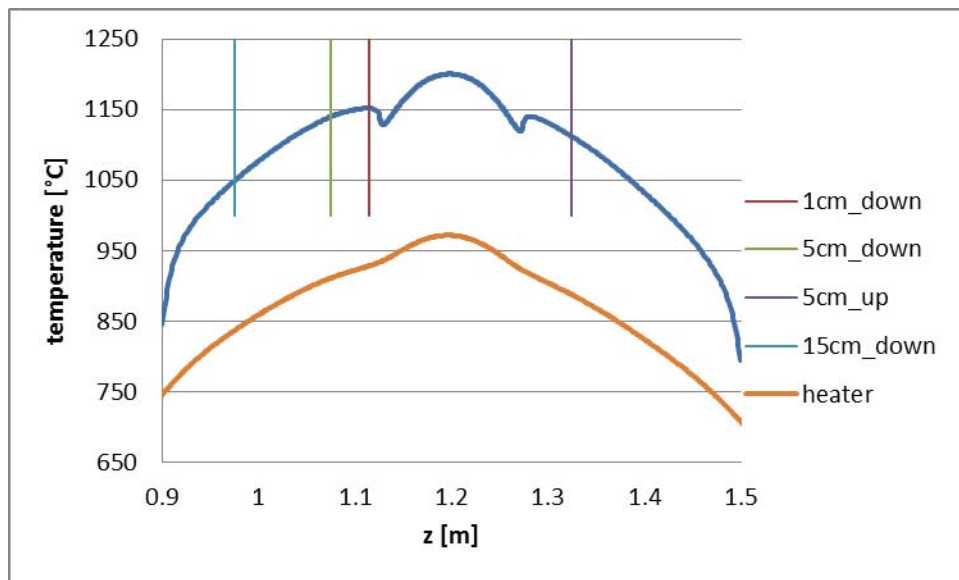


Figure 26. Cladding and heater temperature profile for a typical ballooning (vertical lines represent possible TC location)

Concept of the LORELEI Test Device for LOCA Experiment in the JHR Reactor

N. Moran⁽¹⁾, L. Ferry⁽²⁾, A. Azulay⁽¹⁾, O. Mileguir⁽¹⁾, Y. Weiss⁽¹⁾ and M. Szanto⁽¹⁾

⁽¹⁾ *Rotem Industries LTD, Mishor Yamin, D.N Arava 86800 Israel*

⁽²⁾ *French Atomic Energy Commission (CEA) - Cadarache Centre, France*

INTRODUCTION

Modeling of nuclear fuel cladding behavior during a Loss of Coolant accident (LOCA) is a principal requirement in reactor safety analysis. Former safety criteria were obtained from experiments during the 1970's, conducted mainly with fresh fuels. Changes in modern fuel design, introduction of new cladding materials and motivation towards higher burn-ups have generated a need to re-examine safety criteria and their continued validity. This led to the growing development of both experiments and simulations meant to address this need. The Halden IFA-650 [1] series of experiments for example, beginning in the early 2000's have clearly shown that existing criteria and experimental data are insufficient for the growing demand for higher burn-ups.

In JHR material testing reactor, which is currently under construction, one significant experimental device is the LORELEI testing device. The objective is to examine the LOCA sequence influence on: thermo-mechanical behavior of the fuel clad, possible fuel relocation, corrosion at high temperature, oxidation, hydriding and resulted clad embrittlement. The device is a single rod closed loop system placed on a displacement device inside a defined channel in the reflector. Several operational constraints on the device, as required by the reactor operational philosophy resulted quite a few challenges in the design. Constraints as: pre experimental re-irradiation phase under thermo-syphonic flow, application of active insulation to simulate the surrounding fuel, application of tensile force during refolding simulation, controlling the experiment with non-direct temperature measurement, etc. requires sophisticated solutions. The main objective of the conceptual design was to remove the uncertainties of those challenging requirements. The current presentation describes the approach applied defining the concept of the device, using sophisticated design combined with computational and experimental tools.

Operational requirement

The objective of the LORELEI testing device is to simulate thermo-mechanical behaviour of one LWR rod in the following aspects:

- Ballooning and clad burst with possible fuel relocation inside and outside the rod
- Corrosion at high temperature, oxidation, hydriding and resulting clad embrittlement
- Quenching and post-quench behaviour (mechanical strength)
- Radiological consequences : Fission products source term

Motivations:

- Testing of new cladding material.
- New fuel (UO₂, MOX, additives,..)
- High Burn-Up effect on the cladding material (corrosion and hydriding due to normal operation)
- Investigation of LOCA phenomenology (fuel relocation, possible coupling between fuel and clad behaviour, etc.)

The LOCA sequence realization is according to the plot in Fig. 1.

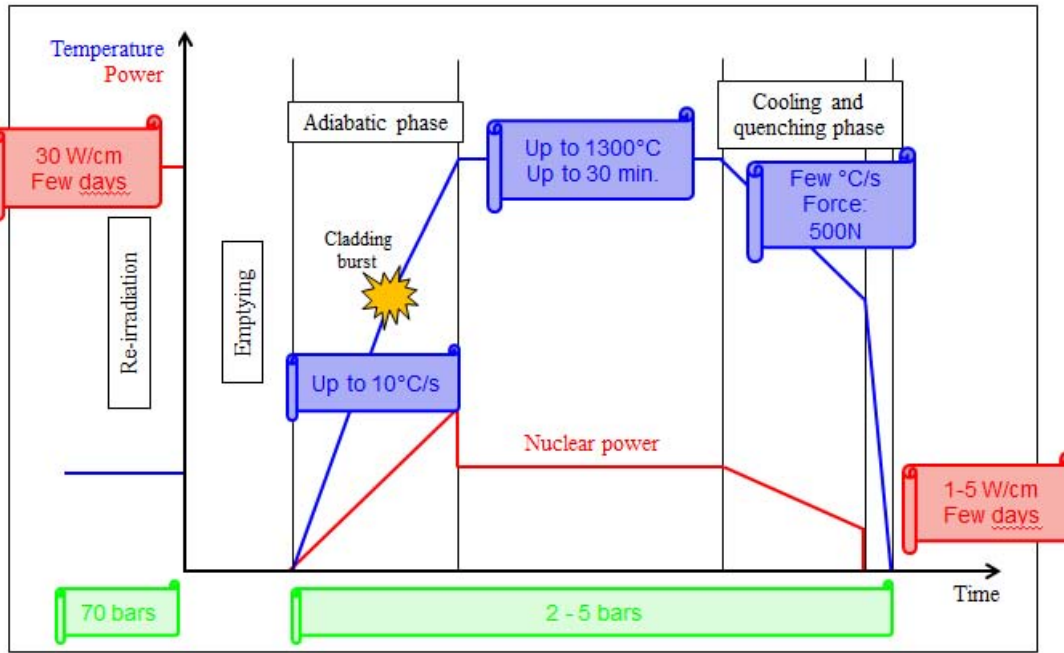


Figure 1: The sequence of the LOCA test.

The experimental device that accomplishes the sequence in Fig. 1 is under development in ROTEM industries. The conceptual design is shown in figure 2.

Among the major challenges in the roadmap toward the design are: Developing a high power and high temperature heating element, realization of a thermo-syphonic heat removal system, non-direct temperature measurement, compliance with nuclear safety regulation and more.

The current presentation describes the conceptual design of the experimental device.

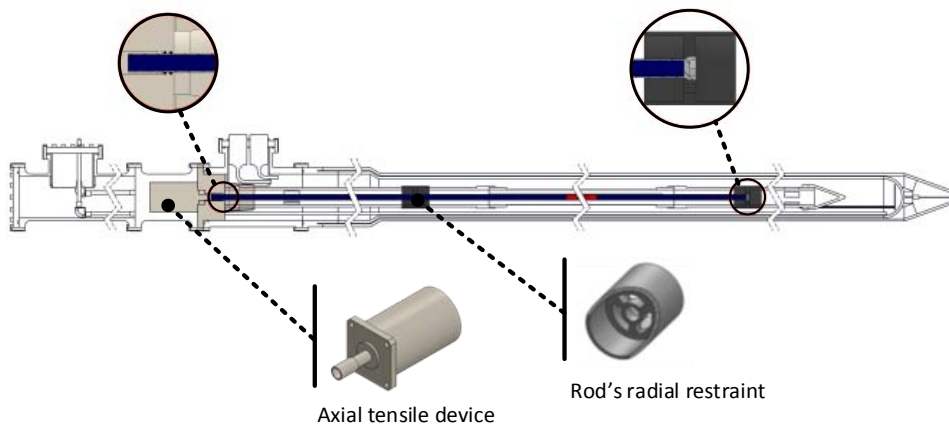


Figure 2: Conceptual design of the experimental device.

REFERENCE

1. Tero Manngård, Ali Massih, Jan-Olof Stengård(VTT), "Evaluation of the Halden IFA-650 loss-of-coolant accident experiments 2, 3 and 4," Quantum Technologies AB, Uppsala, Sweden, 2012.

Numerical Ballooning and Burst Prediction of Fuel Cladding During LOCA Transients in LWR

E. Landau¹, Y. Weiss², M. Szanto²

¹ Ben Gurion University, P.O.B. 653 Beer-Sheva 8410501 Israel

² Rotem Industries LTD, Mishor Yamin, D.N Arava 86800 Israel

INTRODUCTION

Modeling of nuclear fuel cladding behavior during a Loss of Coolant accident (LOCA) is a principal requirement in reactor safety analysis, most former safety criteria were obtained from experiments during the 1970's, conducted mainly with fresh fuels. Changes in modern fuel design, introduction of new cladding materials and motivation towards higher burn-ups have generated a need to re-examine safety criteria and their continued validity.

This led to the growing development of both experiments and simulations meant to address this need. The Halden IFA-650 [1] series of experiments for example, beginning in the early 2000's have clearly shown that existing criteria and experimental data are insufficient for the growing demand for higher burn-ups.

Several codes for reactor core and fuel rod analysis exist nowadays, such as FRAPTRAN1.4 [2] or RELAP5-3D [3]. These are tailor-made codes, designed to predict general core behavior and fuel performance, and while they are also used in predicting core components behavior during accident conditions, including those of cladding ballooning and failure with good accuracy, they contain several limitations on modeling the full transient cladding thermo mechanical phenomena. Limitations such as mechanical models being one dimensional or in axisymmetric geometries only, relying mostly on analytical models therefore having further restricting assumptions in return for accuracy, etc. These limitations disable the simulation of several important aspects, such as modeling 3D azimuthal behavior for example.

The objective of the current work is to develop a comprehensive numerical model for predicting zircalloy cladding thermo mechanical behavior during a LOCA. The model will eventually predicts full cladding ballooning and burst behavior followed by fuel relocation, for fuel rods that can be subjected to 3D distributed flux. The model is fully three dimensional and is created using the commercial FEM numerical simulation software ABAQUS[®] applying coupled user subroutines to describe the complex material behavior during the process.

The target model will eventually display wide simulation capabilities regarding thermo-mechanical phenomenon, and will grow into including multi physics couplings such as fluid-structure interactions, all relying on well tested commercial software. These capabilities will enable conducting computation on complex geometries as well as coupling to various physical phenomena. In addition, in contrary with most tailor made codes, the ABAQUS[®] interface is user friendly and affords a high level of pre and post processing capabilities, as well as being widely available.

The aim is to eventually validate and calibrate the model during the upcoming LORELEI single rod LOCA experiments in the French JHR reactor.

PRELIMINARY RESULTS

In order to validate the model as developed so far, initial results were compared with the chosen benchmark experiment and licensing code overview data from the HALDEN IFA650.2 [1] experiment for as-received cladding, originally meant for initial calibration before testing at higher burn-up fuels.

Figure 1 describes the IFA650.2 [1] applicable and available initial experimental setup data by which the comparison was performed (Figure from reference [1]).

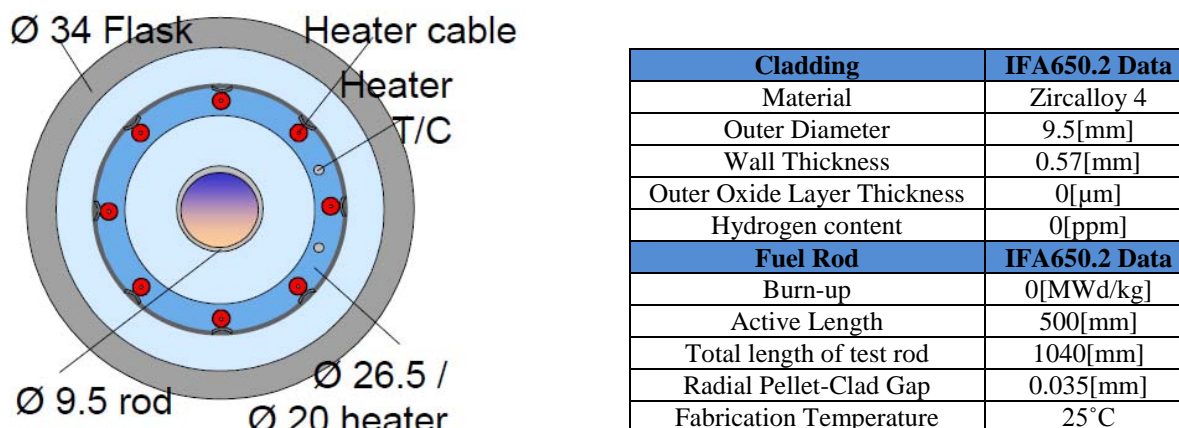


Figure 1. Halden IFA650.2 [1] experiment data for cladding geometry and user inputs.

The current model utilizes the ABQUS/Explicit VUMAT or VUHARD user type subroutines to describe the complex Thermal Elasto-Viscoplastic material behavior through an adapted isotropic hardening algorithm. The subroutine can include the effects of Over-Oxidation, Cold Work, and Irradiation damages, as well as material anisotropy, annealing, and more. Most material properties are taken from MATPRO [3], FRAPCON3.4 [4], and FRAPTRAN1.4 [2] for Zircalloy thermo-mechanical properties.

The current version does not yet however, contain an algorithm for material oxidation or ZrO₂ layer growth and accepts those as constant through the process, given as inputs by the user along with several other user input options for calibration and control.

Benchmark Comparison

Table 1 displays the values calculated by the current model version compared with the HALDEN IFA650.2 Experiment Data and the FRAPTRAN1.4 calculations of the same scenario, Figure 2 and Figure 3 display exemplary visualization of model results.

Test/Parameter	IFA650.2 Experiment	FRAPTRAN1.4 Calculation	Current Model	Deviation from Experiment [%]
Rupture Temperature [°C]	800	773 , 806	788	1.5
Max. diametric cladding Strain [%]	90	82 , 76	84.1	6.5
Internal Pressure at Rupture [MPa]	5.6	5.7 , 5.8	5.9	5.4
Oxide Layer Thickness [μm]	40-50	35	0	--
Axial Location of Rupture [mm]	195-230	--	236	2.5

Table 1. Comparable Results (at Rupture point)

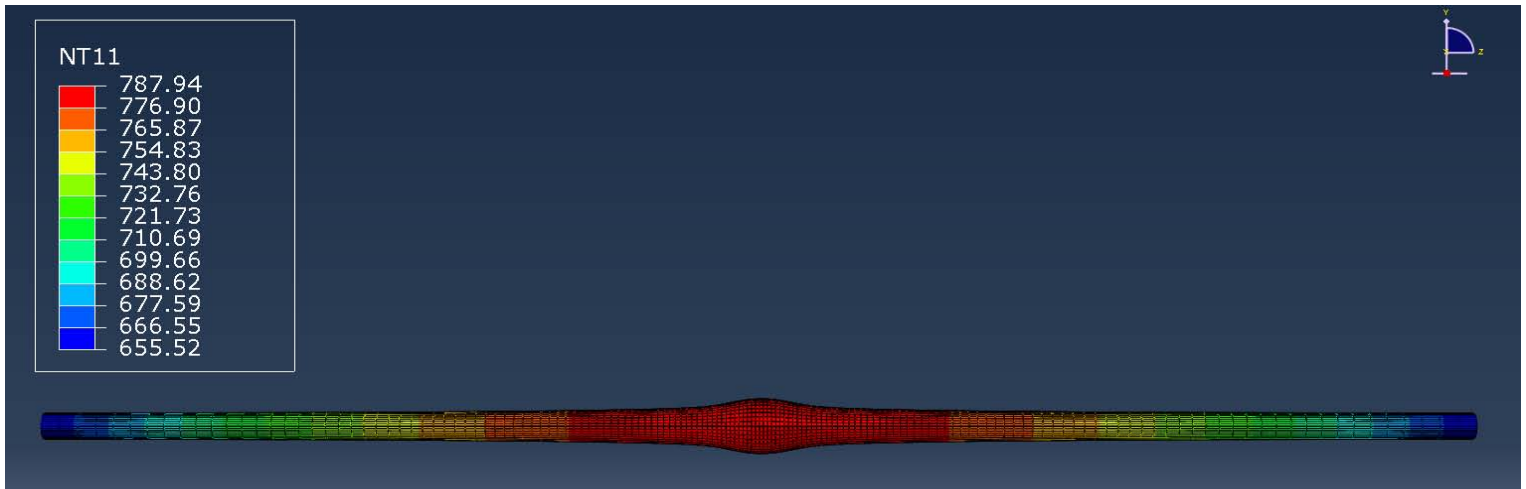


Figure 2. Example of Temperature distribution color-map of clad ballooning before rupture

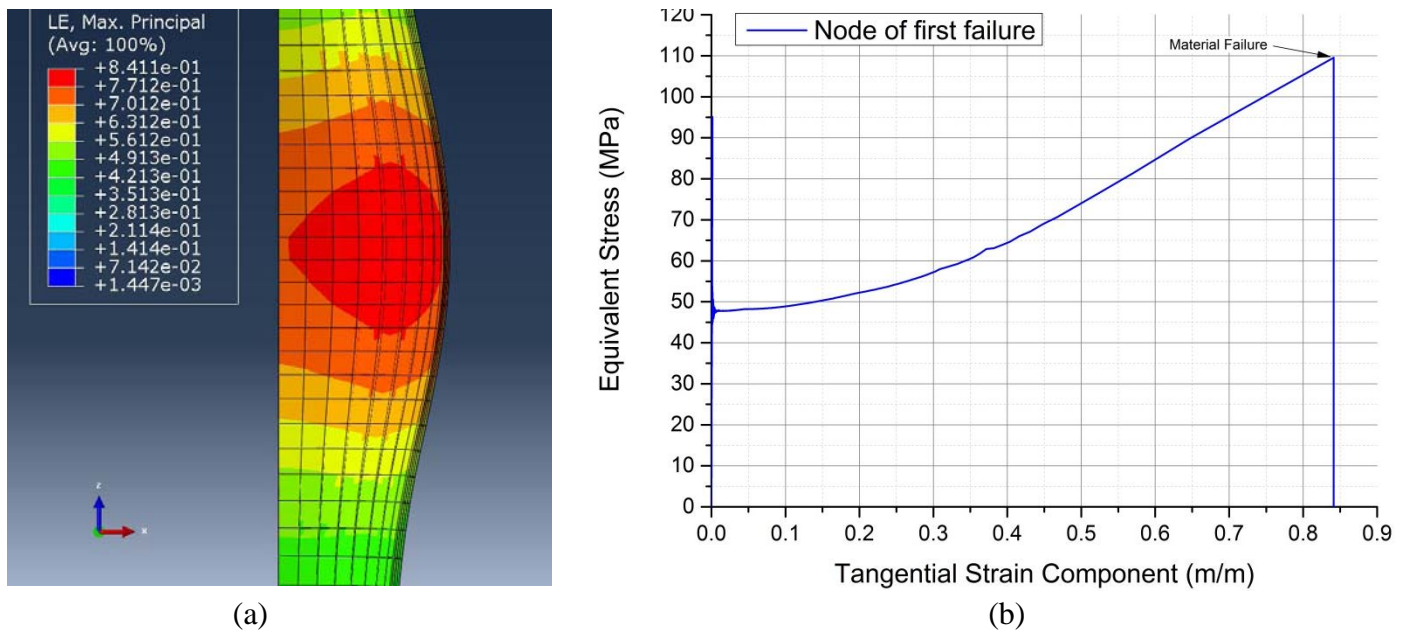


Figure 3. (a) Tangential component of logarithmic strain demonstrated on section view of inner clad diameter (b) Resulting stress-strain for the Thermal Elasto-Viscoplastic behavior (High temperature softening leading to hardening from high train rates)

CONCLUSIONS

- A comprehensive 3D model for clad ballooning and burst behavior prediction was proposed, relying on commercial FEM software with coupled user subroutines.
- Current model displayed here is still in early development stages, preliminary results were compared to the simplified case of the IFA650.2 HALDEN Experiment for as-received material.
- Preliminary results show good agreement with the IFA650.2 experiment.
- Shown here are only the key comparable parameters, many more variables are tracked during the simulation and are available for more in-depth analysis of the problem.
- Amongst Several significant advantages in using an advanced commercial numerical simulations software such as ABAQUS© is the far simpler and better detailed post-processing abilities.

REFERENCES

- [1] Tero Manngård, Ali Massih, Jan-Olof Stengård(VTT), "Evaluation of the Halden IFA-650 loss-of-coolant accident experiments 2, 3 and 4," Quantum Technologies AB, Uppsala, Sweden, 2012.
- [2] K.J. Geelhood, W.G. Luscher, C.E. Beyer, "FRAPTRAN 1.4: A Computer Code for Oxide Fuel Rods," U.S NRC, Pacific Northwest National Laboratory, 2011.
- [3] Code Development Team,, SCDAP/RELAP5-3D© CODE MANUAL, Idaho National Engineering and Environmental Laboratory, 2003.
- [4] K.J. Geelhood, W.G. Luscher, C.E. Beyer, "FRAPCON-3.4: A Computer Code for the Calculation of Steady-State Thermal-Mechanical Behavior of Oxide Fuel Rods for High Burnup," Pacific Northwest National Laboratory, Richland, 2011.

Preliminary I&C Design for LORELEI

S. Korotkin¹, Y. Kaufman¹, E. Grosman¹, B. Guttmann¹, S. Levy¹,
D. Amidan¹, B. Gdalyho¹, T. Cahana¹, A. Ellenbogen¹, M. Arad¹, Y. Weiss²,
A. Sasson², L. Ferry³, F. Bourrelly³, Y. Cohen¹

¹*NRCN, P.O.B 9001, Beer Sheva, Israel*

²*Rotem Industries LTD, Mishor Yamin D.N Arava, Israel*

³*CEA, Cadarache, DER/SRJH, Bâtiment 225-13108 St. Paul lez Durance,
France*

Key words: LORELEI, LOCA, Hybrid simulator, Eutectics, Rod ballooning, Adiabatic heating.

INTRODUCTION

The LORELEI (Light water One Rod Equipment for LOCA Experimental Investigation) device is one of the experimental platforms designed for the Jules Horowitz Reactor (JHR). It is dedicated to reproduce thermal-mechanical conditions of Light Water Reactor (PWR, BWR and VVER) in LOCA (Loss Of Coolant Accident) accident situations. The preliminary design of power, instrumentation and control for LORELEI experiment defines a conceptual I&C architecture with configuration of the control systems and the interfaces to JHR power supply networks⁽¹⁾. Conceptual Configuration of LORELEI's safety and service systems is established as well.

Temperature and position closed loop control rules were determined considering interfaces to displacement device. The automatic control rules are limited to predefined error ranges of temperature and displacement device's position. In any case the operator can intervene and take control of the experiment. The hot spot temperature and thickness of oxidation layer are essential parameters in LORELEI experiment. However, hot spot temperature cannot be measured directly and oxidation layer thickness can be calculated using adequate mathematical models only. Therefore, it is proposed to predict them in real time. Real time prediction can be performed by the proposed Computer Aided Operator Decisions System (CAODS). During the experiment CAODS predicted values will support the operator to take the proper actions. Furthermore, some predicted out of range parameters can be used for prevention or safety functions.

A hybrid simulation system comprising both virtual and real hardware will be developed for LORELEI verification. It will perform both integration cold tests with a partial hardware loop in JHR experimental area and virtual tests for the final I&C design. Additional hardware and software components will be used for simulation of external cooling channel and interfaces to safety systems. The simulator will comply with verification procedures mentioned in IEC 62138⁽²⁾ regarding software aspects for computer based systems category performing B or C functions.

The preliminary design describes considerations regarding appropriate safety and service instrumentation and their technological characteristics⁽³⁾. Preliminary electrical power design was conducted for force and I&C power supply. It determines LORELEI's expected power consumption for service and safeguard and methods for power control of Lorelei's heaters.

METHODS

Remote measurement of hot spot temperature

The study of the first LORELEI experiment will focus on 150mm and 250 mm flattened power profile section and their corresponding clad ballooning. The temperature objective of the hot spot is set to 1200°C while several requirements are dedicated to temperature thresholds or values of the hot spot. Since optical technology for non-contact hot spot temperature measurement is not expected to be available for the first experiment, thermocouples will be used for temperature measurement. The thermocouples should be assembled out-of the hot spot region in order to not interfere with the thermo mechanic phenomena. Moreover the measured temperatures should follow the hot spot temperature as close as possible. Initial position of thermocouples location attached to clad is set to ± 5 cm out of the expected ballooning zone. The clad temperature measurement in this case is limited to 940-1140°C due to eutectics of the TCs sheath. The TCs will be attached to the clad with bands without welding. Another option is to use TCs placed on the coaxial heater to overcome eutectics. The overall temperature range to be covered up to 1200°C will be divided in to two sub ranges. In range up to about 900°C the TCs attached to clad will be taken in to account because they are reliable and available. Beyond this temperature range the TCs of coaxial heater will be available. They will not be used in the first range because the heater will be in operation and remote hot spot temperature measurement will be complicated. TC switching between the ranges should be bump-less. Hot spot temperature measurement for safety is also monitored remotely by TCs, therefore their thresholds should be adjusted properly.

CAODS for real time prediction of hot spot temperature

The hot spot temperature should be monitored and controlled continuously in the LORELEI experiment. However the hot spot temperature cannot be measured directly, it should be predicted using a Computer Aided Operator Decisions System (CAODS). CAODS will be based on prediction algorithms using real time measurements, which will be collected by control system. The prediction algorithms will be obtained by using data from numerical simulations. They will cover the most probable case and at least the extreme cases of ballooning. The data will include time depended thermal responses produced by wide range profiles of electrical and nuclear power (displacement device positions). The thermal responses include hot spot, remote temperature measurements equivalent to clad, coaxial heater and safety TCs. Several algorithms will be considered for prediction such as mathematical relationships, neural networks or fuzzy logic. Validation of each algorithm will related to numerical simulations and real time electrical rod experiments. Best performance algorithm will be applied in programmable automation controller (PAC).

CAODS for real time prediction of oxidation layer thickness

Oxidation layer thickness is critical since it affects the thermo-mechanic properties of the clad and changing its dynamic behavior. Kinetics of non iso-thermal zirconium oxidation reaction caused by water fumes in LOCA scenarios can be described by Baker-Just correlation. The decision to end oxidation phase in LORELEI experiment can be computer aided using CAODS. It will calculate equivalent cladding reacted based on Baker-Just correlation.

Hybrid simulator for LORELEI verification

The hybrid simulator will rely on instrumentation, control systems and electrical cabinets designed for the LORELEI experiment. In order to perform integration cold tests, additional hardware and software components will be used for simulation of external cooling channel and interfaces to safety systems. The hybrid simulator will verify only part of LORELEI loop equipment. Some of the experiment's phases will be

verified by real I/O interfaces related to hardware elements such as peripheral heater and steam generator. The uninstalled equipment will be tested functionally by the programmable automation controller (PAC) using virtual I/O. PAC program sections will simulate virtual I/O in software. Both virtual and real I/O will be resolved simultaneously. Dynamic behavior, such as time delays of valve actuation, can be also implemented within the virtual I/O. Virtual I/O will be used for verification of the remaining phases using experiment's transfer functions. The transfer functions will first be identified from thermo hydraulic calculations.

Temperature regulation for adiabatic heating

LORELEI experiment will simulate the heating resulting from a LOCA accident. In this case the clad should be heated adiabatically with a predetermined heating rate of 5⁰C/s up to 20⁰C/s and the coaxial heater should follow clad's temperature simultaneously. This phase can be achieved automatically by closed loop control in two steps. Initial positioning determination of the displacement device such that it maintains the desired heating rate. The adiabatic heating requirement will be maintained by controlling, in closed loop, the coaxial heater to follow the clad's heating rate. It is very important to reach the desired requirement as fast as possible due to mutual heating affects and sluggish thermal responses.

CONCLUSIONS

This document summarizes the preliminary I&C design for LORELEI experiment. The preliminary design deals with considerations regarding appropriate safety and service instrumentation. The determined closed loop control rules for temperature and position will be implemented in the detailed design. The Computer Aided Operator Decisions System (CAODS) will be used for prediction of hot spot temperature and thickness of oxidation layer using Baker-Just correlation. The proposed hybrid simulation system comprising of both virtual and real hardware will be in-cooperated for LORELEI verification. It will perform both integration cold tests for a partial hardware loop and virtual tests for the final I&C design.

REFERENCES

1. IEC 61226 edition 3.0, *Nuclear Power Plants – Instrumentation and control important to safety – Classification of instrumentation and control functions.* (07/2009).
2. IEC 62138 edition 1.0, *Instrumentation and control important to safety – Software aspects for computer based systems performing category B or C functions.*(01/2004).
3. H.M.Hashemain, *Maintenance of process instrumentation in Nuclear Power Plant*, **ISBN-10 3-540-33703-2** Springer Berlin Heidelberg New York. **ISBN-13 978-3-540-33703-4** Springer Berlin Heidelberg New York, Springer-Verlag Berlin Heidelberg, (2006).

Biodistribution of ^{212}Pb Conjugated Trastuzumab in Mice

N. Schneider¹, M. Lobaugh¹, P. Sandwall¹, S. Glover¹, M. Murry¹, Z. Dong², H. Spitz¹

¹ University of Cincinnati, Cincinnati, OH 45221-0072

² University of Cincinnati Cancer Institute, Cincinnati, OH 45267

INTRODUCTION

The biodistribution and microdosimetry in mice of ^{212}Pb -trastuzumab, a human epidermal growth factor receptor 2 (HER2) targeting immunoglobulin (monoclonal antibody), was investigated for its potential as a therapeutic agent with immunocytotoxic applications. ^{212}Pb -trastuzumab is an alpha-emitting radioimmunoconjugate that can deliver a short-range, high linear energy transfer (LET) radiation dose to targeted tissue. The radionuclide ^{212}Pb , when conjugated with a monoclonal antibody and administered into tumor cells, eventually decays into ^{212}Bi , which emits a 6.09 MeV alpha particle or ^{212}Po , which emits an 8.78 MeV alpha-particle. The half-life of ^{212}Pb is 10.64 hr. The lethal radiation dose delivered to tumor cells by ^{212}Pb -trastuzumab is driven by the 8.78 MeV alpha particles from the decay of ^{212}Po and may promote apoptosis in sensitive tumor cells via a deoxyribonucleic acid (DNA) helical double-strand break.

Trastuzumab (Herceptin®, Genentech Inc., South San Francisco, California) is a humanized recombinant monoclonal antibody. Biologically, it interacts and binds with the high affinity extracellular juxtamembrane domain of the human epidermal growth factor receptor 2, thus preventing the activation of its intracellular tyrosine kinase¹. Monoclonal antibody selection is partially based on the binding affinity plus the specificity of the antibody to its target. Trastuzumab's binding mechanics inhibit the proliferation and survival of the HER2-dependent tumor cells in patients with metastatic cancer which over express the HER2 gene. At therapeutic doses in breast cancer patients, trastuzumab has a mean biological half-life of 5.8 days².

This research investigated the development of HER2 targeting ^{212}Pb -conjugated trastuzumab, a radiopharmaceutical targeted for *in vivo* treatment of HER2 expressing prostate tumor cells. The biodistribution of this radiolabeled antibody was determined in 28 male 10 week-old mice by measuring the radioactivity of ^{212}Pb (as a surrogate for the protein) in nine organs of interest plus the tumor at the time of sacrifice. Orthotopic tumors (PC-3MM2) of prostate cancer cells were used in this study. As organs of interest, the blood, brain, heart, liver, lung, kidney, spleen, bladder, intestine, and tumor were harvested and analyzed for ^{212}Pb content (as a surrogate for the protein) using gamma spectrometry. Two weeks prior to the radioimmunotherapy, the mice were injected with 2×10^5 PC-3MM2 tumor cells into their dorsal prostatic lobe. Each tumor-bearing mouse received approximately 740 kBq (20 μCi) of ^{212}Pb -trastuzumab by intravenous injection. The biodistribution of the conjugated antibody was determined after mice were euthanized at 30 min, 1 hr, 4 hr, 8 hr, 12 hr, 24 hr, 36 hr, 48 hr, 60 hr, and 72 hr post injection.

RESULTS

The concentration of ^{212}Pb in each organ was determined at the time of sacrifice by measuring the 238.6 keV photons and correcting for radioactive decay. The average percentage of injected dose per gram (%ID/g) was determined for each tissue, derived from the activity of ^{212}Pb at sacrifice divided by the injected activity. Results were normalized based upon total organ wet-weights and presented as %ID/g (except for blood which is %ID/mL). Table 1 lists results of the biodistribution of a single intravenous injection of ^{212}Pb -conjugated trastuzumab observed in 28 male mice carrying orthotopic PC-3MM2 tumors. The uncertainty (± 2 SD) listed in parenthesis for each entry is the variation in groups of up to three mice. The percent-injected dose per milliliter (%ID/mL) of ^{212}Pb -trastuzumab in the blood was 11.68 %ID/mL at 30 min and decreased rapidly thereafter to approximately 3.03 %ID/mL at 72 hr. Removal of ^{212}Pb -trastuzumab in blood with time enables transport and uptake in the tumor and other organs where it may remain or eventually be removed by recycling or excretion.

The concentration of ^{212}Pb -trastuzumab in the tumor was 0.48 %ID/g at 30 min, increased to 7.78 %ID/g at 12 hr, and then decreased to 4.28 %ID/g at 72 hr. The greatest retention was observed in the spleen at 60 hr (42.49 %ID/g). Uptake in the kidney ranged from 7.40 %ID/g to 17.94 %ID/g at 30 min and 72 hr, respectively. The concentration in the liver was fairly constant, ranging from 9.89 %ID/g at 30 min to 7.58 %ID/g at 72 hr.

Tissue	Time points (h)									
	0.5	1	4	8	12	24	36	48	60	72
Blood	11.68 (3.12)	11.65 (2.62)	6.92 (1.01)	6.10 (0.39)	5.77 (1.31)	3.68 (2.06)	4.23 (1.15)	3.35 (1.26)	1.88 (0.80)	3.03 (0.00)
Brain	0.32 (0.14)	0.26 (0.01)	0.19 (0.03)	0.17 (0.08)	0.21 (0.04)	0.74 (1.36)	0.16 (0.03)	0.16 (0.05)	0.27 (0.06)	0.38 (0.00)
Heart	3.16 (1.22)	3.29 (0.50)	2.74 (0.45)	2.62 (0.23)	1.53 (2.30)	1.61 (1.36)	2.42 (0.70)	1.56 (0.40)	1.55 (0.54)	1.88 (0.00)
Lung	4.39 (1.28)	4.89 (0.41)	3.18 (0.36)	10.73 (5.96)	3.89 (1.36)	2.01 (0.87)	3.19 (0.54)	3.01 (0.87)	2.74 (0.73)	3.47 (0.00)
Liver	9.89 (2.65)	9.51 (2.61)	9.55 (3.43)	7.31 (0.94)	6.52 (5.03)	8.44 (3.61)	11.99 (3.05)	9.07 (3.74)	7.63 (0.30)	7.58 (0.00)
Spleen	12.86 (5.41)	7.90 (0.33)	4.67 (0.22)	11.70 (6.52)	8.08 (2.21)	11.93 (6.71)	12.47 (5.56)	21.44 (14.29)	42.49 (34.02)	17.16 (0.00)
Kidney	7.40 (0.13)	7.56 (0.88)	7.39 (1.20)	10.21 (4.24)	7.55 (6.39)	10.41 (4.59)	14.61 (0.40)	13.12 (2.16)	10.28 (2.00)	17.94 (0.00)
Bladder	0.55 (0.01)	0.87 (0.32)	1.31 (0.12)	1.97 (0.38)	5.97 (5.24)	4.66 (3.56)	5.97 (4.05)	4.47 (0.89)	4.66 (1.38)	4.19 (0.00)
Intestine	0.36 (0.05)	1.12 (0.78)	1.08 (0.10)	1.46 (1.08)	1.62 (1.40)	1.90 (0.68)	1.17 (0.26)	1.80 (0.46)	3.04 (0.26)	1.56 (0.00)
Tumor	0.48 (0.10)	0.98 (0.36)	1.33 (0.27)	2.60 (1.64)	7.78 (9.03)	3.11 (1.47)	4.19 (0.42)	4.81 (1.19)	5.77 (1.10)	4.28 (0.00)

Table 4: Average percent injected dose of ^{212}Pb -trastuzumab per g of tissue or mL of blood in serially sacrificed mice.

Figure 1 illustrates the relative concentration (%ID/g) of ^{212}Pb -trastuzumab with increasing time post injection in the blood, brain, heart, lung, liver, spleen, kidney, bladder, intestine, and tumor. Results demonstrate that the content of ^{212}Pb -trastuzumab with time was greatest in the liver, spleen and kidney. Accumulation of radioactive ^{212}Pb -trastuzumab in the brain was negligible (< 1 %ID/g).

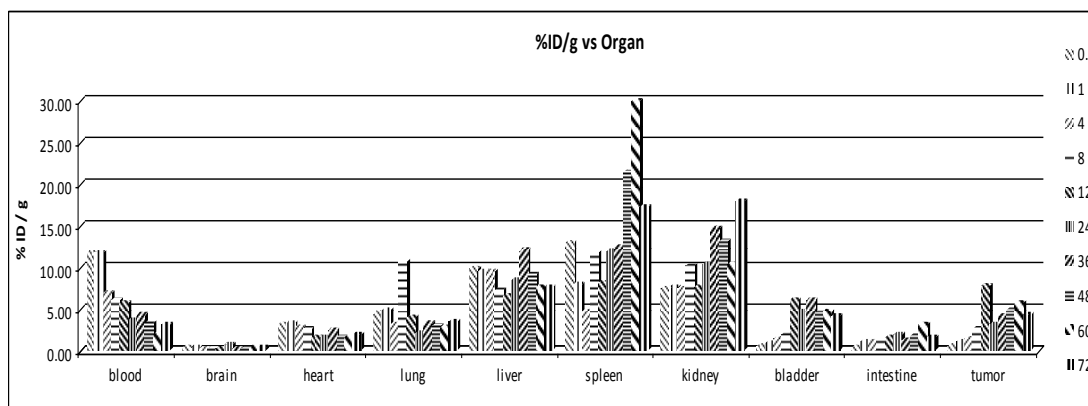


Figure 27: Distribution (% injected/g) of ^{212}Pb -trastuzumab with time (hr) post sacrifice in organs and PC-3MM prostatic tumors of mice.

Removal of ^{212}Pb -trastuzumab from blood and uptake in the prostate tumors is illustrated in Figure 2A and 2B, respectively. The relative distribution in the orthotropic tumors to that in other organs increased over the time from 0.20 % at 30 min to 1.10% at 24 hr. This model can be described using a two-component, exponential increase with time reflecting the binding of trastuzumab with HER2 receptors in tumor cells.

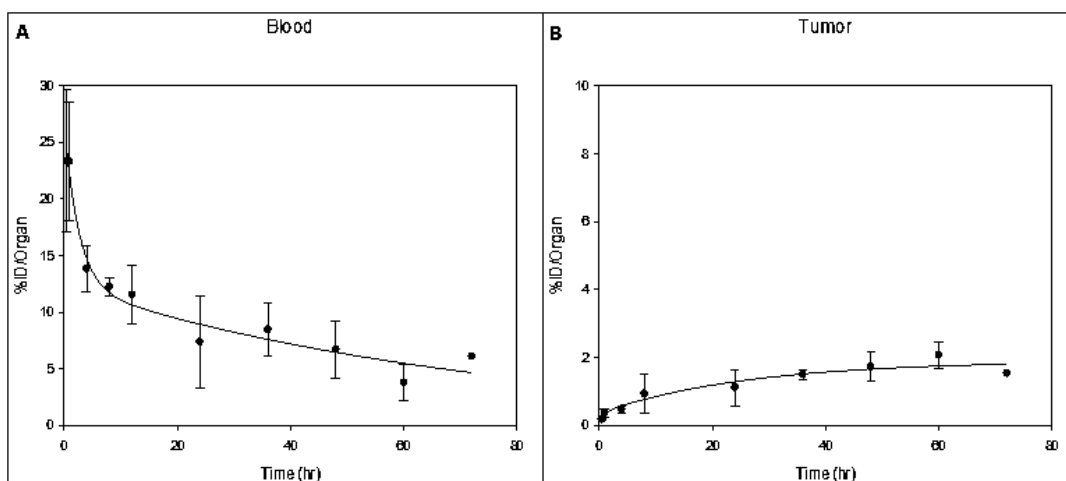


Figure 28: Removal from blood (A) and build-up in PC-3MM2 tumor cells (B) post injection of 740 kBq of ^{212}Pb -trastuzumab. Each point reflects the average percent injected dose for up to three mice at the time of sacrifice (± 2 SD).

Likewise, removal of ^{212}Pb -trastuzumab from blood can be described over the 72 hr period of observation using a two component exponential function ($R = 0.98$, $P = 0.19$). The effective removal half times from blood for the short- and long-term components are 1.77 hr and 51.3 hr, respectively. The slow removal of oncoproteins from the blood is a desirable characteristic that increases the probability that the circulating radiolabeled antibody will bind with the HER2 expressing receptors on tumor cells utilizing this cytotoxic agent to target the vasculature of the tumor. However, removal and excretion may occur as a result of antibody catabolism. Alternatively, retention of ^{212}Pb -trastuzumab in normal organs via metabolic cellular elements decreases availability of the radiolabeled antibody in the blood compartment. The period of observation adopted in this study was limited to 72 hr due to the short half-life of ^{212}Pb . The build-up of ^{212}Pb -trastuzumab in an organ may reflect a transient condition associated with fundamental pharmacokinetic and organ physiology, limited number of receptor sites, or simple diffusion of the antibody in the blood flow. For example, the antibody may be sequestered or phagocytized in the spleen as a natural function of the reticuloendothelium system and this may clarify why the spleen exhibited the greatest percent deposition of ^{212}Pb -trastuzumab observed in this study.

The desired target of the lethal radiation dose is HER2 expressing cells. However, the distribution of ^{212}Pb -trastuzumab deposited in organs other than the tumor demonstrates a need to know the concomitant radiation dose received by these organs (dosimetry) due to the decay of ^{212}Pb and its short-lived alpha- and beta-emitting decay products. Although traditional dosimetry calculations based upon the time dependent concentration of the radioisotope in each organ can easily be determined, it is unclear exactly where in the organ the energy from the short ranged, high LET radiation dose will be deposited³.

Simulations have been performed to predict the radiation dose delivered to blood vessel walls, red and white blood cells, plasma, and tissue surrounding the blood vessels. The percent of the alpha and beta decay energy deposited in the aforementioned compartments was simulated for different blood vessel dimensions and blood flow using the Monte Carlo code MCNPX. Results of simulations demonstrate that the majority of dose from ^{212}Pb -trastuzumab in blood is delivered to blood cells and plasma as well as the walls of the blood vessels. Thus, only a very small fraction of the radiation dose penetrates into organ tissue that is in contact with blood vessels.

CONCLUSIONS

Clinical use of radiolabeled monoclonal antibodies in therapeutic treatment of cancer is increasing. This study demonstrates an increased uptake rate in the tumor over a 72 hr period of observation following a single intravenous injection of ^{212}Pb -trastuzumab in mice. Whereas ^{212}Pb -trastuzumab appeared not to cause systemic toxicity⁴, there may be concomitant uptake in other organs that should be considered in evaluating the risk of radiation toxicity associated with therapy. Additional laboratory and clinical study with ^{212}Pb -trastuzumab should be conducted to define an optimized therapeutic strategy and determine the radiation doses delivered to non-targeted organs and tissues using microdosimetry methods. Results of this

biodistribution study support further investigation of radiolabeled ^{212}Pb -TCMC-trastuzumab, radiobiological organ microdosimetry, and optimal dosing regimens for ^{212}Pb -trastuzumab as a therapeutic agent.

REFERENCES

1. Hudis C A Trastuzumab - Mechanism of Action and Use in Clinical Practice. *New England J of Med* 357:39-51; (2007).
2. Goldenberg M Trastuzumab, a Recombinant DNA-Derived Humanized Monoclonal Antibody, a Novel Agent for the Treatment of Metastatic Breast Cancer. *Clinical Therapeutics* 21:309-317; (1999).
3. Sgouros G, Roeske J, and McDevitt M MIRP Pamphlet No. 22 – Radiobiology and Dosimetry of Alpha Particle Emitters for Targeted Radionuclide Therapy. *Alpha-Particle Emitter Dosimetry* 1-105; (2009).
4. Tan Z, Chen P, Schneider N, Glover S, Cut L, Torgue J, Rixe O, Spitz H, and Dong Z (2012) Significant systemic therapeutic effects of high-LET immunoradiation by ^{212}Pb -trastuzumab against prostatic tumors of androgen-independent human prostate cancer in mice. *International J of Oncology* 40:1881-1888

Medical and Applied Physics (Thursday, February 13, 2014 09:00)

A Novel Drug Delivery System for Preventing the Extension of the Telomeric Ends of DNA and Preventing the Unlimited Proliferation of Cancer Cells

Brenda Laster, Carol Issacson, Maha Msamra, Ekterina Perez, Jospeh Kost

Ben Gurion University, Beer Sheva 84105 Israel

Telomerase is an enzyme present in the majority of malignant tumors (1). It is well-documented that radiotherapy and chemotherapy activate the enzyme telomerase that immortalizes cancer cells (2-6). Telomerase prevents the shortening of the telomeric ends of DNA that is required for cell lethality; therefore, inhibiting its activation would be a useful approach to cancer treatment. However, inhibiting telomerase activation (TA) is no easy task. Despite the plethora of new drugs synthesized as potential clinical candidates for telomerase inhibition (TI) (7-11), their success or failure in the medical clinic will probably be more a function of their mode of administration once they have demonstrated TI in the research laboratory. A major physiological barrier to TI is the absolute requirement for the inhibitor to remain continuously present in the tumor (1) throughout the long term treatment period. This is due to both the reactivation of telomerase that occurs upon the removal of the inhibitor, and the re-lengthening of the telomeres in the absence of the inhibitor (12-16). Because the systemic i.v. administration of drugs is associated with their rapid clearance from the body, the effectiveness of the inhibitor drug would be dramatically reduced due to telomerase re-activation. Under normal conditions, when telomerase is inactive, the telomeres shorten with each cell division until such time as the cell reaches its normal life expectancy (17). The unrestricted proliferation of cancer cells, after treatments that activate telomerase, poses a risk for local recurrence, invasion, metastases, or even second primaries and present an issue that must be addressed. Therefore, critical for clinical success is the identification of an agent whose mechanism of action has been proven to inhibit TA and whose toxicity is negligible. Equally important is the development of a drug delivery system that assures the continuous long-term presence of the drug in the tumor. The latter criterion is required to compensate for the lag time between the inhibition of TA and the time when the telomeres have shortened sufficiently to induce cancer cell lethality (1, 18).

We have identified a highly satisfactory molecule that meets these criteria and have developed a method for sustaining the controlled release of the molecule over the long term. We have done so by developing a controlled-release device that liberates a well-studied telomerase inhibitor for a long period of time (Fig. 1.). Fig. 1 below demonstrates the release characteristics of the telomerase inhibitor, PdTMPyP4, in a gelatin base for up to 52 days. The amount of drug released both initially, and over time, depends upon the weight of the rods. Those rods of greater mass release higher concentrations of the drug over a somewhat shorter time interval. The gelatin base was considered more representative of a tumor environment than water.

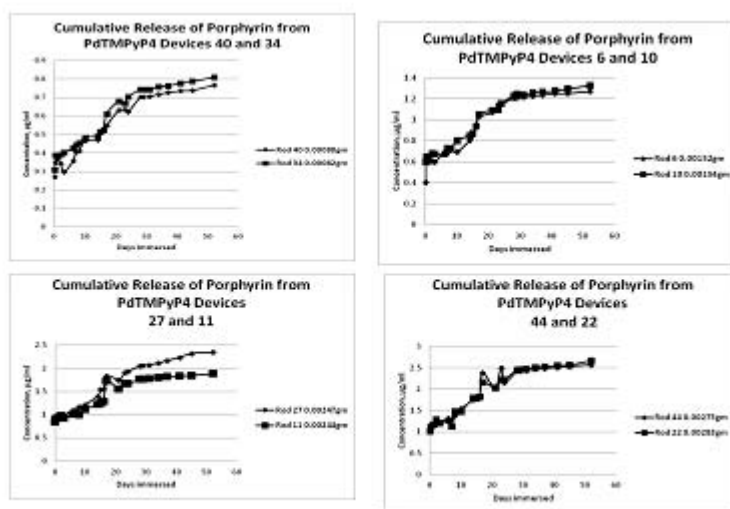


Fig. 1. Release characteristics of PdTMPyP4 in gelatin base. Comparison of release based upon weights of devices. The devices were positioned in the base of a cuvette using gelatin. Upon solidification of the base gelatin, additional gelatin was added to the cuvette. The cuvettes were incubated at 37° in a humidified environment and spectroscopic measurements were taken daily.

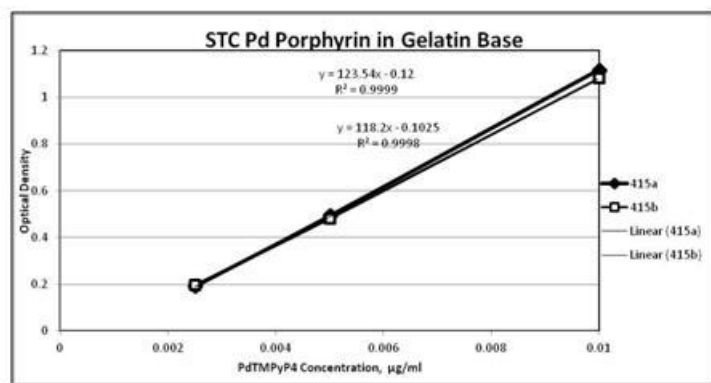


Fig. 2. Standard curve of absorption as a function PdTMPyP4 concentration. Concentration was determined based upon the equation derived from the linear fit of absorption measurements (R^2) as a function of the concentration of known titrated samples (Fig. 2).

The device can be inserted directly into the tumor where it increases tumor loading and reduces systemic toxicity. However, inhibiting telomerase is not necessarily sufficient for shortening the telomeric ends of cancer cell DNA. A number of tumors and cell lines use a recombination-based mechanism, alternative lengthening of telomeres (ALT), to maintain telomere repeat arrays (19). The engagement of the ALT mechanism could be a factor in limiting the success of telomerase inhibition. Therefore, in addition to our method of inhibiting telomerase, we propose that the simultaneous insertion of brachytherapy seeds and our device that releases a telomerase inhibitor directly into the tumor, have a strong probability for controlling the growth of tumors and preventing recurrences. Details are given below.

Our telomerase-inhibiting agent is a meso-5,10,15,20-Tetrakis-(N-methyl-4-pyridyl)porphine (TMPyP4), tagged with palladium (Pd). TMPyP4 binds to G-quadruplex (GQ) structures in DNA such as in the telomeres and in the promoter region of c-myc (20, 21), the most genomically unstable of the oncogenes (22, 23). Its binding stabilizes c-myc, blocking its transcription and over-expression (24-27). Because c-myc stimulates hTERT, a subunit of telomerase that promotes telomerase activation, the blocking of c-myc transcription, in and of itself interferes with the propensity of the oncogene to produce multiple copies of itself, reduces hTERT stimulation and TA (24, 28). The effectiveness of TMPyP4 as a telomerase inhibitor has been well studied. However, we understood that another equally important advantage could be derived by exploiting the robustness of TMPyP4 as a vehicle for transporting and binding high Z atoms to DNA where their physical interaction with radiation could fragment the DNA in a modality called Photon

Activation Therapy (PAT) (29-31). Specifically, we have incorporated PdTMPyP4 into our device that now offers an opportunity to exploit both components of the single molecule, viz., the Pd and the TMPyP4 components, each of which physiologically targets the DNA, but whose actions are entirely independent. Whereas the induction of a photoelectric effect in the Pd atom and its concomitant emission of densely ionizing Auger electrons causes clustered DNA damage, similar to high LET radiation, the TMPyP4 component inhibits telomerase that is activated by radiation. The photoelectric effect can be induced either by the interstitial implantation of appropriate energy brachytherapy seeds directly into the tumor, or by using monochromatic photons produced by finely-tuned synchrotron radiation beams.

We had previously demonstrated an early, significant delay in the growth of the KHJJ murine adenocarcinoma following the i.p. injection of platinum (Pt)-tagged TMPyP4 and the insertion of ^{103}Pd brachytherapy seeds compared to untreated or unirradiated mice (32). Our inability to sustain the delay was attributed to clearance of the drug from tumor. In these studies, we had anticipated that the Pt tag would increase the fragmentation of all GQ sites in DNA through its emission of low energy, short range Auger electrons. The photon energies of the ^{103}Pd seeds (21 keV) were suitable for inducing a photoelectric effect at the L absorption edge of Pt (~14 keV) and promoting concomitant Auger emission. However, the intraperitoneal systemic administration of PtTMPyP4 did not sustain the constant availability of Pt atoms and the resumption of tumor growth was a motivating factors in our pursuit to develop a long term, controlled release drug intratumoral delivery system with incorporated PdTMPyP4. The K absorption edge of Pd is ~24.5 keV and the photon emission from the conventionally-used iodine-125 (^{125}I) brachytherapy seeds is (27 keV) (33, 34). The closer the radiative energy to the K edge of the target atom, the greater the probability of interaction. Therefore, for purposes of the radiotherapeutic approach with PdTMPyP4, the combination is highly suitable. The controlled-release device assures the long term availability of Pd atoms in DNA, so that even during the radioactive decay of the ^{125}I seeds, Auger electrons can continue to densely ionize and fragment the DNA. Additionally, if PdTMPyP4 binds to GQs in the telomeres similarly to TMPyP4, inducing Auger emission at the site of the telomeres would also cause their fragmentation and shortening. Moreover, some immortalized mammalian cell lines and tumors increase the overall length of their telomeres by one or more mechanism with no relationship to telomerase activation (35, 36). This is referred to as alternative lengthening of telomeres (ALT). In these cases, the use of PAT and its Auger emission provides an additional measure to offset ALT.

In summary, our research project has addressed some of the major issues associated with current cancer treatments that might be responsible for their failure in some cases. We propose a new treatment modality that combines both chemotherapy and radiotherapy. It could be administered in a single step that involves the simultaneous insertion of a device that continuously releases a telomerase-inhibiting drug over the long term, and that also potentiates the dense ionization of cancer cell DNA on a highly local basis. The device is biodegradable and the brachytherapy seeds have a relatively short half-life; therefore, insertion of both is permanent. In addition to increasing the sensitivity of the cancer cell to conventional treatments, our proposed therapeutic procedure, in which both the device and the seeds are inserted directly into the tumor, will improve the quality of life of the patient by reducing the frequent visits to the clinic for fractionated radiation or chemotherapy treatments.

REFERENCES

1. Blagoev KB. Cell proliferation in the presence of telomerase. *PLoS One*. 2009;4:e4622.
2. Nakamura M, Masutomi K, Kyo S, Hashimoto M, Maida Y, Kanaya T, et al. Efficient inhibition of human telomerase reverse transcriptase expression by RNA interference sensitizes cancer cells to ionizing radiation and chemotherapy. *Hum Gene Ther*. 2005;16:859-68.
3. von Bueren AO, Shalaby T, Oehler-Janne C, Arnold L, Stearns D, Eberhart CG, et al. RNA interference-mediated c-MYC inhibition prevents cell growth and decreases sensitivity to radio- and chemotherapy in childhood medulloblastoma cells. *BMC Cancer*. 2009;9:10.

4. Wesbuer S, Lanvers-Kaminsky C, Duran-Seuberth I, Bolling T, Schafer KL, Braun Y, et al. Association of telomerase activity with radio- and chemosensitivity of neuroblastomas. *Radiat Oncol*. 2010;5:66.
5. McCaul JA, Gordon KE, Minty F, Fleming J, Parkinson EK. Telomere dysfunction is related to the intrinsic radio-resistance of human oral cancer cells. *Oral oncology*. 2008;44:261-9.
6. Shin JS, Foo T, Hong A, Zhang M, Lum T, Solomon MJ, et al. Telomerase expression as a predictive marker of radiotherapy response in rectal cancer. *Pathology*. 2012;44:209-15.
7. Dikmen ZG, Gellert GC, Jackson S, Gryaznov S, Tressler R, Dogan P, et al. In vivo inhibition of lung cancer by GRN163L: a novel human telomerase inhibitor. *Cancer Res*. 2005;65:7866-73.
8. Gomez-Millan J, Goldblatt EM, Gryaznov SM, Mendonca MS, Herbert BS. Specific telomere dysfunction induced by GRN163L increases radiation sensitivity in breast cancer cells. *Int J Radiat Oncol Biol Phys*. 2007;67:897-905.
9. Joseph I, Tressler R, Bassett E, Harley C, Buseman CM, Pattamatta P, et al. The telomerase inhibitor imetelstat depletes cancer stem cells in breast and pancreatic cancer cell lines. *Cancer Res*. 2010;70:9494-504.
10. Mikami-Terao Y, Akiyama M, Yuza Y, Yanagisawa T, Yamada O, Kawano T, et al. Antitumor activity of TMPyP4 interacting G-quadruplex in retinoblastoma cell lines. *Experimental eye research*. 2009;89:200-8.
11. Beisner J, Dong M, Taetz S, Nafee N, Griese EU, Schaefer U, et al. Nanoparticle mediated delivery of 2'-O-methyl-RNA leads to efficient telomerase inhibition and telomere shortening in human lung cancer cells. *Lung cancer*. 2010;68:346-54.
12. Bazarov AV, Hines WC, Mukhopadhyay R, Beliveau A, Melodyev S, Zaslavsky Y, et al. Telomerase activation by c-Myc in human mammary epithelial cells requires additional genomic changes. *Cell Cycle*. 2009;8:3373-8.
13. Herbert B, Pitts AE, Baker SI, Hamilton SE, Wright WE, Shay JW, et al. Inhibition of human telomerase in immortal human cells leads to progressive telomere shortening and cell death. *Proc Natl Acad Sci U S A*. 1999;96:14276-81.
14. Marie-Egyptienne DT, Brault ME, Zhu S, Autexier C. Telomerase inhibition in a mouse cell line with long telomeres leads to rapid telomerase reactivation. *Exp Cell Res*. 2008;314:668-75.
15. Yaswen P, Stampfer MR. Molecular changes accompanying senescence and immortalization of cultured human mammary epithelial cells. *Int J Biochem Cell Biol*. 2002;34:1382-94.
16. Delhommeau F, Thierry A, Feneux D, Lauret E, Leclercq E, Courtier MH, et al. Telomere dysfunction and telomerase reactivation in human leukemia cell lines after telomerase inhibition by the expression of a dominant-negative hTERT mutant. *Oncogene*. 2002;21:8262-71.
17. Pickett HA, Henson JD, Au AY, Neumann AA, Reddel RR. Normal mammalian cells negatively regulate telomere length by telomere trimming. *Hum Mol Genet*. 2011;20:4684-92.
18. Damm K, Hemmann U, Garin-Chesa P, Huel N, Kauffmann I, Priepke H, et al. A highly selective telomerase inhibitor limiting human cancer cell proliferation. *Embo J*. 2001;20:6958-68.
19. Razak ZR, Varkonyi RJ, Kulp-McEliece M, Caslini C, Testa JR, Murphy ME, et al. p53 differentially inhibits cell growth depending on the mechanism of telomere maintenance. *Molecular and cellular biology*. 2004;24:5967-77.
20. Arora A, Maiti S. Effect of loop orientation on quadruplex-TMPyP4 interaction. *J Phys Chem B*. 2008;112:8151-9.
21. Siddiqui-Jain A, Grand CL, Bearss DJ, Hurley LH. Direct evidence for a G-quadruplex in a promoter region and its targeting with a small molecule to repress c-MYC transcription. *Proc Natl Acad Sci U S A*. 2002;99:11593-8.
22. Prochownik EV. c-Myc: linking transformation and genomic instability. *Curr Mol Med*. 2008;8:446-58.
23. Sheen JH, Woo JK, Dickson RB. c-Myc alters the DNA damage-induced G2/M arrest in human mammary epithelial cells. *Br J Cancer*. 2003;89:1479-85.

24. Grand CL, Han H, Munoz RM, Weitman S, Von Hoff DD, Hurley LH, et al. The cationic porphyrin TMPyP4 down-regulates c-MYC and human telomerase reverse transcriptase expression and inhibits tumor growth in vivo. *Mol Cancer Ther.* 2002;1:565-73.
25. Hurley LH, Von Hoff DD, Siddiqui-Jain A, Yang D. Drug targeting of the c-MYC promoter to repress gene expression via a G-quadruplex silencer element. *Semin Oncol.* 2006;33:498-512.
26. Lemarteleur T, Gomez D, Paterski R, Mandine E, Mailliet P, Riou JF. Stabilization of the c-myc gene promoter quadruplex by specific ligands' inhibitors of telomerase. *Biochem Biophys Res Commun.* 2004;323:802-8.
27. Seenisamy J, Bashyam S, Gokhale V, Vankayalapati H, Sun D, Siddiqui-Jain A, et al. Design and synthesis of an expanded porphyrin that has selectivity for the c-MYC G-quadruplex structure. *J Am Chem Soc.* 2005;127:2944-59.
28. Mikami-Terao Y, Akiyama M, Yuza Y, Yanagisawa T, Yamada O, Yamada H. Antitumor activity of G-quadruplex-interactive agent TMPyP4 in K562 leukemic cells. *Cancer Lett.* 2008;261:226-34.
29. Fairchild RG, Bond VP. Photon activation therapy. *Strahlentherapie.* 1984;160:758-63.
30. Fairchild RG, Brill AB, Ettinger KV. Radiation enhancement with iodinated deoxyuridine. *Invest Radiol.* 1982;17:407-16.
31. Feinendegen LE. Biological damage from the Auger effect, possible benefits. *Radiat Environ Biophys.* 1975;12:85-99.
32. Laster BH, Dixon DW, Novick S, Feldman JP, Seror V, Goldbart ZI, et al. Photon activation therapy and brachytherapy. *Brachytherapy.* 2009;8:324-30.
33. Salembier C, Rijnders A, Henry A, Niehoff P, Andre Siebert F, Hoskin P. Prospective multi-center dosimetry study of low-dose Iodine-125 prostate brachytherapy performed after transurethral resection. *Journal of contemporary brachytherapy.* 2013;5:63-9.
34. Keller B, Sankrecha R, Rakovitch E, O'Brien P, Pignol JP. A permanent breast seed implant as partial breast radiation therapy for early-stage patients: a comparison of palladium-103 and iodine-125 isotopes based on radiation safety considerations. *Int J Radiat Oncol Biol Phys.* 2005;62:358-65.
35. Folini M, Venturini L, Cimino-Reale G, Zaffaroni N. Telomeres as targets for anticancer therapies. *Expert opinion on therapeutic targets.* 2011;15:579-93.
36. McDonald KL, McDonnell J, Muntoni A, Henson JD, Hegi ME, von Deimling A, et al. Presence of alternative lengthening of telomeres mechanism in patients with glioblastoma identifies a less aggressive tumor type with longer survival. *Journal of neuropathology and experimental neurology.* 2010;69:729-36.

Medical and Applied Physics (Thursday, February 13, 2014 09:00)

DNA Topoisomerase-1. A Novel Radiation Exposure Biomarker

R. Gonen¹, U. German¹, Z. B. Alfassi², E. Priel²

¹ Nuclear Research Center, Negev, P.O.B 9001 Beer Sheva, 84190, Israel

² Ben Gurion University of the Negev, Beer Sheva, 84105, Israel

INTRODUCTION

DNA topoisomerases (topo) are essential nuclear enzymes that are responsible for the topological state of DNA. They are involved in a variety of DNA transactions, including replication, transcription, recombination, DNA repair, and nucleosomal condensation ⁽¹⁾.

Topoisomerases are classified as type I or type II and are distinct in sequence, structure, and functions ⁽¹⁾. The eukaryotic type I topoisomerase (topo IB) has an important role in DNA transactions and in maintenance of genomic stability ⁽²⁾ and its inactivation leads to embryonic death at the 4–16 cell stage. Topo IB can relax both positive and negative supercoiled DNA by the formation of a transient single-strand DNA break in which the active site tyrosine becomes attached to the 3-phosphate end of the cleaved strand followed by rotation of the DNA and religation process ⁽²⁾. Mammalian DNA topoisomerases are the targets of several anticancer drugs in current clinical use ⁽¹⁾.

In the present research the influence of the β and γ radiations on the catalytic potential of the important nuclear enzyme DNA- topoisomerase I was investigated, to determine its applicability as a biological radiation dose indicator. The classification of the level of the exposure dose is needed for dose evaluations in accidental and occupational exposure events ⁽³⁾, and the inhibition of the catalytic activity of DNA-topoisomerase I could serve as just such an indicator. For this research we used malignant osteoblast MG-63 cells, and normal peripheral blood lymphocytes. Cells were exposed (acute exposure) to different activities of β and γ radiations (using ³H via HTO exposures and external ⁶⁰Co source). The catalytic activity of topo-I was determined by using a specific Topo-I mixture which includes supercoiled plasmid as the substrate and nuclear protein extracts as the source of Topo-I as described elsewhere ⁽⁴⁾.

RESULTS

Topoisomerase-1 activities from MG-63 Osteoblasts exposed to different HTO concentrations:

The reaction products were analyzed by agarose gel electrophoresis. The gel was stained with ethidium-bromide and photographed using a short UV lamp. Figure 1A shows the Topo-I activity assay results for different exposure levels. A significant dose dependent decrease in the DNA relaxation activity of topo I was observed. Densitometric analysis of the supercoiled plasmids shown in Figure 1A was performed. The amount of the supercoiled plasmids left after the topo I reaction was compared to the activity level of topo I from the control nuclear extract (0 Gy), that was taken as the "100% activity". Band intensities were quantified by densitometric scans using EZQuant-Gel image processing and analysis software. Figures 1B and 1C that summarize the topo I activities by the aid of densitometry analysis, show clearly the inhibition of this enzyme, which is linearly-proportional ($r^2=0.9943$) to the exposure doses.

To examine if this reduction in topo I activity was due to a reduction in the level of topo I protein 50 μ g of the nuclear protein extracts derived from the different HTO activity treatments were subjected to Western blot analysis and reacted with specific anti-topo-I and anti- β -actin antibodies. The results in Figure 2 show that no significant differences can be observed in the levels of both proteins (the same results were obtained by densitometric analysis of the results and the percent of topo-I/ β -actin was calculated). This leads to the conclusion that topoisomerase-1 activity from MG-63 osteoblasts can be partially inhibited by the β

radiation from tritium, dependent on the exposure dose. This inhibition is not due to reduction in the level of the enzyme protein, suggesting possible posttranslational modifications.

A: Inhibition of topoisomerase-1 activity due to exposure of MG-63 osteoblasts to different HTO activities.

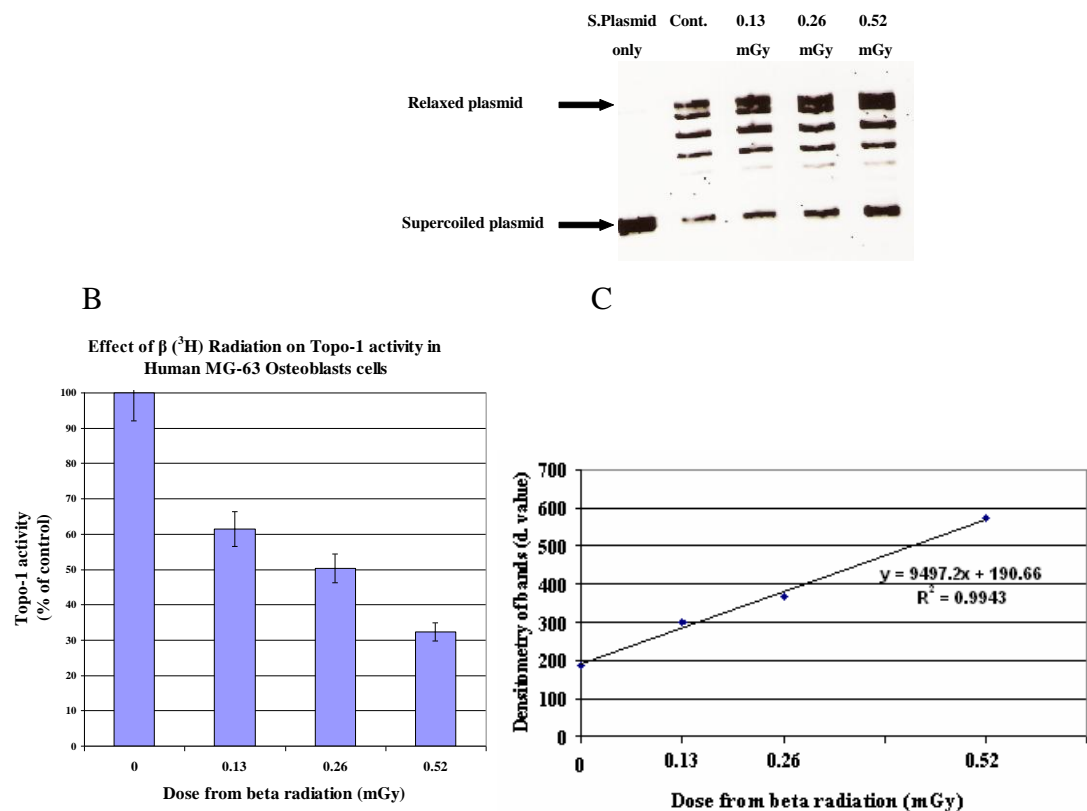


Figure 1: Inhibition of topoisomerase-I activity after exposure of 3 h to different HTO activities.

Notations: Cont. means control (no activity in the growth media)
 1 Ac, 2 Ac, 4 Ac are equivalent to 0.13 mGy, 0.26 mGy, 0.52 mGy.

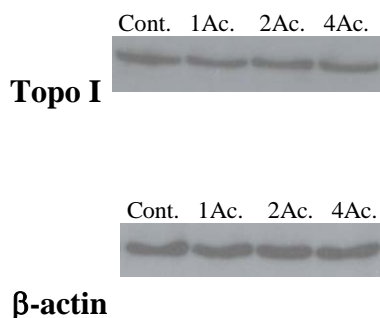


Figure 2: Topo_I protein level Using Western blot analysis with anti- topo I antibodies. β-actin protein served as a control for the amount of nuclear proteins loaded on the gel.

Notations: Cont. means control (no activity in the growth media)
 1 Ac, 2 Ac, 4 Ac are equivalent to 0.13 mGy, 0.26 mGy, 0.52 mGy.

Topoisomerase-1 Activity in Normal Peripheral Blood Lymphocytes

To determine the effect of HTO on normal human cells, the effect of HTO on normal human lymphocytes derived from healthy donors were examined. Equivalent amounts (25 ng) of nuclear proteins obtained from each tritium exposure were added to a topo I reaction mixture, and the reaction was stopped after 90 min. (Reaction activity was calibrated prior to the addition of nuclear proteins so that the control sample,

which was not treated with HTO, could relax the majority of the supercoiled plasmids.) The reaction products were analyzed by agarose gel electrophoresis. The gel was stained with ethidium-bromide and photographed using a short UV lamp. The topo I densitometric results (Figure 3 for different activities indicate a significant reduction in the activity levels of the samples tested. The activity levels of topo I were compared to the activity level of the control nuclear extract (0 Gy), which represent 100% activity. Band intensities were quantified by densitometric scans using EZQuant-Gel image processing and analysis software.

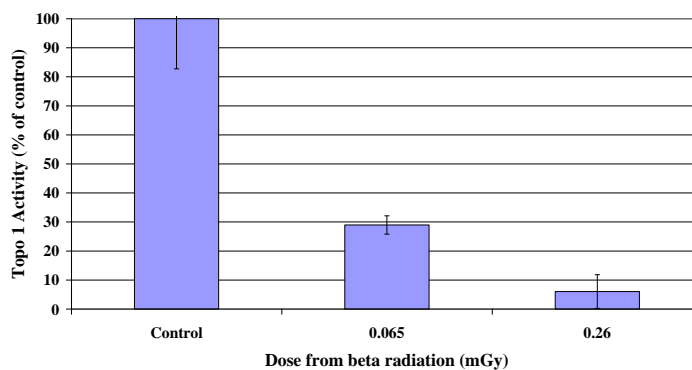


Figure 3: Topoisomerase-1 activity from normal peripheral blood lymphocytes after exposure to different HTO doses. The error bars indicate 3 standard deviations.

Determination of Topoisomerase-1 activity in γ -irradiated MG-63 Osteoblasts

To examine the effect of γ radiation on the activity of topo I in human cells, the MG-63 cells were grown for 5 days. Prior to the irradiation treatment, the cells were centrifuged $\times 400g$ for 5 min, then irradiated with a ^{60}Co source with a dose rate of 2 Gy/min. The cells were dispersed using a sterile pipette and transferred back to the 37 °C incubator for 2 h. The cells were harvested and nuclear extracts were prepared according to the method described elsewhere ⁽⁴⁾. Equal quantities (50 ng) of nuclear extracts from the solutions of different γ exposures were added to topo I reaction mixtures, and the reactions were stopped after 5 min (based on pre-calibration using a non-irradiated control batch). The reaction products were analyzed by agarose gel electrophoresis. The densitometric results (Figure 4) show that topoisomerase-1 activity is inhibited by γ -radiation. This inhibition was found to be dose-dependent and linear up to the dose of at least 0.5 Gy ($r^2=0.9996$).

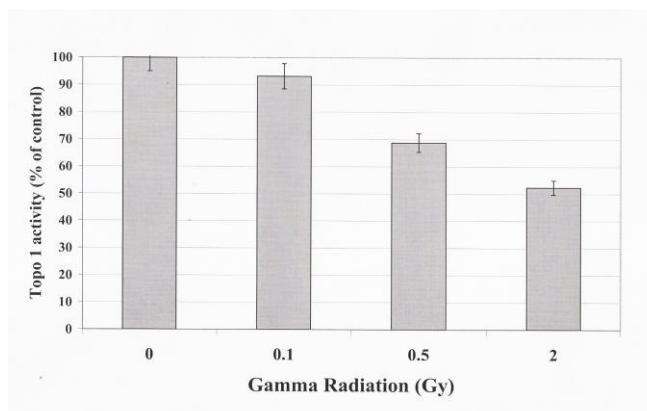


Figure 4 Topoisomerase-1 sensitivity to γ radiation exposure.

CONCLUSIONS

The reduction in topoisomerase I activity after exposure to relatively low doses from tritium and γ radiation may be applicable as a sensitive biomarker, which may be needed in events such as terror attacks involving radioactive materials, measuring chronic exposures to low radiation, and in radiation accidents ⁽³⁾. As this biomarker can be detected in lymphocytes and the effect on its activity can be detected at doses as low as 0.065mGy, it may be applicable also in occupational exposures circumstances.

REFERENCES

1. Wang JC. DNA topoisomerases. *Annu. Rev. Biochem.* **65**, p.635-692, (1996).
2. Champoux JJ. DNA topoisomerases: structure, function and mechanism. *Ann. Rev. Biochem.* **70**, p.369-413, (2001).
3. Durante M. Potential application of biomarkers of radiation exposure in nuclear terrorism events. *Physica Medica*, vol.xix, N (2003).
4. Noach M, Yael S, Itzhak L, Shraga S, Priel E. Modification of topoisomerase 1 activity by glucose and O-GlcNacylation. *Glycobiology*. vol. **17** no.12, p1357-1364, (2007).

Medical and Applied Physics (Thursday, February 13, 2014 09:00)

A New Concept in Radiation Damage Studies: Model System for Self-Induced Radiation Damage Experiments in Thin Films

M. Shandalov¹, T. Tempelman², R. Hevroni³, I. Kelson³, E. Yahel¹ and Y. Golan²

¹*Nuclear Research Center Negev, POB 9001 Beer Sheva 8419001, Israel*

²*Ben-Gurion University, Beer Sheva 8410501, Israel*

³*Tel Aviv University, POB 653, Tel Aviv 6997801, Israel*

INTRODUCTION

Lead chalcogenide semiconductor thin films have been a subject of considerable research due to their technological importance in monocrystalline and polycrystalline forms as infrared radiation detectors, infrared emitters and solar control coatings. A variety of chemical and physical methods have been developed to prepare thin metal chalcogenide films.¹⁻³ Among the different thin film fabrication methods, the chemical bath deposition (CBD) from aqueous solution offers a simple and cost-effective route for the fabrication of high quality semiconductor thin films, without the need for high deposition temperatures, stringent vacuum or plasma generators compared to other sophisticated techniques. PbS, being the most studied material among the lead chalcogenide family, is a narrow, direct band gap semiconductor. The interest in PbS is due to its useful optoelectronic properties for infrared detection and emission. Recently, the interest in nanocrystalline PbS has been dramatically increased due to its potential use in solar cells and visible light sensors.

The properties of irradiated materials have scientific interest and practical importance in nuclear and space applications. Studies of radiation damage are focus on the understanding the changes in physical properties due to the microscopic evolution of the accumulated damage to the lattice. This is usually achieved by irradiating the samples externally in accelerators or reactors. A different branch of radiation damage studies is the change in the properties of materials that are subject to self-irradiation due to their radioactive nature, e.g., metals among the actinide series. The study of the actinides is complicated due to their radioactive and chemical toxicity which require special care and equipment. The ability to carefully control the growth of lead-based thin films such as PbS and alloying it with radioactive thorium, make these materials excellent candidates to become model system for the study of processes, similar to self-irradiation damage.

In the present work, we developed a novel alloying procedure for the incorporation of ²³²Th ($t_{1/2} \sim 10^6$ years) in chemically deposited PbS films, and explored the effect of thorium on the deposition of PbS thin films and their microstructure. Subsequent incorporation of radioactive α -emitting ²²⁸Th ($t_{1/2} = 1.9$ years) presents an innovative possibility for radiation damage studies of thorium-alloyed PbS thin films similar to self-irradiation in non-radioactive samples, thus providing a route for a unique model system. In this work we show for the first time, the incorporation of thorium ions in chemically deposited PbS thin film and report on their remarkable effect on the deposition kinetics and on the film properties.

RESULTS

A comparison between PbS and PbS(Th) films deposited at various deposition times, under the same conditions (30°C, 90-600 min), is given in Fig. 1.

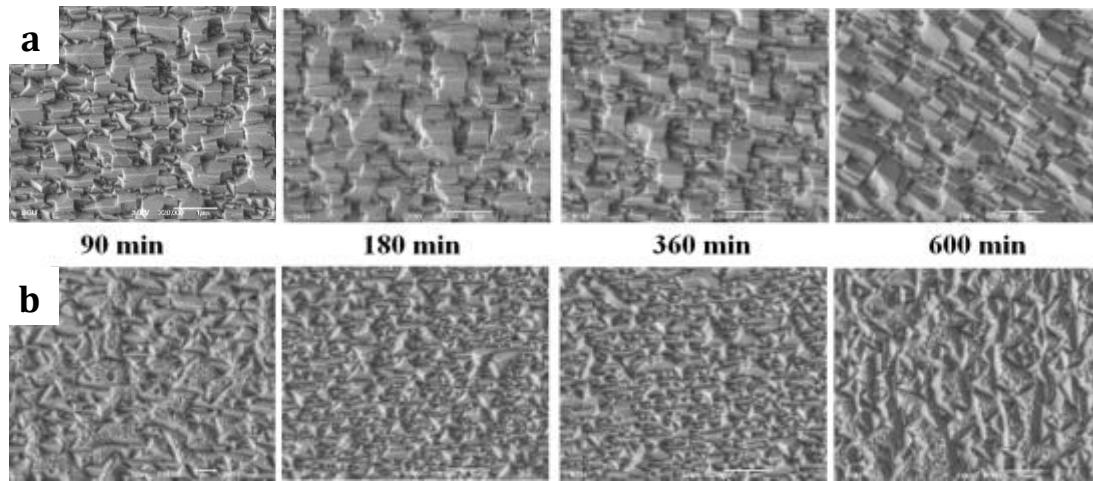


Figure 1. Secondary Electron HR-SEM images of (a) PbS control sample and (b) PbS(Th) films prepared with 0.438 mM thorium concentration in solution, on GaAs(100) at 300C for 90-600 min.

The addition of thorium caused a change in the film morphology from faceted rectangle morphology to triangle morphology.⁴ XPS depth profile indicates that the Th ions are homogenously distributed along the film with average concentration of thorium of 0.5 at% (Fig. 2a).

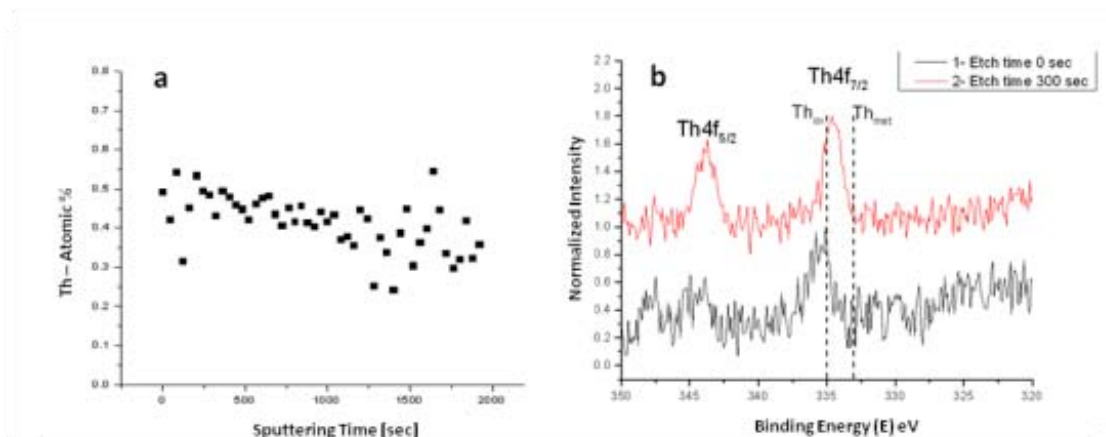


Figure 2. (a) XPS Depth profile of Thorium in PbS(Th) film deposited from solution with Th concentration of 0.438 mM on GaAs(100) at 30°C for 90 min. (b) High-Resolution XPS spectra of Th4f.

High-resolution XPS (HR-XPS) provided invaluable information on the bonding of Th incorporated in the films.⁴ Fig. 2b shows HR-XPS spectrum of Th4f peak in PbS(Th) film deposited on GaAs(100) at 30°C for 90 min. The black curve (Fig. 2b), which corresponds to a spectrum taken at the surface of the film (before etching), matches the oxidized Th state while the red curve, which corresponds to the spectrum after etching the surface, is shifted towards higher binding energies (E_B) compared to that of the metallic Th binding state (333 eV), yet notably lower than the oxidized Th (335 eV). This is expected for thorium bonded with S atoms, since the electronegativity of $O > S > Th$. Considering the observation in Fig. 2 it is reasonable to assume that the Th ions are replacing the lead ions in the PbS lattice.

The optical properties of the obtained PbS(Th) films, investigated by using PL measurements.⁴ PbS(Th) film and PbS control sample were measured. The PL spectra of PbS(Th) sample and PbS control sample is shown in Fig 3.

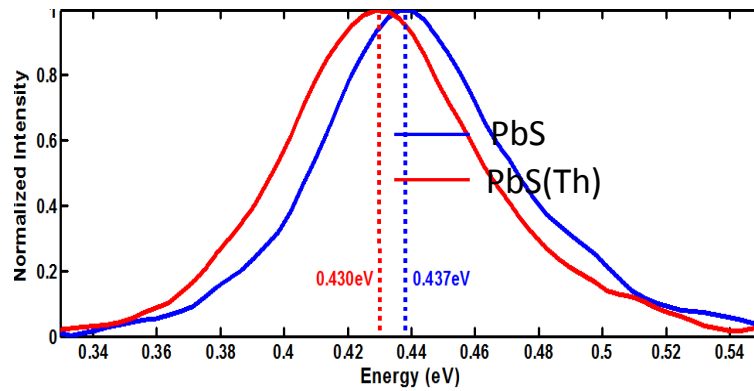


Figure 3. PL spectra of PbS(Th) sample and PbS control sample, grown on GaAs(100) at 30⁰C for 90 min with thorium concentration of 0.438 mM.

PL measurements show a shift of ~7meV between the samples, the measurements were repeated on different sample locations (to make sure the shift is not related inhomogeneous properties of the samples). Assuming x (~0.5% in our case) is small; we can assume linearity in the concentration and estimate the band gap of A_xB_{1-x} as:

$$(1) \quad x \cdot E_g^A + (1-x) \cdot E_g^B$$

The band gap of ThS was estimated from ThS band structure, the estimated shift was found to be 8meV, similar to the measured value (7 meV).

CONCLUSIONS

CBD was successfully applied to create a simple, controllable and cost-effective procedure for alloying PbS thin films with thorium as the first step towards establishing a system designed for the study of radiation damage in thin film semiconductors. The average concentration of thorium along the film was found to be 0.5 at%, regardless of its concentration in the deposition solution (in a 0.438-1.752 mM range). Possibly it is due to the valence difference between the lead (Pb^{2+}) and the thorium (Th^{4+}), thus in order to maintain charge neutrality, a lattice vacancy of Pb is likely to accompany each alloying Th ion. Therefore, large concentrations of alloying thorium in the film should be accompanied by an equal amount of lead vacancies – a situation which is likely to be above the limit of thermodynamic stability. PL measurements show a shift of ~7meV between the reference PbS bandgap and alloyed Pb(Th) bandgap, confirming the concentration of Th in the sample.

PbS(Th) thin films can be applied for radiation damage studies in semiconductor thin films, by using internal radiation sources rather than the conventionally used external radiation. This can now be carried out by replacing the stable isotope ^{232}Th ($t_{1/2} \sim 10^6$ years), with a radioactive isotope ^{228}Th ($t_{1/2} \sim 1.9$ years) which is expected to provide a unique path for studying radiation damage in materials.

REFERENCES

1. G. Hodes, "Chemical Solution Deposition of Semiconductor Films", M. Dekker, New-York, p.12-225,(2003).
2. M. Shandalov and Y. Golan, "Microstructure and Morphology Evolution of Chemical Solution Deposited PbSe Films on GaAs(100)", The European Physics Journal - Applied Physics, **24**, p.13-20,(2003).
3. A. Osherov and Y. Golan, "Chemical Epitaxy of Semiconductor Thin Films", MRS Bulletin, **35**, p.790-796,(2010).
4. M. Biton, A. Shamir, M. Shandalov, E. Yahel and Y. Golan, "Chemical Deposition of Thorium-Alloyed Lead Sulfide Thin Films", accepted for publication in Thin Solid Films, (2014).

Numerical Analysis of the Microwave Auditory Effect

N. M. Yitzhak, R. Ruppin, R. Hareuveny

Soreq NRC, Yavne, Israel

INTRODUCTION

Pulsed microwave and radiofrequency radiation can produce a hearing sensation in human beings and mammals. The correct identification of the thermoelastic expansion as the mechanism responsible for the effect has been proposed by Foster and Finch⁽¹⁾. The absorption of the electromagnetic (EM) energy produces a fast thermal expansion, resulting from a small but rapid temperature rise, of the order of 10^{-6} °K. This launches a thermoelastic wave that travels to the inner ear, which causes an auditory sensation. A detailed review of the results of human, animal and modeling studies, which support this explanation of the hearing effect, has been published by Elder and Chou⁽²⁾.

Several analytical calculations of this phenomenon were presented⁽³⁻⁶⁾. However those calculations assumed a simplified homogeneous spherical head model and an absorption pattern of spherical symmetry. Numerical analyses, employing anatomically based head models, were also presented. These analyses were performed only for an EM plane wave of a single frequency (915 MHz)⁽⁷⁾ or for high-pass birdcage MRI coil for several lower frequencies (64, 300 and 400 MHz)⁽⁸⁾.

In the present work a numerical calculation of the thermoelastic wave propagation in a full male body is performed. The EM energy absorption and the elastic wave propagation are calculated by the finite-difference time-domain (FDTD) technique. An analysis of the results for different pulse width is presented.

METHOD OF ANALYSIS

The calculations were executed in two steps. The first one was the interaction of an incident electromagnetic plane wave with male body model. This was calculated numerically using the Yee FDTD algorithm for solving Maxwell's curl equations. For this step the commercial software XFDTD, supplied by Remcom Inc., State College, PA, USA, was employed. The model, also supplied by Remcom Inc., was of the height of 1.875 m, resolution of $5 \times 5 \times 5$ mm³ and 39 different tissue types. The mesh of this model was converted directly from the data generated by the Visible Human Project sponsored by the US National Library of Medicine.

In the second step a Yee type explicit leapfrog time stepping scheme was employed, in which the stress tensor components and the velocity components were alternately updated⁽⁷⁾. The linear thermal expansion coefficient was taken to be 2.7×10^{-5} °K⁻¹ for hard tissues and 13.0×10^{-5} °K⁻¹ (the value for blood) for soft ones⁽⁹⁾. Since the experimental data on the elastic properties of tissues vary over several magnitudes approximately median values have been taken and those values and a literature review will be published elsewhere.

RESULTS

A typical example of the pressure wave which develops in the cochlea is shown in figure 1 and its fast Fourier transform (FFT) is presented in figure 2. This was calculated for a plane wave pulse of frequency 2450 MHz incident from the back side, with horizontal polarization, pulse width of 70 μs and a power density of 1 mW/cm². The main acoustic frequency is approximately 8 kHz as in a previous analysis⁽⁷⁾.

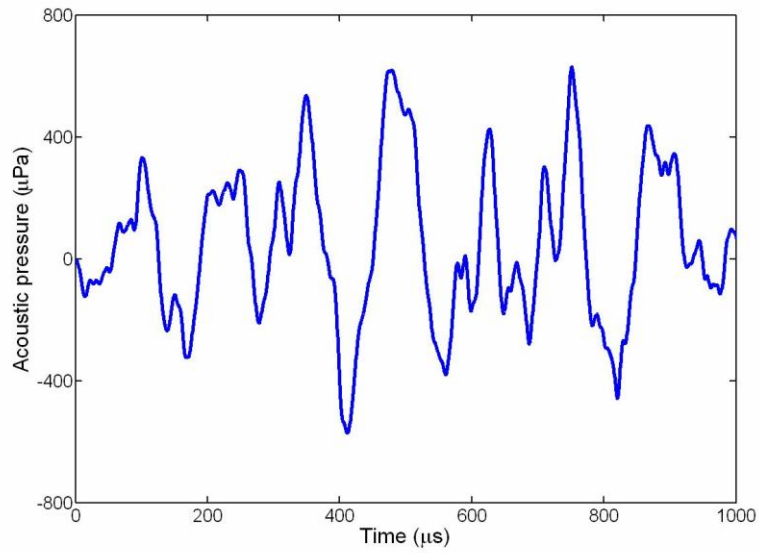


Figure 1. Calculated pressure waveform at the cochlea

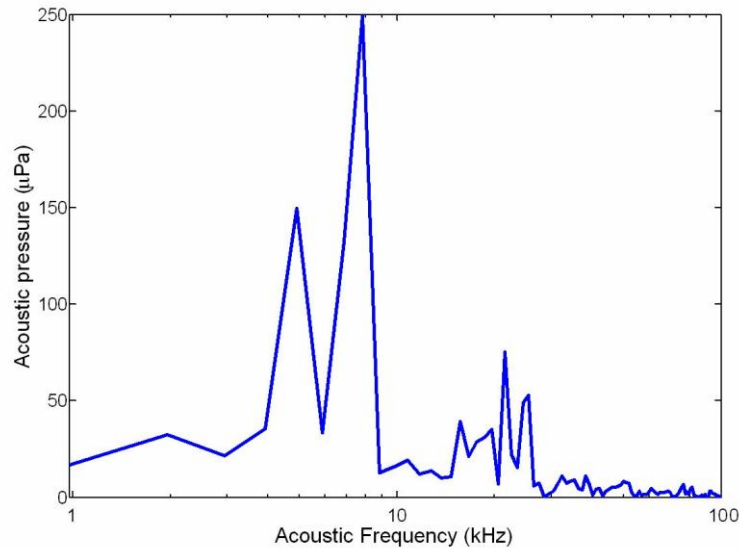


Figure 2. Calculated power spectra of the pressure waves at the cochlea

In the case of the homogeneous spherical head model, for which analytical solutions have been derived⁽⁶⁾ it was found that the pulse width dependence of the induced pressure amplitude anywhere in the head, for acoustic angular frequency ω_m is of the form:

$$P(\tau) = A|\sin(\omega_m \tau/2)| \quad (1)$$

Here τ is the pulse width and the amplitude factor A is independent of the pulse width.

We have found that this dependence on the pulse width holds to a good approximation even for the complicated models treated here. This is demonstrated in figure 3 (calculated for irradiation from the front by a vertically polarized 915 MHz pulse), in which the pulse width dependence of the amplitudes for number of selected acoustic frequencies, as obtained by a FFT of the pressure in the cochlea, is shown by the discrete points and the corresponding curves were obtained by fitting the calculated points to the functional form of the eq. 1, using a nonlinear least squares algorithm.

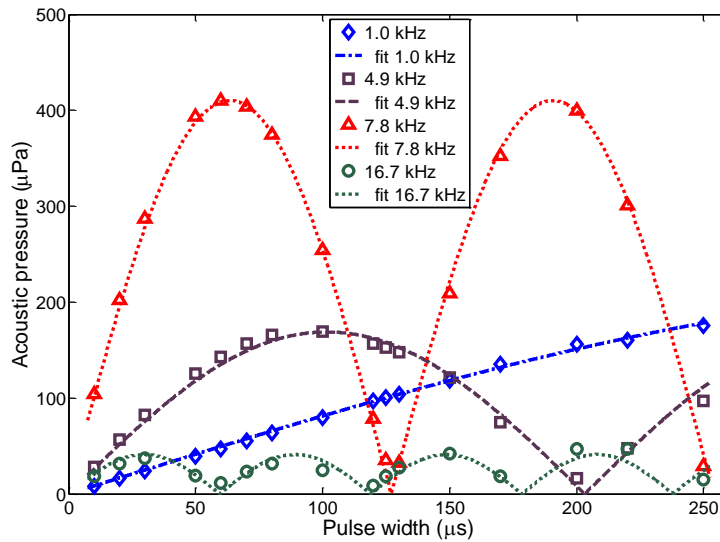


Figure 3. Pulse width dependence of the amplitude of a number of acoustic frequencies and a curve of the analytic dependency.

This dependency might be used to define a new method to analyze this phenomenon. The results of A as defined in eq. 1 as function of the acoustic frequency (calculated for two irradiations of 915 MHz pulse, one is vertically polarized from the front and the second is horizontal polarized from the back) is presented in figure 4. As was mentioned above, the main acoustic frequency is about 8 kHz, but there are more frequencies with non negligible intensity.

CONCLUSIONS

A full male body biological model was used to calculate the excitation of pressure waves at the cochlea following the irradiation by a microwave pulse. We have shown, by a FFT of the pressure waves in the cochlea, that the pulse width dependence of the amplitudes at various acoustic frequencies obeys a simple sinusoidal relation (eq. 1). This is due to the fact that the complicated biological model has an effective resonant cavity for each acoustic frequency.

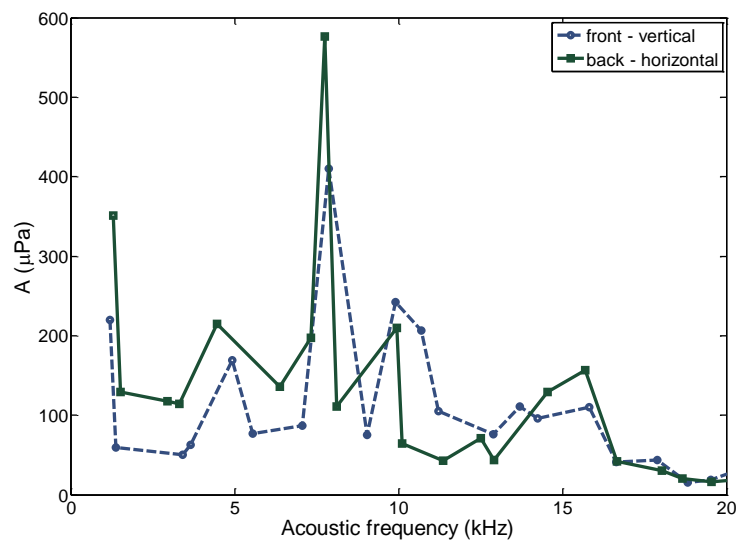


Figure 4. The quantity A as defined in eq. 1 for different acoustic frequencies and two irradiation types.

REFERENCES

1. Foster K. R., Finch E. D. *Microwave hearing: evidence for thermoacoustic auditory stimulation by pulsed microwaves*. Science **185**, p.256-258, (1974).
2. Elder J. A., Chou C. K. *Auditory response to pulsed radio frequency energy*. Bioelectromagnetics **24**, p.S162–S173, (2003).
3. Lin J.C. *On microwave induced hearing sensation*. IEEE Trans. Microw. Theory Tech. **25**, p.605-613, (1977).
4. Lin J.C. *Further studies on the microwave auditory effect*. IEEE Trans. Microw. Theory Tech. **25**, p.938-943, (1977).
5. Shibata T., Fujiwara O., Katoh K., Azakami T. *Calculation of thermal stress inside human head by pulsed microwave irradiation*. IEICE Trans. Commun. **J69-B**, p.1144-1146 (1986)
6. Yitzhak N. M., Ruppin R., Hareuveny R. *Generalized model of the microwave auditory effect*. Phys. Med. Biol. **54**, p.4037–4049, (2009).
7. Watanabe Y., Tanaka T., Taki M., Watanabe S. *FDTD analysis of microwave hearing effect*. IEEE Trans. Microw. Theory Tech. **48**, p.2126-2132, (2000).
8. Lin J. C., Wang Z. *Acoustic pressure waves induced in human heads by RF pulses from high-field MRI scanners*. Health Physics **98**, p.603-613, (2010).
9. Duck F. A. *Physical properties of tissue- a comprehensive reference book*. Academic press, Harcourt Brace Jovanovich, Publishers, p.141, (1990).

Medical and Applied Physics (Thursday, February 13, 2014 09:00)

Archaeological Ceramics: Provenience Based on Neutron Activation Analysis

J. Yellin

The Hebrew University of Jerusalem, Jerusalem, Israel

Compositions of ancient artefacts are examined for a variety of reasons including chronology, provenience, ancient technology and conservation studies. In particular, the elemental composition of archaeological pottery is of prime importance in fixing the origin of the pottery and thereby throwing light on trade routes and inter-regional connections between settlements in antiquity⁴. An intensive program of INAA was conducted at the Institute of Archaeology, The Hebrew University of Jerusalem, during the 1970-1990s⁵. Although that laboratory was closed as were other similar laboratories, new INAA laboratories have sprung up. Despite advances in other methods of analysis, INAA remains the favourite and best method for pottery provenience studies. The bulk of pottery data accumulated over the past five decades is based on INAA. These data, perhaps better than data obtained by other methods, can be integrated providing care is taken in accounting for the different standards employed by different laboratories and the different degrees of precisions attained. As a consequence projects that were suspended with the closure of laboratories can sometimes be concluded by combining resources from different laboratories. Examples will be given on how data from four laboratories, Hebrew University, Lawrence Berkeley National Laboratory, Missouri University Research Reactor⁶ and the University of Texas at Austin are utilized.

⁴ What Aegean “Simple Style” Pottery Reveals about Interconnections in the 13th-Century Eastern Mediterranean, Robert Koehl and Joseph Yellin in: *Krinoi kai Limenes, Studies in Honor of Joseph and Maria Shaw, Prehistory Monographs 22*, Philip P. Betancourt, Michael C. Nelson, and Hector Williams (editors), Chapter 24, pp199-207, INSTAP Academic Press, Philadelphia, Pennsylvania 2007.

⁵ Instrumental Neutron Activation Based Provenience Studies at The Hebrew University Of Jerusalem, With a Case Study on Mycenaean Pottery from Cyprus, Joseph Yellin, *Archaeometry* 49, 2, pp. 271-288 (2007). Four decades of Instrumental Neutron Activation Analysis and its contribution to the archaeology of the ancient land of Israel, Joseph Yellin and Aren M. Maeir, *Israel Journal of Earth Science* 56, pp 123-132 (2008).

⁶ Provenience of LBA II Pottery from the Cultic Repository of Tel Qashish
J. Yellin , M. T. Boulanger and M. Glascock, Atiqot (in press).

The SARAF Accelerator in 2012-2013

L. Weissman, A. Kreisel, D. Berkovits, A. Arenshtam, Y. Ben-Aliz, Y. Buzaglo, O. Dudovitch, I. Eliahu, Y. Eisen, D. Har-Even, Y. F. Haruvy, S. Halfon, T. Hirsh, D. Hirshmann, Z. Horivitz, I. Gertz, A. Grin, G. Feinberg, I. Fishman, B. Keizer, D. Kijel, G. Lempert, Y. Luner, E. Reinfeld, J. Rodnizki, G. Shimel, A. Shor, I. Silverman, E. Zemach

Soreq Nuclear Research Center, Yavne 81800 Israel

INTRODUCTION

Phase I of SARAF [1] consists of a 20 keV/u ECR Ion Source (EIS), a Low Energy Beam Transport (LEBT) section, a 4-rod Radio Frequency Quadrupole (RFQ) injector, a Medium Energy (1.5 MeV/u) Beam Transport (MEBT) section, a Prototype Superconducting Module (PSM), a Diagnostic plate (D-plate), beam dumps (BD) and temporary beam line (Fig. 1).

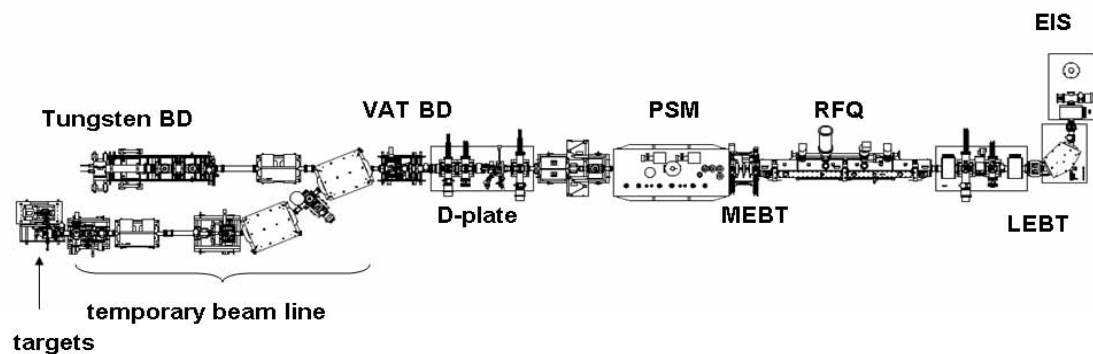


Figure 1. Layout of SARAF Phase I and the temporary beam line.

According to Phase I design specifications; SARAF superconducting linear RF accelerator should yield 2 mA CW beams of protons and deuterons, at energies up to 4 and 5 MeV, respectively. The achieved working points by today are for example; CW proton beams of 1 mA and 3.9 MeV and 1.9 mA at 2.1 MeV and for deuterons a pulsed beam at low duty cycle with 0.8 mA instantaneous current at 4.8 MeV. Nonetheless, during the last two years, alongside with continuous development of the facility, the accelerator has been operated extensively at each opportunity and significant new experience in beam operations has been accumulated. The main achievements in beam operation were demonstration of operation of intense proton beam on a thin foil target and the first experiments with the liquid lithium target.

In this abstract we highlight the accelerator status, some significant improvements of the accelerator subsystems, as well as, experience in beam operations that has been accumulated since the last reports [1].

STATUS of FACILITY and developments OF ITS subsystems

Detailed report on beam operation in 2012-2013 could be found in [2]. We had in average a hundred hours per year of high current proton beam on beam dumps and targets. Many hundreds of hours of beam operation per year were devoted to beam tune and beam studies.

The new developments and modifications of the accelerator subsystems are listed in the table below:

Subsystem	Recent improvements and activities
EIS/LEBT	<ol style="list-style-type: none"> 1. Preparation of the integration of the slow-chopper into the machine safety system 2. Introduction of the new beam blocker/collimator at the exit of the LEBT exit 3. Introduction of two viewports for beam observation 4. Preparation of a test bench for testing the magnetron power supply 5. Beam dynamics simulations to demonstrate second order measured phenomena
RFQ/MEBT	<ol style="list-style-type: none"> 1. Retuning of the RF amplifier to the higher maximum reflected power 2. Introduction of x-ray detectors along the RFQ barrel 3. Introduction of new collimator/blocker at the MEBT exit 4. Improvement of pumping capacity 5. Replacement of the vacuum barriers for water cooling channels 6. Preparation of the new end flange with the electron suppressor
PSM	<ol style="list-style-type: none"> 1. Introduction of the new 4 kW RF amplifiers [3] 2. Replacement of the faulty piezo tuners to superior high voltage ones 3. Testing and introduction of DC breakers for RF couplers 4. Preparation for better cooling arrangement of the couplers [4]
Beam Lines	<ol style="list-style-type: none"> 1. Introduction beam loss monitor system 2. Development and installation of a heavy metal beam dump to overcome the hydrogen blistering problem 3. Testing of a new pins based beam dump prototype [5] 4. Preparation of a new pin based full scale beam dump 5. Installation and commissioning of a new diagnostic chamber before LiLiT 6. Installation and commissioning of the general use station before the beam dump 7. Test residual gas beam profiler from GANIL [6]

The main problems hindering the beam operation were: 1. Electrical power interruptions, 2. Lack of adequate target room infrastructure, 3 Deterioration of the performance of the control system. All the factors above are being addressed and will be improved in the near future.

BEAM OPERATIONS

Beam operation in 2012 was focused on the thin foil target experiment [7]. These targets are very sensitive and in the past we experienced many failures. Significant progress was achieved in 2012; 3.6 MeV proton beam at the intensity of up to 300 μA was kept on targets for period of many tens of hours. The beam current main limit was the foil surface maximum temperature that was limited to 500 ± 50 °C. This was achieved owing to the following two factors; development and improvement of the target design and improvement of the beam diagnostics system and the tuning procedures. The radiation damage accumulated in the foil went up to 1 DPA and the target was still well functioning at this harsh conditions.

In 2013 the focus of beam operation was on the first experiments with the liquid lithium target [8]. Significant efforts were directed on beam tune on the lithium jet target, as the latter has very limited diagnostics possibilities. Two tests with high power CW proton beam were performed with the LiLiT target. The highest current applied on the target was 1.5 mA. The target exhibited robust performance. The first attempts of measurement of neutron capture cross-sections were performed during these tests. In the near future the experiments with LiLiT will be major activity at SARAF phase I.

Beyond the two major projects above a number of minor experiments and tests were performed recently. These activities included: 1. low fluence irradiation of TLD crystals [9], test of a residual gas beam profiler with intense CW beam, test of a new beam dump prototype, test of a beam position monitor from GANIL and others.

CONCLUSION

The beam operation experience in 2012-2013 showed that at Phase I SARAF has potential to become a real user facility with intense beam schedule and high beam availability. The SARAF teams will strive to achieve this goal in 2014-2015.

REFERENCES

1. L. Weissman *et al.*, Proceedings of 26th Israeli Nuclear Societies workshop, Dead Sea, February 21-23, 2012.
2. L. Weissman *et al.*, "SARAF operation in 2012", Soreq NRC report #4444 and L. Weissman *et al.*, "SARAF operation in 2013", in preparation.
3. B. Kaizer *et al.*, proceedings of LINAC 2012.
4. J. Rodnitzki *et al.*, proceeding of SRF 2013.
5. A. Arenstam *et al.*, JINST 8 T07004 (2013).
6. E. Gueroult *et al.*, JINST 8 T08005 (2013).
7. I. Silverman *et al.*, proceedings of ACCAPP 2013.
8. G. Feinberg *et al.*, these proceedings; Sh. Halfon *et al.*, these proceedings.
9. I. Eliahu *et al.*, these proceedings.

Superconducting Accelerating Cavity Pressure Sensitivity Analysis

J. Rodnizki, Z. Horvits, Y. Ben Aliz, A. Grin, L. Weissman

Soreq NRC, Yavne 81800, Israel

INTRODUCTION

The SARAF Prototype Superconducting Module (PSM) Houses six 176 MHz Half Wave Resonators (HWR) and three Super Conducting (SC) 6T solenoids⁽¹⁾. The PSM accelerates protons and deuterons from 1.5 MeV/u to 4 and 5 MeV⁽²⁾. The HWRs are highly sensitive to the coolant liquid Helium pressure fluctuations which might limit the available current to 1-2 mA depending on the output energy. Since new 4 kW amplifiers were installed at SARAF⁽³⁾, reducing the cavity sensitivity may enable SARAF to increase the available current towards 4 mA beams.

To analyze the effect of the HWR eigen mode frequency sensitivity to helium pressure the following formula is used⁽⁴⁾:

$$P_g = \frac{V_c^2}{R_{sh}} \cdot \frac{(1 + \beta)^2}{4\beta} \cdot \frac{1}{\cos^2 \varphi} \left\{ \left[\cos \theta + \frac{I_b R_{sh}}{V_c (1 + \beta)} \cos^2 \varphi \right]^2 + \left[\sin \theta + \frac{I_b R_{sh}}{V_c (1 + \beta)} \cos \varphi \sin \varphi \right]^2 \right\}$$

where P_g is the power required to excite the cavity, V_c is the cavity voltage, R_{sh} is the cavity shunt impedance, β is the cavity coupling constant, I_b is the beam current, and θ is the relative phase angle between the point of maximum acceleration of the cavity RF and the center of the beam bunch being accelerated, and φ is the cavity detuning angle (microphonics).

The effect of the detuning angle φ due to microphonics including the sensitivity to helium pressure Δf_{pk-pk} , $\varphi = \tan^{-1}(\Delta f_{pk-pk}/(f_0/Q_{load}))$, is given in fig. 1 for a set of cavity parameters of the PSM HWR as measured in SARAF and simulated by CST MWS⁽⁵⁾: $Q_0 = 5 \cdot 10^8$, $V_c = 850 \text{ kV}$, $I_b = 4 \text{ mA}$, $R_{sh}/Q_0 = 163$, $\beta = Q_0/Q_{ext}$ and a synchronous phase $\theta = -20^\circ$.

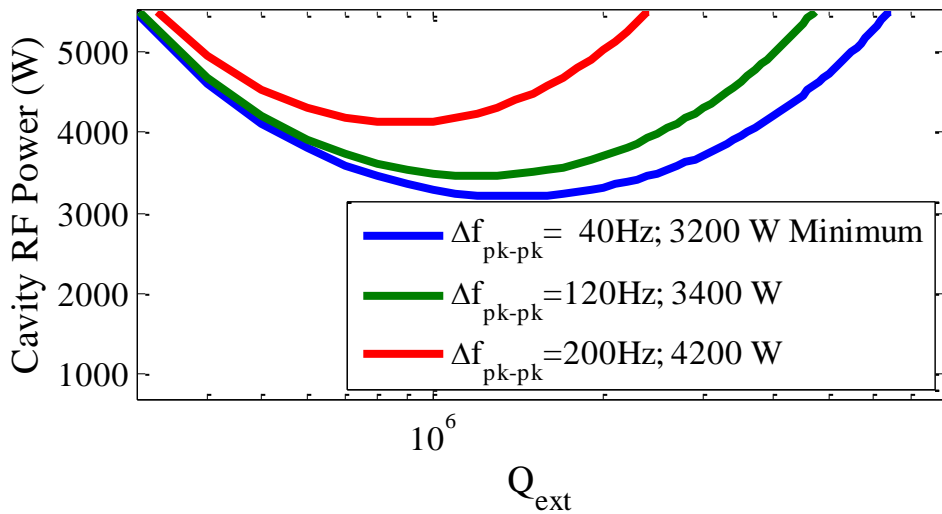


Figure 1. The required cavity RF power for 40, 120 and 200 Hz peak-to-peak microphonics detuning amplitudes, including helium pressure fluctuations.

The SARAF HWRs are extremely sensitive to LHe pressure fluctuations. Detuning signal is dominated by the Helium pressure drift. Detuning sometimes exceeds $\pm 200 \text{ Hz}$ ($\sim \pm 2 \text{ BW}$). The cavity FWHM is

evaluated by: $2\Delta\omega = \omega_0 / Q_{load} = 130\text{Hz}$. The measured sensitivity to helium pressure is 60 Hz/mBar as shown in figure 2⁽⁶⁾.

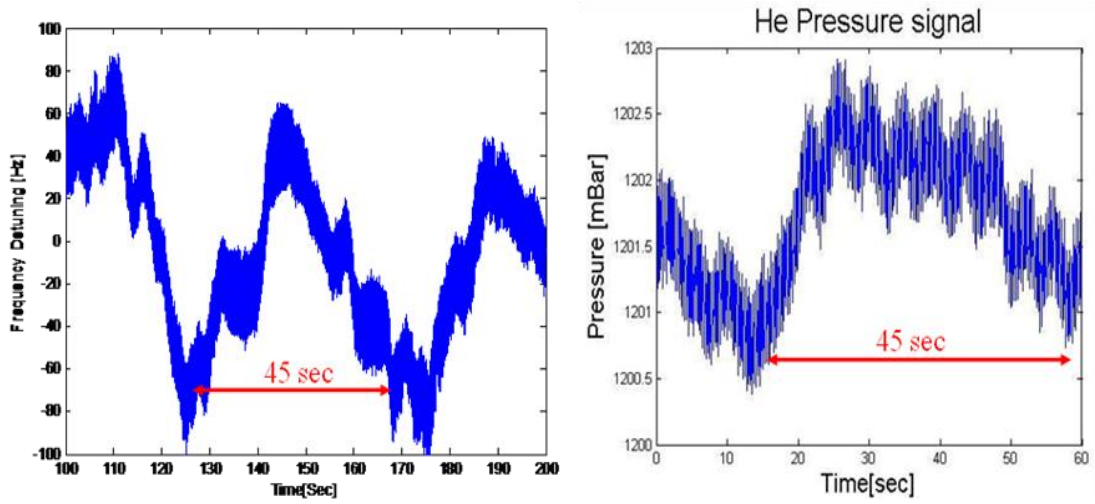


Figure 2. HWR Microphonics measurements (taken from [6]).

ANALYSIS

The high cavity sensitivity is due to the cavity asymmetric radial structure in the vicinity of the beam line. The flat shape of the cavity along the beam line in the area of the high electric field (fig. 3) generates the high sensitivity of the Eigen mode frequency to helium pressure.

The evaluation of the cavity Eigen mode frequency sensitivity to helium pressure fluctuation is based on the following:

The radiation pressure on the cavity surface due to EM fields is evaluated by ⁽⁷⁾:

$$P = \frac{1}{4}(-\epsilon_0 E^2 - \mu_0 H^2)$$

The Eigen mode frequency deviation due to helium hydrostatic pressure HWR cavity surface deformation is evaluated by ⁽⁷⁾:

$$\frac{\Delta\omega}{\omega} = \frac{\Delta U}{U} = \frac{1}{4U} \int_{\Delta V} (\epsilon_0 E^2 - \mu_0 H^2) dV = \frac{1}{4U} \int_S (\epsilon_0 E^2 - \mu_0 H^2) \delta_{norm} ds$$

The HWR EM fields as simulated with the CST MWS. The fields as shown in fig. 3 demonstrate high electric fields in the vicinity of the flat shape of the external conductor around the beam line. In this region the external conductor deformation due to helium hydrostatic pressure gain the maximal value as shown in figure 4. The cavity evaluated sensitivity is in full consistent with the HWR measured values (60Hz/mBar). The found cavity sensitivity values are:

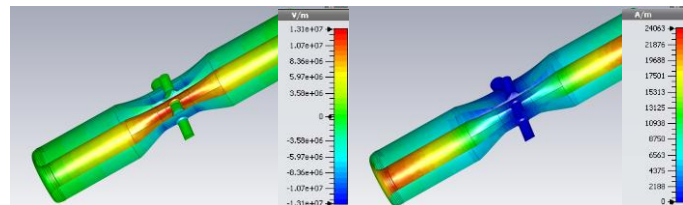


Figure 3. HWR E (left) and H (right) fields.

$$\frac{\partial f}{\partial P} = -60.6 \frac{\text{Hz}}{\text{mBar}}$$

$$P = 10\text{mBar} \Rightarrow$$

$$\delta_{norm\text{beamline}} = -0.7\mu$$

$$\delta_{norm\text{max}} = -0.98\mu$$

$$\sigma_{\text{max}} = 0.56\text{MPa}$$

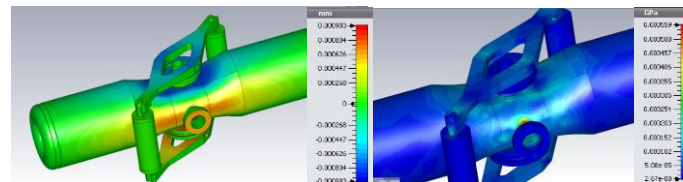
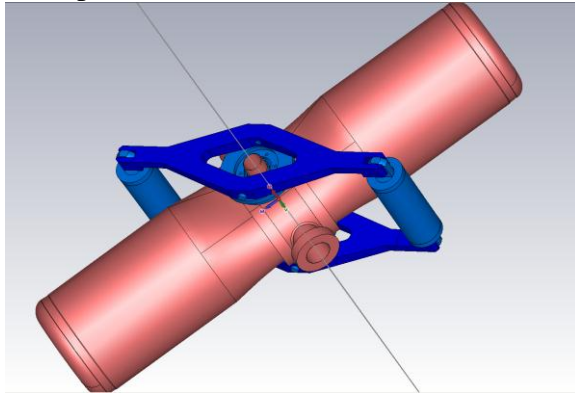


Figure 4. The normal deformation and the stress due to hydrostatic helium pressure.

Increasing the rigidity of the tuning fog and adding ribs at the vicinity of the beam line (fig. 5) may reduce the sensitivity of the HWR to helium pressure: The modified evaluated values are:



$$\frac{\partial f}{\partial P} = -21 \frac{\text{Hz}}{\text{mBar}}$$

$$P = 10 \text{mBar} \Rightarrow$$

$$\delta_{normbeamline} = -0.15 \mu$$

$$\delta_{normmax} = -0.38 \mu$$

$$\sigma_{max} = 0.34 \text{Mpa}$$

Figure 5. A double thick fog with enforced ribs at the cavity neck.

The tuning system operation effect due to helium pressure is demonstrated in fig. 6 for 200 μm tension displacement, both sides both step motor and piezo and 1.2 bar He pressure. This simulation may be used to explore the stresses on the cavity due to cool down and warm up procedure as used in SARAF. The found sensitivity values for the original cavity and tuning system are:

$$P = 1.2 \text{Bar} \quad \delta_{normbeamline} = 39 \mu$$

$$\delta_{piezo \text{ step motor both sides}} \quad \delta_{normmax} = 39 \mu$$

$$= 200 \mu \Rightarrow \quad \sigma_{max} = 62.4 \text{MPa}$$

$$\quad \quad \quad \Delta f = -5.302 \text{kHz}$$

Table 1 summarizes the three simulations scaled to 1.2 Bar.

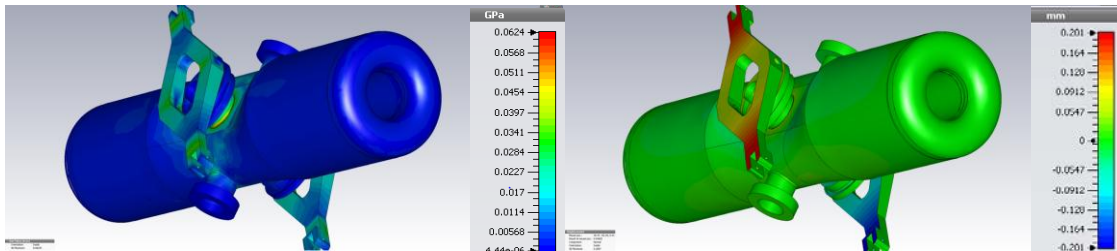


Figure 6. 200 μm tension displacement, both sides both step motor and piezo and 1.2 bar He pressure

Table 1. The three simulated cases scaled to 1.2 Bar

Simulated Case	Δf (kHz)	σ_{max} (MPa)	δ_{beam} (μ)	δ_{max} (μ)
Original cavity	-73	67	84	120
Rigid cavity and fog	-25	41	18	46
Original cavity + 200μ tuning tension excitation	-5.3	62	39	39

CONCLUSIONS

The measured sensitivity of the cavity was evaluated and it is full consistent with the measured values. It was explored that the tuning system (the fog structure) has a significant contribution to the cavity sensitivity. By using ribs or by modifying the rigidity of the fog we may reduce the HWR sensitivity. During cool down and warming up we have to analyze the stresses on the HWR to avoid plastic deformation to the HWR since the Niobium yield is an order of magnitude lower in room temperature.

REFERENCES

1. M. Pekeler et al., DEVELOPMENT OF A SUPERCONDUCTING RF MODULE FOR ACCELERATION OF PROTONS AND DEUTERONS AT VERY LOW ENERGY, Proceedings of LINAC2006, Knoxville, Tennessee USA, 2006.
2. D. Berkovits et al., OPERATIONAL EXPERIENCE AND FUTURE GOALS OF THE SARAF PROTON / DEUTERON LINAC, Proceedings of LINAC2012, Tel-Aviv, Israel,
3. I. Fishman, I. Gertz, B. Kaizer, D. Har-Even, HIGH POWER AMPLIFIER SYSTEMS FOR SARAF PHASE II, LINAC2012 Tel Aviv, Israel, 2012.
4. M. P. Kelly et al, "Microphonics in the ATLAS Upgrade Cryomodule, Proc. of the 14th International SRF Conference, Berlin, Germany, 2009.
5. CST STUDIO SUITE Version 2013 <http://www.cst.com>.
6. A. Perry et al., SARAF SUPERCONDUCTING MODULE COMMISSIONING STATUS, Proc. of the 14th SRF Conference, Berlin, Germany, 2009.
7. H.Gassot, MECHANICAL STABILITY OF THE RF SUPERCONDUCTING CAVITIES, Proceedings of EPAC 2002, Paris, France.

Redesign of SARAF RFQ Modulation for CW Deuteron Acceleration

A. Shor and J. Rodnizki

Soreq Nuclear Research Center, Yavne 81800 Israel

INTRODUCTION

The SARAF radio-frequency quadrupole (RFQ) is a crucial element in the SARAF proton/deuteron accelerator complex - it makes acceleration of high intensity ion beams possible. The RFQ electrodes (Figure 1) consist of 4 four-meter long rods, with adjacent rods at opposite polarity and diagonal rods at same polarity, with the polarity oscillating sinusoidally at 176 MHz, thereby providing the element with very strong transverse focusing capabilities. In addition, properly designed longitudinal modulations on the electrode surfaces enable both acceleration and longitudinal focusing, and thereby the ability to bunch the beam. Bunching is a necessary feature for continuation of the acceleration with the superconducting half-wave resonators.

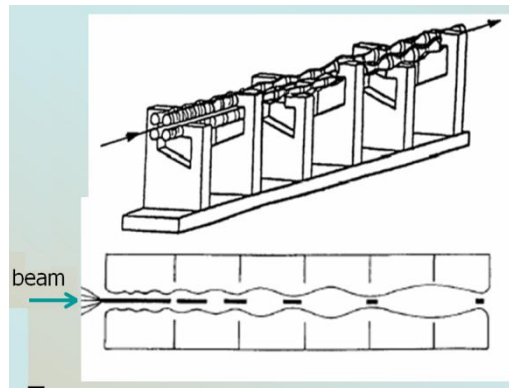


Figure 1. Schematic drawing of RFQ rods (top), and longitudinal cut showing focusing and bunching of beam (bottom).

The SARAF RFQ was designed for CW proton and deuteron acceleration. Proton acceleration requires RF voltage of 32.5 kV, which translates to about 62 kW of power. Deuteron acceleration requires twice the RF voltage and therefore four times the power, or 250 kW. Unfortunately, continuous CW operation of the SARAF RFQ has been successfully achieved only at RF power of somewhat above 170 kW⁽¹⁾.

We have embarked on the re-design of the RFQ rods' modulation parameters for deuteron acceleration at lower voltages to enable CW deuteron operation. This redesign has been done and optimized with the General Particle Tracer (GPT) code⁽²⁾, including code for an RFQ element developed at Soreq using the 8-term potential expansion for the electric fields⁽³⁾. The re-design is based on the SARAF RFQ modulation parameters designed for 65 kV, scaled down to the desired operating voltage of 53.6 kV, which would require 170 kW for CW. At this RFQ voltage, the deuteron energy at the RFQ exit is reduced to 2.56 MeV whereas the original SARAF design was for deuteron exit energy of 3.0 MeV. An energy decrease at the RFQ exit comes at the cost of lower exit energy at the end of the superconducting accelerator and higher beam mismatch at the superconducting linac entrance and so higher beam loss.

RFQ MODULATION AND 8-TERM POTENTIAL EXPANSION

Figure 2 shows a schematic diagram of the RFQ modulation. The quantity $\beta\lambda$ represent the length a particle travels in one RF cycle, where β the particle velocity in units of c and λ the RF wavelength. The quantity a is the minimum transverse radius, and the modulation factor m determines the strength of the longitudinal component (i.e. in z -direction) of the field. One RFQ cell is defined as $\beta\lambda/2$, which must be continuously up-scaled to accommodate for the increase in velocity as a particle traverses the longitudinal electric field.

At first, weak modulation with only very gradual increase allows the RFQ bunches to form adiabatically. Once bunches are formed, the appropriate increase in cell length determines also at which phase the bunch enters into the next RFQ cell. Thus a very careful design and precise machining of the rods is necessary to obtain clean bunching and acceleration for the desired outgoing beam characteristics.

For a realistic RFQ design and simulation, the 8-term potential expansion provides precise electric field distribution. The 8-term potential is given by equation 1,

$$U_{ex}(r, \theta, z) = \frac{V}{2} [A_{01}(r/r_0)^2 \cos(2\theta) + A_{10}I_0(kr) \cos(kz) + A_{03}(r/r_0)^6 \cos(6\theta) + A_{21}I_2(2kr) \cos(2\theta) \cos(2kz) \\ + A_{12}I_4(kr) \cos(4\theta) \cos(kz) + A_{30}I_0(3kr) \cos(3kz) + A_{23}I_6(2kr) \cos(6\theta) \cos(2kz) + A_{32}I_4(3kr) \cos(4\theta) \cos(3kz)]$$

where the I_n are modified Bessel function of order n , and $k = \pi/2\beta\lambda$. We determine the 8-term coefficients by performing a least χ^2 fit for a constant potential on the modulated pole tips surfaces. Further details of this fitting procedure are discussed in reference 3.

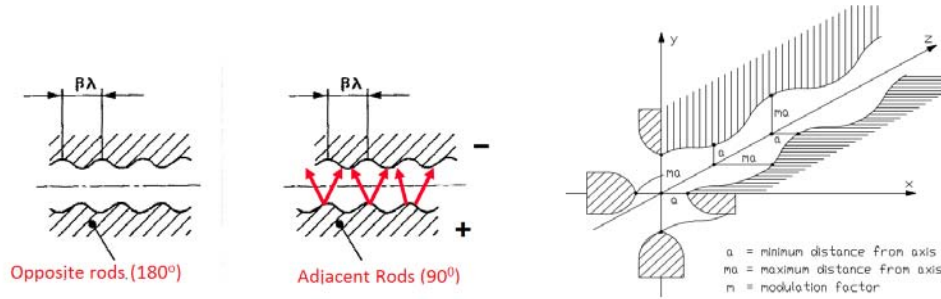


Figure 2 Schematic drawing of RFQ electrodes showing modulation and RFQ cells. Red contours represent field direction.

PROCEDURE FOR DOWN_SCALING EXISTING SARAF RFQ

The consequences of scaling down the RFQ design from 65 kV to 53.6 kV are as follows. To keep the high beam transmission, the transverse focusing strength must be kept the same. In order to do this, the average rod separation, or r_0 , must be down-scaled according to the square root of the ratio of voltages, as is suggested by the leading term of the 8-term potential, or

$$\frac{r_0^{newRFQ}}{r_0^{oldRFQ}} = \sqrt{\frac{V^{newRFQ}}{V^{oldRFQ}}} = \sqrt{\frac{56.3}{65}}$$

The second consequence of scaling down the voltage involves the energy gain (and longitudinal focusing strength) after each cell, which scales as the voltage V . Naively, one can think of modifying the increased cell length following each energy gain according to the ratio of voltages, as suggested by the second term in the potential expansion. Unfortunately, when changing the cell geometry, the 8-term coefficients change, and the phase of the beam entering the next cell is somewhat different. For proper longitudinal development, even small changes in the desired phase can have a detrimental effect for the developing of bunches. Different scaling profiles for the longitudinal cell length development must be attempted, where for each try the 8-term coefficients must be re-calculated using the optimization procedure, before a reliable simulation can be attempted. Once optimum 8-term coefficients are found, terms for the radial matching section must be appropriately adjusted to maintain the radial matching between the incoming beam and the subsequent RFQ modulation.

REDESIGNED RFQ MODULATION FOR CW DEUTERON ACCELERATION

We have successfully obtained RFQ modulation parameters that will allow for deuteron acceleration with pole tip voltage at 53.6 kV, using the scheme described above, including simulation with the 8-term potential expansion for the RFQ electric field. The optimal scaled-down RFQ, with voltage of 53.6 kV, provides a deuteron beam at outgoing energy of 2.56 MeV, with a transmission of 95% for a 0 mA beam, and transmission of 92% for a 5 mA, both for initial beam at $\epsilon_{norm_r.m.s.} = 0.20 \pi\text{-mm-mrad}$.

Figure 1. Simulations for existing SARAF RFQ and re-designed SARAF RFQ

	Voltage for Deuterons	Required Power (kW)	Deuteron Energy (MeV)	Transmission @ 5 mA
Existing SARAF RFQ	65 kV	250	1.5	87 %
Redesigned SARAF RFQ	53.6 kV	170	1.256	92 %

Figure 4 shows the longitudinal phase space plot for the deuteron beam at the exit of the redesigned RFQ for simulation containing 10^5 macro-particles at 5 mA. In the process of obtaining this optimization, great care was made to keep the ΔE of the emerging beam as small as possible so as to minimize the longitudinal drift in the MEBT.

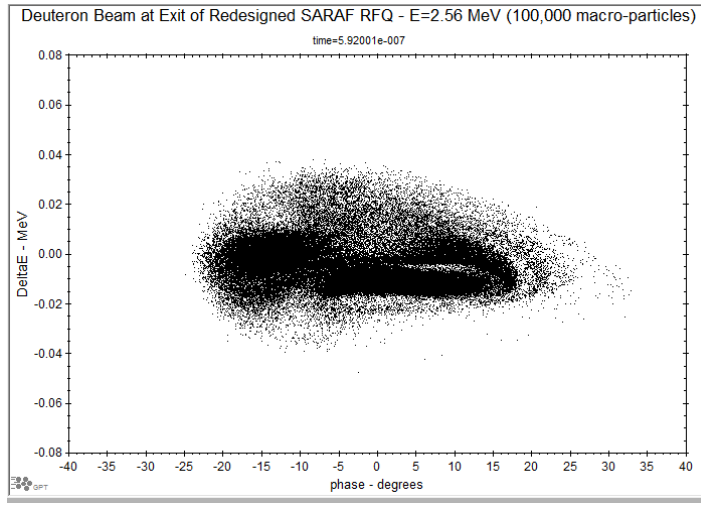


Figure 4. Redesigned RFQ at 53 kV – Longitudinal phase space at RFQ exit

ACCELERATING DEUTERONS FROM REDESIGNED RFQ THROUGH OLD SARAF LINAC

The old design of the SARAF LINAC is flawed in several aspects. There is no buncher in the MEBT section, therefore severe longitudinal focusing is required which puts a strain on the first few HWR cavities. A second flaw is the mismatch between the RFQ emerging beam at $\beta \sim 0.052$ and the first set of HWRs optimized for $\beta = 0.09$. This is especially severe for a RFQ beam at the lower outgoing energy of 2.56 MeV.

Nevertheless, to demonstrate the robustness of the redesigned RFQ concept, a tune of the old SARAF LINAC was made with the beam from the redesigned RFQ. The results for 10^5 deuterons at 5 mA include longitudinal and transverse r.m.s. emittance growth of less than 5 %, with no lost particles, and acceleration up to 42.2 MeV for an initial beam with transverse r.m.s. emittance of $\epsilon_{\text{norm}} = 0.20 \pi\text{-mm-mrad}$.

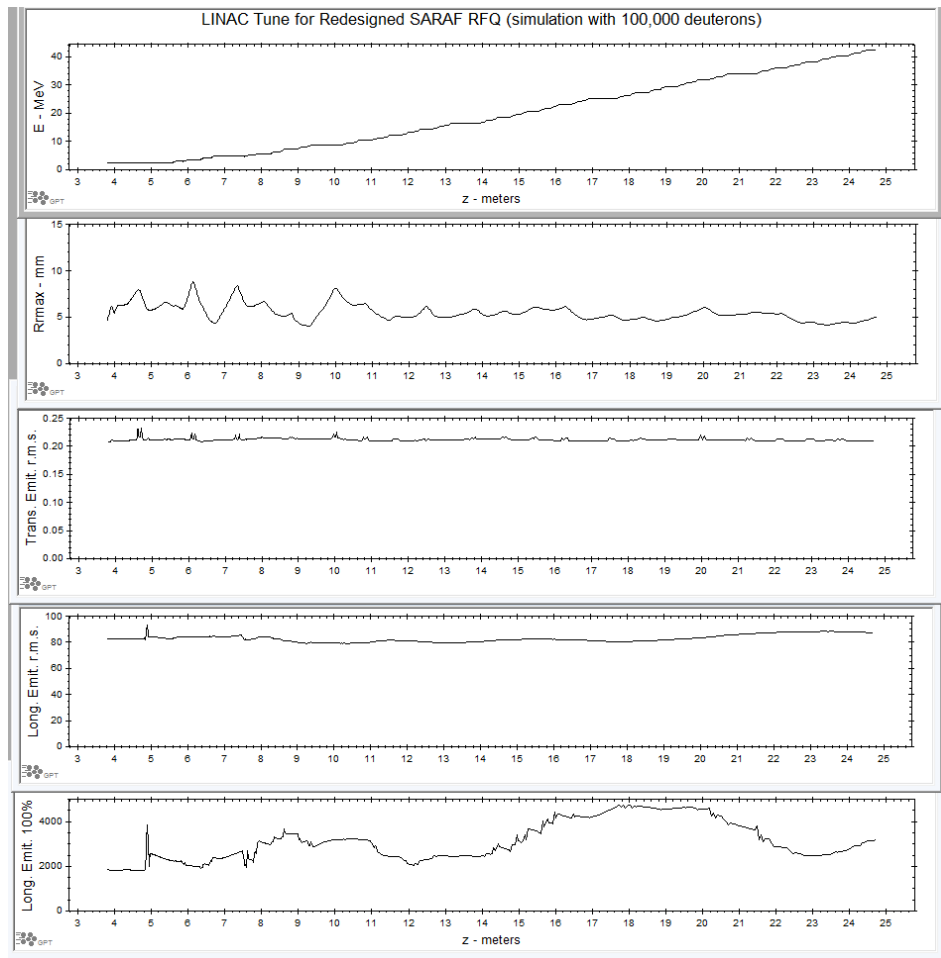


Figure 5. Tune of old SARAF linac for 10^5 deuterons emerging redesigned RFQ
 a) energy development, b) transverse envelope, c) transverse rms emittance
 d) longitudinal rms emittance, and e) 100% longitudinal emittance

[1] L. Weissman et al. Linac 2010, Tsukuba, Japan
 [2] General Particle Tracer simulation package, Pulsar Physics, Netherlands
 [3] B. Bazak, M.Sc. thesis, Racah Institute of the Hebrew University (2008).

Fast Beam Chopper at SARAF Accelerator via RF Deflector before RFQ

B. Kaizer, A. Shor, and L. Weissman

Soreq NRC, Yavne 81800 Israel

INTRODUCTION

Fast beam choppers are necessary in applications where neutron time of flight information is required for measuring and/or selecting the energy of the neutrons⁽¹⁾. Chopping schemes have been developed for high intensity accelerators, which are mostly implemented in the MEBT sections, however at high beam current and energies of several MeV, the power required is formidable and dissipated on the beam dump is significant⁽²⁾. A chopping scheme based on an RF deflector situated before an RFQ has been studied by our colleagues within the framework of the ACCIS project and FNeuRad collaboration⁽³⁾. The deflector effectively chops the pre-RFQ ion beam while the energy is still low, and the transmitted beam is further bunched to even shorter pulse width by the RFQ.

In this paper we present design and simulations of a fast beam chopping system at the SARAF accelerator based on an existing slow chopper consisting of an RF electric-field parallel plate deflector preceding the RFQ. We first discuss operation with the existing deflector for slow chopping. We present measurements made with a fast faraday cup (FFC) showing the micro-structure of the beam emerging the RFQ. We discuss simulations using the General Particle Tracer (GPT) beam dynamics simulation code⁽⁴⁾, where various pulsing regimes were simulated to optimize for successful fast chopping and single bunch selection. The simulations show that fast chopping can be achieved for deflection using alternating positive and negative HV polarities with a fast HV switch where the beam is transmitted to the RFQ during the positive-negative cross-over. The simulations also show that one can obtain efficient deflection of unwanted pulsed, with 60% transmission efficiency for the desired pulse. We discuss implementation for fast chopping at SARAF based on this deflector pulsing scheme, where the current design is for a chopper that will provide 0.3 ns bunches with a repletion rate of $\sim 10^5$ bunches/sec, with future plans for $\sim 10^6$ Hz.

The Saraf Accelerator –Phase I

The SARAF accelerator⁽⁵⁾ is designed to provide CW proton or deuteron beams of up to 5 mA current and 40 MeV energy. Currently, phase I of SARAF has been installed and has undergone commissioning, and is currently operational for experimental work (Figure 1). SARAF phase I consists of an ECR ion source (EIS), a 176 MHz radio-frequency quadrupole (RFQ), and a prototype superconducting module (PSM) for further acceleration. A low energy beam transport (LEBT) transports the beam from the ion source to the RFQ, and consists of a solenoid focusing elements and collimators, a 90° bending magnet, and various diagnostic tools. The RFQ bunches and accelerates the beam to 1.5 MeV/u, providing 300 ps bunches separated by 5.68 nanoseconds. The RFQ was designed for CW operation both for protons and deuterons. A medium energy beam transport (MEBT) matches the beam to the entrance to the PSM. The PSM contains 6 superconducting half-wave resonators (HWR) and 3 superconducting solenoids. The PSM provides further accelerations, up to about 5 MeV, and also allows for longitudinal focusing or bunching (de-bunching). Following the PSM is diagnostic plate (D-plate) with various devices to provide diagnostics of the beam emerging from the PSM. Following the D-plate is a dipole magnet to channel the beam either to a beam dump or to a special beam line to the experimental target area.

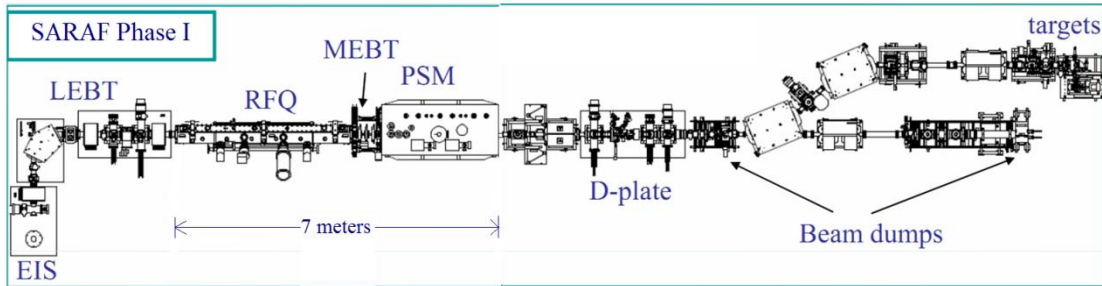


Figure 1. Layout of SARAF phase I showing EIS ion source, LEBT, RFQ, MEBT, PSM, D- plate, and magnetic beam line.

Slow Chopper at Saraf

The slow chopper at SARAF consists of deflection plates and electronics developed at LNS Catania within the SPIRAL II program⁽⁶⁾ and mounted in SARAF for tests and evaluation. The slow chopper consists of a set of parallel plates on which a potential is applied for deflecting a low energy beam at an angle of about 20°. For the duration for which transmitted beam is desired, a fast switch shuts off the HV for the required beam on-time. The electronics provided allows for minimum off-time of about 180 ns and maximum switching repetition rate of up to 800 Hz. The slow chopper was installed in the LEBT between the second and third solenoids. Figure 2 shows a schematic diagram of the LEBT and placement of the slow chopper, including the water cooled beam catcher at 20°, and also the RFQ and MEBT.

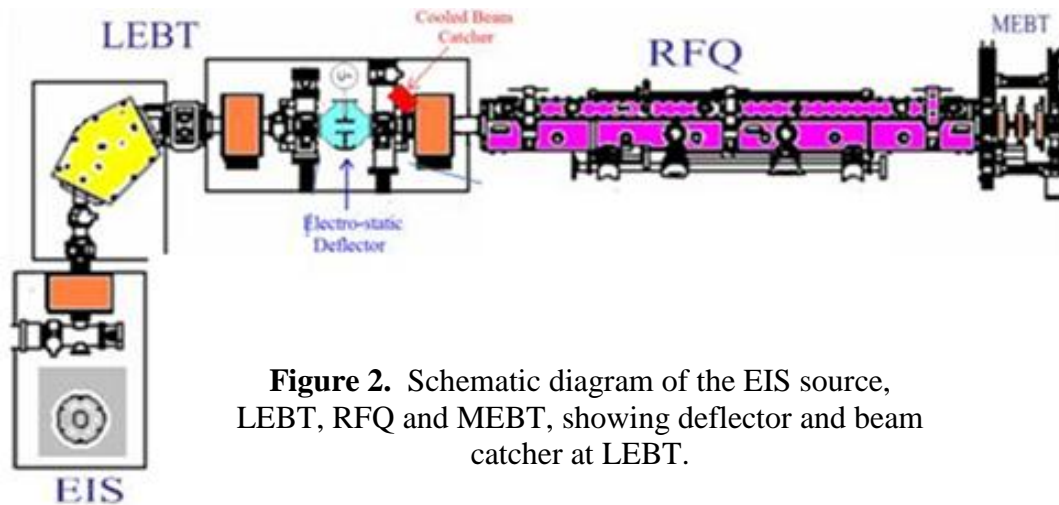


Figure 2. Schematic diagram of the EIS source, LEBT, RFQ and MEBT, showing deflector and beam catcher at LEBT.

Bunched Beam Following RFQ

Figure 3 shows beam trace following the RFQ as measured by the Fast Farraday Cup (FFC). The RFQ bunches are separated by 5.68 ns and have a width of about 0.3 ns. This is very similar to results we obtain from simulations of the RFQ. The big challenge is to develop a scheme for single bunch selection, This will enable producing neutrons at very narrow time windows and thereby providing the capabilities of neutron TOF measurements and neutron energy selection selection at high precision.

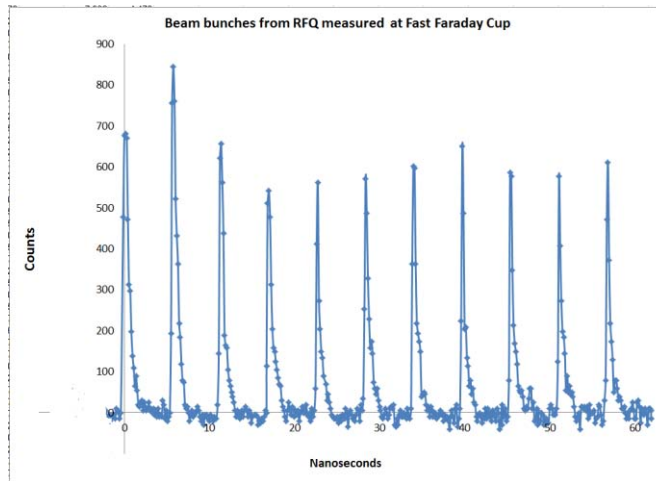


Figure 3. Trace of beam following the RFQ as measured by Fast Faraday Cup (FFC)

Simulations of Single Bunch Selection with Fast Chopper

We have performed beam dynamics simulations of our fast chopping scheme with the GPT (General Particle Tracer) simulation package. We built into GPT a precise parameterization for the LEBT and RFQ, with accurate simulation of beam dynamics with HV applied to the deflection plates. We have tried various HV waveforms to determine which waveform provides the best fast chopping with the least power requirements. The most effective fast switching for our existing configuration was obtained with alternating positive and negative HV of ± 5.5 kV, with fast switching of duration of 20 ns between polarities, where the beam traverses the deflector plates into the RFQ at the crossover at zero voltage. With this scheme, we are able to obtain $\sim 60\%$ transmission of the selected RFQ bunch. The repetition rate for the single bunch selection is simply the frequency of the HV switching.

Electronics for Fast Chopper

We have recently tested electronics that will enable fast chopping for the existing deflector plates. The electronics consist of a Spellman positive HV supply and a negative HV supply, each capable of providing the current necessary for fast switching at high repetition rates. The heart of the electronics is a Behlke fast HV switch with 20 ns HV switching speed. Together, this system enables us to apply ± 5.5 kV, with a switching speed of 20 ns and a repetition rate of up to 100 kHz. This electronics has been tested on the deflection plates situated on the SARAF accelerator floor. A photograph of the fast chopper electronics connected to the LEBT deflector plates, is shown in Figure 4. Note the yellow trace on the scope showing a 20 ns rise from a negative HV of -4500 volts to a positive HV of +4500 volts.

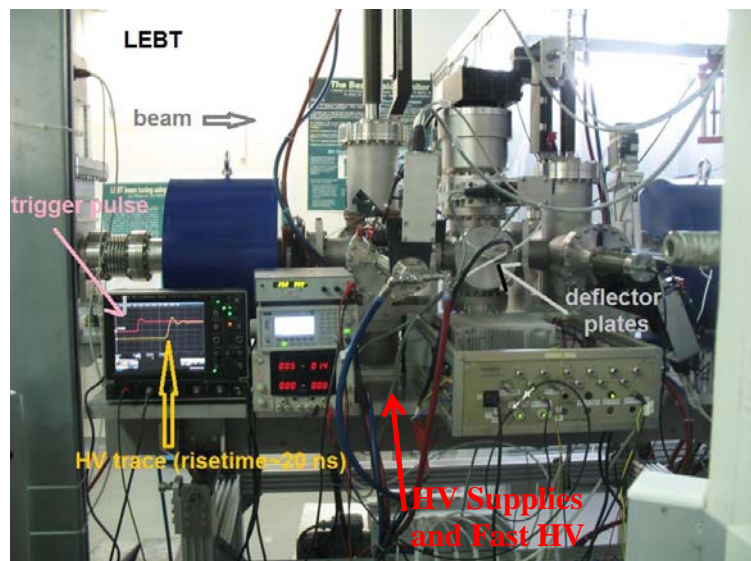


Figure 4. Fast Chopper Electronics connected to Deflector Plates in LEBT

DISCUSSION

A fast chopper will allow single bunch selection from the RFQ and thereby significantly enhance the physics program and applications at SARAF. Our scheme for beam fast chopping at the LEBT with a HV deflector will be both economical, and provide SARAF with important capabilities. We anticipate single bunch selection which will result in 300 ps single bunches, with a single bunch repetition rate of up to 100 kHz, presently, and over 1 MHz with purchase of available off-the-shelf fast electronics. We anticipate that this system will be tested with actual beam in the coming year. Commercial electronics is presently available for higher repetition rates of a MHz or more. Fast chopping at such repetition rates will allow for many interesting experiments and nuclear physics and nuclear technology that requires fast neutron time-of-flight techniques.

REFERENCES

- [1] See for example presentation of I. Mor, *Elemental Reconstruction from Experimental and Simulated Data in Fast-Neutron Resonance Radiography System*, , FNDA 2011 and 2012 JINST 7 C06003.
- [2] T. Kato et al., *Beam Study With RF Choppers in the MEBT of the J-PARC Proton LINAC*, Part. Acc. Conf. 2003, (2003) 1455-1457.
- [3] V. Dangendorf et al., *Proposed work on pulsed fast neutron sources for FNeuRad-Project*, FneuRad proposal, 2007
- [4] General Particle Tracer code, Pulsar Physics, Netherlands
- [5] I. Mardor et al., *The SARAF CW 40 MeV Proton/Deuteron Accelerator* Part. Acc. Conf. 2009 Vancouver,
- [6] A. Caruso et al., *Preliminary Design of the Slow Chopper for the SPIRAL 2 Project*, LINAC 2008,

First Demonstration of High-Power Proton Irradiation and Neutron Production with a Liquid-Lithium Target

S. Halfon^{1,2}, A. Arenshtam¹, D. Kijel¹, M. Paul², L. Weissman¹, D. Berkovits¹, Y. Eisen¹, I. Eliyahu¹,
G. Feinberg^{1,2}, A. Kreisel¹, I. Mardor¹, G. Shimel¹, A. Shor¹, I. Silverman¹ and M. Tessler²

¹Soreq NRC, Yavne, Israel 81800

²The Hebrew University of Jerusalem, Jerusalem, Israel 91904

INTRODUCTION

A free surface liquid-lithium jet target was bombarded for the first time with a high-intensity proton beam at Soreq Applied Research Accelerator Facility (SARAF). The proton irradiation experiments demonstrated the capability the Liquid Lithium Target (LiLiT) to dissipate extremely high ion beam power densities and constitute an intense source of epithermal neutrons produced by the ${}^7\text{Li}(p,n){}^7\text{Be}$ reaction. The LiLiT device will be used to assess the feasibility of accelerator-based Boron Neutron Capture Therapy (BNCT) [1] with a lithium target and for research in stellar [2][3] and Big-Bang [4] nucleosynthesis and Accelerator Driven Systems (ADS) material cross section measurements **Error! Reference source not found.**

The liquid-lithium jet acts both as neutron-producing target and as a beam dump, by removing with fast transport the thermal power generated by high-intensity proton beams (>4 kW). The high intensity is necessary for the high epithermal neutron flux density required for the proposed researches. Of specific concern is the power densities created by the protons at the Bragg peak area, of the order of 1 MW/cm^3 (volume power density), about $150 \mu\text{m}$ deep inside the lithium.

The target was designed based on a thermal model, accompanied by a detailed calculation of the ${}^7\text{Li}(p,n)$ neutron yield, energy distribution and angular distribution **Error! Reference source not found.** Liquid lithium is circulated, driven by an electromagnetic (EM) induction pump, through the target loop (Fig 1c) at $\sim 200^\circ\text{C}$ and generates a stable 1.5 mm-thick, 18 mm-width jet flowing at a velocity up to 7 m/s onto a concave supporting wall (Fig 1a). High power 26 keV electron beam irradiation experiments demonstrated that the liquid-lithium target can dissipate electron power areal densities of $> 4 \text{ kW/cm}^2$ and volume power density of $\sim 2 \text{ MW/cm}^3$ at a lithium flow of $\sim 4 \text{ m/s}$, while maintaining stable temperature and vacuum conditions **Error! Reference source not found.** These power densities correspond to a narrow ($\sigma \sim 2 \text{ mm}$) 1.91 MeV, 3 mA proton beam.

High-intensity irradiation experiments are ongoing, using a 1.91–2.5 MeV, 1-2 mA proton beam from SARAF on LiLiT. The first stages of these experiments, described hereby, demonstrate a safe and stable operation of the system under high power proton beams and high intensity neutron production. Another significant effect that is studied during the experiments is the production of the radionuclide ${}^7\text{Be}$ (through ${}^7\text{Li}(p,n){}^7\text{Be}$), its distribution in the loop and the resulting dose-rate for the surroundings.

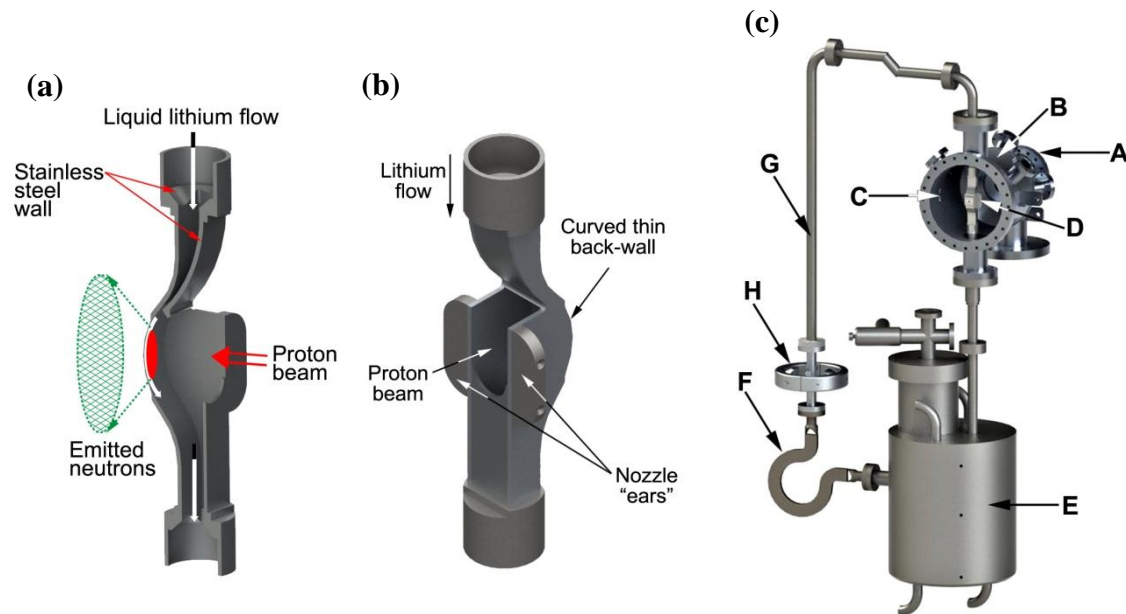


Figure 1: (a) Schematic illustration of the operation of the LiLiT system. The incident proton beam impinges directly on the liquid lithium flow (windowless) and within the first μm 's produces a flux of neutrons. The protons are stopped within the lithium film and the beam power is conveyed by the flow to a heat exchanger. (b) LiLiT nozzle general scheme. (c) schematic drawing of the LiLiT assembly viewed from the neutron exit port: (A) - proton beam inlet port; (B) - target chamber; (C) - neutron port (shown open); (D) - lithium nozzle; (E) - lithium containment tank (including heat exchanger and ^7Be cold trap); (F) - Electromagnetic (EM) pump (only the circulation loop is shown); (G) - loop line; (H) - electromagnetic flow-meter;

Saraf Beam Tune

The proton beam tune for LiLiT requires a relatively small beam size (<4 mm), especially in the horizontal direction, because of the nozzle horizontal size (18 mm). The nozzle side metal slabs (marked as "ears" in Fig1b), located on both sides of the lithium flow, are not cooled and cannot sustain high beam power. Excessive beam heating of the "ears" might cause overheating of the liquid lithium and consequently excessive lithium evaporation, as experienced during the first high power electron beam tests **Error!**

Reference source not found..

The tuning of a narrow high intensity proton beam is challenging, especially due to the lack of reliable beam diagnostics during irradiation of the liquid lithium. A low-current beam diagnostic station was installed 84 cm upstream of the LiLiT nozzle, with wire scanners and quartz and Ta viewers. More wire beam profilers (also relevant only at low current) were located 164 cm upstream the target.

As a first stage a 1.9 MeV high power proton beam tune was achieved upon a dummy LiLiT nozzle, located at the same position as the LiLiT nozzle. The dummy target allowed a measurement of the beam current at the expected target location and a high power CW proton beam (> 1 mA) was used, while all the beam profiles on the viewers and on the wire profilers were monitored. A method was developed to reconstruct the beam profile on the lithium target based on the profile measurements in two positions and on the emittance measurements at the accelerator diagnostic plate ~ 10 m upstream the lithium nozzle.

Proton Irradiation Experiments AT LiLiT

The dummy setup was disassembled and the LiLiT system was attached to the accelerator beam line (Fig. 2). The LiLiT nozzle was aligned with respect to all diagnostic tools installed in the beam lines (wire profilers, two viewers, 4-jaw collimator and the LiLiT collimator).

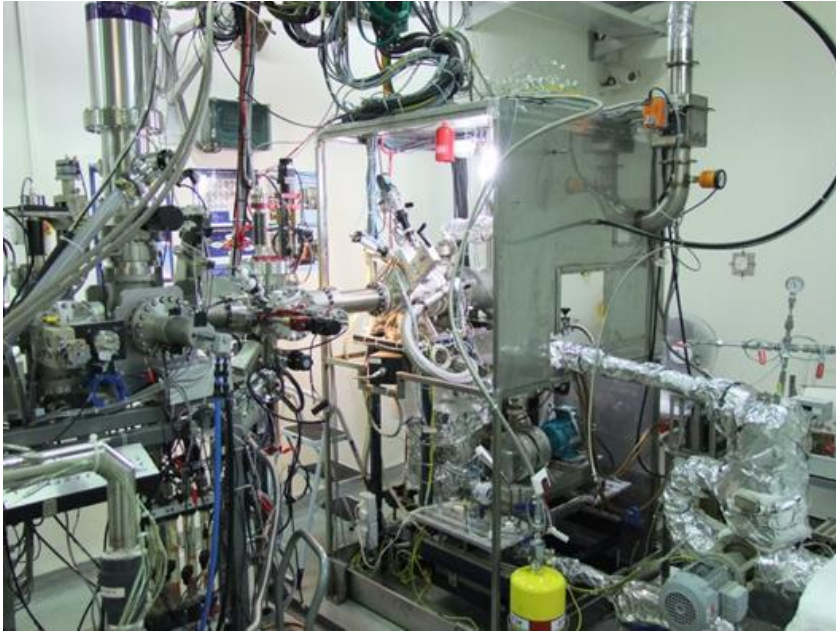


Figure 2: LiLiT installed at the SARAF beam corridor and connected to the SARAF accelerator beam line.

In a typical experiment, a low-power proton beam (around 10 W) was first centered and focused by viewing the beam spot on a retractable thin tantalum diagnostic foil, positioned in front of the lithium nozzle. The beam profiles and emittance were measured and the beam distribution on target was extracted. Following beam tuning, the proton beam was blocked and the tantalum foil was removed from the beam. After the lithium flow was established and the lithium film on the nozzle back wall was confirmed visually and its velocity stabilized at 3-4 m/s, the proton beam was turned on again. In that phase the target parameters (temperatures and vacuum) were recorded and video recordings were made of the beam-on-target image, while increasing the proton beam intensity. When the chamber lights were off, a glow was observed on the nozzle edges close to the flow, starting at relatively low beam power (~ 50 W). At higher currents (>0.5 mA) a glow was observed on the liquid lithium as well. No other glow, disturbances or changes in the lithium jet were noticed during the experiments.

The gamma dose around the target, caused mainly by 478 keV gammas from inelastic proton scattering ${}^7\text{Li}(p,p'\gamma)$, was measured by two gamma Geiger-Müller detectors (GM-42, Rotem) placed on the surrounding walls about 5 m upstream and downstream of the target. The measured gamma dose, in mR/h, was calibrated to monitor the beam current on the target by comparison to charge measurements with a Faraday cup located upstream the target. In the initial experiments the gammas were also measured with a NaI(Tl) spectrometer, located 4 m upstream of the target. The detector indeed showed a peak of gamma radiation at 478 keV but was saturated at proton currents above ~ 100 μA , although tightly collimated by a horizontal slit ~ 0.1 mm wide. The detector was later replaced by a $1'' \times 1''$ LaBr₃ detector located 25 m upstream the target, which showed a clear 478 keV peak that was integrated over the entire run (Fig. 3b).

In the first experiment, the proton beam was tuned to an energy of ~ 1.82 MeV, well below the ${}^7\text{Li}(p,n)$ threshold of 1.880 MeV. The power on the flowing lithium film was increased up to 2.2 kW (1.2 mA) for more than an hour, with no indication of excessive heat in the nozzle and the lithium reservoir and without noticeable evaporation. The proton beam shape (measured at low intensity) could be fitted to a 2D Gaussian with σ_x of 3.8 mm and σ_y of 2.8 mm. This implies a maximum power density of 2.5 kW/cm² and volume density of 0.4 MW/cm³.

Two separate experiments were conducted above the (p,n) threshold, using also a fission chamber detector (PFC16A, Centronic), a ^3He -filled gridded ionization chamber spectrometer (FNS-1, Seforad) and a dosimeter (42-30H, Ludlum **Error! Reference source not found.**) for neutron monitoring (Fig 3). Gold activation foils were attached to the vacuum seal downstream the nozzle.

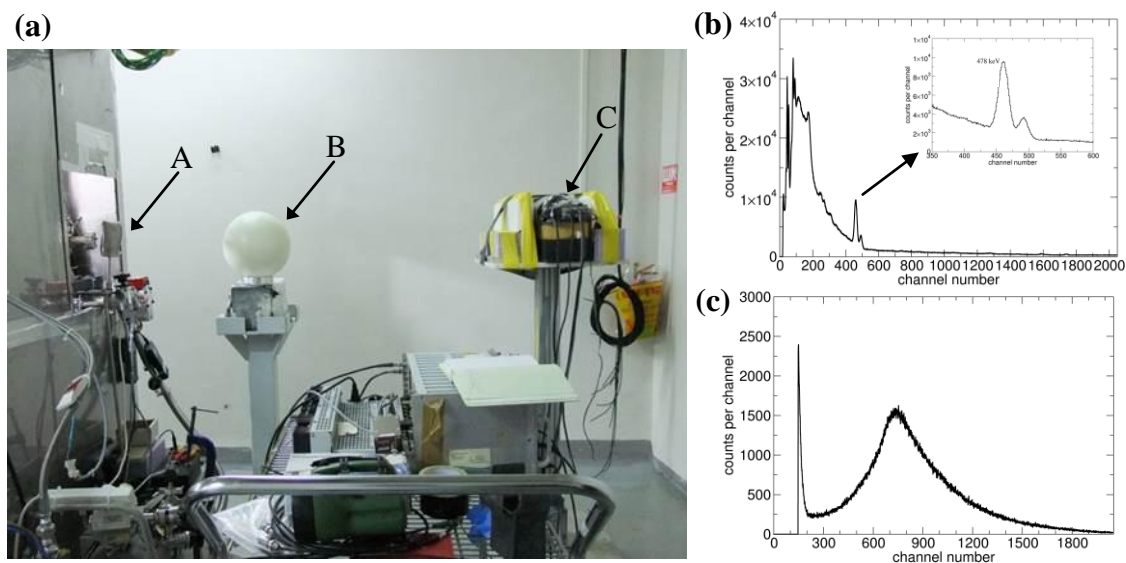


Figure 3: (a)- Neutron detectors setup in front of LiLiT- A- a cadmium covered fission chamber, B- a Ludlum neutron dosimeter, C- a lead shielded Seforad neutron spectrometer; (b)- LaBr_3 gamma spectrum after $\sim 1.34 \text{ mA}\cdot\text{h}$ irradiation; the 478 keV peak (see text) clearly appears; (c)- energy spectrum measured with the fission chamber after $\sim 1.34 \text{ mA}\cdot\text{h}$ irradiation (intrinsic alpha counts below channel ~ 250 were suppressed);

During the experiments above threshold, the Seforad and Ludlum detectors were used only at low current (up to tens of μA) mainly during $^7\text{Li}(p,n)$ threshold scans that were performed for energy calibration. The fission chamber could be used at higher beam currents and its neutron counting rate was also calibrated as a measure of the beam current on the target. The measurements along the most recent experiment, with proton energy around $\sim 1.90 \text{ MeV}$ are shown in Fig. 4. In this experiment the proton current was raised above 1.7 mA, with a long irradiation period around 1.5 mA (Fig. 4). During this irradiation the nozzle maximum temperatures were around 200-220 $^\circ\text{C}$ (Fig. 4). The vacuum in the target chamber was stable around 10^{-7} mbar. No disturbances were observed in the lithium flow.

The system was voluntarily stopped after 45 minutes and no indication for excessive lithium evaporation was found. The average areal power density applied to the liquid lithium, flowing in the nozzle at an estimated velocity of $\sim 4 \text{ m/s}$, was up to $\sim 3.5 \text{ kW/cm}^2$ and the average volumetric power density for $\sim 1.5 \text{ mA}$ is estimated to be $\sim 0.75 \text{ MW/cm}^3$.

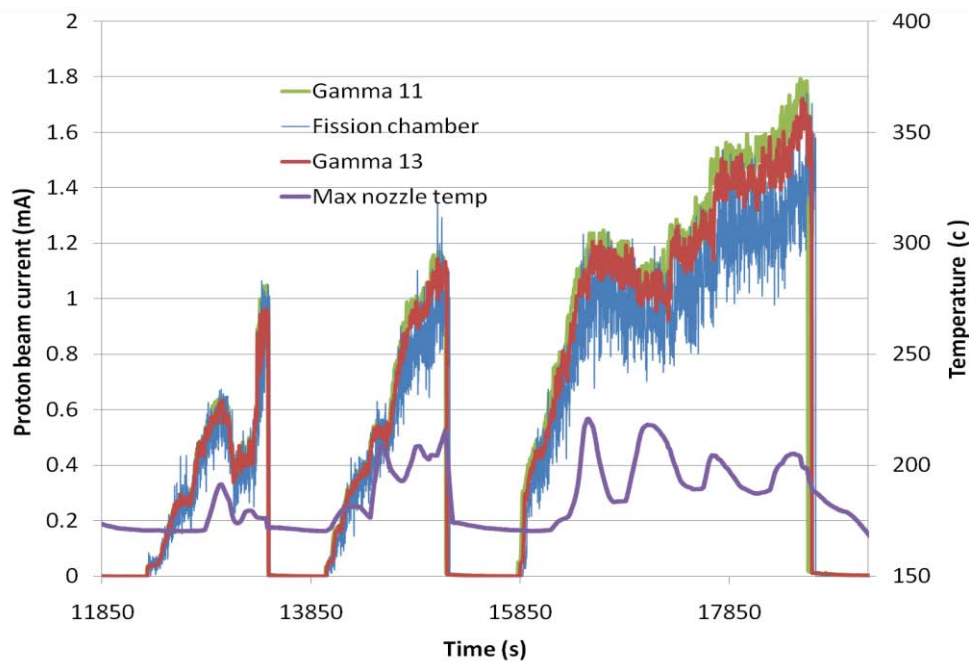


Figure 4: Left scale: Proton beam current evaluations according to the calibrated gamma dose rate (gamma dosimeters Gamma 11 and 13) and the neutron calibrated counting rate (Fission chamber). Right scale: the maximum target nozzle temperature.

According to the integral on the fission chamber measurement, the integrated current on the target was ~ 1.34 mA·h. A consistent value is obtained from the gamma measurement integration. Preliminary analysis of the activation targets, using this value, the simulated neutron spectrum and the known $^{197}\text{Au}(n,g)$ energy-dependent cross section, shows that the proton energy, with an energy spread of 15 keV, was 1900 ± 5 keV, lower by ~ 15 keV than the calibrated energy.

SUMMARY

A high-intensity proton beam irradiation ($\sigma_r = 3\text{-}4$ mm, ~ 1.90 MeV, 1-1.5 mA) of the LiLiT device was performed at SARAF. The experiments are a first demonstration of a free surface liquid lithium target proton irradiation and dissipation of ~ 4 kW/cm² and >0.5 MW/cm³ proton power densities. This high power dissipation shows that the setup at SARAF can be used for the production of high intensity epithermal neutrons and demonstrates the applicability of this new concept to accelerator-based BNCT and for innovative nuclear astrophysics research. We plan to use LiLiT in the future also with a deuteron beam for fast neutron production and radioactive ion production. The experience gained with LiLiT will serve in the design of an upgraded target for higher beam energies (up to 40 MeV) that are expected at Phase II of SARAF.

ACKNOWLEDGMENTS

The authors would like to thank the SARAF accelerator team for providing the conditions necessary for these experiments. We gratefully acknowledge the support of the Pazi Foundation.

REFERENCES

- [1] S. Halfon et al., *High-Power Electron Beam Tests of a Liquid-Lithium Target and Characterization Study of $^7\text{Li}(p,n)$ Near-Threshold Neutrons for Accelerator-Based Boron Neutron Capture Therapy*, App. Rad. Iso., In Press, <http://dx.doi.org/10.1016/j.apradiso.2013.11.043> (2013).
- [2] G. Feinberg et al. these Conference Proceedings.
- [3] M. Friedman et al., *Simulation of the Neutron Spectrum from the $^7\text{Li}(p, n)$ reaction with a Liquid-Lithium Target at Soreq Applied Research Accelerator Facility*, Nucl. Inst. Meth. Phys. Res. A **698** 117 (2013).

- [4] L. Gialanella, *Production and destruction of ^7Be in the universe*, SARAF Workshop 2008, Oct 27-29, 2008, Maale Hahamisha, Israel, <http://www.phys.huji.ac.il/SARAF/gialanella.pdf>.
- [5] C. Domingo-Pardo et al., *New measurement of neutron capture resonances in ^{209}Bi* , Phys. Rev. C 74, 025807 (2006).
- [6] S. Halfon et al., *High-power liquid-lithium jet target for neutron production*, Review of Scientific Instruments **84**, 123507 (2013).

Nuclear Astrophysics at SARAF with LiLiT

G. Feinberg^{1,2}, M. Paul¹, A. Arenshtam², O. Aviv², D. Berkovits², D. Cohen¹, O. Dudovitch², Y. Eisen², I. Eliyahu², M. Friedman¹, Y. Ganon¹, S. Halfon^{1,2}, D. Kijel², A. Kreisel², G. Shimel², A. Shor², I. Silverman², M. Tessler¹, L. Weissman², Z. Yungrais²

¹The Hebrew University of Jerusalem, Jerusalem 91904, Israel

²Soreq NRC, Yavne 81800, Israel

INTRODUCTION

An intense neutron source of new design, based on the ${}^7\text{Li}(p,n){}^7\text{Be}$ reaction using a high-power Liquid-Lithium Target - LiLiT^(1,2) (Fig. 1), was built at the Soreq Applied Research Accelerator Facility – SARAF⁽³⁾. The neutrons, generated by a proton beam at a laboratory energy of ~ 1910 keV (~ 30 keV above the threshold energy $E_{\text{th}} = 1880$ keV), impinging on the thick windowless liquid-lithium target, are forward collimated with angle-integrated energy distribution similar to that of a flux of Maxwellian neutrons at a temperature of $kT \approx 25$ keV⁽⁴⁾. An intense proton beam is required in order to generate a high neutron flux that enables measuring new cross sections that are impossible to measure by traditional techniques. For the first time, stellar-energy neutrons were produced by the SARAF high intensity proton beam and LiLiT and the Maxwellian Averaged Cross Section (MACS) of the ${}^{94}\text{Zr}(n,\gamma){}^{95}\text{Zr}$ and ${}^{96}\text{Zr}(n,\gamma){}^{97}\text{Zr}$ reactions were measured.

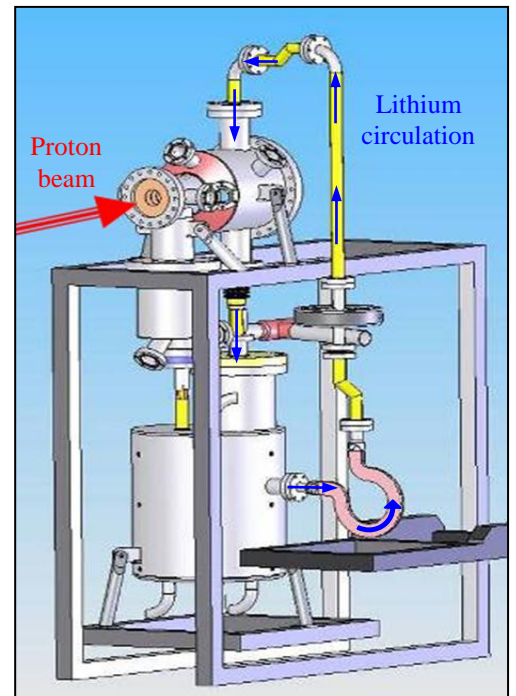


Figure 1. LiLiT 3D scheme. The red arrow represents the proton beam direction.

EXPERIMENTAL SETUP

The setup for MACS measurements was built taking into account the safety constraints for operating a high-intensity machine. In order to protect the accelerator, beamline and LiLiT while enabling activations, a dedicated secondary vacuum (~ 0.1 mbar) chamber was built and connected downstream the LiLiT loop (Fig. 2, right). During operation, the chamber was kept in vacuum and served as a safety beam dump.

As illustrated in Fig. 2 (left), the sample was placed close to the LiLiT vacuum window and about 5 mm from the lithium surface. For the setup design we minimized the materials and components to reduce the effect of activation by scattered neutrons. One of the main objectives of LiLiT is to conduct cross section measurements for reactions

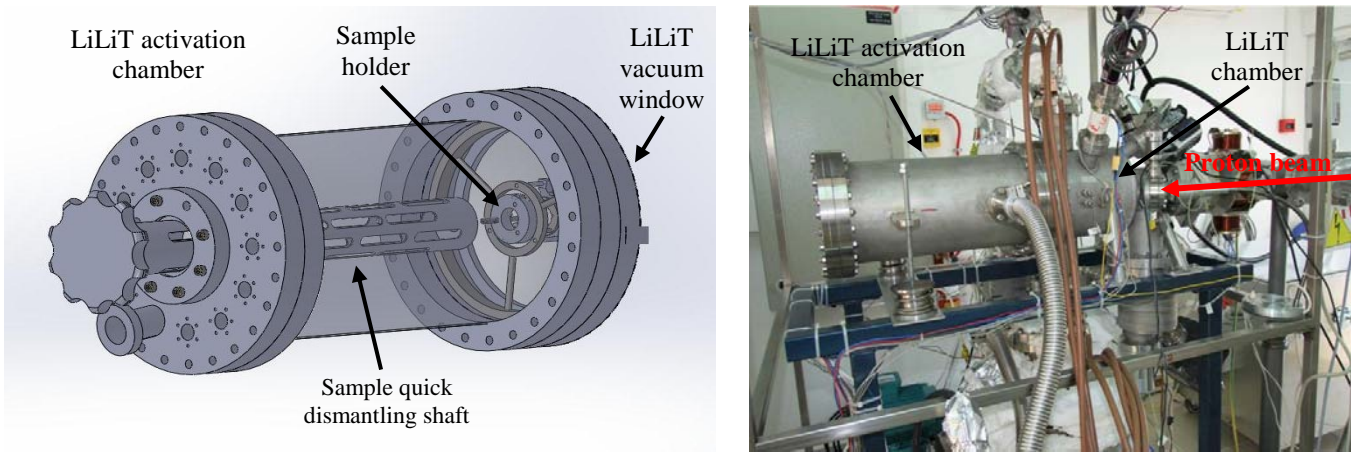


Figure 2. LiLiT activation chamber. Right: connected to the LiLiT loop. Left: the sample is fixed close to the neutron source, quick dismantling after irradiation is done by the shaft.

leading to nuclei with short half lives. In that case – the measurement of the activated sample should be made shortly after the irradiation. The target holder is utilized for quick dismantling of the irradiated target using a long shaft with a bayonet connector. After irradiation, the chamber is open and the sample is pulled out by the shaft through a small port.

RESULTS

A natural Zr disk sample (24 mm in diameter) was irradiated with the LiLiT secondary neutron flux. Two gold disks of same diameter were used to monitor the neutron fluence on both sides of the Zr sample. Preliminary analysis of the irradiated Zr sample was performed to extract the MACS at 30 keV using the gold cross section as reference. The preliminary results are listed in Table 1.

Isotope	MACS (mb)						
	This work	KADoNiS v0.3 ⁽⁵⁾					Recommended
		Toukan 1990	Wyrick 1983	Musgrove 1978	Boldeman 1976	Macklin 1967	
⁹⁴ Zr	28.9 ± 1.3	26.1 ± 1.0	25 ± 4	33 ± 5	26.6 ± 3	-	26 ± 1
⁹⁶ Zr	13.3 ± 1.1	10.7 ± 0.5	12 ± 1	-	-	41 ± 12	10.7 ± 0.5

Table 1. MACS at 30 keV of the ⁹⁴Zr(*n,γ*)⁹⁵Zr and ⁹⁶Zr(*n,γ*)⁹⁷Zr reactions.

Our results are within the range of the reported values although the cross section of both isotopes seems systematically higher than the recommended value. We are presently investigating possible systematic uncertainties which may affect our results.

ACKNOWLEDGEMENTS

The authors would like to thank the SARAF accelerator team for providing the conditions necessary for these experiments. This work is supported in part by the Pazi Foundation.

REFERENCES

1. G. Feinberg et al., *LiLiT - a Liquid-Lithium Target as an Intense Neutron Source for Nuclear Astrophysics at the Soreq Applied Research Accelerator Facility*, Nucl. Phys. A **827**, p.590c-592c, (2009).

2. S. Halfon et al., *High-power liquid-lithium jet target for neutron production*, Review of Scientific Instruments **84**, 123507, (2013).
3. D. Berkovits et al., *Operational experience and future goals of the SARAF proton/deuteron linac*, in Proceedings of Linac 2012, Tel-Aviv, MO1A01, (2012).
4. W. Ratynski and F. Käppeler, *Neutron capture cross section of ^{197}Au : A standard for stellar nucleosynthesis*, Phys. Rev. **C37 (2)**, p.595-604, (1988).
5. I. Dillmann, R. Plag, F. Käppeler, T. Rauscher, Submitted as proceeding of the workshop "EFNUDAT Fast Neutrons - scientific workshop on neutron measurements, theory & applications", April 28-30, 2009, Geel, Belgium (2009). <http://www.kadonis.org>.

Accelerators / SARAF (Thursday, February 13, 2014 11:30)

Status of Cross Section Measurement for the Deuteron Induced Reaction $^{23}\text{Na}(d,p)^{24}\text{Na}$ in the Energy Range 1-20 MeV at NPI Rez and SARAF

A. Kreisel¹, T.Y. Hirsh¹, Y. Eisen¹, J. Mrazek², E.Simeckova², M. Stefanik²

¹*Soreq NRC, Yavne, Israel*

²*NPI Rez, Rez, Czech Rep*

INTRODUCTION

Basic motivation

There is a need for a standard monitoring cross section in order to validate deuteron cross sections at energies 1-40MeV. At energies above 15 MeV the reaction $^{27}\text{Al}(d,p)^{24}\text{Na}$ has been extensively studied in the past and is frequently used to monitor deuteron reactions. It is the aim of the present study to use the same end product nucleus, ^{24}Na , with its reasonable half-life of 15h and high energy gamma rays for low deuteron energy monitoring. This by measuring the $^{23}\text{Na}(d,p)^{24}\text{Na}$ cross section with high precision at energies 1-20MeV. This cross section is much higher than other available monitor reactions such as $^{\text{nat}}\text{Fe}(d,x)^{56}\text{Co}$, $^{\text{nat}}\text{Ti}(d,x)^{48}\text{V}$, and $^{\text{nat}}\text{Ni}(d,x)^{61}\text{Cu}$.

The $^{23}\text{Na}(d,p)^{24}\text{Na}$ cross section has been measured few times in the past [1-4], however the data is not consistent. The objective of this experiment is to perform a modern, accurate and decisive cross section measurement. Preliminary results from the first stage of experiments from April 2013 at Rez are shown together with plans for completion.

Background

1. The Rez LOI (submitted to SPIRAL2 day one experiments) regarding cross section measurements of deuteron induced reactions for the future IFMIF facility is naturally very relevant to SARAF, being a conceptually similar accelerator and by sharing a plan to utilize a lithium loop neutron converter.
2. Based on the list of proposed reactions (for deuterons on structural elements and Li loop contaminations), given in the Rez LOI, we had decided to start with a relatively easy, offline cross sections measurement of the $^{23}\text{Na}(d,p)^{24}\text{Na}$ reaction.

Additional Scientific Motivation

Lithium loop contamination

3. LiLiT (Liquid Lithium Target) at SARAF phase 1 (and probably a similar target at phase 2), will start to operate with ion beam this year.
4. The main contamination of SARAF lithium has found to be sodium with around 100ppm.
5. The main residual activity at the lithium loop is ^7Be from the $^7\text{Li}(p,n)^7\text{Be}$ reaction. A cold trap to catch and shield the ^7Be was built. Then, activation of ^{24}Na (15 hrs) may limit the operation of LiLiT (SARAF is based on an hands-on maintenance accelerator, and the LiLiT is placed at the accelerator beam hall)
6. Similar problem at IFMIF, ^{22}Na production via $^{23}\text{Na}(d,t)^{22}\text{Na}$ (2.6 yrs) may be more of a problem in this case.

Calibration of modern codes for deuteron interactions

7. The experimental data is not complete and contradicting for most regions (3 very early measurements from the 1960s with NaF, NaBr, NaCl and generally with a NaI or CsI scintillators)
8. A precise measurement could farther be used to calibrate the current theoretical models and codes of deuteron induced reactions,

9. For instance, the TALYS code essentially only produce the $^{27}\text{Al}(d,p\alpha)^{24}\text{Na}$ correctly, even after the recent version (with deuteronOMP) .

METHOD OF MEASUREMENT

Complementary measurement at Rez and SARAF phase 1.

- Rez: 5-20 MeV
 - Stack of foils technique using thin NaF targets, evaporated on thin Graphite foils
 - Graphite foil after each target to collect the recoiled products
 - Aluminum foils as an energy degraders between targets
 - ^{24}Na measured off-line in each foil after irradiation with HPGe detector
- SARAF: 3-6 MeV
 - Single thin foil of evaporated NaF
 - Varying the beam energy (SARAF is an independently phase RF LINAC)
 - ^{24}Na measured off-line in each foil after irradiation with HPGe detector

Experiment at Rez

It is not possible to make thin foils of pure sodium (melting at 99 °C) and so NaF foils were used. However, NaF is an electric insulator with poor thermal conductivity and so very delicate during irradiation. The challenge in this experiment is to make thin durable NaF foils with precisely known thickness. The targets stack was composed of 18 targets of ~300 ug/cm² NaF which were evaporated on ~1100 ug/cm² carbon support foils. The Carbon is need both to physically hold the NaF layer and to catch ^{24}Na recoils from the target. Each target is supported by a thin stainless steel frame. Between each target we inserted one or few aluminum degraders in order to achieve a cross section measurement at approximately every 0.8 MeV from 20 MeV down to 6 MeV. The aluminum degraders were separated from the target by another layer of carbon to catch ^{24}Na recoils from the aluminum. We both calculated and tested in the experiment that no ^{24}Na recoil penetrates the carbon layer.

The stack of foils and degraders, all share a common outer diameter of 16mm, was inserted in a standard targets cup, and placed to irradiation at the end of the positive beam line of NPI cyclotron.

The target was irradiated with 20 MeV deuterons beam for 1 hour with a current of ~400 nA, which is recorded with the standard charge integrator of the beam line faraday-cup. Shortly after the irradiation, the target was dismantled and foils were transferred to the HPGe measurement station. Each foil is then measured for a period of 5-20 minutes

Cross Section Calculation

The cross section was calculated using equation 1

$$\langle \sigma \rangle = N_{mes} / \left[Eff \cdot d \cdot \rho \cdot (1 - e^{-\lambda T_2}) \cdot e^{-\lambda T_1} \int_0^{T_1} e^{\lambda t'} I(t') dt' \right] \quad (1)$$

Here T_1 is the time that passed between the start of irradiation to the start of the ^{24}Na decay counting with the HPGe detector, and T_2 is the measurement time with the HPGe detector. N_{mes} is the number of decays measured in a detector with an efficiency Eff in the time interval between T_1 and T_1+T_2 after start of irradiation. $I(t)$ is the current as a function of time as measured by the charge integrator. The term $d \cdot \rho$ is the number of ^{23}Na atoms per area unit.

Measuring the Width or Number of ^{23}Na Atoms Per Area Unit

The thickness of each foil was measured by recording the energy degradation of alpha particles from triple-alpha source of Am, Cm and Pu (~ 5.1 , ~ 5.4 , ~ 5.8 MeV). The carbon layer was measured in prior to the NaF evaporation and then the target was measured again with both layers present. The measured spectrum was corrected by using Monte-Carlo simulations that take into account the full alpha spectrum and the collimator geometry. A few of these measurements were compared to thickness measurements done at the BINA Pelletron accelerator, Bar Ilan University, using elastic back scattering of alpha particles. The comparison shows that relative spread of the difference between the measurements is of the order of 3%

Energy at Target Foil

The energy distribution at each target foil in the stack was calculated using TRIM⁽⁵⁾, and the measured energy distribution of the beam as input.

RESULTS

The measured cross section with comparison to earlier measurements is shown in figure (1)

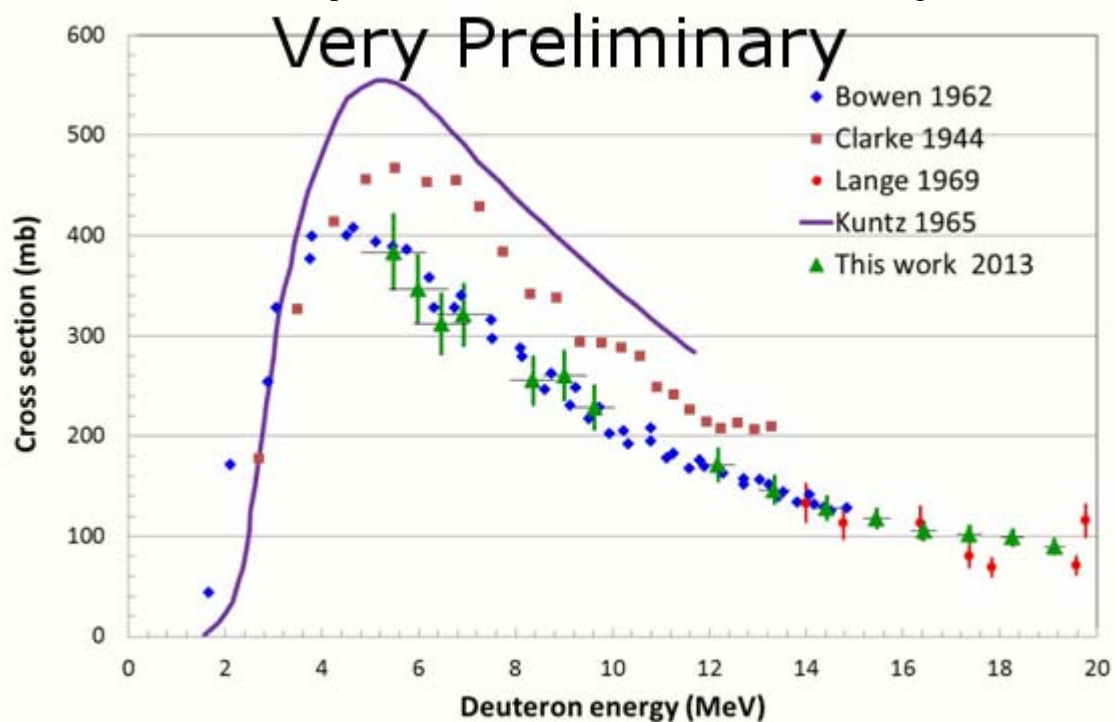


Figure 1. $^{24}\text{Na}(d,p)$ cross section .

CONCLUSIONS

Good agreement with the Bowen measurements from 1962. A new experiment will be performed at Rez with initial deuteron beam energy of 13 MeV in order to reduce the energy spread in the targets below 13 MeV and in order to reach lower energies and an overlap with the SARAF measurements. The complementary experiment at SARAF is planned for early 2014.

REFERENCES

1. E.T. Clarke, J.W. Irvine. Phys. Rev. **66**, p.231, (1944).
2. L.H. Bowen, J.W. Irvine. Phys. Rev. **127**, p.1698, (1962).
3. Kunz et al., *Nuclear Tables*, Pergamon press. **Part II – Nuclear reactions**, (1965).
4. V.J. Lange et al., Radiochimica Acta. **Part I 1969**, p.121, (1968).

Proton Irradiation of LiF:Mg;Ti at SARAF: Optical Absorption Relative Efficiency Calculations using Track Structure Theory

I. Eliyahu^{1,2}, Y.S. Horowitz¹, L. Oster³, L. Weissman², A. Kreisel², S. Druzhyna¹ and I. Mardor²

¹ Ben Gurion University of the Negev, Beersheva, 84105, Israel

² Soreq Nuclear Research Center, Yavne, 81800, Israel

³ Sami Shamoon College of Engineering, Beersheva, 84100, Israel

INTRODUCTION

Irradiation of LiF:Mg;Ti (TLD-100) by a defocused proton beam at the Soreq Applied Research Accelerator Facility (SARAF) has been performed in order to investigate heavy charged particle optical absorption (OA) efficiencies. Experimentally measured and theoretically calculated efficiencies relative to photon/electron irradiation are presented. Proton irradiation was performed at an incident energies of 1.37 MeV with a fluence density of $2 \cdot 10^{11} \text{ cm}^{-2}$. These OA studies were carried out in order to investigate the reliability of track structure theory in the prediction of heavy charged particle radiation effects.

Experimental Setup

The proton irradiations were performed using the SARAF accelerator [1] at Soreq nuclear research center. A sketch of the experimental setup is shown in figure 1. A low-intensity homogeneous beam was obtained using a relatively thick foil upstream to the samples. The beam broadening is created by proton multiple scattering within a gold foil. The foil was located in the diagnostic chamber station at the D-plate, while the sample was placed at the new irradiation station (Fig. 1). The distance between the two stations is 7.05 m. The beam was stopped in a beam dump which also served as a reliable Faraday cup.

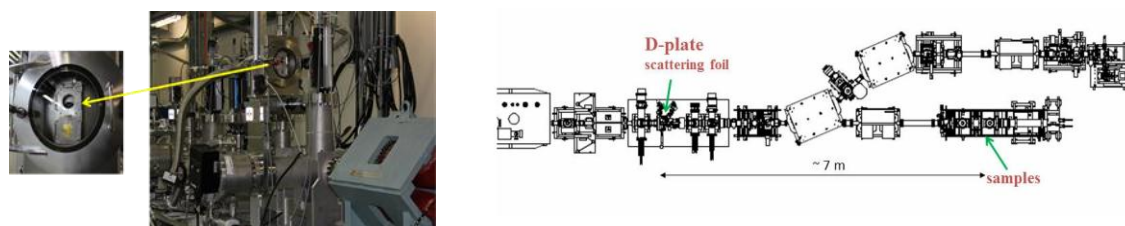


Fig. 1 Picture of the load-lock chamber and diagnostic chamber (left). Layout of the beam line (right)

A silicon detector and the gold foil were placed at 100 degree and 20 degrees to the beam direction respectively (Fig. 2 left). This was done to allow monitoring the beam intensity with rate of the protons scattered to the silicon detector. Prior the irradiation of the samples the counting rate in the detector was calibrated by measuring current in the beam dump. Nine TLD 100 dosimeters were placed at the sample holder. The fluence density on the samples was calculated by TRACK software, given that the beam travels the 7.05 m foil to sample distance with no magnetic elements (fig 2 right).

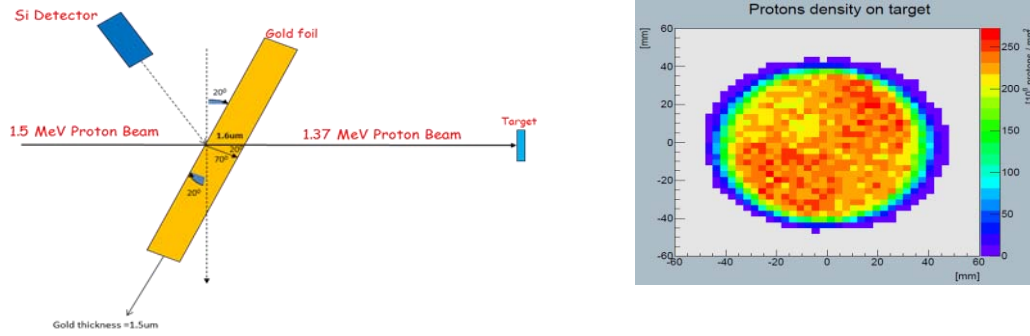


Fig. 2 Experimental setup of the scattering foil (left). Track fluence density calculation result at the target position (right)

The optical density spectra following irradiation were measured for the following OA peaks: 5 eV, 4.77 eV and 5.45 eV. The spectra were deconvoluted into these specific OA bands using peak-fit 4.12 [2].

Heavy Charge Particle (HCP) relative OA efficiencies

The HCP relative efficiency, $\eta_{\text{HCP},\gamma}$ is defined as the ratio of the OA signal following HCP irradiation, I_{HCP} , per energy unit [or per irradiated mass per unit dose (D_{HCP})] divided by the OA signal following photon/electron irradiation, I_{γ} per energy unit (or per irradiated mass per unit dose (D_{γ})).

$$\eta_{\text{HCP},\gamma} = \left[\frac{I_{\text{HCP}}/D_{\text{HCP}}}{I_{\gamma}/D_{\gamma}} \right] = \left[\frac{I_{\text{HCP}}/(E_{\text{HCP}})_{\text{tot}}}{I_{\gamma}/E_{\gamma}} \right]$$

$(E_{\text{HCP}})_{\text{tot}}$ and E_{γ} represent the total kinetic energy absorbed in the sample following HCP and gamma/electron irradiation, respectively. In the case that the HCPs are totally absorbed in the sample, the relation is:

$$(E_{\text{HCP}})_{\text{tot}} = nAE_{\text{HCP}}$$

Where n is the fluence (cm^{-2}), A is the irradiated area of the sample (cm^2) and E_{HCP} is the particle energy. Track Structure Theory (TST) [3,4] assumes that the radiation action of the HCPs is due solely to the radiation action of the secondary electrons liberated during the slowing down of the HCP. The calculation integrates the HCP radial dose, $D(r)$ multiplied by the OA relative efficiency over the entire HCP track as given in the equation below.

$$\eta_{\text{HCP},\gamma} = \eta_{\delta,\gamma} \times \frac{W_{\gamma} \int_0^{R_{\text{max}}} \int_0^{r_{\text{max}}} f_{\delta}(D) D(r,z) 2\pi r dr dz}{W_{\text{HCP}} \int_0^{R_{\text{max}}} \int_0^{r_{\text{max}}} D(r,Z,E) 2\pi r dr dz}$$

The relative efficiency, that is, the relative dose response, $f(D)$, is measured via electron/photon irradiation over an extended dose range as possible. W_{γ} and W_{HCP} are the mean energies required to produce an electron-hole pair by the gamma and HCP radiation, 33.97 eV and 36.0 eV, respectively.

RESULTS

Figure 5 shows the average OA spectra of nine samples exposed to proton irradiation. The main peak known as the F center is located at $\sim 5\text{eV}$.

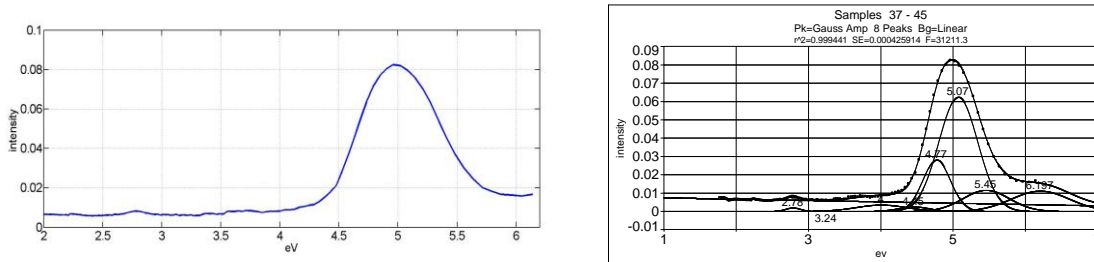


Figure 5. left : the average OA spectra of nine samples irradiated by protons. Right : Deconvolution of the OA spectra.

OA spectra of the nine samples were deconvoluted samples. As can be seen in figure 5, the main peak is 5eV , known as the F center. In addition, peaks at 4.77eV and 5.45eV (CC) are clearly visible. Table 1 and figure 6 show a comparison of the calculated and measured OA relative efficiencies. These measurements of η_{mt} (ratio of measured to theoretically calculated) indicate that the experimental measurements for the F band optical density are 6-9 times higher than the TST calculated efficiencies. Clear evidence supporting the assumption that very significant vacancies/F centers are being radiation-created by the HCPs above the number/Gy created by electrons. The 5.45 eV and 4.77 eV bands also show higher values of η_{mt} which also indicate a link to radiation created vacancies. On the other hand, the maximum value of η_{mt} is ~ 0.3 for the 4 eV band. The 4 eV band is believed to be based on Mg trimers and apparently the created vacancies serve as competitors to the 4 eV electron trap. These results strongly support the basic thrust/postulates that is, radiation created vacancies influence both OA and TL HCP relative TL efficiencies and need to be accounted for in TST calculations.

Table 1. Comparison of measured and calculated OA efficiencies

Particle	OA bands (eV)	Measured this work	Theoretical eq.(3)	η (measured/Theoretical)
		η	η	
protons	5.08	2.85	0.47	6
	5.45	1.36	0.64	2.1
	4.77	3.38	0.89	3.8
	4	0.11*	0.32	0.3

* max value

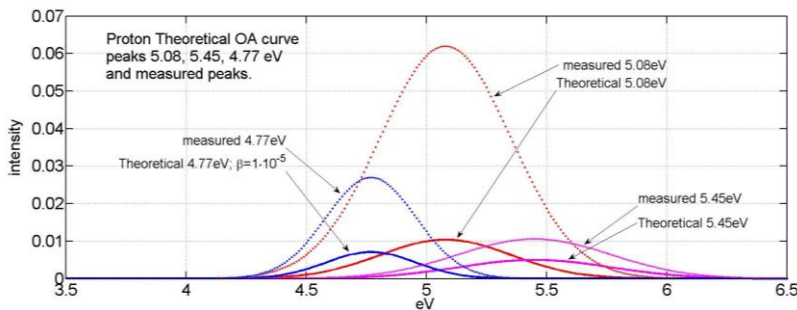


Figure 6. Comparison of measured and calculated OA efficiencies

CONCLUSIONS

A comparison of TST calculated relative OA efficiencies to experimentally measured efficiencies has revealed a significant discrepancy between theory and experiment. Although previous discrepancies have been discovered in TL relative efficiencies [5] a definite decision concerning the applicability of TST in its current form to HCP radiation effects was compromised by various experimental uncertainties in the TL measurements. The current experiment sidesteps these difficulties and leads unambiguously to the conclusion that HCP radiation created defects (eg., radiation created Fluorine ion vacancies leading to F centers) cannot be neglected in the description of HCP induced radiation action. This conclusion applies to TL mechanisms as well since the F center is believed to play a significant role in the production of TL.

REFERENCES

- [1] L. Weissman et al, these proceedings INS27 (2014).
- [2] www.sigmaplot.com
- [3] Y.S. Horowitz, M. Rodriguez-Villafuerte and O. Avila , "Theory of Heavy Charged Particle Dose Response" Solid State Dosimetry School- Advanced Topics in Radiation Dosimetry, Nucl. Instrum. Meths., B184, 85-112 (2001)
- [4] J.K. Ezra, Y.S. Horowitz, Heavy charged particle thermoluminescence dosimetry: Track structure theory and experiments, Int. J. Appl. Radiat. Isot. 33 (1982) 1085-1100.
- [5] O. Avila, I. Gamboa-deBuen, M. Brandan, Study of the energy deposition in LiF by heavy charged particle irradiation and its relation to the thermoluminescent efficiency of the material, J. Phys. D. 32 (1999) 1175.

Radiation Detectors (Thursday, February 13, 2014 11:30)

The SVM Method for Fissile Mass Estimation through Passive Neutron Interrogation: Advances and Developments

C. Dubi, I. Israel Shvili

Nuclear Research Center of the Negev, Israel

INTRODUCTION

Fissile mass estimation through passive neutron interrogation is now one of the main techniques for NDT of fissile mass estimation, due to the relative transparency of neutron radiation to structural materials- making it extremely effective in poorly characterized or dirty samples .

Passive neutron interrogation relies on the fact that the number of neutrons emitted (per time unit) due to spontaneous fissions from the sample is proportional to the mass of the detected sample. However, since the measurement is effected by additional neutron sources- mainly (α ,n) reactions and induced fission chain in the tested sample, a naive estimation, assuming a linear correspondence between the mass of the detected sample and the average number of detections, is bound to give an over estimation of the mass. Since most passive interrogation facilities are based on ^3He detectors, the origin of the neutron cannot be determined by analyzing the energy spectrum (as all neutrons arrive at the detector in more or less the same energy), and a mathematical "filter" is used to evaluate the noise to source ratio in the detection signal. The basic idea behind the mathematical filter is to utilize the fact that the different neutron sources have different statistical attributes- in particular, both the source event rate and the distribution of the number of neutrons released in each event differs between the different sources. There for, by studying the higher moments of the neutron population, new information about the source to noise ration may be obtained.

The most well known method for doing so is the Multiplicity method [1], where the amplitude of the three sources (the spontaneous fission (SF) source, the (α ,n) source and induced fission source) are correlated with the so called Singles, Doubles and Triples rate in the detection signal. Then, by solving a set of three equations with three unknowns, the amplitude of SF source may be isolated. Recently, the authors have introduced a new method, referred to as the SVM method (standing for Skewness, Variance and Mean), correlating between the amplitude of the three sources, and the first three central moments of the number of detections in a given (fixed) time interval [2].

While the new method has the same statistical convergence rate as the Multiplicity method (although a different random variable is sampled) , it enjoys a theoretical "flexibility", allowing us to take into consideration, with relative simplicity, physical effects that have so far been neglected in the physical models, such as the detector dead time effect.

In the present study, we introduce the reader with the SVM method from a practical point of view, demonstrate its advantages and discuss future prospects of the method.

In particular, we demonstrate the method on measurements taken at the JRC (Joint Research Center) at Ispra, Italy (and compare the results with the multiplicity method), and demonstrate how, by fairly simply modifications on the stochastic transport equation describing the dynamics of the distribution of the number of detections, we may obtain analytic formulas for dead time corrections [3] , active neutron pulsed source interrogation [4] and the effect of long fission chains on the measurement [5].

REFERENCES

1. N. Ensslin, W. Harker, M. Krick, D. Langner, M. Pickvell: Application guide to neutron multiplicity counting, Los-Alamos manual, LA-13422-M (1998)
2. C. Dubi, T. Ridnik, I. Israelashvili, J. Bagi, J. Huszti: A method for the estimation of fissile mass by measuring the number of neutron signals within a specific time interval ,Nuclear Instruments and Methods

in Physics Research Section A : Accelerators, Spectrometers, Detectors and Associated Equipment (NIMA), 673, 1 May 2012

3. C. Dubi, T. Ridnik, I. Israelshvili: Analytic model for dead effect in Neutron Multiplicity counting: To appear at "Nuclear Science and Engineering".

4. C. Dubi, T. Ridnik, I. Israelashvili, B. Pedersen: [novel method for active fissile mass estimation with a pulsed neutron source](#), Nuclear Instruments and Methods in Physics Research Section A: Accelerators, Spectrometers, Detectors and Associated Equipment, Volume 715, 1 July 2013.

5. C. Dubi: A stochastic transport equation with induced fission chains in Neutron Multiplicity Counting. Submitted to NIMA .

Radiation Detectors (Thursday, February 13, 2014 11:30)

Alpha Beta Monitoring System Based on a Pair of Simultaneous Multi Wire Proportional Counters

D. Amidan^{1,2}, I. Orion¹

U. Wengrowicz², Y. Yehuda-Zada², Y. Levin², T. Mazor², Y. Kadmon², and Y. Cohen²

¹*Ben-Gurion University of the Negev, Beer Sheva, Israel*

²*Nuclear Research Center-Negev, Beer Sheva, , Israel*

INTRODUCTION

A new approach for a simultaneous alpha beta contamination monitoring system is presented. In nuclear environments or laboratories working with open radioactive sources there exists a risk of contamination. In order to avoid external contamination hazards, hand & foot alpha beta monitoring systems are needed. Usually, monitoring systems are based on large area Multi Wire Proportional Counters (MWPC). Generally, in the MWPC detectors the filling gas is supplied by a continuous gas supply system. The filling gas should not exhibit appreciable electron attachment coefficient. Typically, a noble gas such as Argon Methane, 90%Ar+10%CH₄ is in use. This method of measurement is effective, yet it requires expensive maintenance costs due to gas flow control and periodical replacements. Several hand held commercial detectors such as Rotem Ind. PA-100, are based on free air flow alpha MWPC. Due to the energy released from the alpha particles in the filling gas a large number of ion pairs are formed. Despite the electron attachment coefficient of free air, a measurable pulse is obtained. Contrary to alpha sources, beta emitters deposit only a small part of their energy. In order to obtain a measurable pulse from beta interactions, oxygen free gas is required. Gas sealed detectors which are appropriate for beta measurements, require a relative thick entrance window in order to avoid gas leakage. Thick windows absorb alpha particles so that they are not appropriate for alpha measurement. The presented approach combines a pair of simultaneous MWPC assembled in a "pancake" type configuration; the sealed gas beta counter is located behind a free air alpha detector. This approach enables simultaneous alpha-beta measurement without needing continuous gas supply.

METHODS

Some of the most popular types of radiation detectors are based on the effects produced when a charged particle passes through a gaseous medium. Due to coulomb forces interactions, charged particles cause ionization and excitation of gas molecules throughout their track in the medium. Gas filled detectors such as ion chambers, proportional counters and Geiger-Muller (G.M.) tubes, are based on sensing the direct ionization created by the passage of the charged particles [1]. In order to distinguish between alpha and beta emitters, pulse amplitude discrimination methods are typically applied in the signal processing system. G.M tubes and continuous current ion chambers are not suitable. The low primary charge produced by the radiation interaction with the gas, limits the effective detection availability that exceeds the electrical noise of the pulse processing circuitry. Therefore, the most appropriate gas filled detectors are the proportional counters. The free electrons from the primary ionization are easily accelerated by the electric field and achieve a large kinetic energy when undergoing a collision with another gas molecule. If this energy is greater than the ionization energy of these molecules, it is possible that an additional ion pair will be created and secondary electrons will be released. This process is reproduced according to the intensity of the electric field. The signal multiplication process forms a cascade known as a Townsend avalanche. This phenomenon occurs at very large electric fields that are practically created by a radial electric field. The proportional output pulses are much larger than those from ion chambers, and their amplitude depends on the primary ionization and the intensity of the electric field. Typical proportional counters are made of cylindrical geometry, where the negative electrode is a metal cylinder and the positive electrode is made of a very thin

tungsten or stainless steel wire, typically 1/1000". The cylindrical geometry limits the effective area of the proportional counters, therefore, at CERN laboratories, a Multi Wire Proportional Chamber was developed by the noble price laureate G. Charpak and his team [2]. These detectors are being used worldwide for particles detection and contamination measurements. These detectors are constructed by a grid of anode wires placed between two large flat plates that serve as cathodes. Recent researches are currently performed in order to improve the sensitive area homogeneity [3].

In this work, the simultaneous alpha-beta MWPC properties have been researched in order to improve the detector performances without gas supplying. Factors influencing the output signal amplitude including: type of filling gas, distribution of electrical field, distance between the anode wires, anode wires diameter and distance to cathode plate, were investigated. As part of this research, the electric field around the anode wires had been simulated by Comsol 4.2 software. The simulation consists of a two-dimension model, where the cathode parallel plates on the top and bottom of the detector have been earthed and high DC voltage was supplied to the anode wires. The simulation of the electrical potential around a seven-wire MWPC model is presented in Figure 1. The model shows that the behavior of the electrical potential close to the thin anode wire is very similar to the classic cylindrical geometry applied in proportional gas filled chambers. The simulation results comply with the electrical field equation [2].

The beta detector entrance window properties and the energy deposition of beta particles in the sensitive gas area were tested and simulated using MCNP-4C software. The beta detector entrance window avoids penetration of alpha particles into the beta detector sensitive area, yet, it is made as thin as possible in order to reduce the beta energy deposition. Further improvements in the entrance window will be performed in order to avoid gas leakage. Different types and pressures of gas filling were investigated as well. The energy deposition for ^{90}Sr 196 keV average beta energy was simulated by MCNP-4C software for different gasses and pressures, see Figure 2. Simulations for ^{90}Y and other beta emitters are being investigated as well.

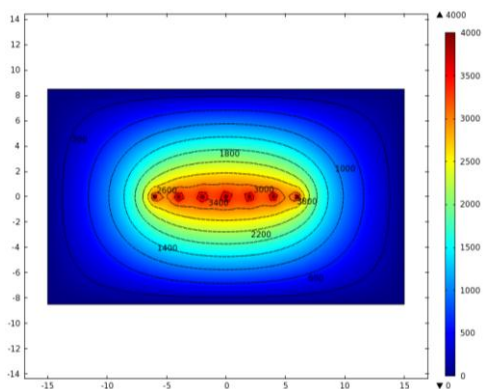


Figure 1: electrical potential around a seven wire MWPC model

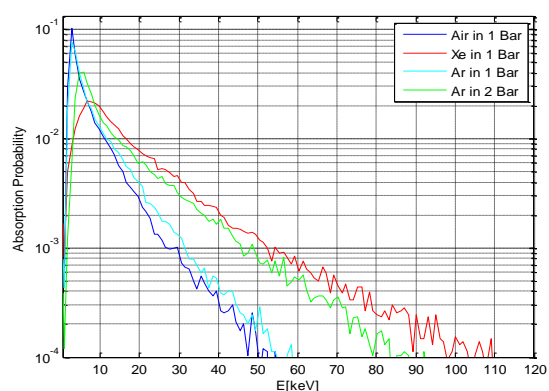


Figure 2: Comparison of different gas proportional detectors

RESULTS

The Comsol 4.2 software efficiency was compared to previous theoretical works and a MWPC detector prototype has been designed according to the simulated model results. According to the gas model simulations results, Xenon at one bar is the best filling gas for long time sealing and maximum energy deposition. Approximate results of energy deposition can be achieved by 2 bar Argon methane filling gas, but this requires higher challenging sealing methods.

REFERENCES

- [1] F.knoll, Glenn. *Radiation detection and measurement*. 3rd. Ed. : John Wiley & Sons.
- [2] *Some developments in the operation of multiwire proportional chambers*. G. Charpak.. : Nuclear instruments and methods, 80, s.1, pp. 13-34. (1970).
- [3] B.Olshvanger, G.Bogorodzki. *High efficiency and high homogeneity large-area gas-filled radiation detector*. US patent No. 7,470,913 B1 Dec 30, 2008.

Radiation Detectors (Thursday, February 13, 2014 11:30)

Aerial Measuring System (AMS)/ Israel Atomic Energy Commission (IAEC) Joint Comparison Study

I. Halevy¹ and P. Wasiolek²

1. *Israel Atomic Energy Commission, Israel*
2. *U.S. Department of Energy National Nuclear Security Administration Remote Sensing Laboratory, USA*

Israeli Team: I. Halevy, S. Dadon, M. Sheinfeld, A. Broide, S. Rofo and I.Yaar

American Team: AMS team – RSL LV

Piotr Wasiolek, Rusty Malchow, Carson Riland, Manuel Avaro, Ray Arsenault
Ed Zachman, Mike Lukens, Joe Keller, Jaz Stampahar and John Gelsthorpe

In support of the U.S. Department of Energy (DOE) International Emergency Management and Cooperation (IEMC/NA-46) Program, the comparison of the U.S. and Israeli Aerial Measuring Systems (AMS) study was proposed and accepted. The study, organized by the DOE/National Nuclear Security Administration (NNSA) Remote Sensing Laboratory (RSL), involved the DOE/NNSA Aerial Measuring System Project based at the RSL and operated under a contractor agreement by National Security Technologies, LLC (NSTec), and the Israel Atomic Energy Commission (IAEC) Aerial Measuring System. The operational comparison was conducted at RSL-Nellis in Las Vegas, Nevada, during week of June 24–27, 2013. The Israeli system, Air RAM 2000 (figure 1, down), was shipped to RSL-Nellis and mounted together with the DOE Spectral Advanced Radiological Computer System, Model A (SPARCS-A, figure 1 up) on U.S. DOE Bell-412 helicopter for a series of aerial comparison measurements at local test ranges, including the Desert Rock Airport and Area 3 at the Nevada National Security Site (NNSS). A four-person Israeli team from the IAEC, Nuclear Research Center – Negev (NRCN) supported the activity.

The main objective of this joint comparison was use the DOE/RSL Bell-412 helicopter aerial platform, perform the comparison study of measuring techniques and radiation acquisition systems utilized for emergency response by IEAC and NNSA AMS [1].

MEASURING SYSTEMS

One advantage of acquiring aero-radiometric measurements lies in the high collection rate of data over large areas and rough terrain. Typical aero-radiometric systems record and save gamma-ray spectra, correlated with the Global Positioning System (GPS) derived location information (latitude, longitude, elevation over GPS ellipsoid=GPS altitude) in regular time intervals of 1 to 2 seconds. Such data can be used to locate radiation anomalies on the ground, map ground contamination, or track a radioactive airborne plume. Acquiring spectral data of this type allows separation of natural radioactivity from that of man-made sources and identification of specific isotopes, whether natural or man-made.

During the acquisition the flight altitude is kept constant, with typical values recorded between 50 and 985 feet (ft) (15 and 100 meters [m]) above ground level (AGL). The helicopter ground speed is maintained constant, in the case of DOE Bell-412, 70 knots (130 km/h).

For the comparison study, AMS and IAEC used their emergency response radiation detection systems, Israel's Air RAM 2000, and the DOE's SPARCS. For altitude measurements the AirRAM 2000 system uses a barometric altimeter with the range of 0–8000 ft, which is calibrated at 1000 ft by a radar altimeter. The SPARCS system uses radar altimeters for vertical positioning (altitude over the ground) and Differential GPS for location.

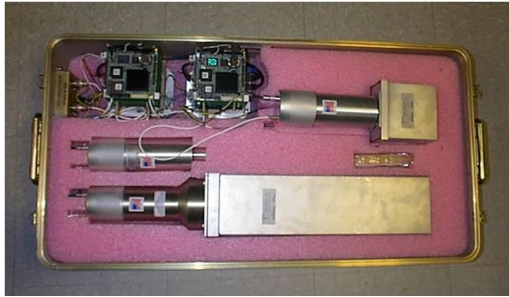


Figure 1. Interior of the SPARCS-A pod and The SPARCS ATU connections, up. The Air ram2000, down.

Survey Aircraft

The DOE Bell-412 helicopter was used as the airborne platform to carry out the comparison study (figure 2). The Bell-412 is a twin engine utility helicopter that has been manufactured by Bell Helicopter since 1981. With a standard fuel capacity of 330 gallons, it is capable of flying for up to 3.7 hours, with a maximum range of 356 nautical miles and a cruising speed of 122 knots. However, with the AMS radiation survey configuration of 12 detectors, four crew members (two pilots, a mission scientist, and an equipment operator), with a survey speed of 70 knots (120 ft/sec) at survey altitude of 300 ft AGL, the Bell-412 was capable of 2.5 hours of flight time.



Figure 2. DOE Bell-412 helicopter during survey

RESULTS

Attenuation and Sensitivity

Lake Mohave Calibration Line

The altitude spiral flight over the Lake Mohave Calibration Line was used to derive the local effective air attenuation coefficient, obtain the sensitivity of both acquisition systems, and estimate their inherent background. The altitude spiral consists of passes between two waypoints programmed into helicopter navigation system over the land calibration line and water line at several different altitudes. During the exchange, the altitudes were 50, 100, 200, 300, 750, 1500, and 3000 ft AGL. The path plots of the altitude spiral flight plotted independently by both groups are presented in Figure 3.



Figure 3. The AirRAM 2000 inside the DOE Bell-412 helicopter

The count rate ratio of the SPARCS single 2" × 4" × 16" NaI detector to the AirRAM 2000 two 2" × 2" inch detectors of about 18 (Table 1) compares very well with the ratio of volumes between systems of 16 [128 inch³ (2" × 4" × 16")/8 inch³ (2" × 2" × 2")].

From the altitude spiral, the effective air attenuation coefficient and sensitivity of the detectors can be derived by plotting each altitude flight's net gross counts versus altitude on a semi-log plot (Figure 4) and exponentially fitting the gross counts expression:

$$Calt = CGC \times \exp[\mu_{air} \times (H - H_{avg})]$$

Where:

Calt = gross counts normalized to the averaged survey altitude, (cps).

CGC = total terrestrial count rate or gross counts, (cps).

μ_{air} = gamma ray air attenuation coefficient, ft⁻¹.

H, H_{avg} = average radar altitude, ft AGL.

The difference in sensitivity between the SPARCS single 2" × 4" × 16" NaI detector to the AirRAM 2000 two 2" × 2" inch detectors is remarkable, ~18 times.

Table 1. Average count rate from different detectors at the calibration line

Altitude (ft)	Count rate (cps)					
	Land Line			Water Line		
	SPARCS NaI 2"×4"×16	AirRAM two NaI 2"×2"	Count Ratio	SPARCS NaI 2"×4"×16	AirRAM two NaI 2"×2"	Count Ratio
50	2620	151	17	159	11	14
100	2450	141	17	155	10	16
200	2139	118	18	165	11	15
300	1887	102	18	172	10	17
750	993	53	19	190	12	16
1500	405	22	18	173	11	16
3000	223	13	17	196	12	16

The slope in figure 4 is the gamma ray air attenuation coefficient (0.00186 ft^{-1}). From the graph it is clear that the heights altitude for detecting $8.5 \mu\text{R/hr}$ is $\sim 1950 \text{ ft}$.

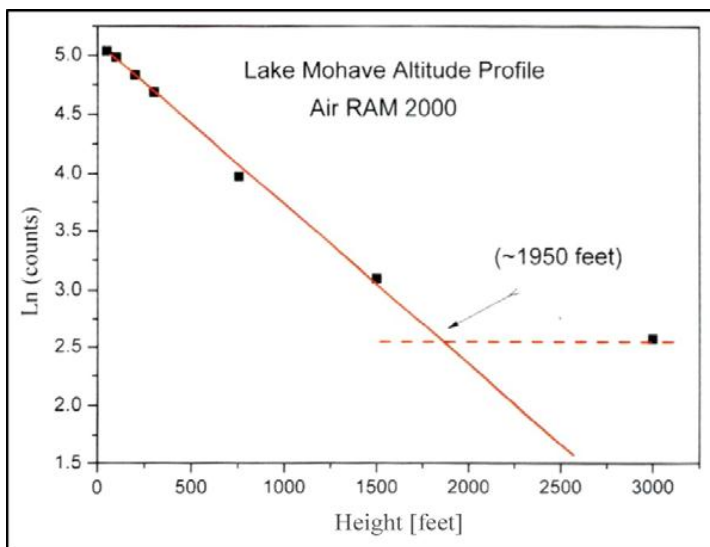


Figure 4. Results of the curve fit of the altitude spiral data collected with AirRAM and analyzed by IAEC.

Desert Rock Airport Sources Overfly

Three radioactive sources listed in Table 2 were placed approximately 1500 ft (450 m) apart along the runway at the Desert Rock Airport (Figure 5). Using the visual flight rules, several passes directly over the sources (marked with orange cones) were executed. To study the response of the SPARCS and AirRAM, the flight altitude and speed were varied from 50 to 150 ft AGL and from 35 to 150 knots. The results of the source flyover are presented in Figure. The SPARCS data (gross counts from the $2'' \times 4'' \times 16''$ NaI crystal) show an elevated count rate at any combination of flight altitude and speed tested, from 50 ft AGL at 50 knots to 150 ft AGL at 100 knots. The AirRAM, due to much lower detector volume, failed to detect the smaller ^{60}Co source at 100 ft and both ^{60}Co sources at 150 ft AGL. A higher flight speed of 100 knots, combined with lower sampling frequency (sample every 2 seconds) affected the AirRAM capability to spatially locate the sources.

Table 2. Activity and location of the radioactive sources used in the study

	Activity (mCi)	Longitude	Latitude
^{137}Cs	20.6	-116.028505	36.624740
^{60}Co	3.6	-116.031402	36.621293
^{60}Co	1.7	-116.034129	36.617998

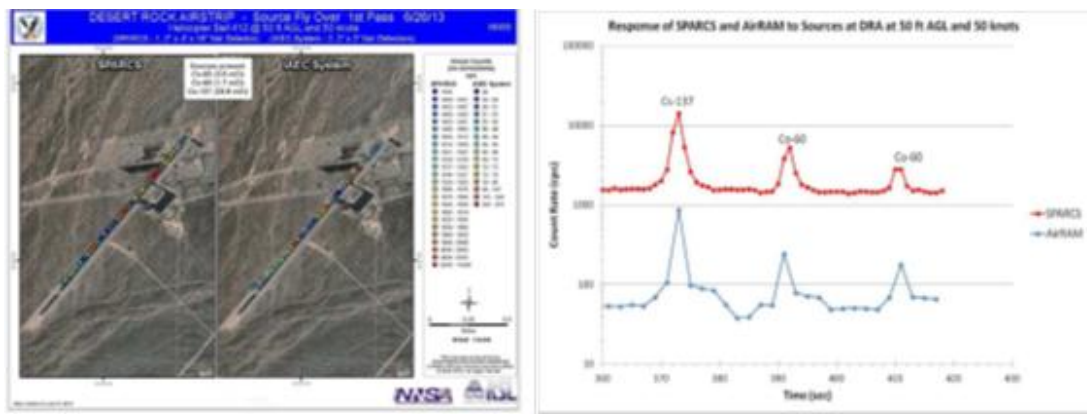


Figure 5. Source flyover at Desert Rock Airport at 50 ft AGL altitude at 50 knots ground speed presented spatially (left) and as time series (right)

Contours

Natural Background

To compare responses of the SPARCS and AirRAM to variable natural radiation background, the AMS test/evaluation area (Government Wash) was surveyed using standard AMS techniques of flying uniformly spaced parallel lines over survey area. The actual flight lines flown during the exchange are shown in Figure 6.

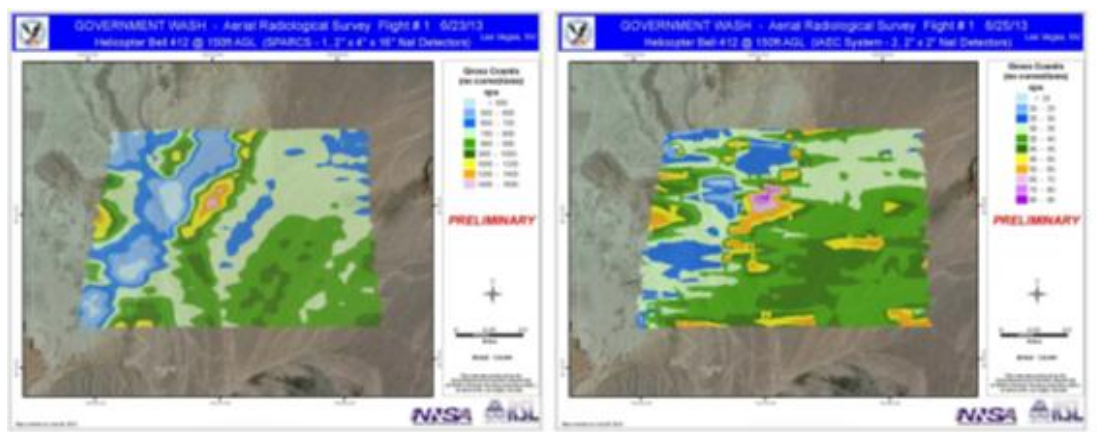


Figure 6. Gross-count contour of the natural background area (Government Wash) created using IAEC AirRAM detection system and AMS data processing techniques

[1] PIOTR WASIOLEK and ITZHAK HALEVY, AERIAL MEASURING SYSTEM (AMS)/ ISRAEL ATOMIC ENERGY COMMISSION (IAEC) JOINT COMPARISON STUDY REPORT, Nevada National Security Site June 24–27, 2013 , DOE/NV/25946--1941

Radiation Detectors (Thursday, February 13, 2014 11:30)

Design of Stack Monitoring System for PET Medical Cyclotron Facilities with Isotope Identification and Released Activity Concentration Measurement

A. Osovizky¹, D. Ginzburg¹, V. Pushkarsky¹, D. Shmidov¹, E. Vax², Y. Knafo¹,
N. Semyonov¹, L. Kaplan¹, Y. Kadmon², Y. Cohen² and T. Mazor²

¹ Rotem Industries Ltd, Israel

² Nuclear Research Center Negev, Israel

INTRODUCTION

Cyclotrons are commonly used for production of radioactive isotopes utilized for Positron Emission Tomography (PET) imaging and other purposes⁽¹⁾. During the isotopes production process there are routine releases of nonhazardous amounts of radioactive isotopes into the atmosphere. The activity concentration of radioactive effluents, released into the atmosphere are subjected to restrictions by national regulations based on international recommendations⁽²⁾. Uncontrolled isotopes emission through the ventilation system would increase the radiation hazard potential to nearby population. In order to control and prevent such emissions, monitoring and assessment of the released activity concentration is required.

For this purpose, a radiation detection system is required to be installed in the ventilation stack. The design of such a monitoring system should cope with two main difficulties: the capability to detect low concentration level and the capability to accurately assess the emitted activity per released isotope.

In this work, we present innovative stack monitoring detection system that combines new detector design, electronics, friendly interface software and unique algorithms that provide a comprehensive solution for the above-mentioned requirements. Activity releases measured by the system are discussed along with calculation for the system sensitivity, detectable level and isotope identification algorithm.

METHODS

The innovating stack monitoring system is aimed to measure the released activity concentration and to report the activity according to the produced isotope. In order to achieve accurate and correct measurements, the design should allow for the following considerations:

- a. Release vs. decay: distinguish the detector reading that is caused by an actual activity release into the atmosphere from a decay that is caused by absorption of the released radiopharmaceutical on the duct surface or in the charcoal filters.
- b. Release vs. external radiation field: distinguish the detector reading that is caused by an actual activity release into the atmosphere from readings that are produced by short term events of radiation located outside the duct. These events can occur due to radiation source located at the chemical hot laboratory during the routine activity of the radiopharmaceutical production and shipping.
- c. High sensitivity: accurate measurement of pulsed releases with low activity concentration (about 1000 Bq/m³).
- d. PET isotope identification: distinguish between the readings caused by the commonly used positron emitting isotopes (¹⁵O, ¹³N, ¹¹C, ¹⁸F)⁽³⁾.
- e. Conversion and calibration: converting the detector reading in counts per second (CPS) into activity concentration units that will fit different duct systems.
- f. Installation: design a system appropriate for outdoor conditions that can be easily installed, maintained and checked for proper and accurate operation.

The block diagram of the designed stack monitoring system is described on Figure 1. It is designed to be installed inside the duct for increased sensitivity. For achieving maximal efficiency, the innovating system was designed to measure both the positron energy, which is different for each of the PET isotopes, and the 511 keV gammas produced by the annihilation process that are common to all the isotopes. The mean free pass of the β^+ particle is limited therefore in order to detect the positron the detector surface should be in

direct contact with the released air. Detection of the penetrating 511 keV gamma photon is less complex; however the effect of the external background has to be considered.

The system is based on two plastic scintillation detectors mounted back to back. On this configuration detector 2 measures both the gamma and beta while detector 1 measures only the gamma. By comparing between the two detector's reading it is possible to assess the contribution of the released activity while subtracting other interferences caused by external radiation or radiation decay of the material which is absorbed on the duct surface or within the filters.

On this configuration, the reading obtained by detector 2 is affected by both the kinetic energy loss of the positron prior to the annihilation and the 511 keV gamma photons produced by the annihilation process. Because the PET isotopes have different positron energies, the spectrum that is obtained when measuring the same activity concentration is specific to the isotope.

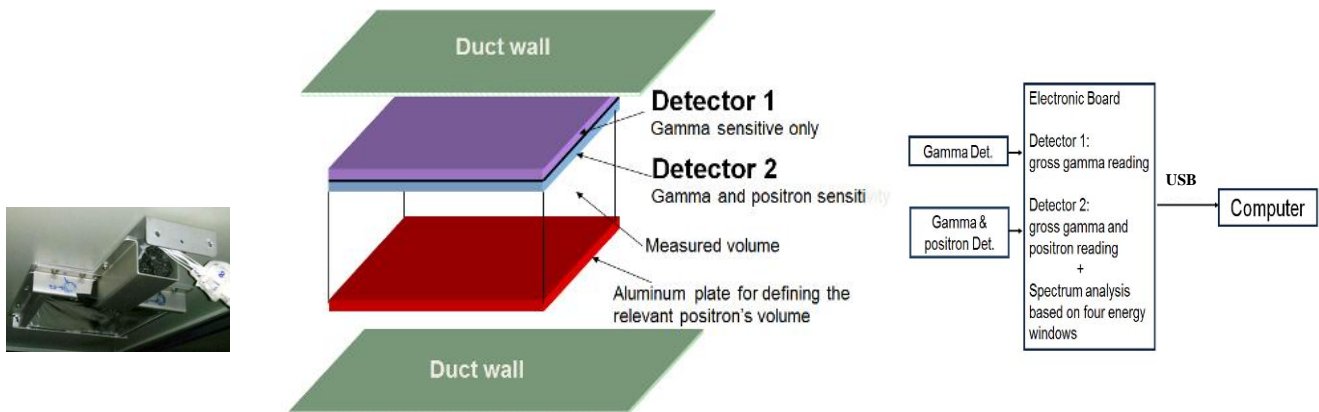


Figure 1. Block diagram of the detector design

The detection volume is defined by an aluminum frame, thus enabling to dissociate the activity assessment from the actual duct size and therefore has a predefined conversion factor for the detector's reading into concentration units. In case that higher sensitivity is required, the design enables to increase the number of detectors or the detectors size and to improve the detectability.

The detector geometry has a negligible effect on the airflow; no shield is required to maintain background rejection for improving the detection level. As a result of the predefined installation geometry and considering the stack size, it is possible to obtain a calibration factor regardless to the actual stack size and thus prevent the need for local calibration. The signal processing electronics supports energy windows discrimination, enabling PET isotope identification. The microprocessor controls the counting process and the communication to the dedicated interface software. The software presents on-line the release concentration and the reporting is based on the detector's gross counts reading and the air volume flow. The software algorithm analyzes the ratio between counts in each of the energy windows and enables automatic computation of the released activity with correlation to each of the isotopes including gamma background subtraction.

RESULTS

Measurements were performed in a radiopharmaceutical production cyclotron facility. The facility produces two different isotopes (N-13 and F-18).

Figure 3 presents the gross counts reading that is obtained by both detectors and the subtraction, which represents the positron contribution only.

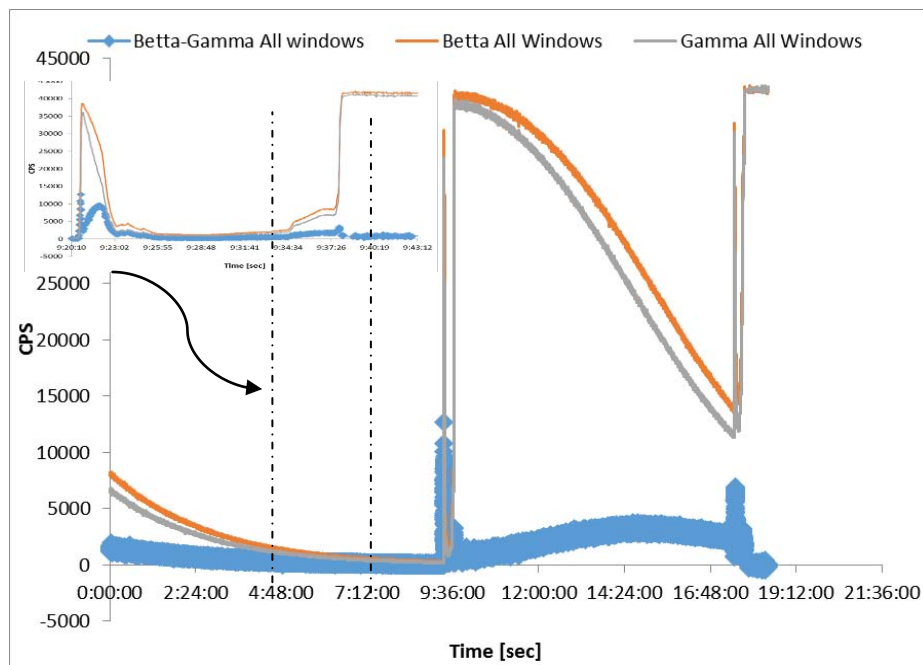


Figure 3. Gross counts reading: Orange line – Gamma and positron contribution, as obtained from detector 2; Grey line – Gamma contribution only, as obtained from detector 1; Blue line – the subtraction of the readings from both detectors, that represent positron contribution only. The inlay graph shows the zooming of the area framed by dashed lines.

Spectral measurements were also performed using an external MCA for the purpose of energy calibration of the detectors. A sample of the obtained spectra is presented in Figure 4.

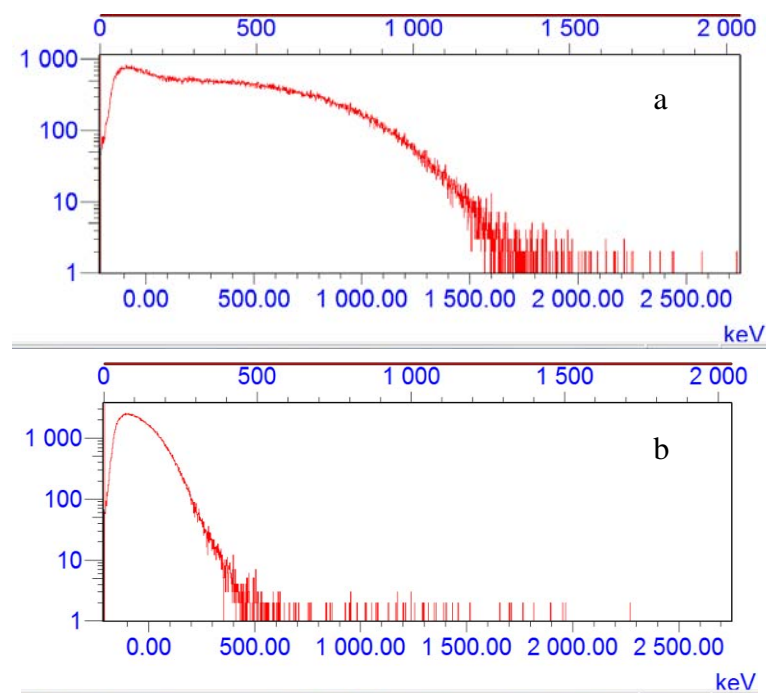


Figure 4. Measurement of Sr-90 beta emitting calibration source: a) as obtained with detector 2. B) as obtained with detector 1.

CONCLUSIONS

- A new design for a stack monitoring system is presented
- The preliminary results support the design methodology
- The system novel design provides a method for isotopes identification, predefined calibration and reliable documentation of the activity releases
- Further study of the system performances is underway at PET isotopes production facility.

REFERENCES

1. IAEA, Technical Reports Series no. 465, Cyclotron Produced Radionuclides: Principles and Practice, Vienna, (2008).
2. International Commission on Radiological Protection, ICRP Publication 103 (2007).
3. Introduction to PET Physics
http://depts.washington.edu/nucmed/IRL/pet_intro/intro_src/section2.html

Key words: Stack monitoring, PET isotopes, detection, identification

Radon Daughters Background Reduction in Alpha Particles Counting System

S. S. Dadon¹, O. Pelled¹, I. Orion²

¹*NRCN, POB 9001, Beer-Sheva, Israel*

²*Ben-Gurion University of the Negev, Beer-Sheva, Israel*

INTRODUCTION

Nuclear alpha counting system for air monitoring samplers does not subtract accurately the contribution of Radon Daughter Progeny (RDP) background in most cases, and a delayed counting is needed to overcome the RDP contribution⁽¹⁾. Others RDP background reduction methods use prior information on the RDP background, and requires that measurements of the artificial isotopes should be conducted under the same calibration conditions.

The pseudo coincidence counting method is using a serially occurring events of the beta decay of the ²¹⁴Bi followed by alpha decay of the ²¹⁴Po that accure almost simultaneously ($T_{1/2}=164 \mu\text{sec}$), to detect the Pseudo Coincidence Event (PCE) from the RDP, and to subtract them from the gross alpha counts. The Radon Daughter Progeny decay series is shown in fig.1.

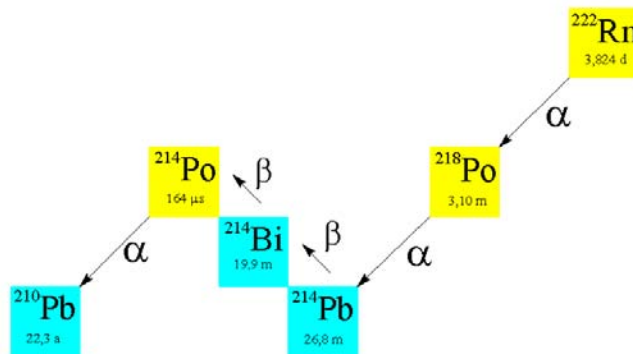


Fig.1: Radon daughter progeny decay series.

The aim of this work was to develop and to optimize an Alpha Beta Pseudo Coincidence (ABPC) counting method for real time RDP background reduction, including subtracting the ²¹⁸Po contribution, based on a solid state silicon *PIPS* detector.

MATERIALS AND METHODS

A PCE experimental system was developed consisting : a single solid state silicon *PIPS* detector for alpha and beta detection, amplification unit, identification and stretching beta pulse circuit, identification and shaping alpha pulse circuit, PCE circuit to capture sequence of beta→alpha decay, and measurement modules and data processing. The electronics system diagram is shown in Fig. 2.

The nuclear analog pulses obtained at the output of the detector (*PIPS*), due to alpha/beta particles, are amplified and delivered to the energy discriminator circuit that transfer and shapes the nuclear pulses of the alpha/beta particle. The shaped beta pulses are delivered to PCE circuit which opens a narrow time gate (hundreds of μs) so any detected alpha event that occurs in this time window is supposed to be originated from RDP and considered as a background to be subtracted from the total counts obtained from alpha emitting (TOTAL alpha) by the Measurement and Processing Modules obtaining the net isotope activity.

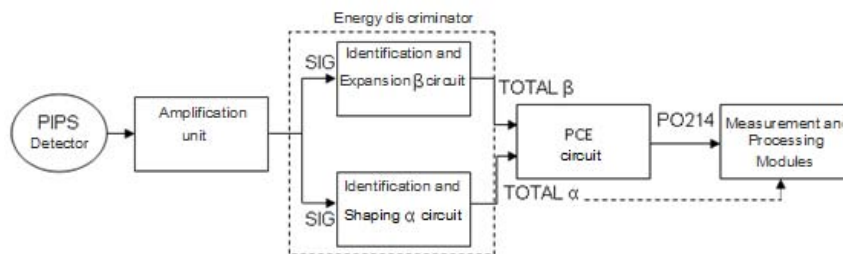


Fig 2-Diagram of the electronics system.

EXPERIMENTAL AND RESULTS

1. Background measurements

One hour background counting cycles were performed with a clean filter for 24 hours. The average background was 0.05 ± 0.012 cpm for the alpha channel, and 5.00 ± 0.129 cpm for beta channel and 0.00 cpm for PCE channel.

2. Accuracy of the PCE system

An air filter that was adsorbed with RDP⁽³⁾ was combined with a 22 Bq of ²³⁸U calibration source, and was counted for 4 hours by the PCE system. Fig.3 shows the *total alpha counts* without the RDP reduction, and it can be seen that after four hours the counts rate is mainly due to the ²³⁸U emission obtaining an average value of 525 ± 20 cpm. The "*Net ALPHA counts*" in fig.3 represent the total alpha counts after the subtraction of the ²¹⁴Po background counts using the PCE method. According to fig.3, it can be seen that after 20 minutes, a good match between the true value of the ²³⁸U calibration source and the net alpha count rate was achieved. Until the 20th minute it can be notice the influence of ²¹⁸Po on total counts, due to the fact that the PCE system do not reduced a non PCE. After 20 minutes the ²¹⁸Po was strongly decayed, and its contribution became negligible.

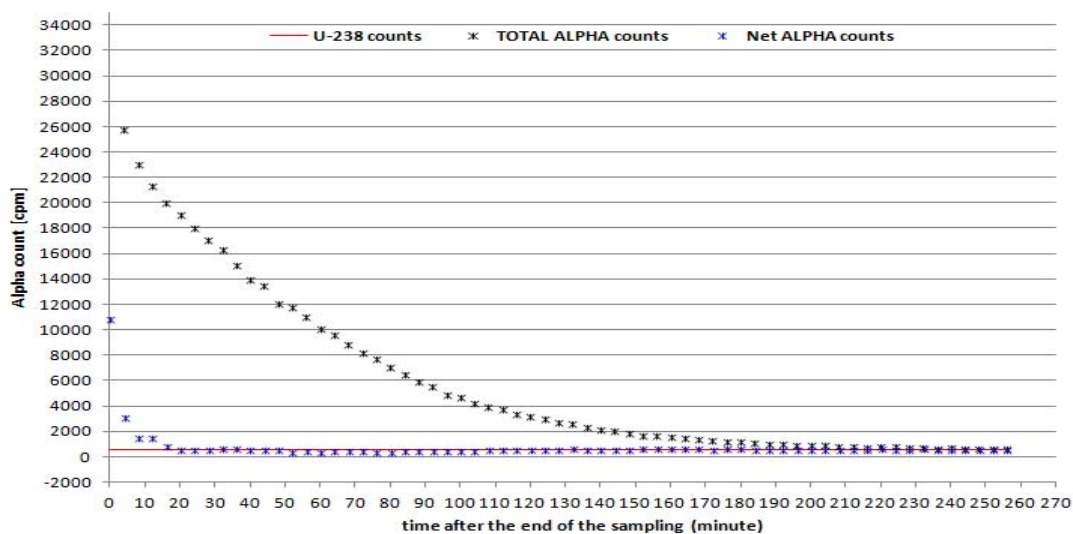


Fig 3 - Counting of ²³⁸U source combined with RDP air filter adsorbed.

In order to examine the effect of a non RDP beta emitter source on the PCE circuit, which can produce a false PCE, combined filter adsorb with RDP and a ⁹⁰Sr calibration source was used. The results showed that there is an over compensation of the PCE system in the first 40 minutes, due to the false random coincidence events of the alpha emitted by the ²¹⁸Po and the beta events emitted by the ⁹⁰Sr source.

In order to determine the false PCE due to a non RDP alpha source, a check was performed with a high activity 8.6 kBq alpha source to test its effect on the output of PCE circuit. Table 1 shows that the of false counts percentage obtained at the output of the PCE circuit were smaller than 0.1%. The results show that the PCE circuit was not influenced by non RDP alpha emitters.

Table 1 - False counts of the PCE circuit

TIME CNT	TOTAL α [counts]	False PCE [counts]	False PCE [%]
1min	164681	97	0.06
1min	166190	108	0.06
1min	166258	124	0.07
30min	4966335	3155	0.06
30min	4965819	3115	0.06
30min	4972584	3165	0.06

3. Improving the PCE method by real time ^{218}Po subtraction

The PCE reduction subtracts only the alpha emission due to the ^{214}Po decay, and cannot compensate the alpha contribution due to the ^{218}Po decay which is dominate at the first 20 minutes after the air filter removal from the air sampler. In order to overcome this limitation, mathematical matching calculations was made with the ^{214}Po and the ^{218}Po decay equations No. 1 and 2 respectively^(4,5,6), the total counting rates of the $^{218}\text{Po} + ^{214}\text{Po}$, and the ^{214}Po count rate after the 20th minute, obtaining the $A_{\text{Po}_{214}(0)}$ and the $A_{\text{Po}_{218}(0)}$.

$$(1) A_{\text{Po}-214 \text{ decay}}(t) = A_{\text{Po}_{214}[0]} \frac{\lambda_4}{\lambda_4 - \lambda_3} \left[e^{-\lambda_3 t} - \frac{\lambda_3}{\lambda_4} e^{-\lambda_4 t} \right] [\text{cpm}]$$

Where, $\text{Po}_{214}[0]$ represents the initial activity of ^{214}Po at time zero ($t=0$); $A_{\text{Po}-214 \text{ decay}}(t)$ represents the activity of ^{214}Po at time t ; $\lambda_3 = 4.3097 \times 10^{-4} \text{ sec}^{-1}$ and $\lambda_4 = 5.8040 \times 10^{-4} \text{ sec}^{-1}$ are the decay constants for ^{214}Pb and ^{214}Bi respectively⁽⁵⁾⁽⁶⁾:

$$(2) A_{\text{Po}-218} = A_{\text{Po}-218[0]} * e^{-\lambda_{\text{Po}-218} t} [\text{cpm}]$$

Fig. 4 shows a good matching of the total measured count rate "TOTAL PO218+PO214 MEASURE" with the calculated decay curve " ^{214}Po CALCULATE" and the " ^{218}Po CALCULATE2". Fig. 4, shows the calculated decay curve using the equation 2.

From several different measurements, a constant ratio of 1.4 of $A_{\text{Po}_{214}(0)} / A_{\text{Po}_{218}(0)}$ was obtained. This ratio can be used in order to estimate the count rate of the ^{218}Po at the first 20 minutes, and subtract it from the total count rate in order to obtain a correct RDP reduction, "NET COUNT", as shown in Fig. 4.

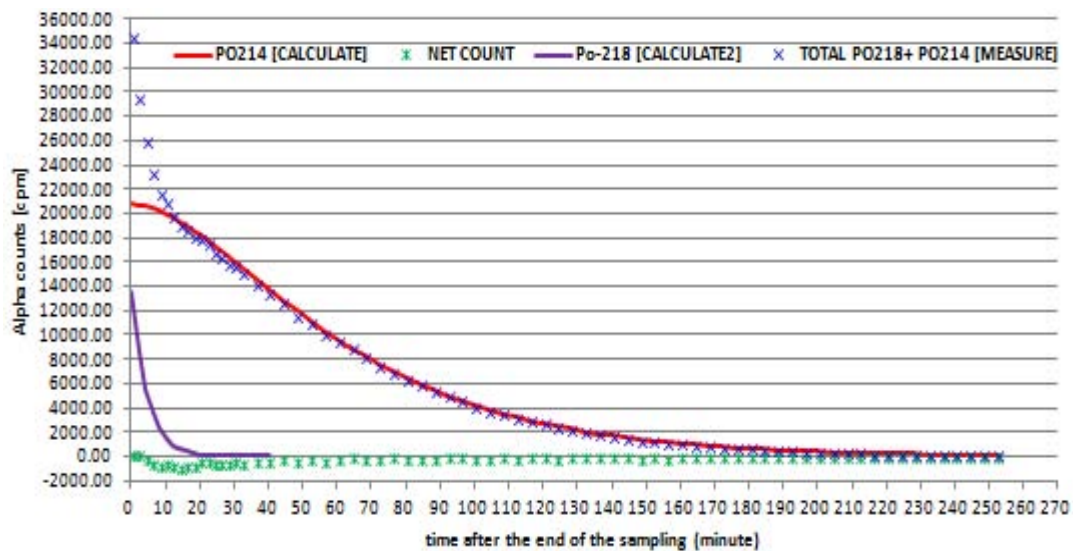


Fig 4 - Decay curve of ^{218}Po , ^{214}Po measured against calculated.

CONCLUSIONS

The ABPC method is using a serially occurring events of the beta decay of the ^{214}Bi follow by alpha decay of the ^{214}Po that take place almost simultaneously to detect the Pseudo Coincidence Event (PCE) from the RDP, and to subtract them from the gross alpha counts.

This work showed that it is possible to improve the efficiency of RDP background reduction, including subtracting the ^{218}Po contribution by using the ABPC method based on a single solid state silicon *PIPS* detector.

False counts percentage obtained at the output of the PCE circuit were smaller than 0.1%. The results show that the PCE circuit was not influenced by non RDP alpha emitters.

The PCE system did not reduce the non PCE of the ^{218}Po . After 20 minutes the ^{218}Po was strongly decayed, and its contribution became negligible. In order to overcome this disadvantage, a mathematical matching calculations for the ^{214}Po and the ^{218}Po decay equations were employed, and a constant ratio of the $\text{APo}_{214(0)} / \text{APo}_{218(0)}$ was obtained. This ratio can be used to estimate the count rate of the ^{218}Po at the first 20 minutes, and to subtract it from the total count rate in order to obtain correct RDP reduction.

REFERENCES

- [1] Darrel Scogging, Radon detection and compensation Methods, Alpha compensation for Radon Progeny Interference Using a Pseudo coincidence Method, 19/5/2009, Protean Instrument Corporation.
- [2] Canberra Inc, NAN 0010 5/93, ALPHA PIPS DETECTORS PROPERTIES and APPLICATIONS.
- [3] PYLON ELECTRONICS INC, RADIOACTIVE SOURCES, RN-190.
- [4] Susan Vanderzyl, Radioactive Decay Laws-General Properties and Related Applications, Full chapter Radioactivity and Radioactive Decay Laws ver. 030310.
- [5] Glenn F.Knoll, Radiation detection and measurement, (3-ed), 2000, Jhon. Wiley&Sons, CH 1, 3.
- [6] Robley D.Evans, The Atomic Nucleus, T M H Edition, 1995, Jhon. Wiley&Sons, CH 15.

Monte Carlo Simulation for Optimizing ${}^6\text{LiF:ZnS(Ag)}$ based Neutron Detector Configuration

Y. Yehuda-Zada^{1,4}, I. Orion¹, L. Dongwon², O. Hen⁵, A. Beck⁴, Y. Kadmon⁴, Y. Cohen⁴, J. Zigler²,
N. Maliszewskyj², A. Osovizky^{2,3}

¹*Ben Gurion University of the Negev, Beer-Sheva, Israel*

²*NIST Center for Neutron Research, Gaithersburg, USA*

³*Rotem Industries Ltd, Rotem Industrial Park, Israel*

⁴*Nuclear Research Center Negev, Beer-Sheva, Israel*

⁵*Tel Aviv University, Tel Aviv, Israel*

Key words: ${}^6\text{LiF:ZnS(Ag)}$, GEANT4, Neutron Detector

INTRODUCTION

Research for developing a cold neutron detector for Chromatic Analysis Neutron Diffractometer Or Reflectometer (CANDOR)⁽¹⁾ is underway at the NIST center for neutron research. The neutron detector is based on ${}^6\text{LiF:ZnS(Ag)}$ ⁽²⁾ scintillation material. The development required optimization of the detector design by simulating the nuclear interactions, light yield for different ${}^6\text{LiF:ZnS:Binder}$ mixture ratios and the grain sizes effect on the light production.

This optimization goal was achieved by using Geant4, a Monte Carlo based simulation software⁽³⁾. The software enables the investigation of the Neutron interaction with the detector, the ionization process and the light transfer process following the nuclear process.

Two neutron sensor configuration were evaluated, one with a mixture ratio of: 1:2:0.3 (${}^6\text{LiF:ZnS:Binder}$ ⁽²⁾) and the other with ratio of 1:3:0.3. The simulation included the captured process of a cold neutron (mean value of 3.62 meV) by the ${}^6\text{Li}$ in the scintillator and the production of an Alpha and a Triton particles. The particles ionize the ZnS(Ag), and blue light photons are created. Because the ionizing particles lose their energy to all of the compound components the number of light photons produced per neutron interaction can vary and a proper design can increase the energy transfer to the ZnS(Ag).

METHOD

The main goal is to simulate all the processes including the neutron interaction, energy loss of nuclear reaction fission products (Alpha & Triton), define the energy transferred for ionizing the ZnS(Ag) and the light travel inside the detector

The simulation enables optimizing the detector design in order to increase the energy transfer to the ZnS(Ag) and therefore enhance the light yield and improve the detection efficiency. The detection efficiency is based on two parameters:

- The stopping power of the scintillator - the probability of having an interaction between the cold neutrons and the ${}^6\text{Li}$.
- Light output - getting a measurable light output signal from the ZnS(Ag) ionization.

There is a contradiction between these two parameters. For maximal stopping power the scintillation mixture should contain high concentration of ${}^6\text{Li}$, but in order to get high light output a high concentration of ZnS(Ag) is required. Furthermore, the ZnS(Ag) is opaque and not transparent to its own luminescence, therefore the concentration of ZnS(Ag) must be controlled.

The simulation output should support the analysis of the following parameters for the two investigated mixture ratios:

- Alpha and Triton Free path in ${}^6\text{LiF}$, ZnS and the Binder
- Probability of the ${}^6\text{Li}(n,\alpha){}^3\text{H}$ reaction for different detector width (up to 1mm).
- Alpha and Triton energy deposition in ZnS(Ag) while traveling in the sensor (grain size dependent, starting with the manufacturer grain size of $\sim 8\mu\text{m}$ ⁽⁷⁾).
- Light attenuation inside the detector.

RESULTS

Geant4 simulation was written in order to find out the scintillator efficiency at different thicknesses and evaluate the stopping power. A horizontal neutron beam with a diameter of 6mm and energy of 3.62meV was placed in front of a scintillator (30mm height, 10mm width and a variable thickness), The scintillator was defined as a mixture of ⁶LiF:ZnS:Binder in two different mass ratios. For each thickness, 100,000 neutrons events were recorded.

Table 1 – Thickness dependent Neutron capture efficiency (Alpha + Triton creation)

Det Width [mm]	Neutron capture Eff[%]	
	1:2:0.3	1:3:0.3
0.25	76.69	69.64
0.5	94.30	90.50
0.75	98.30	96.87
1	99.33	98.78

As can be seen in Table 1, Neutron capture efficiency of the 1:2:0.3 ratio scintillator is higher. At this ratio the ⁶LiF constitute 34% of the total detector volume compared to volume portion of 28% in the 1:3:0.3 compound. However, the dense design (low binder portion) provide high capture efficiency also in the compound with ratio of 1:3:0.3.

Since the ZnS(Ag) in the scintillator mixture is grained powder of about 8 μ m⁽⁷⁾ diameter, and the free path of heavy particles such as Alpha and Triton is very limited, another simulation block was written in order to find out the free path and energy loss of the Alpha and Triton in the scintillator materials.

Three material blocks (⁶LiF, ZnS, Binder) with dimensions of 10cm³ were created, Alpha and Triton isotropic point sources with the above mentioned energies were placed in the middle of each block. For each simulation step the distance and energy loss were recorded.

A comparison was made between the Geant4 maximum free path results and SRIM⁽⁶⁾ software results as shown in Table 2. Results were found to be very similar.

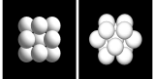
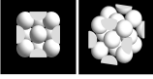
Table 2. Maximum Geant4 free Path compared to SRIM output

	Alpha Path [μ m]		Triton Path [μ m]	
	Geant4	SRIM	Geant4	SRIM
LiF	~6.5	6.05	~32	33.57
ZnS	~7	5.95	~33.5	31.85
Binder	~9	8.92	~51	52.02

Since the Alpha path shown in Table 2 is very small, ZnS grain size can affect the energy deposition in the ZnS grains greatly and following it the scintillator light yield.

In order to simulate the scintillator with different ZnS grain size, a small cube shaped unit cell containing ⁶LiF:Binder in the ratio of 1:0.3 was created and different diameter grains of ZnS were implemented inside it. After creating one unit cell it was replicated in order to build the detector with the required dimensions. Table 3 shows the unit cell configuration for each of the ratios and grains size.

Table 3 – Unit cells configuration for each mixture ratio and ZnS grain size

Mixture Ratio	Grain Diameter [μ m]	ZnS Grains	Cell Dimensions [cc]	Grains Deployment
1:2:0.3	16/8/4	16/16/16	40/20/10	
1:3:0.3	16/8/4	13/13/13	40/20/10	

As can be seen in Figure 1, the smaller the grain size is, the energy deposition distribution in ZnS is closer to normal distribution, has a better (narrow) FWHM and most important a higher mean energy value.

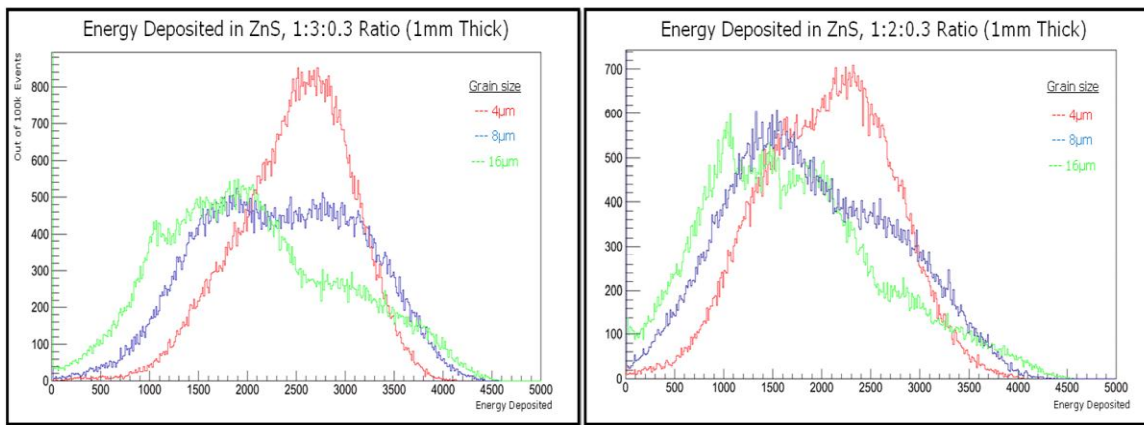


Figure 1. Energy Deposited in ZnS grains for two mixture ratio and three ZnS grain size

When setting an energy threshold to the histogram as can be seen in Figure 2, one can see that as the threshold increases, the light yield of the 1:2:0.3 ratio decreases rapidly while the 1:3:0.3 maintains high efficiency.

From examining Figure 2, it appears that the 1:3:0.3 ratio scintillators are far more effective than the 1:2:0.3, and that the grain size of 4µm in the 1:3:0.3 ratio, maintains its efficiency up to a discrimination level of 1250keV and drops only to 75% when the discriminator level is set to 2000 keV. The 1:3:0.3 ratio with a 8µm grain size is the best to maintain its efficiency when setting up a discrimination level of 2750 keV.

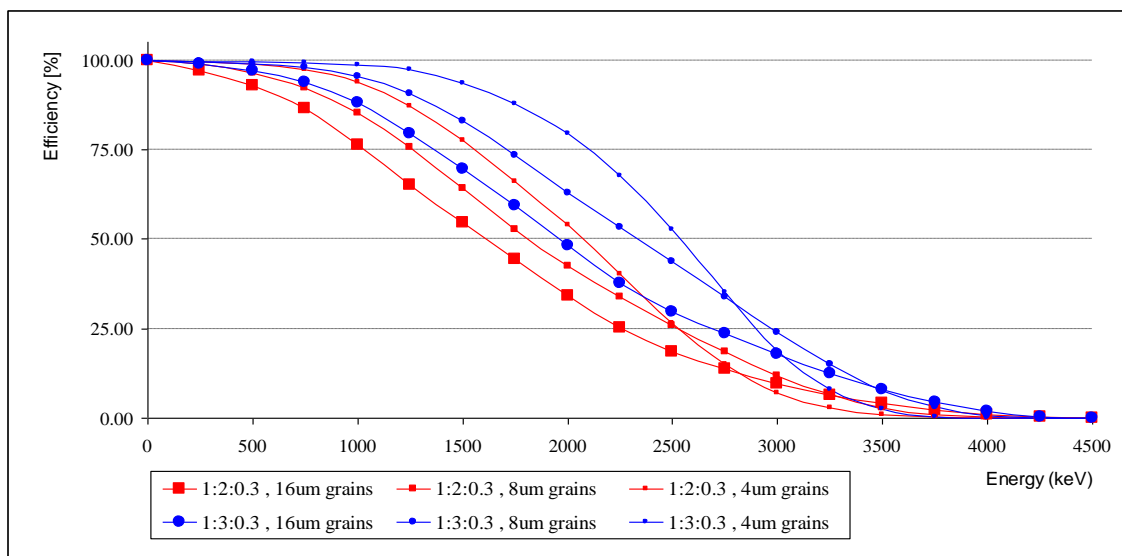


Figure 2. Threshold and grain size dependant scintillator efficiency

CONCLUSIONS

- The 1:2:0.3 ratio scintillator has a better capturing efficiency but lower light yield, it would be good to use it when directly coupled to a light sensor.
- In our case (Great light loss due to detector dimensions, self light absorption and poor WLS fibers efficiency), the 1:3:0.3 will probably provide higher efficiency.
- The smaller the ZnS grain size is, a higher mean value of “scintillating energy” is obtained and has a more uniform distribution.
- 1:3:0.3 has a much better light yield but since it has more ZnS this compound would probably have higher light attenuation than the 1:2:0.3. Although preliminary calculations present small variance between the effective light attenuation of the two compounds, however further investigation is required.
- At a later stage, a full simulation including the WLS fibers, reflectors and solid state light sensor will be performed.

REFERENCES

1. http://www.ncnr.nist.gov/expansion2/individual_instruments/CANDOR053007.html
2. http://www.eljentechnology.com/images/stories/Data_Sheets/Neutro+n_Detectors/EJ426-data-sheet-June12.pdf
3. <http://Geant4.web.cern.ch/geant4/>

4. V.S. Litvin, A.D. Belyaev, S.M. Ignatov, et al., "ZnS(Ag)/6LiF and LiI(Eu) scintillators and silicon photomultipliers for thermal neutron detectors with high space and time resolution", Bulletin of the Russian Academy of Sciences: Physics February 2009, Volume 73, Issue 2, pp 219-221
5. http://www.hep.ph.ic.ac.uk/fets/pepperpot/docs+papers/zns_602.pdf
6. J. F. Ziegler and J. P Bierasck and M. D. Ziegler (2008). "SRIM – The stopping and Range of Ions in Matter". SRIM Co. ISBN 0-9654207-1-X
7. <http://www.eljentechnology.com>, "EJ-600 ZnS:Ag PHOSPHOR POWDER"



POSTERS SESSION I

- 1**
Gamma Scintillator System Enhancement for Neutron Detection using Boron Carbide for Homeland Security
Yuval Ben-Galim¹, Udi Wengrowicz², Itzhak Orion¹, Avi Raveh³
¹*Department of Nuclear Engineering, Ben Gurion University (BGU) of the Negev, Israel*
²*NRC-Negev, Israel*
³*Advanced Coatings Center, Rotem Industries Ltd, Israel*
- 2**
Zero Time of Transitory Nuclear Events Derived by Parent-Daughter Systems
Yoram Nir-El
Reut, Israel
- 3**
Optimized Activity Concentration Monitoring System for Ventilation Duct at Positron Emitters Production Center
Eran Vax¹, Vlad Bronfenmacher², Amir Broide¹, Dimitry Ginzburg², Vitaly Pushkarsky², Lawrence Kaplan², Tzahi Mazor¹, Yagil Kadmon¹, Alon Osovizky²
¹*NRCN, Israel*
²*ROTEM Industries Ltd., Israel*
- 4**
Flattening the Energy Response of a Scintillator Based Gamma Dose Rate Meter Coupled to SiPM
Y. Knafo¹, A. Manor¹, D. Ginzburg¹, M. Ellenbogen¹, A. Osovizky¹, U. Wengrowicz², M. Ghelman², R. Seif², T. Mazor², Y. Kadmon², Y. Cohen²
¹*ROTEM Industries Ltd., Beer-Sheva, Israel*
²*Nuclear Research Center-Negev, Beer-Sheva, Israel*
- 5**
Neutron Dose Measurement Using a Cubic Moderator
M. Sheinfeld¹, T. Mazor¹, Y. Cohen¹, Y. Kadmon¹, I. Orion²
¹*Electronics R&D, NRCN, Israel*
²*Ben Gurion University of the Negev, Beer-Sheva, Israel*
- 6**
Composites Based on Fly Ash and Clay
Emilija Fidancevska¹, Vojo Jovanov¹, Biljana Angusheva¹, Vineta Srebrenkoska²
¹*Faculty of Technology and Metallurgy, Ss Cyril and Methodius University, Macedonia*
²*Faculty of Technology, Goce Delcev University, Macedonia*
- 7**
Glass Ceramics Fabricated from Coal Fly Ash and Waste Glass
Biljana Angjusheva¹, Vojo Jovanov¹, Vineta Srebrenkoska², Emilija Fidancevska¹
¹*Faculty of Technology and Metallurgy, Ss Cyril and Methodius University, Macedonia*
²*Faculty of Technology, Goce Delcev University, Macedonia*
- 8**
Narrow Lead Aprons under Medical Fluoroscopy Procedures
Avi Ben-Shlomo
Safety Division, Soreq NRC, Israel
- 9**
Medical Staff X-Ray Dose Reduction by Changing the Patient Examination Side
Avi Ben-Shlomo
Safety Division, Soreq NRC, Israel
- 10-20**
"ORCHID" Project

- 1**
DNA Topoisomerase-I Inhibition due to Exposure to X-Rays
Rotem Daudee¹, Rafi Gonen¹, Uzi German¹, Itzhak Orion², Esther Priel²
¹*Nuclear Research Center Negev, Israel*
²*Ben-Gurion University of the Negev, Israel*
- 2**
A Program for Follow-Up and Quality Assurance of Electret Results
Beny Sarusy¹, Shmuel Levinson¹, Natan Lavi², Uzi German¹
¹*NRCN, Israel*
²*Environmental Lab, Ben-Gurion University of the Negev, Beer Sheva, Israel*
- 3**
Application of the "GammaGen" Computer Code for NORM Synthetic Spectra Analysis
Beny Sarusi¹, Shmuel Levinson¹, Uzi German¹, Sergey Antropov², Konstantin Kovler³
¹*NRCN, Israel*
²*Amplituda, Israel*
³*Technion - Israel Institute of Technology, Haifa 32000, Israel*
- 4**
Matrix Materials for Preparation of Marinelli Calibration Standards
Shmuel Levinson¹, Natan Lavi², Uzi German¹
¹*NRCN, Israel*
²*Environmental Lab BGU, Israel*
- 5**
Radioactivity in Soils and Foodstuff Samples in Israel
Shmuel Levinson¹, Natan Lavi², Hisham Nassar³, Uzi German¹
¹*NRCN, Israel*
²*Environmental Lab BGU, Israel*
³*Ministry of Environmental Protection, Israel*
- 6**
Using Cherenkov Counting For Fast Determination of ⁹⁰Sr/⁹⁰Y Activity in Milk
Shimon Tsroya¹, Bella Dolgin¹, Uzi German¹, Omer Pelled¹, Zeev Benjamin Alfassi²
¹*NRCN, Israel*
²*Ben-Gurion University of the Negev, Israel*
- 7**
Study of Cleanup Procedures for Contaminated Area: Examination of Rubidium as a Surrogate to Cesium
Ofra Paz Tal, Ronen Bar Ziv, Roni Hakmon, Eitan Borojovich, Andrey Nikoloski, Tsion Ohaion, Rinat (Yanosh) Levi, Ilan Yaar
Nuclear Research Center Negev, Israel
- 8**
A Computerized QC Analysis of TLD Glow Curves for Personal Dosimetry Measurements Using TagQC Program
Sabi Primo¹, Hanan Datz¹, Amit Dar²
¹*Radiation Safety Division, Soreq Nuclear Research Center, Israel*
²*Empiric Technologies consulting, Israel*
- 9**
Electronic and Magnetic Properties of NpNi5
 A. Hen^{1,2}, E. Colineau¹, R. Eloirdi¹, J. - C. Griveau¹, J. - P. Sanchez⁴, A. B. Shick^{1,5}, I. Halevy^{2,3}, I. Orion², R. Caciuffo¹
¹*Institute for Transuranium Elements, European Commission, Joint Research Centre, Germany*
²*Nuclear Engineering Department, Ben Gurion University, Israel*
³*Physics Department, Nuclear Research Center Negev, Israel*
⁴*UMR-E CEA/UJF-Grenoble, SPSMS, UMR-E, France*
⁵*Academy of Sciences of the Czech Republic, Institute of Physics, Czech Republic*
- 10**
Radioactive Contamination Estimation from micro-copters or helicopter Airborne survey: Simulation and Real Measurements
Itzhak Halevy, M. Ghelman, Y. Yehuda-Zada, A. Manor, A. Sharon, I. Yaar
Physics Department, Nuclear Research Center – Negev, Israel

11

Prospects for the SMR Technology

Barak Tavron, Dan Rene Marouani
Israel Electric Corporation, Israel

12

Mechanical properties characterization for a cylindrical fuel clad using the segmented expanding cone-mandrel (SEM) method

Matan Tubul, Barak Ostraich, Eugene Shwageraus,
Nuclear Engineering, Ben Gurion University, Israel

13

Ground Shock Resistant of Buried Nuclear Power Plant Facility

David Ornai, Amir Adar, Erez Gal
Structural Engineering, Ben-Gurion University of the Negev, Israel

14

Performance of SNRC in MAPEP Proficiency Tests During 2005-2013

Ofer Aviv, Zohar Yungrais, Sharon Moscovici, Michal Brandis, Carmela Tzur, Lea Broshi, Tal Reimer, Reut Oren-Shemesh, Gustavo Haquin
Radiation Safety, Soreq Nuclear Research Center, Israel

15

Natural Circulation Modeling in MTR Fuel Geometry in Research Reactors

Yosef Aharon
NRCN, Israel

16

A New Approach to Analyze the Effect of Initial Conditions on Steam Explosion in Coolant Injection Mode

Idan Baruch¹, Galit Widenfeld²
¹*Nuclear Engineer, Ben Gurion University of the Negev, Israel*
²*NRCN, Israel*

17

Geological Disposal of Radioactive Waste

Ofra Klein Ben David, Avraham Dody
NRCN, Israel

18

Safety Issues of the LORELEI Test Device

Roni Sarusi¹, L. Ferry², D. Drapeau², M. Szanto³, N. Moran, M. Katz¹, Y. Weiss¹
¹*Safety, NRCN, Israel*
²*CEA, Cadarache, France*
³*Rotem Industries LTD, Israel*

Posters (Wednesday, February 12, 2014 10:15)

Gamma Scintillator System Enhancement for Neutron Detection using Boron Carbide for Homeland Security

Y. Ben-Galim¹, U. Wengrowicz², I. Orion¹, A. Raveh³
¹Ben Gurion University (BGU) of the Negev, Beer Sheva, Israel
²NRC-Negev, P.O. Box 9001, Beer-Sheva 84190, Israel
³Rotem Industries Ltd, Mishor Yamin D.N. Arava 86800, Israel

INTRODUCTION

An efficient and low cost ^{10}B based thermal neutron detector as a replacement for ^3He based neutron detectors is suggested. The detection is based on an enhancement to a scintillator gamma-rays detector. ^3He supply for neutron detectors is gradually become harder to obtain⁽¹⁾ since the commercial production of this isotope has been practically ended. The $^{10}\text{B}(n,\alpha)^7\text{Li}$ interaction is characterized with two energetic ion and a 478 keV gamma photon which is emitted from the excited ^7Li in 94% of the interactions⁽²⁾. A tailored Monte-Carlo code for the detector model was written in MATLAB in order to assess the detector's efficiency. The simulation model is based on ENDF/B-VII.0⁽³⁾ libraries for neutrons cross sections, and XCOM⁽⁴⁾ database for gamma absorption coefficients. By varying the B_4C thickness, optimal efficiency was obtained both for natural occurring ^{10}B compound with atomic abundance of 19.8% as well as for boron-10 enriched to 96%.

RESULTS

The simulation results showed intrinsic thermal neutron efficiency (ITNE) of about 40-45% both for natural and enriched compounds. This suggests that a coupling of natural B_4C converting layer with an existing gamma-rays scintillator detector will produce an effective low cost neutron detector. This coupling enables neutron detection by capturing the 478 keV gamma-photon. Validation of the MATLAB code for the suggested detector was accomplished through comparison with a Monte Carlo N Particle (MCNP4C2⁽⁵⁾) simulation results for the same detector configuration. An experimental model was assembled for verification of the simulation results. The boron used for the experiment was a B_4C disc (2" diameter, 0.125" thick) supplied by PLASMATERIALS (USA) coupled with a CsI scintillator detector with dimensions of 3" diameter and height of 3" and a photomultiplier (PMT). The experiment configuration is pictured in figure 1.

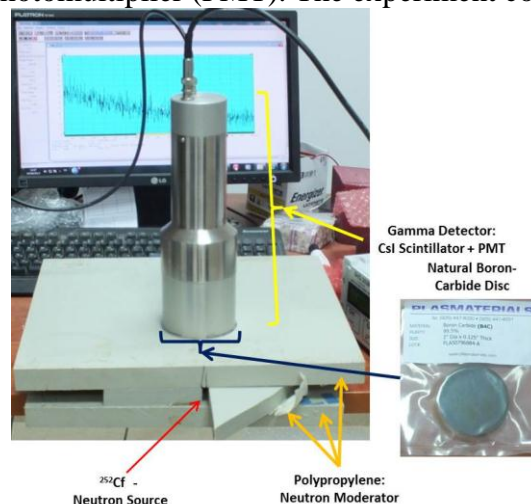


Figure 1: The experiment set-up configuration.

The measured efficiency from the experiment shows good agreement with both model's approximations and yielded a total measured efficiency of ~12.4% (count spectrum in figure 2).

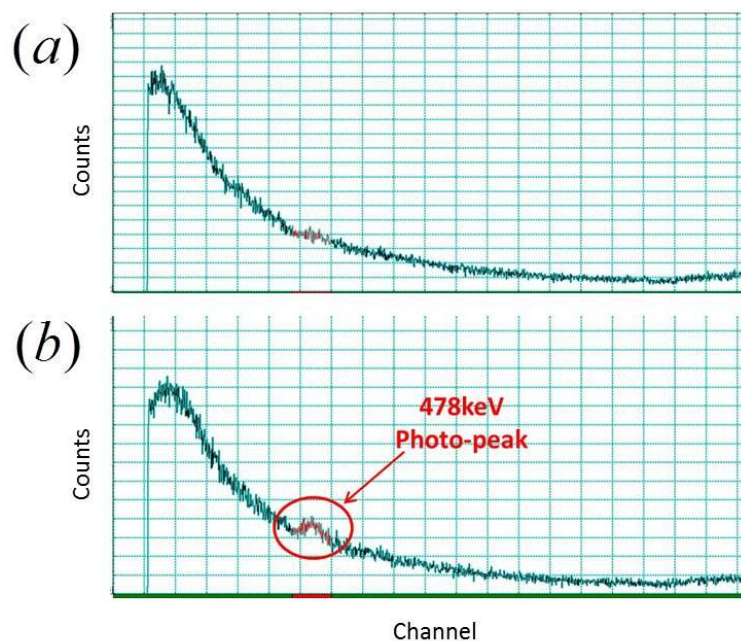


Figure 2: Spectrum of intensity vs. energy. (a) the scintillator positioned in front of the ^{252}Cf source. (b) B_4C disc was added as a neutron absorber.

CONCLUSIONS

The implementation of natural B_4C rather than enriched boron-10 compounds and the usage of an existing gamma-ray detector makes this detector easy to assemble and relatively inexpensive. Moreover, since B_4C is virtually transparent to gamma, thick neutron converting layers may be applied in order to increase neutron absorption probability without degrading the overall efficiency as oppose to ion capture methods. The analysis for various applications where gamma detectors are widely available such as Homeland Security can be performed by subtracting the signals from two similar scintillator detectors; one is a reference and the second is coupled with a B_4C converting layer. For other applications, it is feasible to develop an electronic circuit that can collect only the desired photo-peak counts.

REFERENCES

1. R. T. Kouzes, *The ^3He Supply Problem*, Pacific Northwest National Laboratory, 2009.
2. G. F. Knoll, *Radiation Detection and Measurement*, third edition, John Wiley & Sons, Inc, 2000.
3. *ENDF/B-VII.0 Libraries*, Organisation for Economic Co-Operation and Development (OECD) - Nuclear Energy Agency (NEA) - JANIS 3.4. [Online]. Available: <https://www.oecd-nea.org/janis/>
4. *XCOM - Photon Cross Sections Database*, National Institute of Standards and Technology (NIST), [Online]. Available: <http://www.nist.gov/pml/data/xcom/index.cfm>
5. *Monte Carlo N-Particle Transport Code System*, version 4C2, Technical Report LA-13 709-M, Los Alamos National Laboratory, NM, USA, 2001.

Zero Time of Transitory Nuclear Events Derived by Parent-Daughter Systems

Y. Nir-El

125 Lilac Street, P.O.Box 1476, Reut 71799, Israel

INTRODUCTION

The detection and identification of a nuclear event that results in the dissemination of radioactive products into the environment can be realized by dating the age of the event. In order to correct observed activities for the decay since the occurrence of the event, the age must be known to a high level of confidence. Previous papers^(1,2) described the method to date the age of a nuclear event by measuring the activity of two fission products, which constitute the clock in this application.

Within the proficiency test programme for radionuclide laboratories supporting the CTBT, a simulated gamma spectrum with the characteristics of an atmospheric test of a Chinese thermonuclear device, was used to determine the zero time by calculating the theoretical peak area ratio of $^{95}\text{Nb}/^{95}\text{Zr}$ ⁽³⁾. Their approach used only the main gamma lines at 766 and 757 keV and assigned the same detection efficiency to both these close lines. Their methodology of calculating the uncertainty of zero time is subject to comments because it takes the sum of two components (nuclide ratio and activity ratio as function of time) in quadrature.

In another paper⁽⁴⁾, the activity of ^{95}Nb as a function of time was presented without any development or expression for the zero time.

Analytical equations for zero time and the associated uncertainty calculations were derived in a recent paper⁽⁵⁾ using a measured activity ratio of two nuclides and illustrating the procedure by data from the Chinese test. The evaluation of the zero time uncertainty was performed by a very large set of very complicated analytical equations.

The present paper aims at developing a procedure to determine the zero time and its uncertainty in a transitory nuclear event by treating a parent-daughter system of 3 nuclides, where one daughter feeds the other one, in addition to its direct feeding by the decay of the parent.

ACTIVITY OF PARENT AND DAUGHTERS

Transitory (brief duration) nuclear events are e.g. an explosion of a nuclear device, or an accidental release of radioactivity due to a start-up failure in a reactor loaded with fresh nuclear fuel. An accurate and precise age of a nuclear event can be determined by the gamma spectrometric measurement of activities of a parent-daughter system and their dependence on time. This relation excludes the complications and misleading results arising from physicochemical fractionation effects in non-isobaric fission products.

The analysis of measured parent and daughters that are not in equilibrium is non-trivial and a wrong decay correction of the daughter activity can be an explanation for discrepancies in proficiency test exercises. Some commercial softwares perform an on-line analysis for merely two members, e.g. ^{140}Ba (parent)- ^{140}La (daughter). Hence, the analysis of parent-daughter cases of 3 members should be performed off-line solving differential equations that express the rate of change of the number of atoms.

At the time $t = 0$, only the parent ^{95}Zr (nuclide #1 in the decay chain) is present in the sample and the number of atoms of both daughters $^{95\text{m}}\text{Nb}$ (nuclide #2) and ^{95}Nb (nuclide #3) is assumed to be zero. This is the case of a radiochemical separation of ^{95}Zr which takes place at $t = 0$, or the situation of the transitory nuclear events, i.e. device explosion or reactor start-up failure, where the direct (independent) fission production of both #2 and #3 is practically null compared to the direct fission production of ^{95}Zr .

Parent ^{95}Zr , nuclide #1, $T_{1/2} = 64.032(6)$ d

$$\frac{dN_1(t)}{dt} = -\lambda_1 N_1(t)$$

$$A_1(t) = A_1(0)e^{-\lambda_1 t}$$

Daughter $^{95\text{m}}\text{Nb}$, nuclide #2, $T_{1/2} = 3.61(3)$ d

$$\frac{dN_2(t)}{dt} = -\lambda_2 N_2(t) + a\lambda_1 N_1(t) \quad a = 0.0108(7)$$

$$A_2(t) = \frac{aA_1(0)}{1 - \frac{\lambda_1}{\lambda_2}} (e^{-\lambda_1 t} - e^{-\lambda_2 t})$$

Daughter ^{95}Nb , nuclide #3, $T_{1/2} = 34.991(6)$ d

$$\frac{dN_3(t)}{dt} = -\lambda_3 N_3(t) + (1-a)\lambda_1 N_1(t) + b\lambda_2 N_2(t) \quad b = 0.944(6)$$

$$A_3(t) = A_1(0) (f_1 e^{-\lambda_1 t} + f_2 e^{-\lambda_2 t} + f_3 e^{-\lambda_3 t})$$

$$f_1 = \frac{1}{1 - \frac{\lambda_1}{\lambda_3}} \left(1 - a + \frac{ab}{1 - \frac{\lambda_1}{\lambda_2}} \right)$$

$$f_2 = -\frac{ab}{\left(1 - \frac{\lambda_1}{\lambda_2}\right) \left(1 - \frac{\lambda_2}{\lambda_3}\right)}$$

$$f_3 = \frac{ab}{1 - \frac{\lambda_1}{\lambda_2}} \left(\frac{1}{1 - \frac{\lambda_2}{\lambda_3}} - \frac{1}{1 - \frac{\lambda_1}{\lambda_3}} \right) - \frac{1-a}{1 - \frac{\lambda_1}{\lambda_3}}$$

The reference time of activity is the start of measurement t_1 , as required in many applications, e.g. proficiency test exercises, and t_2 is its end. Integration of the count rate gives

$$A_3(t_1) = \frac{\lambda_3 I_3}{\varepsilon_3 P_3 C_3} - A_1(t_1) f_1 \left(\frac{\lambda_3 C_1}{\lambda_1 C_3} - 1 \right) - \left[A_2(t_1) - \frac{aA_1(t_1)}{1 - \frac{\lambda_1}{\lambda_2}} \right] \frac{b}{1 - \frac{\lambda_2}{\lambda_3}} \left(\frac{\lambda_3 C_2}{\lambda_2 C_3} - 1 \right)$$

$$C_i = 1 - e^{-\lambda_i(t_2-t_1)}, \quad i = 1, 2, 3.$$

Private case

$a = 0$, that is no feeding of $^{95\text{m}}\text{Nb}$.

$$A_3(t_1) = \frac{\lambda_3 I_3}{\varepsilon_3 P_3 [1 - e^{-\lambda_3(t_2-t_1)}]} - \frac{A_1(t_1)}{1 - \frac{\lambda_1}{\lambda_3}} \cdot \left\{ \frac{\lambda_3 [1 - e^{-\lambda_1(t_2-t_1)}]}{\lambda_1 [1 - e^{-\lambda_3(t_2-t_1)}]} - 1 \right\}$$

This is exactly the equation of a ‘one parent-one daughter’ case, see e.g. in the Genie 2000 software. A similar equation is used to calculate the activity of $^{95\text{m}}\text{Nb}$,

$$A_2(t_1) = \frac{\lambda_2 I_2}{\varepsilon_2 P_2 [1 - e^{-\lambda_2(t_2-t_1)}]} - \frac{A_1(t_1)}{1 - \frac{\lambda_1}{\lambda_2}} \cdot \left\{ \frac{\lambda_2 [1 - e^{-\lambda_1(t_2-t_1)}]}{\lambda_1 [1 - e^{-\lambda_2(t_2-t_1)}]} - 1 \right\}$$

Private case

$a = 1$, that is ^{95}Zr decays entirely to $^{95\text{m}}\text{Nb}$.

$$A_3(t) = b\lambda_2\lambda_3 A_1(0) \left[\frac{e^{-\lambda_1 t}}{(\lambda_2 - \lambda_1)(\lambda_3 - \lambda_1)} + \frac{e^{-\lambda_2 t}}{(\lambda_1 - \lambda_2)(\lambda_3 - \lambda_2)} + \frac{e^{-\lambda_3 t}}{(\lambda_1 - \lambda_3)(\lambda_2 - \lambda_3)} \right]$$

This is identical to the Bateman solution for $n = 3$, where the branching of member #2 towards member #3 is b .

ZERO TIME

The ratio of the activity of ^{95}Nb to ^{95}Zr is given by

$$\frac{A_3(t)}{A_1(t)} = 2.204892(541) + 0.001243(82) \cdot e^{-0.181183t} - 2.206135(549) \cdot e^{-0.008984t}$$

Table 1 shows calculated activities of A_1 and A_3 , and their ratio A_3/A_1 , as a function of the time t , for $A_1(0) = 1$ Bq.

Table 1. Activities of ^{95}Zr and ^{95}Nb

t (d)	A_1 (Bq)	A_3 (Bq)	A_3/A_1
0	1.0000	0.0000	0.0000
10	0.8974	0.1692	0.1885
20	0.8053	0.2912	0.3616
30	0.7227	0.3758	0.5200
40	0.6486	0.4311	0.6648

The equation of $A_3(t)/A_1(t)$ is transcendental and can be solved to give the age t of the event by a numerical analysis method, e.g. the method of *Regula Falsi*⁽⁶⁾ requiring several iterations until a target convergence criterion is accepted.

As an example for applying the method, the data of the Chinese test in Ref. (3) are used:

$A_1(t) = 17.668$ Bq; $A_3(t) = 5.396$ Bq; Reference Time(= start measurement) = 25/09/2003 08:58.

Then, $A_3(t)/A_1(t) = 0.3054$ and therefore, by Table 1, the age is in the interval 10 to 20 d. Four iterations by *Regula Falsi* give 16.75247, 16.65740, 16.65464, and 16.65456 d. The fourth iteration changes the third by 7 time seconds. Hence, 3 iterations are sufficient for a 5×10^{-6} convergence at 16.6546 d. The zero time is found to be 08/09/2003 17:15, in perfect agreement with Ref (3), where the difference is approximately 1 time minute.

UNCERTAINTY OF ZERO TIME

The standard ($k = 1$) uncertainty $u(t)$ of the age t is given by

$$u^2(t) = \sum_{i=1}^n \left(\frac{\partial t}{\partial x_i} \right)^2 u^2(x_i)$$

where t is a function of n independent variables x_i , $i = 1, 2, \dots, n$, $\frac{\partial t}{\partial x_i}$ is the partial derivative of t with

respect to x_i , and $u(x_i)$ is the standard uncertainty ($k = 1$) of x_i . The equation of the activity ratio $R(t) = A_3(t)/A_1(t)$ cannot be solved analytically to render an explicit function of t . Hence, we cannot determine partial derivatives. Our approach is to invert the relationship, that is to calculate the uncertainty $u(R)$ according to

$$u^2(R) = \sum_{i=1}^6 \left(\frac{\partial R}{\partial v_i} \right)^2 u^2(v_i)$$

where $u(R)$ is known from the measurement, the 6 variables v_i are λ_1 , λ_2 , λ_3 , a , b , and t . The age $t = 16.6546$ d had been already found and the unknown is $u(t)$. By Ref. (3), $u(R)$ is 0.002932 (0.96%). Then, $u(t)$ is calculated to be 0.168 d = 4.037 h. This value disagrees with 0.26 d = 6.2 h in Ref. (5) which presents a rather complex procedure of calculating the uncertainty of zero time. On the other hand, Ref.(3) presents the value $u(t) = 0.17$ d, but their prescription of uncertainty budget and computing the combined uncertainty is questionable. It is worthwhile to note that the 0.17 d uncertainty is obtained by ignoring the $^{95\text{m}}\text{Nb}$ nuclide and using the equation of one parent-one daughter⁽¹⁾

$$t = \frac{1}{\lambda_1 - \lambda_2} \ln \left[1 - \left(1 - \frac{\lambda_1}{\lambda_2} \right) \left(\frac{A_3}{A_1} \right) \right]$$

This equation gives $t = 16.60$ d.

REFERENCES

1. Nir-El Y. *Dating the age of a nuclear event by gamma spectrometry*, Appl. Radiat. Isot. **60**, p.197-201, (2004).
2. Nir-El Y. *Dating the age of a recent nuclear event by gamma-spectrometry*, J. Radioanal. Nucl. Chem. **267**, p.567-573, (2006).
3. Karhu P., De Geer L.-E., McWilliams E., Plenteda R., Werzi R. *Proficiency test for gamma spectroscopic analysis with a simulated fission product reference spectrum*, Appl. Radiat. Isot. **64**, p.1334-1339, (2006).
4. Harms A., Johansson L., MacMahon D. *Decay correction of ^{95}Nb* , Appl. Radiat. Isot. **67**, p.641-642, (2009).
5. Pan P., Ungar R. K. *Nuclear event zero-time calculation and uncertainty evaluation*, J. Environ. Radioactivity **106**, p.65-72, (2012).
6. Hildebrand F. B. *Introduction to Numerical Analysis*, McGraw-Hill, New York, NY, 1956.

Optimized Activity Concentration Monitoring System for Ventilation Duct at Positron Emitters Production Center

E. Vax¹, V. Bronfenmacher², A. Broide¹, D. Ginzburg², V. pushkarsky², L. Kaplan², T. Mazor¹, Y. Kadmon¹,
A. Osovizky²

¹ Nuclear Research Center Negev, Beer Sheva, Israel

² Rotem Industries Ltd, Israel

INTRODUCTION

Monitoring the radioactive isotopes concentration released from cyclotron center is mandatory for complying with the site operational license and federal regulations. Cyclotrons are commonly used for production of radioactive isotopes for Positron Emission Tomography (PET). The isotopes are short half life β^+ emitters used for medical imaging purposes. There exist routine releases of small amounts of isotopes during the production process. The possibility of uncontrolled isotopes emission through the ventilation system, in case of malfunction, increases the radiation hazard potential to nearby population. Since the relatively short time decay of these isotopes made the wide use of cyclotrons next to populated areas possible. As a protection, any factory license requires activity release management for compliance with the total radionuclides activity emission limit. The limit is set to ensure no member of the public receives an effective dose equivalent above 10 mrem/year⁽¹⁾.

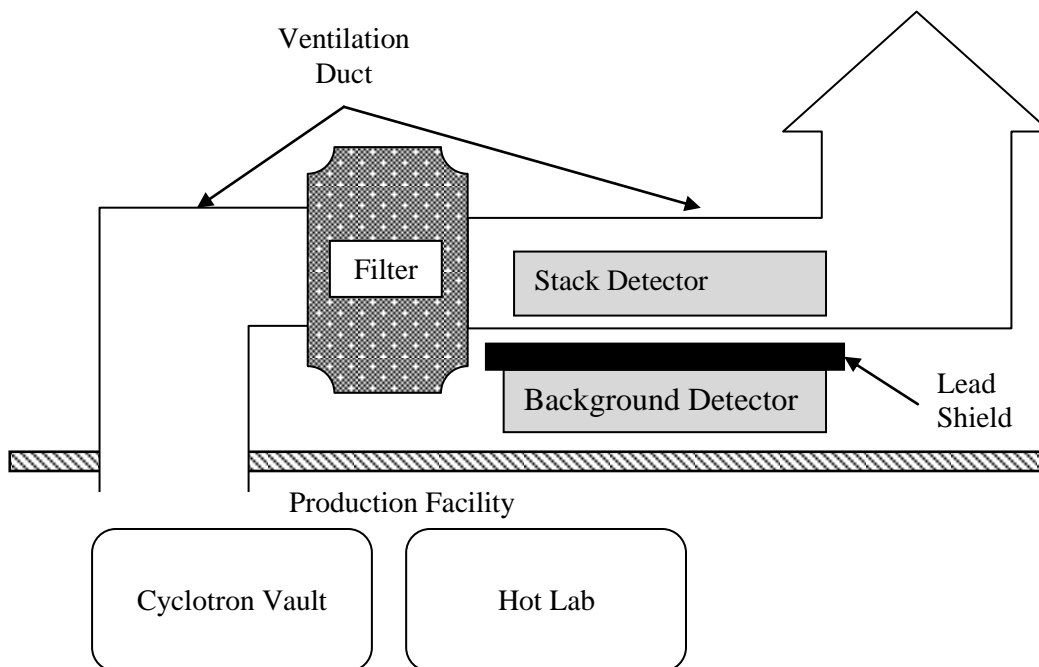


Figure 1: System block diagram. The stack detector location enables a high sensitivity to the activity concentration releases however it also sensitive to radiation field caused by the site routine activity, the shining filters and releases at neighbored stacks.

The design of a system that monitors the total activity released should address two main requirements: (1) adequate sensitivity (2) accurate report about the emitted activity. The sensitivity should comply with detection of very low concentration level of PET isotopes. In addition the report should provide an accurate estimation of the released activity based on the detector's gross counts reading and the air volume flow. These two requirements are in a contradiction. The best sensitivity is achieved by installing the detector inside the ventilation duct. On the other hand, correct release identification and accurate activity calculation, require a distant and shielded measuring point, where the effect of the shining filters or radioactive sources movement at the hot-lab can be reduced and even eliminated.

METHOD

Mapping the obstacles for accurate release calculation is a necessary step in designing a system with the ability to suppress the different noises while identifying and calculate correctly the activity release. The noise is comprised of statistical fluctuations, external radiation source readings not caused by activity concentration that flows inside the ventilation duct, and background changes due to absorption of isotopes in the filter and their decay. Table 1 lists all the noise sources and the methods chosen to overcome it.

Table 1: Obstacles for accurate activity release calculation and the overcome methods

radiation field source	Solution
Shining filter	Background detector has higher readings,
Site Routine activity	Background detector has higher readings + atypical rise shape
Natural background	Electronic energy window + accumulate only fast rise
Chemical absorption	software algorithm local background subtraction
Release through a neighboring duct	Background detector
Routine maintenance	Calibration point

The analysis of these noises led to the following system design. The configuration is based on two scintillation based radiation detectors (2"x2" NaI(Tl)) with an electronic discriminator for the 511keV energy window and software interface with implemented algorithm used to identify the release itself. The first detector (stack detector) is located inside the ventilation duct for maximum proximity to the isotopes release, thus accomplish the required sensitivity. The second detector (background detector) is located just below the ventilation duct and shielded from above, as shown in Figure 1. The combination of the data from the two detectors infers about the source of the radiation field, e.g. whenever the signal is stronger in the background detector (Figure 2), one can eliminate this as an external activity.

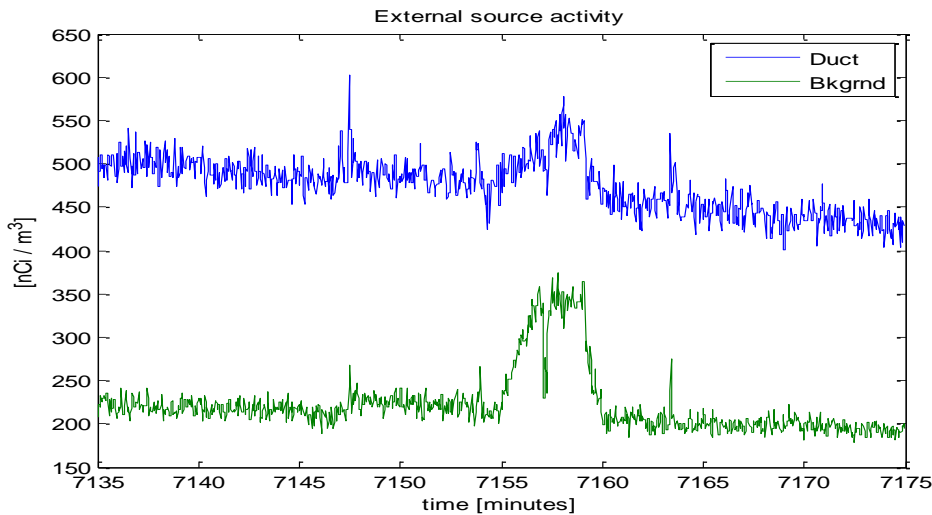


Figure 2: External source signal

RESULTS

The experimental data demonstrates the ^{18}F isotope, which is the most common PET isotope. The nature of the emission can be characterized as pulsed release or as slow release. A pulsed release of a gassed $^{18}\text{F}_2$ isotope causes a fast rise in the detector readings spread for about a minute, due to the air flow. This is followed by a small rise of the steady state reading caused by the air filter absorbing a small amount of the $^{18}\text{F}_2$. A slow release, on the other hand, shows a rise of the readings for 10-40 minutes, indicating that most of the ^{18}F particles released were absorbed in the air filter. Following the release one can see a slow decrease in the raw reading of the detector fitting the 110 minutes half life time of the isotope. A case study (Figure 3) shows a 20 minutes rise due to slow release of ^{18}F accumulated in the air filter, followed by the slow decrease in the readings due to the isotope activity decay. Two fast releases can be observed riding the tail of the decay. Zooming in on these pulses (Figure 5), shows a step rise in the readings of the detector

followed by a fast return to the previous level, indicating that nearly all of the isotopes passed through the filters and close to the detector.

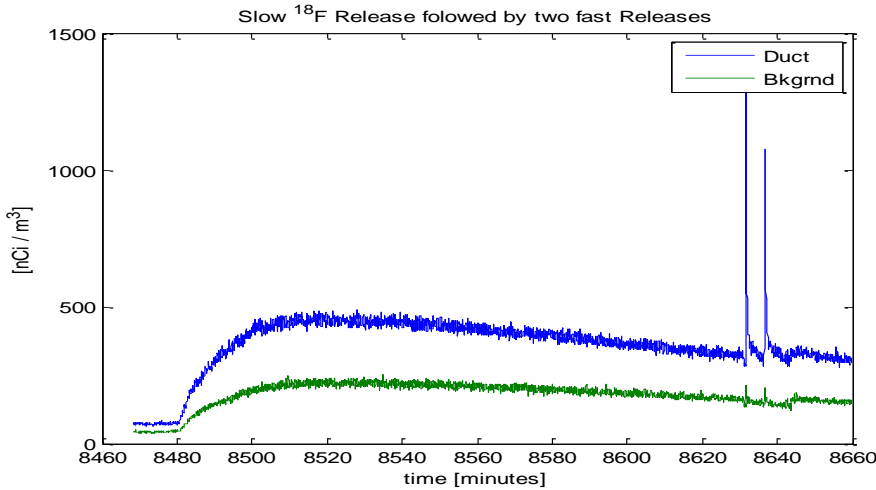


Figure 3: Slow Release of ^{18}F followed by two fast Releases

In order to suppress the statistical fluctuations, detect peaks of the right shape and eliminate the local bias, we used a correlation of the detector readings with the correlation function shown at Figure 4. This function has zero mean and one unit power. It is designed to locate 20 seconds peaks, and subtract the local average excluding the peak. It also takes into account that there is a small background elevation following the release. The correlation function should be fine tuned for each stack detector according to its unique installation. One can modify the pulse length, its shape (exponential, symmetric or non-symmetric triangle) and the background averaging time, before and after the pulse, which effects the background elevation expected. These parameters are equivalent to a change in air speed, filter efficiency and the detector proximity to the filter.

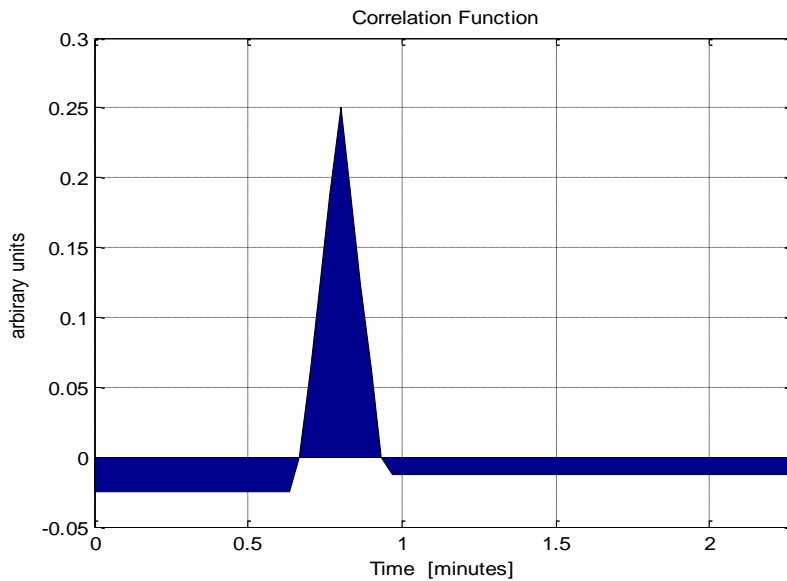


Figure 4: Slow correlation function for finding peaks

After locating the peaks, logic was constructed to determine whether the peaks were caused by a release or by a source outside the ventilation duct. For each release peak, we find its boundaries and accumulate the total readings (Figure 5) subtracting the background trapezoid total reading estimation (below the red line). This translates into the total activity emitted from the air duct.

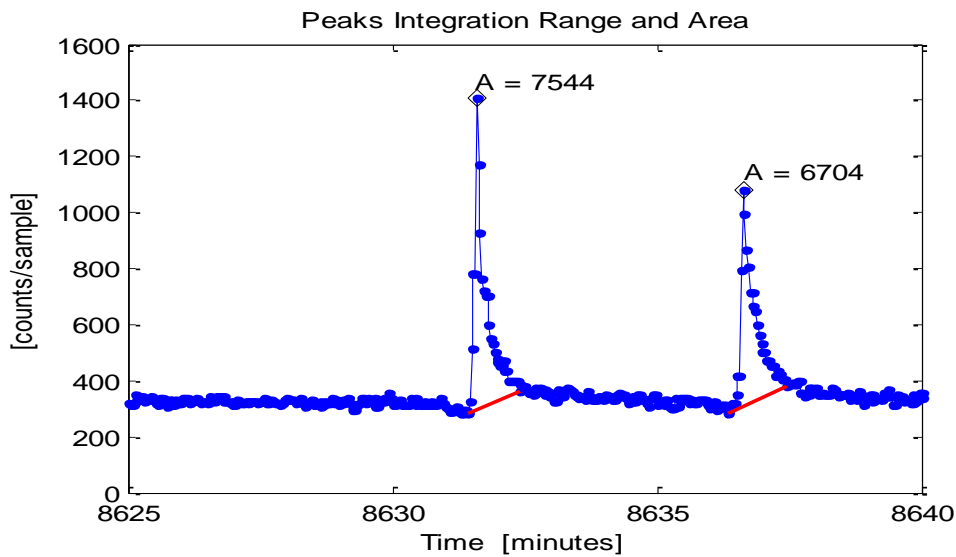


Figure 5: The algorithm final results: Peaks found (black marker), their boundaries (red) and the accumulated readings (above the red line) for each peak (black 'A')

DISCUSSION

The main obstacle of the radiation stack monitoring system is to define accurately the activity release out of the gross detector readings. As discussed, the stack detector readings originate in the activity flowing in the ventilation duct and several other sources which should not be accumulated as part of the activity release. The described system designed to overcome this complication by using the double detectors configuration and smart algorithm analyzing the data offline. Table 1 summarizes all the optional reasons for the detector reading that should not count as an activity release, and the methods used for improving the activity release documentation.

REFERENCES

1. *National Emission Standards for Emissions of Radionuclides Other Than Radon from Department of Energy Facilities*, National Emission Standard for Hazardous Air Pollutants (NESHAPS) 40 CFR 61 Subpart H,
2. D. Ginzburg, et al., *Methods for Determining the Activity Concentration Calibration Factor for Ventilation Duct in Cyclotron Sites*, The 24th Conference of the Nuclear Societies, p.151-153, Dead-Sea, Isreal, Feb. (2008)

Flattening the Energy Response of a Scintillator Based Gamma Dose Rate Meter Coupled to SiPM

Y. Knafo¹, A. Manor¹, D. Ginzburg¹, M. Ellenbogen¹, A. Osovizky¹
U. Wengrowicz², M. Ghelman², R. Seif², T. Mazor², Y. Kadmon², Y. Cohen²

¹*ROTEM Industries Ltd., Beer-Sheva, Israel*

²*Nuclear Research Center-Negev, Beer-Sheva, Israel*

INTRODUCTION

Among the newest emerging technologies that are used in the design of personal gamma radiation detection instruments, the silicon photomultiplier (SiPM) light sensor is playing an important role. This type of photo sensor is characterized by low power consumption, small dimensions and high gain. These special characteristics present applicable alternatives for the replacement of traditional gamma sensors based on scintillator coupled to Photomultiplier tubes (PMT) or on Geiger-Muller(G.M.) sensors. For health physics applications, flat energy response is required for a wide range of radio-nuclides emitting gamma rays of different energies. Scintillation based radiation instrumentation provides count rate and amplitude of the measured pulses. These pulses can be split in different bins corresponding to the energy of the measured isotopes and their intensity. The count rate and the energy of the measured events are related to the dose rate. The conversion algorithm applies a different calibration factor for each energy bin in order to provide an accurate dose rate response for a wide range of gamma energies. This work describes the utilization of an innovative approach for dose rate conversion by using the abilities of newest 32-bit microcontroller based ARM core architecture.

METHODS

Radiation survey meters that are based on G.M tubes are widely used for the measurement of gamma levels. In these types of instruments, a single pulse is obtained for each gamma photon interaction in the sensitive volume of the sensor. The counting efficiency for gamma rays depends on the probability of a gamma photon interacting with the cathode wall and producing an electron, and also on the probability that the electron will ionize the gas in the sensitive volume of the sensor. These probabilities drastically reduce the detection efficiency and are usually not related to the energy of the measured photons. The gamma field intensity depends on the source distance, on his activity and the energy of the emitted photons. Neglecting the distance and the medium material within the source and the detector, it is possible to assume that 1 gamma/s from 662 keV ¹³⁷Cs source produce a similar field response [mR/h] to the one produced by 11 gamma/s from 59.5 keV ⁶⁰Am source. In order to obtain a flat energy response, the G.M is usually enclosed into a mechanical filter which surrounds the tube. The filter absorbs most of the low energy gamma rays in order to reduce the low energy over response. The intrinsic sensitivity is the ratio between the detected pulses and the gamma rays fluency within the sensor active volume. For G.M. based sensor, the intrinsic sensitivity for high energy photons such as gamma rays is about 1% [1].

In order to increase the gamma rays detection efficiency while maintaining or even reducing the detector dimensions scintillation based sensors are used. These sensors usually provide a high stopping power. The scintillator light pulses intensity depends on the energy absorbed within the crystal. The light emitted by the interaction of gamma photons with scintillation material is determined by the photon energy and the scintillation material properties. Those pulses can be measured using a sensitive light detector such as a photodiode, a PMT or a SiPM. The intrinsic efficiency depends on the gamma energy, the crystal density and the dimensions. The light sensor optical properties and the photo-coupling to the crystal influence also on the intrinsic efficiency. A small 1cc CsI(Tl) crystal, has nearly 100% intrinsic efficiency for 100keV photons. For a similar dimensions crystal, the efficiency of rapidly drops to a few percents for higher gamma energy such as 662keV ¹³⁷Cs gamma rays.

The output pulse amplitude of scintillator based detectors is related to the energy deposited in the crystal by the gamma photons. Accurate dose rate measurement is achieved by splitting the measured pulses into

various bins related to their amplitude. Then, dose rate is calculated according to the count rate and a calibration factor for each bin. For low count rate, this procedure enables a flat energy response.

In modern instrumentation, a microcontroller unit (MCU) implements the flat energy response algorithm for the obtained pulses. Usually, the output signal is sampled by a digital to analog converter (DAC). This approach can last a relative long time and is power consuming for hand held instrumentation requirements. To overcome these obstacles, we implement the approach using an array of voltage comparators. Each comparator with his appropriate threshold is connected to a hardware counter. Due to the lack of many hardware counters in older families of 8-bit MCUs, the traditional way to perform the accumulation is to configure some general purpose input/output ports (GPIO) of the MCU to an interrupt port. By the MCU software, every measured pulse is accumulated in the according bin. In this way, a lot of processing time is required to manage the interrupt routine. For high count rate applications, the processing time limits the available resources required for other algorithms real-time tasks.

Newest 32-bit MCU ARM based cortex-M3 architectures provide at least 4 hardware counters. Among many other features, this type of MCU provides: more communication peripherals, like 3xUSART(universal synchrony/asynchrony receive transmit), 2xSPI, 2xI2C, 10 timers, 128KB Flash memory for the application code, internal 4KB EEprom for calibration parameters storage and event log accumulation. All of these features are achievable without external components reducing energy consumption and instrument dimensions. The dose rate is calculated by measuring the hardware counters even for high count rates. By this approach, essential processing time and resources are released from the MCU to focus in real-time algorithms. For accurate dose rate calculations, many energy bins are required. Sometimes, the number of measured bins is higher than the available counters in the MCU. In this case, low energy output pulses are measured by hardware counters and high energy pulses which occurs seldom, are measured by the traditional method of software counters under interrupt routines without consuming MCU processing time.

RESULTS

The described algorithm was satisfactory implemented in the new Rotem Ind. survey meter named PDS-GO (Figure 1). The new PDS-GO (presented here), is based on 32-bit MCU ARM. His sensor, consists of a 3 cc CsI(Tl) crystal coupled to SiPM. The instrument was originally designed to meet the scope of specifications defined by Home-Land Security (HLS) standards for Personal Radiation Detector (PRD). For HLS applications, it is mandatory that the device will be highly sensitive, small, and robust and width long operating hours. Yet, regarding dose rate accuracy, the HLS standards are more tolerable than survey meter standards. The new PDS-GO, includes five different energy windows (bins) for improved dose rate calculation. The energy response (related to ^{137}Cs), is within $\pm 15\%$ from 60 keV up to 1.3 MeV gamma rays. This response, meets standard requirement for survey meters instrumentation. This improvement has been achieved while maintaining the existing capabilities for HLS applications.



Figure 1. PDS-GO survey meter

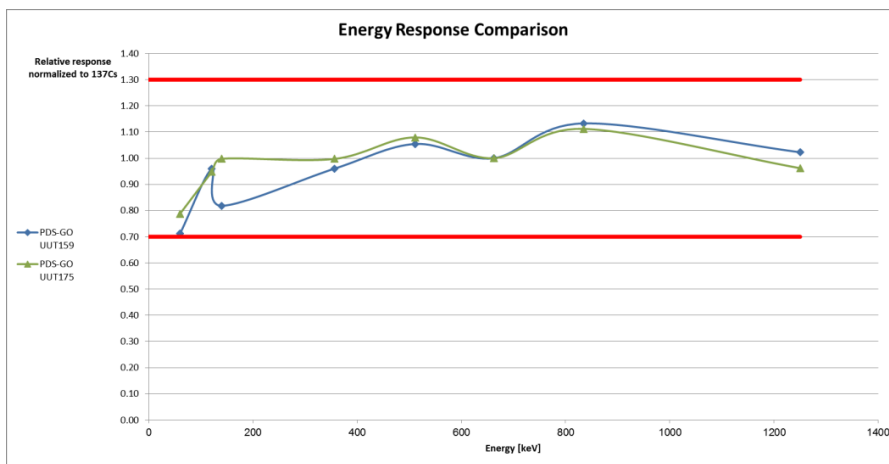


Figure 2. Energy response of the PDS-GO as measured for the following isotopes: ^{241}Am , ^{152}Eu , $^{99\text{m}}\text{Tc}$, ^{133}Ba , ^{22}Na , ^{137}Cs , ^{54}Mn , ^{60}Co

CONCLUSIONS

A new approach for high sensitive scintillator based gamma radiation survey meter is presented. The new PDS-GO meets the requirements for gamma survey meters and the specifications of PRDs for HLS applications as well. The ^{137}Cs relative response for different gamma sources is presented in Figure 2. The new electronics that maintain a larger number of hardware counters enable an improved accurate energy response over a wider gamma energy range.

REFERENCES

1. Centronic. Geiger Muller Tubes Data book, Croydon, England.
2. Rotem Ind. PDS-GO user manual, doc. No.17, rev. 1, Oct. 2013.
3. A. Osovizky et al. SENTIRAD – An innovative personal radiation detector based on a scintillation detector and a silicon photomultiplier, Nuclear Instruments and Methods in Physics Research A, 652, Issue 1, pp. 41-44 (2011).
4. D. Ginzburg et al. Optimizing the design of a silicon photomultiplier-based radiation detector, Nuclear Instruments and Methods in Physics Research A, 652, Issue 1, pp. 474-478 (2011).

Neutron Dose Measurement Using a Cubic Moderator

M. Sheinfeld¹, T. Mazor¹, Y. Cohen¹, Y. Kadmon¹, I. Orion²

¹ Nuclear Research Center-Negev, P.O.Box. 9001, Beer Sheva 84190, Israel

² Ben Gurion University of the Negev, Beer-Sheva, Israel

INTRODUCTION

The Bonner Sphere Spectrometer (BSS), introduced In July 1960⁽¹⁾ by a research group from Rice University, Texas, is a major approach to neutron spectrum estimation. The BSS, also known as multi-sphere spectrometer, consists of a set of a different diameters polyethylene spheres, carrying a small LiI(Eu) scintillator in their center. What makes this spectrometry method such widely used, is its almost isotropic response, covering an extraordinary wide range of energies, from thermal up to even hundreds of MeVs.

One of the most interesting and useful consequences of the above study is the 12" sphere characteristics, as it turned out that the response curve of its energy dependence, have a similar shape compared with the neutron's dose equivalent as a function of energy⁽²⁾. This inexplicable and happy circumstance makes it virtually the only monitoring device capable providing realistic neutron dose estimates over such a wide energy range. However, since the detection mechanism is not strictly related to radiation dose, one can expect substantial errors when applied to widely different source conditions.

Although the original design of the BSS included a small 4mmx4mmØ ⁶Li(Eu) scintillator, other thermal neutron detectors has been used over the years: track detectors⁽³⁾, activation foils⁽⁴⁾, BF₃⁽⁵⁾ filled proportional counters, etc. In this study we chose a Boron loaded scintillator, EJ-254⁽⁶⁾, as the thermal neutron detector. The neutron capture reaction on the boron ¹⁰B(n,αγ)⁷Li has a Q value of 2.78 MeV of which 2.34 MeV is shared by the alpha and lithium particles.

The high manufacturing costs, the encasement issue, the installation efficiency and the fabrication complexity, led us to the idea of replacing the sphere with a cubic moderator.

This article describes the considerations, as well as the Monte-Carlo simulations done in order to examine the applicability of this idea.

THE METHOD

The Monte-Carlo simulations were implemented on the MCNP-4C platform, using the cross-section tables obtained from the ENDF/B-VI library. The reference system included a polyethylene sphere, having a 5% natural boron loaded scintillator detector in its center irradiated by a surface neutron source shaped as a 12" diameter disk. The source was placed 5 meters from the detector, perpendicular to an imaginary line connecting both centers. Since neutron creation probability is uniform all over the disk source, the probability density function will be proportional to r, with no dependence on the polar angle θ⁽⁸⁾:

$$p(r, \theta) dA = \frac{dA}{\pi R^2} = \frac{r dr d\theta}{\pi R^2}$$

$$p(r) dr = \int_0^{2\pi} \frac{r dr d\theta}{\pi R^2} = \frac{2r dr}{R^2}$$

$$p(r) = \frac{2r}{R^2} \propto r$$

Therefore, the source distribution can be programmed into its probability function as a linear function of the radius, by inclusion of a bias function to the source which will minimize the variance of the detector response.

In order to acquire meaningful results, Tally 4 and Tally multiplier FM4 have been used to obtain the average neutron flux in the scintillator. Theoretically, F4 is calculated by ⁽⁷⁾:

$$F4 = \int_V \int_t \int_E E \cdot \Phi(\vec{r}, E, t) dE dt \frac{dV}{V} = \int_V \int_E \int_s E \cdot \frac{N(\vec{r}, E, t) ds}{\text{Track Length Density}} dE \frac{dV}{V}$$

Where: $\Phi(\vec{r}, E, t)$ - Particles flux
 E - Particle energy
 V - The volume in which particles interactions occur

Tally FM4 card was used to normalize the result obtained by the F4 card with the multiplicative constant acquired by:

$$(^{12}\text{C}_{\text{Atomic Density}} + \text{H}_{\text{Atomic Density}} + ^{10}\text{B}_{\text{Atomic Density}} + ^{11}\text{B}_{\text{Atomic Density}}) \times \text{barn} \times \text{Volume}_{\text{Plastic Scintillator}}$$

Substituting EJ254 manufacturer data with the above parameters, gives the constant the value: 0.61092751. Moreover, this card was also used to select only the reactions contributing to the EJ254 total photon production.

The necessity for the long distance between the detector and the neutron source was derived from the assumption that the detector will respond differently when encompassed in a sphere rather than in a cube, especially due to differences in spatial angular response. All that was left was to verify the theory that when the distance between the source and the detector is long enough, the behavior of cube moderator will resemble the spheres.

The following 3 criterions for cube's side length were examined:

1. **Cube's side length equals the sphere diameter:** under this criterion it appeared that although the resemblance between graphs was satisfying, the comparison of total counts ratio at 22 neutron energies, gave:

$$0.90 \leq \frac{\text{Sphere Counts}}{\text{Cube Counts}} \leq 3.39$$

Meaning an average of 1.73 and standard deviation 0.893.

2. **Equal volumes for the cube and the sphere:** in this case the counts ratio gave:

$$0.46 \leq \frac{\text{Sphere Counts}}{\text{Cube Counts}} \leq 0.71$$

Meaning an average of 0.6 and standard deviation 0.092.

Where cube side length was Calculated by:

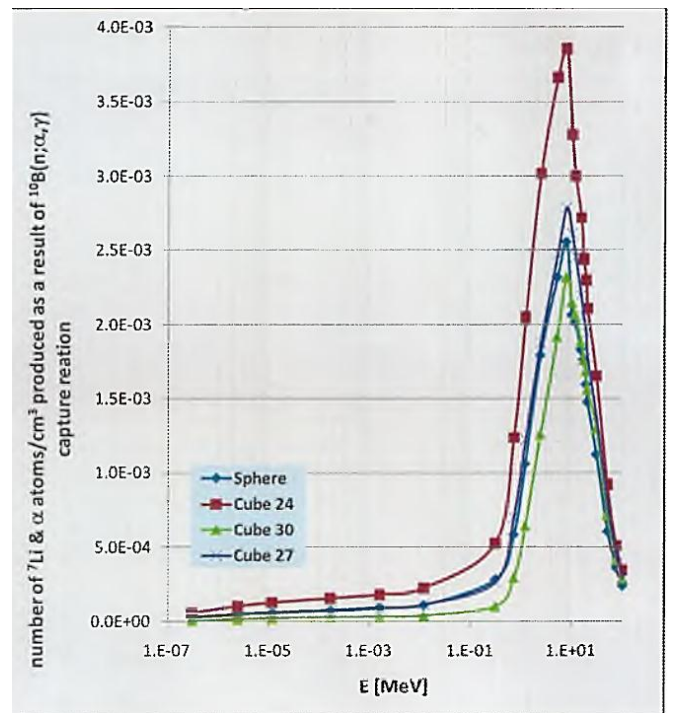


Fig. 1: Comparison between the sphere and cubes

$$a = \sqrt[3]{\text{Sphere Volume}} = \sqrt[3]{\frac{4}{3}\pi(6'')^3} = 24.566\text{cm}$$

3. Equal cross-section area at the detector's location: cube side length was calculated by:

$$a = \sqrt{\pi(6'')^2} = 27.012\text{cm}$$

in this case the counts ratio gave $0.46 \leq \frac{\text{Sphere Counts}}{\text{Cube Counts}} \leq 0.71$ Meaning an average of 0.9528 and standard deviation 0.124.

The 3rd criterion brought the highest behavioral compatibility between the cube and the sphere, but the cube was irradiated only from one of its facets. To prove a higher level of compatibility we needed to examine the cube's behavior when irradiated from other directions. To accomplish this goal, the coordinate's transformation card, TR, was used.

It has been decided that the neutron disk source will be diverted by 45° with respect to XYZ axes (see fig. 2), while the distance between the source's and the detector's centers will remain 5 meters.

Using the Pythagorean and the Cosine theorems, the rotation matrix was found to contain the following angles:

$$\begin{aligned} \angle_{xx'} &= 60^\circ, \angle_{yx'} = 60^\circ, \angle_{zx'} = 45^\circ, \\ \angle_{xy'} &= 135^\circ, \angle_{yy'} = 45^\circ, \angle_{zy'} = 90^\circ, \angle_{xz'} = 120^\circ, \\ \angle_{yz'} &= 120^\circ, \angle_{zz'} = 45^\circ. \end{aligned}$$

All MCNP simulations were repeated under the rotation data and the 3rd criterion above.

The counts ratio this time was:

$$0.82 \leq \frac{\text{Sphere Counts}}{\text{Cube Counts}} \leq 1.35$$

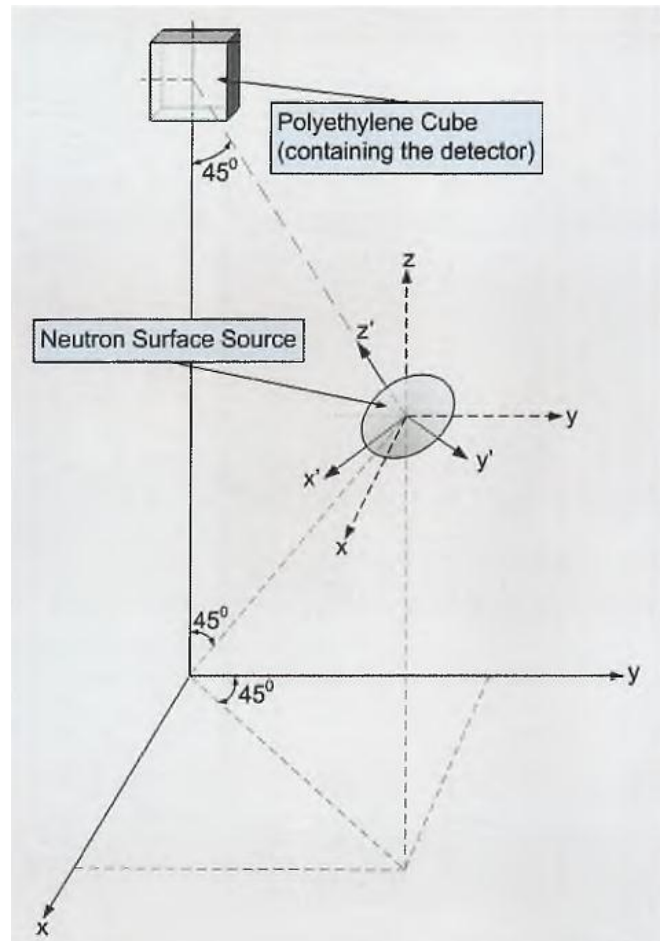


Fig. 2: Source shifting with respect to the irradiated cube

Having an average of 1.0163 with standard deviation 0.12991.

SUMMARY AND CONCLUSIONS

After confirming the correctness of the MCNP input file, by comparison to the literature ⁽²⁾, other MCNP simulations were conducted using a cubical neutron moderator.

Three criteria for cube side length were studied, where the optimum was set as the closest Resemblance to the behavior of the sphere moderator over a wide energy range. Therefore, the 3rd criterion was selected, giving

$$\frac{\text{Sphere Counts}}{\text{Cube Counts}} \cong 1$$

The angular dependency of the cube configuration has been studied too, giving satisfactory results.

The conclusion from this study is that whenever the measurement of neutron's dose equivalent is required, one can always use the cubic moderator, under the conditions stated in this paper (distance from source, accuracy demands, manufacturing costs, installation limitations etc.).

Furthermore, this study was just theoretical, requiring extensive laboratory experiments in order to confirm the commercial usage of the cubic configuration.

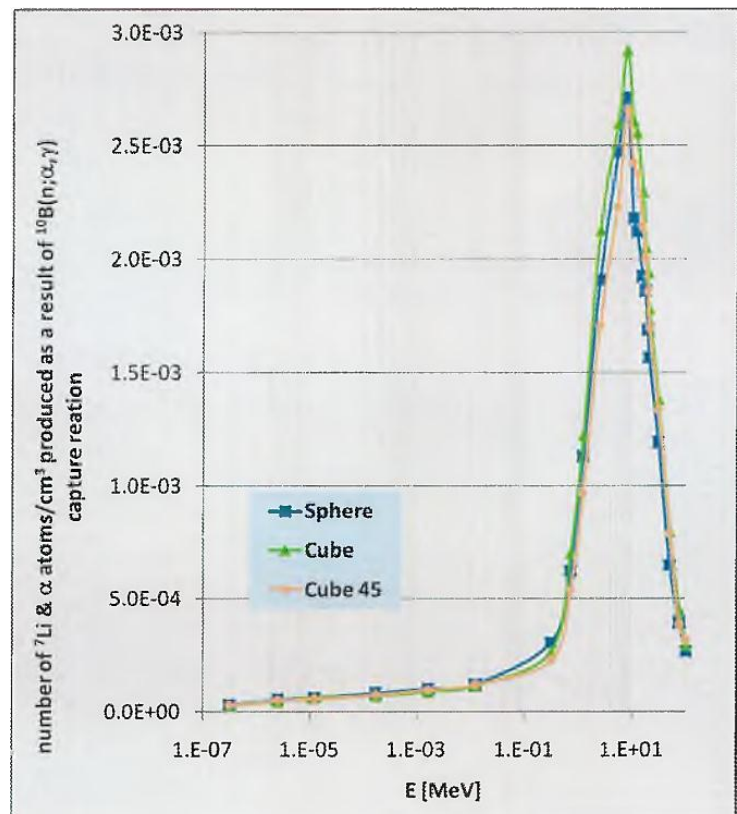


Fig. 3: The spatial dependency of neutron detection using cube moderator in comparison to sphere moderator

REFERENCES

1. R. L. Bramblett, R. I. Ewing and T. W. Bonner, *A Type of Neutron Spectrometer*, Nuclear Instrumentation and Methods 9(1), July 1960.
2. Glen F. Knoll, *Radiation Detection and Measurement*, 3rd edition, pp. 539-540.
3. M. P. Dhairyawan, P. S. Nagarajan and G. Venketaraman, *Further Studies on the Response of Spherical Moderated Neutron Detectors*, Nucl. Instrum. Methods 175,1980, pp 561-564.
4. W. G. Alberts et al., *European Workshop on Neutron Dosimetry for Radiation Protection*, Physikalisch Technische Bundesanstalt Report PTB-ND-17, Braunschweig, Germany, 1979, pp. 1-43.
5. A. V. Alevra and D. J. Thomas, *Radiation Protection Dosimetry*107, 2003, p. 36.
6. www.eljentechnology.com, *EJ-254 Datasheet*, ELGEN Technology.
7. *Monte Carlo N-Particle Transport Code System*, Version 4C2, Technical Report LA-13 709-M, Los Alamos National Laboratory, NM, USA, 2001.
8. B. J. Macdougall, *The effect of Bonner Sphere Borehole Orientation on Neutron Detector Response*, Master's Thesis, University of Tennessee, 2010

Composites Based on Fly Ash and Clay

E.Fidancevska¹, V.Jovanov¹, B.Angusheva¹, V.Srebrenkoska²

¹Faculty of Technology and Metallurgy, Ruger Boskovic 16, 1000 Skopje, Republic of Macedonia

²Faculty of Technology, Krste Misirkov, 2000 Stip, Republic of Macedonia

INTRODUCTION

Fly ash is a waste generated from the coal combustion during the production of electricity in the thermal power plants. It presents industrial by-product containing Technologically Enhanced Natural Occurring Radioactive Materials (TENORM) with the great potential for valorisation⁽¹⁾. Fly ash is successfully utilized in cement and concrete industry⁽²⁾, also in ceramics industry⁽³⁾ as component for manufacturing bricks and tiles, and recently there are many investigations for production of glass-ceramics⁽⁴⁾ from fly ash. Although the utilization of fly ash in construction and civil engineering is dominant, the development of new alternative application for its further exploitation into new products is needed. This work presents the possibility for fly ash utilization for fabricating dense composites based on clay and fly ash with the potential to be used in construction industry.

RESULTS

Fly ash (from the thermal power plant REK Bitola, Republic of Macedonia) with the chemical composition (SiO₂:52.00wt.%, Al₂O₃:23.61wt.%, Fe₂O₃:7.31wt.%, CaO:7.42wt.%, MgO:2.11wt.%, Na₂O:0.90wt.%, K₂O:1.67wt.%, SO₃:1.20wt.%, LOI: 3.12wt.%) was used as raw material for fabricating composites. The particle size distribution of the fly ash showed that the content of the fine fraction (less than 0.063mm) was dominant (47.10wt.%) and it was used in this investigation. The phase compositions of the fly ash consisted of: quartz, albite, hematite, anorthite, anhydrite and an amorphous phase. The concentrations of the natural radionuclides in fly ash as industrial by product were: ²⁶⁶Ra:59±6 Bq/kg; ²³²Th:76±8 Bq/kg; ⁴⁰K:376±29Bq/kg and are in accordance with the reported⁽⁵⁾. The typical morphology of the fly ash is presented in the figure 1. It is evident the presence of spherical particles and particles with irregular geometry and dimensions. The evident presence of diatomite can be seen from the honey sake morphology (fig. 1 b).

Clay (with granulometry less than 0.063mm) from the same region with the similar chemical composition (SiO₂:58.48wt.%, Al₂O₃:19.18wt.%, Fe₂O₃:7.44wt.%, CaO:6.18wt.%, MgO:1.43wt.%, Na₂O:2.10wt.%, K₂O:2.51wt.%, LOI: 2.05wt.%) was introduced to fly ash varying the quantity from 10 to 90wt.%. Quartz, feldspar, aragonite, illite, chlorite and calcite were the major crystalline phases present in clay. The composites were consolidated by uniaxially pressing at 45 MPa and the green samples were dried (105^oC) prior to sintering. Sintered composites were fabricated by firing at temperatures: 900, 1000, 1050, 1100^oC in chamber furnace with heating rate of 10^oC/min with a 60 min dwell at maximum firing temperature.

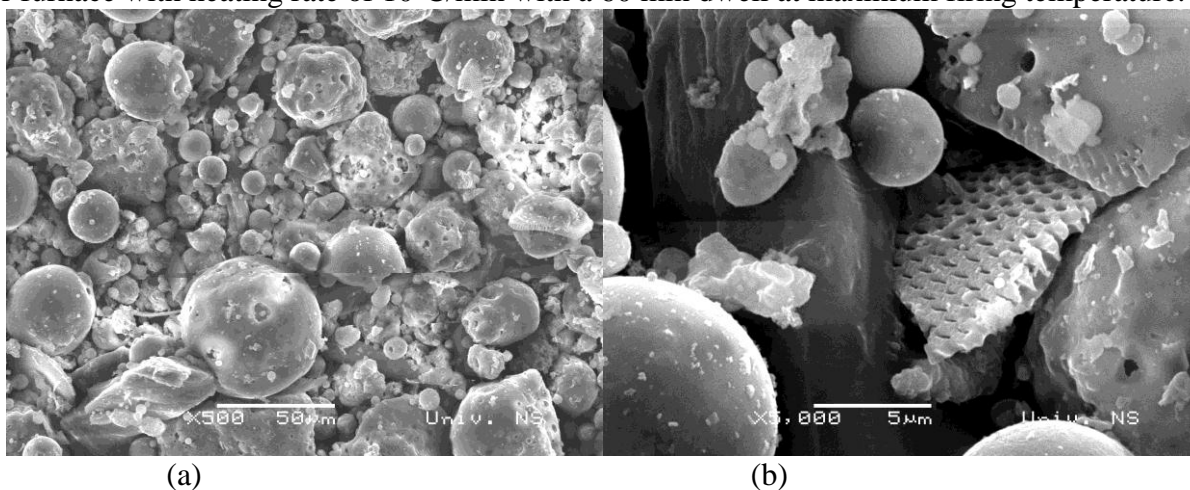


Figure 1. Morphology of the fly ash (a). bar 50μm, (b). bar 5 μm

The dependence of density and water absorption from the temperature for different fly ash –clay composites is presented in figure 2 and figure 3 presents the dependence of bending strength and E-modulus from temperature for the same composites.

Chemical durability of composites (sintered at 1050 and 1100⁰C) was tested using the standard methods for glass and ceramics. It was determined as mass lost after treatment in neutral (H₂O) and aggressive mediums (0.1M HCl and 0.1M Na₂CO₃) during the period of 24, 168 and 720 hours. The results of the leach testing of the composites in acid medium (0.1MHCl) are presented in figure 4.

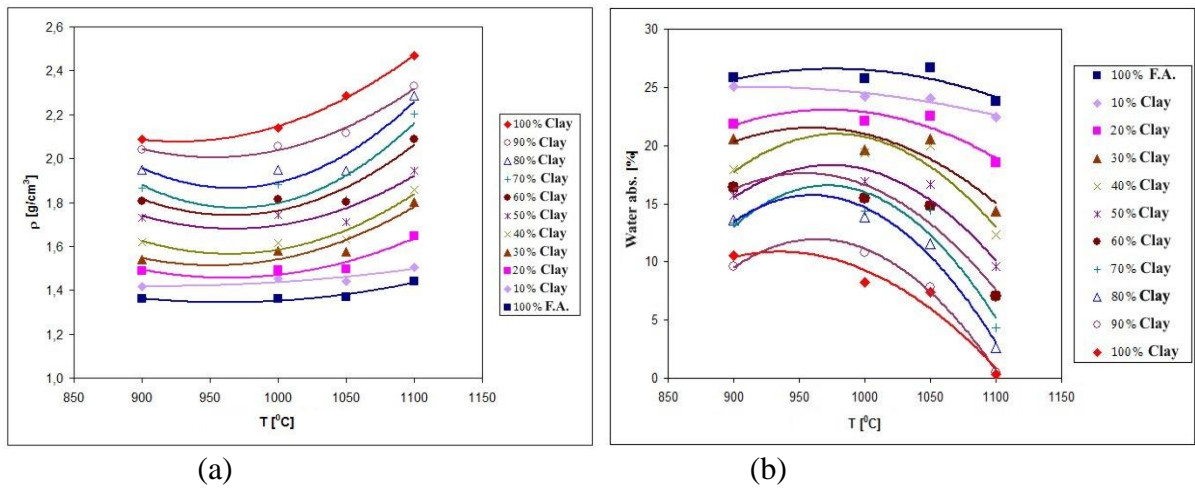


Figure 2. Dependence of : a. density from sintering temperature; b. water absorption from temperature

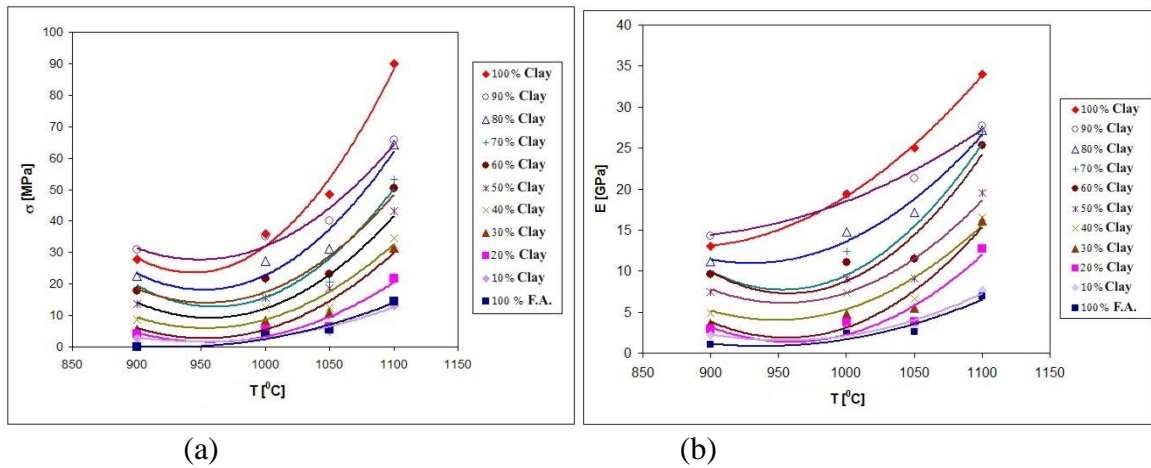


Figure 3. Dependence of: a. bending strength from temperature; b. E-modulus from temperature

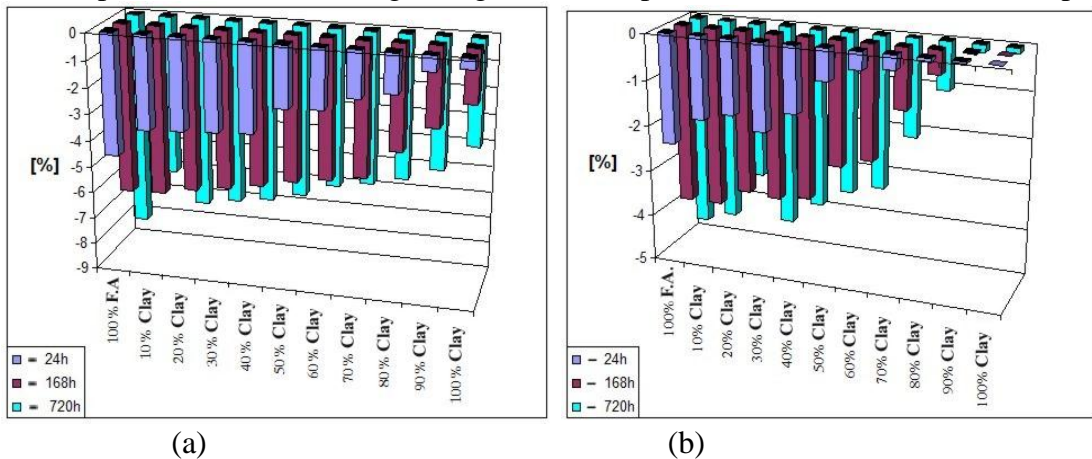


Figure 4. Leaching of the composites in acid medium (0.1MHCl) a. composites sintered at 1050⁰C, b. composites sintered at 1100⁰C

It is evident from the the figure 2 that clay content generally influences on the incensement of density and decrease mant the water absorption. Significant densification of the compacts was achieved by increasing the temperature from 1050⁰C to 1100⁰C. The mechanical properties (bending strength and E-modulus), figure 3, of the composites also increase with the addition of clay and the rapid densification was at temperature of 1100⁰C.

The clay content influenced positively on the durability of the compacts and it is directly connected to the density of the compacts. Namely, the densest composites i.e composites with higher content of clay have lower mass lost i.e. higher durability.

From the above investigation, as an optimal was chosen a composite containing 60wt.% clay and 40wt.% fly ash sintered at 1100⁰C. The density and water absorption of the composite were 2.09 g/cm³ and 7.02%, respectively, and the mechanical properties i.e bending strength and E-modulus were 50.47 MPa and 25.35GPa, respectively.

The microstructures of the composites with fly ash content of 40wt.%, sintered at 1050 and 1100⁰C are presented in figure 5.

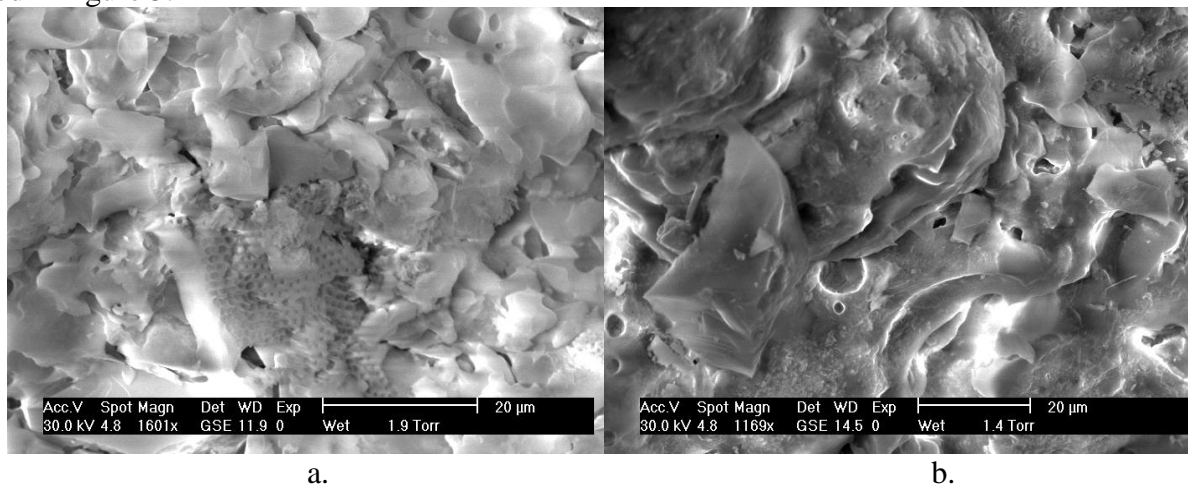


Figure 5. Microstructures of composites with 40wt.% fly ash content (bar 20µm) a. sintered at 1050⁰C
b. sintered at 1100⁰C

The degree of densification is evident, namely at temperature of 1050⁰C the morphology of diatomite is still present, but at 1100⁰C the composite is extensively sintered (more homogenous and smoother) with the evident appearance of small closed pores.

CONCLUSION

Fly ash as industrial by product can successfully replace certain quantity of clay as naturally occurring raw material to fabricate composites which can be potentially used as dense ceramics in construction industry.

REFERENCES

1. Somlai J., Jobbágy V., Kovács J., Tarján S., Kovács T. *Radiological aspects of the usability of red mud as building material additive*. J. Haszard. Mater. **150(3)**, p.541-546, (2008)
2. Kockal N U., Ozturan T. [*Effects of lightweight fly ash aggregate properties on the behavior of lightweight concretes.*](#) J. Hazar. Mater., **179(1-3)**, p. 954-965 (2010)
3. Queralt I., Querol X., Lopez-Soler A., Plana F. *Use of coal fly ash for ceramics: a case study for a large Spanish power station*, Fuel **76** p.787-791 (1997)
4. Barbieri L., Lancellotti I., Manfredini T., Queralt I., Rincon J.M., Romero M. *design obtainment and properties of glasses and glass-ceramics from coal fly ash*. Fuel **78** p.271-276 (1999)
5. http://www.irpa12.org.ar/KL/III.4.4/Haquin_fp.pdf (accessed on 30.12.2013)

Glass Ceramics Composites Fabricated from Coal Fly Ash and Waste Glass

B. Angjusheva¹, V. Jovanov¹, V. Srebrenkoska², E. Fidancevska¹

¹University "Ss Cyril and Methodius" Rudjer Boskovic 16, Skopje, Republic of Macedonia

²University Goce Delcev, Krste Misirkov bb, 2000 Stip, Republic of Macedonia

INTRODUCTION

Great quantities of coal ash are produced in thermal power plants which present a double problem to the society: economical and environmental. This waste is a result of burning of coal at temperatures between 1100-1450⁰C. Fly ash available as fine powder presents a source of important oxides SiO₂, Al₂O₃, Fe₂O₃, MgO, Na₂O, but also consist of small amount of ecologically hazardous oxides such as Cr₂O₃, NiO, MnO. The combination of the fly ash with waste glass under controlled sintering procedure gave bulk glass-ceramics composite material. The principle of this procedure is presented as a multi barrier concept ⁽¹⁾. Many researches have been conducted the investigations for utilization of fly ash as starting material for various glass-ceramics production ⁽²⁻⁴⁾. Using waste glass ecologically hazardous components are fixed at the molecular level in the silicate phase and the fabricated new glass-ceramic composites possess significantly higher mechanical properties.

The aim of this investigation was to fabricate dense glass ceramic composites using fly ash and waste glass with the potential for its utilization as building material.

RESULTS

Fly ash from the thermal power plant REK Bitola, Republic of Macedonia (from forth zone of electro filter with particle size lower than 63µm) and a type of waste glass from laboratory inventory (particle size lower than 63µm) were used as raw materials for this investigation. The compacts were coded as follows: fly ash - FA, waste glass - WG, FA50WG – glass ceramics composite with glass content from 10 to 50wt.% i.e. FA10WG – composite consisted of fly ash with 10wt.% waste glass). Chemical analysis of the fly ash was carried out by X-ray fluorescence (model ARL 9900XP) and the chemical composition of the waste glass was declared from the manufacturer Pyrex ⁽⁵⁾. The chemical compositions of the investigated waste materials are given in Table 1.

Table 1. Chemical compositions of the industrial wastes

	SiO ₂	Al ₂ O ₃	Fe ₂ O ₃	CaO	MgO	Na ₂ O	K ₂ O	SO ₃	B ₂ O ₃	LOI	Σ
FA [wt%]	49.51	17.62	7.91	13.77	3.36	0.69	1.46	3.52	/	1.57	99.41
WG [wt%]	83.34	1.33	/	0.03	/	4.08	0.04	/	11.19	/	100

Fly ash belongs to the silicates due to the evident presence of the SiO₂, Al₂O₃ and Fe₂O₃ as basic oxides constituencies. The level of CaO and SO₃ are relatively high, while the level of MgO and other alkali metal oxides are typical as the other ashes.

The morphology of the fly ash is presented in figures 1. It is evident the presence of primary spherical particles with dimension cca 10µm and particles with irregular geometry with dimensions from 5 to 20µm. Also the presence of agglomerates is evident. The particles of waste glass are with irregular geometry and dimensions from 10 to 60µm, figure 2.

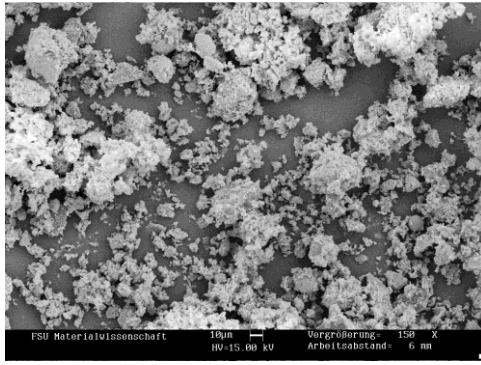


Figure 1. SEM micrograph of the FA, (bar 10µm)

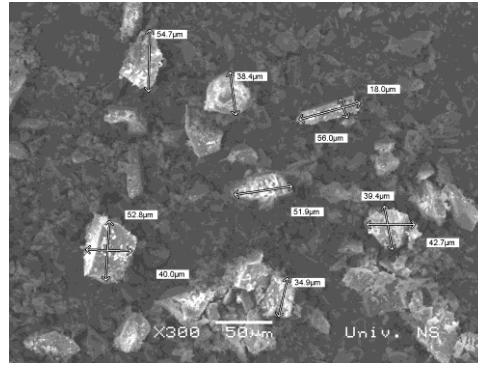


Figure 2. SEM micrograph of the WG, (bar 50µm)

Glass-ceramics composites were fabricated by adding waste glass in quantity from 10 to 50wt.% to the fly ash. One of the reasons was to increase mechanical properties of the composites and secondly to encapsulate the particles of industrial wastes into matrix. Prior to the consolidation the milling and homogenization of the fly ash and waste glass were realized in the planetary mill (Fritsch pulverisette 5) during 60 min. Pressing of the samples was performed by uniaxial press (Weber Pressen KIP 100) at P=45 MPa using PVA as a binder. Dense composites with different densities were obtained by varying the sintering temperatures: 900, 1000 and 1050°C with the holding time at a maximum temperature of 1 hour. The applied heating rate was 10⁰/min. FA50WG composites sintered at 1000°C and 1050°C were deformed. The sintered glass ceramics composites were tested using three point bending tester (Netzsch 401/3) to determine mechanical properties (bending strength and E-modulus).

According the obtained results in this investigation the whole spectrum of the glass ceramics composites were fabricated, but the properties (density, bending strength, E-modulus, porosity and linear shrinkage) of WG (sintered at 700°C), FA and the optimal glass ceramics composites (FA10WG, FA40WG) sintered at 1000°C (chosen as optimal sintering temperature) are presented in Table 2.

Table 2. Sintering temperature, density, bending strength, E –modulus, porosity, and linear shrinkage of fly ash, waste glass and the optimal glass ceramics composites

Compacts	Sinter.temp./ time[°C/h]	ρ [g/cm ³]	σ [MPa]	E [GPa]	Θ [%]	$\Delta L/L$ [%]
FA	1000/1h	1.433	9.41	4.90	43.69	1.96
WG	700/1h	2.233	69.08	27.31	14.43	15.77
FA10WG	1000/1h	1.470	17.98	7.34	42.21	3.05
FA40WG	1000/1h	2.214	63.62	32.31	10.65	13.84

It is evident that glass addition influenced on the incensement of the mechanical properties. Namely, the bending strength of FA is 9.41MPa, but for the glass ceramics composites FA10WG and FA40WG it increased to 17.98MPa and 63.62MPa, respectively. The E-modulus for the composites FA10WG and FA40WG increased to 7.34 and 32.3GPa, respectively in comparison to the pure FA (4.90GPa). The porosity of the FA compacts and FA40WG composites decreases from 43.69 to 10.65%, respectively and the shrinkage increased from 1.96 to 13.84% .

The microstructure of the fractured surface and EDS analysis of the FA10WG composite are presented in figure 3.

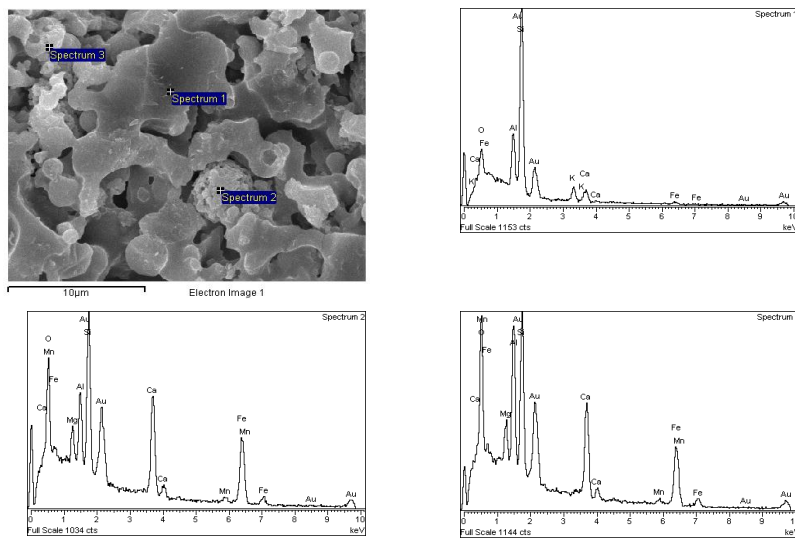


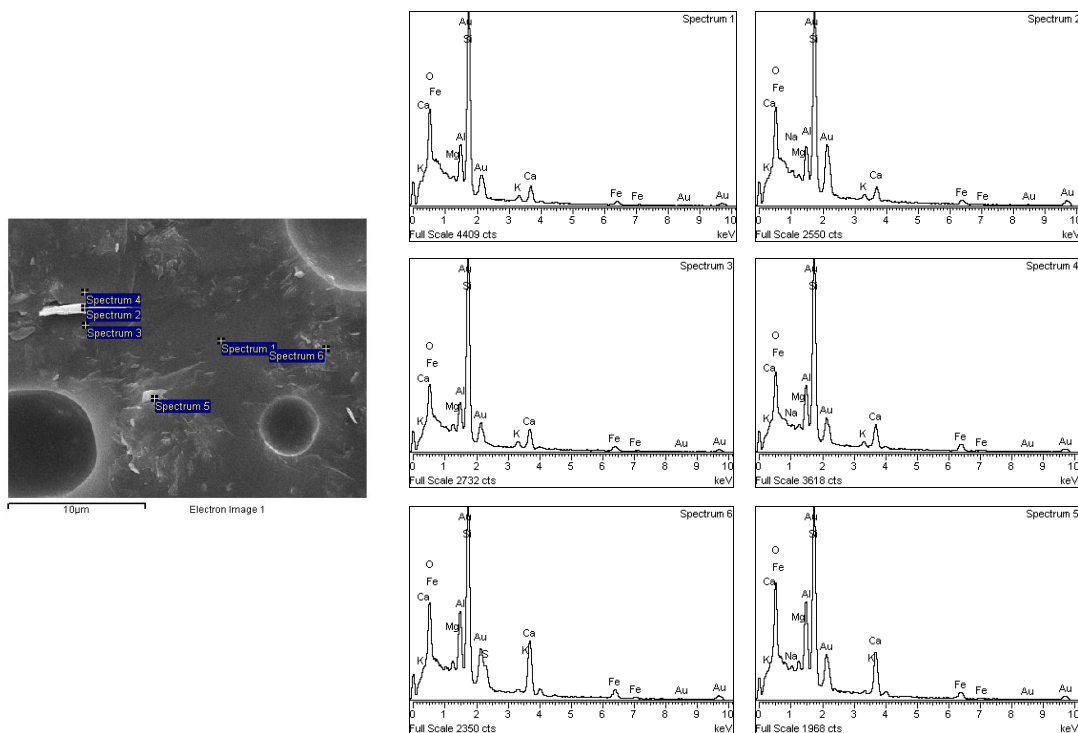
Figure 3. SEM micrograph and EDS spectra (1-3) of composites FA10WG, $t=1000^{\circ}\text{C}$

The fractured surface of the FA10WG composite is granular. It is evident presence of the liquid glassy phase, but also recognisable grains from the original morphology of the FA particles. EDS analysis confirmed that point 2 and point 3 correspond to the FA composition and the point 1 could be characterized as the region of the glassy phase.

Figure 4 shows that the microstructure of the fractured surface of the glass-ceramic FA40WG is homogeneous and smoother in comparison to the FA10WG composite. There are no recognisable grains from the FA and they are well encapsulated in the silica matrix. There is significant formation of closed spherical pores with dimensions between 5-10 μm . The formation of the spherical pores is connected with softening of the glassy phase and evolution of gas⁽⁶⁾. According to the similarity of the peaks (1-6) from the EDS analysis of glass ceramics composite FA40WG it can be concluded that FA particles are uniformly distributed in the glassy matrix.

CONCLUSIONS

As a general it can be concluded that it is possible to produce dense glass-ceramic composites using high percentage of coal fly ash and waste glass. The new glass-ceramic composites possess significantly higher mechanical properties which make them suitable for a wide range of application in the building industry.



REFERENCES

- [1] G.Ondracek, *Waste treatment and recycling to remineralized products with multibarriers structure*. Monatshefte, 7 273 (1994)
- [2] C.Leroy, M.C.Ferro, R.C.C. Monteiro, M.H.V. Fernandes. *Production of glass-ceramics from coal ashes*. J. of Eur. Cer. Soc. 21 p.195-202, (2001)
- [3] B.Angjusheva, *Production and characterization of glass-ceramics from waste materials*, Qual.of life, 2 (1-2) p.13-20, (2011)
- [4] J.P.Wu, A.R Boccaccini, P.D. Lee, M.J.Kershaw, R.D. Rawlings, *Glass ceramic foams from coal ash and waste glass: production and characterization*. Adv. in App. Cer. 105 1 p.32-39, (2006)
- [5] www.scilabware.com/Glass_technical/, Accessed on 15 June 2011
- [6] M.Ilic, C.Cheeseman, C.Sollars, J.Knight. *Minerology and microstructure of sintered lignite coal fly ash*. Fuel, 82 (30), p.331-336 (2003)

Posters (Wednesday, February 12, 2014 10:15)

Narrow Lead Aprons under Medical Fluoroscopy Procedures

A. Ben-Shlomo

Soreq NRC, Yavne, Israel

INTRODUCTION

Lead aprons are the major protective item of the medical staff whose work involves x-ray exposure. Heart catheterization and angiography procedures represent the most common exposures of the medical staff. The lead equivalent thickness of lead aprons worn by the medical staff is defined by many national standards. The frontal side of the aprons should be 0.25 mm lead equivalent at working conditions under 100 kV, 0.35 mm for working conditions above 100 kV, and 0.5 mm for heart catheterization and angiography. The back side of the body needs less protection and usually is covered by 0.25 mm of lead equivalent. The lead equivalent thickness is defined at the 80 kV level.

Most of the hospital's lead aprons are purchased with general specifications and some of them too narrow and aren't suitable for the body of specific members of the medical staff. It can be assessed in Israel that at least 10% of the medical staff in fluoroscopy rooms are using lead aprons that are too narrow.

Most of the lead aprons in Israeli medical institutions are built in a way that the needed protection of the apron is obtained from two protective layers, each of half the needed lead equivalent thickness. The overlapping of these two layers gives the needed thickness and staff protection. The requirement for the two layer's thickness extends from one side of the body (R LAT) to the other side of the body (L LAT). When the body size is too large for a given apron, the overlapping width of the two layers is reduced and the two lateral sides of the body (along the whole body) get only the half needed protective lead equivalent thickness.

This work is based on Monte Carlo simulation under PCXMC 2.0 software¹. The effective dose calculations were performed for a reference adult (73.2 kg, 178.6 cm), 100 kV, focus to skin distance (FSD) of 100 cm, and entrance surface air kerma of 1 mGy. The number of photons in the simulation was 250,000 (the simulation error was $\pm 0.3\%$).

The radiation spectrum was formed by filtration of a 2.5 mm Al and tungsten target.

The main location of the x-ray source for the medical staff is the imaging volume of the patient, which causes scattered radiation. The simulation radiation angle towards the medical staff was taken as -20° in the cranial-caudal direction (z-axis) and $+45^\circ$ and -45° in the lateral direction (xy plane). These directions were chosen as the typical exposure angles of the staff.

The simulation was performed for whole body radiation (at the above angles) and for partial exposure of the lateral side to simulate the over-exposed area and only one apron layer protection (the field size width at this part of the simulation was one half of the body at LAT view, towards the back, along the full body length). This partial area simulates the half thickness of the protective apron.

The next step after the effective dose simulation was to calculate x-ray penetration through the apron. The calculations were performed for direct x-ray spectrum, using an IPEM spectrum processor². The calculation results give entrance surface air kerma after full apron protection (0.5 mm lead equivalent) and half protection (0.25 mm lead equivalent). Inputs to the calculations include similar kV and basic filtration that are used in the PCXMC 2.0 Monte Carlo simulation. Calculations of the final staff effective dose were obtained from the sum of the full body irradiation and the partial irradiation, using the shielding influence of the full and half protection protective clothing.

RESULTS

X-ray transmission through the protective apron is presented in Table 1.

Table 1: x-ray transmission through the lead apron.

Shielding thickness (mm lead equivalent)	X-Ray transmission (%)
0.25	9.61
0.5	3.02

The overall effective dose was calculated by the effective dose differences of the partial shielding (0.25 mm) and full shielding (0.5 mm) plus the whole body effective dose calculation with full shielding. Table 2 shows the calculation results.

Table 2: Staff effective dose per 1 mGy air kerma outside the apron and projection of -20° in the z-axis.

Lead Apron	Projection	mSv/mGy*
Full cover	AP	0.0152
Partial cover	45° to right	0.0116
Full cover		0.0106
Partial cover	45° to left	0.0134
Full cover		0.0122

It is clearly shown that partial apron cover raises the effective dose of the medical staff.

CONCLUSIONS

It can be assessed in Israel that at least 10% of the medical staff in fluoroscopy rooms are using lead aprons that are too narrow. The medical staff effective dose while wearing inappropriate lead aprons was assessed as an excess of 9-10% under 100 kV x-ray radiation. It can be compared to about double the dose of not wearing thyroid shielding during x-ray fluoroscopy procedures.

REFERENCES

1. **Tapiovaara M., Siiskonen T.** (2007) *A PC-based Monte Carlo Program for Calculating Patient Dose in Medical X-Ray Examinations*. STUK – The Finnish Radiation and Nuclear Safety Authority. Report STUK-A139. Helsinki, Finland.
2. **IPEM (1997).** *Spectrum processor software*, based on IPEM report 78.

Medical Staff X-Ray Dose Reduction by Changing the Patient Examination Side

A. Ben-Shlomo

Soreq NRC, Yavne, Israel

INTRODUCTION

The major x-ray procedures that expose the medical staff at hospitals are angiography and heart catheterization. Most of those procedures take place while the medical staff is standing to the right side of the patient (the patient is lying on his back). It is possible to change some of those examinations and make those invasive procedures on the left side of the patient instead of the right side of his body.

The position of the medical staff influences the staff's x-ray effective dose. The choice of the x-ray projection, as AP, PA, left lateral, or right lateral projections, causes effective dose differences. These differences arise from the asymmetrical positioning of tissues and organs inside the body, x-ray shielding of organs by other organs, and different radiation sensitivity of each organ¹.

The physicians usually stand close to the patient pelvis, keeping some distance from the x-ray source. Thus, standing on the right side of the patient in angiography and heart catheterization usually exposes the left side of their body (in most of the cases, their standing position is not frontal towards the patient's irradiated volume).

Based on anatomical indicators, the traditional concept of building x-ray equipment was to fix the x-ray accessory items at the left side of the patient bed so the medical staff is standing to the right of the patient. Modern x-ray equipment in fluoroscopy rooms for angiography and heart catheterization is built to allow easy and comfortable working from both sides of the patient.

This work shows the differences in the effective dose of the medical staff working in fluoroscopy procedures and standing to the right side of the patient compared to working at his left side. The work is based on Monte Carlo simulation under PCXMC 2.0 software². The effective dose calculations were performed for a reference adult (73.2 kg, 178.6 cm), 100 kV, focus to skin distance (FSD) of 100 cm, and entrance surface air kerma of 1 mGy. The number of photons in the simulation was 250,000 (the simulation error was $\pm 0.3\%$).

The radiation spectrum was formed by filtration of a 2.5 mm Al and tungsten target.

The imaging volume of the patient is the source of scattered radiation towards the medical staff. The simulation radiation angle was taken as -20° in the cranial-caudal direction (z-axis) and $+45^\circ$ and -45° in the lateral direction (xy plane). These directions were chosen as the typical exposure angles of the staff.

The effective dose calculation considers the x-ray penetration through the apron. The calculations were performed for direct x-ray spectrum, using IPEM spectrum processor³. The calculation results produced entrance surface air kerma after full apron protection (0.5 mm lead equivalent). Calculation of the staff effective dose was obtained by using the effective dose of the full body irradiation at the above specific angle and considering the shielding influence.

RESULTS

The standard lead apron thickness for angiography and heart cauterization is 0.5 mm lead equivalent. This protection layer transmits only 3.02% of the x-ray spectrum, formed by tungsten target, 100 kV, and 2.5 mm Al spectrum³.

PCXMC 2.0 effective dose simulation results and the shielding of the protective apron combined to assess the medical staff's effective dose while the staff member stand to the right or left sides of the patient bed.

Table 1: Staff effective dose per 1 mGy Air kerma outside the lead apron and staff irradiation angles of -20° in the cranial-caudal direction (z-axis) and $+45^\circ$ and -45° in the lateral direction (xy plane).

Projection	mSv	45° to left/45° to right projection effective dose ratio (%)
45° to left	0.0122	114.8
45° to right	0.0106	

The results in Table 1 show that standing at the right side of the patient (i.e., exposing the left side of the medical staff member at 45°) causes a larger effective dose than standing at the left side of the patient in the same conditions.

CONCLUSIONS

This work simulate the differences in the effective dose of the medical staff working in angiography and heart catheterization procedures and standing to the right side of the patient compared to working at his left side. This Monte Carlo exposure simulation of the medical staff, while they are standing to the right side of the patient, shows effective dose excess of 114.8% compared to standing in the same conditions at the left side of the patient.

REFERENCES

3. **Ben-Shlomo A., Bartal G., Shabat S and Mosseri M.** (2013). Effective Dose and Breast dose reduction in pediatric scoliosis X-Ray radiography by an optimal positioning. *Radiat. Prot. Dosimetry* 156(1):30-36.
4. **Tapiovaara M., Siiskonen T.** (2007). *A PC-based Monte Carlo Program for Calculating Patient Dose in Medical X-Ray Examinations*. STUK – The Finnish Radiation and Nuclear Safety Authority. Report STUK-A139. Helsinki, Finland.
5. **IPeM** (1997). *Spectrum processor software*, based on IPeM report 78.

DNA Topoisomerase-I Inhibition due to Exposure to X-Rays

R. Daudee¹, R. Gonen¹, U. German¹, I. Orion², E. Priel²

¹*Nuclear Research Center Negev, Beer-Sheva, Israel*

²*Ben-Gurion University of the Negev, Beer-Sheva, Israel*

INTRODUCTION

In events such as radiological terrorism, accidents involving radioactive materials and occupational exposures, there is a great need to identify exposures to relatively low radiation levels. In many situations, the evaluation of radiation doses is not possible using physical dosimeters as they are not worn, and it is desirable to achieve this based on sensitive biomarkers^(1,2,3).

DNA Topoisomerase-I (Topo-I) is an essential nuclear enzyme that is responsible for the topological state of the DNA. The enzyme is involved in a variety of DNA transactions, including replication, transcription, recombination and DNA repair^(4,5). The aim of the present work was to investigate the influence of X-ray radiation on the catalytic activity of this enzyme, and to evaluate its applicability as a biological dosimeter.

RESULTS

Osteoblast-like cell line MG-63 were cultured for 2 days, then harvested to six 50ml sterile tubes. The tubes containing the cells were irradiated using a X-ray source with a dose rate of 1Gy/min for different periods of time. The X-ray source used was an RS-2000 Biological system manufactured by RAD SOURCE company. It produces x-rays with an average energy of about 50keV. After irradiation, the cells were transferred back to the incubator for 2 hours, and then the nuclear protein was extracted from the cells using a common method described in the literature⁽⁶⁾.

The Topo-I catalytic activity was measured using a specific Topo-I reaction mixture which includes supercoiled plasmid as the substrate and nuclear protein extracts as the source of Topo-I⁽⁷⁾. Topo-I relax supercoiled DNA provides topoisomers which are seen by the agarose gel as a ladder of DNA molecules which differ in their topological structure. Equivalent amounts (50 ng) of nuclear proteins were added to a specific Topo-I reaction mixture and the reaction was stopped after 10 min (the reaction activity was calibrated prior to the addition of the nuclear proteins so that the control sample, which was not irradiated, could relax the majority of the supercoiled plasmids).

Figure 1 shows the Topo-I activity assay results of samples exposed to different levels of x-ray radiation, which reveal significant differences in the activity levels between the six samples tested.

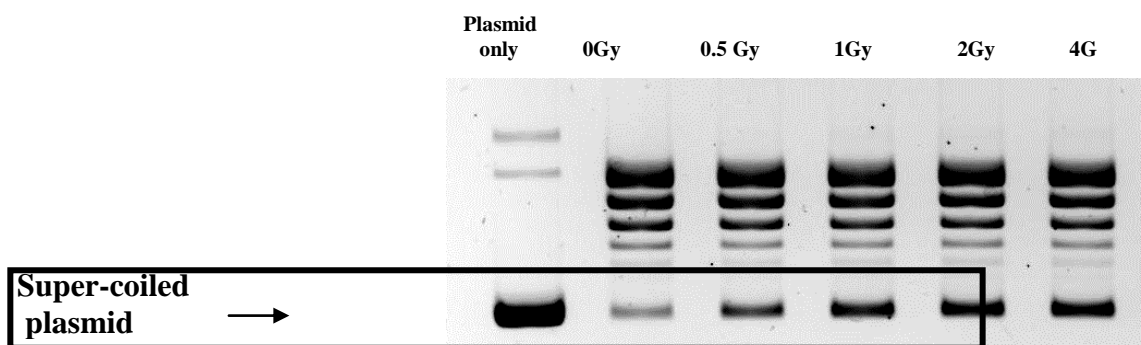


Figure 1: Topoisomerase-I assay results for nuclear extracts of MG-63 cells exposed to different doses of X-ray radiation.

Band intensities were quantified by densitometric scans using EZ-Quant-Gel image processing and analysis software (Figure 2). The inhibition was found to be linear up to a dose of about 1Gy ($r^2 \approx 1$). For exposures

higher than 1Gy there is a significant deviation from linearity, but still, inhibition of the enzyme's catalytic activity can be seen.

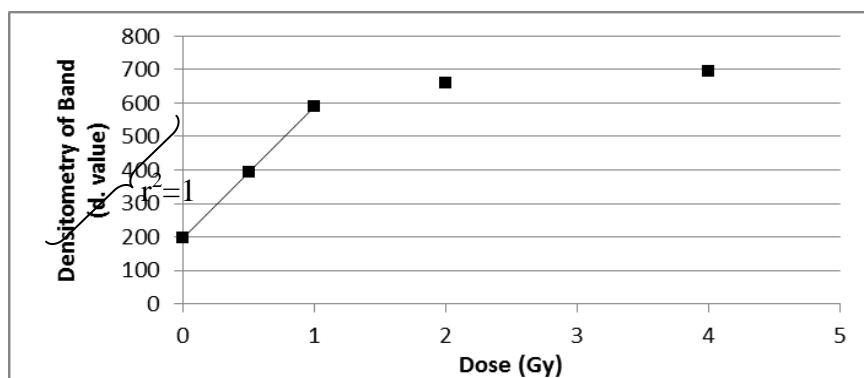


Figure 2: Densitometry results of supercoiled plasmid obtained from Fig. 1

The amount of supercoiled plasmid left after the reaction (see figure 1) was compared to the activity level of the un-irradiated control (0 Gy), that was taken as 100% activity. Figure 3 shows the comparison of the relative activities.

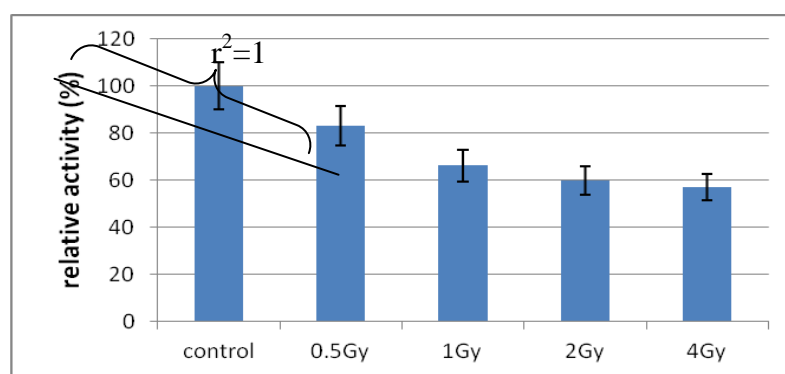


Figure 3: Inhibition of Topoisomerase-I activity after exposure of MG-63 cells to different doses of X-ray radiation.

For purposes of quality control, in order to verify that equivalent amounts of Topo-I were used in the Topo-I assay, the nuclear protein was analyzed by western blot⁽⁸⁾ and reacted with specific anti-topo I and anti β -actin antibodies. Band intensities were quantified by densitometric scans using EZQyant-Gel image processing and analysis software. The relative level of Topo-I protein was calculated using the equation: $[(\text{Topo-I})/(\beta\text{-actin})] \times 100$. The results show no significant differences between the levels of the proteins, leading to the conclusion that topoisomerase-1 activity is inhibited by X-Rays.

CONCLUSIONS

In the present work it was found that exposing MG-63 cells to X-ray irradiation resulted in a significant inhibition of DNA-Topoisomerase-I catalytic activity. The inhibition was found to function in the range of up to at least 4Gy, and up to 1Gy the inhibition was found to be linear with dose. As equal DNA-Topoisomerase-I were used, it is suggested that the cellular mechanism of Topo-I inhibition can be attributed to posttranslational modifications. The reduction in Topo-I activity after exposure to X-ray may be applicable as a biological dosimeter (biomarker) mainly in the range of 0-1 Gy. Further studies are needed to elucidate the limit of detection (LOD) of the dose that can be detected by the enzymes inhibition's activity.

REFERENCES

1. Brooks A.L. *Biomarkers of Exposure and Dose: state of the art*, Radiation Protection Dosimetry, Vol. 97 (1), p.39-46, (2001).
2. Durante M., *Potential application of biomarkers of radiation exposure in nuclear terrorism events*, Physica Medica, Vol. XIX (3), p.191-212, (2003).
3. Guipaud O., Benderitter M., *Protein biomarkers for radiation exposure: towards a proteomic approach as a new investigation tool*. Ann Ist Super Sanita, Vol.45 (3), p.278-286, (2009).

4. James C. Wang, *DNA topoisomerases*, Annu. Rev. Biochem, Vol. 65, p. 635-692,(1996).
5. Champoux JJ., *DNA topoisomerases: structure, function and mechanism*. Annu. Rev. Biochem., Vol 70, p.369-413, (2001).
6. Auer B., Vosberg HP, Buhre U., Klocker H., Hirsh-Kauffman M., Shweiger M., *Intracellular distribution of DNA topoisomerase I in fibroblasts from Fanconi patients*, Hum. Genet, Vol. 61, p.369-371, (1982).
7. N. Noach, Y. Segev, I. Levi, S. Segal, E. Priel, *Modification of topoisomerase I activity by glucose and by O-GlcNAcylation of the enzyme protein*, Glycobiology, Vol.17(12), p.1357-1364, (2007).
8. J. Sambrook, Fritch EF, Maniatis T., *Molecular cloning: a laboratory manual*, Cold spring Harbor, NY: Cold spring Harbor Laboratory Press, (1989).

Posters (Wednesday, February 12, 2014 15:30)

A Program for Follow-Up and Quality Assurance of Electret Results

B. Sarusi¹, S. Levinson¹, N. Lavi², U. German¹

¹ *Nuclear Research Center, Negev, P.O.B 9001 Beer Sheva, 84190, Israel*

² *Ben-Gurion University of the Negev, Beer Sheva, 84105, Israel*

INTRODUCTION

The most important naturally occurring radio-nuclides in the environment are ^{40}K and ^{238}U and ^{232}Th , which are heads of decay series. Building materials may also contain enhanced levels of naturally occurring radioisotopes which may be sources of external and internal radiation exposure in dwellings. The external exposure is due to the direct radiation from the radioisotopes in the decay series of ^{238}U and ^{232}Th , and among these daughters, two Radon isotopes are produced: ^{222}Rn is a daughter in the chain of decay of ^{238}U and ^{220}Rn is a daughter in the ^{232}Th chain. Radon is a gas, it undergoes diffusion in the building material and exhalation to the surrounding. Besides, radon is emanated also from soil and its concentration can be significant in radon prone areas. Inhalation of air with increased level of Radon causes internal exposure, which is the greatest contribution to the exposure of individuals to natural radiation. Therefore, accurate measurement of radon concentration is of great importance.

There are several methods to determine the radon concentration in air. The Israeli regulation for measuring the radioactive content in building materials⁽¹⁾ specifies three methods for radon concentration measurements: applying continuous monitoring, using Electrets and using active charcoal cassettes. Using Electrets is convenient, as a relatively simple stand-alone system can be used. The follow-up and quality assurance of Electrets results is the subject of the present work. For this purpose a computer program was developed which handles the Electrets results database and applies various tools for analysis.

MATERIALS AND METHODS

An Electret is a charged Teflon® disk, mounted inside a small chamber^(2,3). Radon gas diffuses into the chamber through filtered inlets, and the alpha particles emitted by the decay ionize air molecules. Negative ions produced inside the chamber are collected on the positively charged Electret, causing a reduction of its surface charge. Thus, the Electret serves both as a source of electrostatic field and as a sensor. The change in voltage, which is a function of the radon concentration, is measured by a sensible voltage reader. In the present work EIC's (Electret ion chambers) made by Rad Elec Inc. (5714-C Industry Lane, Frederick, MD 21704, USA) were used. The basic components of the E-PERM® Electrets system are shown in Fig.1. The Electrets are accurate devices, but they are susceptible to some environmental effects, which may induce significant errors. The main effects are mechanical shocks, dirt/dust, humidity^(4,5,6). Also improper operation of the shutter handle when measuring the voltage may produce results deviating from the proper values. Therefore, at least 2 equal sequential measurements are needed for a valid result.



Figure 1. The E-PERM® Electrets system

THE COMPUTER PROGRAM

The general flow chart of the computer program is presented in Fig. 2. The main database contains information on each Electret, characterized by its unique serial number. All Electrets readings are displayed, as well as the time of reading, the readout equipment used and the reading status (voltage follow-up, voltage check before exposure, readout after exposure, etc.). All historical data is contained in the database, from beginning of use of each Electret. to ensure reliable check points and quality assurance of the reader, reference Electrets are also defined in the system. These are highly stabilized Electrets and in addition a blank Electret. Full information on the reference Electrets and their history is included in the database as well.

The database is used to check compliance with all the requirements of the manufacturer and the regulator (ministry of environmental protection) and to issue proper alerts for action. New Electrets come loaded to 700 – 780 volts which allows for 500 usable volts. A valid Electret reading must be higher than 200V, otherwise it must be sent back to the manufacturer for charging. In order to ensure a correctly functioning reader, weekly readings of reference Electrets should be within $\pm 3V$ of the manufacturer certified readings and the blank ("zeroing") Electret reading should be in the range $\pm 2V$. The warning limits can be changed by the administrator of the system, but not by the operator.

The program establishes communication between the reader and the database. The Electret number is written in barcode format and is transmitted directly to the database. Also the voltage values are received from the reader and are input automatically into the database.

A valid reading is defined as the value of two consecutive equal voltages out of up to 10 readings. In order to facilitate the follow-up, to enable an efficient handling of problems, and to observe trends, a graphical presentation of the voltage readings as a function of the reading time is available.

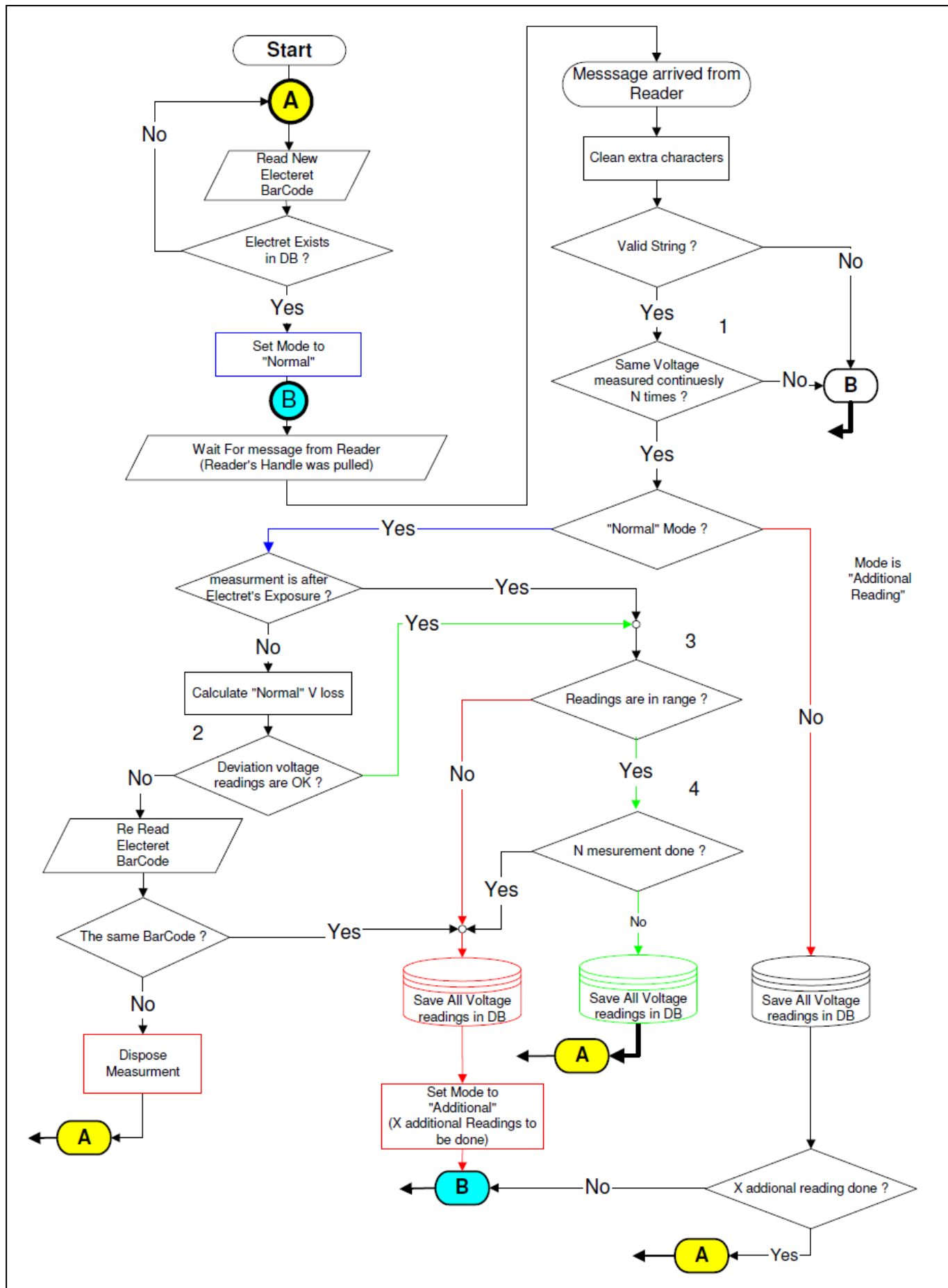


Figure 2. Flow chart of the computer program.

EXAMPLE OF RESULTS

Two typical graphic presentations are given. The first one (Fig. 3) presents data of a valid radon exposure measurement. Before exposing the Electrets, the voltage values are stable. Also after exposure the voltage remains stable and the radon concentration can be calculated from the voltage difference before and after the exposure. A different case can be seen in Fig. 4.

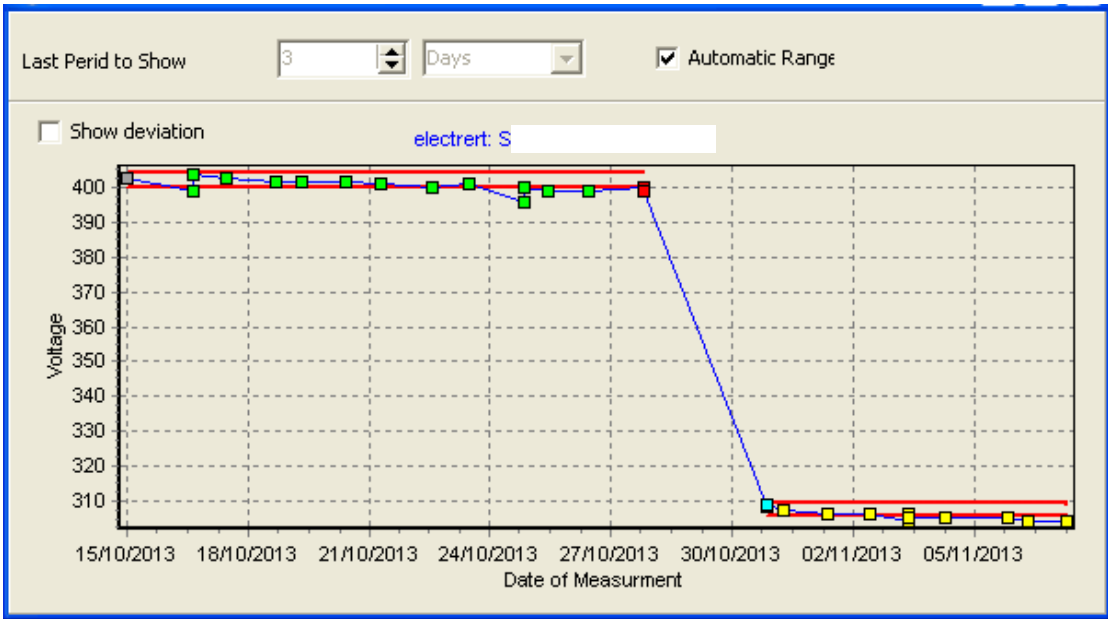


Figure 3. Data of a valid radon exposure measurement.

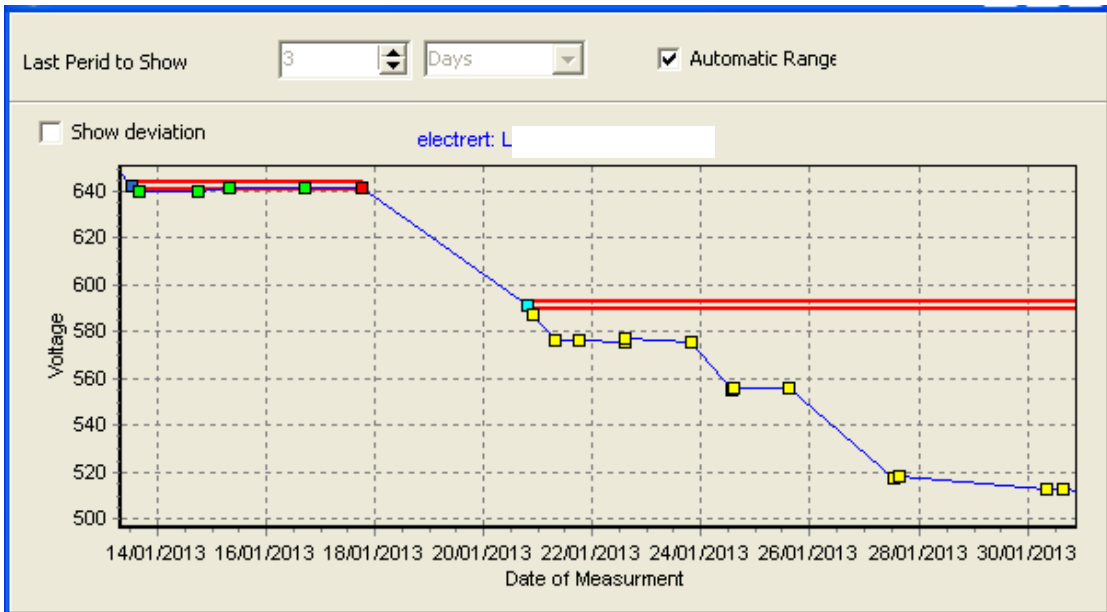


Figure 4. Data of an invalid exposure measurement.

Before the exposure the voltage was stable, but after the exposure there is a non-normal behavior. The first two readings were close, but afterwards a slip of about 15V occurred. The next 4 readings were stable, but then another drift occurred. This behavior does not allow us to determine with acceptable accuracy the radon concentration. It is possible that this drift was caused by some dirt accumulated on the Electret during its use.

CONCLUSIONS

A computerized tool was developed which greatly improves the handling and follow-up of data used to evaluate the radon concentrations by Electrets. The voltage readings are directly placed into the database, statistical analysis is performed and the validity of the readings are checked. All readings of the reference Electrets are included in the database as well. The graphic presentation of data enables a clear observation of behavior and trends. Using the program greatly improves the quality assurance of radon concentration determination when using Electrets. The program is under development. Its expansion will include calculations of radon concentrations based on the voltage readings.

REFERENCES

1. SI 5098, 2009. Content of radioactive elements in building products. The standards institution of Israel.
2. Kotrappa, P., Brubaker, T., Dempsey, J.C., Stieff, L.R., 1992. Electret ion chamber system for measurement of environmental radon and environmental gamma radiation. *Radiation Protection Dosimetry* 45, 107–110.
3. US Patent nr. 4,992,658. Ramsey Jr. et al. 1991.
4. Denman, A.R., Groves-Kirkby, C.J., Phillips, P.S., Krockett, R.G.M., Woolbridge, A., Gillmore, G.K., 2005. The practical use of Electrets in a public health radon remediation campaign. *J. of Envir. Radioactivity*, 84, 375-391.
5. Mahat, R.H., Bradley, D.A., Amin, Y.M., Wong, C.Y., Su, L.D., 2001. The effect of humidity on the accuracy of measurement of an Electret radon dosimeter. *Radiat. Phys. Chem.* 61, 489–490.
6. Sorimachi, A., Takahashi, H., Tokonami, S., 2009, Influence of the presence of humidity, ambient aerosols and thoron on the detection responses of Electret radon monitors. *Rad. Measurements* 44, 111-115.

Posters (Wednesday, February 12, 2014 15:30)

Application of the "GammaGen" Computer Code for NORM Synthetic Spectra Analysis

B. Sarusi¹, S. Levinson^{*1}, U. German¹, S. Antropov², K. Kovler³

¹*Nuclear Research Center, Negev, P.O.B 9001 Beer Sheva, 84190, Israel.*

²*"Amplituda" Research Center, POB 120, Moscow 124460, Russia*

³*Technion - Israel Institute of Technology, Haifa 32000, Israel*

INTRODUCTION

"GammaGen" (GG) is a computer software developed to simulate gamma ray spectra obtained from NaI(Tl) or Ge detectors. The detector efficiency, resolution and peak to Compton ratios are used to generate synthetic pulse height spectra for specific detector and geometrical configurations.

GG was used in the past for several applications, as to predict the detector response to different radio-nuclides mixtures [1-3], to predict the pulse height spectra near a nuclear spent fuel site as a function of the shielding thickness and cooling time [4] and for homeland security purposes [5, 6]. An updated version of the GG program was developed, and the application presented in the present work consists of building a library and simulating the detection and analysis of synthetic spectra to check the performance of a commercial spectrometry system based on a NaI(Tl) detector intended for NORM analysis, which was developed by *Amplituda/Russia* [7].

MATERIALS AND METHODS

The basic application of the GG computer program is to generate a calculated spectrum, mainly for complicate cases of many photo-peaks from different radioisotopes mixtures, for visual inspection and comparison with measured spectra. The spectrum for a chosen radio-nuclide is generated based on its activity and its photo-peaks energies and yields taken from a data library such as the "Raddecay" program [8]. The detector efficiency, resolution and the peak to Compton ratios are determined specifically for a certain detector system, as well as the counting geometry which is chosen by the user. The spectra can be displayed in several modes: as energy lines of the photo-peaks, as Gaussians of each photo-peak, or as sum of all Gaussians. Compton distributions of the predicted accumulated counts in each channel can be included. The resulting spectra are displayed for visual analysis together with peaks and radio-nuclides data. All spectra can be exported to formats required by commercial spectra analyzing programs and to Excel format.

THE COMPUTER PROGRAM

This new version of the GG program simulates the multichannel analyzer (MCA) operation. According to the activity determined for each radionuclide and the counting time, the GG program displays the spectrum accumulation as it is done in MCA. The counts are summed to a temporary variable as a function of time. If the count is greater than 1, Gaussian randomization is performed based on the normal standard deviation and if the random value is greater than 1 its integer value is added to the previous counts of the specific channel. The temporary variable is cleared for the next iteration. The same procedure is done for all the spectrum channels and the accumulation progress is refreshed and displayed every second, which is the basic unit time. This way, the channel content of spectra of low activity samples may be updated only after several seconds, as it really occurs in actual counting systems. The user can control the accumulation procedure with all the features that are in common MCA systems.

The "Progress" program developed at *Amplituda/Russia* [5] is commonly used to analyze NORM spectra, including the ¹³⁷Cs radionuclide. The analysis is basically performed by the Linear Least Squares technique on 12 Regions of Interests (ROIs) [9, 10]. Its library was replaced by a synthetic, calculated library consisting of NORM radioisotopes and ¹³⁷Cs, prepared by the GG program. The "Progress" program was applied to analyze complex pulse height spectra, also prepared by the GG program with statistical fluctuations taken into consideration.

EXAMPLE OF RESULTS

A spectrum of the NORM materials ^{226}Ra , ^{232}Th , ^{40}K with an activity of 1000 Bq/kg each, with added 1000 Bq/kg of ^{137}Cs in 1 liter Marinelli container [11] for 10 minutes counting time was calculated by the GG program, when using a NaI(Tl) flat 3"x3" detector (as installed in the "Progress" system). The spectrum was transferred and analyzed by the "Progress" program, that was pre-calibrated for this specific geometry and detector characteristics by GG spectra. In figure 1 the predicted "measured" spectrum and the analyzed and fitted spectrum by the "Progress" program are given. The analysis results reported by the "Progress" program can also be seen in the insert. Table 1 summarizes the "Progress" analysis results. It can be seen that for all radio-isotopes the accuracy is better than about 2%, except for ^{40}K where the difference from the target value is about 2.5%. However, also the standard deviation of the calculated ^{40}K activity is much higher than for other radio-isotopes (more than 5% compared to about 1%), indicating a lower statistical accuracy of the counts in the ^{40}K energy peak.

Table 1. The accuracy of the analysis performed by the "Progress" program on a simulated spectrum of a mixture of 1000 Bq/kg NORM radio-nuclides and ^{137}Cs .

Radio-nuclide	Calculated content [Bq /kg]	Difference [%]
^{226}Ra	1020.6 ± 8.7	2.06
^{232}Th	1001.6 ± 10.3	0.16
^{40}K	974.8 ± 52.6	2.52
^{137}Cs	999.6 ± 8.3	0.04

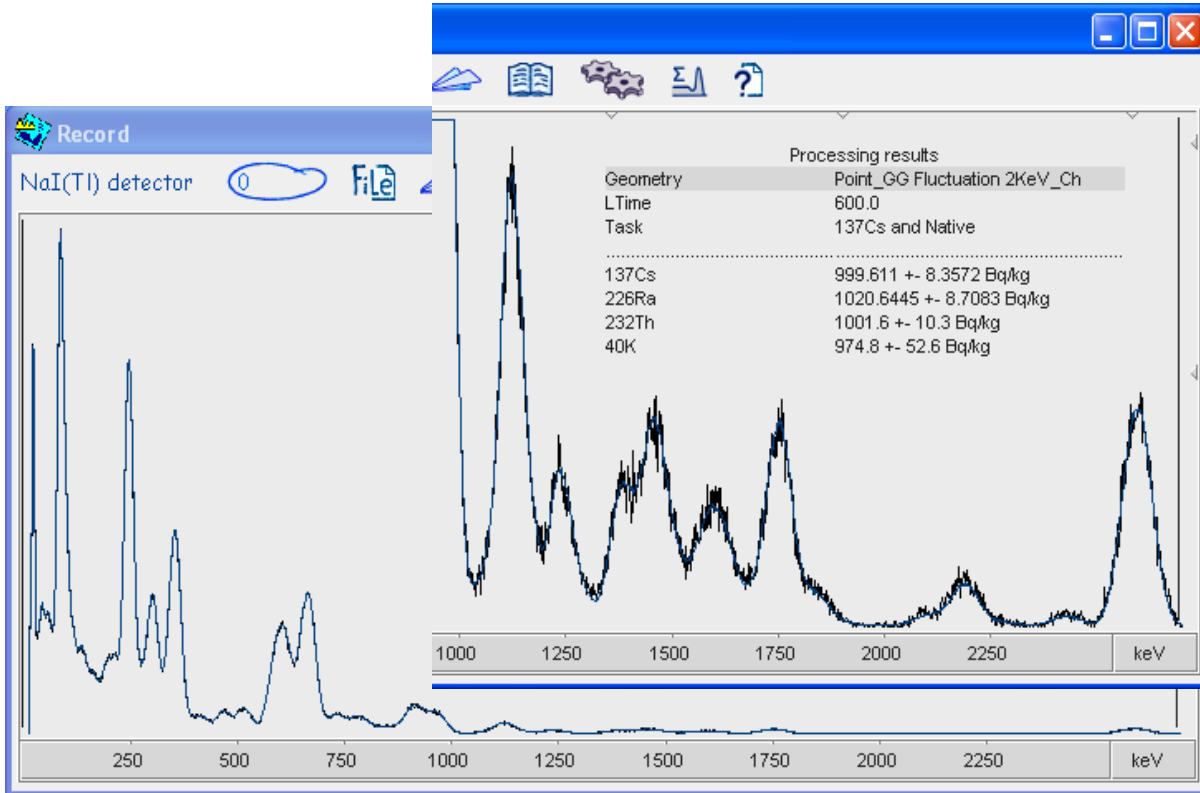


Figure 1: NORM + ^{137}Cs NaI(Tl) spectrum created by GG program and analyzed by the "Progress" program.

CONCLUSIONS

The new version of the GG program enables prediction of "real" spectra, including counting statistics. It simulates the operation of the multichannel accumulation process. The program was used to prepare the library components of the commercial "Progress" analysis system, in order to check its performance when analyzing NORM spectra. The "Progress" program was applied to analyze a synthetic mixture of 1000 Bq/kg of NORM materials+¹³⁷Cs contained in a Marinelli beaker, and the results for all radio-isotopes were obtained within an accuracy range of 2.5%

The new version of the GG program enables future investigations of counting and analyzing complex spectra, especially in the case of NaI(Tl) detectors, where significant overlapping may occur. Producing synthetic spectra can be used for example to determine the MDA of radio-nuclides in complex mixtures with various activities. The main advantage is that no sample preparation is needed, as well as no laboratory work.

REFERENCES

1. "GammaGen - a computer code for gamma-ray spectra generation". S.Levinson, B. Sarusi, O. Pelled, U. German. The 24th conference of the nuclear societies of Israel, Dead-Sea, Israel, February 19-21, 2008, p.137-140
2. "Simulation of pulse height spectra from NaI(Tl) and Ge detectors near the location of a nuclear reactor accident". S.Levinson, U.German, B.Sarusi, O.Peled. IRPA Regional Congress for Central and Eastern Europe, Brasov, Romania, 24-28 September 2007, p. 261
3. "A computer code for synthetic gamma-ray spectra generation". S. Levinson, B. Sarusi, O. Peled, U. German. IRPA-12 international congress of the international radiation protection association, Buenos-Aires, Argentina, 19-24 October 2008, TS I.1.1-2418, p. 31
4. "Gamma-ray spectra prediction for radioactive waste". S. Levinson, B. Sarusi, O. Peled, U. German, Z. Alfassi. MRS Materials research society, the 33nd international symposium, scientific basis for nuclear waste management, Saint Petersburg, Russia, 24-29 May 2009, RP-21, p. 177
5. "Synthetic gamma ray spectra for homeland security radio-nuclides analysis". S.Levinson, B.Sarusi, A.Osovizky, V.Pushkarsky, U.German, E.Marcus, Y.Cohen, I.Belaish. Nuclear science symposium Medical Imaging conference, Orlando, Florida, U.S.A, 25-31 October 2009, N13-81, pp. 504-508
6. "Homeland security - masking of special nuclear materials (SNM) by Natural Occurring Radiation Materials". B.Sarusi, S.Levinson, A.Osovitzki, U.German, T.Mazor, Y.Cohen, I.Belaish. The 25th conference of the nuclear societies in Israel, 16-18 February 2010, Dead-Sea, Israel, pp. 249-253
7. "Amplituda" Research Center, POB 120, Moscow 124460, Russia
8. "Raddecay", Version 3 March 1999. <http://rad-decay.software.informer.com>.
9. "Determination of Radionuclide Content of Building Materials by Means of Scintillation Spectrometry". K. Kovler, Z. Priluzky, S. Antropov, N. Antropova, V. Bozhko, Z. Alfassi, N. Lavi. The 25th conference of the nuclear societies in Israel, 16-18 February 2010, Dead-Sea, Israel, pp. 284-289
10. "Can scintillation detectors with low spectral resolution accurately determine radionuclides content of building materials?" K. Kovler, Z. Prilutskiy, S. Antropov, N. Antropova, V. Bozhko, Z.B. Alfassi, N. Lavi. Applied Radiation and Isotopes 77 (2013) 76-83
11. Isotrak Nuclitec Eckert & Ziegler, Germany, 1 liter Marinelli beaker type 1N FZ-1262-001 with internal hole of 77 mm dia.

Posters (Wednesday, February 12, 2014 15:30)

Matrix Materials for Preparation of Marinelli Calibration Standards

S. Levinson¹, N. Lavi², U. German¹

¹ Nuclear Research Center, Negev, P.O.B 9001 Beer Sheva, 84190, Israel

² Ben Gurion University of the Negev, Beer Sheva, 84105, Israel

INTRODUCTION

Due to the very low concentrations of radioactive nuclides in environmental samples (soils, water, plants, building materials, etc.) high volume samples are used when employing γ -ray spectrometry. A convenient procedure is to employ Marinelli beakers, which surround the spectrometer and enhance the detection efficiency. The spectrometry system must be calibrated to the Marinelli beaker geometry, but due to the great variety of the environmental samples, their density may vary in the general range $0.2 - 2 \text{ g cm}^{-3}$. Variability in the sample chemical composition is not a major problem, since mass attenuation coefficients differ only slightly from one environmental sample to another, but the wide range of densities results in large differences in γ -ray attenuation factors within the samples. Therefore, measurements of radionuclides from environmental samples by γ -ray spectrometry require a correction for self-attenuation of γ -rays. This correction can be minimized or avoided by direct calibration with certified γ -ray standard sources in matrices with a composition close to that of environmental samples to be assayed. The preparation of the standards can be made using "in house procedures". This can be done by homogeneously incorporating certified standard radionuclide sources into inactive matrices with a composition and density as close as possible to the samples.

Many possible matrices are described in the literature for preparation of the Marinelli standards. De Sanoit⁽¹⁾ describes the preparation and characterization of a low density (0.27 g cm^{-3}) silica matrix spiked with mixed γ -ray standards. Daraban et. al⁽²⁾ used a composition of CaCO_3 , CaSO_4 , SiO_2 and Al_2O_3 to simulate "artificial soil". Lavi and Alfassi⁽³⁾ proposed CaCO_3 for a matrix with a density of $1.1 - 1.3 \text{ g cm}^{-3}$ mixed with known amounts of ThO_2 . The Netherlands Standard for radioactivity measurements in building materials⁽⁴⁾ mentions stearic acid, starch, gypsum and quartz powder as suitable matrix materials. Taskaeva et.al⁽⁵⁾ gave a detailed description on preparation of low activity efficiency calibration standards of different densities with natural organic and inorganic materials, including widespread food products as coffee, sugar and honey.

The Marinelli matrix density is indeed an important parameter which influences the calibration accuracy, but the natural radioactivity content of the various added bulk materials may also contribute by adding spurious background to the spectra originating from the certified γ -ray emitting radioisotopes, as the calibration for NORM determination is usually performed with very low standard activities. In the present work, an investigation of the specific activity content in selected inorganic and natural organic products regarded as potential matrix materials was performed. As the main natural occurring radioisotopes are ^{226}Ra , ^{232}Th and ^{40}K , their specific activity in the various samples was measured. ^{137}Cs which was added in the last decades to the environment due to the increased nuclear activity was measured as well.

MATERIALS AND METHODS

Marinelli beakers of 1 liter volume supplied by Isotrak- Ekert &Ziegler were used. The bore diameter of these beakers is 79 mm and fits to the 2.75” diameter of the HPGe detector employed in this work (Ortec, 20% efficiency). The samples were counted several times (50,000 to 300,000 sec) in order to achieve a desirable statistical accuracy.

The following samples were analyzed :

- Sand collected from the shore of the Mediterranean Sea
- White Sugar
- White Flour
- Several organic food products: Rice, Maize (corn), Red and green Lentils, White beans, Broad beans and Humous beans and green Pea.

The samples were grinded to a fine powder, were homogenized and transferred to Marinelli standard beakers. The content of each beaker was compressed to obtain maximum density and the beakers were tightly closed, The counting was delayed for 21 days to allow equilibrium between ^{226}Ra and its daughters, due to Radon emanation from the natural ^{226}Ra . The system was calibrated using a standard ^{226}Ra 1 liter Marinelli beaker with an activity of 3080 Bq and density of 1.08 gr cm^{-3} .

RESULTS AND DISCUSSION

The ^{226}Ra , ^{232}Th and ^{40}K activity in the samples checked is presented in Figures 1-3. The specific weights of the various samples are given in Table 1.

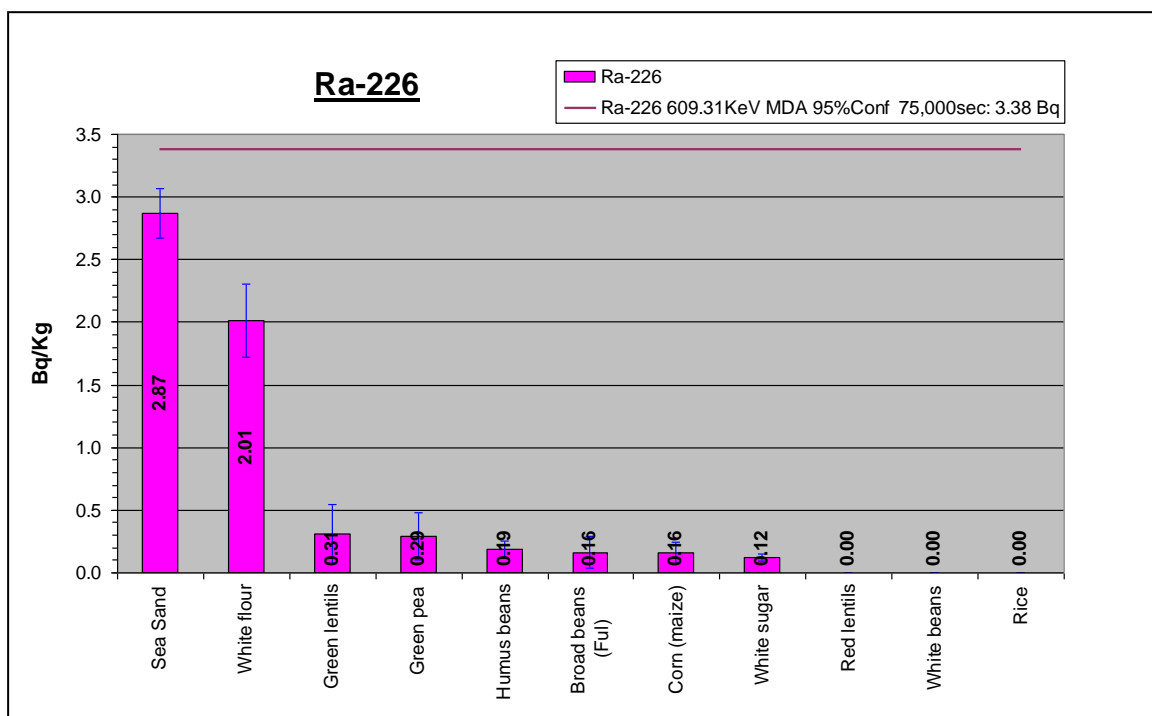


Figure 1: The ^{226}Ra specific activity of the different samples.

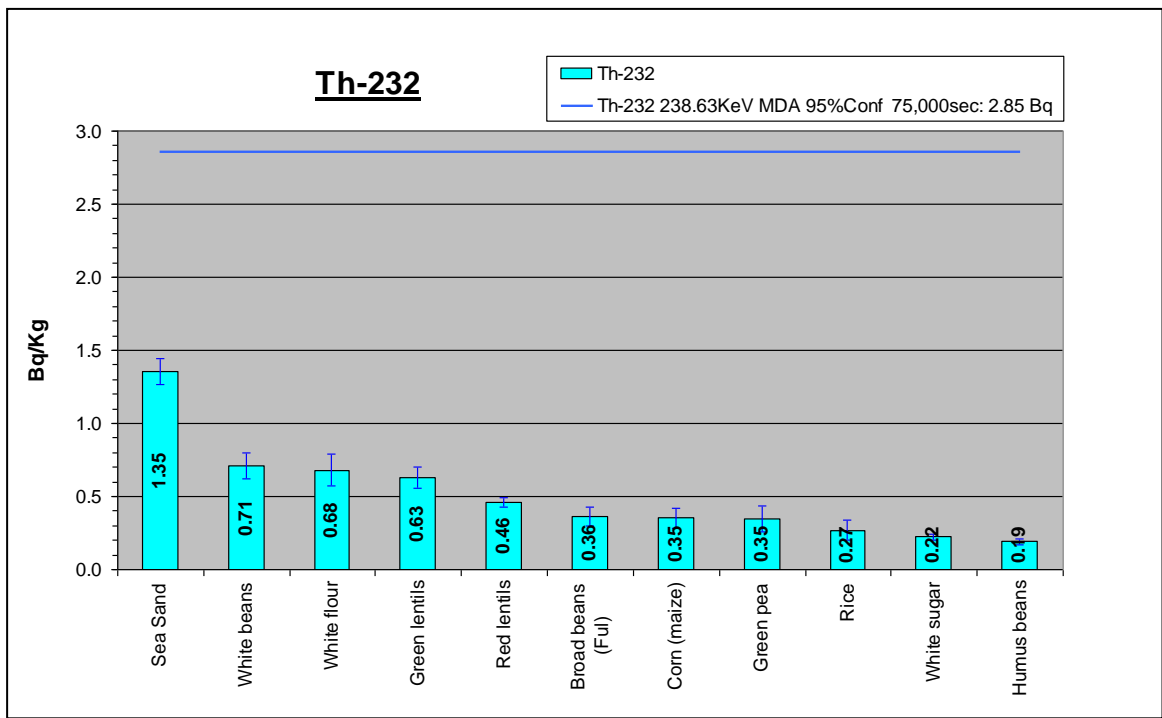


Figure 2: The ^{232}Th specific activity of the different samples.

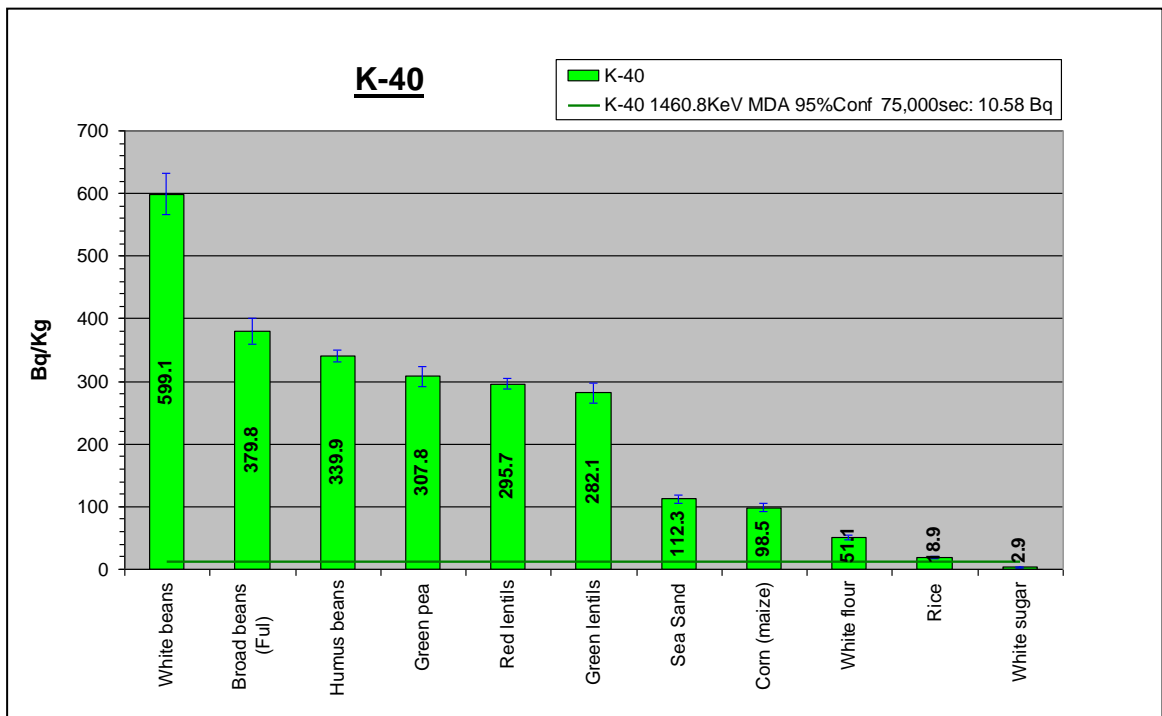


Figure 3: The ^{40}K specific activity of the different samples.

Table 1: Specific weight of the checked materials

	White	Broad	Humus	Red	Corn	White	Rice	Green	Green	Sand
Material	flour	Beans (ful)	beans	lentils	(maize)	sugar		lentils	pea	
Density (kg/liter)	0.78	0.84	0.92	0.94	0.95	0.98	1.03	1.04	1.04	1.83

DISCUSSION

It can be seen that except sea sand, white flour and broad beans the specific weight of all samples is in the range 0.9 - 1.1 kg L⁻¹. However, significant differences are present regarding the radio-nuclides content. The ²²⁶Ra and ²³²Th activity for all samples is below the MDA value for the applied counting time. However, the ⁴⁰K content is considerably higher in all samples, the highest value being 599 Bq kg⁻¹ in white beans and only 2.9 Bq kg⁻¹ in sugar. Traces of ¹³⁷Cs (0.006 Bq kg⁻¹) were found only in the sand sample. It seems that grinded white sugar is the best choice for matrix material, with the lowest NORM concentration and density close to 1.

REFERENCES

1. de Sanoit J., Silica spiked with mixed γ ray standards for use as environmental reference material. *Radiochimica Acta* 65, 249-257, 1994.
2. Daraban L., Iancu D. Nita D., Daraban L., Efficiency calibration in γ spectrometry by using ²³²Th series radionuclides. *Rom. Journ. Phys.* Vol 58, Suppl. P, S99-S107, 2013.
3. Lavi N., Asfassi Z.B., Development of Marinelli beaker standards containing thorium oxide and application for measurements of radioactive environmental samples. *Rad. Measurements*, 38, 15-19, 2005.
4. NEN 5697, Radioactivity measurements-Determination of the natural radioactivity in stony building materials by means of semiconductor gamma-ray spectrometry. Netherlands Standard, 2001
5. Taskaeva M., Taskaev E., Penev I., On the preparation of efficiency calibration standards for γ -ray spectrometers. *Appl. Radiat. Isot.*, Vol 47, 981-990, 1996.

Posters (Wednesday, February 12, 2014 15:30)

Radioactivity in Soils and Foodstuff Samples in Israel

S. Levinson¹, N.Lavi², H.Nasar³, U.German¹

¹ Nuclear Research Center, Negev, P.O.B 9001 Beer Sheva, 84190, Israel.

² Ben Gurion University of the Negev, Beer Sheva, 84105, Israel.

³ Ministry of Environmental Protection, Jerusalem POB 34033, Israel

INTRODUCTION

A new series of measurements was performed to determine the current NORM radionuclide content in cultivated soils and selected foodstuff. An HPGe detector (EG& G Ortec) system with a 20% efficiency (relative to 3"x3" NaI(Tl) at 1332 keV) was used for gamma ray spectrometry. Due to the low amount of radioactivity in natural materials, 1 liter of soil samples were measured in Marinelli beakers as well as the foodstuff samples which were concentrated and homogenized. Calculation of the radioactivity transfer factors from the cultivated soils to foodstuff was performed on the basis of dry weight data, as described elsewhere in the literature [1,2]. In order to ensure the equilibrium of ²²²Rn and its daughters in the ²²⁶Ra chain, the measurements were performed after a waiting time of at least 21 days.

MATERIALS AND METHODS

The foodstuff and soil samples were collected from several locations in Israel: Ein Carmel (North), Nehalim, Beerot Ytzhak and Bne Atarot (Center) and Arad (South). The samples of cultivated soils were taken from the top 5 cm of the soil, were dried at 105° C, homogenized and transferred into Marinelli Beakers of 1 liter [3]. Two types of foodstuff samples were prepared from each sampling place and were transferred to Marinelli beakers for counting:

- 1) Samples in natural form (raw materials) grinded and homogenized.
- 2) Samples dried and blended to fine powder. The average drying temperature was 150° C, which differs from a previous technique that was used in the past [4]. The drying process took about 16 hours and required continuous blending.

γ spectrometry was performed for all samples, after calibration for the Marinelli beaker geometry. In order to get acceptable counting statistics the measurements lasted between 8 and 80 hours, depending on the radioactivity content in the samples. The appropriate background was subtracted from each spectrum and density corrections were applied.

RESULTS AND DISCUSSION

Fig. 1 presents the ratio of the dry foodstuff weight to the natural weight, defined as the dryness fraction. The sort of foodstuffs and their collection location are noted in the figure. The dryness fraction obviously depends on the kind of foodstuff. It varies in the range from 4.5% to 22.1% with an average value of about 12%.

The specific activity of the dried soil samples from the various locations is given in Fig. 2. The average activity of ²²⁶Ra is 12.72 Bq/kg, of ²³²Th is 23.10 Bq/kg and of ⁴⁰K is 245 Bq/kg. The contribution of ¹³⁷Cs, which became significant after the Chernobyl accident, can also be seen with an average activity of 3.77 Bq/kg.

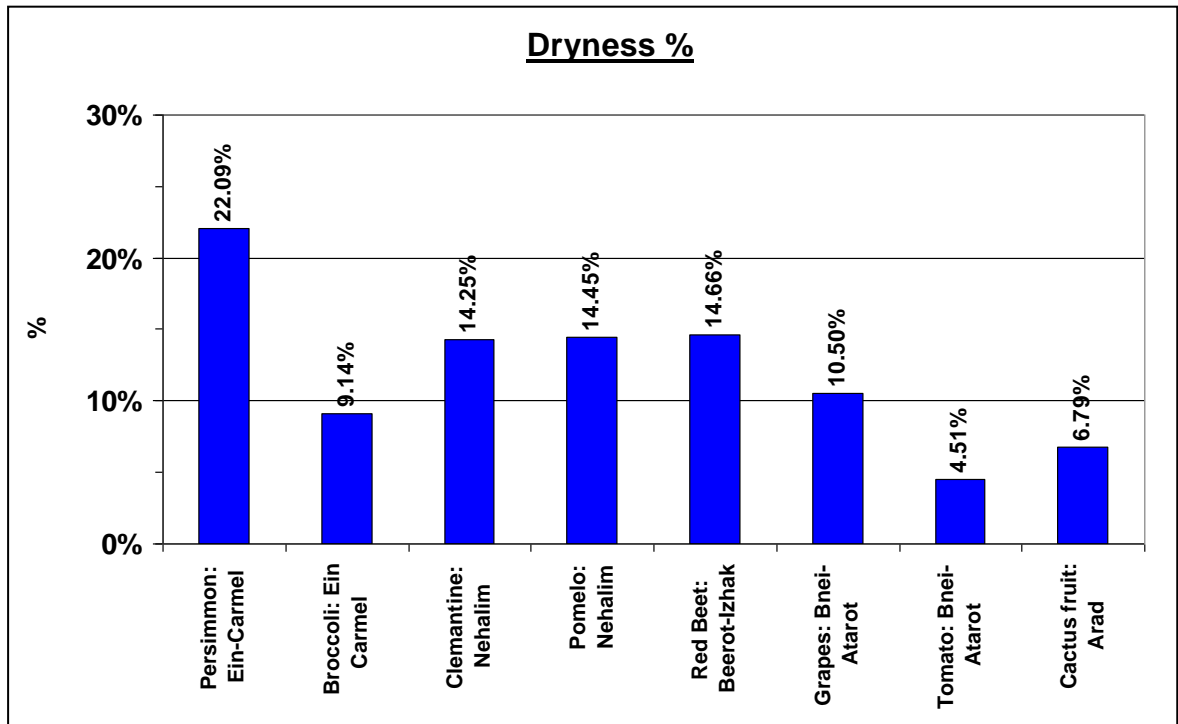


Figure 1: Dryness fractions of various foodstuffs.

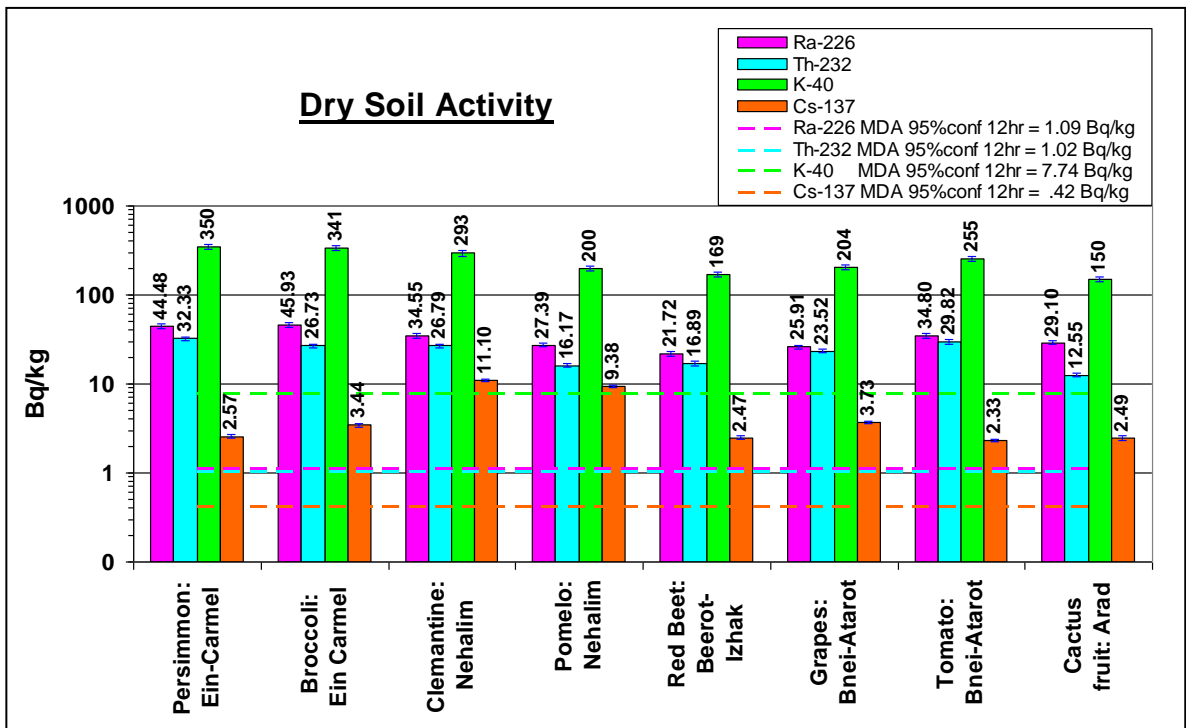


Figure 2: The specific activity of the soil samples from different locations.

Due to the great variation in dryness fraction between the different foodstuff sorts, it is important to notice the differences between the specific activities normalized to the natural weight (as consumed) and normalized to the dry weight (the actual plant specific activity). Both specific NORM activities for the selected foodstuffs can be seen in Fig. 3. No measurable ^{137}Cs amounts were detected.

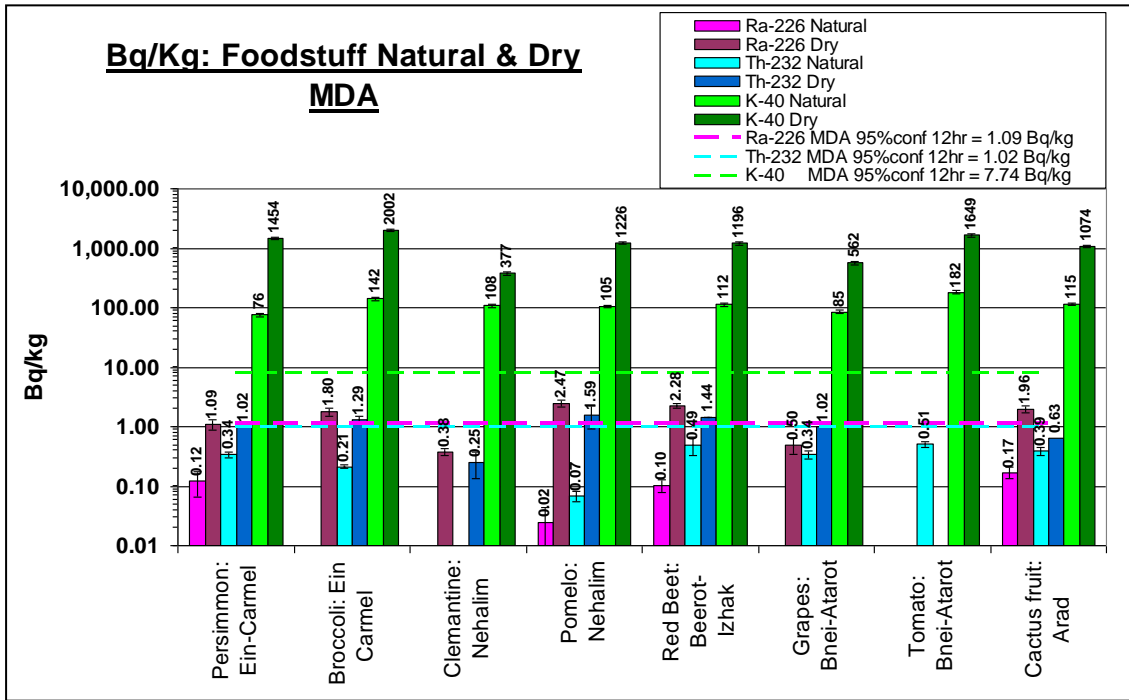


Figure 3: Specific activities of NORM radio-nuclides in natural and dried foodstuff samples.

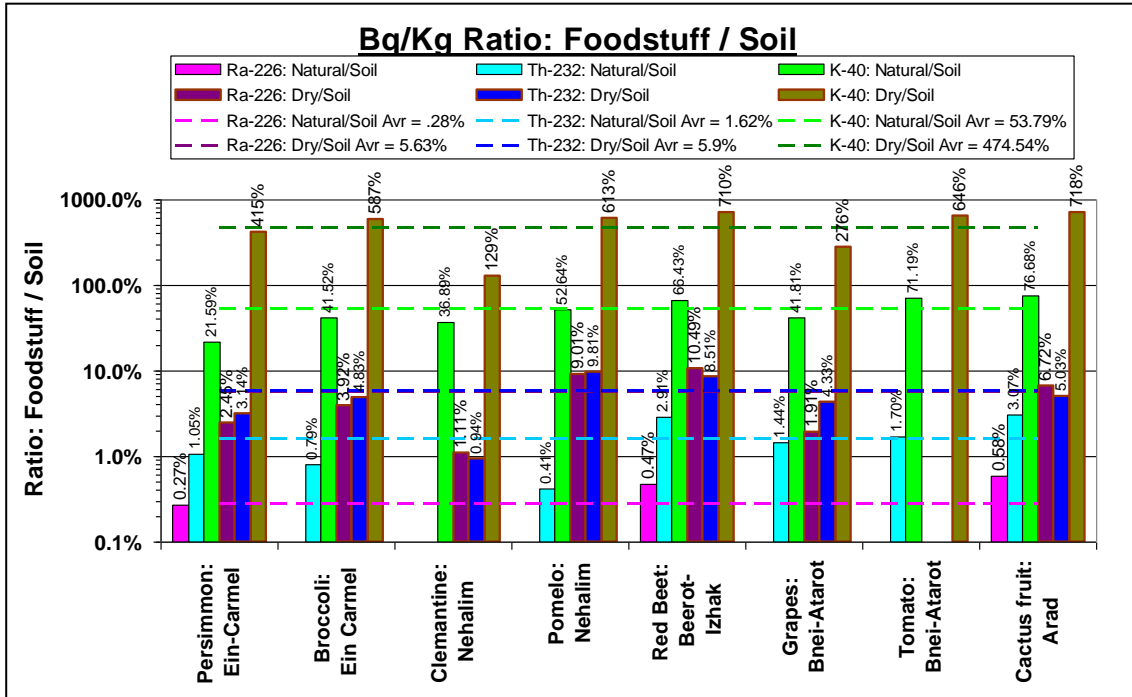


Figure 4: Transfer fraction of NORM radio-nuclides from soil to natural and dried foodstuff samples.

The transfer fraction of NORM radio-nuclides was calculated for the natural and dried foodstuff samples and is given in figure no 4. For ^{226}Ra in natural samples the average transfer fraction is 0.35% and for dried samples 5.09%. For ^{232}Th the average transfer fraction is 1.63% for natural samples and 5.23% for dried samples. For ^{40}K the results are very different compared to ^{226}Ra and from ^{232}Th . An average transfer fraction of 51.09% was obtained for the natural samples and 511.58% for dried samples. Although also the soil contains a much higher ^{40}K activity relative to ^{226}Ra and ^{232}Th (about one order of magnitude – see Fig 2), the ^{40}K activity in foodstuff is enhanced further to a factor of about 100 relative to ^{226}Ra and ^{232}Th . The reason for this seems to be that in the growing process fertilizers containing significant portions of potassium are added to the soil. Part of the potassium excess is absorbed by the plants (increasing its ^{40}K activity), but most of it is washed away from the soil by irrigation or rain and the ^{40}K content in the soil is reduced, leading to an excess in the ^{40}K ratio between plants and soil.

CONCLUSIONS

Gamma-ray spectrometry was used to determine the NORM radionuclide content in foodstuff samples and in cultivated soils in Israel during the year 2013. The transfer fractions from soil to foodstuff were determined as well, and excess values were found for ^{40}K , most probably due to added fertilizers which contain significant amounts of potassium. The activity measured in the checked foodstuff is very low and is in the general frame of values published in the literature [4,6,7].

REFERENCES

1. L.H.Staven, K.Rhoads, B.A. Napier and D.L. Strenge, "A Compendium of Transfer Factors for Agricultural and Animal Products". PNNL-13421, June 2003.
2. W.E. Kennedy, D.L. Strenge. "Residual Radioactive contamination from Decommissioning: Technical Basis for Translating Contamination Levels to Annual Total Effective Dose Equivalent". NUREG-5512 (PNL-7994), Pacific Northwest Laboratory, Richland, Washington. 1992.
3. Isotrak Nuclitec Eckert & Ziegler, Germany, 1 liter Marinelli beaker type 1N FZ-1262-001.
4. N.Lavi, G.Golob, Z.B. Alfassi. "Monitoring and surveillance of radio-caesium in cultivated soils and foodstuff samples in Israel 18 years after Chernobyl disaster". Radiation Measurements. 41, (2006) 78-83.
5. IAEA Technical Reports Series no. 295. "Measurement of Radionuclides in Food and the Environment" – a guidebook, IAEA library 0-000002-316-30, 1989.
6. T.V. Ramachadran, U.C. Mishra. "Measurement of Natural Radioactivity Levels in Indian Foodstuffs by Gamma Spectrometry". Appl. Radiat. Isot. 40, (1989) 723-726.
7. P.R. Maul, J.P. O'Hara. "Background Radioactivity in Environmental Materials". J. Environ. Radioactivity. 9, (1989) 265-280.

Using Cherenkov Counting For Fast Determination of $^{90}\text{Sr}/^{90}\text{Y}$ Activity in Milk

S. Tsroya¹, B. Dolgin¹, U. German¹, O. Pelled¹, Z. B. Alfassi²

¹ Nuclear Research Center Negev, P.O.B. 9001, 84190 Beer Sheva, Israel

² Ben-Gurion University of the Negev, 84105 Beer Sheva, Israel

1. INTRODUCTION

^{90}Sr is one of the main long-lived fission products, and it is transferred into human body primarily by food, with milk being a substantial contributor. Due to its biochemical similarity to calcium, most strontium is efficiently incorporated into bone tissues. ^{90}Sr is characterized by a long physical half life (28.8 y) and decays by beta particles with an E_{max} of 0.546 MeV to ^{90}Y . This daughter isotope has a half life of 64 h and decays into ^{90}Zr by beta particles with an E_{max} of 2.284 MeV.

The milk components produce a high turbidity and light attenuation, causing a significant decrease of the counting efficiency in liquid scintillation counting (LSC) systems, mostly used for beta emitters detection. Most methods proposed in the past are time-consuming, as they are based on several stages of chemical and physical treatments, including precipitation, ashing, ion exchange and extraction (Wikins et al., 1984, Porter et al, 1961, Kimura et al., 1979).

When measuring $^{90}\text{Sr}/^{90}\text{Y}$ activity by Cherenkov counting, most of the Cherenkov radiation is produced by ^{90}Y (about 98.6%), due to the much higher energy of its beta particles relative to these from ^{90}Sr . The counting efficiency varies strongly with color quenching, at a greater extent than in standard liquid scintillation counting (L'Annunziata, 2012), and therefore the quench correction is critical. The "external source area ratio" (ESAR) quench correction method was applied to measure $^{90}\text{Sr}/^{90}\text{Y}$ activities in aqueous samples with a wide range of quenching levels (Tsroya et al., 2009). This method was proved to be superior to all other quench correction methods (Tsroya et al., 2012) and is applicable also for determination of $^{90}\text{Sr}/^{90}\text{Y}$ in human urine (Tsroya et al., 2013). In the present work the applicability of the ESAR method to measurement of $^{90}\text{Sr}/^{90}\text{Y}$ activities in milk and some of its products was investigated.

2. MATERIALS AND METHODS

2.1 The ESAR method

A Quantulus 1220TM LSC system (manufactured by Wallac Oy, Finland) is operated at Soreq Nuclear Research Center, Israel. It has an external ^{152}Eu source, emitting radiation of sufficient energy to produce Cherenkov radiation. The ESAR method was developed for aqueous samples and is described in detail in a former publication (Tsroya et al., 2009). It is also described shortly in the latest edition of Handbook of radioactivity analysis (L'Annunziata, 2012).

The experiments in the present work were performed using a $^{90}\text{Sr}/^{90}\text{Y}$ calibrated and certified liquid standard with a specific activity of 4070 Bq/g of ^{90}Sr in 0.1 M HCl solution, provided by Amersham International. Polyethylene vials were used, as it is generally accepted that they are superior to glass vials for Cerenkov counting (Takiue (1996), L'Annunziata (2002)). The vials volume was 20 ml.

2.2 The milk samples

A set of representative milk samples was collected from the local supermarkets. The set contained 1% fat fresh and 1% UHT pasteurized skimmed cow milk (produced by Tnuva dairies), 3% fresh and UHT pasteurized cow milk, 3.7% fresh whole goat milk, about 6% raw sheep milk, 8% buffalo milk, and two cream types with different fat content: 15% (cooking cream) and 32% (whipping cream). A second set was also used, which contained 2% fat enriched milk, 3% fresh milk, 3.6% natural milk and 10% cooking. The fat contents mentioned above are as indicated on the packages.

3. RESULTS AND DISCUSSION

3.1 The parameters analysis

Due to the opaqueness of the milk bulk which is influenced by its complex composition and the variety of the milk matrix characteristics, it is expected that the counting efficiency will be influenced by the specific

properties of the various milk products (density, fat content, conductivity, etc.) in different ways. Six parameters were chosen for investigation in the present work: fat content, electrical conductivity, specific gravity, transmittance at 420nm, transmittance at 650 nm and the ESAR quench indicator parameter. The efficiency was the response function. The Minitab statistical software tool (Minitab 16) automatically performs a variance analysis for each factor and the interaction between them. For a quantitative analysis, a best subsets linear regression of the efficiency using different parameters sets (variants) was performed. The regression results obtained are presented in Table 1. The parameters (predictors) included in each specific model are marked in the property columns. The results for one parameter presenting a simple linear regression are given only for illustration, to stress their relative values.

Table 1. The best subsets regression results

Variants	R ² [%]	Stdev	Property (predictor)					
			Fat content	Specific gravity	Conductivity	Transmission 450nm	850nm	ESAR
1	46.1	2.81	√					
1	94.7	1.00						√
2	96.7	0.82		√				√
3	97.0	0.80	√	√				√
4	97.7	0.72	√			√	√	√
5	98.2	0.67	√		√	√	√	√
6	98.2	0.70	√	√	√	√	√	√

A best fitting line to the experimental points will be obtained when the correlation (R²) of the function (efficiency) expressed by the variables (predictors) in the model is as large as possible. "Stdev" is the standard deviation, representing the random experimental error in the efficiency values, and it should be as small as possible.

As seen in Table 1, for ESAR alone the R² is about 95%, more than twice the value for fat alone. Based on the experimental data and the defined statistical criteria, the best linear regression should include 5 variables, but we can see that adding more variants to the fit has only a minor influence on the R² compared to ESAR alone.

3.2 The contribution of ⁴⁰K

The ⁴⁰K contribution to Cherenkov counting can be estimated by assessing separately the activity of ⁴⁰K by HPGe (High Pure Germanium) gamma detector and converting the activity to counts using the efficiency calibration function.

The actual concentration of potassium in milk may depend on several factors, as the kind of milk giving animal and its diet. 8 samples from each of the milk types investigated in the present work were analyzed by γ spectrometry using an HPGe system with calibrated containers. The counting time was 100,000 s for each sample. The average activity concentration of ⁴⁰K for the different milk products is presented in Table 2.

Table 2: ⁴⁰K activities in different milk products

Milk type*	Activity[Bq/L]
1% - skimmed	54.0 ± 10.4
1% - skimmed UHT	38.6 ± 6.4
3%	50.9 ± 7.1
3% - UHT	57.5 ± 7.3
3.7% - goat milk	49.3 ± 7.4
6% - sheep raw milk	42.1 ± 5.9
8% - buffalo milk	29.8 ± 6.1
15% - cooking cream	60.4 ± 9.2
32% - whipping cream	≤MDA (18.1 Bq/L)

- Cow milk if not otherwise noted

The average activity in all types of milk products (except the 32% cream), is 47.8±10.3 Bq/l. The standard deviation within each group is up to about 20%. No significant variation of ⁴⁰K activity can be observed for all milk products examined within the given uncertainties. The efficiency of the ⁴⁰K Cherenkov counting was

estimated by measuring milk samples after adding a known amount of potassium. As each milk product has a different composition, the quenching effect will be type-dependent, therefore, the ^{40}K contribution will also be type-dependent. ^{40}K counting efficiency was obtained as a function of the relative ESAR index of the different milk products. The ^{40}K counting efficiency range is from 2.3% (for 32% fat cream) to 7.3% (for 1% skimmed milk).

4. $^{90}\text{Sr}/^{90}\text{Y}$ activity determination in milk samples

4.1 Application of the ESAR quench correction method

Samples were prepared by adding 16 Bq of $^{90}\text{Sr}/^{90}\text{Y}$ (as solution) to 20 ml from the different milk types. A linear function was fitted to the efficiency results obtained for all milk samples, and Fig. 5 presents the ESAR dependent efficiency curve. The full line in Fig. 5 relates to all natural milk samples, starting with 1% fat content up to 6% (raw sheep milk). The striped line includes the milk cream products, with 15% and 32% fat content. Standard $^{90}\text{Sr}/^{90}\text{Y}$ calibration solutions were added to 3% fat milk samples which were not used in the preparation of the calibration curve. These samples are shown in Fig.5 as open circles.

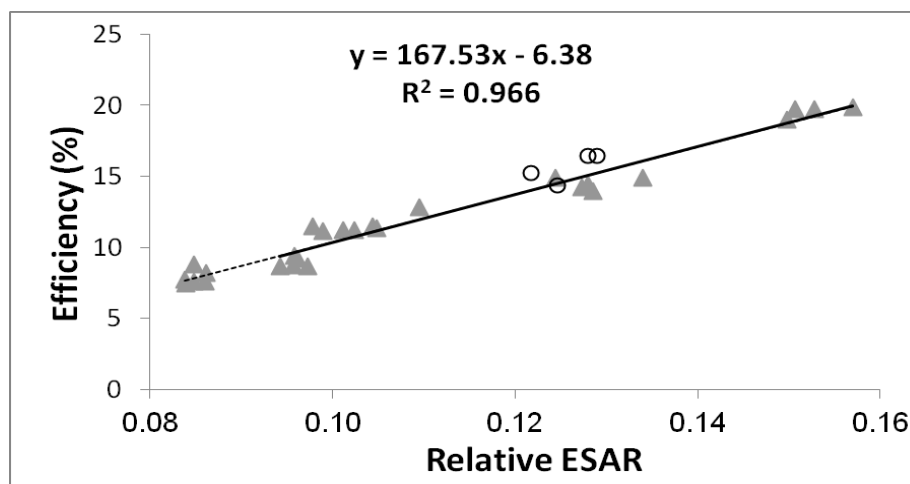


Figure 5. Correlation of the Cherenkov counting efficiency of $^{90}\text{Sr}/^{90}\text{Y}$ to the ESAR quenching indicator parameter in milk samples.

By using the quenching efficiency curve given in Fig 5, the $^{90}\text{Sr}/^{90}\text{Y}$ activity in any milk sample and milk products can be determined, without considering its source or fat content. The evaluated activities and the difference from the known activity added to "unknown" samples are presented in Table 3.

Table 3: ^{90}Sr activity determination in four different kinds of milk products (3 natural drinking milk sorts and a 10% fat cooking cream).

<u>Fat [%]</u>	<u>Actual activity [Bq]</u>	<u>Evaluated activity [Bq]</u>	<u>Difference [%]</u>
2	8.29 ± 0.18	8.41 ± 0.30	1.45
2	8.29 ± 0.18	8.07 ± 0.29	-2.65
2	16.59 ± 0.36	18.02 ± 0.64	8.62
2	16.59 ± 0.36	17.47 ± 0.62	5.30
3	8.29 ± 0.18	8.53 ± 0.64	2.90
3	8.29 ± 0.18	8.79 ± 0.66	6.03
3	16.59 ± 0.36	16.32 ± 1.22	-1.63
3	16.59 ± 0.36	17.91 ± 1.34	7.96
3.6	8.29 ± 0.18	8.64 ± 1.41	4.22
3.6	8.29 ± 0.18	8.70 ± 1.42	4.95
3.6	16.59 ± 0.36	15.67 ± 2.56	-5.55
3.6	16.59 ± 0.36	17.23 ± 2.81	3.86
10	8.29 ± 0.18	10.02 ± 2.80	20.87
10	8.29 ± 0.18	10.27 ± 2.87	23.88
10	16.59 ± 0.36	21.15 ± 5.90	27.49
10	16.59 ± 0.36	20.51 ± 5.72	23.63

For the natural milk samples (2%, 3% and 3.6% fat), the mean difference between the actual and real activity is about 4% and the results for all samples are within 8.6% from the target values. For the 10% cooking cream there is an average difference of about 24% from the target values. Although this difference is within the uncertainty range of the evaluated values, there seems to be a bias (as all differences are in the same direction).

4.2 The limit of detection

Due to its simplicity and short processing time, the Cherenkov counting method is especially suitable for emergency situations. However, if assessing ^{90}Sr activity in milk and its products without applying any pre-concentration procedure, a relatively high MDA (minimum detectable activity) is expected. The applicability of the proposed method was checked against the corresponding regulations for emergency situations. The results are presented in Fig. 6 for 4 hours counting time.

The highest MDA for drinking milk is for the buffalo milk (containing the maximum fat percent in natural drinking milk - 8%), which is about 108 Bq/l, lower than both limits of the FDA (160 Bq/kg) and the European regulations (125 Bq/l - EU No 961/2011, FDA 1998). For the most popular and widespread drinking milk products (1%-3% fat content) the MDA for ^{90}Sr when applying direct Cherenkov counting for 4 h is much below 100 Bq/l. For the processed milk products (creams) with the highest fat content of 32% the MDA values approach the limiting levels, but due to their related high uncertainties applying the ESAR index in this case seems not to be applicable.

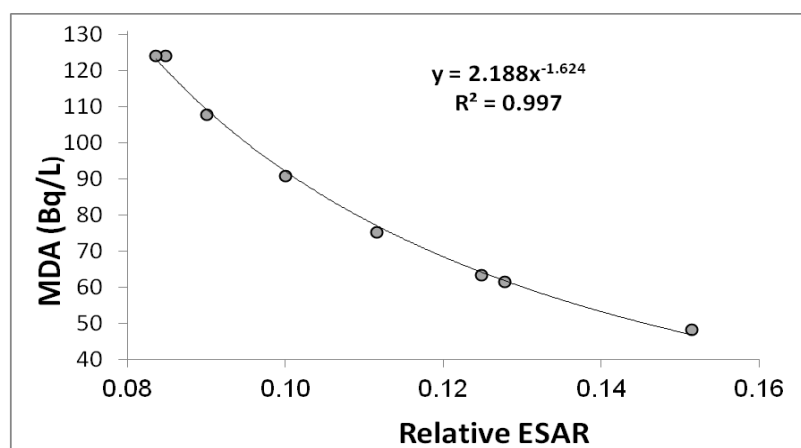


Figure 6. The ^{90}Sr MDA levels for 4 h counting time in milk products for various ESAR values.

5. CONCLUSIONS

Cherenkov counting is a fast, reliable and non-destructive method for detecting high energy beta emitters in aqueous solution, but it is sensitive to quench correction, especially for colored or semi-opaque media as milk. The ESAR quench correction index is shown to work well also for milk, in spite of the high turbidity and strong light attenuation. The ESAR index is the main parameter which uniquely defines the counting efficiency for all kinds of milk tested. There are no major differences in the ^{40}K content in different sorts of drinking milk, enabling a direct evaluation of the $^{90}\text{Sr}/^{90}\text{Y}$ based only on the ESAR value.

REFERENCES

- EU No 961/2011. Special conditions governing the import of feed and food originating in or consigned from Japan following the accident at the Fukushima nuclear power station and repealing Regulation (EU) No 297/2011. EU commission implementing regulation of 27.11.2011. L 252/10.
- FDA 1998. Food and Drug Administration. Accidental Radioactive Contamination of Human Food and Animal Feeds: Recommendations for State and Local Agencies. Federal Register 63:43402-43403; 1998.
- Kimura, T., Iwashima, K., Ishimori., T., Hamada, T., 1979, Separation of Strontium-89 and -90 from Calcium in Milk with a Macrocyclic Ether. Anal. Chem. 51, 1113-1116.
- L'Annunziata, M.F., Passo, C.J., 2002. Cherenkov counting of yttrium-90 in the dry state; correlations with phosphorus-32 Cherenkov counting data. Appl. Radiat. Isot. 56, 907-916.
- L'Annunziata, M.F., 2012. Cherenkov Counting. pp. 935-1019, in "Handbook of radioactivity analysis", Third ed. (M.F. L' Annunziata, Ed.) Elsevier, Oxford.
- Minitab 16, <http://www.minitab.com/en-US/products/minitab/default.aspx>

- Porter, C., Cahill, D., Sshneider, R., Robbins, P., Perry, W., Kahn, B., 1961. Determination of Strontium-90 in Milk by an Ion Exchange Method. *Anal. Chem.* 33, 1306-1308.
- Takiue, M., Natake, T., Fujii, H., Aburai, T., 1996. Accuracy of Cerenkov Measurements Using a Liquid Scintillation Spectrometer. *Appl. Radiat. Isot.* 47, 123-126.
- Tsroya S., Pelled, O., German, U., Marco, R., Katorza, E., Alfassi, Z.B., 2009. Color quench correction for low level Cherenkov counting. *Appl. Radiat. Isot.* 67, 805-808.
- Tsroya S., Pelled, O., German, U., Katorza, E., Abraham A., Alfassi, Z.B., 2012. A comparative study of color quenching correction methods for Cherenkov counting. *Appl. Radiat. Isot.* 70, 397-403.
- Tsroya S., German, U., Pelled, O., Katorza, E., Alfassi, Z.B., 2013. Determination of $^{90}\text{Sr}/^{90}\text{Y}$ activity in urine samples using Cherenkov counting. *Appl. Radiat. Isot.* 73, 12-16
- Wilkins, B.T., Green, N., Dodd, N.J., Smith, D.M., 1984. Concentrations of Strontium-90 and Cesium-137 in milk produced in the Channel Islands. *Rad. Prot. Dosim.* 8, 253-255.

Posters (Wednesday, February 12, 2014 15:30)

Study of Cleanup Procedures for Contaminated Areas: Examination of Rubidium as a Surrogate to Cesium

O. Paz Tal, R. Bar Ziv, R. Hakmon, E. J. C. Borojovich, A. Nikoloski, T. Ohaion, R. (Yanosh) Levi, I. Yaar

Nuclear Research Center Negev, POB 9001 Beer Sheva 84190, Israel

A radiological weapon, or radiological dispersion device (RDD), is designed to spread radioactive materials (^{137}Cs , ^{60}Co , ^{241}Am , ^{252}Cf , ^{192}Ir , ^{238}Pu , ^{90}Sr , ^{226}Ra , etc) over a large area, in order to cause severe contamination. The dispersed radioactive material can be strongly bound to surfaces if not effectively removed shortly after the event.

An effective decontamination agent for such cases is the commercial polymer Decongel-1101¹. It can be applied onto contaminated surfaces by brushing or spraying. Upon drying, it forms stable films that can be peeled off the surface, together with most of the contaminating materials.

One of the most dangerous isotopes that can be used by terrorist to make a RDD is ^{137}Cs ². Therefore, it is important to examine the effectiveness of the polymer Decongel-1101 in removing it. Due to the difficulty in working with ^{137}Cs in large scale experiments, It was suggested to replace it with the short lived radioisotope ^{86}Rb (~18.6 days). This isotope is a good simulator for ^{137}Cs , having similar chemical properties and migration behavior.

This work is aimed at verifying whether ^{86}Rb can indeed serve as a simulator to ^{137}Cs in cleanup procedures of large contaminated areas. The first step will be a small scale comparison, on porous and non-porous surfaces, of the decontamination efficiency of this procedure tested on Rb versus Cs. These elements were spread on the examined surfaces as known concentration solutions of natural Rb and Cs salts. The decontamination efficiency was measured by peeling off the dry polymer and measuring the concentrations of the two elements in the polymer by various analytical methods.

¹<http://decongel.com/documents/1101%20Product%20Data%20Sheet%20v080612.pdf> (Last accessed on 18.1.14).

²J.L.Conca, J.R. Wischnewsky and M.D. Johnson, Reducing the Threat of a Serious ^{137}Cs Dirty Bomb, Proceedings of the DHS Conference; Working Together – Research & Development Partnerships in Homeland Security, the Seaport Hotel and World Trade Center, Boston, MA, April 27-28 (2005).

A Computerized QC Analysis of TLD Glow Curves for Personal Dosimetry Measurements Using TagQC Program

S. Primo⁽¹⁾, H. Datz⁽¹⁾ and A. Dar⁽²⁾

⁽¹⁾ *Soreq Nuclear Research Center, Yavne, Israel*

⁽²⁾ *Empiric Technologies consulting (e.t.c) Ltd. Modiin, Israel*

INTRODUCTION

The External Dosimetry Lab (EDL) at the Radiation Safety Division at Soreq Nuclear Research Center (SNRC) is ISO 17025 certified and provides its services to approximately 13,000 users throughout the country from various sectors such as medical, industrial and academic. About 95% of the users are monitored monthly for X-rays, γ and β radiation using Thermoluminescence Dosimeter (TLD) cards that contain three LiF:Mg,Ti elements and the other users, who work also with thermal neutrons, use TLD cards that contain four LiF:Mg,Ti elements. All TLD cards are measured with the Thermo 8800pc reader.⁽¹⁾

Suspicious TLD glow curve (GC) can cause wrong dose estimation so the EDL makes great efforts to ensure that each GC undergoes a careful QC procedure.⁽³⁾ The current QC procedure is performed manually and through a few steps using different softwares and databases in a long and complicated procedure: EDL staff needs to export all the results/GCs to be checked to an Excel file, followed by finding the suspicious GCs, which is done in a different program (WinREMS), According to the GC shapes (Figure 1 illustrates suitable and suspicious GC shapes) and the ratio between the elements result values (see graph in Figure 2), the inspecting technician corrects the data.⁽³⁾

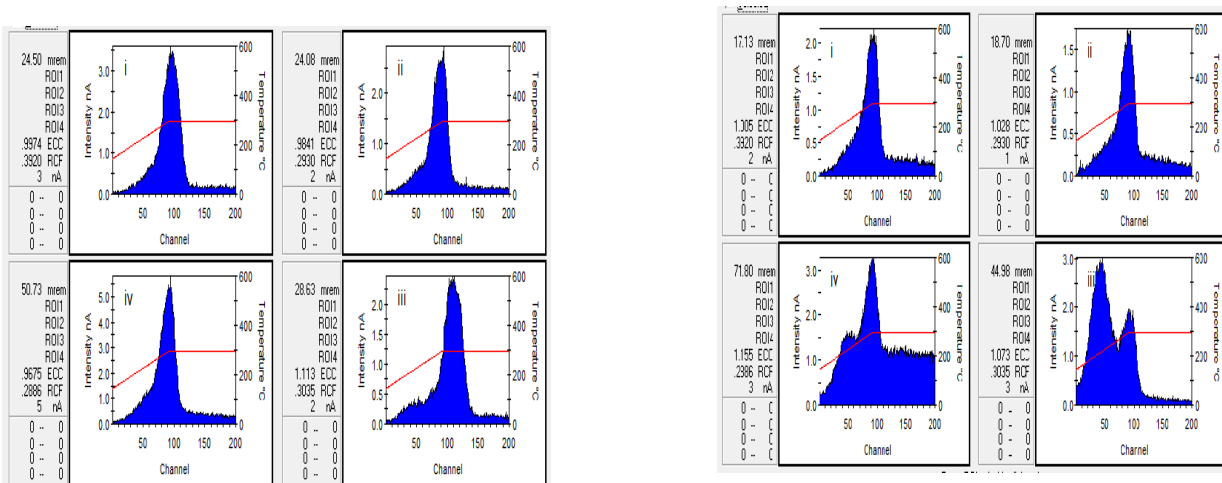


Figure 1. Typical LiF: Mg, Ti glow curve following ^{137}Cs irradiation (a) suitable GC; (b) suspicious GC

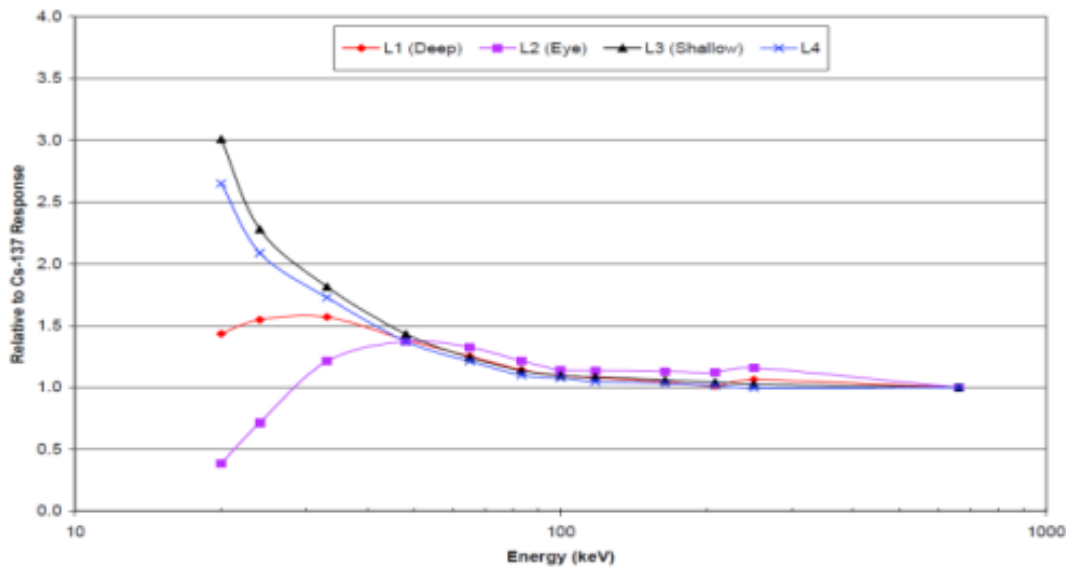


Figure 2. LiF:Mg,Ti TLD elements response⁽²⁾

The motivation for developing the new program is the complicated and time consuming process of our the manual procedure to the large amount of TLDs each month (13,000), similarly to other Dosimetry services that use computerized QC GC analysis.^(4,5) it is important to note that only ~25% of the results are above the EDL recorded level (0.10 mSv) and need to be inspected. Thus, the purpose of this paper is to describe a new program, TagQC, which allows a computerized QC GC analysis that identifies automatically, swiftly, and accurately suspicious TLD GC.

TagQC program description.

The source file is copied (to avoid damage of the raw data) to a destination file and all the corrections are made and saved on it.

A morphologic classifier is embedded in TagQC, for pointing out "*Suspicious*" GC using the following general method:

- a. A canonic GC is defined (to which the analyzed GC is compared. during the classifier).
- b. Each GC is first canonized & passes a noise filter. a too high noise figure in a GC renders it as "*Suspicious*".
- c. The location and shape of the main lobe of the GC is checked, in several parameters: the start (first channel) of the lobe, the end of the lobe (last channel) - both using the wavefront, The slopes of the front and end of the lobe, the width of the lobe, its similarity to a parabola (difference from quadratic fit), and the shift of the peak from its canonic location. Finally the skewness and kurtosis of the GC is compared to the canonic ones. Any diversion from the canonic parameters that are too large renders the analyzed GC *suspicious*.
- d. The last step is comparison between the values of the parameters of the various elements on the tag (if possible), and pointing out outliers as "*suspicious*".

Once the above process is complete, the program automatically indicates the faulty GC by painting the suspicious element with a different color (red), as shown in Figure 3.

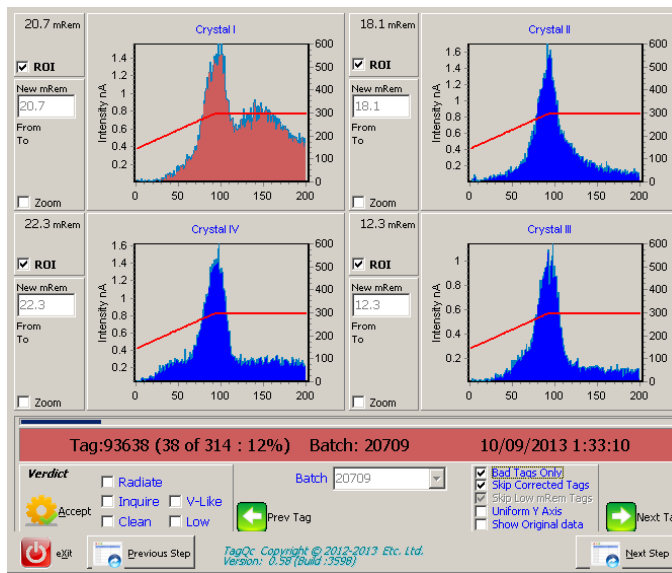


Figure 3. TagQC screen with marked suspicious GC (upper left GC)

The operator can choose from a number of options to correct the abnormal data:

1. Use ROI (region of interest) by dragging the GC's borders to fit the correct GC and dose value (as shown at the bottom of Figure 4).
2. Select "Low" check box to correct all the doses to a value which is set at the preferences page, as a limit of detection (as shown at the bottom of Figure 3).
3. Selecting a specific check box, when only the third TLD element is suspicious, to determine the value of the third element to the average dose of the first and second elements. Shown in Figure 5.

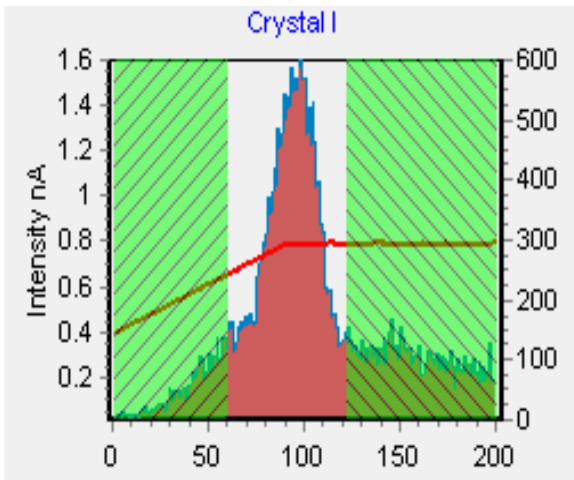


Figure 4. TagQC ROI correction

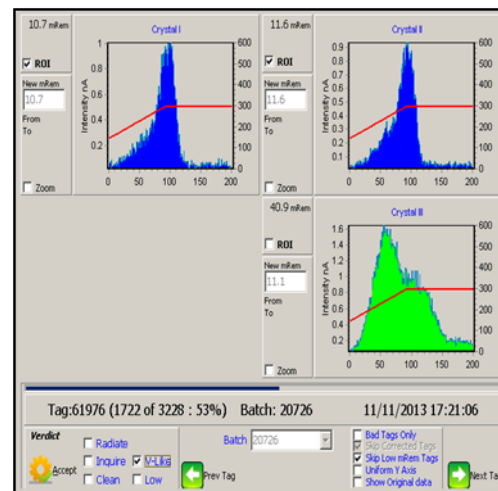


Figure 5. 3rd element value correction

In addition to abnormal data correction, the operator can perform more QC steps:

1. Selecting the "Irradiate" checkbox, the TLD will be manually exposed to a known dose and re-measured prior to the shipment to the user.
2. Selecting the "Inquire" checkbox will e-mail a print screen of the GC to the EDL supervisor for a second opinion and approval.

When all the TLD cards are checked, a log report is issued containing all the information of any card that underwent results intervention.

CONCLUSION

TagQC is a useful program that automatically will indicate suspicious TLD elements results and allows correcting the data in a reliable and fast way. In addition, it will allow the EDL staff to view and to check only the suspicious TLD results, which will make the QC procedure much faster and accurate.

The TagQC program is currently being examined at the EDL. At the completion of the examination and validation, TagQC will be used in routine activities and thus will improve the efficiency and quality assurance of EDL service.

REFERENCES

1. Model 8800 Automatic TLD Card Reader with WinREMS Operator's Manual. Publication No 8800-W-O-1200-006.
2. WinAlgorithms: Dose calculation Algorithm for 8805, 8810, 8814, and 8815 Dosimeters user's manual. Publication No. ALGM-W05-U-0903-001
3. LiF:Ti, Mg Methodology - Guidelines for GC Analysis. Publication No. LiFM-G-C-1091-001-Bicron/Saint-Gobain/Norton Industrial Ceramics Corporation.
4. Harvey.A.John, Rodriguse L.Miesher, J.Kearfott.J. *Computrized glow curve analysis (GCA) method for WinREMS thermoluminescent dosimeter data using MATLAB*. Applied Radiation and Isotopes **69**, 1282-1286, (2011).
5. Chase, W.J, Bezaire, M.D, Vanderzwet, F.P., Taylor, C.E., *A glow curve analyzer (GCA) for routine analysis of personnel thermoluminescent dosimeter results*. Radiation Measurement **43**, 621-625, (2008).

Electronic and Magnetic Properties of NpNi₅

A. Hen,^{1,2} E. Colineau,¹ R. Eloirdi,¹ J.-C. Griveau,¹ J.-P. Sanchez,⁴
A. B. Shick,^{1,5} I. Halevy,^{2,3} I. Orion,² and R. Caciuffo¹

¹European Commission, Joint Research Centre, Institute for Transuranium Elements, Postfach 2340, D-76125 Karlsruhe, Germany

²Ben Gurion University, IL84105 Beer-Sheva, Israel

³Nuclear Research Center Negev, P.O. Box 9001, IL84190 Beer-Sheva, Israel

⁴SPSMS, UMR-E CEA/UJF-Grenoble 1, INAC, FR-38054 Grenoble, France

⁵Academy of Sciences of the Czech Republic, Na Slovance 2, CZ-182 21 Prague, Czech Republic

The physical properties of binary actinides and transition metal alloys are of great importance for the safety assessment of nuclear fuels. Since transition metals are major components of the cladding material of fuel rods (stainless steel, HT-9 etc.), the physical properties of those compounds formed by accidental fuel-cladding interactions could have limiting factors on the fabrication, life time operation and disposal of nuclear fuels. Binary compound of the form ReT₅ (Re = rare earth, T = Transition metal) has been in the focus of interest mainly because of their magnetic properties (small Re to T stoichiometric ratio, large spontaneous magnetization and high Curie temperature) and their ability to store large amount of hydrogen per formula unit (f. u.)

Reported in 1997 [1], NpNi₅ was synthesized and identified to have hexagonal (D_{2d}) CaCu₅ crystallographic structure, with room-temperature lattice parameters $a = 8.3107(1)$ Å and $c = 8.1058(1)$ Å. In the present study, NpNi₅ has been synthesized and characterized by means of powder x-Ray diffraction (**Fig. 2** left panel), Superconducting – Quantum – Interference – Device magnetometry (SQUID, **Fig. 2** right panel), ²³⁷Np Mössbauer spectroscopy [2] (**Fig. 3** left panel) and specific heat measurements (**Fig. 3** right panel).

Magnetization curves indicate that NpNi₅ is a ferromagnet ($T_C \sim 16$ K), fit of the paramagnetic part to the Curie–Weiss law ($C \sim 1.7$ emu·K/mol, $\theta_P \sim 14.6$ K) gives an effective moment $\mu_{\text{eff}} \sim 3.7 \mu_B$ per f.u. – no magnetization hysteresis was observed. The isomer shift ($\delta_{\text{IS}} \approx -11.1$ mm/s vs. NpAl₂) observed in Mössbauer spectra suggests a tetravalent Np state, but considering the influence of conduction electrons we determine a Np³⁺ (5f⁴ configuration) oxidation state. The hyperfine field determined by fitting of the spectra (~ 439 T) gives an ordered moment at the Np site $\mu_{\text{Np}} \sim 2 \mu_B$ per Np ion ($1 \mu_B = 215$ T [3]). The magnetic transition is clearly visible in the temperature dependence of the specific heat, and a magnetic phase diagram as a function of temperature and external magnetic field was generated.

In this communication we will present the results obtained and discuss them in the light of theoretical considerations.

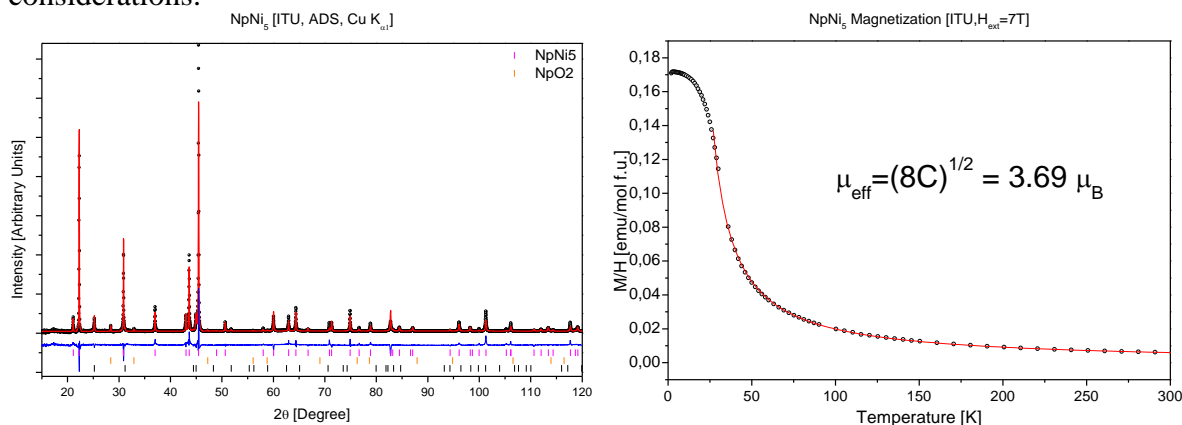


Fig. 2 Left: Powder x-ray diffraction pattern of NpNi₅, black dot – measured data, red line – fitted profile, blue line – difference profile, vertical tick – angular position of Bragg peaks. **Right:** Temperature dependence of the magnetic susceptibility, red line – fit to the Curie-Weiss law.

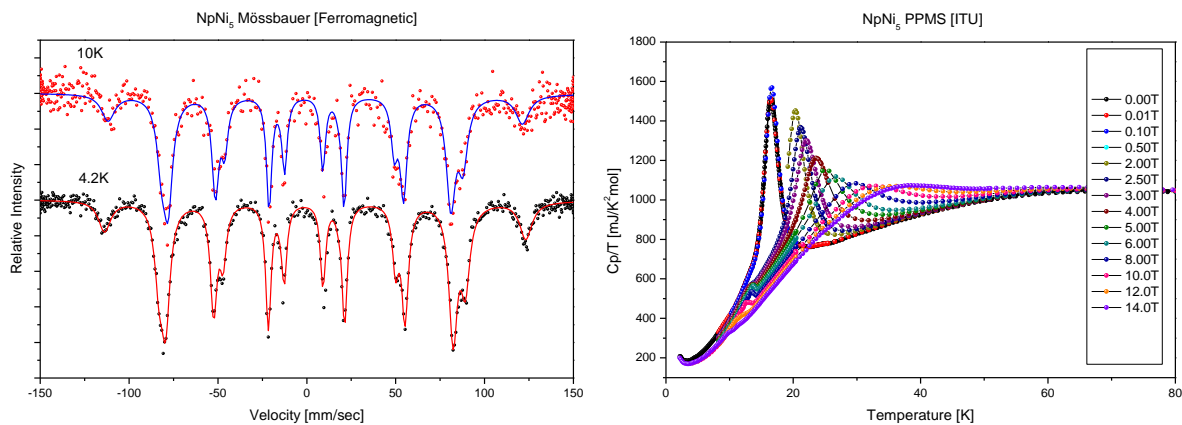


Fig. 3 **Left:** Mössbauer spectra taken in the ferromagnetic region, dots – measured data, lines – fits of hyperfine fields to the measured data, spectrum is composed of one hyperfine field as expected from the crystallography.

Right: Normalized heat capacity as a function of temperature in various external magnetic fields.

ACKNOWLEDGEMENTS

The high purity Np metals required for the fabrication of the compound were made available through a loan agreement between Lawrence Livermore National Laboratory and ITU, in the frame of a collaboration involving LLNL, Los Alamos National Laboratory and the US Department of Energy.

REFERENCES

- [1] M. Akabori et al. , Journal of Alloys and Compounds 257 (1997) 268-272.
- [2] R.L. Mössbauer., Zeitschrift für Physik, Bd. **151**, S. 124-143 (1958).
- [3] B. D. Dunlap and G. M. Kalvius, in Handbook on the Physics and Chemistry of the Actinides, edited by A. J. Freeman and G. H. Lander (North-Holland, Amsterdam, 1985), Vol. 2, p. 329.

Posters (Wednesday, February 12, 2014 15:30)

Radioactive Contamination Estimation from Micro-Copters or Helicopter Airborne Survey: Simulation and Real Measurements

I. Halevy, M. Ghelman, Y. Yehuda-Zada, A. Manor, A. Sharon and I. Yaar

Nuclear Research Center – Negev, P. O. Box 9001, Be'er-Sheva 84190, Israel

One of the main advantages of acquiring aero-radiometric measurements lies in the high collection rate of data over large areas and rough terrain. Typical aero-radiometric system records and saves gamma ray spectrum, correlated with the GPS derived location information in regular time intervals of one to two seconds. Such data can be used to locate radiation anomalies on the ground, map ground contamination or track a radioactive airborne plume. Acquiring spectral data of this type allows separation of natural radioactivity from that of man-made sources and identification of specific isotopes, natural or man-made.

The data acquisition can be done by helicopter or micro-copters at wide range of heights from few meters to few kilometers.

Usually the flight altitude will be kept constant to make the data analysis easier. Rough terrain will jeopardize that assumption. The radioactive particles are not always on the ground, they can be in a cloud above the ground or on roofs or trees. Speed of survey with a helicopter is in the range from hovering to ~120 Knots, while the speed of micro-copters is much lower, from hovering to ~30 Knots. Both, the helicopter and the micro-copters are suffering from limited abilities while severe weather conditions.

The main advantages of micro-copters are the ability to fly even indoor and without exposing the measuring team to radiation or extra flight risks.

When the survey is done or even during the survey, the main challenge is to estimate the radiation field and the contamination in the scene.

An iterative algorithm was suggested to estimate the radioactive contamination for analyzing an airborne survey [1].

In that work this algorithm will be tested on real scenario while spreading radioactive material, ^{99m}Tc , simulating an RDD events by explosion [2, 3].

In those simulations it is clear that a lower-height survey can improve the space resolution. Slow flight will improve the detection sensitivity but will take much more time.

This survey can be for detection only or it can bring also isotope identification by energy resolution. In our software, four energies windows can be set as our PDS-1000 flying detector.

We simulated a spread of radioactive sources on a radioactive background. A radioactive field at a survey height was calculated. From that data we found the spread of radioactive sources by our iterative algorithm.

There is no clear proof that the results are unique. The highest background we have the less significant map of spread radioactive sources can be achieved.

Few new results of simulation and real surveys are depicted in the next figures.

Mikro-Kopter / multi-rotor

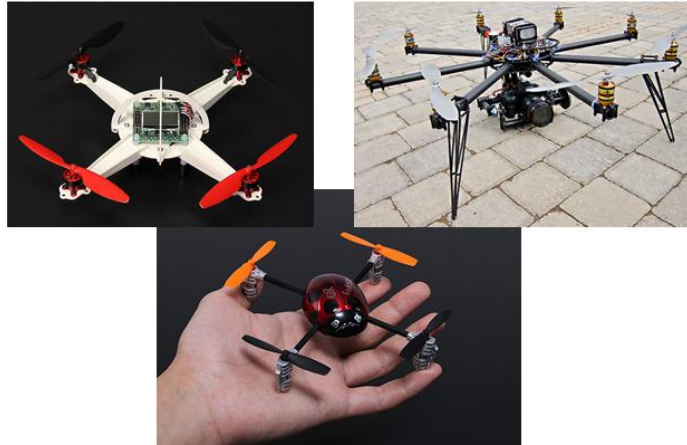
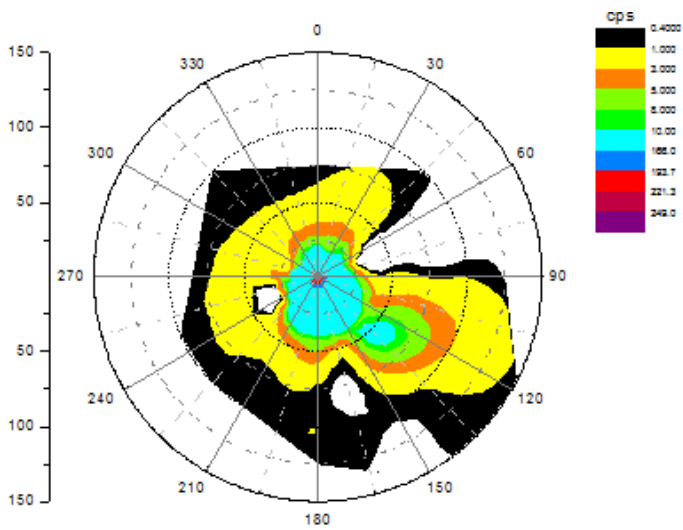


Figure 1: Mikro-Kopter / multi-rotor (upper)
Airborne radiation survey of ^{99m}Tc from “Green field” (Open field) test compared with ground survey (lower) [2].



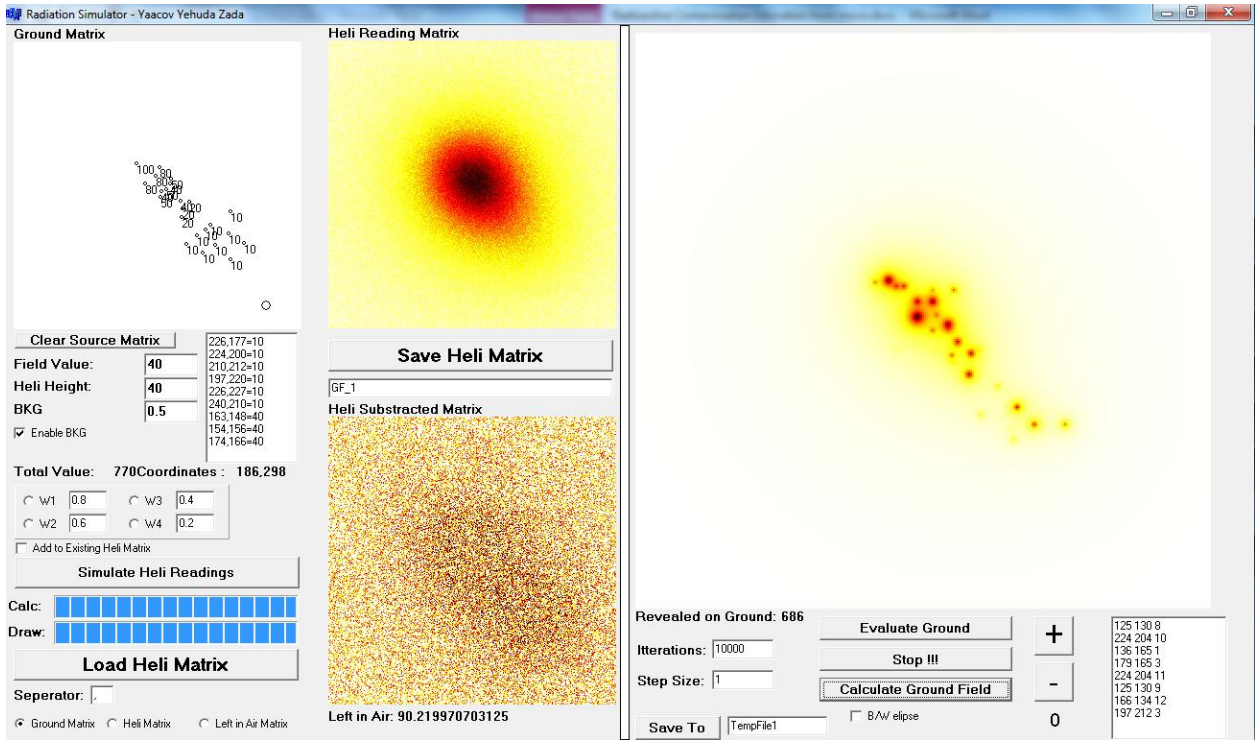


Figure 2: Airborne radiation survey analysis of ^{99m}Tc from “Green field” (Open field) test compared with ground survey [2].

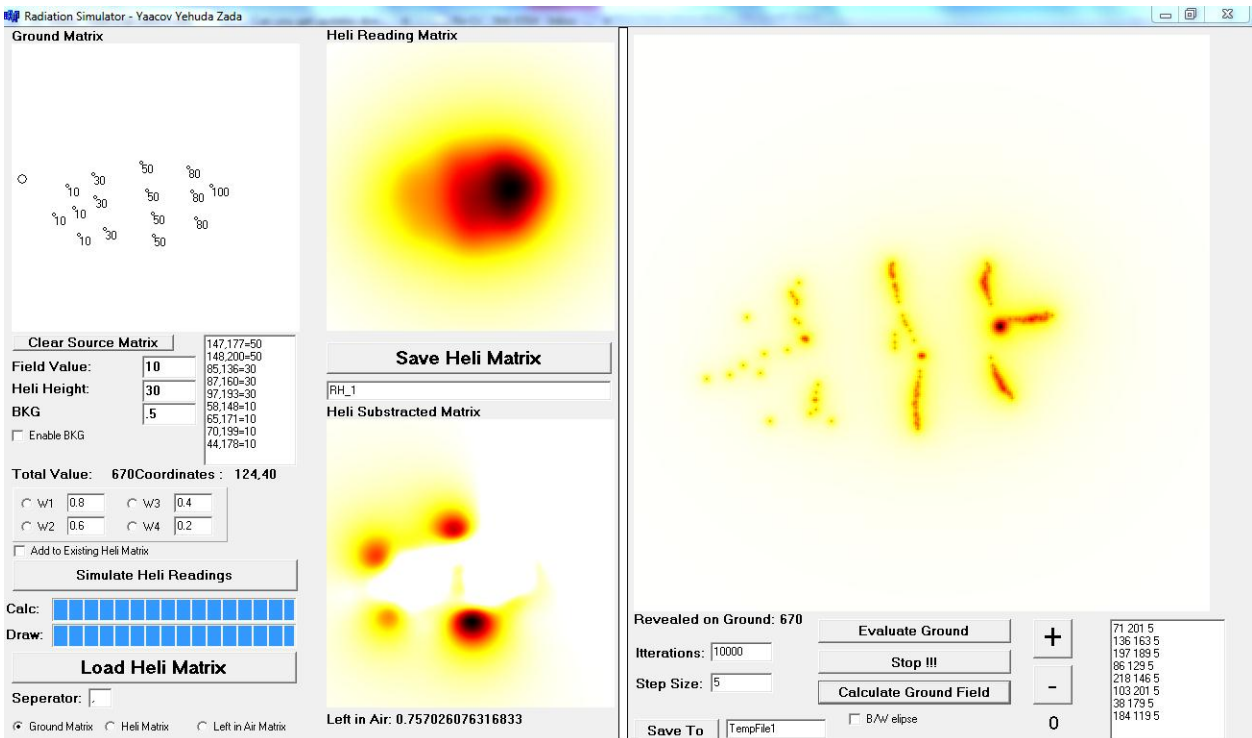
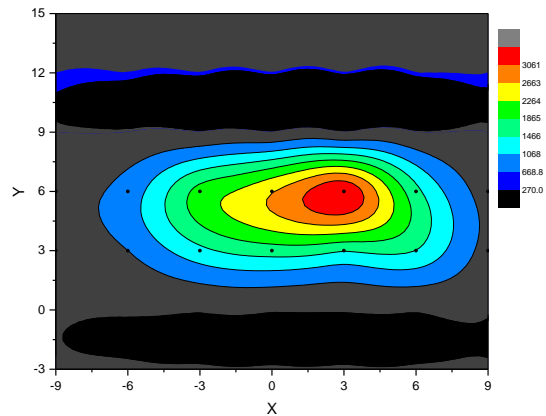


Figure 3: Airborne radiation survey of ^{99m}Tc from “Red-House” (Indoor) test compared with ground survey [3].

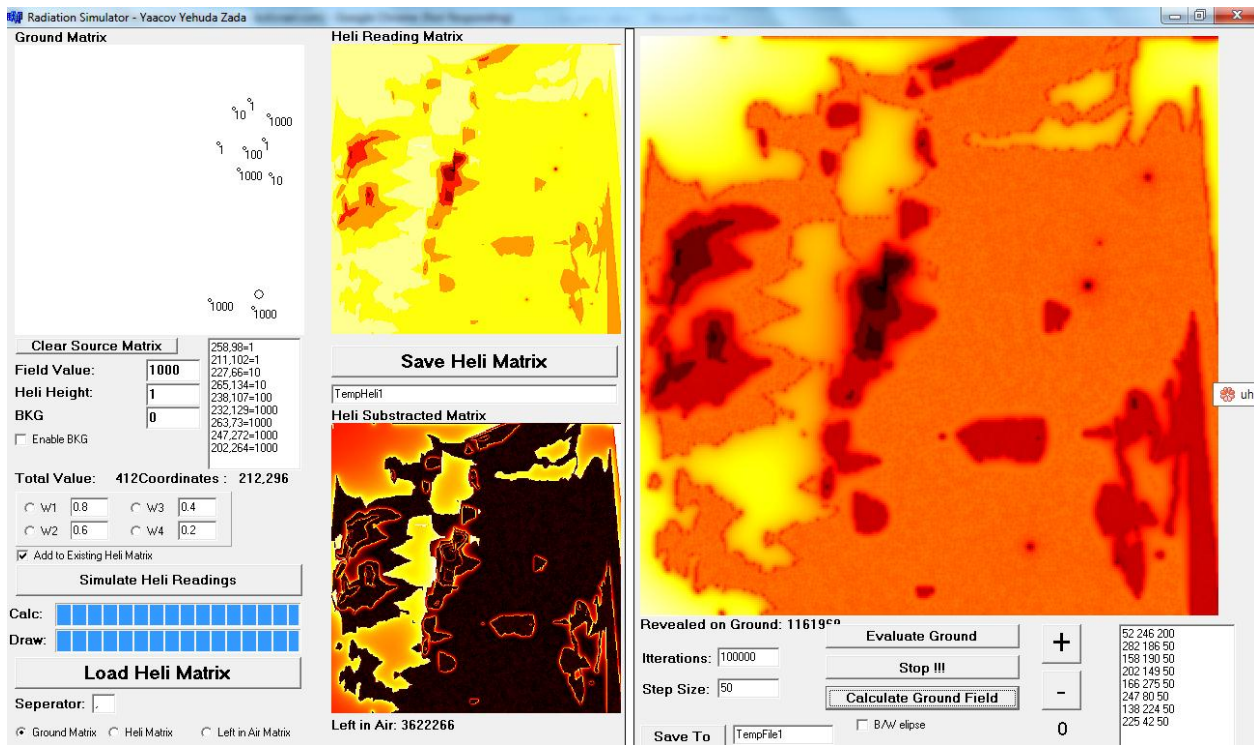


Figure 4: Airborne radiation survey of natural background from Air RAM 2000 measurements at the Government Wash area [4].

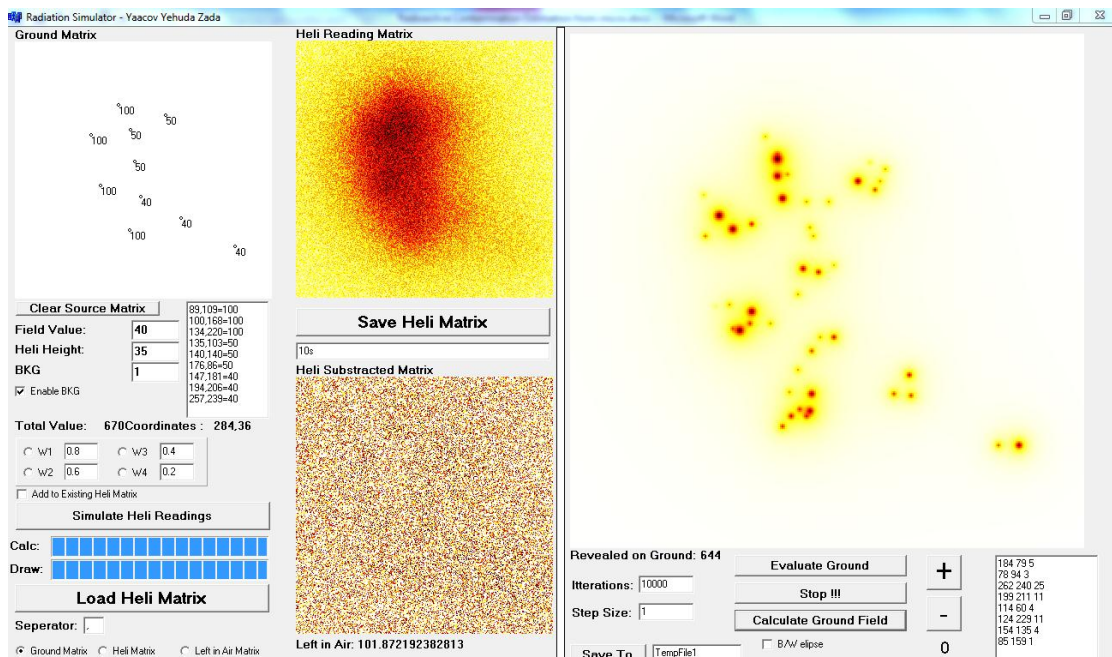


Figure 5: Airborne radiation simulation of natural background with ten spread sealed sources.

REFERENCES

- [1] M. Ghelman, M. Sheinfeld, A. Manor, E. Vax, Y. Kadmon and D. Tirosch The 25th Conference of the Nuclear Societies in Israel 16-18 February 2010, Crown Plaza Hotel, Dead Sea, Ein Bokek, ISRAEL (PDF)
- [2] A. Sharon, D. Sattinger, I. Halevy, R. Neuman, A. Ashkenazi and I. Yaar Cloud Rise Model for a "Dirty Bomb" Event The 25th Conference of the Nuclear Societies in Israel 16-18 February 2010, Crown Plaza Hotel, Dead Sea, Ein Bokek, ISRAEL (PDF)

- [3] Cloud Rise Model for an Explosion Inside a Building A. Sharon, D. Sattinger, I. Halevy, R. Neuman, A. Ashkenazi and I. Yaar The ²⁵th Conference of the Nuclear Societies in Israel 16-18 February 2010, Crown Plaza Hotel, Dead Sea, Ein Bokek, ISRAEL (PDF)
- [4] Aerial Measuring System (AMS) / Israel Atomic Energy Commission (IAEC) Joint Comparison Study Report Piotr Wasiolek and Itzhak Halevy: DOE/NV/25946-1941

Prospects for the SMR Technology

B. Tavron , D. R. Marouani

Israel Electric Corporation, Haifa, Israel

ABSTRACT

The nuclear power industry which suffered from prolonged recession has got additional slowdown by the Fukushima nuclear accident. Nuclear safety and security concerns together with cheap fossil fuel alternatives are among main reasons for this recession. Small Modular Reactor (SMR) technologies which feature enhanced safety, security and economics features may restore confidence in nuclear power and lead the nuclear energy renaissance. SMR unit sizes (up to 300MWe), match common existing oil, coal and gas unit sizes and present the environmentally suitable candidate for replacing old polluting plants. Moreover, SMR unit sizes and their enhanced load following capabilities match well future electricity system requirements.

SMR technology, safety and security features

SMR is referred by IAEA as Small-Medium size Reactor, and is defined to have power in the range of up to 700MWe. Here we will refer to the other commonly used term for SMR - Small Modular Reactors, referring to the factory made module feature of SMR of up to 300MWe. In the IAEA advanced reactor database - <https://aris.iaea.org/> - there are about 30 SMR types, based mainly on Light Water Reactor (LWR), Heavy Water Reactor (HWR), Gas Cooled Reactor (GCR) and Liquid-Metal Cooled Reactor (LMCR) technologies. Most of SMR designs are at various stages of development. SMR of 3 technologies are under-construction: the HTR-PM (200MWe) Pebble-Bed reactor in China, the KLT-40S floating nuclear power (35MWe PWR) in Russia and the CAREM 27 MWe Integral Pressurized Water Reactor in Argentina. Research is being carried out on SMR design for electricity generation, process heat production, desalination, hydrogen generation and other applications

SMR are expected to have improved safety performance mainly due to its reduced source term. The reduced power level means also lower decay heat allowing for simplified and/or passive emergency heat removal systems. Many SMR variants feature integral design which has less vulnerable components therefore reducing accident probabilities. The small reactor size makes also their seismic design simpler and more robust. The improved safety performance results in increased safety margins reduced shielding, reduced site exclusion and emergency planning zones.

Security measures for small reactors may be easier to implement. Some SMR types feature underground reactor design which improves resistance to external hazards. SMR may also include proliferation-resistant fuel cycle design [1].

SMR economics

Large reactors benefit from the economy of scales due to saving expenses which are independent from reactor size. Siting multiple SMR units at the same site, with the common infrastructure may also improve SMR economics. SMR also benefit in cost savings from factory module fabrication. Increasing SMR fabrication efficiency is anticipated at conditions of "mass production". Shorter construction times of SMR, will significantly save the interest payments. SMR will have additional cost savings from incrementally adjusting installed site capacity to demand growth and financial conditions. The SMR initial investment level is significantly lower than for large reactors reducing the finance risk and therefore enabling the private sector involvement. Since SMR are still in development stages, no detailed cost estimates are available; some general evaluations have estimated that SMR can be competitive especially when applying "carbon tax" on fossil fuel generation plants [2].

SMR and future electricity systems

Discoveries of large shale gas resources (especially in the US), environmental considerations and the energy sector reforms are some of main factors contributing to the change of electricity systems during the last decade. In the US the CCGT (Combined Cycle Gas Turbine) technology become the leading generation expansion technology on the account of coal, and oil fueled plants. Greenhouse gases emitting technologies are being phased-out by renewable energy technologies, like wind and solar, due to environmental concerns. Introduction of intermittent renewable energy sources, like solar and wind (both with up to 30% capacity factor), requires flexible backup generation capacity with steep load-following capabilities. In addition, government policies for renewable energy such as subsidies and dispatch priorities have to be set in order to make them acceptable. Hence, the operation of future grids will be a more complex task, and various "Smart grid" management programs are in development [3]. "Smart grid" control systems manage energy production, grid operations and demand side management for optimizing system performance. Energy market reform programs are promoting electricity production by the private sector, which has usually limited abilities to raise capital for very large plants. Energy market reforms also result with distributed generation systems.

SMR have the right unit size for integration into the future electrical system. Enhanced load following and relatively modest capital cost requirements of SMR also suitable for future electrical systems.

SUMMARY AND CONCLUSIONS

SMR have good safety, security and economics features. The SMR siting, and operation features may suit well the future electrical systems. Moreover, SMR integration in future electrical system may be part of the solution for achieving environmental goals along with energy security of supply.

Whether SMR will fulfill the prospects for clean, secure and affordable electricity supply and the prospects for the nuclear industry renaissance – it will depend on the commitment of governments to promote building and operating SMR that will demonstrate the enhanced features and regain the public confidence in nuclear energy, as well as continuous investment in SMR R&D.

Such positive developments may be suitable for Israel conditions since the SMR suite both to Israel future electrical grid as well as to the Shivta site in the Negev intended to the first nuclear power plant.

REFERENCES

1. *"INTERIM REPORT OF THE ANS PRESIDENT'S SPECIAL COMMITTEE ON SMR GENERIC LICENSING ISSUES"*, American Nuclear Society (ANS), 2010.
2. D. Shropshire, *"Economic viability of small to medium -sized reactors deployed in future European energy markets"*, Progress in Nuclear Energy 53 (2011) 299-307.
3. http://www.smartgrid.gov/the_smart_grid#smart_grid

Posters (Wednesday, February 12, 2014 15:30)

Mechanical Properties Characterization for a Cylindrical Fuel Clad Using the Segmented Expanding Cone-Mandrel (SEM) Method

M. Tubul, B. Ostraich, E. Shwageraus

Ben Gurion University P.O.B. 653 Beer-Sheva 8410501 Israel

INTRODUCTION

Rotem Industries is one of the partners in the JHR project. The Project deals with research reactor facilities. To train future employees for recruitment, The Company supports and assists students in undergraduate and master's degrees. This work is part of an MSc thesis accompanied by Rotem Industries instructors.

Modern demand for higher burn-up of nuclear fuels presents complicated safety related challenges for testing of both new and existing fuel cladding materials for integrity during long term operations, and especially for several known phenomena that may be expected to occur during the fuel rod operation.

Irradiation damage, as well as temperature and pressure induced creep along with several other factors have significant effect on cladding mechanical properties. Also, the small (usually about 300 μm) fuel to clad gap in as-received fuel usually closes rather rapidly due to high external pressure and the thermal expansion (swelling) of the fuel pellet.

The combination of these effects often leads to full contact between the pellet and the cladding inner wall. Since the fuel pellet is also subjected to non-uniform temperature gradient and operates at high temperatures⁽¹⁾, radial pellet cracking may incur, potentially compromising the integrity of the cladding and allowing fission products release to the coolant⁽²⁾. This process is known as PCI (Pellet cladding interaction) and it is of high importance in reactor safety and licensing considerations.

PCI also affects the fuel pellet itself, the ceramic UO₂ pellet geometry often distorts from cylindrical geometry into hour glass shaped sections. It is induced also by several other phenomena (Stress Corrosion Cracking, Chemical reactions, etc.), and leads to stress concentrations in some contact areas between fuel and clad. It is in fact one of the major cladding failure mechanisms. Therefore, it must be addressed when designing the fuel.

The characterization of mechanical properties is very important in the fuel design stages to adequately address the phenomena mentioned above.

Usually, the stress strain curves, produced in uni-axial tests, describe the mechanical properties of materials sufficiently well. In the case of fuel cladding, the stress regime is tri-axial. Therefore, properties obtained in uni-axial tests do not provide sufficient information on material properties required for obtaining an accurate prediction of cladding behavior. As a result, a requirement is emerging for a new simulation method of the PCMI phenomenon, suitable also for irradiated materials. Several works on this subject were published. In one of these works, the SEM⁽³⁾ (segmented expanding cone mandrel) test is used. This test simulates the clad loading due to thermal expansion of cracked fuel, by inducing clad radial loading through expanding segments, which are placed inside the cladding tube (Fig 1).

In this work, we propose a method for obtaining a more accurate evaluation of the material properties. By using a three-dimensional FEM model based on the SEM test, our method allows a better understanding of the three-dimensional complex stress fields occurring during pellet-cladding interaction⁽⁴⁾, including stress concentrations at the edges of the segments. In addition, our model takes into account the normal and shear stress distribution in all directions, the friction between all surfaces, the reaction force and the strain distribution in the clad. For validation of the proposed method, the FEM simulation predictions are compared with experimental data from the literature.

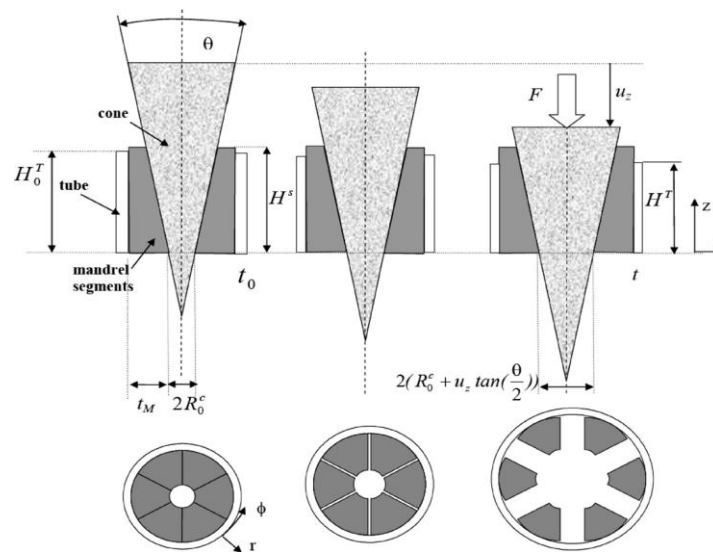


Figure 29-Schematic illustration of the principles for the cone mandrel test ^[1]

Finite element modeling

The following analysis concentrates on the segmented expanding mandrel (SEM) test ⁽³⁾ shown in Fig.1, in which a Cartesian and cylindrical coordinate system is defined. The SEM includes a cylinder (cladding), a segment, cone and block. The parametric FEM is performed using the finite element software ANSYS-APDL. The 3D eight-node solid element SOLID186 is used to mesh the structure. The effects of friction are represented by the Ansys Coulomb friction model algorithm on the contact between the clad segment cone and block. The finite element mesh model is shown in Fig.2.

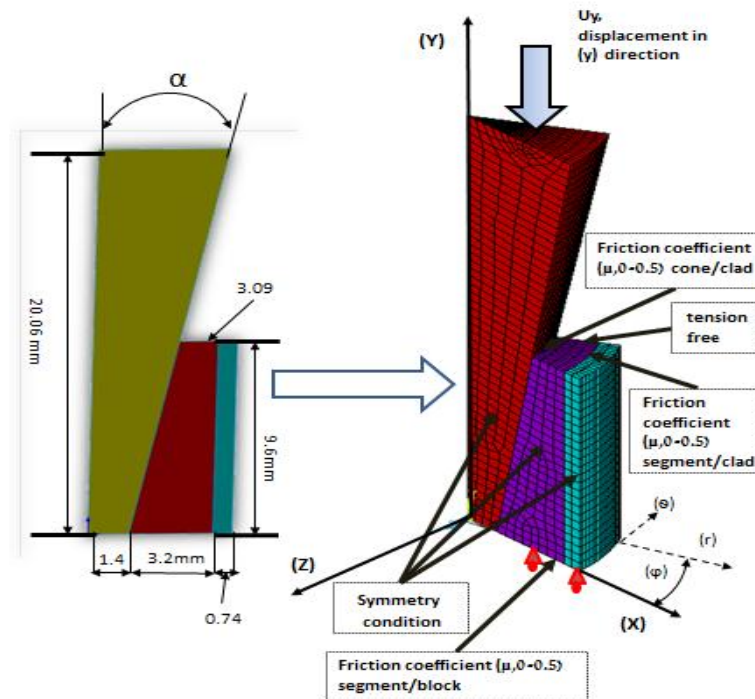


Figure 30-meshing and boundary condition

RESULTS

The reaction forces from the 3D-FE model are compared to the SEM test ⁽¹⁾ experimental results. The load displacement curves are shown in Fig 3. The model results are in good agreement with the experimental curves. This suggests that the friction coefficient (μ) in both cases is similar and equal to 0.04. The difference between the FE model and experimental curves comes from the difference between the material model fed into the 3D-FE model and the actual properties of the material used in the experiment.

Fig 4a presents the stress-strain curves of Zircaloy 2 obtained by: 1. uniaxial tensile test. This data is the material model fed into the 3D-FE model 2. Ansys 3D-FE model. The data in this curve is calculated for the clad outer perimeter. 3. Feeding the data in fig 3 to a semi-analytical model ⁽³⁾, transforming it to stress-strain. Curves 2 and 3 are calculated using $\mu=0.04$. It can be seen that all curves are similar. In the case of

$\mu=0.5$ (Fig 4b), the curves are very different from each other: In the semi-analytical curve, the material strength is much lower, the elastic slope is lower and the strain hardening is more moderate. All results assume isotropic material. Clearly, the friction coefficient has a large effect on the Semi-analytical computed stress-strain curve. In order to reduce this effect dramatically, a correction for the semi-analytical model was developed. Its effect can be seen in Fig. 4b, the stress-strain curve calculated using the semi-analytical model changed when the friction coefficient increased, but material mechanical properties are expected to be independent of the friction in the measuring system. Thus, the semi-analytical model needs to be modified by adding a mathematical expression that fits the semi-analytical curve to the FE model curve. Eq. 1 presents such an expression.

$$(1) \quad \sigma_{\theta} = \begin{cases} \text{if } \varepsilon \leq 0.0034 ; E * \varepsilon \\ \text{if } \varepsilon > 0.0034 ; K * \varepsilon^n \end{cases}$$

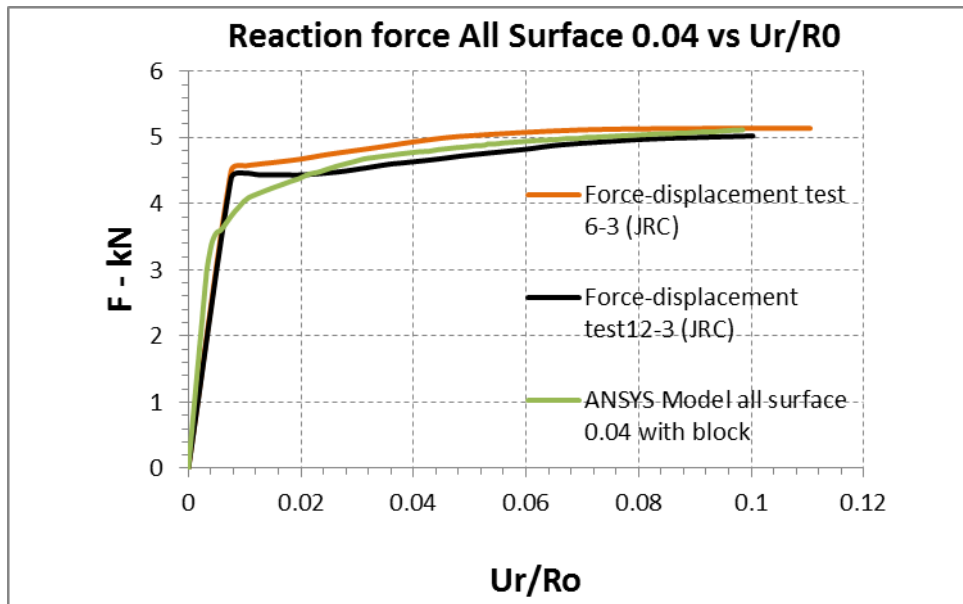


Figure 31-Force-displacement relationship with a friction coefficient of 0.04 cone / segment, segment /clad compared with experiment cone segment produced from STAVAX [3]

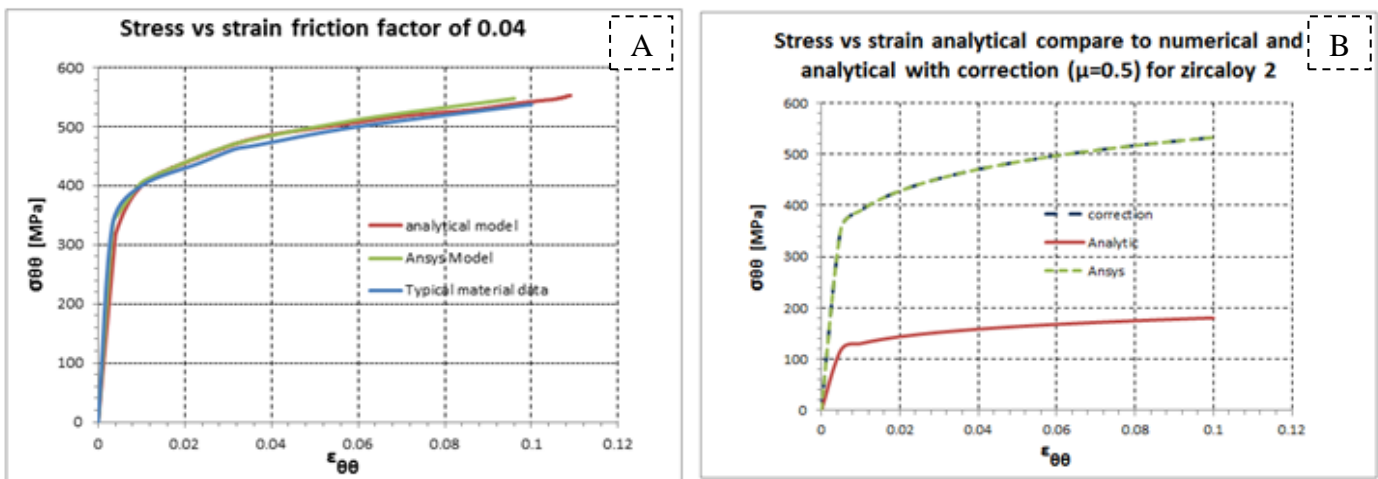


Figure 4- calculated stress-strain curve in ANSYS versus stress-strain curve calculated using force curve (Figure 4) taken through the calculation results on ANSYS model and entered the semi-analytical model [3]. A- Friction coefficient of 0.04 B- friction coefficient of 0.5

CONCLUSIONS

In the current stage of the research, the following conclusions can be drawn:

- The 3D FE model can accurately reproduce the experimental results after calibrating the friction coefficient.
- The 3D FE model is suitable for the analyses of local failure mechanisms and distribution of stresses/strain and stress concentration in the clad segmented interaction.
- A correction for the semi-analytical model was developed using the 3D-FE model. The corrected semi-analytical model is independent of the friction coefficient.
- The 3D-FE model can be used to obtain the friction coefficient from experimental results.

For summing up, a 3D model is developed to correct the analytical model which intends to compute the stress-strain curve of a clad from SEM test. The analytical model happens to fail at high friction factors. The analytical correction, developed by the 3D model, reduces the dependency of the results at the friction and suggests useful method for compiling SEM models.

REFERENCES

- [1] Lustman, B., 1979. *Zirconium technology – twenty years of evolution*. In: *ASTM-STP 681. American Society for Testing and Materials*, pp. 5–18.
- [2] Cacuci, D.G., 2010. *Handbook of Nuclear Engineering, Volume 1, Nuclear Engineering Fundamentals*. Springer
- [3] Karl-Fredrik Nilsson, Oliver Martin, Cesar Chenel-Ramos, Jose Mendes *The segmented expanding cone-mandrel test revisited as material characterization and component test for fuel claddings*.
- [4] Nakatsuka, M., Koizumi, K., Hayashi, Y., Kawahara, A., 1982. *Measurement of friction coefficient and strain concentration of barriered fuel claddings under mechanical interaction with pellets*. *J. Nucl. Sci. Technol.* 19 (4), 336–339.
- [5] Pickman, D.O., 1994. *Zirconium alloy performance in light water reactors: a review of UK and Scandinavian experience*. In: *ASTM-STP 1245. American Society for Testing and Materials*, pp. 19–32.

Posters (Wednesday, February 12, 2014 15:30)

Ground Shock Resistant of Buried Nuclear Power Plant Facility

D. Ornai, A. Adar, E. Gal

Ben-Gurion University of the Negev, PO Box 653, Beer-Sheva, 84105, Israel

Ground Shock Resistant of Buried Nuclear Power Plant Facility

D. Ornai^{1,2}, A. Adar¹, E. Gal¹

¹*Department of Structural Engineering, Ben-Gurion University of the Negev*

²*Protective Technologies Research & Development Center, Ben-Gurion University of the Negev,
PO Box 653, Beer-Sheva, 84105, Israel*

INTRODUCTION

Nuclear Power Plant (NPP) might be subjected to hostile attacks such as Earth Penetrating Weapons (EPW) that carry explosive charges. Explosions of these weapons near buried NPP facility might cause collapse, breaching, spalling, deflection, shear, rigid body motion (depending upon the foundations), and in-structure shock. The occupants and the equipment in the buried facilities are exposed to the in-structure motions, and if they are greater than their fragility values than occupants might be wounded or killed and the equipment might be damaged, unless protective measures will be applied. NPP critical equipment such as pumps are vital for the normal safe operation since it requires constant water circulation between the nuclear reactor and the cooling system, including in case of an immediate shut down. This paper presents analytical- semi empirical formulation and analysis of the explosion of a penetrating weapon with a warhead of 100kgs TNT (Trinitrotoluene) that creates ground shock effect on underground NPP structure containing equipment, such as a typical pump. If the in-structure spectral shock is greater than the pump fragility values than protective measures are required, otherwise a real danger to the NPP safety might occur.

NUMERICAL EXAMPLE

Underground explosion creates free field motions formulated by Drake & Little [1], [2], [3]. The analysis of NPP buried facilities resistant to the in-structure shock caused by the external ground motions is based on the response shock spectra method [2],[3],[4]. A response spectrum is calculated and presented on a special figure with four logarithmic axes. Both the spectral motions (displacement, velocity, and acceleration) of a damped structure subjected to support excitations as a function of frequency and the installed equipment fragility spectrum are presented on the same figure (for example see figure 3). If the spectral in-structure motions are greater than the equipment fragility than the equipment is supposed to be damaged with direct implication on the NPP unsafe operation. Hence, for an existing structure the equipment may be mounted to proper isolator. In a new facility external base isolators may decrease the excessive motions, and additional external protective layers may lower the ground shock and the in-structure shock as required. A numerical example of a response spectrum of an underground structure with an internal pump coping with motions caused by explosive charge stand-off distances of 5m and 10m was carried. The configuration of the structure and the explosive charge is presented in Figure 1.

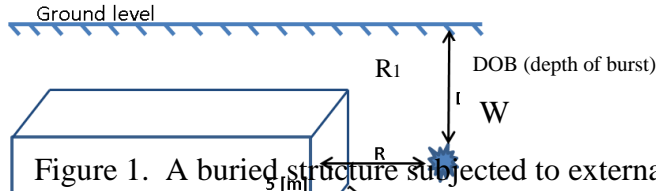


Figure 1. A buried structure subjected to external underground explosion

The soil properties of dense and poorly graded dry sand are as follows [2]: seismic velocity $c=365.76$ [mps (meters per seconds)], and attenuation coefficient $n= 2.6$. The explosion parameters are: weight of charge $W=100(\text{kgs})_{\text{TNT}}=73(\text{kgs})$ C4, and coupling factor $f=1$ (fully coupled). The US army and air force protective structures manuals [2],[3] suggests the following procedure to evaluate the in-structure response spectrum including some fragility spectrums of typical equipment exposed to shock. The in-structure motions are the average ground motions ranging between the front wall that is exposed directly to the explosion and the back wall. The formulas for the averaged acceleration- $A(\text{g}'\text{s})$, velocity- $V[\text{fps}$ (feet per seconds)], and displacement- $D(\text{ft})$ are:

$$A_{avg} = \frac{50 * f * c * W^{\frac{n+1}{3}} * [R_1^{-n} - R_2^{-n}]}{W^{\frac{1}{3}} * n * [R_2 - R_1]} \quad [g's]$$

$$V_{avg} = \frac{160 * f * W^{\frac{n}{3}} * [R_1^{-n+1} - R_2^{-n+1}]}{(n - 1) * [R_2 - R_1]} \quad [fps]$$

$$D_{avg} = \frac{W^{\frac{1}{3}} * 500 * f * W^{\frac{n-1}{3}} * [R_1^{-n+2} - R_2^{-n+2}]}{c(n - 2) * [R_2 - R_1]} \quad [ft]$$

f , c , n , W , and R_1 , R_2 are the coupling factor (for deep explosion $f=1$), soil seismic velocity (fps), dimensionless attenuation coefficient, charge weight (in lbs of C4 high explosive that are equal to 1.37 lbs of TNT), distance between the explosive charge and the front wall, and distance between the explosive charge the back wall.

The values of the free field ground motion are larger than those in the structure since the distances to the various points on the structure's front wall are larger than the shortest distance to the wall center, R_1 . Using a reduction factor approach proposed by [2] corrects the ground motions in relation to the explosion stand-off and the structure geometry as shown in Figure 2.

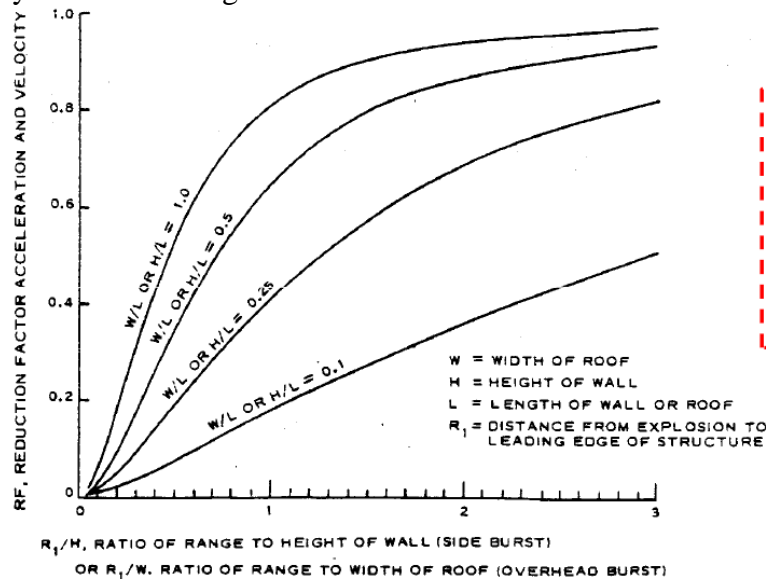


Figure 2. Reduction factor of in-structure acceleration and velocity regarding side burst ($H=5\text{m}$, $L=10\text{m}$)

For small amounts of structural damping (5-10% of the critical damping ratio) it is recommended to multiply the maximum motions by factors 1, 1.5 and 2 for displacement, velocity and acceleration respectively [2]. The physical units of the shock spectrum are taken in inches (in) for the displacement, inches/sec (in/sec) for

the velocity and g's (gravity multiplier) for the acceleration. The calculated spectral in-structure motions are shown in Table 1.

Table 1. Spectral motion values due to in-structure shock caused by two external underground explosions

Explosion stand-off, R	Motion type	Average Values	RF-Reduction Factor	Spectrum factor	Spectral motion values
5[m] , 16.4[ft]	Acceleration [g's]	9.38	0.63	2	18.76[g's]
	Velocity [in/sec]	7.52		1.5	11.28[in/sec]
	Displacement [in]	0.91		1	0.91[in]
10[m] , 32.8[ft]	Acceleration [g's]	1.98	0.84	2	3.95[g's]
	Velocity [in/sec]	2.96		1.5	4.44[in/sec]
	Displacement [in]	0.47		1	0.47[in]

At a stand-off of 5 meters the blast produces base motions that for some frequencies are greater than the pump fragility, hence protective measures are necessary (Figure 3). At a stand-off of 10 meters the blast produces motions that are smaller than the pump fragility and there is no need for protection.

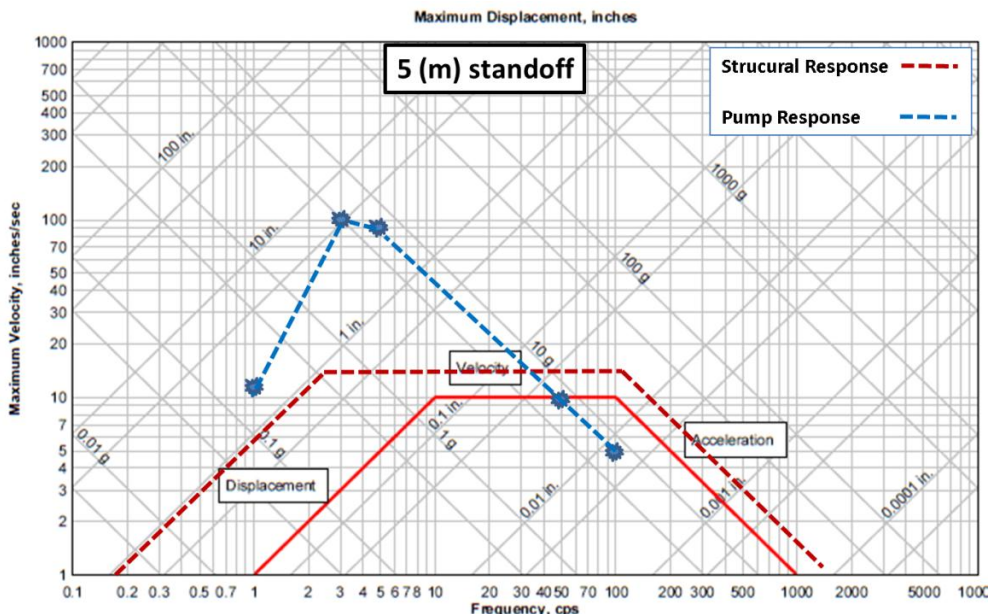


Figure 3. Pump fragility versus in-structure shock spectra due to external 100 kg TNT exploding 5 meters from the structure

SUMMARY

Analytical semi empirical method based on Little & Drake method enabled in-structure motion analysis due to external buried explosion. At 5 meters stand-off between the explosive charge and the front wall the blast creates in-structure motions that are greater than the pump fragility. In the case of existing structure protective measures such as mounting the pump to a proper isolator is required. For a new designed structure using base isolators or external protective layers should be considered. Similarly any underground NPP facility may be analyzed.

REFERENCES

1. Drake J.L., and Little, C.D.Jr. *Ground shock from penetrating conventional weapons*, The interaction of non-nuclear munition with structures, Symposium proceedings, Colorado USA (1983).
2. *Fundamentals of Protective Design for Conventional Weapons, TM5-855-1*. US Army, (1986).
3. Drake, J., Twisdale, L., Frank, R., Dass, W., Rochefort, M., Walker, R., Britt, J., and Sues, R. *Protective construction design manual ESL-TR-87-57*. US Air Force

Engineering and Services Center, Tyndall Air Force Base, Florida, (1989).

4. Harris, C. M., and Piersol, A. G. *Harris' shock and vibration handbook*, McGraw-Hill, New York, (2002).

Posters (Wednesday, February 12, 2014 15:30)

Performance of SNRC in MAPEP Proficiency Tests During 2005-2013

O. Aviv, Z. Yungrais, S. Moscovici, M. Brandis, C. Tzur, L. Broshi, T. Reimer, R. Oren-Shemesh,
G. Haquin

Soreq Nuclear Research Center, Yavne 81800, Israel

INTRODUCTION

The Mixed Analyte Performance Evaluation Program (MAPEP) is organized by the United States Department of Energy as a quality assurance tool for radiological and chemical laboratories around the world. Matrices of vegetation, soil, air filter and water, spiked with mixed radionuclides and stable elements are prepared and sent to participating laboratories every 6 months. The participating labs are required to identify and quantify radionuclides and stable elements using their standard methods⁽¹⁾ and report the results within sixty days. False positives are also routinely examined. The performances are assessed and sent to the participating laboratories.

The radiation measurements laboratories at the Radiation Safety Department (RSD) at Soreq Nuclear Research Centre (SNRC) continually participates in MAPEP since 2005 for gross alpha and beta, tritium and uranium in water and gamma emitting radionuclides in the previously mentioned matrices. In this paper we present an analysis of SNRC performance up today.

MATERIALS AND METHODS

Gamma emitting radionuclides are measured from the four matrices by gamma spectrometry using a high purity germanium (HPGe) detector. Efficiency, true coincidence summing corrections and decay corrections are applied where required.

Gross alpha and beta in liquid samples are measured by low background coincidence proportional counting. Tritium in water is performed by low background liquid scintillation using a Quantulus1220 (PerkinElmer) while for uranium isotopes selective extraction liquid scintillation alpha counting using the same type of instrument.

In the following we specify the materials supplied by MAPEP and the preparation procedure for the actual samples which are measured.

Vegetation: Two plastic jars consisting of 95 gr and 10 gr of finely milled grass hay (identically spiked) are supplied. The sample with 10 gr are placed in a dedicated plastic container and sealed with silicon.

Soil: Sample containing 300 gr of soil is supplied in a plastic jar. All 300 gr are transferred into a dedicated plastic container which fits to the measuring apparatus.

Air filter: A thin air filter (diameter of 47 mm, width of 1 mm) made of glass fiber is supplied. The filter is measured "as is", i.e. without any preparation.

Water: Two bottles of 1 liter of water each are supplied. One bottle is used for identification of gamma, alpha and beta emitters (RSD labs participates in the measurement of ^3H , ^{234}U , ^{238}U only). The other bottle is used for gross alpha-beta measurements. For gamma emitters, the preparation method involved transfer of 200 ml into a dedicated plastic container. For gross alpha measurement the standard co-precipitation method⁽²⁾ is used. The method consists of co-precipitation of Ra, U and Th isotopes with BaSO_4 , FeO_3 . Gross beta sample preparation is according to the standard evaporation method⁽²⁾. For Tritium in water, a sample of 150 ml of water is cleaned and purified through active charcoal powder and then filtered and distilled (boiling and condensed) to achieve a constant quenching property of the sample mixed with the inorganic scintillation solution. For uranium isotopes measurements (^{234}U and ^{238}U), a sample of 200 ml of water is transferred into a dedicated container which is first heated to remove radon and CO_2 . After cooling, the sample is mixed with the extraction cocktail (HDEHP and liquid scintillator), and later a known portion is measured by a low background liquid scintillation counter (Quantulus1220, PerkinElmer).

The evaluated parameters in the proficiency tests are the activity concentration and the corresponding uncertainty for each nuclide and for each matrix. Reporting of activity⁷ was performed in accordance to

⁷For cases where a nuclide was not identified, the minimal detection activity was reported.

MAPEP instructions (i.e. decay corrected to the requested reference time). The acceptance criteria for receiving a passing grade (“A”) defined by MAPEP is given for a result which is within a relative deviation⁸ of <20% than the reference value. A passing grade with warning (“W”) is given for a relative deviation within 20%-30%. A fail grade (“N”) is given for a relative deviation of >30%.

RESULTS

Table 1 shows the performance level in percent (i.e. number of “A”+“W” grades) for all of the examined radionuclides in each of the four matrices for all tests during 2005-2013. Tests involving detection and quantification of the most of the gamma emitters (⁴⁰K, ⁵⁴Mn, ⁵⁷Co, ⁶⁰Co, ⁶⁵Zn, ¹³⁴Cs, ¹³⁷Cs, ²⁴¹Am) in all matrices as well as Uranium isotopes and gross alpha and gross beta in water are mostly graded “A”. The low energy gamma emitters ²⁴¹Am and ⁵⁷Co were given the highest amount of fail grades in water and vegetation matrices. Tests with ³H were only partly good, though we note that since 2010 a significant improvement was achieved after a validation process was performed.

Submitted data including activity concentrations, and the reference values within the period of 2005-2013 (conducted once/twice per year, altogether 16 tests) were processed and analyzed. Figure 1 (left) shows the average deviation (over all tests) between the submitted result and the reference value for the studied nuclides and for the four matrices (vegetation, soil, filter, and water).

Non-zero deviations⁹ are observed in practically all matrices and radionuclides. The deviations in the gamma emitters may be attributed to a significant offset in the used efficiency curve. The relatively large deviation in the low gamma energy emitter ²⁴¹Am is attributed to the very low activity concentration of the nuclide which is best suited for alpha spectrometry methods rather than for gamma spectrometry as the minimal detection activity level of the HPGe detection system is usually above the reference values.

The large deviation in ³H is attributed to a previous sample preparation method which was updated in 2010. Since then the performance was successful.

The few deviations in Uranium isotopes results are attributed to non-equilibrium between the isotopes in depleted uranium samples. The updated measurement method (since 2011) accurately determines the uranium activity concentration not depending on uranium depletion/enrichment.

Nuclide	Success Level			
	Vegetation	Soil	Filter	Water
⁴⁰ K	-	100%	-	100%
⁵⁴ Mn	100%	100%	100%	100%
⁵⁷ Co	93%	100%	100%	100%
⁶⁰ Co	100%	100%	100%	100%
⁶⁵ Zn	100%	100%	100%	100%
¹³⁴ Cs	100%	100%	100%	100%
¹³⁷ Cs	99%	100%	98%	98%
²⁴¹ Am	80%	100%	87%	64%
³ H	-	-	-	90%
²³⁴ U	-	-	-	85%
²³⁸ U	-	-	-	93%
Gross α	-	-	-	94%
Gross β	-	-	-	94%

Table 5: Grades per nuclide and per matrix for MAPEP tests during 2005-2013.

⁸For gross alpha/beta emitters, the acceptable values are within a relative deviation of <70%.

⁹Deviations in reported results caused by typos were omitted from this average as this report studies technical expertise.

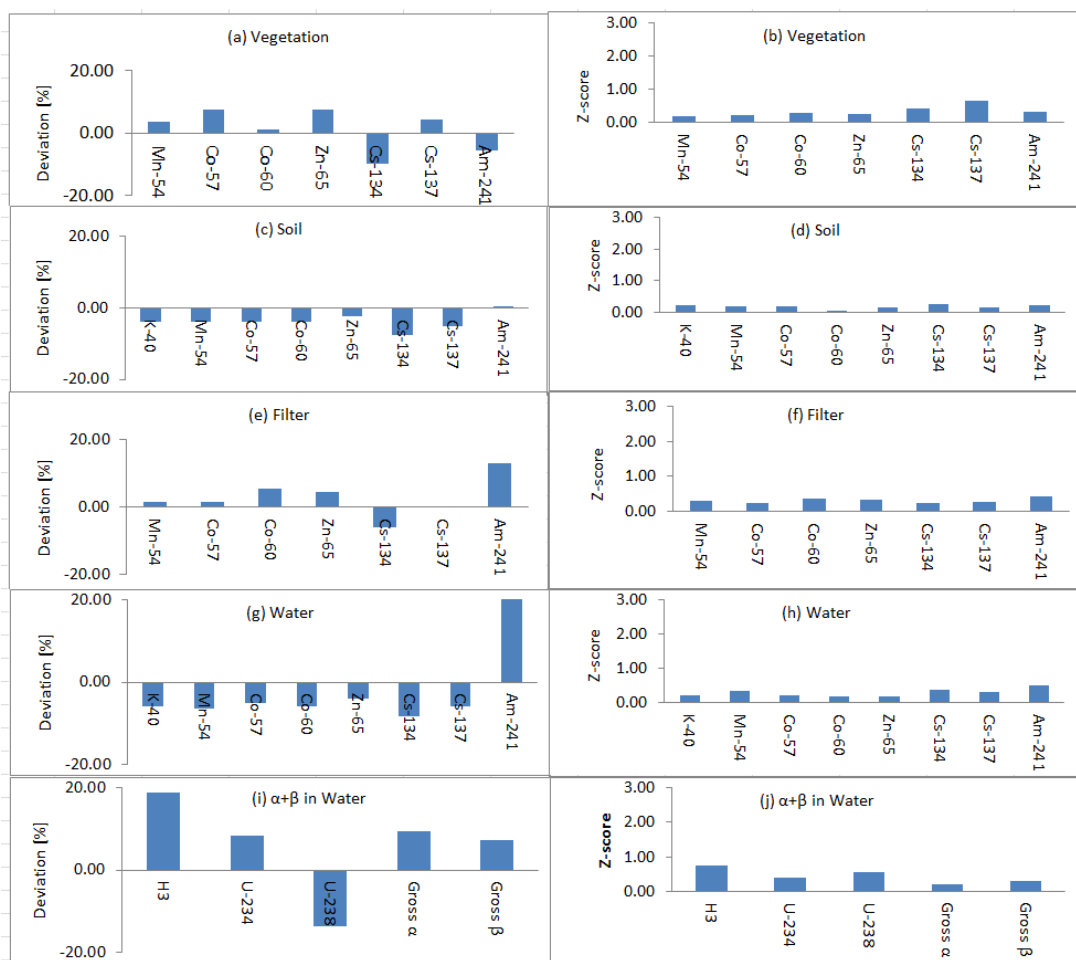


Figure 32: Averaged deviation (left – a,c,e,g,i) and averaged z-score (right – b,d,f,h,j) for the examined radionuclides in four matrices: vegetation, soil, filter and water.

Most of the reported results for nuclides in the four matrices are within the accepted values, while alpha and beta emitters exhibit slightly elevated Z-scores.

An additional performance evaluation has been carried out using the statistical test Z-score which takes into account the relative deviation between the assigned value and the lab result together with the corresponding uncertainties, given by $\zeta = \frac{|A_{lab} - A_{ref}|}{\sqrt{\Delta A_{lab}^2 + \Delta A_{ref}^2}}$. Where A_{lab} is the reported activity; A_{ref} is the assigned activity;

ΔA_{lab} and ΔA_{ref} are the corresponding uncertainties. Results with $\zeta < 3$ are considered accepted values.

Figure 1 (right) shows the averaged (over all tests) Z-score per nuclide and per matrix.

Figure 2 shows the performance of the lab in MAPEP tests over the period 2005-2013 in terms of success level in percent (= [number of “A” + “W” grades]/[total nuclides examined]). The lab exhibited good performance over the years for all matrices, though occasional failures were recorded in some years especially for vegetation and water matrix. The main reason for these failures is miss-quantification in the low energy gamma emitters (^{241}Am and ^{57}Co).

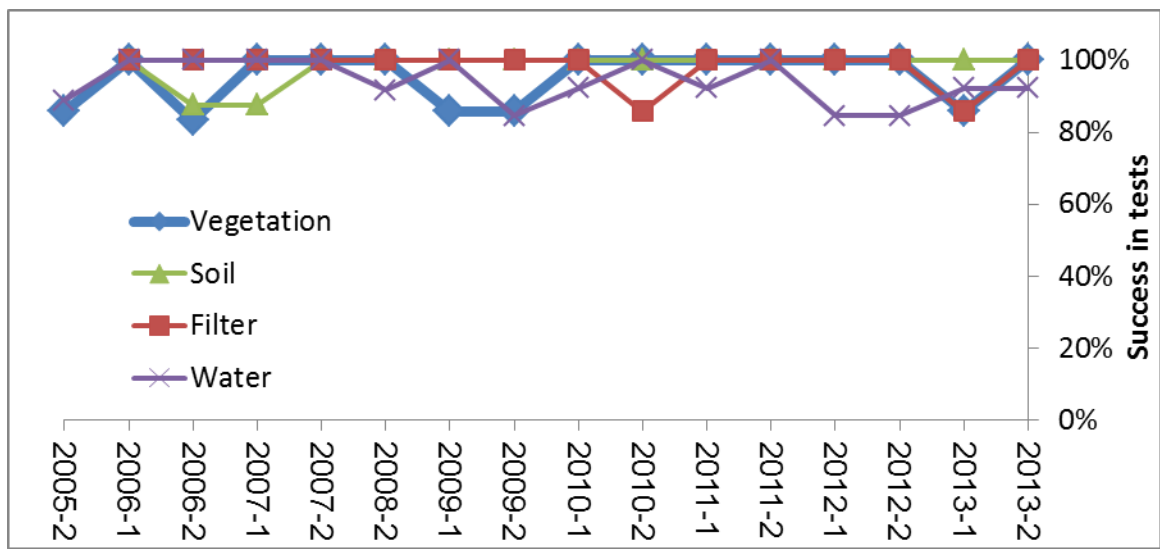


Figure 33: Success level for the four matrices in MAPEP tests during 2005-2013.

CONCLUSIONS

The performance of the radiation measurements laboratories at Soreq Nuclear Research Centre in MAPEP proficiency tests has been presented. There is a very good overall success in these tests over the years, although deviations were found in some nuclides which need to be addressed.

REFERENCES

1. DOE\MAPEP website: <https://mapep.inl.gov/>
2. Standard methods for the examination of water and waste water 22nd edition, American Public Health association (2012).

Natural Circulation Modeling in MTR Fuel Geometry in Research Reactors

Y. Aharon

NRCN, P.O.B. 9001, Beer – Sheva, Israel

INTRUDUCTION

In many research reactors the reactor can operate under either forced or natural convection modes. Under forced convection, the primary cooling system removes the heat generated in the reactor core through a heat exchanger to the secondary cooling system, which releases this thermal energy through the cooling tower to the atmosphere. Under natural convection operating mode, the generated nuclear power imply heats up the pool water, and is ultimately dissipated through the pool surface to the containment atmosphere. Hence, the large pool provides a heat sink for the energy generated within the core. The pool surface is open to the containment atmosphere, where thermal energy exchange via evaporation and convection heat transfer can occur. In case of electrical supply failure or mechanical / electrical failure in the pumps, a Loss of Flow Accident (LOFA) will occur. In this case natural circulation mechanism may be the only mechanism that can be use to remove the decay heat from the core.

Modeling and modeling validation of natural circulation is an important issue in designing and commissioning of nuclear reactors. Most of the designers are using commercial codes like RELAP5, TRAC and THYDE-W to simulate the behavior of the core under natural circulation. Validation of those cods is done by comparing between different codes and comparing the calculated results with results from scaled experimental systems. In the last two decades, CFD calculations are also used for calculations and validation of the commercial codes⁽¹⁾.

In case of research reactors and in case of Loss of Flow Accident, a simple analytical model can be use for preliminary and advanced calculations of the reactors.

The purpose of this paper is to present and validate a simple model for thermohydraulic calculation of research reactor in natural circulation mode.

THE MODEL

The flow loop in a pool type research reactor, in case of natural circulation, consists of the heat source (the core) which works in low power (up to about 100 kW) or in case of decay heat after shutdown. The inlet of the water from the pool to the lower plenum of the core is through the flapper valves which are opened automatically when the flow rate reaches a limiting value of about 10% of the nominal flow rate. The water entering the lower plenum and flowing up trough the inlet nuzzle of the fuel rod to the fuel plates / pins zone. In most of the research reactors the water continues to flow through the exit nozzle of the fuel rod and mixing with the water in the pool. In few research reactors like the Australian MAPLE and the Korean HANARO and also in the commercial heating reactor SLOWPOKE, the water continue to flow to a chimney and than mixing with the water in the pool.

Modeling of a natural circulating in that loop based on a balance between the friction losses along the loop due to the flow rate ($\Delta p_{tot,f}$) and the moving force (pressure drop) due to the density decreased by the heating of the water which causing buoyancy force ($\Delta p_{tot,b}$).

$$(1) \quad \Delta p_{tot,f} = \Delta p_{tot,b}$$

In each zone the friction losses were calculated as follow.

For the longitudinal friction losses: (2)
$$\Delta p_{L,i} = \left(f \frac{L}{D_H} \rho \frac{v^2}{2} \right)_i$$

And for local friction losses: (3)
$$\Delta p_{loc,i} = \left(K \rho \frac{v^2}{2} \right)_i$$

The friction coefficient f in eq. 1 was taken according to the Reynolds number in the calculated zone. In case of natural circulation the Reynolds number is usually defined a laminar flow regime. In this case the friction coefficient f is calculated as follow: (4) $f = C/Re$

where the value of the constant C depends on the channel geometry. For the local friction losses the constant K was taken as approximated value $K=1$.

The velocity v in each zone is calculated from the mass flow rate and the cross section of the calculated channel.

The moving force (buoyancy pressure drop) is depending on the mass flow rate of the coolant, the heating power of each zone and the inlet and outlet level of the calculated zone as follow:

$$(5) \quad \Delta p_{b,i} = g\Delta z(\rho_{inf} - \rho_i)$$

Where Δz is the elevation difference between the inlet and the exit of the channel, ρ_{inf} is the pool water density and ρ_i is the average density value of the water in the calculated zone. The density value in each zone is varying with the coolant temperature. That value was calculated by using a curve fitting of the density vs. temperature of the water. The water temperature gradient in each zone (ΔT_i) was calculated from the energy equation:

$$(6) \quad \Delta T_i = T_{in} + \frac{q_i}{\dot{m}Cp}$$

Where T_{in} is the inlet temperature to the calculated zone, q_i is the heating power which supply to the water along the calculated zone, \dot{m} and Cp are the mass flow rate and the heat capacity of the coolant, respectively. In case of heating zone (along the fuel plates) the average temperature was calculated between the inlet and the outlet temperature and the average density was calculated from the density function with that temperature.

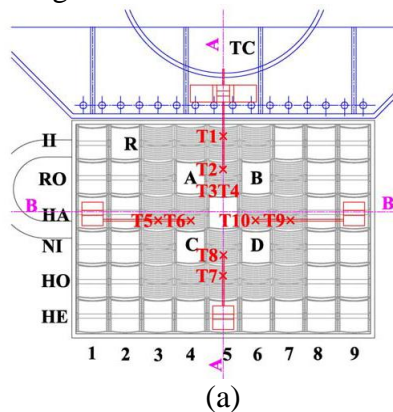
Model Validation

To validate the present model, experimental data from the Kyoto University Research Reactor (KUR) was used which is a pool type 5MW research.

Experimental temperature measurements of water in various locations in the core in natural circulation mode of the KUR are presented in ref. 2. The description of the KUR core is presented in Fig. 1(a) and the fuel rode in Fig. 1(b). The core consists of 19 standard fuel rods and 5 control rods (A,B,C,D and R in Fig. 1). Standard fuel rode consist of 18 fuel plates 1.5 mm in thick and 625.5 mm in length and 75.9 mm in with. Between the fuel plates, there is a 2.8 mm width water channel for the coolant flow. The location of the water temperatures measurements is presented in Fig. 1(a) and the power distribution between the fuel rods for 100 kW operation power is presented in Table 1. It was also mentioned in reference 2 that the ratio between the thermal power and the nutronic power is 0.9. The two thermocouples T3 and T4 were respectively arranged in the vertical positions of 5 cm and 10 cm above the position of thermocouple T2.

The channel power from Table 1 was normalized with the core power to get the values in various operation core powers.

In the model it was assumed that the main flow resistance in the flow loop is the resistance of the channels between the fuel plates and the inlet nozzle of the fuel rod, where the flow resistance inside the lower plenum is negligible. Sensitivity calculation was done for the inlet flapper resistance. In ref. 2 the dimensions of the flapper are not provided and we assumed that the flapper has (in total open position) typical circular tube geometry of 0.2 m inside diameter and length of 0.5 m⁽³⁾.



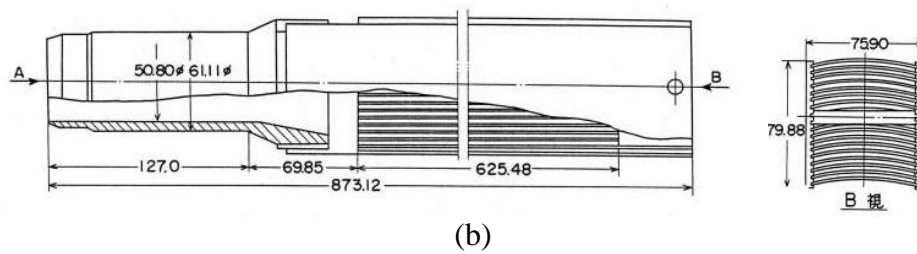


Figure 1: a- Fuel rods arrangement in the KUR core. b- Fuel rod geometry ⁽²⁾.

Table 1: Power distribution between the fuel rods at reactor operating power of 100 kW⁽²⁾.

Output Power : 100kW									
	1	2	3	4	5	6	7	8	9
II	G	1.79	3.75	4.21	4.22	3.79	SSS	G	G
RO	G	G	4.66	2.94	5.77	2.64	3.92	G	G
HA	G	G	4.90	6.11	Hyd	5.71	4.24	G	G
NI	G	G	4.68	3.02	5.93	2.84	4.11	G	Pn2
HO	G	G	3.94	4.48	4.57	4.27	3.52	G	Pn3
HE	G	G	G	G	G	G	G	G	Pn1

Unit: kW

The total flow resistance of the flapper was taken as a sum of local flow resistance ($K=1$) due to a sudden entrance of the water from the pool to the valve and longitudinal friction losses along the flapper valve tube. It was also assumed that the pool has no resistance to the flow. For conservative calculation it was assumed also that the flow rate through the flapper is the hottest channel flow rate times the number of the fuel rods. The measured temperatures versus the time are presented in ref. 2 for to fuel channels HA-3 and HA-4 for various core operating power up to 100 kW. Comparison between the measured temperatures and the calculated values is presented in Fig. 2.

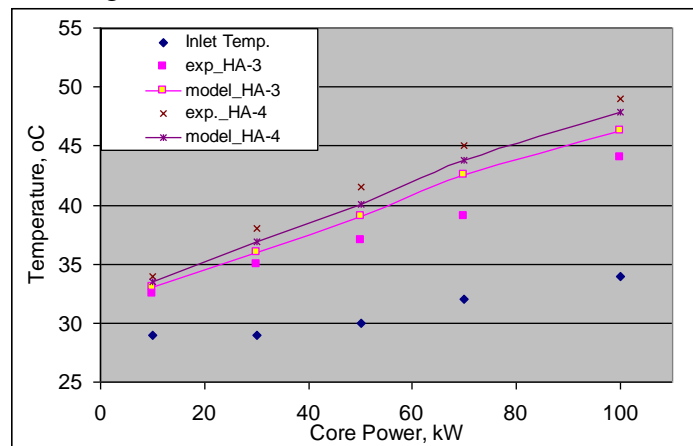


Figure 2: Comparison between calculated and measured exit temperatures

As it can be observed from Fig. 2, a good agreement was achieved between the calculated and the measured values where in fuel rod AH-3 there is a small over prediction of the model and in fuel rod AH-4 the model has a small under prediction in the calculated values.

For calculation of the water and the fuel temperature along the fuel rods it was assumed that the power distribution has a chopped cosine shape with a 30% heat flux value at the plate edge. The fuel plates temperature $T(z)_{wall}$ was calculated as follow:

$$(7) \quad T(z)_{wall} = T_b(z) + \frac{q''(z)}{h}$$

Where $T_b(z)$ and $q''(z)$ are the local water temperature and heat flux, respectively and h is the convective heat transfer coefficient. Based on the Reynolds number in the channel the flow regime is laminar. In this case the value of h was calculated as proposed in ref. 4 by using the following correlation: (8)

$$Nu = \max[Nu = 4(const), eq(9)] \quad \text{for } Re < 2000$$

$$(9) \quad Nu = 0.17 Re_f^{0.33} Pr_f^{0.43} \left(\frac{Pr_f}{Pr_w} \right)^{0.25} \left\{ \frac{g \beta D_H^3 (T_w - T_b)}{\nu^2} \right\}_f^{0.1}$$

The calculated water and the fuel temperatures are presented in Fig. 3 (a) and (b) for fuel rod HA-3 and HA-4 respectively for core power of 100 kW.

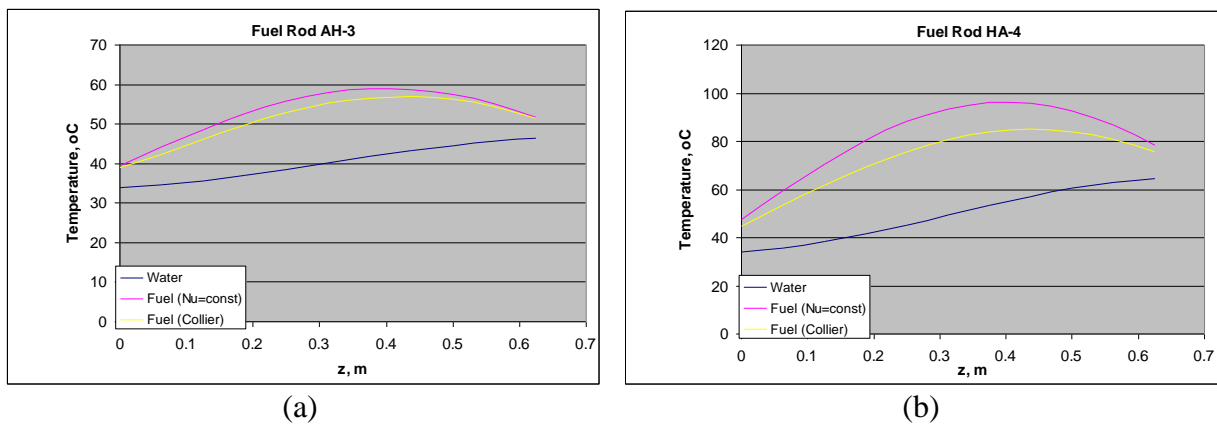


Figure 3: Calculated water and fuel temperature for fuel rod AH-3 (a) and AH-4 (b) at 100 kW core power.

CONCLUSIONS

- a. A good agreement was achieved by the present model in calculating of the flow rate and the exit water temperatures in a natural circulation mode in plates geometry fuel rod.
- b. It was found that the inlet plenum and the flapper valve have a negligible flow resistance comparing to the flow resistance of the flow channels in the fuel element.
- c. Fuel temperature was calculated based on correlations from literature. Validation of those correlations can be done by comparing with experiments from literature.

REFERENCES

1. Y. Yan, R. Uddin and N. Sobh, CFD Simulation of a Research Reactor, Mathematical and Computation Supercomputing, Reactor Physics and Nuclear and Biological Applications, France, 2005
2. J. Zhang, X. Z. Shen, Y. Fujihara, T. Sano, Y. Takahashi, K. Oono, A. Nakamori, N. Maruyama, K. Hasegawa, T. Tsuchiyama, K. Minami, K. Okumura, T. Yamamoto and K. Nakajima, Experimental Investigation on Natural Circulation Capacity of Kyoto University Research Reactor, NURETH15-125, Pisa, Italy, 2013
3. C. Park, M. Tanimoto, T. Imaizumi, M. Miyauchi, M. Ito, M. Kaminga, Preliminary Accident Analysis for a Conceptual Design of a 10 MW Multi-purpose Research Reactor, Japan Atomic Energy Agency, JAEA – Technology 2012 – 039, 2013
4. Y. Sudo, H. Ando, H. Ikawa, N. Ohnishi, Core Thermohydraulic Design with 20% LEU Fuel for Upgraded Research Reactor JRR-3, J. Nucl. Science and Technology, 3, pp. 551-564, 1985

A New Approach to Analyse the Effect of Initial Conditions on Steam Explosion In Coolant Injection Mode

I. Baruch¹, G. Widenfeld²

¹*Ben Gurion University of the Negev, Ben Gurion 1, Beer-Sheva, Israel*

²*NRCN, Israel*

ABSTRACT

Reaction between water and molten metal can lead to a very severe accident, caused by Steam Explosion (SE). Although the SE has been widely studied, the effect of dynamic parameters and material properties are still not well established. This study presents a new approach that based on the influence of material properties, jet characteristics and the initial temperatures on the feasibility of SE occurrence in coolant injection (CI) mode. Data from four different studies were cross-referenced, comparing various parameters such as melt and water initial temperatures, material properties and jet parameters for different melts such tin, aluminium, zinc and lead-bismuth eutectic mixture. This study showed that in tin-water system, the thermal interaction boundaries which varied with the jet dynamic properties, indicating that other parameters affecting the phenomena. Regions of low Weber number found as regions where spontaneous SE did not occur. This study shows that analysing the occurrence conditions solely by the melt and water initial temperatures is not applicable, and offers a new approach for further examination of jet parameters and material properties together with melt and jet initial temperatures.

INTRODUCTION

Violent thermal interactions resulting from the sudden contact of a cold vaporizable liquid and a hot liquid may cause high pressure explosions. In nuclear reactors the Steam Explosion (SE) might damage the core vessel and the containment integrity, release radioactive fission products to the environment and risk human health and pollute the environment for years to come. Fuel Coolant Interaction (FCI) can be form in one of these contact modes: Melt Injection (MI), Coolant Injection (CI), Free Fall Melt Drop (FFMD) into coolant and melt flooding by coolant. The current study uses TIZ map together with dynamic properties in order to reveal the SE occurrence conditions.

Due to the complexity of the CI experimental system, there is a lack of experimental data in the literature. Experimental data of the FFMD mode, found useful in interpreting the CI mode data. TIZ (Thermal Interaction Zone) map is the most conventional method to display the conditions leading to SE. These maps depict the areas where SE occur or does not occur depending on the initial melt and water temperatures. TIZ theoretical boundaries commonly defined as melting point (MP) temperature or homogenous nucleation (HN) temperature and minimum film boiling (MFB) temperature, at the interface temperature (1) between the two liquids.

$$T_i = T_{jet} + \frac{T_{melt} - T_{jet}}{1 + \sqrt{\beta}}, \text{ where } \beta = \frac{(k \cdot \rho \cdot C_p)_{jet}}{(k \cdot \rho \cdot C_p)_{melt}} \quad (1)$$

Although a TIZ map analysis is commonly used, this map does not provide sufficient information of other parameters affecting the feasibility for SE occurrence at CI mode. These parameters include jet dynamic properties such as diameter, nozzle height from melt surface, velocity and the amount of water. Material properties such as: thermal conductivity, specific heat, MP, density, surface tension, heat of fusion and more.

The examination of experiments^[1-4], shows that the contact mode has a major influence on the feasibility for SE to occur. From comparison of two experiments in CI mode, conducted with the same materials and initial temperatures, it was found that one may generate SE while the other ends in a violent boiling regime. The main cause for these different results is the jet dynamic characteristics. This fact emphasize that it is impossible to predict SE occurrence in CI mode by using only TIZ map.

Triggering thermal interaction is an essential stage for escalating violent boiling to SE. Some materials as tin have spontaneous triggering mechanism while others, like aluminium or zinc, do not spontaneously triggered. It well known that the triggering mechanism leading towards SE is a local vapour film collapse that generates a shock wave, which moves through the water and extends the film collapses to other sites. Y. Abe et al^[4] found that SE trigger cannot be satisfied when the interfacial temperature (Ti) between the molten material and water is lower than the material melting temperature, even if the vapour film around the

molten material collapsed by the external pressure pulse. However, analysing G. Widenfeld^[1] experiments results of water injection into tin melt, SE does occur even beneath the MP boundary at the interface temperature. External triggers may generate SE, by forcing the film boiling to collapse, at non self-triggered materials like aluminium and zinc. From Y. Abe et al^[4] experiments includes external triggering of aluminium and zinc, it was found that **0.5 [MPa]** pressure pulse triggers both materials.

A vast experimental data from different studies collected and analysed. Table 1 shows the main experiments parameters from the studies^[1-4] used in the current study.

Table 6: [1-4] experiments main parameters.

Experiment	Mode of contact	Materials (melting point [°C])	Melt mass [kg]	Jet dia. [mm]	Jet velocity [m/s]	Jet temp. [°C]	Melt temp. [°C]
G. Widenfeld ^[1]	CI	*Sn(231.9), Al(660.3), Zn(419), different Sn- Zn mixtures(198.5,300,350)	1.4	0.5-5	9-25	25,31	240-750
Y. Sibamoto et al ^[2]	CI	Pb-Bi eutectic mixture (125)	2	6	5-8	25-90	230-550
Y. Perets ^[3]	CI	Sn(231.9)	1	0.7	13-14	25-98	240-590
Y. Abe et al ^[4]	FFMD	Sn(231.9), Al**(660.3), Zn(419)	$5 \cdot 10^{-3}$	NA	50mm free fall	Water pool temp 25,57	Al:710,746 Zn:575,590

* Only Sn experiments were analysed. ** Only Al and Zn experiments were analysed.

The experiments results from studies [1-4] compared by: melt point temperature, water to melt thermal inertial ratio (β), surface tension, kinematic viscosity, jet diameter and velocity and jet theoretical breakup length. Examination of this vast field of parameters is possible by using dimensionless numbers that describes the material properties, jet characteristics and the initial temperatures. The dimensionless numbers, which were used to describe the phenomena, are Weber ($We = \frac{\rho v^2 d}{\sigma}$), Froude ($Fr = \frac{v}{d_{jet} g^{1/2} (\rho_{jet} - \rho_{melt})^{1/2}}$), $\frac{T_m}{T_{MP}}$ and β . With this new approach, further insights concerning the SE trends and boundaries exposed.

RESULTS

Drawing TIZ map for studies [1] and [3], in tin-water system, shows that TIZ boundaries relevance for one study are not matching to the other. In Fig.1, TIZ map shows melt temperature as function of water temperature, the "x" sign represents no SE occurrence and a full diamond is a SE event. The boundaries divided to theoretical boundaries as mentioned before (T_{MFB} , T_{MP} , and T_{HN}) and empirical boundaries. Y. Perets^[3] found empirical boundary (marked as RBTIZ - right boundary TIZ) for tin – water system. Figure 1 shows that SEs above the RBTIZ may occur as was found at G. Widenfeld^[1] experiments using higher jet diameters and velocities.

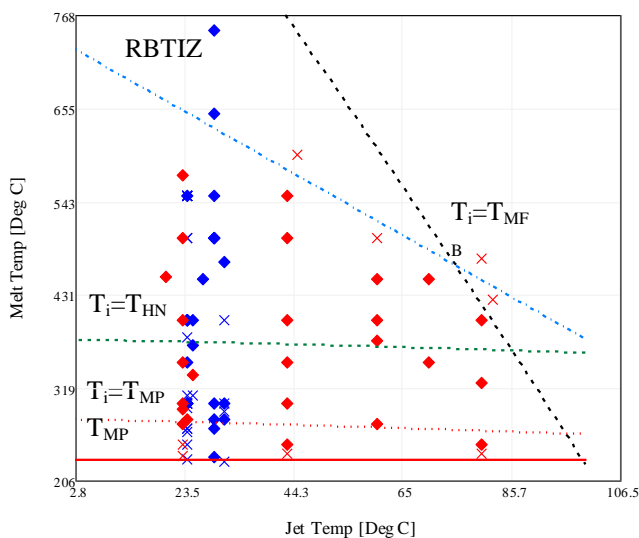


Fig. 5. Thermal interaction zone for tin-water system in CI mode from [1, 3] experiments.

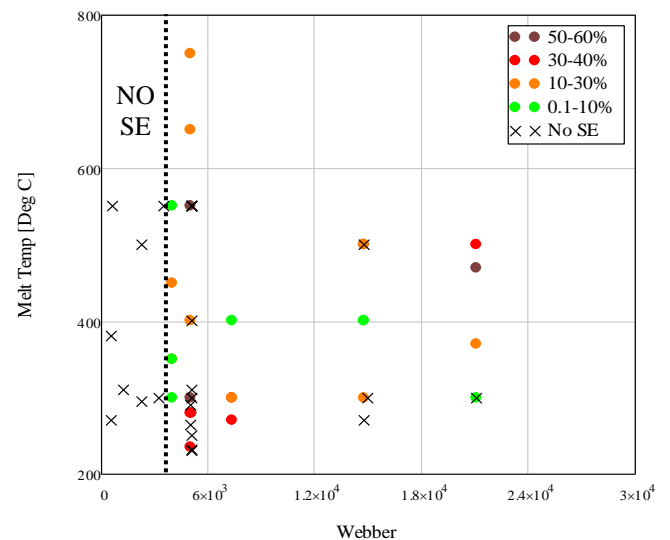


Fig.5. Tin melt percentage splattered from the crucible versus melt temperature and Weber number from G. Widenfeld^[1] experiments. Jet temperature is around **25°C**.

Further, it was found that SE occurs even beneath the melting point at the interface temperature in both experiments, suggesting that jet inertial forces influencing the triggering mechanism.

Using a combination of dynamic and TIZ maps may draw, more accurate initial conditions leading towards SE event. Therefore, further testing of parameters such as Weber and Froude numbers shows that dynamic properties have to be treated. Fig.2. Shows the melt initial temperature of tin, versus Weber number. "x" signs indicate no SE event and the colour scheme representing the percentage of melt splattered from the crucible, that may implies on the explosion intensity. No explosions appeared below jets with Weber number of 3900, indicating that a minimal inertial force is required to generate SE. The theoretical breakup length matching this Weber value is 7.5 mm for tin – water system. From Y. Perets^[3] images of the melt surface, it was found that at low flow rates the water jet could not penetrate the melt surface. Examinations of the splattered melt percentage (as shown in fig.2) shows that SE intensity is not a function of jet dynamic properties or melt temperature.

A further examination of β value was done. Figure 3 shows melt to melting point ratio as function of β for studies [1-4]. It was found (see Fig.3.) that the non-self-triggered materials (aluminium and zinc) sharing low β values (0.014) and melting points above HN temperature. While materials (tin and lead bismuth mixture) with β higher then 0.04 and melting point below the HN temperature generates spontaneous SE. Further experimental data is required in order to confirm that β may consider as occurrence conditions.

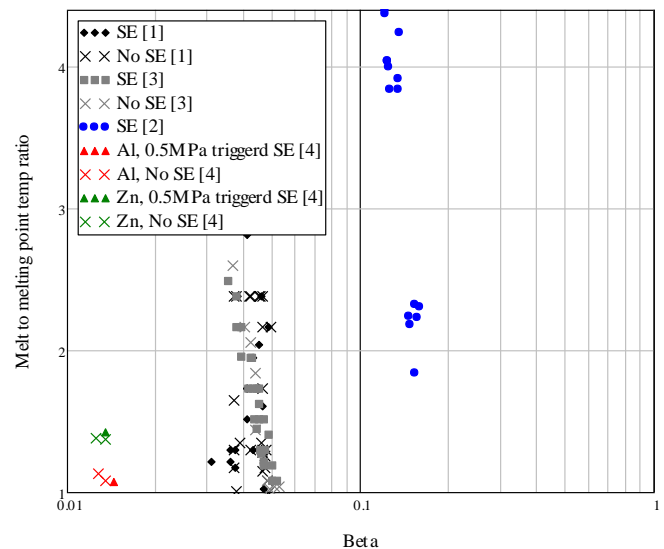


Fig.3. Different regions of triggering mechanism map for different materials

Conclusions

In this study, data from four different studies was cross-referenced by comparing jet parameters, initial temperatures and material properties for different melts. It was found that TIZ boundaries varied with the jet dynamic properties. Weber number was found as a minimum limit for dynamic occurrence condition. This study shows that analyse the SE occurrence conditions solely by the TIZ map, will not be accurate for CI mode. From dynamic properties, analyse together with the TIZ map the ability to predict SE events increases. Further experimental data required to understand the complete effects of jet properties on the occurrence conditions.

REFERENCES

- [1] G. Widenfeld, Y. Aharon, R.Harari, I. Hochbaum and Y. Weiss, Steam Explosion Induced by Water Injection onto Molten Metal, 29th Israel Conf. of Mechanical Engineering, 2003.
- [2] Y .Sibamoto, Y. Kukita And H. Nakamura. "Small-scale Experiment on Subcooled Water Jet Injection into Molten Alloy by Using Fluid Temperature-Phase Coupled Measurement and Visualization." *Journal of NUCLEAR SCIENCE and TECHNOLOGY*, Vol. 44, No. 8, p. 1059–1069 (2007)
- [3] Perets, Yaron. Thermal Reaction By Impinging Coolant on Liquid Metal - Vapor Explosion. Thesis, Beer Sheva: Ben Gurion University of the Negev, Department of Mechanical Engineering, 2003.
- [4] Yutaka Abea, Hideki NARIAI and Yukihiro HAMADA. "The Trigger Mechanism of Vapor Explosion." *Journal of NUCLEAR SCIENCE and TECHNOLOGY*, 39, no. 8 (August 2002): 845-853.

Geological Disposal of Radioactive Waste

A. Dody, O. Klein Ben David

NRCN, Israel

INTRODUCTION

Disposal of radioactive waste imposes complicated constraints on the regulator to ensure the isolation of radioactive elements from the biosphere. The IAEA (1995) states that "The objective of radioactive waste management is to deal with radioactive waste in a manner that protects human health and the environment now and the future without imposing undue burdens on future generation". The meaning of this statement is that the operator of the waste disposal facilities must prove to the regulator that in routine time and in different scenarios the dose rate to the public will not exceed 0.3 mSv/y in the present and in the future up to 10,000 years.

For low and intermediate level waste (LILW), these constraints can be accommodated using near surface repositories. However, for high level waste (HLW), transuranics waste (TRU) and spent fuel; these conditions cannot be fulfilled by near surface repositories, which depend strongly on the nature of their engineered barriers, climate and the intensity of geomorphology processes. Such construction (e.g. cements, steel etc.) have a life span of hundreds to thousands of years. In the case of HLW the activity after such periods of time can still be many orders of magnitudes above the clearance level. Additionally, The IAEA recommends an institutional control period of 300 years after the disposal site's closure, including passive and active monitoring. This period may be too short regarding the long lived and toxic radionuclides (RNs). Moreover, climate changes and erosion processes can impose strong constraints on the life-span of engineered barriers and on contamination migration from them.

Thus the IAEA (2006) recommended deep geological disposal as long-term solution for HLW, such as TRU and spent fuel. A geological disposal is defined as : isolating long lived radioactive waste from human environment by placing them deep underground in repositories located in host rocks characterized by high stability and low or no groundwater flow" (IAEA, 2003). A geological repository is considered as the best approach to ensure the isolation of the HLW from the biosphere. Construction, operation and closing of geological repository require considerable technical and scientific background in the design, engineering and safety assessment of such a facility (IAEA, 2003).

The depth of a geological formation and its characteristics are the ultimate barriers between the waste and the environment in the long run. Thus, to accommodate these characteristics a relevant geological formation must have: 1) Low hydraulic conductivity. 2) Low fractures and joint density. 3) High distribution coefficient (Kd) for RN contaminants. 4) Low or no groundwater flow.

There are three major lithologies that were investigated and considered as adequate for a deep disposal site. Clay-rich formations are considered adequate principally because of their very low permeability and high adsorption coefficients (Kd) for most RNs. Salt rock, when under hyper saline solution conditions, is insoluble and highly impermeable. Finally, crystalline rocks (e.g. granite), when unfractured, also have low permeability and relatively high Kd.

IMPLEMENTATION OF GEOLOGICAL DISPOSAL AROUND THE WORLD

Today, no country has an authorized and operating geological disposal facility. The main obstacles in the regulation process arise public acceptance issues and stakeholders approval, together with the regulatory and authorization applied requirements. Specifically, the demand for retrievability of the buried waste in the future, in some countries (e.g. France) imposes much safety, regulatory and engineering challenges. Additionally, far future (i.e. 10^5 y) modeling and speculation create large uncertainties and difficulties in communicating with the public.

Nevertheless, most of the western countries have taken significant steps towards the implementation of such repository, examples of which are given below.

USA: Waste Isolation Pilot Plant (WIPP) is operating in New Mexico at 655 m depth in a 600 m thick of salt formation that has been stable for more than 2000 million years. It is defined as storage and not as final

burial site. The site is aimed for military TRU waste only. On the other hand, 30 years of research into the implementation of geological disposal site in Yucca Mountain, Nevada in a tuff formation have been ended in extinguishing the project and in search for a new location for the site/France: The French National Radioactivity Management Agency (ANDRA) is constructing a deep disposal site at about 500 m depth in clay-argillite of Callovo-Oxfordian formation. At the Meuse/Haute-Marne Underground Research Laboratory (URL) located at Bure (300 km east of Paris). The site is expected to become operational in 2020.

Belgium: A clay formation (boom clay) at a depth of about 240 m in north east of the country is being considered as a possible disposal site, but so far no final decision has been made.

Germany: The Gorleben salt dome was investigated for its feasibility as a repository since the mid-1980s. In 2000 a moratorium was imposed on the Gorleben site and it was re-opened for investigation in 2010. Decision about the future use the site is expected in 2020.

Sweden: A site in granite bedrock about 500 m below surface was located at Fosmark. The site is expected to be opened in 2025 and to be in full use in 2027.

Finland: Finland is constructing a national repository named Onkalo in a crystalline bedrock formation. The repository is located in Olkiluoto at a depth of 400-500 m. An underground rock characterization facility was established at the site. The repository is expected to be operational by 2020.

Switzerland: Two active undergrounds research labs were established. One in an Opalinus clay formation (Mont Terri) and one in granite rock (Grimsel). No decision has been made on the final location the repository.

Other countries: Russia and Hungary have sited specific locations and defined the geological formation and aimed for suitable kind of disposal. The UK and Canada are in the stage of approaching local communities for consent to entrain geological repository.

In summary, it can be seen that most western countries involved in nuclear activity are in the process of locating, investigation and acquiring public acceptance in their quest towards geological disposal implementation.

THE ISRAELI CASE – PRELIMINARY RESULTS

The small size of Israel, the large population density in the central and northern parts and the proximity to an active fault zone (the Dead Sea Rift) make the choice of suitable site difficult. Additionally, the common target rocks for geological disposal (e.g. salt, clay, and granite) are unavailable in Israel in thick, depth and un-fractured formations.

The Yamin Plateau (YP) in the north east of the Negev holds the Israeli national site for radioactive waste since the 1969th. LLW is disposed in near surface trenches. However, other waste forms (i/e. spent fuel) are stored as being inadequate for near surface disposal. The government of Israel gave the NRCN through the IAEA the mandate to examine the possibility of locating a geological waste disposal site in YP. The marl and chalk lithologies of the Mount Scopus Group are being examined for their suitability to serve as host rocks for geological repository. These lithologies are characterized by low hydraulic conductivity and high retardation capacity for RNs. It should be noted the Judea and Kurnub aquifers (Fig. 1) reside 200-300 m below the target formation.

Four boreholes of 3" diameter perpendicular to the geological structure (Figs. 1, 2) were drilled down to 300 m depth in order to investigate the stratigraphy, depth and thickness of the target units. The presence, direction and joints' density were studied using a unique camera (TeleViewer). Cores were sent for geotechnique analyses to check the parameters of mass rock quality. In-situ inspections within boreholes were conducted to measure the hydraulic conductivity values, using "double packer" technique, and the bulk densities of the rocks unit through P and S seismic velocities. Additionally, primary estimation of the rocks retardation capacity for the expected contamination (through their stimulants) was done, yielding satisfactory values. So far, the main finding is that none of these measured parameters negate the possibility of geological waste disposal in those deep formations, but more research is needed

REFERENCES

- IAEA, 2006. Geological Disposal of Radioactive Waste. SR. No. WS-R-4.
- IAEA. 2003. Scientific and Technical Basis for Geological Disposal of Radioactive Wastes. Technical Reports Series No. 4.
- IAEA, 1995. Principles of Radioactive Waste Management. Safety Series No. 111-F.

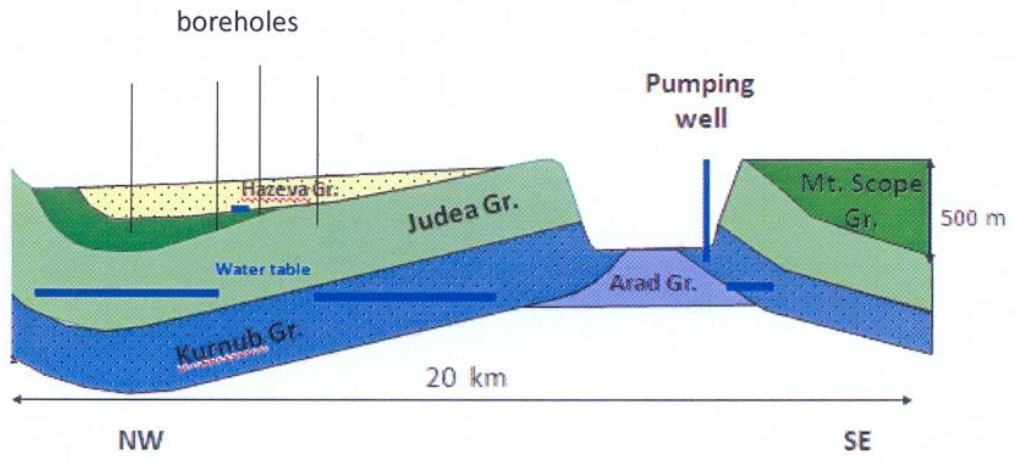


Figure 1: The geology structure of Yamin Plateau

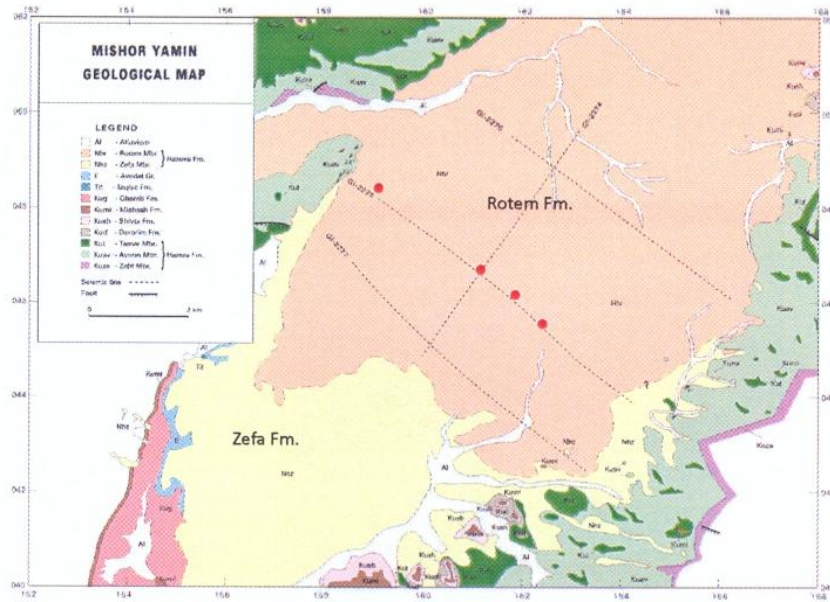


Figure 2: Geology map of Yamin Plateau

Safety Issues of the LORELEI Test Device

R. Sarusi⁽¹⁾, L. Ferry⁽²⁾, D. Drapeau⁽²⁾, M. Szanto⁽³⁾, N. Moran,
M. Katz⁽¹⁾, Y. Weiss⁽¹⁾

(1) NRCN, P.O.Box 9001 Beer Sheva, , Israel

(2) CEA, Cadarache, France

(3) Rotem Industries LTD, Mishor Yamin, D.N Arava 86800 Israel

1. INTRODUCTION

The LORELEI (Light-Water One-Rod Equipment for LOCA Experimental Investigation) test device is dedicated for the study of fuel during a Loss of Coolant Accident (LOCA).

The safety of this project is been done with a collaboration between the Israeli and the French teams and will have to be authorized by the French regulation authority (ASN).

The main challenges in safety are:

1. Preparing a safety reports according to the French regulations and standards.
 2. Learning and obtaining knowledge on the safety philosophy of experimental devices in French.
2. The safety approach include:

2.1. Identification of all the dangers from the device in all the working situations:

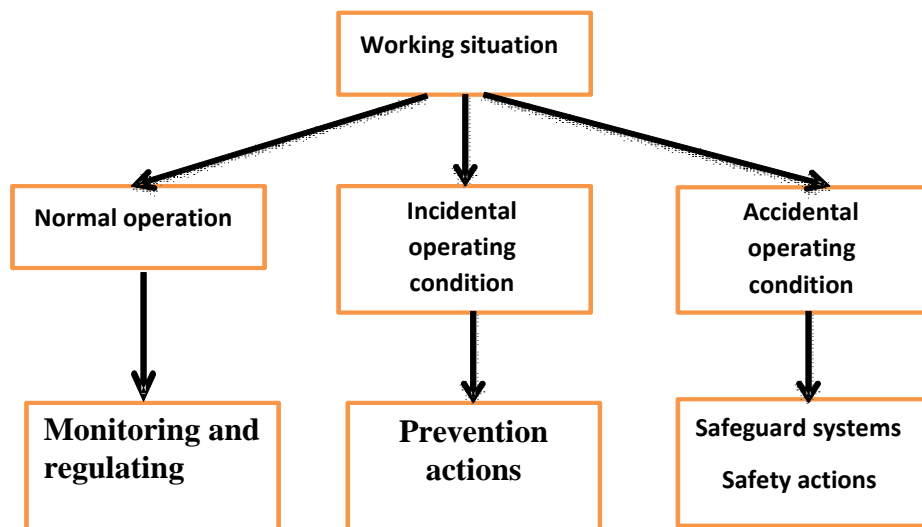


Figure 1: Classification of working situation

2.2. Identification of the number of barriers needed:

2.2.1. The term barrier refers to a physical envelope of the device design to contain the effects of “dangerous sources” due to the device itself.

2.2.2. The recommended approach aims at identifying the barriers for the in-Core section of the device which is directly exposed to flux and/or Capable of leading to interactions with the reactor core.

2.3. Identification of the anti fly-off systems needed:

2.3.1. A hypothetical total failure of the in-core section of the device- is considered as the retraction of the in-core device which can lead to a reactivity insertion depending on the configuration.

2.3.2. Consequently, the reactivity of the device and any possible causes of fly-off must be examined.

3. Safety analysis is based on FMEA (Failure Mode and Effect Analysis) method:

- 3.1. A systematic technique that takes all the components of the device and analyzed them in normal and accidental situations.
- 3.2. Bottom- up technique.
- 3.3. Evaluate the means (defense lines) that needed in each component failure.

4. Defense in Depth approach is adopted:

	Level of defence in depth	Objective of the level	Essential means	Associated Plant condition categories
Original design of the plant	Level 1	Prevention of abnormal operation and failure	Conservative design and high quality in construction and operation	Normal operation
	Level 2	Control of abnormal operation and failure	Control, limiting and protection systems and other surveillance features	Anticipated operational occurrences
	Level 3	Control of accident within the design basis	Engineered safety features and accident procedures	Design basis accidents (postulated single initiating events)
Beyond design situations	Level 4	Control of severe plant conditions that were not explicitly addressed in the original design of currently operating plants owing to their very low probabilities	Complementary measures and accident management	Multiple failures Severe accidents
Emergency planning	Level 5	Mitigation of radiological consequences of significant releases of radioactive materials	Off-site emergency response	-

In SF-1 published in 2006, the IAEA stressed that independency effectiveness of the different levels of defence is a necessary element of DiD concept.

Table 1: Defense in Depth approach

- 5. The approach of the experimental devices is deterministic.
- 6. There are 5 stages to prepare the hazard analysis:
 - 6.1. Classification of the components to ISE1...ISE3 – table of classification.
 - 6.2. Evaluation the consequences of a component failure (according to his functions)- the result is the working situation- table WS1...WS4.
 - 6.3. Checking if the safety classification of the components (ISE1...ISE3) is relevant with the classification of the working situation WS1...WS4.
 - 6.4. Determination of the means (options) needed for the device according to the Defense in Depth criteria (level 1...level 4).
 - 6.5. Possible actions from LORELEI device for the control of the experiment

The analysis scheme

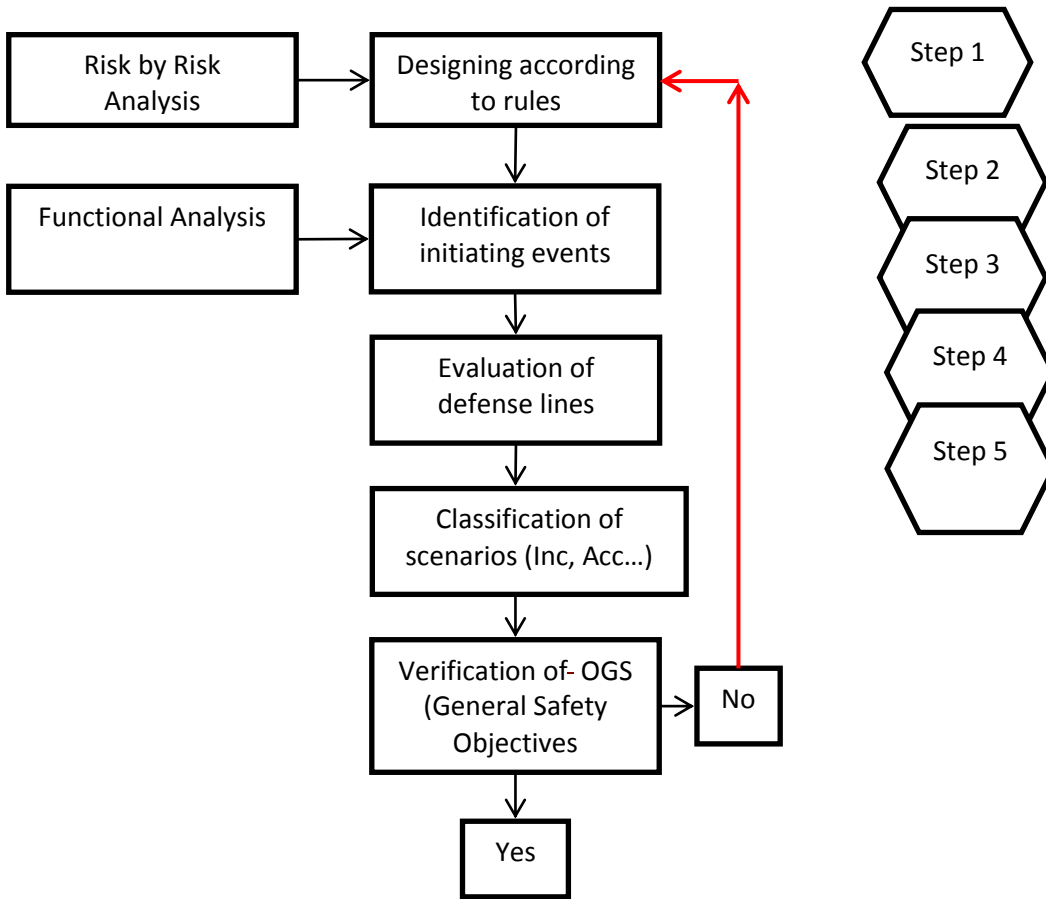


Figure 2: Hazard Analysis scheme

